

# ICFA HIB2021

High Intensity and High-Brightness Hadron Beams

64th ICFA Advanced Beam Dynamics Workshop

Fermilab, Batavia, Illinois USA

Monday October 4 to Friday October 8 2021

# PROCEEDINGS



## Foreword: Welcome to the HB2021 Workshop Proceedings

The 64th ICFA Advanced Beam Dynamics Workshop on High Intensity and High Brightness Hadron Beams was hosted by Fermilab from October 4 to October 9, 2021. Known in the community as an ICFA HB workshop, this series is the premier international event, focused on the latest developments and insights into the physics of high-intensity hadron beams. The HB series originated at Fermilab in 2002 (AIP Conf. Proc. 642 (2002)) as the 20<sup>th</sup> ICFA Advanced Beam Dynamics Workshop and we are very proud to continue its traditions of high-quality contributions and scholarly discussions. HB2021 provided a platform to present and discuss new projects, concepts, and physics ideas into high-power, high-brightness, and high-intensity beams, as well as updates, progress, and new developments in existing hadron accelerators and beam physics. The workshop scientific program was planned by the HB International Organizing Committee (IOC), chaired by Prof. Ingo Hofmann.

Because of the COVID-19 pandemic restrictions, the workshop was organized as a virtual event. Unfortunately, multiple time zones were not conducive to day-long workshop sessions. The program therefore included shorter invited talks both in plenary and in parallel sessions of 5 Working Groups: (1) Beam Dynamics in Rings, (2) Beam Dynamics in Linacs, (3) Accelerator Systems, (4) Commissioning and Operations, and (5) Beam Instrumentation and Beam Interaction. The workshop had 175 registered participants.

During the IOC meeting at HB2021, the next HB workshop (HB2023) was decided to be held at CERN (Switzerland). It follows the tradition of the HB workshop biennial cycle rotating between the three regions -- Europe, Asia, and North America.

Eliana Gianfelice-Wendt (LOC chair)

Sergei Nagaitsev (LOC co-chair)

## International Organizing Committee (IOC)

Yuri Batygin	LANL	USA
Mike Blaskiewicz	BNL	USA
Sarah Cousineau	ORNL	USA
Mohammad Eshraqi	ESS	Sweden
Shinian Fu	IHEP	China
Eliana Gianfelice	FNAL	USA
Simone Gilardoni	CERN	Switzerland
Ingo Hofmann	<b>Chair</b> GSI	Germany
Hideaki Hotchi	KEK	Japan
Ji-Ho Jang	IBS	Republic of Korea
Dong-O Jeon	IBS	Republic of Korea
In Soo Ko	POSTECH	Republic of Korea
Srinivas Krishnagopal	BARC	India
Jean-Michel Lagniel	GANIL	France
Valeri Lebedev	FNAL	USA
Yoshiharu Mori	Kyoto University	Japan
Andrea Pisent	INFN	Italy
Sergey Polozov	NRNU MEPhI	Russia
Christopher Prior	RAL	UK
Ji Qiang	LBL	USA
Thomas Roser	BNL	USA
Todd Satogata	JLab	USA
Mike Seidel	PSI	Switzerland
Gennady Stupakov	SLAC	USA
Jingyu Tang	IHEP	China
Jiuqing Wang	IHEP	China
Jie Wei	FRIB	USA
Yoshishige Yamazaki	FRIB	USA
Xueqing Yan	Peking University	China
Hongwei Zhao	IMP	China

## Local Organizing Committee (LOC)

Robert Ainsworth	
Paul Derwent	
Marilyn Franck	
Eliana Gianfelice	<b>Chair</b>
Jonathan Jarvis	
Lisa Lopez	
Marco Mambelli	<b>Scientific Secretary</b>
Sergei Nagaitsev	<b>Co-Chair</b>
Vladimir Nagaslaev	
Jean-François Ostiguy	
Giulio Stancari	
Alexander Valishev	
Susan Winchester	

## JACoW Editorial Team (JET)

Dong Eon Kim  
Michael Marx  
Volker RW Schaa

**Editor-in-Chief**

PAL, Republic of Korea  
DESY, Germany  
GSI, Germany

## Working Groups and Conveners

---

**WGA: Beam Dynamics in Rings**

Jeffrey S. Eldred (Fermilab)  
Wolfram Fischer (BNL)  
Elias Metral (CERN)

**WGB: Beam Dynamics in Linacs**

Yuan He (IMP)  
Peter Ostroumov (FRIB)  
Ciprian Plostinar (ESS)

**WGC: Accelerator Systems**

Moses Chung (UNIST)  
Cheng-Yang Tan (Fermilab)  
Daniel Wollmann (CERN)

**WGD: Commissioning and Operations**

Michele Comunian (INFN/LNL)  
Sarah Cousineau (ORNL)  
Susumu Igarashi (KEK)  
Sheng Wang (IHEP)

**WGE: Beam Instrumentation and Interaction**

Willem Blokland (ORNL)  
Peter Forck (GSI)  
Naoki Hayashi (J-PARC/JAEA)  
Michiko Minty (BNL)

---

# Contents

<b>Preface</b>	<b>i</b>
Foreword . . . . .	iii
Committees . . . . .	iv
Contents . . . . .	vi
<b>Papers</b>	<b>1</b>
MOIP11 – 1 MW J-PARC RCS Beam Operation and Further Beyond . . . . .	1
MOAC3 – Development of an Injection-Painted Self-Consistent Beam in the Spallation Neutron Source Ring . . . . .	7
MOCC3 – First Experience of Crystal Collimators During LHC Special Runs and Plans for the Future . . . . .	12
MOP01 – Improvement of Capture Ratio for an X-Band Linac Based on Multi-Objective Genetic Algorithm . . . . .	18
MOP02 – Recent Improvements in the Beam Capture at Fermilab Booster for High Intensity Operation . . . . .	23
MOP03 – Longitudinal Emittance Measurements at PIP2IT . . . . .	27
MOP04 – Status of the JAEA-ADS Superconducting LINAC Design . . . . .	30
MOP05 – Reduction of the Beam Jitter at the PIP2IT Test Accelerator . . . . .	35
MOP06 – Resonance Compensation for High Intensity and High Brightness Beams in the CERN PSB . . . . .	40
MOP07 – Chromaticity Measurement Using Beam Transfer Function in High Energy Synchrotrons . . . . .	46
MOP08 – Recent Progress on Nonlinear Beam Manipulations in Circular Accelerators . . . . .	52
MOP09 – HL-LHC Beam Dynamics with Hollow Electron Lenses . . . . .	59
MOP10 – Closed Form Formulas of the Indirect Space Charge Wake Function for Axisymmetric Structures . . . . .	65
MOP11 – Controlled Longitudinal Emittance Blow-Up for High Intensity Beams in the CERN SPS . . . . .	71
MOP12 – Understanding of the CERN-SPS Horizontal Instability with Multiple Bunches . . . . .	77
MOP13 – Influence of Transverse Motion on Longitudinal Space Charge in the CERN PS . . . . .	83
MOP14 – The PS Booster Alignment Campaign and a New Tune Control Implementation After the LHC Injectors Upgrade at CERN . . . . .	89
MOP15 – Threshold for Loss of Longitudinal Landau Damping in Double Harmonic RF Systems . . . . .	95
MOP16 – New Analytical Criteria for Loss of Landau Damping in Longitudinal Plane . . . . .	100
MOP17 – End-to-End Longitudinal Simulations in the CERN PS . . . . .	106
MOP18 – Injection Chicane Beta-Beating Correction for Enhancing the Brightness of the CERN PSB Beams . . . . .	112
MOP19 – Optimised Transverse Painting Schemes for the New 160 MeV $H^{-}$ Injection System at CERN . . . . .	118
MOP20 – Space Charge Resonance Analysis at the Integer Tune for the CERN PS . . . . .	124
MOP21 – 3D Symplectic Space Charge Implementation in the Latest Mad-X Version . . . . .	129
MOP22 – A Dedicated Wake-Building Feedback System to Study Single Bunch Instabilities in the Presence of Strong Space Charge . . . . .	135
MOP23 – Coupled Bunch Instabilities Growth in the Fermilab Booster During Acceleration Cycle . . . . .	140
MOP26 – Status of Layout Studies for Fixed-Target Experiments in Alice Based on Crystal-Assisted Halo Splitting . . . . .	146
MOP27 – The Design and Implementation of Fast Machine Protection System for CSNS . . . . .	151
TUIP1 – An Operationally Integrated Approach to the SNS 2.8 MW Power Upgrade . . . . .	156
TUAC1 – Self-Consistent Long-Term Dynamics of Space Charge Driven Resonances in 2D and 3D . . . . .	160
TUAC2 – Impact of Power Supply Ripple on the Beam Performance of the Large Hadron Collider and the High-Luminosity LHC . . . . .	170
TUEC2 – Operational Experience with Nanocrystalline Injection Foils at SNS . . . . .	176
TUEC4 – Test of Machine Learning at the CERN LINAC4 . . . . .	181
WEBC3 – MYRRHA-MINERVA Injector Status and Commissioning . . . . .	186
WEDC1 – Study on the Injection Beam Commissioning and Painting Methods for CSNS/RCS . . . . .	191
WEDC2 – Acceleration of the High Current Deuteron Beam Through the IFMIF-EVEDA RFQ: Confirmation of the Design Beam Dynamics Performances . . . . .	197
WEDC3 – Status of FRIB Commissioning . . . . .	203
THAC1 – Beam Instability Issue and Transverse Feedback System in the MR of J-PARC . . . . .	208
THAC3 – Exploring Quasi-Integrable Optics with the IBEX Paul Trap . . . . .	214
THDC1 – Slow Extraction Operation at J-PARC Main Ring . . . . .	219
THDC2 – Commissioning of the ESS Front End . . . . .	225
THBC1 – Beam Acceleration with the Upgraded Riken Heavy-Ion Linac . . . . .	231

<b>Appendices</b>	<b>235</b>
List of Authors . . . . .	235
List of Institutes . . . . .	239
List of Participants . . . . .	244



# 1 MW J-PARC RCS BEAM OPERATION AND FURTHER BEYOND

H. Hotchi<sup>1†</sup>, H. Harada<sup>2</sup>, N. Hayashi<sup>2</sup>, M. Kinsho<sup>2</sup>, K. Okabe<sup>2</sup>, P.K. Saha<sup>2</sup>, Y. Shobuda<sup>2</sup>,  
 F. Tamura<sup>2</sup>, K. Yamamoto<sup>2</sup>, M. Yamamoto<sup>2</sup> and M. Yoshimoto<sup>2</sup>  
 Accelerator Division, J-PARC Center, <sup>1</sup>KEK/<sup>2</sup>JAEA, Tokai, Ibaraki, Japan

## Abstract

The J-PARC 3-GeV rapid cycling synchrotron has achieved a 1-MW beam operation with considerably low fractional beam loss of a couple of  $10^{-3}$ . Following this successful achievement, we have recently conducted further high-intensity beam tests toward a higher beam power beyond 1 MW. This paper reviews our continuous efforts for beam loss mitigation including the recent result of a 1.5-MW-equivalent high-intensity beam test.

## INTRODUCTION

The J-PARC 3-GeV rapid cycling synchrotron (RCS) is a world leading high-power pulsed proton driver, which has the goal of achieving a 1-MW beam power [1, 2]. A 400-MeV negative hydrogen ion ( $H^-$ ) beam from the injector linac is delivered to the RCS injection point, where it is multiturn charge-exchange injected through a carbon foil over a period of 0.5 ms (307 turns). The RCS accelerates the injected protons up to 3 GeV with a repetition rate of 25 Hz. Most of the RCS beam pulses are delivered to the materials and life science experimental facility (MLF), while only four pulses every several seconds (2.48 s or 5.2 s) are injected to the main ring (MR) by switching the beam destination pulse by pulse.

Figure 1 shows the history of the RCS beam power. In 2015, the beam power reached 500 kW. But it caused premature failures of the neutron production target two times in a row as shown by white arrows in Fig. 1, so that the beam power was reduced to 150–200 kW to prioritize availability for users. In 2017, a new improved target was installed. Since then, the beam power has been stepped up again while carefully monitoring the durability of the target. It now reaches 740 kW. If there are no unexpected troubles with the target from now on, the routine beam power will reach nearly 1 MW in two years.

Thus, we are still in the course of gradually increasing the beam power to 1 MW, but the accelerator itself has already well established a 1-MW beam operation. The most important issues in realizing such a MW-class high-power beam operation are controlling and minimizing beam loss, which are essential for sustainable beam operation that allows hands-on maintenance [3].

In high-power machines such as the RCS, there exist many factors causing beam loss, such as space charge, lattice imperfections and foil scattering. Besides, beam loss generally occurs through a complex mechanism involving several factors. In the RCS, numerical simulations have played a vital role in solving beam loss issues in combination with actual beam experiments; various ideas for beam loss mitigation were proposed with the

help of the numerical simulations, and verified by experiments. As a result of such continuous efforts including several hardware improvements, we have recently accomplished a 1-MW beam acceleration with considerably low fractional beam loss of several  $10^{-3}$  [4, 5].

This paper reviews our approaches to beam loss issues that we faced in the course of beam power ramp-up. Our recent efforts to further beam power ramp-up beyond 1 MW are also presented.

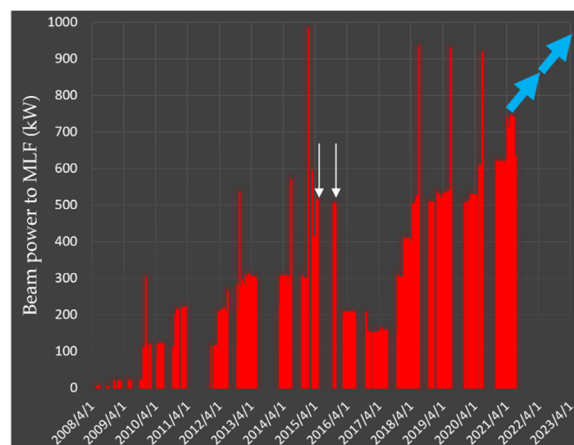


Figure 1: History of the RCS beam power.

## REVIEW OF BEAM TUNING FOR BEAM LOSS MITIGATION

### Beam Loss Mitigation by Injection Painting

In high-intensity proton synchrotrons, space charge in the low-energy region is one of the most crucial sources of beam loss. To mitigate this, the RCS adopts transverse and longitudinal injection painting.

In transverse injection painting [6], the phase space offsets between the centroid of the injection beam and the ring closed orbit are varied during multi-turn injection. By this way, the injection beam is uniformly distributed over a required phase-space area. On the other hand, in longitudinal injection painting [7, 8], a momentum offset to the rf bucket is introduced during multi-turn injection. In this way, a uniform bunch distribution is formed through emittance dilution by a large synchrotron motion excited by the momentum offset. In addition, the second harmonic rf and its phase sweep are introduced, which enable further bunch distribution control through a dynamical change of the rf bucket potential. By this way, the charge density peak in the longitudinal direction is effectively reduced.

Figure 2 shows the beam survival rates measured without and with the injection painting. In the case with no

† email address hideaki.hotchi@j-parc.jp

Content from this work may be used under the terms of the CC BY 3.0 licence (© 2021). Any distribution of this work must maintain attribution to the author(s), title of the work, publisher, and DOI

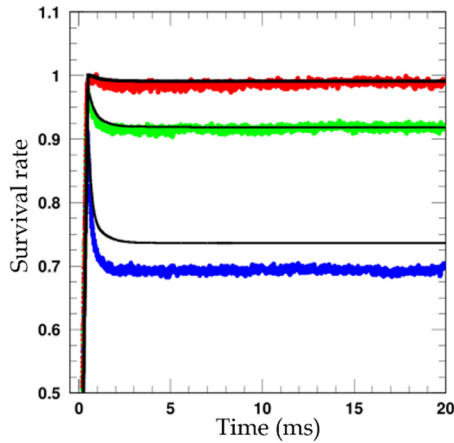


Figure 2: Beam survival rates measured without painting (blue), with longitudinal painting (green), and with transverse and longitudinal painting (red). The black solid curves show the numerical simulation results.

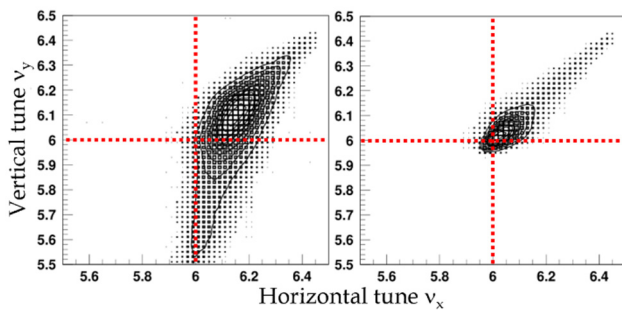


Figure 3: Numerical simulation results; tune footprints at the end of injection calculated without (left) and with injection painting (right).

painting, a critical 30% beam loss occurred in the low-energy region, where space charge is most serious. But the beam loss was drastically mitigated by the combination of the transverse and longitudinal painting. Figure 3 shows the tune footprints at the end of injection simulated without and with the injection painting. In the case with no painting, a core part of the beam particles crosses the integers ( $\nu_{x,y}=6$ ) due to the large space-charge detuning. On the integers, all-order systematic resonances are excited. The 30% large beam loss is ascribed to large emittance growth caused by the stopbands. As shown in Fig. 3, the injection painting well decreases the space-charge detuning. This mitigates the effect of the stopbands, as a result, leading to the significant beam loss reduction. This experiment clearly demonstrated the excellent ability of the injection painting for space-charge mitigation [4].

### Approach to Solving Beam Loss Issue Caused by the Combined Effect of Image Charge and Dipole Field Ripple

By introducing injection painting, the beam loss was drastically reduced as mentioned above, but there still remained nonnegligible beam loss of  $\sim 2\%$ , as shown in

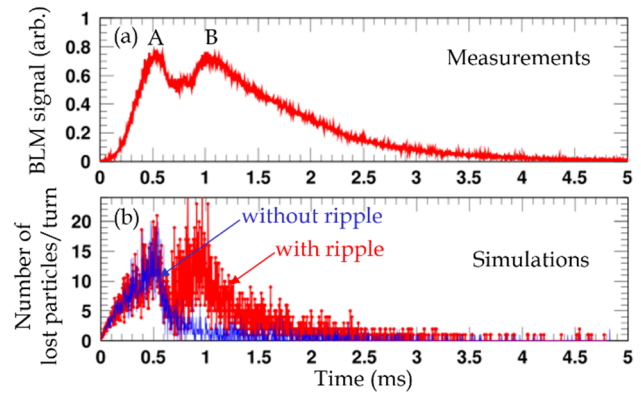


Figure 4: (a) Experimental result; time structure of beam loss. (b) Corresponding numerical simulation results.

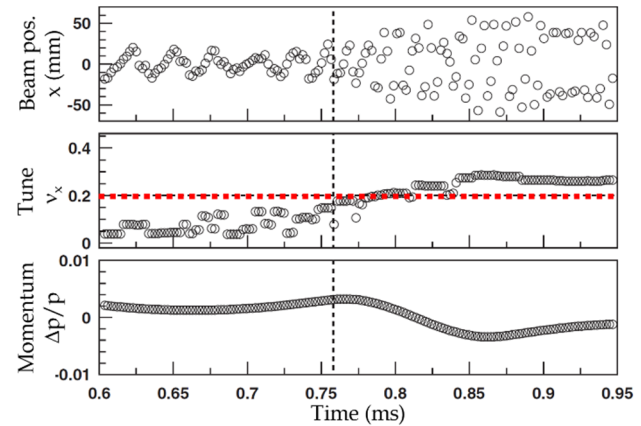


Figure 5: Numerical simulation result; single-particle motion near the resonance.

Fig. 4 (a). Further reduction of this beam loss was the next subject in our beam study. As shown in Fig. 4 (a), the beam loss consists of two peak structures; (A) and (B). The first beam loss (A) is caused by foil scattering during charge exchange injection. This is a very simple beam loss mechanism. On the other hand, the second beam loss (B) has a relatively complex mechanism. This beam loss is caused by a beam oscillation induced by a dipole field ripple [9], but it cannot be explained only by the presence of the beam oscillation. For understanding the beam loss mechanism, we have to additionally consider the effect of the image charge of the beam; the numerical simulation suggested that the beam loss (B) is caused by a betatron resonance driven by the combined effect of the beam oscillation and the image charge [4].

The image charge has a simple defocusing effect on a beam particle, but the strength varies depending on the square of the beam position. Thus, if the beam position oscillation is excited, the defocusing effect of the image charge periodically varies with two times higher frequency than that of the beam position oscillation. The oscillating defocusing force drives a second-order resonance, affecting the beam.

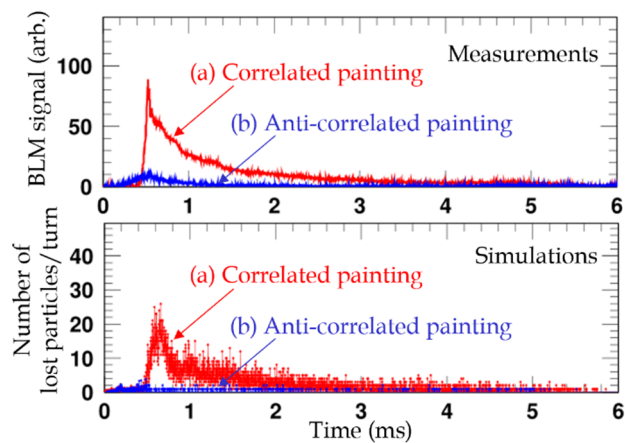


Figure 6: (Upper) Experimental results; time structure of beam loss. (Lower) Corresponding numerical simulation results.

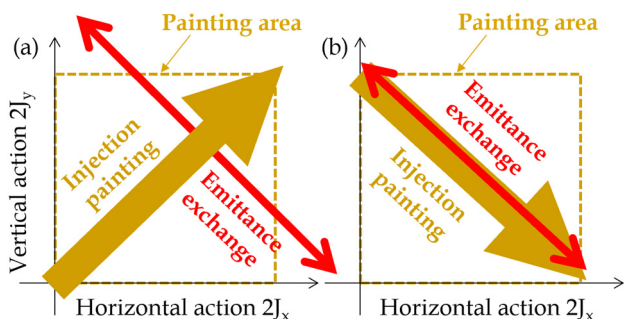


Figure 7: (a) Schematic of the geometrical relationship between correlated painting and emittance exchange in the  $(J_x, J_y)$  space. (b) Similar schematic for anti-correlated painting.

Figure 5 shows the motion of a beam particle near the resonance. The frequency of the beam position oscillation is  $\sim 100$  kHz, which corresponds to  $\sim 0.2$  in the wavenumber per turn, so that the resonance is excited at 0.2 in the betatron tune space. In Fig. 5, one can find that the amplitude of the betatron motion of the beam particle sharply increases when the betatron tune gets on the resonance. The beam loss (B) is ascribed to a beam halo formation caused by the resonance.

As shown in Fig. 4 (b), the experimental beam loss was well reproduced by the numerical simulation by including the measured dipole field ripple and also by considering the realistic boundary condition. The characteristic of this resonance is that it is an intensity-dependent phenomenon, and that it occurs at unusual betatron frequency depending on the frequency of the beam position oscillation. Receiving this study result, the power supply of the injection bump magnets, which was the source of the dipole field ripple, was improved. As a result, the dipole field ripple was drastically reduced, and the beam loss (B) was successfully removed [4].

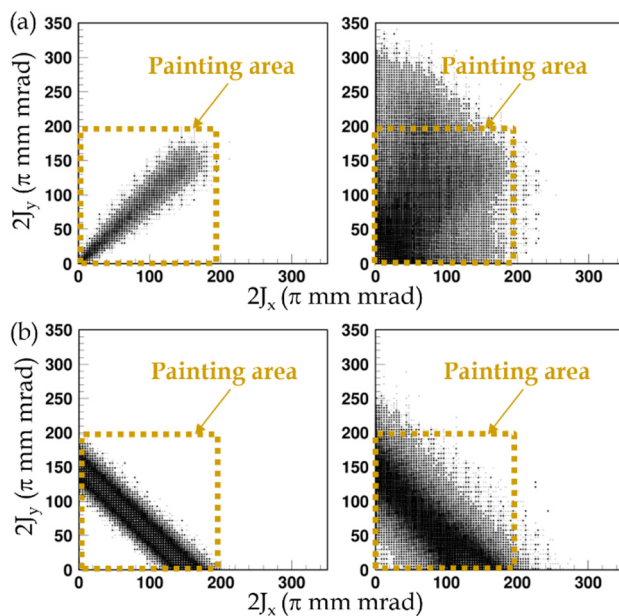


Figure 8: Numerical simulation results; scatter plots between the horizontal and vertical actions at the end of injection calculated without (left) and with (right) space charge. The upper (a) is for correlated painting, while the lower (b) is for anti-correlated painting.

### Approach to Solving Beam Loss Issue Caused by the Montague Resonance

The next subject in our beam study was to further reduce the residual beam loss coming from foil scattering during injection. The foil scattering beam loss occurs in proportion to the foil hitting rate during injection. One possible solution to reduce the foil hitting rate is to expand the transverse painting area, which serves to more quickly move the circulating beam away from the foil. The original painting area was  $100\pi$  mm mrad. In this case, the average number of foil hits per particle is as large as 20.0. This number can be reduced by  $\sim 1/4$  if the painting emittance is doubly enlarged. But it was not so easy to expand the painting area.

By introducing a large painting of  $200\pi$  mm mrad, the foil scattering beam loss was well reduced as expected, but another significant beam loss occurred as shown by (a) in the upper panel of Fig. 6. But the numerical simulation provided a clue to solve this issue. As shown by (a) in the lower panel of Fig. 6, the numerical simulation well reproduced the experimental beam loss and clearly showed that the beam loss is caused by the Montague resonance,  $2\nu_x - 2\nu_y = 0$  [10]. This resonance is excited mainly by the nonlinear space-charge field, causing emittance exchange between the horizontal and vertical planes.

Figure 7 (a) shows a 2d space of the horizontal and vertical actions, showing the mechanism of the beam loss. The yellow arrow shows the path of injection painting; the injection beam is painted from the middle to the outside on both the horizontal and vertical planes (called correlated painting). To this direction of injection painting,

the emittance exchange occurs in the orthogonal direction. Figure 8 (a) shows scatter plots of the horizontal and vertical actions at the end of injection calculated without and with space charge. In this figure, one can see that the beam particles are greatly diffused by the space charge, and some of them are greatly out of the painting area. The numerical simulation clearly showed that this diffusion of beam particles is caused by the emittance exchange ( $J_x$ - $J_y$  exchange of each particle) that occurs perpendicularly to the path of injection painting. This is the mechanism of the beam loss.

To solve this issue, the path of injection painting was modified as shown in Fig. 7 (b); the direction of vertical painting was reversed. That is, the injection beam is painted from the middle to the outside on the horizontal plane, but from the outside to the middle on the vertical plane (called anti-correlated painting). In this case, the direction of the injection painting is the same as that of the emittance exchange. This geometrical relationship between injection painting and emittance exchange has an advantage, which minimizes the diffusion of beam particles. In Fig. 8 (b), one can find that most of beam particles stay in the painting area though emittance exchange occurs, because the directions of the injection painting and the emittance exchange are the same.

As shown in Fig. 6, the beam loss was successfully reduced by changing the path of injection painting, as predicted by the numerical simulations [4]. By this effort, the painting area was doubly expanded with no additional beam loss, and thereby the foil scattering beam loss was sufficiently reduced.

### Mechanism of the Residual Beam Loss

By continuous efforts, the beam loss in the 1 MW beam operation was finally reduced to the order of  $10^{-3}$ , as shown by (b) in Fig. 6. The numerical simulation well reproduced the experimental beam loss, and found the residual beam loss mainly arises from the effect of  $3\nu_x=19$  driven by the sextupole field components intrinsic in the injection bump magnets [11].

As shown in Fig. 9, four sets of same-type pulsed dipole magnets, SB1-4, are utilized for forming a horizontal injection orbit bump of 93 mm; they are excited over 0.5 ms for multiturn injection and then sharply turned down within the next 0.35 ms. Figure 10 shows the measured field distributions of the SB 1, 2, 3, and 4 [12, 13]. In this figure, one can clearly see that each SB has a significant sextupole component.

Ideally, the SBs generate the same magnetic field distribution except polarity. That is, the SB fields including the high-order field components cancel with each other through the integration over the SB1-4. In such an ideal case, the SB fields have no significant influence on the beam. But the actual situation is different from that. As shown in Fig. 9, the SBs are installed very close to each other. Besides, the distances of SB1-2 (SB3-4) and SB2-3 are different. Also, the SB1 and SB4 are very close to the quadrupole magnets. Due to such actual situations, each SB has a different magnetic interference with each nearby

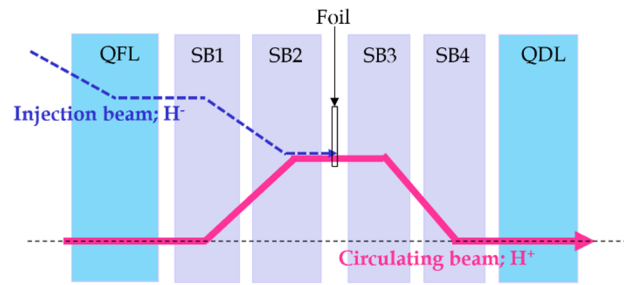


Figure 9: Schematic of the injection area.

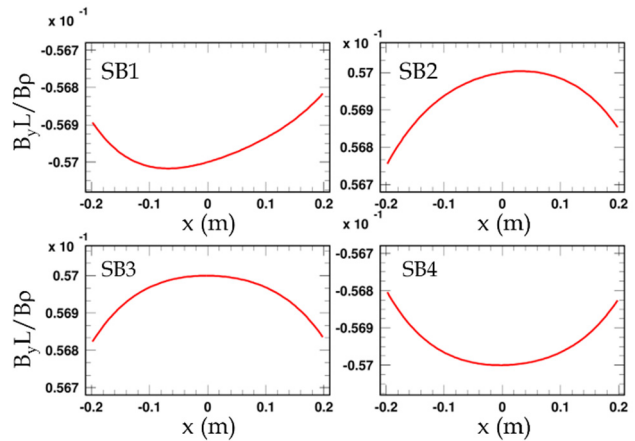


Figure 10: BL distributions ( $y=0$ ) measured for SB1-4.

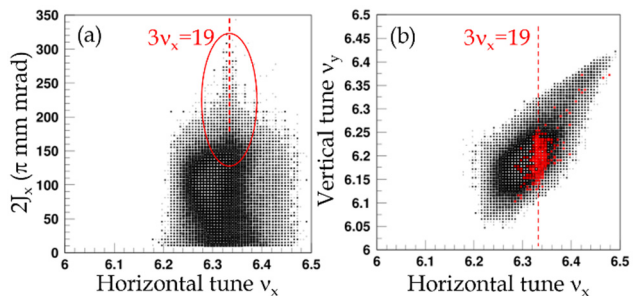


Figure 11: Numerical simulation results; (a) scatter plot of the horizontal tune and the horizontal action, and (b) tune footprint, calculated at the end of injection, where the particles painted red correspond to the beam halo particles found in (a).

component. Therefore, the actual field distributions of the SBs are not identical. In the actual beam operation, the SB fields are adjusted so that their dipole field components are compensated through the integration over the SB1-4. But, as to the higher-order field components, such a field compensation is incomplete due to the effects of the magnetic interferences. The residual sextupole component ( $K_2=0.012 \text{ m}^{-2}$ ), not cancels, excites the 3rd-order betatron resonance,  $3\nu_x=19$ .

Figure 11 (a) and (b) show the 2d plot of the horizontal tune and horizontal action and the tune footprint, calculated at the end of injection. In this figure, one can find that a horizontal beam halo is generated on the 3rd-order reso-

nance. This horizontal beam halo is the main cause of the residual beam loss. To correct the 3rd-order resonance, we need at least two sets of additional sextupoles with individual power supplies. But they are not urgent, because the residual beam loss is already small sufficiently.

### Demonstration of 1 MW Beam Operation

The amount of the residual beam loss in the 1-MW beam operation is as low as the order of  $10^{-3}$ . It is concentrated in the injection energy region, most of which is well localized at the collimator section. Under this condition, we performed a  $\sim 2$ -day continuous 1-MW beam operation at 25 Hz for users right before the summer maintenance period in 2020. During this beam operation, no serious issues were found. Besides, no unexpected increases in the residual radiation levels were found; the machine activations in the RCS were still maintained at sufficiently low levels of  $<80 \mu\text{Sv/h}$  at the injection area,  $<350 \mu\text{Sv/h}$  at the collimator area, and  $<3 \mu\text{Sv/h}$  at the high dispersion area, which were measured at 30 cm, 5 hours after the beam stop. Now we can say the accelerator itself including the linac is ready for the routine 1-MW beam operation.

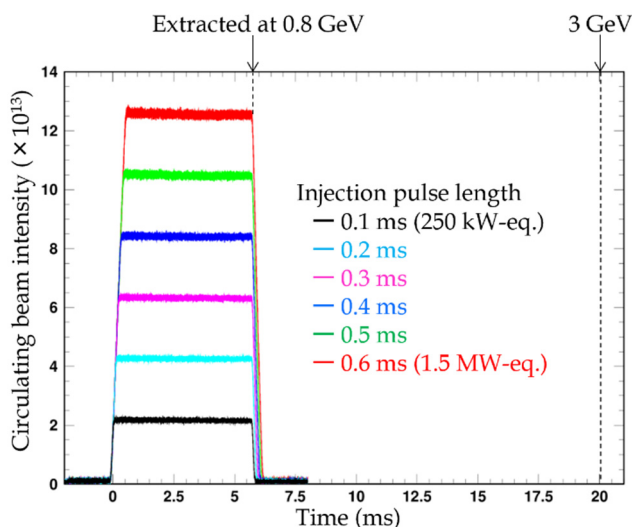


Figure 12: Experimental results; circulating beam intensities from injection to extraction.

### 1.5-MW BEAM TEST

The successful achievement of the low-loss 1-MW beam operation opened the door to further beam power ramp-up beyond 1 MW [4, 5].

We have recently performed a further high-intensity beam test by increasing both injection peak current (50 mA to  $>60$  mA) and injection pulse length (0.5 ms to 0.6 ms). The beam intensity reached  $1.26 \times 10^{14}$  particles per pulse, which corresponds to 1.5 MW at 3 GeV and 25 Hz. Due to the limitation of the ring RF system, the full acceleration of up to 3 GeV was not reached, but we achieved a 0.8 GeV acceleration for the high-intensity beam. Beam loss usually occurs for low energy region

below 0.8 GeV, so that we were able to complete sufficient beam loss studies even under the limited situation.

Figure 12 shows the result of the high-intensity beam test, showing the circulating beam intensity from injection to extraction, where the red one shows the maximum beam intensity which corresponds to 1.5 MW. In this figure, one can find that there is no significant beam loss; it's almost flat from injection to extraction. The beam loss in the low energy region, which was the most concern, was successfully reduced to the order of  $10^{-3}$  even for the 1.5-MW-equivalent high-intensity beam.

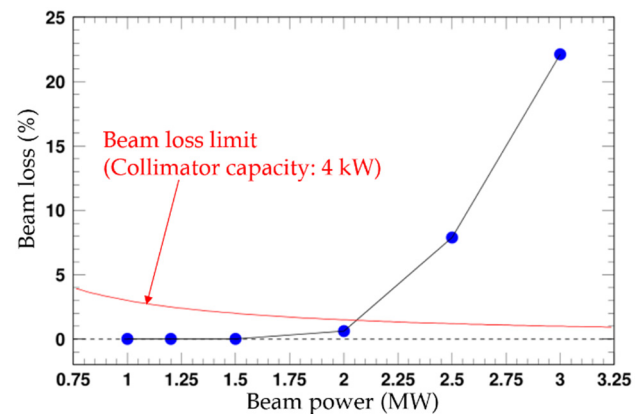


Figure 13: Numerical simulation results; intensity dependence of beam loss from 1 MW to 3-MW-equivalent intensity.

To realize the actual 1.5-MW beam operation, we need several hardware upgrades, such as the upgrade of the ring RF system [14]. But this experiment clearly demonstrated that the J-PARC RCS has a sufficient potential to realize a higher-power beam operation beyond 1 MW. The numerical simulation, which is displayed in Fig. 13, also supports the experimental result; it suggests the possibility of a low-loss 2-MW beam operation [5]. Looking ahead to future upgrades of J-PARC including the construction of the second target station, we will continue high-intensity beam studies aiming for a 1.5–2 MW beam power.

### SUMMARY

We are still in the course of gradually increasing the beam power to 1 MW while carefully monitoring the durability of the neutron production target, but the accelerator itself is ready for the routine 1-MW beam operation. By continuous efforts for beam loss mitigation including several hardware improvements, we have recently established a 1-MW beam operation with considerably low fractional beam loss of the order of  $10^{-3}$ . This beam loss amount corresponds to  $<1/10$  the typical value in the previous high-intensity proton synchrotrons. This achievement of the low-loss 1-MW beam operation opened the door to further beam power ramp-up beyond 1 MW. We are now

developing high-intensity beam tests toward achieving a 1.5-MW beam power or more with promising results.

## REFERENCES

- [1] High-intensity Proton Accelerator Project Team, J-PARC, JAERI Report, No. JAERI-Tech 2003-044, 2003.
- [2] H. Hotchi *et al.*, “Beam commissioning of the 3-GeV rapid cycling synchrotron of the Japan Proton Accelerator Research Complex”, *Phys. Rev. ST Accel. Beams*, vol. 12, p. 040402, Apr. 2009.  
doi:10.1103/PhysRevSTAB.12.040402
- [3] H. Hotchi, “High-power proton accelerators for pulsed spallation neutron sources”, *AAPPS Bull.*, vol. 31, p. 23, Oct. 2021. doi:10.1007/s43673-021-00025-0
- [4] H. Hotchi *et al.*, “Achievement of a low-loss 1-MW beam operation in the 3-GeV rapid cycling synchrotron of the Japan Proton Accelerator Research Complex”, *Phys. Rev. Accel. Beams*, vol. 20, p. 060402, Jun. 2017.  
doi:10.1103/PhysRevAccelBeams.20.060402
- [5] H. Hotchi *et al.*, “J-PARC 3-GeV RCS: 1-MW beam operation and beyond”, *JINST*, vol. 15, p. P07022, Jul. 2020.  
doi:10.1088/1748-0221/15/07/P07022
- [6] H. Hotchi *et al.*, “Beam loss reduction by injection painting in the 3-GeV rapid cycling synchrotron of the Japan Proton Accelerator Research Complex”, *Phys. Rev. ST Accel. Beams*, vol. 15, p. 040402, Apr. 2012.  
doi:10.1103/PhysRevSTAB.15.040402
- [7] F. Tamura *et al.*, “Longitudinal painting with large amplitude second harmonic rf voltages in the rapid cycling synchrotron of the Japan Proton Accelerator Research Complex”, *Phys. Rev. ST Accel. Beams*, vol. 12, p. 041001, Apr. 2009. doi:10.1103/PhysRevSTAB.12.041001
- [8] M. Yamamoto *et al.*, “Simulation of longitudinal beam manipulation during multi-turn injection in J-PARC RCS”, *Nucl. Instrum. Methods*, vol. 621, p. 15, 2010.  
doi:10.1016/j.nima.2010.04.050
- [9] Y. Shobuda *et al.*, “Analytical method for the evaluation of field modulation inside the rf-shielded chamber with a time-dependent dipole magnetic field”, *Phys. Rev. ST Accel. Beams*, vol. 12, p. 032401, Mar. 2009.  
doi:10.1103/PhysRevSTAB.12.032401
- [10] H. Hotchi, “Effects of the Montague resonance on the formation of the beam distribution during multiturn injection painting in a high-intensity proton ring”, *Phys. Rev. Accel. Beams*, vol. 23, p. 050401, May 2020.  
doi:10.1103/PhysRevAccelBeams.23.050401
- [11] H. Hotchi *et al.*, “J-PARC RCS: high-order field components inherent in the injection bump magnets and their effects on the circulating beam during multi-turn injection”, *J. Phys. Conf. Ser.*, vol. 1350, p. 012102, 2019.  
doi:10.1088/1742-6596/1350/1/012102
- [12] T. Takayanagi *et al.*, “Measurements of the injection bump magnets at J-PARC 3 GeV RCS”, in *Proc. the 4th Annual Meeting of Particle Accelerator Society of Japan*, Wako, Japan, Aug. 2007, p. 85.
- [13] H. Harada *et al.*, “Modelling for the injection bump system at the J-PARC 3 GeV Rapid Cycling Synchrotron”, in *Proc. the 4th Annual Meeting of Particle Accelerator Society of Japan*, Wako, Japan, Aug. 2007, p. 88.
- [14] M. Yamamoto *et al.*, “Conceptual design of a single-ended MA cavity for J-PARC RCS upgrade”, *J. Phys. Conf. Ser.*, vol. 1067, p. 052014, 2018.  
doi:10.1088/1742-6596/1067/5/052014

# DEVELOPMENT OF AN INJECTION-PAINTED SELF-CONSISTENT BEAM IN THE SPALLATION NEUTRON SOURCE RING

A. Hoover, University of Tennessee, Knoxville, U.S.A.

N. J. Evans\*, T. Gorlov, J. Holmes, Oak Ridge National Laboratory, Oak Ridge, U.S.A.

## Abstract

A self-consistent beam maintains linear space charge forces under any linear transport, even with the inclusion of space charge in the dynamics. Simulation indicates that it is possible to approximate certain self-consistent distributions in a ring with the use of phase space painting. We focus on the so-called Danilov distribution, which is a uniform density, rotating, elliptical distribution in the transverse plane and a coasting beam in the longitudinal plane. Painting the beam requires measurement and control of the orbit at the injection point, and measuring the beam requires reconstruction of the four-dimensional (4D) transverse phase space. We discuss efforts to meet these requirements in the Spallation Neutron Source (SNS) ring.

## INTRODUCTION

We define a self-consistent beam as one that maintains linear space charge forces under any linear transport, even with the inclusion of space charge in the dynamics. Several desirable properties stem from the linearity of the space charge force: the emittance is conserved, the space charge tune shift is minimized, and the space charge tune spread is eliminated. An ongoing project is to determine whether a self-consistent beam can be approximated in reality.

Various self-consistent distributions were derived in [1]; of particular interest for our purposes is the so-called Danilov distribution, which is a uniform density ellipse in the transverse plane and a coasting beam in the longitudinal plane. Particles in the distribution occupy elliptical modes so that the four-dimensional (4D) transverse emittance vanishes. Equivalently, one of the intrinsic emittances  $\varepsilon_{1,2}$  vanishes depending on the sign of the angular momentum [2]. The intrinsic emittances are conserved even with space charge, but the apparent emittances  $\varepsilon_{x,y}$  are not [3].

In the linear approximation, it is possible to create an approximate Danilov distribution in a circular machine using phase space painting. This can be done by moving the injection coordinates along an eigenvector of the ring transfer matrix with square root time-dependence. In other words,

$$\mathbf{x}(t) = \sqrt{2J} \operatorname{Re} \{ \mathbf{v} e^{-i\mu} \} \sqrt{t}, \quad (1)$$

where  $\mathbf{x} = (x, x', y, y')$  is the phase space location of the injection beam in the frame of the circulating beam,  $J$  is an amplitude,  $\mu$  is a phase,  $\mathbf{v}$  is an eigenvector of the ring transfer matrix, and  $t$  is a time variable normalized to the range [0, 1]. We call this *elliptical painting*. The turn-by-turn projection of the eigenvector onto any 2D subspace

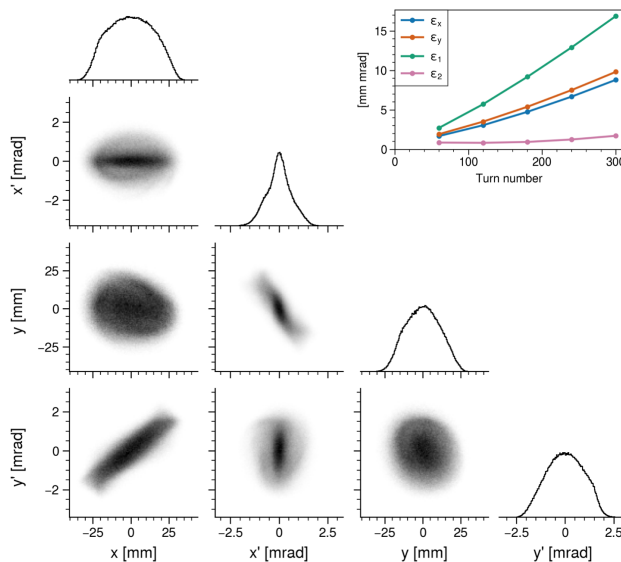


Figure 1: ORBIT simulation of elliptical painting in the SNS ring. Bottom left: 2D projections of the final 4D phase space distribution. Top right: emittance growth during injection.

of the 4D phase space will trace an ellipse, and the square root time-dependence ensures the uniform density of the projected distributions at all times. Since the particles lie along an eigenvector, the intrinsic emittance associated with the other eigenvector will be zero. We note that performing this method in an uncoupled lattice results in a flat beam ( $\varepsilon_x = 0$  or  $\varepsilon_y = 0$ ) unless the horizontal and vertical tunes are equal.

Simulations suggest that the various conditions required for elliptical painting to produce a self-consistent beam will approximately hold in the Spallation Neutron Source (SNS) [4]. Figure 1 shows the results of one such simulation. The core of the final 1D projections resemble those of ideal elliptical projections, and it can also be seen from the linear emittance growth and constant/small  $\varepsilon_2$  that the beam remains reasonably close to a Danilov distribution during injection.

Several steps were necessary to achieve this simulated result. First, the painting path was chosen to follow a line in the  $x$ - $y'$  plane. Deviation from this path was found to increase beam losses due to machine specifics. Additional motivation for  $x$ - $y'$  painting comes from study of the beam envelope equations in [3]. The beam tilts throughout the ring, but the matched solution with space charge is upright at locations where  $\alpha \approx 0$  such as the injection point. A tilted beam at

\* evansnj@ornl.gov

Content from this work may be used under the terms of the CC BY 3.0 licence (© 2021). Any distribution of this work must maintain attribution to the author(s), title of the work, publisher, and DOI

these locations leads to severe mismatch oscillations due to linear coupling from space charge. Second, the apparent emittances were kept nearly equal, again in consideration of the matched beam. Third, the ring RF cavity voltages were decreased to better approximate a coasting beam. Fourth, the beam energy was lowered to 0.6 GeV to increase the effective kicker strength; the number of injected turns was decreased to 300 to compensate for the resulting increase in space charge strength. Fifth, orbit corrector dipoles in the injection region were used to assist the vertical kickers. With these settings, a maximum vertical slope of 1.7 mrad was reached. Finally, a solenoid magnet was added to the ring to mitigate the effect of fringe fields near the difference resonance  $\nu_x - \nu_y = 0$  by splitting the eigentunes of the ring transfer matrix.

In the rest of this paper, we report on the development of tools at the SNS to (a) measure and control the orbit in the injection region and (b) measure the 4D phase space of the painted beam. We then present initial experimental results.

## RING INJECTION CONTROL

The closed orbit in the injection region is controlled by varying the current in eight independent dipole kicker magnets — four in each plane. Each magnet is given a square root waveform; what remains is to determine the initial/final voltages to produce the desired phase space coordinates at the injection point. An OpenXAL application was developed to this end [5].

The positions and angles at the injection point are estimated in the following way. A single minipulse from the linac is injected and stored in the ring with the kicker magnets at a constant voltage and a turn-by-turn signal is collected from a beam-position-monitor (BPM) in the ring. The average signal over multiple minipulses is fit with a Gaussian-damped sinusoid of the form [6]:

$$x(t) = A_0 + Ae^{kt^2} \cos(\mu + \mu_0), \quad (2)$$

where  $t$  is the turn number. The parameter  $A$  gives the betatron amplitude,  $\mu/2\pi$  gives the fractional tune, and  $\mu_0$  gives the particle phase at the BPM. The phase space coordinates at the injection point are recovered by combining these parameters with the linear ring model. This is repeated for each BPM to give an estimated mean and standard deviation of the phase space coordinates at the injection point. An example fit is shown in Fig. 2.

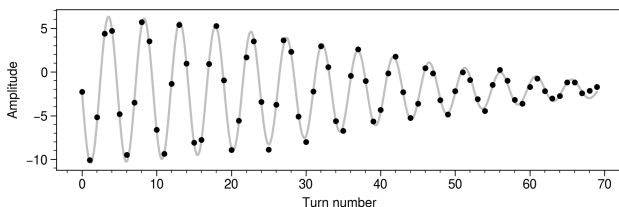


Figure 2: Turn-by-turn BPM signal fit with Eq. (2).

The next issue is how to control the phase space coordinates at the injection point. Each kicker magnet is calibrated by applying a voltage difference to the magnet and measuring the orbit response using the ring BPMs; the angular kick associated with the magnet is varied until the model orbit agrees with the measured orbit. It was also found that slight quadrupole corrections are necessary for the model to agree with measurements. The standard deviation of the measured phase space coordinates is small after this calibration. One can then ask the model for a change in coordinates, update the kickers accordingly, and measure the new coordinates, iterating if necessary.

The kicker magnets have limited strengths and are unipolar, which limits the minimum distance from the and the maximum angle at the injection point. In fact, the closed orbit cannot reach the foil at production energy (1 GeV). As mentioned previously, the beam energy can be lowered to increase the effective kicker strength; however, this is a significant task for SNS operators due to issues related to the SNS timing system. Attempts to lower to 0.6 GeV were unsuccessful, but an energy of 0.8 GeV was recently achieved. The use of orbit corrector dipoles to assist the kickers is complicated by the fact that the correctors are turned on during production, so their variation leads to significant closed-orbit waves throughout the ring. The use of orbit correctors is left as a future optimization.

## FOUR-DIMENSIONAL PHASE SPACE MEASUREMENT

Determining how closely a painted beam resembles a Danilov distribution requires measurement of the 4D transverse phase space distribution. A direct measurement such as a slit-scan is not possible, so the phase space distribution must be reconstructed from lower-dimensional projections.

### Reconstruction from 1D Projections

The transverse covariance matrix can be reconstructed 1D projections by estimating the  $\langle xx \rangle$ ,  $\langle yy \rangle$ , and  $\langle xy \rangle$  moments at four or more locations or optics settings [7,8]. Four reliable wire-scanners are available to perform this measurement in the ring-target beam transport (RTBT) section of the SNS, just before the target, each equipped with a horizontal, vertical, and diagonal wire. The wire-scanners can be run in parallel in approximately five minutes. The optics in the RTBT can be changed, but there are several constraints. First, the  $\beta$  functions must be kept reasonably small throughout the RTBT to minimize beam loss. Second, the beta functions at the target must be kept at their nominal values. Third, control of the optics *between* the wire-scanners is limited by the fact that two power supplies control the eight quadrupoles in the measurement region.

We tested the method on a production beam by scanning the phase advances at WS24 (the last wire-scanner in the group) in a 30-degree window over ten steps. At each step, the two power supplies (eight quadrupoles) upstream of WS24 were varied to obtain the correct phase advances, then

five quadrupoles downstream of WS24 were varied to reset the  $\beta$  functions at the target. The results are shown in Fig. 3. The colored lines are defined by  $x = \sqrt{\langle xx \rangle}$  at the wire-scanners transported back to the reconstruction location. The coordinates are normalized by the reconstructed Twiss parameters.

Errors can appear in the transfer matrix elements or measured moments. Errors in the measured moments are expected to be small since there is very little bunch-to-bunch variation in the profiles, while the correlation between  $x$  and  $y$  could have a larger error since it is calculated indirectly. Errors in the transfer matrix are also expected to be small since the reconstruction location is close to the wire-scanners. We use the standard deviations of the ten reconstructed moments obtained from the linear least squares estimator in our analysis and propagate these to obtain the uncertainties in the beam parameters [9]. The reconstructed Twiss parameters are close to the model parameters computed from the linear transfer matrices of the ring and RTBT. The intrinsic emittances are almost equal to the apparent emittances, showing that there is very little cross-plane correlation in the beam.

We found that two measurements (eight profiles) produced nearly the same values and uncertainties as the entire scan, but that the reconstruction failed when using only one measurement (four profiles), producing imaginary intrinsic emittances. This is a known problem; certain optics between wire-scanners lead to an ill-conditioned system of equations [10]. To solve this problem, we varied the phase advances at WS24 and recorded the number of failed fits from a Monte Carlo simulation at each setting. This revealed

that the measurement sensitivity can be made tolerable by changing the horizontal(vertical) phase advance at WS24 by 45(-45) degrees.

### Reconstruction from 2D Profiles

The SNS target nose is prepared with a luminescent Cr:Al<sub>2</sub>O<sub>3</sub> coating that allows imaging of the beam distribution on the target [11]. The target imaging system is immediately useful for our purposes to verify the shape, density, and tilt of the painted beam, especially relative to a production beam. It is also possible to vary the phase advances from a point upstream of the target to the target, which effectively shows a 2D projection of the distribution at different "angles" in 4D phase space. Tomographic methods could be employed to reconstruct the 4D phase space distribution using these 2D projections [12]. We are currently determining the feasibility of this approach.

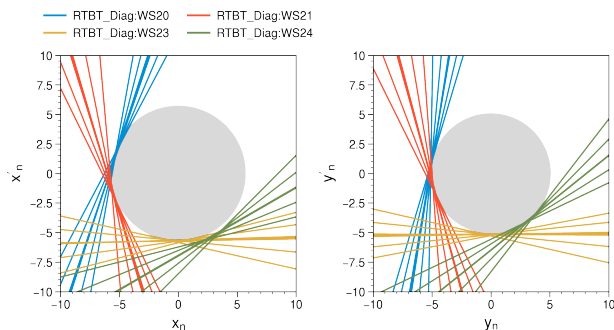
## INITIAL RESULTS

We first discuss the 4D phase space measurement of a production beam for later comparison. The SNS operates at 1 GeV during neutron production and employs correlated painting with an initial offset of the closed orbit from the foil [13]. We used the same painting waveforms but decreased the painting time so that only 500 minipulses are injected instead of 1000; i.e., the final beam is the same size but half the intensity. We are free to extract and measure the beam at any point during injection; we chose to collect measurements every 50 turns.

The wire-scanner measurements and reconstructed emittances are displayed in Fig. 4. The initial orbit offset from the foil is evident in the hollow wire-scanner profiles. The reconstructed emittances indicate very small cross-plane correlation throughout injection. Since in these cases the cross-plane moments are solved for exactly using four wire-scanners, we cannot use the uncertainty estimate from linear least squares for the intrinsic emittances; instead, we use the worst case from Fig. 3 of approximately 4% uncertainty.

We now discuss our first attempt at elliptical painting. The beam energy was lowered to 0.8 GeV to reach the closed orbit to the foil, and the ring tunes were then set equal at 6.18. With these machine settings, a maximum vertical slope of 1.1 mrad was attained, and we chose to paint to a maximum horizontal position of 20 mm over 500 turns. The bunch length was set to approximately half of the ring length, and the ring RF cavities were left untouched. The measurement from Fig. 4 was then repeated. The results are displayed in Fig. 5.

The measured apparent emittances increase linearly from near zero as intended, and the wire-scanner profiles are no longer hollow. There is a small amount of cross-plane correlation present during injection, but the 4D emittance is not close to zero. The wire-scanner profiles are also somewhat peaked as opposed to the elliptical profiles that would be present in a uniform density elliptical beam. The measured Twiss parameters are not the same as the model Twiss pa-



Parameter	Measurement	Model
$\beta_x$ [m/rad]	$22.06 \pm 0.29$	22.00
$\beta_y$ [m/rad]	$4.01 \pm 0.02$	3.81
$\alpha_x$ [rad]	$2.33 \pm 0.04$	2.37
$\alpha_y$ [rad]	$-0.49 \pm 0.01$	-0.60
$\varepsilon_1$ [mm mrad]	$33.02 \pm 0.05$	-
$\varepsilon_2$ [mm mrad]	$25.67 \pm 1.03$	-
$\varepsilon_x$ [mm mrad]	$32.85 \pm 0.05$	-
$\varepsilon_y$ [mm mrad]	$25.87 \pm 0.12$	-

Figure 3: Reconstructed beam parameters and graphical output from the multi-optics emittance measurement of a production beam.

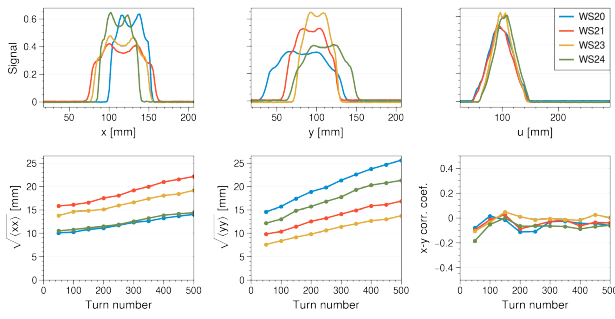


Figure 4: Measured beam during correlated painting. Top: measured wire-scanner profiles after injection. Middle: measured beam moments during injection. Bottom: reconstructed emittances during injection.

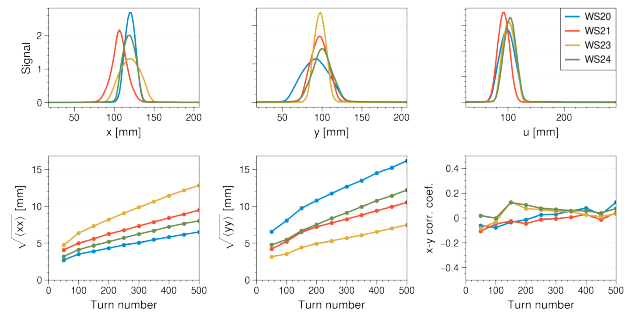


Figure 5: Measured beam during elliptical painting. Top: measured wire-scanner profiles after injection. Middle: measured beam moments during injection. Bottom: reconstructed emittances during injection.

rameters; this is expected for higher space charge since the beam Twiss parameters will adjust to the matched solution with space charge in the ring.

The left column of Fig. 6 shows a simulation of this case using PyORBIT [14]. The cross-plane correlation is largely eliminated by fringe fields early on; however, the intrinsic emittances split around turn 100 and remain significantly different than the apparent emittances for the rest of injection. It is known from previous studies that the space charge force in an elliptical beam has a stabilizing effect similar to solenoid fields. Although blurred, the  $x$ - $y'$  projection of the distribution has a higher density along the painting path. The reason for the disagreement between this simulation and our measurements is under investigation.

Several modifications could bring the painted beam closer to a self-consistent state. The first is to decrease the space charge strength by increasing the painted emittances and/or decreasing the beam intensity. It is evident from the simulated emittance growth in the second half of injection that the space charge effect on the beam is quite strong. There is no limit on the horizontal emittance since it is increased by lowering the kicker voltages, but the vertical emittance is fixed unless the orbit corrector dipoles provide additional help. Although it is undesirable to greatly separate the horizontal and vertical emittances, simulation indicates that increasing  $x_{max}$  from 21 mm to 31 mm has a positive effect. As seen in the right column of Fig. 6,  $\epsilon_2$  remains nearly constant during the second half of injection, and the final  $x$ - $y'$  projection is clustered along the painting path. A second

possible improvement is to insert a solenoid magnet in the ring to mitigate fringe field effects; this is planned to occur in early 2022. A third possibility is to modify the ring RF voltages and bunch length to better approximate a coasting beam.

## CONCLUSION

Several issues have been resolved in our project to create an approximately self-consistent beam in the SNS ring. First, an application has been developed to measure and control the closed orbit at the injection point. Second, a method to reconstruct the transverse covariance matrix from 1D projections has been implemented and the optics have been modified to minimize the measurement time. Third, the SNS energy has been lowered to inject particles directly onto the closed orbit. Elliptical painting has been carried out and compared with simulation and with correlated painting. Although the resulting beam is distinguishable from a normal production beam, it does not exhibit the desired relationships between the phase space coordinates; however, modifications to both the lattice and painting parameters have the potential to provide a significant improvement in future experiments.

## REFERENCES

- [1] V. Danilov, S. Cousineau, S. Henderson, and J. Holmes, “Self-consistent time dependent two dimensional and three dimensional space charge distributions with linear force”, *Phys. Rev. Accel. Beams*, vol 6, p. 094202, 2003. doi: 10.1103/PhysRevSTAB.6.094202

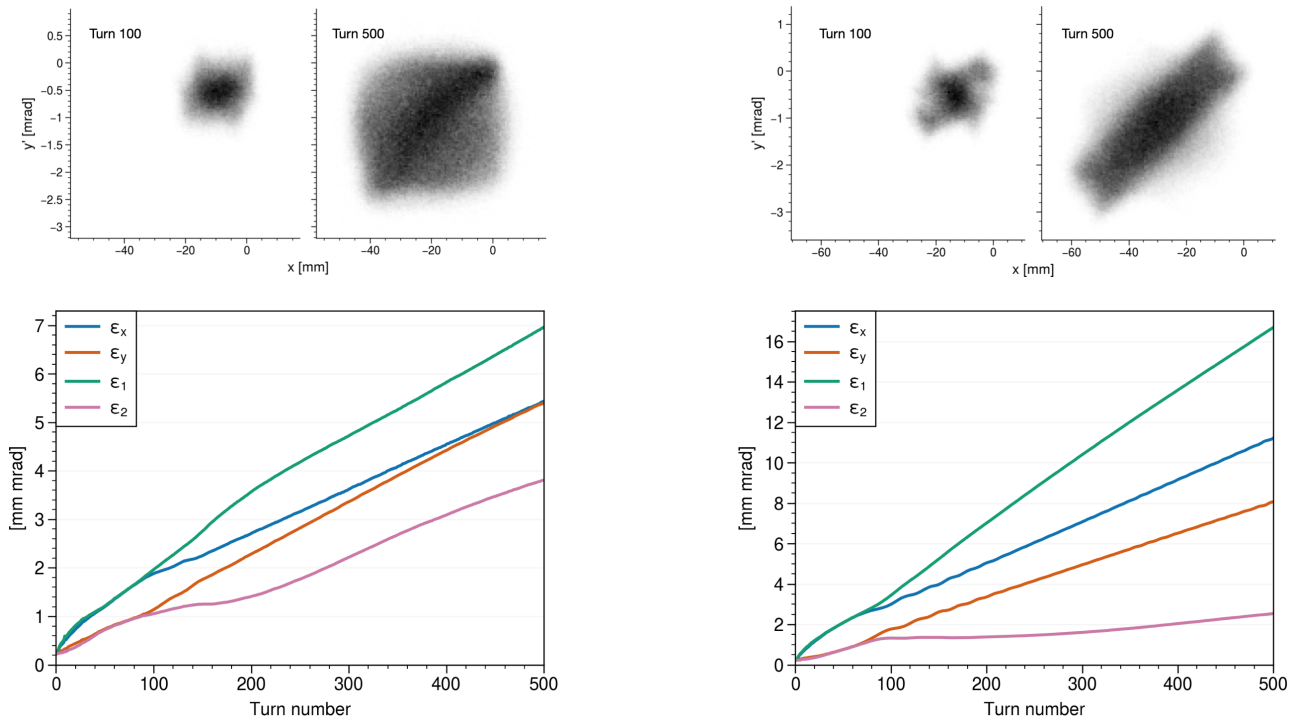


Figure 6: PyORBIT simulation of elliptical painting in the SNS ring without solenoids. In both columns,  $y'_{max} = 1.1$  mrad. In the left column,  $x_{max} = 21$  mm, while in the right column,  $x_{max} = 31$  mm. The lower plots show the emittance growth during injection, while the upper plots show the  $x$ - $y'$  projections at turn 100 and 500.

- [2] L. Groening, C. Xiao, and M. Chung, “Particle beam eigen-emittances, phase integral, vorticity, and rotations”, *Phys. Rev. Accel. Beams*, vol. 24, p. 054201, 2021. doi:10.1103/PhysRevAccelBeams.24.054201
- [3] A. Hoover, N. J. Evans, and J. A. Holmes, “Computation of the matched envelope of the Danilov distribution”, *Phys. Rev. Accel. Beams*, vol. 24, p. 044201, 2021. doi:10.1103/PhysRevAccelBeams.24.044201
- [4] J. A. Holmes, T. Gorlov, N. J. Evans, M. Plum, and S. Cousineau, “Injection of a self-consistent beam with linear space charge force into a ring”, *Phys. Rev. Accel. Beams*, vol. 21, p. 124403, 2018. doi:10.1103/PhysRevAccelBeams.21.124403
- [5] N. Milas *et al.*, “Open XAL Status Report 2021”, in *Proc. IPAC'21*, Campinas, Brazil, May 2021, pp. 3421–3423. doi:10.18429/JACoW-IPAC2021-WEPAB319
- [6] T. Pelaia, “Parameter Estimation of Gaussian-Damped Sinusoids from a Geometric Perspective”, <http://arxiv.org/abs/1604.05167/>, 2021.
- [7] E. Prat and M. Aiba, “Four-dimensional transverse beam matrix measurement using the multiple-quadrupole scan technique”, *Phys. Rev. Accel. Beams*, vol. 17, p. 052801, 2014. doi:10.1103/PhysRevSTAB.17.052801
- [8] “Measurement and Correction of Cross-Plane Coupling in Transport Lines”, in *Proc. LINAC'00*, Monterey, CA, USA, Aug. 2000, paper MOC19, pp. 196–198.
- [9] A. Faus-Golfe, J. Navarro, N. Fuster Martinez, J. Resta Lopez, and J. Giner Navarro, “Emittance reconstruction from measured beam sizes in ATF2 and perspectives for ILC”, *Nucl. Instrum. Methods Phys. Res. A*, vol. 819, pp. 122-138, 2016. doi:10.1016/j.nima.2016.02.064
- [10] I. Agapov, G. A. Blair, and M. Woodley, “Beam emittance measurement with laser wire scanners in the International Linear Collider beam delivery system”, *Phys. Rev. Accel. Beams*, vol. 10, p. 112801, 2007. doi:10.1103/PhysRevSTAB.10.112801
- [11] W. Blokland, T. McManamy, and T. J. Shea, “SNS Target Imaging System Software and Analysis”, in *Proc. BIW'10*, Santa Fe, NM, USA, May 2010, paper TUPSM003, pp. 93–97.
- [12] K. M. Hock and A. Wolski, “Tomographic reconstruction of the full 4D transverse phase space”, *Nucl. Instrum. Methods Phys. Res. A*, vol. 726, pp. 8–16, 2013. doi:10.1016/j.nima.2013.05.004
- [13] S. Henderson *et al.*, “The Spallation Neutron Source accelerator system design”, *Nucl. Instrum. Methods Phys. Res. A*, vol. 763, pp. 610-673, 2014. doi:10.1016/j.nima.2014.03.067
- [14] A. Shishlo, S. Cousineau, J. Holmes, and T. Gorlov, “The Particle Accelerator Simulation Code PyORBIT”, *Procedia Comput. Sci.*, vol. 51, p. 1272, 2015. doi:10.1016/j.procs.2015.05.312

# FIRST EXPERIENCE OF CRYSTAL COLLIMATORS DURING LHC SPECIAL RUNS AND PLANS FOR THE FUTURE\*

M. D’Andrea<sup>1,2†</sup>, V. Avati<sup>1,3</sup>, R. Bruce<sup>1</sup>, M. Butcher<sup>1</sup>, M. Di Castro<sup>1</sup>, M. Deile<sup>1</sup>, B. Dzedzic<sup>4</sup>,  
 H. Garcia Morales<sup>1,5‡</sup>, Y. Gavrikov<sup>1,6</sup>, K. Hiller<sup>7</sup>, S. Jakobsen<sup>1</sup>, J. Kašpar<sup>1,8</sup>, K. Korcyl<sup>4</sup>,  
 I. Lamas Garcia<sup>1</sup>, A. Masi<sup>1</sup>, A. Mereghetti<sup>1,§</sup>, D. Mirarchi<sup>1,9</sup>, S. Redaelli<sup>1</sup>, B. Salvachua Ferrando<sup>1</sup>,  
 P. Serrano Galvez<sup>1</sup>, M. Solfaroli Camillocci<sup>1</sup>, N. Turini<sup>10</sup>

<sup>1</sup>CERN, European Organization for Nuclear Research, Geneva, Switzerland

<sup>2</sup>Università degli Studi di Padova, Padova, Italy

<sup>3</sup>AGH University of Science and Technology, Kraków, Poland

<sup>4</sup>Institute of Nuclear Physics, Polish Academy of Sciences, Kraków, Poland

<sup>5</sup>Royal Holloway University of London, Egham Hill, Egham, United Kingdom

<sup>6</sup>Petersburg Nuclear Physics Institute, NRC “Kurchatov Institute”, Gatchina, Russia

<sup>7</sup>Deutsches Elektronen-Synchrotron, Hamburg, Germany

<sup>8</sup>Institute of Physics of the Czech Academy of Sciences, Prague, Czech Republic

<sup>9</sup>The University of Manchester, Manchester, United Kingdom

<sup>10</sup>Università degli Studi di Siena and Gruppo Collegato INFN di Siena, Siena, Italy

## Abstract

Bent crystals can deflect charged particles by trapping them within the potential well generated by neighboring crystalline planes and forcing them to follow the curvature of the crystal itself. This property has been extensively studied over the past decade at the CERN accelerator complex, as well as in other laboratories, for a variety of applications, ranging from beam collimation to beam extraction and in-beam fixed target experiments. In 2018, crystal collimators were operationally used for the first time at the Large Hadron Collider (LHC) during a special high- $\beta^*$  physics run with low-intensity proton beams, with the specific goal of reducing detector background and achieving faster beam halo removal. This paper describes the preparatory studies carried out by means of simulations, the main outcomes of the special physics run and plans for future uses of this innovative collimation scheme, including the deployment of crystal collimation for the High-Luminosity LHC upgrade.

## INTRODUCTION

The CERN Large Hadron Collider (LHC) is routinely used to accelerate and collide high-intensity proton beams [1]. Throughout Run 2 (2015-2018), it was operated at a top energy of 6.5 TeV, with typical beam populations of a few  $10^{14}$  protons per beam. In addition to the high-intensity, high-energy operation, special runs with dedicated machine and beam configurations were also performed in order to achieve specific experimental conditions.

In October 2018, one of the aforementioned special runs was carried out at the injection energy of 450 GeV, using low-intensity beams (up to about  $6 \cdot 10^{11}$  protons per beam)

and a special optics with a  $\beta^*$  (i.e. the optical function at the Interaction Points, IPs) larger than in normal operation. This special run was requested by the forward physics community to measure the proton-proton elastic cross section and extrapolate its nuclear part towards low values of momentum transfer [2]. Dedicated detectors housed in movable Roman Pots (XRP) [3] are transversely placed very close to the circulating beams in order to intercept particles scattered at small angles as result of collisions with low momentum transfer at the IP. Two sets of XRP stations are installed downstream of IP1 and IP5, and are operated by the ATLAS (ALFA) [4] and TOTEM [5] collaborations respectively. Only the vertical two-sided stations, whose layout is schematically illustrated in Fig. 1, were used for this run.

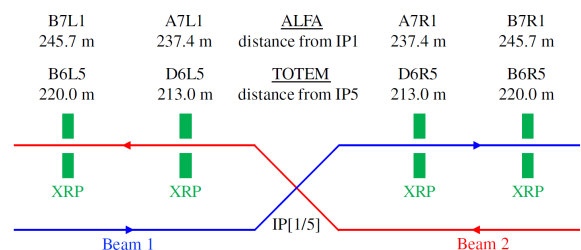


Figure 1: Illustrative layout of the vertical ALFA and TOTEM XRP stations around IP1 and IP5 [6].

The setup of this run posed several challenges from the accelerator physics point of view, requiring the design of dedicated beam optics [7] and collimation settings [8]. While machine protection requirements were relaxed thanks to the low stored beam energy of about 40 kJ (with respect to the stored energy of 350 MJ in nominal operation), the background induced at the detectors would have been intolerable without a dedicated halo collimation system. The feasibility of tight collimator settings necessary to position the XRPs as close as possible to the beam was identified as a major concern for the success of the run. In the standard LHC col-

\* Work supported by the HL-LHC Project

† marco.dandrea@cern.ch

‡ Currently at University of Oxford, Oxford OX1 2JD, United Kingdom

§ Currently at Fondazione CNAO, Strada Campeggi 53, 27100 Pavia, Italy

limation system [9–11], multiple stages of amorphous collimators installed in two dedicated Insertion Regions (IRs) are used to progressively outscatter halo particles in a multiturn cleaning process. However, an innovative technique which makes use of crystal collimators has been extensively studied as a way to improve the efficiency of the LHC collimation system, promising a faster cleaning process via a reduced multiturn halo population [12]. The peculiar needs of this special physics run provided an ideal scenario for the first operational use of crystal collimation at the LHC.

## CRYSTAL COLLIMATION AT THE LHC

Atoms in a crystal are arranged in a highly ordered microscopic structure, called a *crystalline lattice*. If the crystal is well oriented with respect to the trajectory of an impinging charged particle, the lattice is seen as a sequence of ordered planes of atoms. A particle impinging onto the crystal with specific impact conditions can then be trapped inside the electrostatic potential well generated by two neighboring planes and forced to travel in the nearly empty space between them for the full length of the crystal. This process is called *planar channeling*. If a particle is channeled by a bent crystal, its trajectory will be forced to follow the curvature of the crystalline planes. A few millimeter long crystal can thus be used to efficiently steer beam halo particles by tens of  $\mu\text{rad}$ , an effect corresponding to that of a magnetic field of hundreds of Tesla over the same length at nominal LHC beam energies. In a crystal-based collimation system, bent crystals are used as the primary collimation stage and deflect beam halo particles towards a single absorber, as schematically shown in Fig. 2. This innovative technique has been studied over the past decade to improve the performance of the LHC collimation system in view of its High-Luminosity upgrade (HL-LHC) [13–16], in particular for operation with nominal heavy-ion beam intensities.

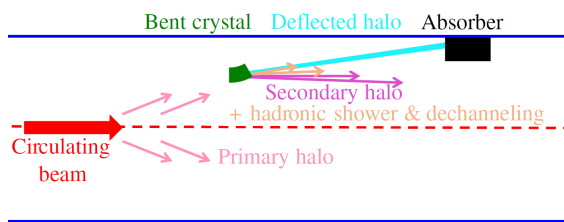


Figure 2: Schematic representation of the working principle of a crystal-based collimation system [6].

A test stand consisting of four silicon crystal collimators, two per beam and one per plane, is presently installed in the betatronic collimation Insertion Region (IR7) of the LHC [17]. The two vertical crystals used in the special physics run are provided by the UA9 collaboration and built at the Petersburg Nuclear Physics Institute (PNPI). Each crystal is mounted on a high-resolution goniometer, equipped with a piezo actuator and a stepper motor for the rotational and linear stage, respectively. The same high-performance motors with  $5\ \mu\text{m}$  resolution developed for standard LHC collimators are used for the linear movement. The piezo

Table 1: Settings (in Beam  $\sigma$ ) of Relevant Vertical Collimators for Different Configurations at Injection Energy

Collimator	IR	Nominal	Special Run Standard	Special Run Crystal
TCTPV.4[R/L]1.B[1/2]	2	13.0	2.7	13.0
TCTPV.4[R/L]5.B[1/2]	5	13.0	2.7	13.0/2.7
TCP.D6[R/L]7.B[1/2]	7	5.7	3.2	3.2
TCPCV.A6[L/R]7.B[1/2]	7	OUT	OUT	2.5
TCLA.A6[R/L]7.B[1/2]	7	10.0	2.5	2.7
TCLA.C6[R/L]7.B[1/2]	7	10.0	2.7	2.7
TCTPV.4[R/L]8.B[1/2]	8	13.0	2.7	13.0
TCTPV.4[R/L]1.B[1/2]	1	13.0	2.7	2.7/13.0

actuator provides an angular resolution below  $0.1\ \mu\text{rad}$  and an accuracy below  $1\ \mu\text{rad}$  [18]. These parameters are necessary in order to achieve and maintain channeling conditions throughout the entire machine cycle, as the channeling acceptance at LHC energies varies from about  $9.5\ \mu\text{rad}$  at 450 GeV to about  $2.5\ \mu\text{rad}$  at 7 TeV.

## PREPARATION OF THE SPECIAL PHYSICS RUN

Dedicated settings for the LHC collimation system were devised in order to comply with the specific goal of reducing the background rate at the XRPCs, placed close to the beams with an opening of  $3\ \sigma$  (where  $\sigma$  is the r.m.s. beam size, assuming a Gaussian distribution and normalized emittance  $\varepsilon^* = 3.5\ \mu\text{m}$ ). The nominal settings of vertical primary (TCP), absorber (TCLA), tertiary (TCT) and crystal (TCPC) collimators for normal operation at injection are reported in Table 1 in units of  $\sigma$ , along with the two schemes developed for the special run.

In what will be referred to in the following as the *standard scheme*, tungsten collimators (TLCAs and TCTs) are deployed in a two-stage hierarchy characterized by the tightest normalized settings ever used in the LHC [8]. In particular, a  $0.2\ \sigma$  retraction is present between the primary and secondary stage, with an additional  $0.3\ \sigma$  retraction between the secondary stage and the XRPCs. Tungsten collimators were chosen because of their higher absorption efficiency compared to all other collimators.

The *crystal scheme* was developed in parallel as an alternative way to achieve possibly even lower background rates [6]. The same settings as the standard scheme were taken as a starting point, but using a bent crystal as the primary stage. These settings were then optimized to relax margins and reduce the risk of small orbit drifts breaking the collimation hierarchy, while also improving the overall performance.

Semianalytic studies were carried out to evaluate if the channeled halo could be intercepted by the secondary stage even in these extreme conditions, by calculating the trajectory of deflected particles using the transfer matrix formalism. The final layout was then validated by complete multiturn tracking simulations performed with SixTrack, a

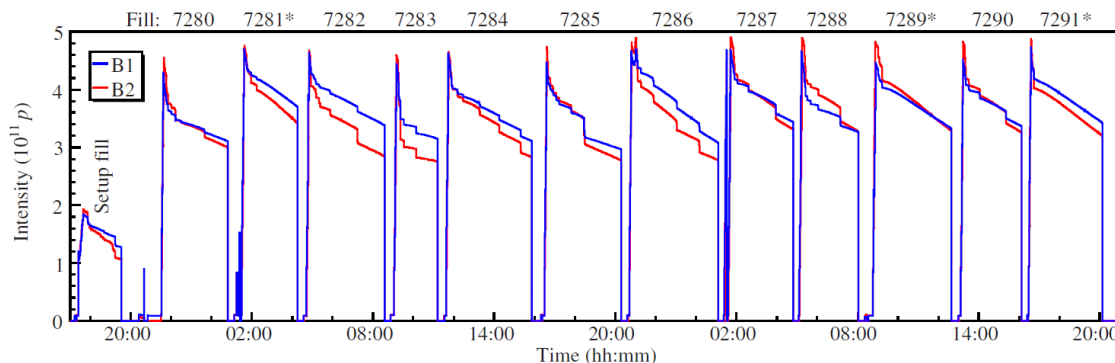


Figure 3: Beam intensity in fills performed during the special physics run. Crystal collimation fills are marked by \* [6].

single-particle tracking code widely used at CERN for simulating beam dynamics in circular accelerators [19–23]. A dedicated Monte-Carlo simulation routine within SixTrack models the interaction between proton beams and crystal collimators [24–27]. This setup allowed the expected background at the XRP and the improvement provided by crystals compared to standard collimation to be estimated.

An initial test run was carried out on 2 October 2018, during which promising results were obtained with both collimation schemes. In particular, the reference linear and angular positions to maximize the channeling performance were found for both crystals, allowing their deployment in operation interleaved with standard collimation settings.

## PERFORMANCE DURING THE SPECIAL PHYSICS RUN

The special physics run took place from 11 to 13 October 2018 with 450 GeV proton beams. After a first setup fill to validate the results obtained in the initial tests, two physics fills were dedicated to data taking with the standard and crystal collimation schemes, respectively. A preference for the standard scheme was expressed by ALFA, while TOTEM had better data quality with the crystal scheme but was also satisfied with the standard scheme. Thus, it was initially decided to keep the standard scheme for the subsequent fills. However, after four fills, it was necessary to recenter some of the collimators in order to keep the very tight margins between the primary and secondary collimation stages. As a result of this operation, the data quality for TOTEM was significantly worsened in the following fills. It was then decided to use the crystal scheme for two final fills, interleaved by a fill dedicated to ALFA using the standard scheme. A total of nine and three fills were carried out using the standard and crystal schemes, respectively. The beam intensity during each fill is shown in Fig. 3.

During each fill using the standard scheme, the background on the XRP was observed to increase over time up to values that could have jeopardized the measurement. As a result, it was necessary to perform a rescraping of the beam – a deep cut of the beam tails down to  $2\sigma$ , as done at the beginning of every fill – about once every hour. The tungsten collimators are inserted towards the beam in order to dispose of the accumulated multiturn beam halo and

bring the background rate down to a satisfactory level. During this operation, the ALFA XRP needed to be retracted from the beam due to concerns for radiation to electronics. Thus, the whole procedure took about 6 minutes each time. The rescrapings can be seen in Fig. 3 as decreasing steps in beam intensity during fills which make use of the standard scheme. In the fills using the crystal scheme, on the other hand, the background rate was observed to increase much more slowly and no rescraping was needed, leading to a 10% more efficient data taking. Furthermore, crystals were quickly deployed using an automated sequence to insert them directly in optimal channeling using the reference positions and orientations identified during the test run. A quick check was nevertheless performed after each insertion, confirming that the crystals could reliably be deployed. These observations are an important milestone, showing the efficiency of the current crystal collimator hardware and controls.

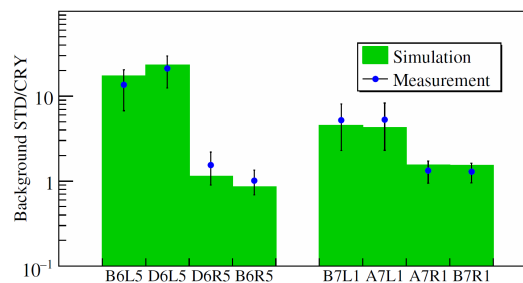


Figure 4: Comparison of the measured and simulated background ratio at the XRP stations [6].

The beam-related background with the two schemes was evaluated using non-colliding bunches, in order to remove the contribution of physics background coming from collisions. High-sensitivity data provided by ALFA and TOTEM were used to quantify the observed background rate. The ratio between the background measured with the crystal and standard system at the XRP stations is in very good qualitative and quantitative agreement with simulations, as shown in Fig. 4. The background rate is directly linked to the multiturn halo, formed by particles that keep circulating in the machine after their first interaction with the collimation system. These particles need to be absorbed as quickly as possible to achieve efficient cleaning. A dedicated simulation campaign showed that 99% of the particles impacting on

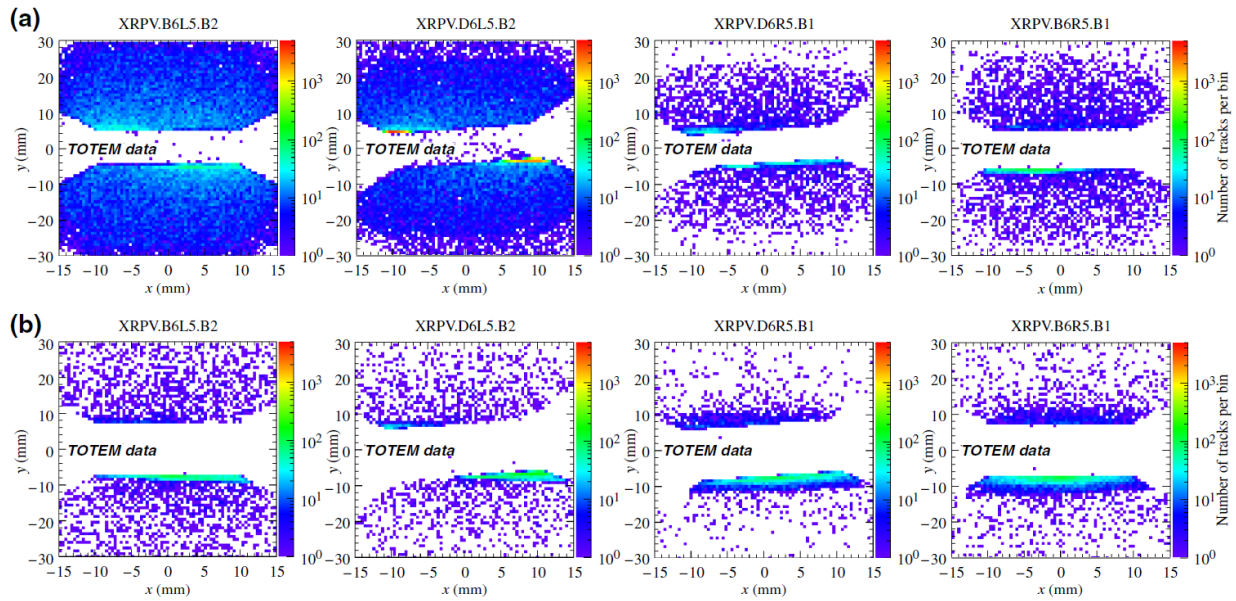


Figure 5: Measured background hit pattern at the TOTEM XRP stations using standard (a) and crystal (b) collimation [6].

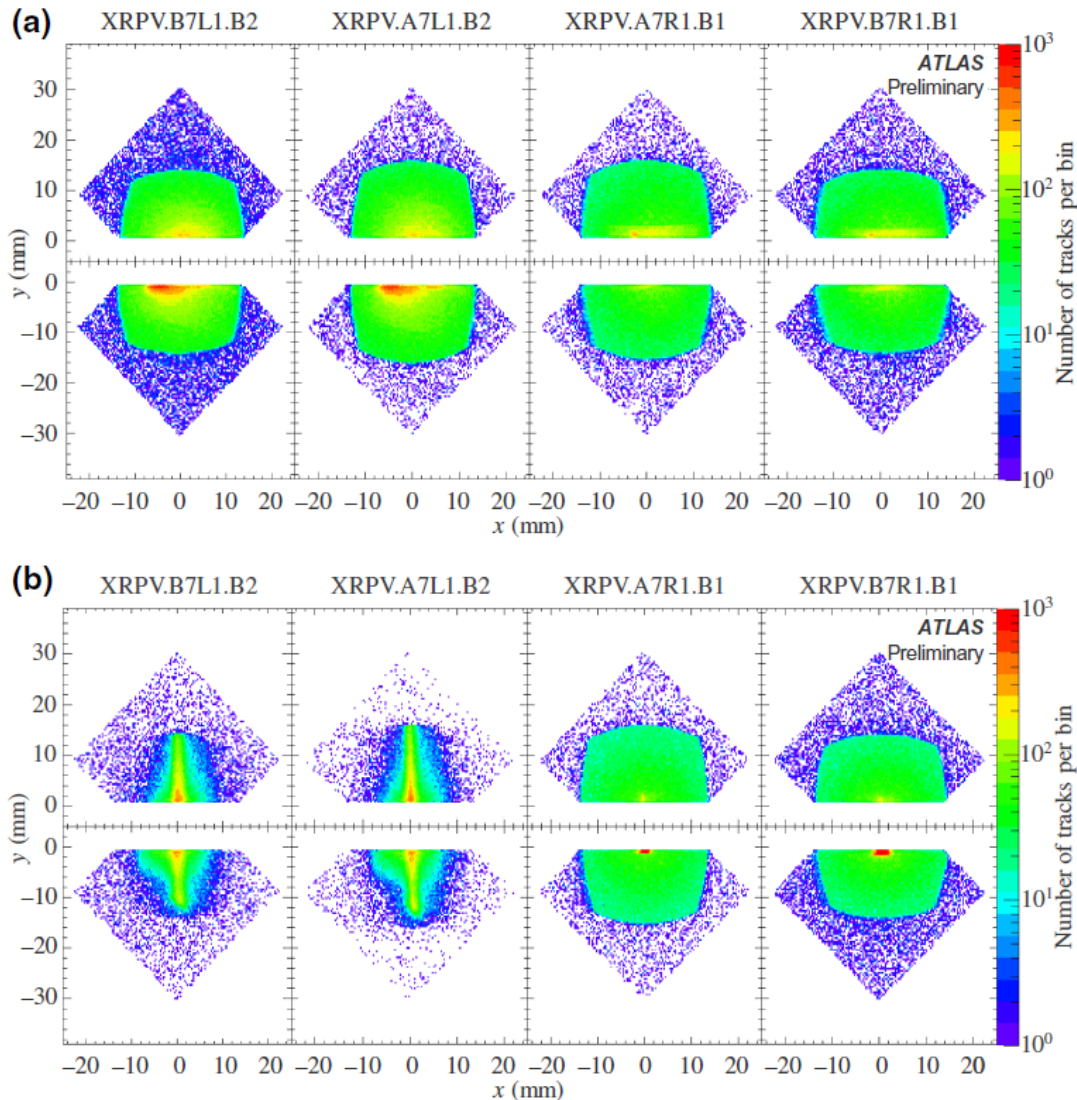


Figure 6: Measured background hit pattern at the ALFA XRP stations using standard (a) and crystal (b) collimation [6].

a crystal primary collimator are absorbed by the collimation system in the same turn, while this percentage is reduced to only 66% for a standard primary collimator. The observed performance provides evidence for the faster halo removal achievable with crystals. More details can be found in [6].

Figures 5 and 6 show the background hit pattern measured with non-colliding bunches at the TOTEM and ALFA XRP's respectively, using the two collimation schemes. In both cases, the observed pattern is in very good agreement with simulations [6]. In particular, structures due to the multiturn halo hitting the detector edges facing the beam are significantly suppressed when crystals are used. This enabled efficient offline event reconstruction and an improved data quality for TOTEM. For ALFA, however, the hit pattern on the Beam 2 XRP's when crystals are used is more focused on the central region, where the physics signal is expected, leading to a less efficient offline background subtraction. This problematic feature of the background distribution was not identified during preliminary studies as the main focus was the optimization of the background rate, rather than the hit pattern. A full offline analysis showed that the irreducible background is increased from about 0.5% with the standard scheme to about 1.5% with the crystal scheme, which is still satisfactory for the measurement. Nevertheless, a dedicated simulation campaign was carried out after the physics run in order to understand this behavior and investigate possible mitigation solutions. The source of the hit pattern was found to be particles that undergo dechanneling after hitting the crystal in IR7 and bypass the secondary stage because of the lower deflection acquired. These particles then circulate in the machine for about 10 turns before hitting a tungsten collimator in IR3. A fraction of these particles escape the collimator and finally hit the ALFA XRP's in Beam 2 on the same turn. The peculiar shape of the hit pattern is related to the fractional betatron phase advance between the collimator and the XRP's. Simulations show that retracting the IR3 collimator would have removed the problematic distribution and led to an even larger background rate reduction for ALFA, while the gain would have been reduced for TOTEM. More details can be found in [6].

## FUTURE PROSPECTS OF CRYSTAL COLLIMATION

The performance achieved by the crystal scheme in the special physics run is a crucial milestone, proving the maturity and reliability reached by this innovative collimation technique, as well as by the associated hardware and control systems. Furthermore, the good qualitative and quantitative agreement between observed results and simulations is a good indicator of the accuracy of the currently available tools. The predictive power of simulations could make it possible to achieve even better performance should this scheme be defined as baseline for future low-intensity special runs.

The main challenge for the use of crystal collimation in operation with high-intensity proton beams is the safe disposal of the power from channeled halo particles that can reach

up to 500 kW, requiring the design of a special absorber. However, much lower power depositions are expected with high-intensity ion beams, allowing the channeled halo to be safely intercepted with a standard secondary collimator [28]. The good outcome of the special physics run and the demonstration of the cleaning improvement provided by crystal collimation with Pb ion beams [15] were key ingredients in the decision to include crystal collimation in the HL-LHC upgrade baseline programme for use in operation with ion beams starting in Run 3 [29, 30].

Bent crystals are highly versatile tools that lend themselves to a variety of purposes aside from collimation, including advanced techniques of beam extraction and manipulation, as well as applications to fixed target experiments currently studied in the Physics Beyond Colliders framework [31–33]. The outcome of this special physics run shows that crystals can be deployed safely and efficiently in these highly specialized scenarios.

## CONCLUSIONS

Crystal collimation was used in operation at the LHC for the first time during a special high- $\beta^*$  physics run. Crystals were aligned during preparatory tests and automatically deployed in channeling orientation during the physics fills. Data provided by the ATLAS (ALFA) and TOTEM collaborations show that the experimental background at the detectors was significantly reduced thanks to the faster halo cleaning process provided by the crystal collimation scheme. This led to a more efficient data taking and an improved data quality with respect to the standard collimation scheme. Additional simulation studies show that the background hit pattern could be improved by adjusting the settings of other collimators, leaving room for further optimization in view of future runs. The good performance achieved in this run was a crucial milestone demonstrating the maturity reached by this innovative collimation scheme, as well as that of the associated hardware and control system, allowing bent crystals to be safely and efficiently used for beam manipulations in state-of-the-art machines such as the LHC. This opens the way for more synergies between accelerator and high-energy physics, and, along with the demonstrated cleaning performance with high-intensity ion beams, was a contributing factor in the decision to include crystal collimation in the baseline for the next runs of the LHC and HL-LHC.

## ACKNOWLEDGEMENTS

The experimental data gathered during the special physics run were kindly provided by the ATLAS (ALFA) and TOTEM collaborations. Crystal collimation tests at the LHC are carried out with the support of the UA9 collaboration, which provided and characterized the bent crystals prior to the installation in the machine. The crystals used in the special run were manufactured by PNPI. Research on crystal collimation for the LHC is supported by the HL-LHC Project. Crucial contributions from the CERN BE-ABP, BE-CEM, BE-OP and SY-STI groups to the preparation and carrying out of the run are also kindly acknowledged.

## REFERENCES

- [1] O. Brüning *et al.*, “LHC Design Report”, in *CERN Yellow Reports Monographs*, 2004. doi:10.5170/CERN-2004-003-V-1
- [2] G. Antchev *et al.*, “First determination of the  $\rho$  parameter at  $\sqrt{s} = 13$  TeV: Probing the existence of a colourless C-odd three-gluon compound state”, *Eur. Phys. J. C*, vol. 79, p. 785, 2019. doi:10.1140/epjc/s10052-019-7223-4
- [3] M. Oriunno *et al.*, “The Roman Pot for the LHC”, in *Proc. EPAC’06*, Edinburgh, UK, 2006, paper MOPLS013, pp. 562–564.
- [4] S. A. Khalek *et al.*, “The ALFA Roman Pot detectors of ATLAS”, *J. Instrum.*, vol. 11, p. 11013, 2016. doi:10.1088/1748-0221/11/11/P11013
- [5] G. Anelli *et al.*, “The TOTEM experiment at the CERN Large Hadron Collider”, *J. Instrum.*, vol. 3, p. 08007, 2008. doi:10.1088/1748-0221/3/08/S08007
- [6] D. Mirarchi *et al.*, “Reducing Beam-Related Background on Forward Physics Detectors Using Crystal Collimation at the Large Hadron Collider”, *Phys. Rev. Applied*, vol. 14, p. 064066, 2020. doi:10.1103/PhysRevApplied.14.064066
- [7] H. Burkhardt, “High-Beta Optics and Running Prospects”, *Instruments*, vol. 3, p. 22, 2019. doi:10.3390/instruments3010022
- [8] H. Garcia Morales *et al.*, “Tightest collimation system in the LHC”, (to be published).
- [9] R. Assmann *et al.*, “The final collimation system for the LHC”, in *Proc. EPAC’06*, Edinburgh, UK, Jun. 2006, paper TUODFI01, pp. 986–988.
- [10] R. Bruce *et al.*, “Simulations and measurements of beam loss patterns at the CERN Large Hadron Collider”, *Phys. Rev. Spec. Top.-Accelerators Beams*, vol. 17, p. 081004, 2014. doi:10.1103/PhysRevSTAB.17.081004
- [11] S. Redaelli, R. Bruce, A. Lechner, and A. Mereghetti, “Chapter 5: Collimation system”, in *CERN Yellow Reports Monographs*, vol. 10, pp. 87–114, 2020. doi:10.23731/CYRM-2020-0010.87
- [12] W. Scandale and A. Taratin, “Channeling and volume reflection of high-energy charged particles in short bent crystals. Crystal assisted collimation of the accelerator beam halo”, *Phys. Rep.*, vol. 815, pp. 1-107, 2019. doi:10.1016/j.physrep.2019.04.003
- [13] W. Scandale *et al.*, “Observation of channeling for 6500 GeV/c protons in the crystal assisted collimation setup for LHC”, *Phys. Lett. B*, vol. 758, p. 129, 2016. doi:10.1016/j.physletb.2016.05.004
- [14] R. Rossi, “Experimental assessment of crystal collimation at the Large Hadron Collider”, Ph.D. thesis, Università La Sapienza di Roma, Roma, Italy, 2017.
- [15] M. D’Andrea, “Applications of crystal collimation to the CERN Large Hadron Collider (LHC) and its High Luminosity upgrade project (HL-LHC)”, Ph.D. thesis, Università degli Studi di Padova, Padova, Italy, 2020.
- [16] HL-LHC Crystal Collimation Day, <https://indico.cern.ch/event/752062/>
- [17] D. Mirarchi, G. Hall, S. Redaelli, and W. Scandale, “Design and implementation of a crystal collimation test stand at the Large Hadron Collider”, *Eur. Phys. J. C*, vol. 77, p. 424. doi:10.1140/epjc/s10052-017-4985-4
- [18] A. Masi *et al.*, “Goniometer and controls”, presented at HL-LHC Crystal Collimation Day, 2018.
- [19] SixTrack – 6D Tracking Code, <http://sixtrack.web.cern.ch/SixTrack/>.
- [20] F. Schmidt *et al.*, “SixTrack users’s reference manual, Version 5.4.3”, CERN, Geneva, Switzerland, 2019.
- [21] G. Ripken and F. Schmidt, “A symplectic six-dimensional thin lens formalism for tracking”, CERN, Geneva, Switzerland, 1995, Rep. CERN-SL-95-12-AP.
- [22] G. Robert-Demolaize, R. Assmann, S. Redaelli, and F. Schmidt, “A New Version of SixTrack with Collimation and Aperture Interface”, in *Proc. PAC’05*, Knoxville, TN, USA, May 2005, paper FPAT081, pp. 4084–4086.
- [23] R. Bruce *et al.*, “Status of SixTrack with collimation”, in *CERN Yellow Report Conference Proceedings*, vol. 2, pp. 1–10, 2015. doi:10.23732/CYRCP-2018-002.1
- [24] D. Mirarchi, S. Redaelli, and W. Scandale, “Crystal implementation in SixTrack for proton beams”, in *CERN Yellow Report Conference Proceedings*, vol. 2, pp. 91–108, 2015. doi:10.23732/CYRCP-2018-002.91
- [25] V. Previtali, “Performance evaluation of a crystal-enhanced collimation system for the LHC”, Ph.D. thesis, EPFL, Lausanne, Switzerland, 2010.
- [26] D. Mirarchi, “Crystal collimation for LHC”, Ph.D. thesis, Imperial College, London, UK, 2015.
- [27] D. Mirarchi, G. Hall, S. Redaelli, and W. Scandale, “A crystal routine for collimation studies in circular proton accelerators”, *Nucl. Instrum. Methods Phys. Res. Sect. B*, vol. 355, pp. 278–382, 2015. doi:10.1016/j.nimb.2015.03.026
- [28] C. Bahamonde, A. Lechner, and R. Rossi, “Crystal channeling of ions on different TCSG materials”, presented at LHC Collimation Upgrade Specification Meeting, 2018.
- [29] O. Aberle *et al.*, “High-Luminosity Large Hadron Collider (HL-LHC): Technical design report”, in *CERN Yellow Reports Monographs*, vol. 10, 2020. doi:10.23731/CYRM-2020-0010
- [30] M. D’Andrea *et al.*, “Crystal collimation of 20 MJ heavy-ion beams at the HL-LHC”, in *Proc. IPAC’21*, Campinas, SP, Brazil, May 2021, pp. 2644–2647. doi:10.18429/JACoW-IPAC2021-WEPAB023
- [31] J. Jaeckel, M. Lamont, and C. Vallée, “The quest for new physics with the Physics Beyond Colliders programme”, *Nat. Phys.*, vol. 16, p. 393, 2020.
- [32] C. Barschel, “Report from the LHC Fixed Target working group of the CERN Physics Beyond Colliders Forum”, CERN, Geneva, Switzerland, 2019, Rep. CERN-PBC-REPORT-2019-001.
- [33] D. Mirarchi, A. Fomin, S. Redaelli, and W. Scandale, “Layouts for fixed-target experiments and dipole moment measurements of short-lived baryons using bent crystals at the LHC”, *Eur. Phys. J. C*, vol. 80, p. 1, 2020. doi:10.1140/epjc/s10052-020-08466-x

# IMPROVEMENT OF CAPTURE RATIO FOR AN X-BAND LINAC BASED ON MULTI-OBJECTIVE GENETIC ALGORITHM\*

Junyang Li, Tongning Hu<sup>†</sup>, Jun Yang, Bingqian Zeng, Hongjie Xu, Lanxin Nie  
Huazhong University of Science and Technology, Wuhan, China

## Abstract

Electron linear accelerators with an energy of ~MeV are widely required in industrial applications. Whereas miniaturized accelerators, especially those working at X-band, attract more and more attention due to their compact structures and high gradients. Since the performance of a traveling wave (TW) accelerator is determined by its structures, considerable efforts must be made for structure optimization involving numerous and complex parameters. In this context, functional key parameters are obtained through deep analysis for structure and particle motion characteristics of the TW accelerator, then a multi-objective genetic algorithm (MOGA) is successfully applied to acquire an optimized phase velocity distribution which can contribute to achieving a high capture ratio and a low energy spread. Finally, a low-energy X-band TW tube used for rubber vulcanization is taken as an example to verify the reliability of the algorithm under a single-particle model. The capture ratio is 91.2%, while the energy spread is 5.19%, and the average energy is 3.1MeV.

## INTRODUCTION

Electron beams with energy of ~MeV have been widely applied in life and materials sciences, industrial radiography, wastewater treatment, non-destructive testing, and other fields [1-4]. In recent years, Chiang Mai University in Thailand has researched applying electron beam of ~MeV to rubber vulcanization. The research on vulcanization of rubber was carried out by Chiang Mai University in Thailand Considering the difference in material thickness and density, the beam energy is generally 1-4 MeV [5-7].

RF linac is a commonly used scheme to obtain electron beam of ~MeV, but the traditional S-band accelerator structure and supporting power sources are relatively large, which is not suitable for cargo inspection and other occasions requiring accelerator miniaturization [8]. In contrast, the X-band increases the operating frequency by about three times, which has the advantages of a high acceleration gradient and compact structure. At present, many accelerator laboratories have developed X-band accelerators [9-13].

In the design of phase velocity for the TW tubes, it is often necessary to try repeatedly according to engineering experience, which is time-consuming and difficult to gain the optimal performance parameters. In 2002 Deb proposed nondominated sorting genetic algorithm II (NSGA-II), which has good convergence and diversity in solving multi-objective problems [14]. Based on NSGA-II, many

accelerator-related optimization problems have been completed, such as beam matching and beam transport in the low and medium energy section of a modern hadron linac [15], undulator taper profile and focusing scheme of a seeded free electron laser (FEL) [16], the optimal working point of a linac driver for a seeded FEL [17], the nonlinear lattice and dynamic aperture for the high energy photon source storage ring [18,19].

In consequence, it is of engineering significance to optimize the phase velocity of low-energy X-band TW tubes by using the multi-objective genetic algorithm. After introducing the mathematical and physical model of TW acceleration structure, NSGA-II is used to obtain the Pareto front with the goal of high capture ratio and low energy spread. At last, one of the points in the Pareto front is selected to analyze single-particle motion.

## DESIGN CONSIDERATIONS OF X-BAND LINAC

As mentioned in the last section, MOGA is a good choice for optimizing the TW tubes. For sake of applying the algorithm better, it is necessary to convert physics problems into mathematics problems reasonably.

### Basic Theory

Designing the TW tubes with the iris-loaded waveguide structure requires the relationships between the field strength  $E$  and the power  $P$ , as a consequence of beam loading effect must be considered in actual operation, the relationships should be expressed as follows.

$$E(z) = \sqrt{2\alpha Z_s P(z)} \quad (1)$$

$$\frac{dP(z)}{dz} = -2\alpha P(z) - IE(z) \quad (2)$$

where  $\alpha$  is the attenuation factor,  $Z_s$  is the shunt impedance,  $z$  is the longitudinal position in the TW tubes, and  $I$  is the average beam current.

As for Eq. (1) and (2),  $P$  is given at the beginning of the design,  $\alpha$  and  $Z_s$  are determined by designing the structure according to the target field strength.  $\alpha$  could be directly obtained by the two-dimensional electromagnetic field software SUPERFISH, while  $Z_s$  could be calculated by the group velocity  $v_g$ , the quality factor  $Q$ , and the angular frequency  $\omega$ , stated as the following.

$$\alpha = \frac{\omega}{2v_g Q} \quad (3)$$

The above-mentioned field strength distribution should be designed according to the quality requirements of the

\* Work supported by National Natural Science Foundation of China (NSFC) under Project Numbers 11905074.

<sup>†</sup> TongningHu@hust.edu.cn

output particles. The longitudinal motion of particles under the field strength is shown as:

$$\frac{d\gamma}{dz} = -\frac{eE}{m_0c^2} \sin \varphi \quad (4)$$

$$\frac{d\varphi}{dz} = \frac{2\pi}{\lambda} \left( \frac{1}{\beta_p} - \frac{\gamma}{\sqrt{\gamma^2 - 1}} \right) \quad (5)$$

where  $\gamma$  is the relativistic mass factor,  $\varphi$  is the phase,  $e$  is the electron charge,  $m_0c^2$  is the rest energy of the electron,  $\lambda$  is the radio frequency wavelength, and  $\beta_p$  is the cavity phase velocity.

### Preparations for Optimizing Design

As introduced in the last subsection,  $\alpha$  and  $Z_s$  are calculated by SUPERFISH, while different  $\beta_p$  have different  $\alpha$  and  $Z_s$ . The following Fig. 1 shows the 1.5 cell model at  $\beta_p=0.50$  in SUPERFISH and the corresponding single-cavity three-dimensional model.

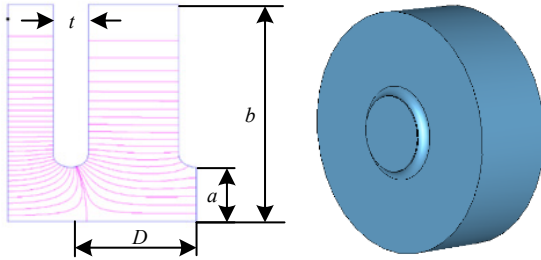


Figure 1:  $\beta_p=0.50$  (a) 1.5 cell two-dimensional model, (b) three-dimensional model of single-cavity, where  $D$  is the cavity length,  $a$  is the iris radius,  $b$  is the waveguide radius, and  $t$  is the iris thickness.

As we know, the low-energy linac needs to rely on the variable  $\beta_p$  to achieve particle capture, so the front end of the TW tubes has a wide variation. Thus, a reasonable design will be considered about the distribution of  $\beta_p$  in the cavity chain to obtain a higher capture ratio. The application of the MOGA can improve the design efficiency, but the relationship between the parameters needs to be established in advance, especially the changes of  $\alpha$  and  $Z_s$  with  $\beta_p$ .

Taking the initial power of 1 MW and the initial beam energy of 45keV as an example, to achieve an acceleration of about 3MeV and a high capture ratio, firstly calculate the field strength according to Eq. (1) and Eq. (2) for each cavity, then exit energy and phase could be obtained according to Eq. (4) and Eq. (5), which determines capture ratio and energy spread. As the key parameters, the calculations for  $\alpha$  and  $Z_s$  are time-consuming and inconvenient because SUPERFISH must be re-called cell by cell in the programming. The range of  $\beta_p$  is selected as [0.35,1.11] due to the initial energy of the electrons and several points of  $\alpha$  and  $Z_s$  are chose to fit. To improve

efficiency, the variation of  $\alpha$  with  $\beta_p$  is expressed by Gaussian fitting and the variation of  $Z_s$  with  $\beta_p$  is expressed by polynomial fitting. The expressions are written as.

$$\alpha = 25510 \exp \left( - \left( \frac{\beta_p + 0.8152}{0.3694} \right)^2 \right) + 18.73 \exp \left( - \left( \frac{\beta_p + 0.5809}{0.6113} \right)^2 \right) + 1.888 \exp \left( - \left( \frac{\beta_p + 0.8879}{2.733} \right)^2 \right) \quad (6)$$

$$Z_s = -132.05\beta_p^5 + 657.31\beta_p^4 - 1320.5\beta_p^3 + 1292.7\beta_p^2 - 434.43\beta_p + 47.908 \quad (7)$$

Corresponding fitting curves of  $\alpha$  and  $Z_s$  are displayed in Fig. 2. Obviously, the fitting curves are consistent with the calculation results of SUPERFISH well. The sum of squares due to error (SSE) of the attenuation factor is  $9.3391 \times 10^{-5}$  and coefficient of determination R-square is 1, SSE of the shunt impedance is 0.0046 and R-square is also 1. Since the closer R-square is to 1, the better the data fit, it is feasible to solve  $\alpha$  and  $Z_s$  by fitting functions.

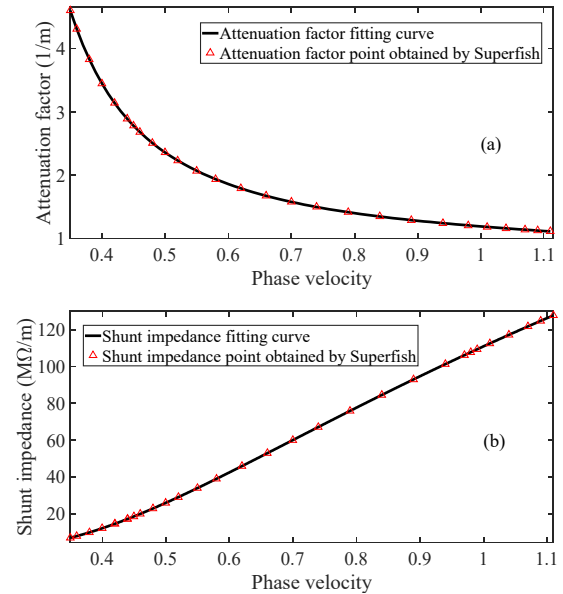


Figure 2: Fitting at different phase velocities (a) attenuation factor, (b) shunt impedance.

Note that, to simplify the structure design and realization, the same iris radius is used here. Combining previous literature and engineering experiences [20], the structure of the six-segment cavity chain is adopted. As the energy of the electron is lower, the increment of the electron phase velocity  $\Delta\beta_e$  to a certain energy increase is larger, so it is reasonable that the number of cavities in each segment gradually increases while the corresponding variable range of  $\beta_p$  gradually decreases. The initial energy of the electron

Content from this work may be used under the terms of the CC BY 3.0 licence (© 2021). Any distribution of this work must maintain attribution to the author(s), title of the work, publisher, and DOI

is 45 keV, and the corresponding electron phase velocity  $\beta_e$  is 0.394. Let the variable range of the first segment  $\beta_p$  is around 0.394, then gradually increase the value of each segment  $\beta_p$ . Finally, the range of  $\beta_p$  and the number of cells for the six segments are shown in the table below.

Table 1: The Range of  $\beta_p$  and the Number of Cells for the Six Segments

	1	2	3	4	5	6
$\beta_{p\min}$	0.36	0.50	0.72	0.92	0.96	0.98
$\beta_{p\max}$	0.43	0.57	0.75	0.95	0.97	0.99
Number of cells	4	5	5	6	6	16

### SIMULATIONS BASED ON MOGA

To verify the optimizing scheme, NSGA-II is applied to chase phase velocity distribution in this section.

#### MOGA Combined with the TW Tubes

In the cases of multi-objective X-band TW tubes,  $\beta_p$  of each cavity is chosen as the variable, while the capture ratio  $\eta$  and the energy spread  $\sigma$  are set as the goals.  $\eta$  and  $\sigma$  are determined by the energy and phase at the exit of the linac.

The electrons that can be stably accelerated in the TW tubes are called captured electrons. The expression of  $\eta$  is as follows:

$$\eta = \frac{M}{N} \times 100\% \quad (8)$$

where  $N$  is the initial number of electrons whose entrance phase is uniformly distributed in  $[-360^\circ, 0]$ . Suppose  $\varphi_1$  is the median phase of these  $N$  electrons at the last cell, and  $M$  is the number of electrons whose phase at the exit is  $[\varphi_1 - 180^\circ, \varphi_1 + 180^\circ]$ . In this context,  $N$  is set to 500, so that the accuracy of the capture ratio is 0.2%.

Since the program obtains  $M$  energy points, it is more convenient to measure energy spread in the form of root mean square. The expression of  $\sigma$  is as follows:

$$\sigma = \frac{1}{\bar{W}} \sqrt{\frac{1}{M} \sum_{i=1}^M (W_i - \bar{W})^2} \quad (9)$$

where  $W_i$  is the exit energy of different initial phases, and  $\bar{W}$  is the average energy. Both  $W_i$  and  $\bar{W}$  are for the captured particles.

The optimization process of the TW tubes structure is shown in Fig. 3. First, 200 population individuals with different  $\beta_p$  are initialized, and then the fitness function values of individuals in the population are calculated and fast non-dominated sorting is performed. The individuals with a small non-dominated serial number are selected through

the tournament. If the serial number is the same, the previous individual will be chosen. After crossover and mutation, the first generation of offspring population is obtained and merged with the parent population. Then calculate the fitness function value for the merged population and get the stratification result after fast non-dominated sorting. After completing the above steps, calculate the crowdedness of the individuals and fill in the individuals with small non-dominated serial numbers and high crowdedness into the new parent population up to 200. Finally, select, crossover and mutation as before to get the offspring population. After 30 generations of cycles, the individuals with the smallest non-dominated serial number are output.

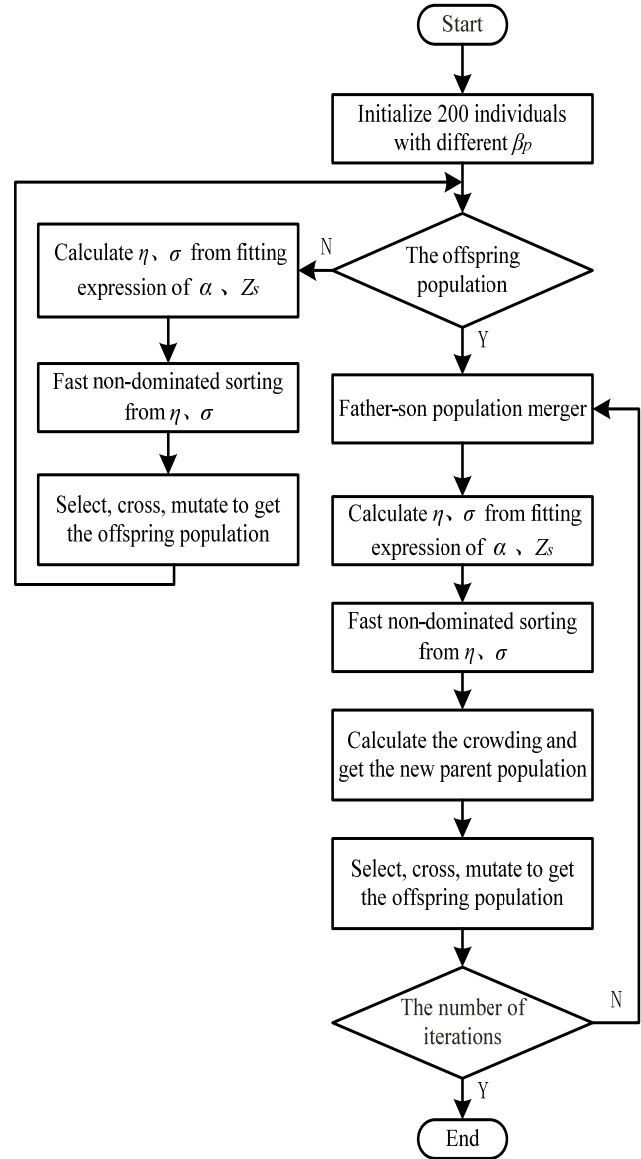


Figure 3: Flow chart of optimizing the TW tubes with NSGA-II.

The eight Pareto front points obtained by using NSGA-II are shown in Fig. 4(a). The corresponding capture ratio ranges from 87.4% to 92.0%, and the energy spread ranges from 4.18% to 5.52%.

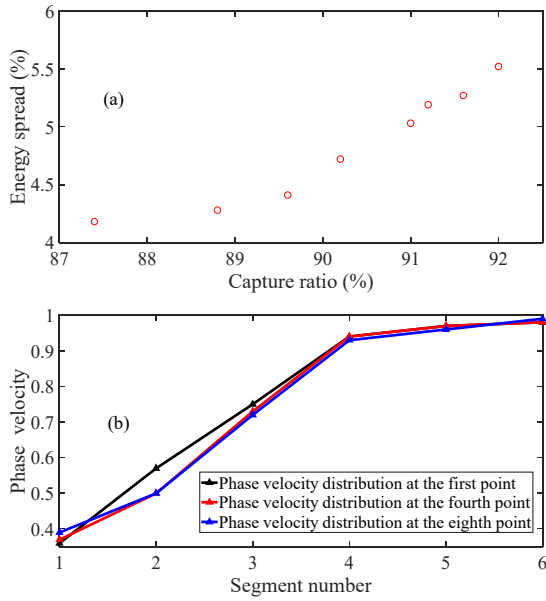


Figure 4: Pareto front and phase velocity distribution.

In Fig. 4(a), take the representative points 1, 4, and 8 from left to right and gain the corresponding phase velocity distribution as shown in Fig. 4(b). It can be seen that the capture ratio and energy spread are related to the first two segments of the cavity chain. The greater the phase velocity of the first segment, the higher the capture ratio and the smaller the energy spread.

### Beam Dynamics Based on Single-particle Model

To analyze the movement process of electrons in the TW tubes, the sixth Pareto front point of Fig. 4(a) from left to right is selected. The phase and energy change along with the longitudinal position of the TW tubes are shown in the Fig. 5 below.

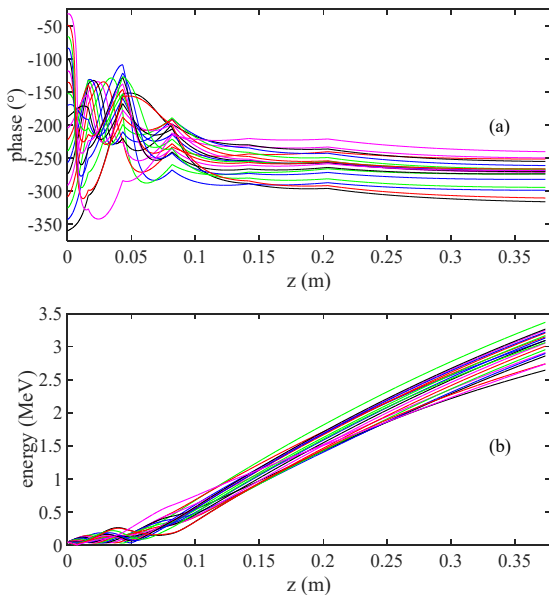


Figure 5: Change along with the longitudinal position  $z$  of the TW tubes (a) Phase, (b) Energy.

It can be seen from Figure 5(a) that  $328^\circ$  can be captured with an initial phase width of  $360^\circ$ , and the capture ratio is 91.2%. The captured electrons oscillate in phase in the first half of the cavity chain, and the phase gradually decreases and stabilizes after 0.1m in the longitudinal position. There are non-differentiable points in the phase distribution due to the sudden change of  $\beta_p$  at the segment junction, and its number and position corresponding to the number and position of  $\beta_p$  sudden change. It can be seen from Fig. 5(b) that the energy of the captured electrons oscillates with the phase oscillation in the first half of the cavity chain. Since the phase gradually stabilizes after 0.1m in the longitudinal position, the energy increases approximately linearly.

To analyze the capture ratio and energy spread, the distributions of phase and energy at the exit of the TW tubes are plotted as shown in the Fig. 6 below.

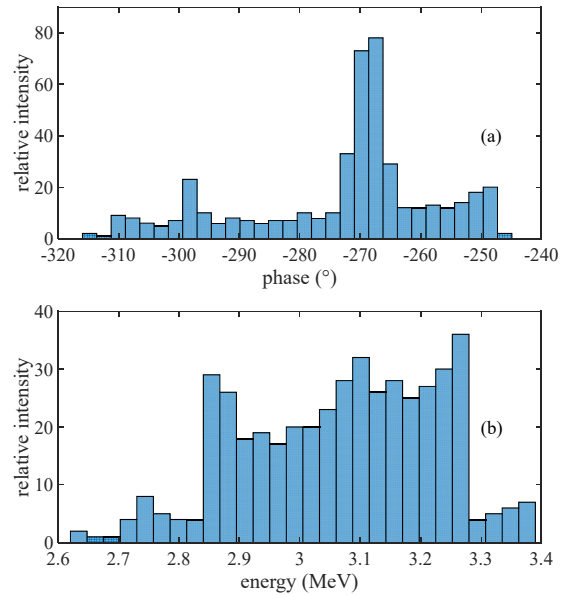


Figure 6: Distribution (a)exit phase, (b)exit energy.

It can be seen from Fig. 6(a) that the exit phase of the captured electrons is compressed to  $75^\circ$ . The exit phase of most electrons is concentrated at the maximum acceleration phase of  $-270^\circ$ , so the cavity with  $\beta_p$  of 0.99 can be expanded to increase the exit energy. It can be seen from Fig. 6(b) that the exit energy of the captured electrons is distributed within 2.6~3.4MeV, most of which are concentrated in 2.9~3.3MeV. The average energy is 3.1MeV and the energy spread is 5.19%.

## CONCLUSION

For the reasonable application of the MOGA in improving the design efficiency for X-band linac, the fitting of the attenuation factor and the shunt impedance with respect to the phase velocity distribution of the acceleration unit is proposed in the structure of identical iris radius. The coefficient of determination R-square shows that the fitted model is feasible. To simplify the structural design and improve the capture ratio, the form of six segments is adopted and the variable phase velocity range of each section is

given. By establishing a quantitative relationship between capture ratio, energy spread and exit phase, exit energy, the fitness function is linked to the output of the single-particle model. Based on NSGA-II, the phase velocity distribution with high capture ratio and low energy spread is obtained, which provides the design basis for ~MeV TW cube that can be used in the industry. In addition, the algorithm can be extended to the situation where the phase velocity and field strength can be changed cell by cell, resulting in a higher capture ratio and lower energy spread.

## REFERENCES

- [1] V. M. Tsakanov *et al.*, "AREAL low energy electron beam applications in life and materials sciences," *Nuclear Instruments and Methods in Physics Research Section A: Accelerators, Spectrometers, Detectors and Associated Equipment*, vol. 829, pp. 248-253, 2016. doi:10.1016/j.nima.2016.02.028
- [2] A. J. Antolak, "Overview of Accelerator Applications for Security and Defense," in *Reviews of Accelerator Science and Technology*: World Scientific, 2016, pp. 27-36. doi:10.1142/9789813108905\_0002
- [3] S. Machi, "Trends for Electron Beam Accelerator Applications in Industry," *Reviews of Accelerator Science and Technology*, vol. 04, no. 01, pp. 1-10, 2011. doi:10.1142/S1793626811000562
- [4] W. A. Reed, "Nondestructive Testing and Inspection Using Electron Linacs," in *Industrial Accelerators and Their Applications*: World Scientific, 2011, pp. 307-369. doi:10.1142/9789814307055\_0008
- [5] P. Apiwatanakul and S. Rimjaem, "Electron beam dynamic study and Monte Carlo simulation of accelerator-based irradiation system for natural rubber vulcanization," *Nuclear Instruments and Methods in Physics Research Section B: Beam Interactions with Materials and Atoms*, vol. 466, pp. 69-75, 2020. doi:10.1016/j.nimb.2020.01.012
- [6] S. Rimjaem, E. Kongmon, M. W. Rhodes, J. Saisut, and C. Thongbai, "Electron linear accelerator system for natural rubber vulcanization," *Nuclear Instruments and Methods in Physics Research Section B: Beam Interactions with Materials and Atoms*, vol. 406, pp. 233-238, 2017. doi:10.1016/j.nimb.2016.11.016
- [7] J. Saisut, M. W. Rhodes, E. Kongmon, S. Rimjeam, and C. Thongbai, "RF System of Linear Accelerator for Natural Rubber Research," *Journal of Physics: Conference Series*, vol. 1144, p. 012157, 2018. doi:10.1088/1742-6596/1144/1/012157
- [8] S. V. Kutsaev, "Novel Technologies for Compact Electron Linear Accelerators (Review)," *Instruments and Experimental Techniques*, vol. 64, no. 5, pp. 641-656, 2021. doi:10.1134/S0020441221050079
- [9] S. V. Kutsaev *et al.*, "Compact X-Band electron linac for radiotherapy and security applications," *Radiation Physics and Chemistry*, vol. 185, p. 109494, 2021. doi:10.1016/j.radphyschem.2021.109494
- [10] J. Shi, A. Grudiev, and W. Wuensch, "Tuning of X-band traveling-wave accelerating structures," *Nuclear Instruments and Methods in Physics Research Section A: Accelerators, Spectrometers, Detectors and Associated Equipment*, vol. 704, pp. 14-18, 2013. doi:10.1016/j.nima.2012.11.182
- [11] G. Gatti *et al.*, "X-band accelerator structures: On going R&D at the INFN," *Nuclear Instruments and Methods in Physics Research Section A: Accelerators, Spectrometers, Detectors and Associated Equipment*, vol. 829, pp. 206-212, 2016. doi:10.1016/j.nima.2016.02.061
- [12] S. Kim *et al.*, "Development of a compact X-band linear accelerator system mounted on an O-arm rotating gantry for radiation therapy," *Review of Scientific Instruments*, vol. 92, no. 2, p. 024103, 2021. doi:10.1063/5.0030271
- [13] X. Huang, W. Fang, Q. Gu, and Z. Zhao, "Design of an X-band accelerating structure using a newly developed structural optimization procedure," *Nuclear Instruments and Methods in Physics Research Section A: Accelerators, Spectrometers, Detectors and Associated Equipment*, vol. 854, pp. 45-52, 2017. doi:10.1016/j.nima.2017.02.050
- [14] K. Deb, A. Pratap, S. Agarwal, and T. Meyarivan, "A fast and elitist multiobjective genetic algorithm: NSGA-II," *IEEE Transactions on Evolutionary Computation*, vol. 6, no. 2, pp. 182-197, 2002. doi:10.1109/4235.996017
- [15] M. Yarmohammadi Satri, A. M. Lombardi, and F. Zimmermann, "Multiobjective genetic algorithm approach to optimize beam matching and beam transport in high-intensity hadron linacs," *Physical Review Accelerators and Beams*, vol. 22, no. 5, p. 054201, 2019. doi:10.1103/PhysRevAccelBeams.22.054201
- [16] J. Wu *et al.*, "Multi-Dimensional Optimization of a Terawatt Seeded Tapered Free Electron Laser with a Multi-Objective Genetic Algorithm," *Nuclear Instruments and Methods in Physics Research Section A: Accelerators, Spectrometers, Detectors and Associated Equipment*, vol. 846, 2016. doi:10.1016/j.nima.2016.11.035
- [17] R. Bartolini, M. Apollonio, and I. P. S. Martin, "Multiobjective genetic algorithm optimization of the beam dynamics in linac drivers for free electron lasers," *Physical Review Special Topics - Accelerators and Beams*, vol. 15, no. 3, p. 030701, 2012. doi:10.1103/PhysRevSTAB.15.030701
- [18] J. Wan, P. Chu, Y. Jiao, and Y. Li, "Improvement of machine learning enhanced genetic algorithm for nonlinear beam dynamics optimization," *Nuclear Instruments and Methods in Physics Research Section A Accelerators Spectrometers Detectors and Associated Equipment*, p. 162683, 2019. doi:10.1016/j.nima.2019.162683
- [19] W. Gao, L. Wang, and W. Li, "Simultaneous optimization of beam emittance and dynamic aperture for electron storage ring using genetic algorithm," *Physical Review Special Topics - Accelerators and Beams*, vol. 14, no. 9, p. 094001, 2011. doi:10.1103/PhysRevSTAB.14.094001
- [20] C. Yao, *Electron Linear Accelerator*, China: Science Press, 1986.

# RECENT IMPROVEMENTS IN THE BEAM CAPTURE AT FERMILAB BOOSTER FOR HIGH INTENSITY OPERATION\*

C. M. Bhat<sup>†</sup>, S. J. Chaurize, P. Derwent, M. W. Domeier, V. Grzelak, W. Pellico, J. Reid, B. A. Schupbach, C.Y. Tan, A. K. Triplett, Fermilab, Batavia IL, USA

## Abstract

The Fermilab Booster uses multi-turn beam injection with all its cavities phased such that beam sees a net zero RF voltage even when each station is at the same maximum voltage. During beam capture the RF voltage is increased slowly by using its paraphase system. At the end of the capture the feedback is turned on for beam acceleration. It is vital for present operations as well as during the PIP-II era that both the HLRF and LLRF systems provide the proper intended phase and RF voltage to preserve the longitudinal emittance from injection to extraction. In this paper, we describe the original architecture of the cavity phase distribution, our recent beam-based RF phase measurements, observed significant deviation in the relative phases between cavities and correction effort. Results from the improved capture for high intensity beam are also presented.

## INTRODUCTION

Fermilab has undertaken major improvements to the existing accelerators in recent years to meet the high intensity proton demands for HEP experiments both onsite as well as long baseline neutrino experiments. An important program was the “Proton Improvement Plan” (PIP) [1, 2]. PIP had the baseline goal of extracting beam at 15 Hz from the Booster with about 4.3E12 ppp (protons per pulse). PIP completed its goals successfully in late 2016. During PIP-II [3], the plan is to increase the Booster beam intensity per cycle by >50%, and the cycle rate from 15 Hz to 20 Hz. The injection energy will be increased from 400 MeV to 800 MeV by using a newly built superconducting RF LINAC which will be completed around 2027. We have an intermediate beam intensity goal of achieving ~5E12 ppp in about two years. This will enable us to increase the beam power on the NuMI target from 700 kW to >900 kW. Concurrently, we will continue to provide 8 GeV beam to multiple low energy neutrino experiments before PIP-II comes online. The intermediate power increase helps us to better prepare Booster for the PIP-II era.

Booster is the oldest rapid cycling synchrotron (RCS) in operation in the world. Mitigation of beam losses during current operations continue to be a challenge and is of high priority. The allowed beam loss must be  $\leq 475$  W in the Booster ring or an average 1 W/m during its operation. Figure 1 displays a typical snapshot of the RF voltage, beam current and beam loss from its current operation.

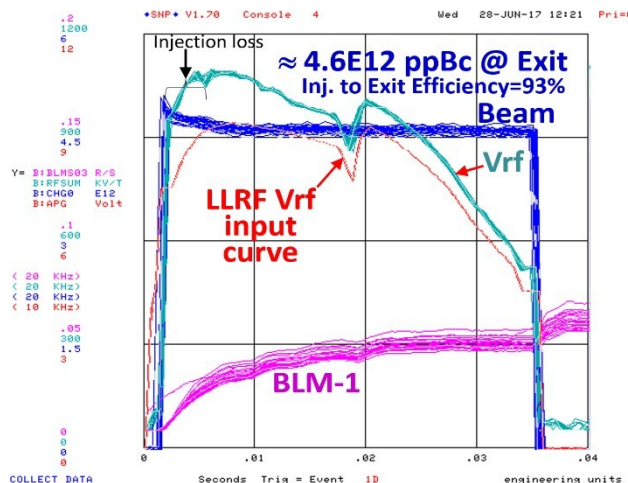


Figure 1: These are snapshots of the RF voltage, beam current, and a beam loss monitor at every 15 Hz tick.

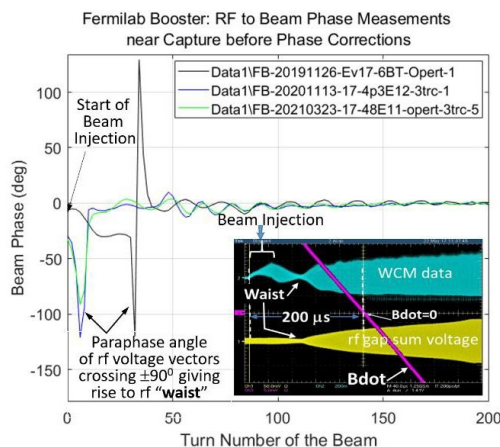


Figure 2: RF to beam phase measurements during injection and capture. The inset shows the wall current monitor (WCM) data (cyan), RF waveform (yellow), Bdot curve (magenta) during the first 400  $\mu$ s of the beam cycle.

The Booster beam cycle starts with a multi-turn H<sup>-</sup> injection scheme with no RF buckets opened. The injected beam debunches and loses its LINAC bunch structure by the end of beam injection. Next, the injected beam is captured by raising the RF voltage by changing the phase angle between two groups of RF cavities called A and B (see Figs. 3(a), 3(b)). A and B have the same number of RF stations (see Fig. 4). This method of manipulating the phase is called RF paraphase.

Since 2015 we have adopted an early injection scheme [4] by adding ~200  $\mu$ s to the beam cycle for adiabatic beam capture. The aim is to improve the capture efficiency and reduce any beam loss arising from longitudinal beam dynamics dur-

\* Work supported by Fermi Research Alliance, LLC under Contract No. De-AC02-07CH11359 with the United States Department of Energy

<sup>†</sup> cbhat@fnal.gov

Content from this work may be used under the terms of the CC BY 3.0 licence (© 2021). Any distribution of this work must maintain attribution to the author(s), title of the work, publisher, and DOI

ing the first 5 ms of the beam cycle. On average, although the early injection scheme improved the longitudinal emittance by nearly 15% to the downstream machines, it did not help improve capture efficiency. Prior to our work described later in this paper, the best injection to extraction efficiency imposed a waist like structure in the RF sum voltage and in the WCM data at  $\sim 100 \mu\text{s}$  as shown in the inset of Fig. 2. The measured RF to beam phase around the waists, displayed in Fig. 2, for three different operational cases, shows sudden phase glitches in a matter of few turns. This observation contradicted results from simple longitudinal beam dynamics simulations which showed a smooth transition from injection to beam capture without any RF waist or RF phase glitch. In addition to this issue, the Booster RF voltage measured using synchrotron frequency measurements [5] was about 5% smaller than the sum of the magnitude of RF voltages from individual gap monitor outputs ( $V_{\text{rf}}$  shown in Fig. 1). One explanation for this reduction in the vector sum of the RF voltage is that the RF vectors from individual stations are not properly phased. These two issues led us to revisit the current configuration of the Booster HLRF and LLRF systems.

### INJECTION SIMULATIONS

A clue for the possible causes for beam loss in the early part of the beam cycle that has an RF waist came from injection simulations described in Ref. [6]. Simulations were done using ESME [7]. The LLRF paraphase system used in the Booster during injection and beam capture is shown in Fig. 3(a) and (b) that has phase or magnitude errors. RF measurements during injection indicated that the observed waist in the WCM data might arise from the  $V_a$  and  $V_b$  vectors (dashed lines in Fig. 3(a)) not being anti-parallel.  $V_a$  and  $V_b$  are the vector sums of the RF voltages of all the cavities in groups A and B respectively. In the current operations, we have ten RF cavities in each group. Figure 3(b) shows an example of a phase error between cavity voltage vectors. These errors give rise to emittance growths and possible beam particle losses. The simulation results for an ideal case with  $|\theta_a| = |\theta_b| = 90 \text{ deg}$  during injection and  $|\theta_a| = |\theta_b|$  at the

end of beam capture with  $|V_a| = |V_b|$  are shown in Fig. 3(c) and 3(d). This illustrates a case with no emittance growth. If  $|V_a/V_b| \neq 1$  and or, one of the paraphase angle  $>90 \text{ deg}$  at injection, then as the paraphase angle starts changing during the beam capture process, the magnitude of the RF voltage sum vector reaches a minimum value resulting in beam acceleration or deceleration along with debunching. In the illustration shown here, the de-bunching took place in  $\sim 20 \mu\text{s}$  which is much faster than the synchrotron period at that time. This led to  $>30\%$  emittance dilution. Figures 3(e) and 3(f) show the phase space distributions from the end of injection to the end of beam capture, respectively. Further simulations showed that if cavities in groups A and/or B have phase errors or magnitude differences (as shown in Fig. 3(b)) then there is emittance growth even without any RF waist. Therefore, it is quite important to ensure that the cavities have the proper phase and have comparable gap voltages that are within a few percent.

### RF PHASE MEASUREMENTS

The Booster uses 20 RF cavities in operation (with two additional cavities as backup), each with a gap voltage of 50 kV. During beam acceleration, the RF frequency ramps from 37.92 MHz to 52.81 MHz. Figure 4 shows a schematic of the RF cavity phasing diagram and arrangement of group A and B cavities in the Booster. Theoretically, the closest pair of A and B cavities must be  $\beta\lambda$  apart for acceleration. But due to space constraints, they are closer to  $\beta\lambda/2$ . The solution to this problem is for the LLRF to send RF to groups A and B that has a phase difference of 180 deg plus phase compensation that ensures that the A and B cavities are exactly  $\beta\lambda/2(+\eta\beta\lambda)$  apart. For example, the arrangement and spacing of four consecutive cavities are shown in Fig. 5. The center-to-center distance between two adjacent cavities in a sector (sectors 14 and 15 as shown in Fig. 4) is 2.385 m that is  $< \beta\lambda/2 = 2.816 \text{ m}$ . Between any two sectors the spacing is  $\eta\beta\lambda + \Delta\theta\beta\lambda/2\pi$ . The quantity  $\Delta\theta = 28 \text{ deg}$ , is the required phase compensation because the cavity separation is not exactly an integer multiple of  $\beta\lambda/2$ . The fanout phase shifter (also called a *brass box*) shown in Fig. 5 adds the required phase compensation provided the connecting cables from each cavity to the LLRF box are identical.

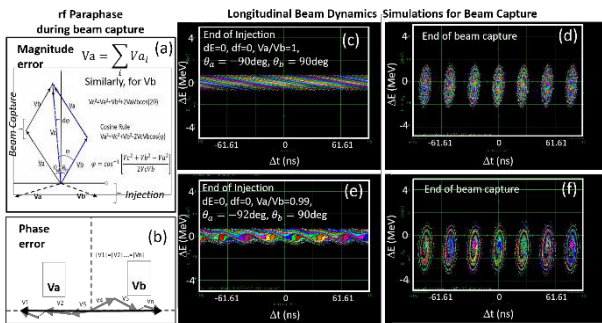


Figure 3: (a) and (b) are schematics of two scenarios of paraphase RF voltage vectors during beam injection into Booster. (c) - (f) are simulated  $(\Delta E, \Delta t)$ -phase space distributions for these two scenarios of paraphase.

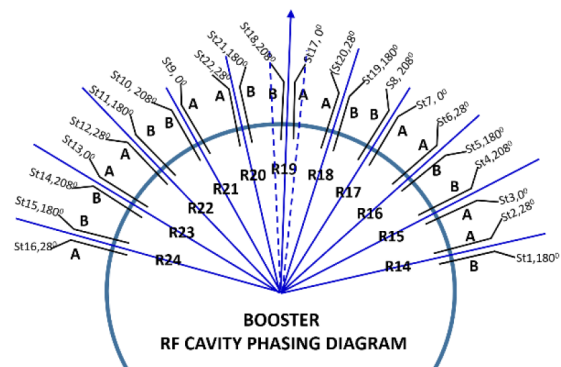


Figure 4: Schematic of the Booster RF cavity configuration for 22 RF cavities with added phases between cavities.

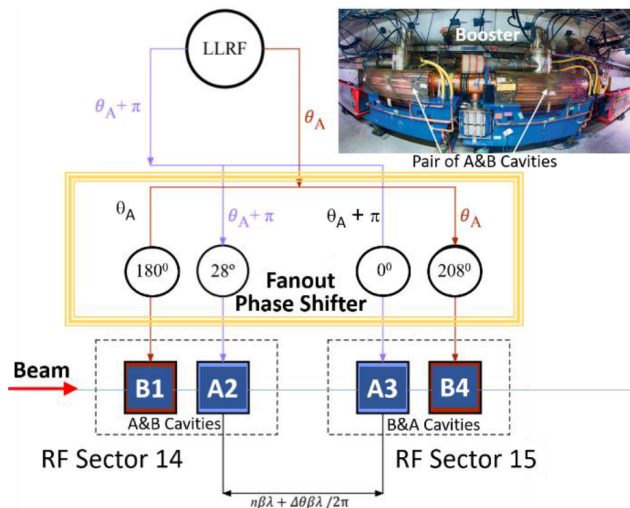


Figure 5: Schematic of Booster RF cavity configuration with fanout phase shifter for a set of four cavities.

To measure the relative phase between any pair of RF cavities, we performed the following: i) Booster was put into a non-ramping state at the injection energy of 400 MeV with the RF frequency held constant, ii) in the para-phase module, the paraphase angle between A and B RF stations were set to 180 deg. In principle, if the system is perfect, A and B RF voltage vectors should be anti-parallel, iii) the magnitude of the RF voltage vector for each station is set to ~30 kV (within about 2%). We chose one cavity in group A to be the master station and then used beam to measure the phase of each cavity in group B. We expected that if A and B was perfectly anti-parallel, then there is no bunching, i.e., there is no RF component (37.92 MHz) carried by the beam. In practice, this was not the case because we see this component. We could measure the phase error between these two cavities by simply knobbing the para-phase angle until the RF component carried by the beam vanishes.

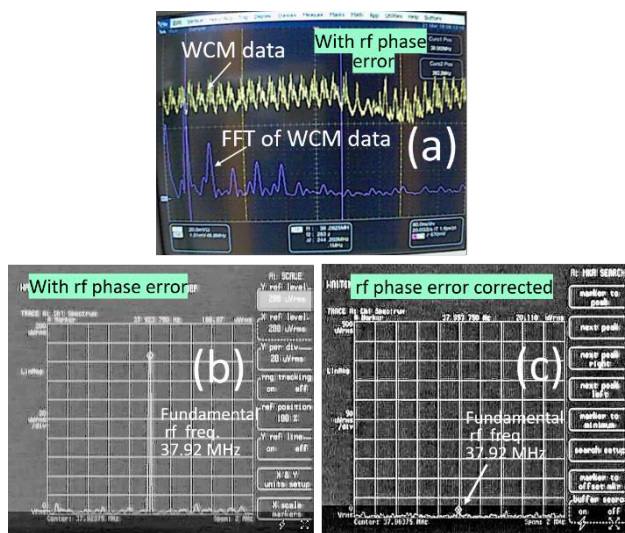


Figure 6: (a) A typical time domain and (b), (c) VSA data of the beam before and after phase correction.

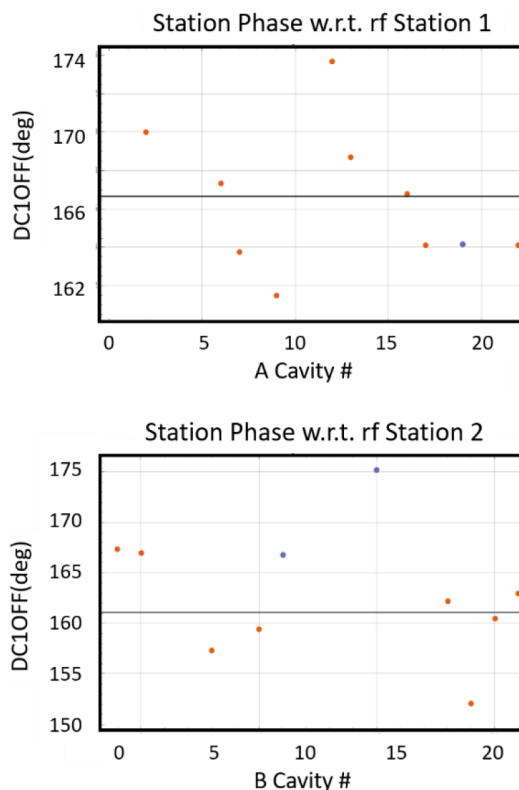


Figure 7: (top) The measured phase differential offset of all group A cavities relative to station-1 (group B cavity) and (bottom) similar measurement of all group B cavities relative to station 2 (group A cavity) before phase correction.

A typical WCM data and its FFT measured with a Tektronix, TDS7154B Digital Phosphor about 1 ms after injection that shows bunching is shown in Fig. 6(a). The WCM data measured with a vector signal analyzer (VSA) is shown in Fig. 6(b).

Since we can see the 37.92 MHz component prominently in Fig. 6(b), this indicates that these two RF cavities are not anti-parallel. To make them anti-parallel, we adjusted a phase differential offset device DC1OFF in the LLRF system until the 37.92 MHz component disappears. Figure 6(c) shows the VSA data after adjustment. The value (DC1OFF -180) deg when this component disappears is the phase error between these pair of cavities. After working on this pair, the same method was used to measure DC1OFF for the remaining pairs. The as found measured DC1OFF are shown in Fig. 7. The average DC1OFF before any correction was 166.7 deg between group A stations to a reference group B station (station 1). And 161.1 deg between group B stations to a reference group A station (station 2). If there was no phase error, we expected DC1OFF to be 180 deg.

The observed systematic phase error can come from a) the LLRF system, b) from the mismatch of cable lengths from the LLRF system to fanout phase shifter box, fanout phase shifter box to the cavities or from cavities to the fanback sum box (the last one will not affect the observed phase error, but has an effect on the measured Vrf), c) the circuits inside the fanout phase shifter box or d) from the improper

Content from this work may be used under the terms of the CC BY 3.0 licence (© 2021). Any distribution of this work must maintain attribution to the author(s), title of the work, publisher, and DOI

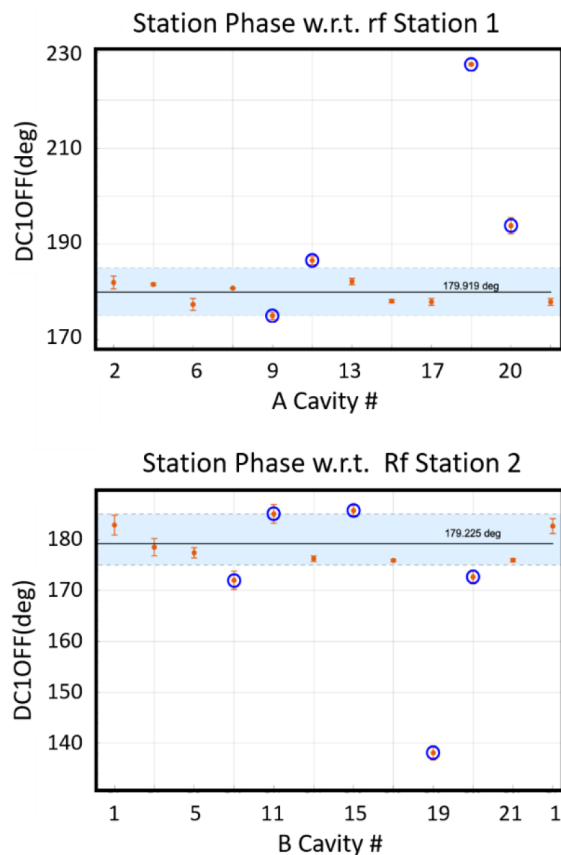


Figure 8: Phase measurement after correction. Figure description is same as that for Fig. 7.

cavity spacing in the Booster ring. Or from all the above. We looked at each of these items as a possible source of the error but ruled them all out except for the Booster LLRF. We found that the paraphase module in the LLRF was the major source of the error because of an incorrect cable length. We fixed the problem and remeasured DC1OFF after correction.

Figure 8 displays measurement results for all the cavities after the phase error was corrected. We found that the average DC1OFF is 179.9 deg and 179.2 deg for group A stations relative to the reference group B station (station-1) and group B stations relative to the reference group A station (station-2), respectively. This met our specification of <5 deg from 180 deg. Stations 19 and 20 were outliers during these measurements, and they were corrected later. These two stations will need further beam-based phase measurements to verify their corrections.

### OBSERVED IMPROVEMENTS

After correction, the measured RF to beam phase during injection and beam capture is shown in Fig. 9 for an extraction intensity of  $4.5E12$  ppp with about 94% injection to extraction efficiency. This is the normal intensity for 15 Hz operation. The measurement results look like our simulation results for a properly corrected RF system. There was also a noticeable improvement in the capture process: under low beam repetition conditions, we had up to about  $5.7E12$  ppp

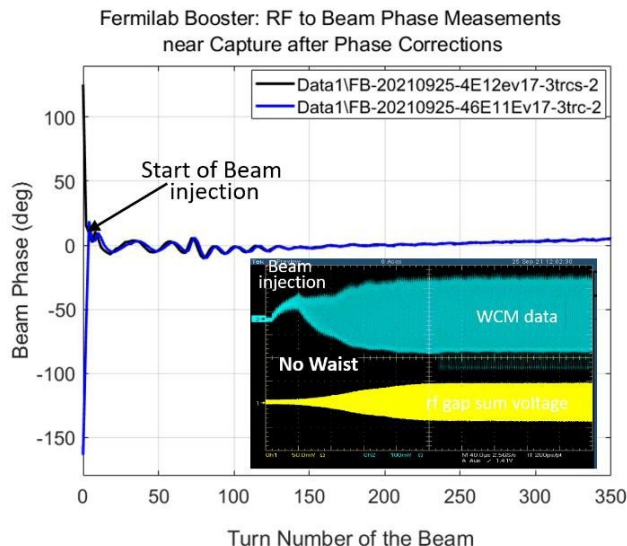


Figure 9: The RF to beam phase measurements during injection and capture after all RF cavities have been phased correctly. The shown data is for  $4.5E12$  ppp in the Fermilab Booster.

at extraction with a comparable injection to extraction efficiencies. Currently we are optimizing the Booster for higher intensity as per users' demand.

### ACKNOWLEDGEMENTS

Special thanks due to RF personnel and MCR crew for their help during these measurements.

### REFERENCES

- [1] F. G. Garcia *et al.*, “Proton Improvement Plan Design Handbook”, Fermilab-Beams-doc-4053-v4, 2012.
- [2] W. Pellico *et al.*, “FNAL - The Proton Improvement Plan (PIP)”, in *Proc. IPAC'14*, Dresden, Germany, June 2014, pp. 3409–3411. doi:10.18429/JACoW-IPAC2014-THPME075
- [3] “The PIP-II Reference Design Report”, 2015, [https://indico.fnal.gov/event/9939/attachments/75550/90629/PIP-II\\_RDR\\_v1.0.pdf](https://indico.fnal.gov/event/9939/attachments/75550/90629/PIP-II_RDR_v1.0.pdf)
- [4] C. M. Bhat, “R&D on Beam Injection and Bunching Schemes in the Fermilab Booster”, in *Proc. HB2016*, Malmö, Sweden, June 2016, pp. 293–298. doi:10.18429/JACoW-HB2016-TUPM3X01
- [5] C. M. Bhat and S. Bhat, “Beam Based RF Voltage Measurements & Longitudinal Beam Tomography at the Fermilab Booster”, in *Proc. DPF2017*, Fermilab, Aug. 2017. arXiv:1710.07372
- [6] C. M. Bhat, “Beam Injection and Capture in the Fermilab Booster for PIP”, in *Fermilab Workshop on Megawatt Rings & IOTA/FAST Collaboration Meeting*, 7 May 2018, Beams Doc. 6294. <https://indico.fnal.gov/event/16269/contributions/36557/attachments/22679/28120/PIPWorkshop-talk2018cbhat-BD6294.pptx>
- [7] J. A. MacLachlan, “Multiparticle Dynamics in the E- $\varphi$  Tracking Code ESME”, *AIP Conference Proceedings*, vol. 642, p. 68, 2002. doi:10.1063/1.1522585

# LONGITUDINAL EMITTANCE MEASUREMENT AT PIP2IT\*

Mathias El Baz<sup>†</sup>, Université Paris Saclay, Orsay, France  
 Jean-Paul Carneiro, Fermilab, Batavia, USA

## Abstract

The PIP-II particle accelerator is a new upgrade to the Fermilab accelerator complex, featuring an 800 MeV  $H^-$  superconducting linear accelerator that will inject the beam into the present Fermilab Booster. A test accelerator known as PIP-II Injector Test (PIP2IT) has been built to validate the concept of the front-end of PIP-II [1]. One of the paramount challenges of PIP2IT was to demonstrate a low longitudinal emittance at the end of the front end. Having a low longitudinal emittance is crucial in order to ensure the stability of the beam in the accelerator. We present a longitudinal emittance measurement performed at 14.3 MeV by scanning the SSR1-8 cavity phase and measuring the corresponding beam rms bunch length with a Fast Faraday Cup (FFC) located in the High Energy Transport line (HEBT). The FFC signal is recorded by a high-bandwidth oscilloscope.

## INTRODUCTION

The PIP-II Injector Test facility (PIP2IT) is a model of the Front End of PIP-II which will accelerate the  $H^-$  ion beam up to 25 MeV. As shown in Fig. 1, the injector is made of an Ion Source, a Low Energy Beam Transport (LEBT) made of three solenoids that matches the beam into a 162.5 MHz Radiofrequency Quadrupole (RFQ), a Medium Energy Beam Transport (MEBT) that prepares the beam for injection into two superconducting (SC) cryomodules: one containing eight Half-Wave Resonators (HWR) cavities operating at 162.5 MHz and one containing eight Single-Spoke Resonator (SSR1) cavities operating at 325 MHz. At the end of the injector a High-Energy Beam Transport (HEBT) brings the beam to a dump.

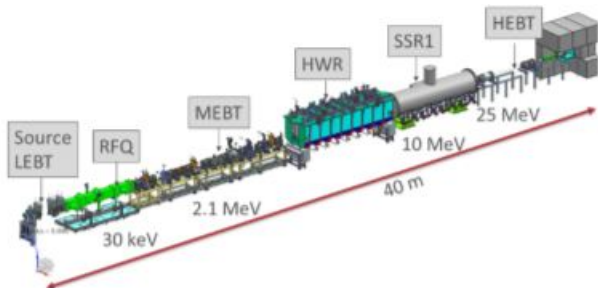


Figure 1: Sketch of PIP2IT.

During normal operation of the injector, the ion source operates with long pulses (usually few ms) and at 20 Hz repetition rate. A beam chopper, located upstream of the third LEBT solenoid, cut pulses of up to 0.55 ms of beam at

\* This work was supported by the U.S. Department of Energy under contract No. DE-AC02-07CH11359

<sup>†</sup> mathias.el-baz@universite-paris-saclay.fr

a repetition rate of 20 Hz. At the exit of the RFQ, the beam has an energy of 2.1 MeV. The MEBT has two purposes: first the MEBT performs a bunch-by-bunch selection using two kickers that decreases the average current in the macro-pulse from 5 mA down to 2 mA, and second the MEBT matches the beam into the HWR cryomodule using 3 buncher cavity (operating at 162.5 MHz), 2 doublets and 7 triplets. During normal operation, the beam is expected to reach an energy of 10.3 MeV at the exit of the HWR cryomodule and 25 MeV at the exit of the SSR1 cryomodule. The transverse focusing is performed by 8 SC solenoids in the HWR cryomodule and by 4 SC solenoid in the SSR1 cryomodule. The HEBT is made of 2 quads.

The goal of the longitudinal emittance measurement performed at PIP2IT is to quantify the beam quality at the end of the injector. A low longitudinal emittance ensures a small bunch length and little variations of the longitudinal momentum inside the bunch, and therefore, a high stability of the beam with negligible losses along the PIP2 linac.

## MEASUREMENT SCHEME

### Injector Settings

During the commissioning of the PIP2IT injector (from Spring 2020 to Spring 2021), the 3 first HWR cavities were not operational because of a frequency offset for the two first cavities and a coupler issue for the third one. Furthermore, due to multipacting effects, the 2 last HWR cavities (HWR#7 and #8) were operated at lower accelerating gradient than originally anticipated (respectively 8.5 MV/m and 8 MV/m vs 9.7 MV/m). As a consequence of these HWR cavities adjustments, the beam was longitudinally matched from the MEBT into the fourth HWR cavity reaching a beam energy of 8 MeV at the end of the HWR cryomodule and further accelerated to 16.2 MeV by the SSR1 cryomodule. During our longitudinal emittance measurement, and in order to lower the beam power in the Fast Faraday Cup (FFC), the pulse length was limited to 10  $\mu$ s and the repetition rate to 1 Hz. The average beam current of 5 mA at the exit of the RFQ was chopped down to 2 mA by the 2 MEBT kickers. Under these conditions, the beam was transported with minimal uncontrolled losses until the dump at the end of the HEBT.

### Beam Dynamic Simulations

Figure 2 shows the transverse and longitudinal envelope along the PIP2IT injector from Tracewin [2] for the above-mentioned injector settings used during the longitudinal emittance measurement. The simulation starts with a  $792 \times 10^3$  input distribution at the MEBT ( $z = 0$  in Fig. 2). This input distribution was built from a start-to-end model of the Ion Source, LEBT and RFQ, this later being simulated using

Content from this work may be used under the terms of the CC BY 3.0 licence (© 2021). Any distribution of this work must maintain attribution to the author(s), title of the work, publisher, and DOI

the code Toutatis [2]. The injector was modeled in Tracewin using 3D fields for all cavities, solenoids, quadrupoles and correctors.

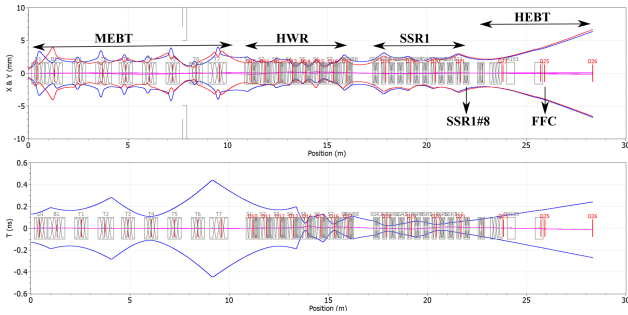


Figure 2: Transverse (upper) and Longitudinal (lower) envelope along the PIP2IT injector for the phase scan measurement. The beam is longitudinally matched from the MEBT into the 4<sup>th</sup> HWR cavity. From Tracewin.

### Description of the Cavity Phase Scan

The schematic of the cavity phase scan measurement section is represented in Fig. 3. The objective is to estimate the longitudinal emittance at the entrance of the eighth and last SSR1 cavity (noted SSR1#8 on Fig. 3). The SSR1#8 cavity phase is scanned from  $-10^\circ$  to  $-45^\circ$  (with a  $5^\circ$  step) and at fixed field amplitude of 10 MV/m changing the beam energy from 16.2 MeV to about 15.6 MeV according to Tracewin.

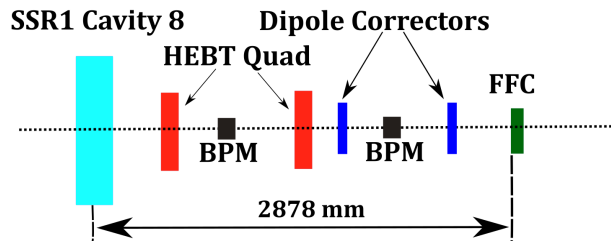


Figure 3: Schematic of the section of interest for the scan.

The cavity acts like a thin lens whose focal length depends on its phase. Therefore, the bunch length at an upstream location varies during the scan. We can reconstruct the longitudinal emittance from the variation of the bunch length. The ions are collected at the end the HEBT by a FFC and the corresponding waveforms are recorded by a high-bandwidth oscilloscope located outside the cave enclosure and with a 10 ps interpolation sampling. The rms bunch length at the FFC is estimated using a Gaussian fit of the FFC waveform. The FFC has a collimating aperture of 0.8 mm and efforts have been made during the cavity phase scan to keep the beam centered with the FFC aperture using BPMs and correctors located upstream of the FFC. Two quadrupoles located between the cavity and the FFC have also been used during the measurement in order to maximize the signal at the FFC. As indicate in Fig. 3, the distance between the middle of the SSR1#8 cavity and the FFC is 2878 mm. A detailed description of the FFC is given in [3] and [4].

### Analysis of the Waveform

Figure 4 shows a FFC signal for operation of the SSR1#8 cavity at 10 MV/m and a phase of  $-15^\circ$ . The signal is fitted with a Gaussian curve and the rms bunch length of the beamlet is extracted. A detailed analysis of the beam distribution at the FFC obtained from Tracewin simulation have shown that the rms bunch length of the beamlet is representative of the rms bunch length of the core of the beam representing about 90% of the full beam.

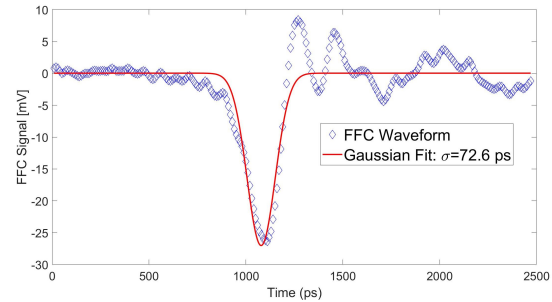


Figure 4: FFC waveform for a field on SSR1#8 of 10 MV/m and a phase of  $-15^\circ$  with Gaussian fit, 10  $\mu$ s pulse, 1 Hz, 2 mA average beam current.

As discussed, the FFC waveform analysis is based on the assumption of a Gaussian-shape bunch. However, as shown in Fig. 4, the bunch diverges from the Gaussian model. The bunch is skewed to the right and the baseline oscillates after the bunch. These distortions are very unlikely due to discrepancies of the beam. Since the oscilloscope is out of the cave, the long cable between the FFC and the oscilloscope could explain the skewed feature characteristic of cable dispersion. The oscillations after the bunch are likely due to reflections near the FFC. We estimate the error between the Gaussian bunch length RMS and the real bunch length to be below 7%. The estimation of the longitudinal emittance with error bar (and discussed in the last section) is deduced from the uncertainty on the bunch length.

## LONGITUDINAL EMITTANCE RECONSTRUCTION

The beam is first focused by the SSR1-8 cavity and needs to pass a 2878 mm drift before being collected by the FFC. The transport matrix  $M$  modelling the evolution of the beam between the input of SSR1-8 and the FFC is the product of the drift matrix and the SSR1-8 matrix [5]:

$$M(\Phi_s) = \underbrace{\begin{pmatrix} 1 & L \\ 0 & 1 \end{pmatrix}}_{\text{Drift}} \times \underbrace{\begin{pmatrix} 1 & 0 \\ \frac{-2\gamma^2 k \sin(\Phi_s)}{(\beta\gamma)_f} & \frac{(\beta\gamma)_i}{(\beta\gamma)_f} \end{pmatrix}}_{\text{RF}}$$

with:

$$k \hat{=} - \frac{\pi}{\beta^2 \gamma^2 \lambda} \frac{Q}{A} \frac{E_0 T L}{m_u c^2}$$

where  $(\beta\gamma)_i$  and  $(\beta\gamma)_f$  are respectively the relativistic coefficients at the entrance and the exit of SSR1-8,  $L$  is the drift

length,  $\Phi_s$  is the cavity phase, and  $k$  is the focusing strength of the cavity. The phase dependence of  $M$  is also contained in  $(\beta\gamma)_f$ .  $M$  is numerically calculated for each cavity phase using the different values of  $(\beta\gamma)_f$  given by the Tracewin simulation.

The beam matrix at the FFC is linked to the beam matrix at the input of SSR1-8 by:

$$\Sigma_{FFC}(\phi_s) = M(\phi_s) \Sigma_{SSR1-8} M(\phi_s)^T$$

One can notice that the determinant of the beam matrix is not conserved since the determinant of  $M$  is strictly less than 1. Therefore, the longitudinal emittance and the beam energy at the output of SSR1-8 are phase dependent. Only the (1,1) coordinate of  $\Sigma_{FFC}$  is measured and can be expressed as a function of the  $M$  and  $\Sigma_{SSR1-8}$  coordinates:

$$\begin{aligned} \sigma_z^{FFC}(\phi_s)^2 &= \Sigma_{11}^{SSR1} M_{11}(\phi_s)^2 + 2M_{11}(\phi_s) M_{12}(\phi_s) \Sigma_{12}^{SSR1} \\ &\quad + M_{12}^2(\phi_s) \Sigma_{22}^{SSR1} \\ &= \underbrace{\Sigma_{11}^{SSR1}}_a X^2 + \underbrace{2\Sigma_{12}^{SSR1}}_b XY + \underbrace{\Sigma_{22}^{SSR1}}_c Y^2 \end{aligned}$$

where  $X = M_{11}(\phi_s)$  and  $Y = M_{12}(\phi_s)$ .  $\sigma_z^{FFC}(\phi_s)^2$  is a polynomial function of  $X$  and  $Y$ . We can fit the evolution of  $\sigma_z^{FFC}(\phi_s)^2$  in order to estimate the polynomial coefficients  $a, b$  and  $c$  (Fig. 5). The longitudinal emittance measurement is computed from the estimation of these coefficients:

$$\begin{aligned} \epsilon_z^{SSR1} &= (\beta\gamma)_i \sqrt{ac - \frac{1}{4}b^2} \\ &= (\beta\gamma)_i \sqrt{\Sigma_{11}^{SSR1} \Sigma_{22}^{SSR1} - (\Sigma_{12}^{SSR1})^2} \\ &= 0.29 \text{ mm} \cdot \text{mrad} \end{aligned}$$

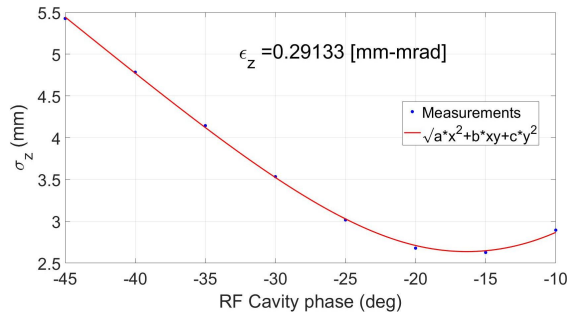


Figure 5: Measured rms bunch length at the FFC as a function of the SSR1#8 cavity phase and reconstruction of the longitudinal emittance at SSR1#8 cavity entrance.

## DISCUSSION

As previously mentioned, we estimate the error between the Gaussian bunch length RMS and the real bunch length to be below 7%. The estimation of the longitudinal emittance with error bar is deduced from the uncertainty on the bunch length and estimated to be:

$$\epsilon_z^{SSR1} = (0.29 \pm 0.02) \text{ mm.mrad.}$$

This measured emittance is in good agreement with the Tracewin simulation reported in Fig. 6 which shows the 90% longitudinal phase space at the SSR1#8 cavity and the corresponding longitudinal emittance of 0.3 mm-mrad.

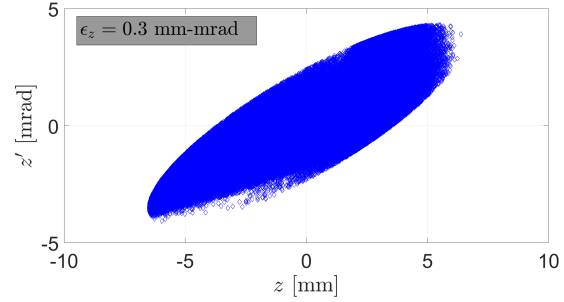


Figure 6: Simulated 90% longitudinal phase space distribution at the entrance of the SSR1#8 cavity. From Tracewin.

The longitudinal phase space distribution of Fig. 6 corresponds to the distribution at the entrance of the SSR1#8 cavity for the envelope shown in Fig. 2 and for which 10% of the beam with the largest longitudinal action has been removed. Analysis of the Tracewin distribution at the FFC shows that the core of the beam sampled by the FFC of about 0.8 mm diameter is representative of the rms bunch length of about 90% of the full beam. As a consequence, we consider the emittance measurement reported in this document as being representative of the core (about 90%) of the beam and in good agreement with simulations.

## ACKNOWLEDGEMENT

We want to thank the team members for their expertise and assistance on all the aspects of our study and for their help in writing this article. We especially thank Eduard Pozdeyev, Alexander Shemyakin, Arun Saini, Bruce Hanna and Lionel Prost for their help in the analysis and Victor Scarpine for giving us his expertise in instrumentation.

## REFERENCES

- [1] PIP-II Collaboration, “PIP-II Reference Design Report”, FNAL, Batavia, IL, USA, 2015.
- [2] Tracewin and Toutatis codes, <http://irfu.cea.fr/Sacm/logiciels/>
- [3] A. Shemyakin *et al.*, “Characterization of the beam from the RFQ of the PIP-II Injector Test”, in *Proc. IPAC'17*, Copenhagen, Denmark, May 2017, pp. 2425–2428. doi:10.18429/JACoW-IPAC2017-TUPVA139
- [4] J.-P. Carneiro *et al.*, “Longitudinal beam dynamics studies at the PIP-II injector test facility”, *International Journal of Modern Physics A*, Vol. 34, no. 36, p. 1942013, 2019. doi:10.1142/S0217751X19420132
- [5] USPAS Notes, Chapter 3: Basic of beam dynamics, 2013. [https://uspas.fnal.gov/materials/13Duke/SCL\\_Chap3.pdf](https://uspas.fnal.gov/materials/13Duke/SCL_Chap3.pdf)

# STATUS OF THE JAEA-ADS SUPERCONDUCTING LINAC DESIGN

B. Yee-Rendon\*, Y. Kondo, J. Tamura, S. Meigo and F. Maekawa  
 JAEA/J-PARC, Tokai-mura, Japan

## Abstract

The Japan Atomic Energy Agency (JAEA) is working in the research and development of an Accelerator Driven Subcritical System (ADS) for the transmutation of nuclear waste. To this end, JAEA is designing a 30 MW cw proton linear accelerator (linac) with a beam current of 20 mA. The JAEA-ADS linac starts with a Normal Conducting (NC) up to an energy of 2.5 MeV. Then, five Superconducting (SC) sections accelerate the beam up to 1.5 GeV. The biggest challenge for this ADS linac is the stringent reliability required to avoid thermal stress in the subcritical reactor, which is higher than the achieved in present accelerators. For this purpose, the linac pursues a strong-stable design that ensures the operation with low beam loss and fault-tolerance capabilities to continue operating in case of failure. This work presents the beam dynamics results toward achieving high reliability for the JAEA-ADS linac.

## INTRODUCTION

The Japan Atomic Energy Agency (JAEA) is doing R&D in an Accelerator Driven Subcritical System (ADS) for the transmutation of minor actinides to reduce the long lifetime and high radiotoxicity of nuclear waste. The JAEA-ADS project is composed of a 30 MW cw proton linac, a spallation target, and an 800 MW thermal power subcritical reactor [1], as shown in Fig. 1.

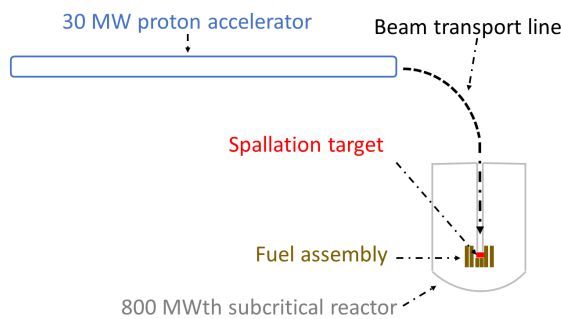


Figure 1: General scheme for the ADS.

A summary of the main specifications of the JAEA-ADS linac is provided in Table 1. Among them, the restricted number of beam trips is the main challenge for the ADS, which is beyond the present high-intensity linacs [2]. Thus, the JAEA-ADS linac seeks a reliability-oriented accelerator by achieving a robust beam optics design and fault-tolerance capabilities [3].

## BEAM OPTICS DESIGN

The beam optics design pursues strict control beam loss and beam properties such as energy spread and emittance

\* byee@post.j-parc.jp

Table 1: Main Characteristics of the JAEA-ADS Accelerator

Parameter	Beam trip duration	
Particle	Proton	
Beam current (mA)	20	
Beam energy (GeV)	1.5	
Duty factor (%)	100 (cw)	
Beam loss (W/m)	< 1	
Length (m)	429	
Beam trips per year [4]	$2 \times 10^4$	$\leq 10$ s
	$2 \times 10^3$	from 10 s to 5 min
	42	> 5 min

growth; simple lattice arrangement; operation with de-rated elements to reduce the failure probabilities and applied fault-tolerance schemes.

Figure 2 shows that JAEA-ADS linac has a normal conducting (NC) part, a so-called Injector, and a superconducting (SC) part known as the Main Linac. The Main Linac employs five groups of SC cavities to achieve high accelerating efficiency and compact design. The Half Wave Resonator (HWR) and Single Spoke Resonator (SSR) use a configuration solenoid-cavity inside the cryomodule. For the HWR region, the period is composed of one solenoid and one cavity; on the contrary, the SSR periods have two SC cavities for SSR1 and three for SSR2. Five-cell Elliptical Resonators (EllipRs) employ doublet NC quadrupoles with three and five SC cavities per cryomodule for EllipR1 and EllipR2, respectively [5].

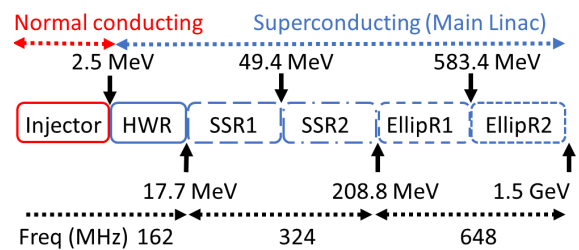


Figure 2: Linac lattice configuration.

At the normal operation, the maximum accelerating gradient ( $E_{acc}$ ) for the SC cavities was chosen to operate with an electric peak up to 30 MV/m to reduce the possibility of a malfunction in the cavity. Moreover, in case of an SC cavity failure, it enables the increase of  $E_{acc}$  to apply for fault-tolerance compensations.

The beam optics was developed using the programs GenLinWin and Tracewin [6]. The beam loss was minimized by reducing the beam halo and emittance growth. This was achieved by pursuing an equipartitioning model, avoiding parameter resonances, among others [5]. The lattice design was optimized first in ideal conditions, i.e., without errors,

Table 2: Parameters of the Main Linac

Parameters	
Input $\varepsilon_x$ ( $\pi$ mm mrad)	0.24
Input $\varepsilon_y$ ( $\pi$ mm mrad)	0.23
Input $\varepsilon_z$ ( $\pi$ MeV deg/mm mrad)	0.08/0.39
Number of Cavities	293
Number of magnets	153
Length (m)	416

tracking large beam distributions with  $1 \times 10^7$  macroparticles obtained from the RFQ design [7]. Table 2 presents the relevant parameters of the Main Linac. This ideal case is known as the Ideal Machine (IM) case. The IM case did not record beam loss; furthermore, it has reasonable control of the normalized root-mean-square  $\varepsilon$ , see Fig. 3.

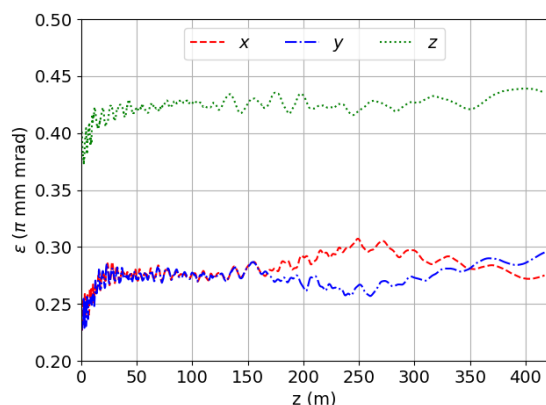


Figure 3: Normalized rms emittance in the linac.

Then, the robustness of the lattice was tested using element errors and input beam errors (IBE). The former are misalignments and parameters fluctuations of the cavities and magnets. They are divided as statics elements errors (SEE) and dynamics element errors (DEE). On the contrary, IBEs are errors from Injector part such as emittance growth and energy fluctuations. Reference [8] provides a detailed explanation of the errors and their application. Figures 4 and 5 present a comparison of the  $\varepsilon$  growth and the maximum radial envelopes for the error cases and the IM one. From all the error cases simulated, only the static errors registered beam loss; however, the corresponding maximum power loss was 20 mW/m, two orders of magnitude lower than the limit for hand-on maintenance.

## FAULT-TOLERANCE

Fault-tolerance is achieved by using parallel or serial redundancy. For the former, the linac lattice is partially or completely duplicated. In contrast, serial redundancy exploits the modularity of the linac by using the neighbors' elements of the faulty element to compensate for the unwanted effect produced by the faulty one. This study was focused on serial redundancy; however, the general strategy is to use both schemes to decrease the duration and the number of beam trips. Figure 6 illustrates the serial redundancy

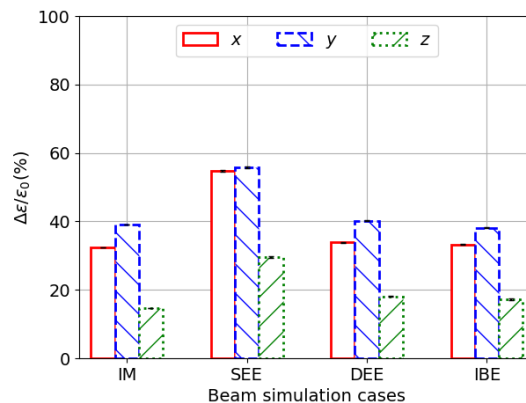


Figure 4: Normalized rms emittance growth for the different beam simulation cases.

for a faulty SC cavity; nevertheless, the compensation for a magnet failure follows the same proceeding.

Based on the Fault-tolerance schemes reported by Biarrotte [9, 10], two schemes were applied: beam stopping compensation scheme and beam continue compensation scheme. Figure 7 provides a summary of both schemes. The main difference between both schemes is that the first one begins with the compensation after the faulty element is detuned. Subsequently, the compensation setting is less complex because it does not require to be updated. On the contrary, the continue case starts the compensation when the faulty element is acting in the beam. Thus, the compensation settings need to be continually updated according to the transient behavior of the faulty element; consequently, the scheme becomes more complex and requires a large RF power budget.

The nonstop beam scheme is more attractive than the stopped one because it implies the beam operation is not interrupted; however, it is more challenging. Nevertheless, when the fault element is detuned, both cases have the same compensation settings. The three main challenges of both schemes are a fast-reliable diagnostic, an accurate large compensation database, and fast control system. In addition, these configurations are temporary; thus, after recovery of the fault, the element settings will be returning to the design configuration at a certain proper time.

The schemes were optimized to fulfill the next requirements:

- Beam loss  $< 1$  W/m.
- Energy difference  $< \pm 1\%$ .
- $\Delta\varepsilon_{trans}/\varepsilon_{0,trans} < 2$ .
- Mismatch  $< 0.4$ .
- Increase of  $E_{acc}$  up to 20 % and 50 % for the stopping and continue case, respectively.
- Increase of the magnetic field up to 20 %.

The energy,  $\varepsilon$ , and mismatch are with respect to the design case, also known as the IM case. The values were calculated using beam tracking simulations using  $2 \times 10^5$  macroparticles.

The beam stopping strategy has been reported in previous conferences [11, 12]. Figure 8 presents the compensation

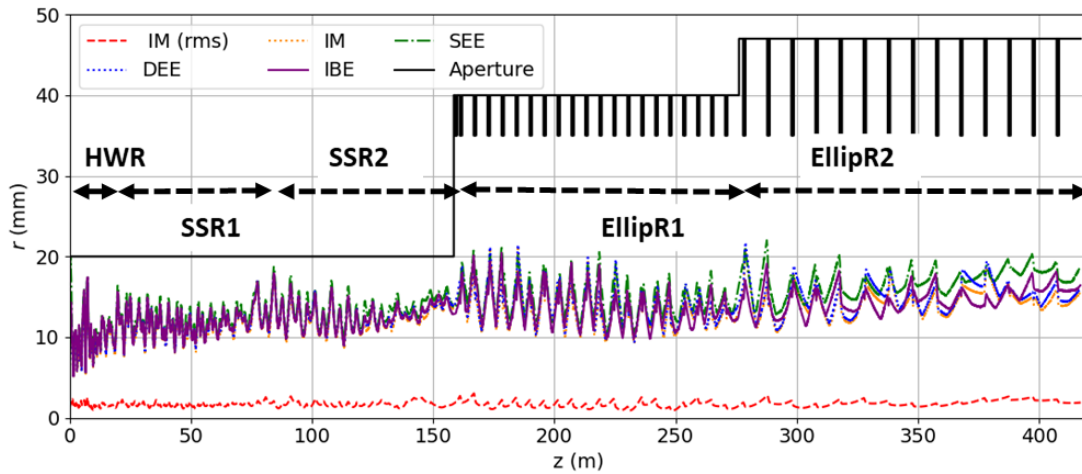


Figure 5: Maximum radial beam size along the Main Linac for the different cases. The aperture and the rms size, for the IM case, are included as a reference.

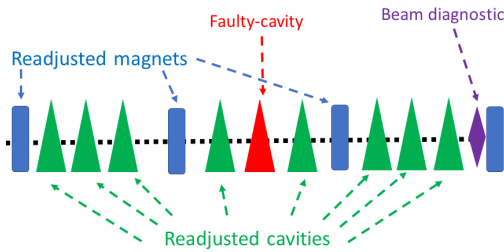
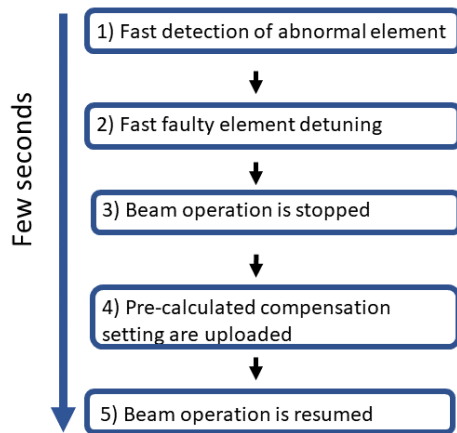


Figure 6: Serial redundancy scheme.

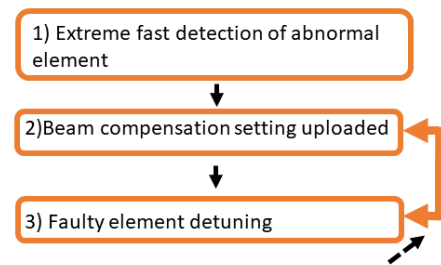
for a failure in the last cavity of the EllipR1 section using this scheme.  $E_{acc}$  and  $\phi_s$  around the faulty SC cavity are readjusted to restore the beam energy at the closest downstream period. Studies indicated that this procedure is suitable for faulty elements in the last four sections of the Main Linac SC cavity. The overall results registered no beam loss, an energy difference below 0.3 %, and the largest mismatch was 0.17. In addition, Fig. 9 presents the transverse and longitudinal  $\epsilon$  growth for the worst compensation performance in a cavity and magnet failure for the SSRs and EllipRs section. This strategy is effective for decreasing the number of beam trips that take longer than 10 s.

For the beam continue compensation scheme, only SC cavities were tested. In addition, the transient behavior of the cavities was computed considering only the detuning contributions of the cold tuning system and Lorentz force [10]. For instance, a failure at the end of the SSR1 section is discussed below. Figure 10 shows the transient behavior of the  $E_{acc}$  and  $\phi_s$  for the faulty cavity. The failure was arbitrarily chosen to occur 500  $\mu$ s after the simulation started, and 1 ms later, the cavity operated with almost the same  $E_{acc}$  as the design; but,  $\phi_s$  suffered a change of  $-150^\circ$ . Figure 11 presents the output energy dropped to zero after 230  $\mu$ s after the failure. It suggests that the adjustment scheme could start at 230  $\mu$ s after the failure, but beam loss is recorded at 160  $\mu$ s later the failure occurred. After a trade-off among a lower number of cavities, stable compensation, and real-

a) Beam **stopping** compensation scheme



b) Beam **continue** compensation scheme



Continuous update according to the transitory behavior of the faulty element.

Figure 7: Serial redundancy strategies.

istic response time, it was decided to use two SC cavities before and three SC after the faulty SC cavity and begin the adjustment 130  $\mu$ s after the failure.

Figure 12 shows that the final energy becomes stable after some hundred microseconds after the compensation is applied. Between the failure starts until a stable compensation is reached, the particles are transported through the linac with an acceptable beam performance.

Content from this work may be used under the terms of the CC BY 3.0 licence (© 2021). Any distribution of this work must maintain attribution to the author(s), title of the work, publisher, and DOI

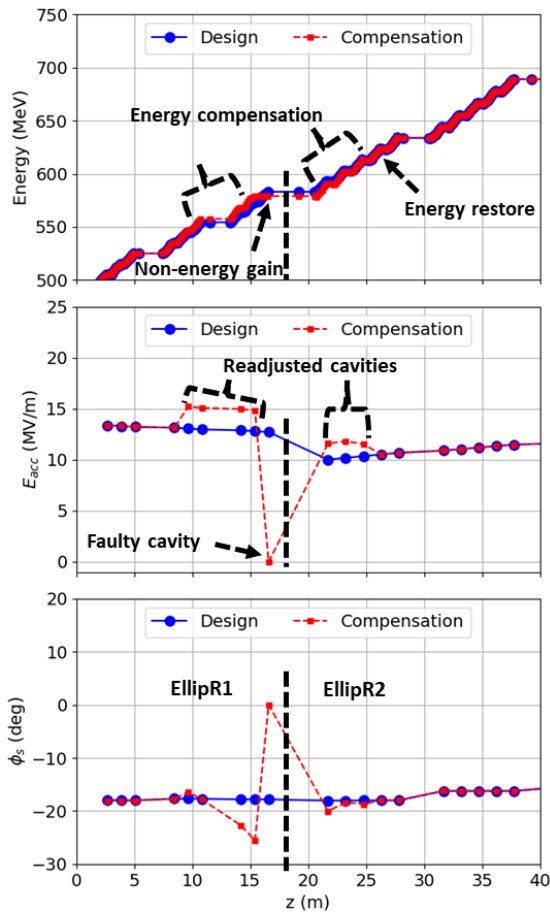


Figure 8: Compensation scheme for the failure in the last EllipR1's cavity. The black-dotted vertical line indicates the transition between EllipR1 and EllipR2 regions.

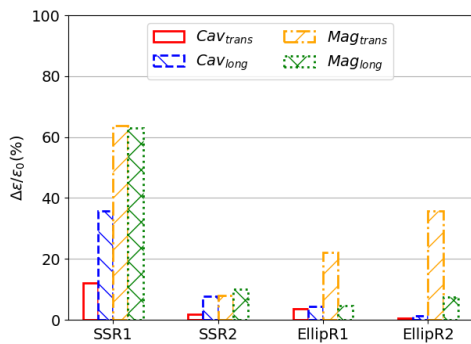


Figure 9: Transverse and longitudinal  $\epsilon$  growth for the worst compensation case in SC regions, excluding the HWR section.

Additionally, Fig. 13 presents the maximum radial envelopes for the design, beam failure, and compensated case. In the beam failure scenario, i.e., without compensation, the beam envelope reached the aperture at the SSR2 section. On the contrary, the envelope for the beam compensated has a similar evolution as the design one. The largest radial beam envelopes in Fig. 13 are smaller than Fig. 5 because the number of macroparticles was reduced as a compromise

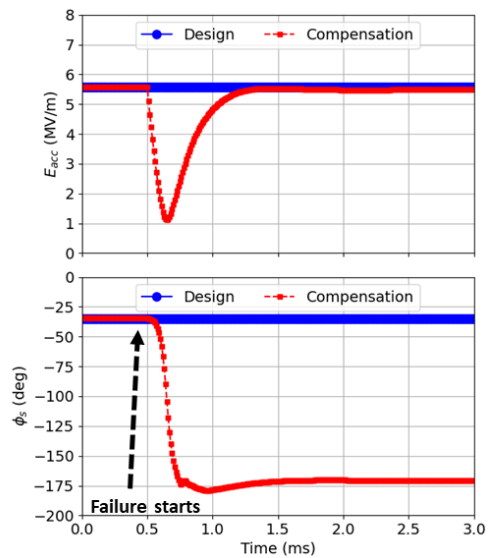


Figure 10:  $E_{acc}$  (top) and  $\phi_s$  (bottom) for the faulty cavity.

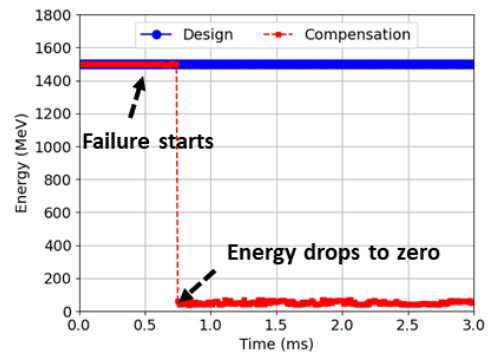


Figure 11: Output energy for the failure case.

between high statistics and the available computational resources. This procedure showed the feasibility of continuing operating the linac in the presence of faulty cavities.

## CONCLUSION

The JAEA-ADS linac pursues a robust beam optics design with fault-tolerance capabilities to avoid thermal stress in the subcritical reactor. The multiparticle tracking studies showed a beam operation with beam losses of 20 mW/m in

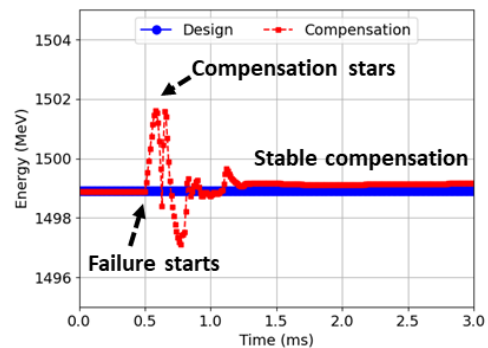


Figure 12: Final energy for the compensation case.

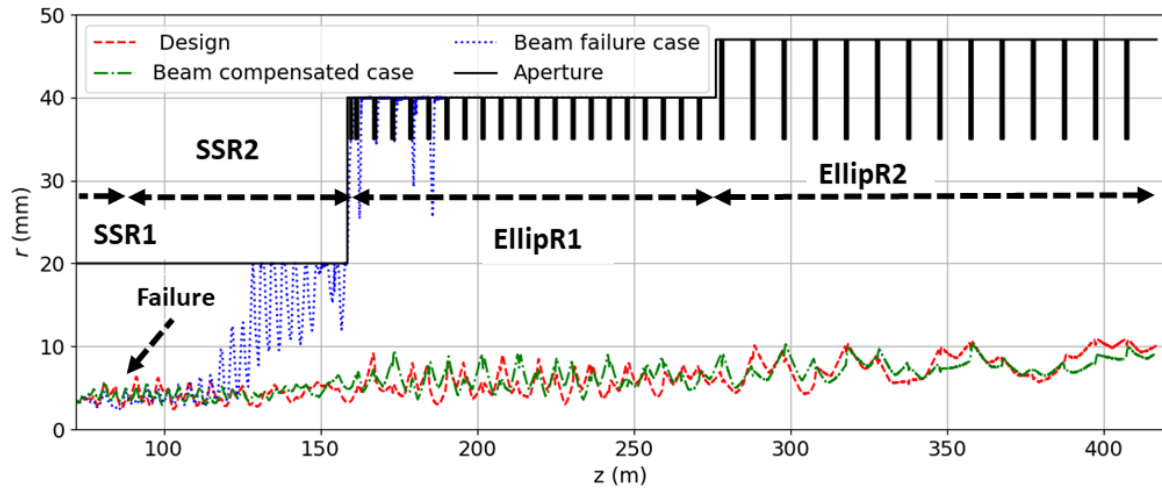


Figure 13: Maximum radial beam size from some periods before the failure starts to the end of the linac.

error cases. In addition, the beam optics design has proper control of the beam envelopes and emittance growth.

The fault-tolerance analysis proved serial redundancy could be applied from the spoke section to the end of the linac to fulfill the stringent reliability with acceptable beam output properties and without compromise the cavity operation or neither a significant increase of the RF power budget. These schemes indicate the possibility of a total or partial reduction of the failure time in the SC cavities and magnets of the linac. Therefore, they represent key conditions to meet the strict reliability of the ADS project.

### ACKNOWLEDGMENTS

The authors would like to thank to the members of the JAEA-ADS for their comments and suggestions. This work is supported by the Subvention for ADS development.

### REFERENCES

- [1] K. Tsujimoto *et al.*, “Neutronics design for lead-bismuth cooled accelerator-driven system for transmutation of minor actinide”, *J. Nucl. Sci. Technol.*, vol. 41, no. 21, p. 21, Jan. 2004. doi:10.1080/18811248.2004.9715454
- [2] D. Vandeplassche and L. Medeiros-Romao, “Accelerator Driven Systems”, in *Proc. 3rd Int. Particle Accelerator Conf. (IPAC’12)*, New Orleans, LA, USA, May 2012, paper MOYAP01, pp. 6–10.
- [3] J.L. Biarrotte, “Reliability and fault tolerance in the European ADS project”, CERN, Geneva, Switzerland, Rep. CERN-2013-001.481, Jun. 2011.
- [4] H. Takei, K. Nishihara, K. Tsujimoto, and H. Oigawa, “Estimation of acceptable beam-trip frequencies of accelerators for accelerator-driven systems and comparison with existing

- performance data”, *J. Nucl. Sci. Technol.*, vol. 49, p. 384, Sep. 2012. doi:10.1088/00223131.2012.669239
- [5] B. Yee-Rendon *et al.*, “Present Status of the R&D of the Superconducting Linac for the JAEA-ADS”, *J. Phys. Soc. Jpn.*, vol. 33, p. 011043, March 2021. doi:10.7566/JPSCP.33.011043
- [6] GenLinWin Manual, <http://irfu.cea.fr/dacm/logiciels/TraceWin/Manual>, <http://irfu.cea.fr/dacm/logiciels>
- [7] Y. Kondo, J. Tamura, and B. Yee-Rendon, “Reference Design of the RFQ for JAEA ADS Linac”, *JPS Conf. Proc.*, vol. 33, p. 011015, March 2021. doi:10.7566/JPSCP.33.011015
- [8] B. Yee-Rendon, J. Tamura, Y. Kondo, F. Maekawa, S. Meigo, and H. Oguri, “Error Studies for the JAEA-ADS Linac”, in *Proc. 17th Annual Meeting of Particle Accelerator Society of Japan (PASJ’20)*, Matsuyama, Japan, Sept. 2020, paper WEOT01, pp. 33–37.
- [9] J.-L. Biarrotte, M. Novati, P. Pierini, H. Safa, and D. Uriot, “Beam Dynamics Studies for the Fault Tolerance Assessment of the PDS-XADS Linac Design”, in *Proc. 9th European Particle Accelerator Conf. (EPAC’04)*, Lucerne, Switzerland, Jul. 2004, paper TUPLT057, pp. 1282–1284.
- [10] J.-L. Biarrotte and D. Uriot, “Dynamic compensation of an rf cavity failure in a superconducting linac”, *Phys. Rev. ST Accel. Beams*, vol. 11, p. 072803, July 2008. doi:10.1103/PhysRevSTAB.11.072803
- [11] B. Yee-Rendon *et al.*, “Progress on SRF Linac Development for the Accelerator-Driven Subcritical System at JAEA”, in *Proc. 20th International Conf. on RF Superconductivity (SRF’21)*, USA., July 2021, paper TUPFAV001, to be published.
- [12] B. Yee-Rendon *et al.*, “Fast Fault Recovery Scenarios for the JAEA-ADS Linac”, in *Proc. 18th Annual Meeting of Particle Accelerator Society of Japan (PASJ’21)*, Japan, Aug. 2021, paper TUOA01, to be published.

# REDUCTION OF THE BEAM JITTER AT THE PIP2IT TEST ACCELERATOR\*

A. Shemyakin<sup>†</sup>, G. Saewert, A. Saini, Fermilab, Batavia, IL 60510, USA

## Abstract

Analysis of the beam position monitor (BPM) signals at the H- test linear accelerator PIP2IT showed that a large portion of the signals scatter comes from the beam jitter. BPM position measurements of the jitter modes were compared with beam orbit responses to perturbations excited by driving various beamline parameters in a low frequency sinusoidal manner. The main contributor to the jitter was found to be a low-frequency noise in the input reference to the ion source high voltage (HV) power supply. Filtering the HV power supply reference signal decreased the rms scatter in BPM readings by a factor of 2-3.

## INTRODUCTION

The PIP-II Injector Test (PIP2IT) [1] was an H<sup>-</sup> ion linac that was assembled in several stages in 2014-2021 to test critical elements of the front end of the PIP-II accelerator currently under development at Fermilab [2]. In its final configuration (Fig. 1), the PIP2IT consisted of a 30 kV, 15 mA H<sup>-</sup> DC ion source, a 2 m long Low Energy Beam Transport (LEBT), a 2.1 MeV CW 162.5 MHz RFQ, a 10 m Medium Energy Beam Transport (MEBT), two cryomodules (HWR and SSR1) accelerating the beam up to 17 MeV, a High Energy Beam Transport (HEBT), and a beam dump.

Transverse focusing was provided by solenoids in the LEBT and cryomodules, and by quadrupole doublets and triplets in the MEBT and HEBT. Each doublet/triplet or solenoid (except in the LEBT) was accompanied by a BPM operating at 162.5 MHz.

The PIP2IT beam was operated in the pulse regime with 20 Hz repetition rate and the bunch population corresponding to the pulse current of 5 mA. The pulse duration varied up to 25 ms, but all measurements described in this paper were performed at 10  $\mu$ s.

Soon after beginning of MEBT operation, it was observed that the pulse-to-pulse variation in the positions measured by BPMs significantly exceeded the expected electronics noise. The scatter was analysed, similar to what

has been reported before (e.g. see Ref. [3]), by simultaneous recording of signals from all BPMs for tens of minutes and applying Singular Value Decomposition (SVD) to the resulting matrix. The scatter was dominated by a single mode. The ratio between the first and second eigenvalues was found to be about 10, and the components beyond the second eigenvalue were already at the noise floor [4].

The first spatial eigenvector was found to be a linear combination of the MEBT betatron modes starting from the RFQ exit. It clearly indicated that the BPM position scatter was dominated by the beam jitter originated upstream of the MEBT. Initial attempts to identify the source of the jitter by checking parameters readbacks in the ion source and LEBT were unsuccessful because of a high level of noise in the reading channels themselves.

While additional analysis [5] showed that the increase in projected emittances due to the jitter is small, the BPM readings scatter did negatively affect quality of measurements. Consequently, in the final run of PIP2IT additional efforts were made to find and correct the source of the jitter.

## CHARACTERIZATION OF BEAM JITTER

An example of beam jitter characterization is shown in Fig. 2. In this measurement, the beam was propagating to the middle of the MEBT at the energy of 2.1 MeV, and beam positions, averaged over a pulse, were recorded by horizontal (X) and vertical (Y) channels of 7 BPMs for 500 seconds at 20 Hz pulse rate. The typical rms scatter was about 0.1 mm (Fig. 2a). The resulting ( $m=10000$ )  $\times$  ( $n=14$ ) matrix  $M$  was decomposed with SVD in MathCad into a product of three matrices:

$$M = ULV^T, \quad (1)$$

where  $L$  is a diagonal  $n \times n$  matrix populated with eigenvalues ordered in the descending order;  $U$  is an  $m \times n$  matrix composed of temporal eigenvectors, and  $V$  is a  $n \times n$  matrix of spatial eigenvectors.

As Fig. 2b shows, the 1<sup>st</sup> eigenvalue exceeded the 2<sup>nd</sup> by a factor of 6. The Fourier spectrum of the 1<sup>st</sup> temporal

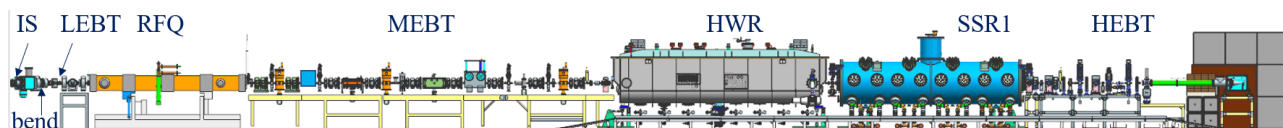


Figure 1: Side view of the PIP2IT.

eigenvector (Fig. 2c) is composed mainly by low-frequency ( $< 4$  Hz) components, with a prominent peak at 1.1 Hz. While this peak was not a dominant contributor to the rms jitter value, it was a convenient marker to match while looking for the noise source. To describe the spatial

\* This manuscript has been authored by Fermi Research Alliance, LLC under Contract No. DE-AC02-07CH11359 with the U.S. Department of Energy, Office of Science, Office of High Energy Physics  
<sup>†</sup> shemyakin@fnal.gov

eigenvector, it is compared with the simulated betatron motion.

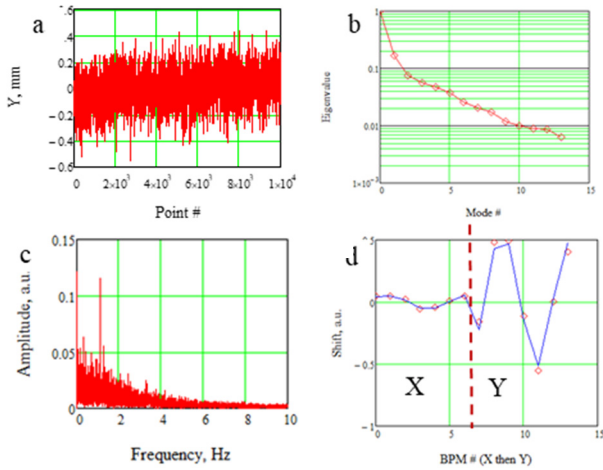


Figure 2: Example of jitter characterization. a- raw signal in Y channel of BPM #3, b- eigenvalues, c- temporal spectrum of the first mode. d- fitting of the 1<sup>st</sup> spatial eigenvector (red dots) to a sum of the betatron modes (blue line). The horizontal axis is the BPM channel number, first X and then Y channels.

First, four “base” trajectories are simulated using OptiM [6] code with the initial conditions at the exit of the RFQ, corresponding to a non-zero value (1 mm or 1 mrad) of only one degree of freedom (either offset or initial angle) in either horizontal or vertical plane. Any beam trajectory in the MEBT is a sum of these base trajectories with coefficients equal to the initial conditions  $(x_n, x'_n, y_n, y'_n)$ . Consequently, the set of initial conditions corresponding to the best fit of the spatial eigenvector (as in Fig. 2d) was used as a characteristic of the noise mode. To express all elements of such set in the same units, they were transformed to canonical variables using the simulated Twiss parameters  $\alpha_x, \beta_x, \alpha_y, \beta_y$ , thus forming the characteristic vector  $R_n$ :

$$R_n = \left( \frac{x_n}{\sqrt{\beta_x}}, \sqrt{\beta_x} x'_n + \frac{\alpha_x x_n}{\sqrt{\beta_x}}, \frac{y_n}{\sqrt{\beta_y}}, \sqrt{\beta_y} y'_n + \frac{\alpha_y y_n}{\sqrt{\beta_y}} \right). \quad (2)$$

A good fit in Fig. 2d indicates that the mode was indeed associated with beam motion and was originated upstream of the first BPM.

## FINDING THE ORIGIN OF THE JITTER

Since no direct position measurements were available upstream of the MEBT, a different procedure was developed to search for the jitter origin. Responses of the beam orbit in the MEBT to various ion source and LEBT parameters were recorded. An orbit response was defined as a difference between BPM readings at nominal settings and with one of parameters (e.g. current of a dipole corrector in the LEBT) changed. Then, the resulting patterns were compared with the spatial distribution of the MEBT noise described in the previous section.

Initial measurements, performed in 2018, literally followed this orbit response definition. The difficulty with such measurements was their poor accuracy. At small parameter variations, contributions of the jitter and parameters drifts were significant as indicated by poor fits to the base trajectories. An increase in the number of pulses measured for each orbit did not significantly improve the actual scatter in the results. An explanation could be that the increased time between orbit measurements enhanced contribution of slow drifts. On the other hand, larger parameter variations resulted in non-linear orbit responses due to beam dynamics in the RFQ.

To resolve this issue, in 2021 the orbit responses were measured with an “oscillating trajectory” method, where a small amplitude sine wave variation was applied to the parameter value, and the Fourier component in the spectrum of all BPMs corresponding to the excitation frequency was recorded, with a proper normalization, as the response. The method was eventually implemented for all orbit response measurements at PIP2IT [7]. This technique applied in the NSLS-II ring had been discussed in Ref. [8]. Example of such measurement at PIP2IT is shown in Fig. 3.

$$\cos \theta_i = \frac{R_n \cdot R_i}{|R_n| |R_i|}, \quad (3)$$

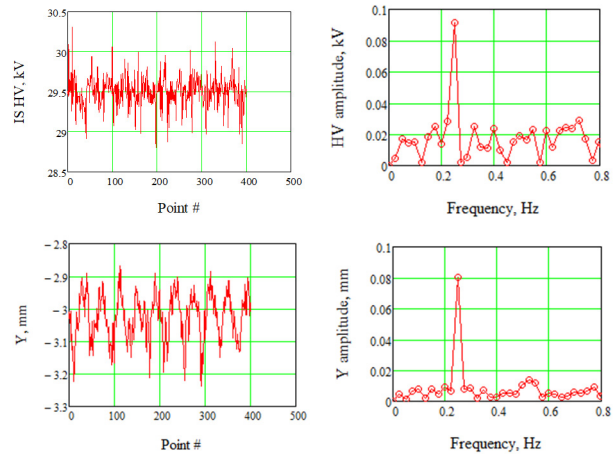


Figure 3: Example of orbit response measurement with oscillating trajectory: response of Y channel of the 1<sup>st</sup> BPM to excitation of the ion source high voltage at 0.25 Hz. 402 points are recorded at 10 Hz. Top row shows readings of IS HV, and the bottom row is the BPM. Left column presents the raw signals, and the right column is the relevant part of the Fourier spectra.

The recorded orbit response was fitted to the base trajectories, and the initial condition vector  $R_i$  was obtained for each tested parameter in the same manner as shown in Eq. (2).

The noise measurements were repeated at the same shift when the orbit responses were measured to ensure identical focusing. In this case, any trajectory is fully determined by its initial conditions, and initial condition vectors of similar trajectories should be colinear. Therefore, the angle  $\theta_i$  between the orbit response and noise vectors was chosen as a measure of similarity, with the angle calculated as

$$\cos \theta_i = \frac{R_n \cdot R_i}{|R_n||R_i|}, \quad (3)$$

where dot represent the scalar product of the vectors.

The results for the 1st and 2nd modes are presented in Table 1 for excitation by the ion source high voltage (IS HV), 5 dipole correctors, LEBT bend, and LEBT chopper. Two measurements repeated at different amplitudes (with the corrector P:L10CYI and with the LEBT bend) show a reasonable reproducibility.

Table 1: Absolute Values of the Angle Between Noise and Orbit Response Vectors

	Mode 1	Mode 2
Ion Source HV	0.018	1.540
P:L00CXI	0.995	0.625
P:L00CXI	0.771	0.849
P:L10CXI	0.590	1.030
P:L10CYI	1.191	0.333
P:L10CYI	1.038	0.485
P:L20CXI	0.025	1.502
P:L20CYI	1.148	0.472
P:L30CXI	1.138	0.386
P:L30CYI	0.663	0.957
LEBT bend	0.366	1.254
LEBT bend	0.344	1.276
LEBT chopper	1.235	0.597

Two excitations, highlighted in the table, with the IS HV and P:L20CXI (the horizontal corrector in the second solenoid), both produce the angles close to zero. Their spatial distributions fitted to the first jitter mode are shown in Fig. 4.

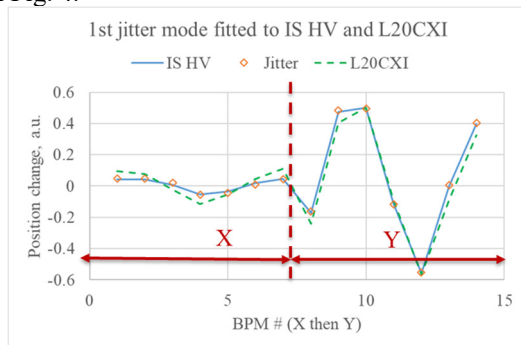


Figure 4: Comparison of the first spatial mode of the beam jitter in the MEBT (orange diamonds) with the best fits of responses to excitation by IS HV (solid line) and corrector P:L20CXI (dashed line).

To explain the observed beam jitter using the fit shown in Fig. 4, the noise in the P:L20CXI corrector current needed to be by about 8 times higher than the noise value measured in its readback. Therefore, the corrector was ruled out as the primary source of the jitter.

On the other hand, the fit assuming that the jitter was originated in the IS HV required 56 V rms noise (out of 30 kV DC), while its readback delivered the noise with 200 V rms.

The presented results were considered conclusive enough to justify additional efforts of investigating the ion source high voltage stability.

Note that instead of the described procedure of comparing the initial vectors corresponding to the noise and the tested component with Eq. (3), initially we directly fitted the measured orbit responses to the noise spatial vector as it was done for Fig. 4. In this approach, the figure of merit was the rms error of fitting. Applying this procedure to the measurements used in Table 1 eventually gave the same result, pointing to IS HV as the jitter source. However, introduction of the intermediate step of fitting to the base trajectories helped to eliminate bad measurement sets and appeared to make the procedure more reliable and accurate.

## REDUCTION OF THE JITTER

Following the conclusion derived in the previous section, a commercial 50 kV resistive divider was installed to monitor the 30 kV DC IS HV power supply (PS) output. This signal was buffered and isolated from the instrumentation ground to eliminate any common mode noise that might be between the PS and instrumentation. A low frequency spectrum analyzer readily showed the frequencies of interest, and particularly the 1.1 Hz line (Fig. 5 left).

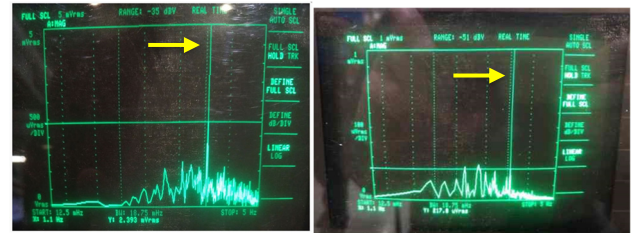


Figure 5: Screenshots of the low frequency spectrum analyzer showing the signal from the resistive divider before (left) and after (right) installation of the filter. The arrows indicate the 1.1 Hz marker. The vertical scale is 5 mV in the left plot and 1 mV on the right.

This analyzer was an HP 3561A Dynamic Signal Analyzer with 0.125 mHz to 100 kHz bandwidth. It was used with AC coupling that suppressed the signal below ~0.1 Hz.

The ripple specified for the IS HV PS, Glassman LT40N50, is small, < 12 V rms [9]. Therefore, we suspected that the noise could be caused by the reference DAC signal and/or common mode noise between the DAC and PS. The same spectrum analyzer was used to measure the ground signals between the 30 kV PS and the DAC reference chassis and showed the same noise spectrum at about the expected amplitude. Hence, a low-pass R/C filter having a cut-off frequency pole at 0.12 Hz was installed at the PS reference input, attenuating both the common mode and single-ended noise arriving over the long cable from the DAC reference.

Content from this work may be used under the terms of the CC BY 3.0 licence (© 2021). Any distribution of this work must maintain attribution to the author(s), title of the work, publisher, and DOI

The measurements of the HV output spectrum, repeated after installation of the filter, showed a significant decrease of the noise (Fig. 5 right). For example, the rms amplitude of the characteristic 1.1 Hz line decreased from 2.4 to 0.22 mV.

The measurements of the BPM scatter were repeated for same transverse focusing before and after installation of the filter with the beam propagated through the entire PIP2IT without acceleration in the cryomodules. Comparison of the rms scatter in each BPM channel is shown in Fig. 6. After installation of the filter, the rms scatter, averaged over all BPMs, decreased by 2.5 times in X and by 3.1 times in Y.

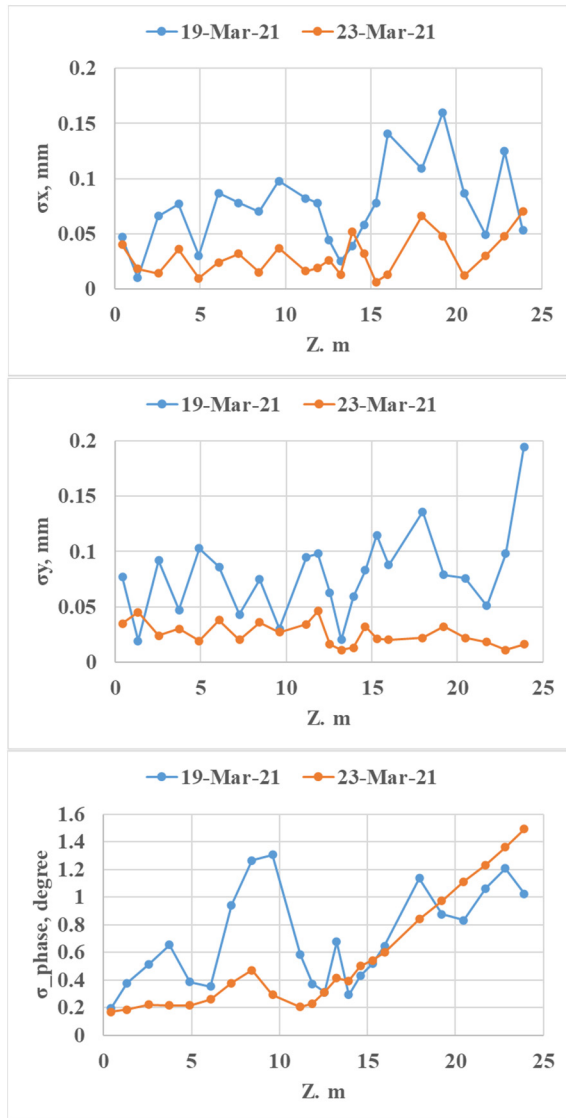


Figure 6: Comparison of the scatter in BPM readings before (marked 19-Mar-21) and after (23-Mar-21) installation of the IS HV PS reference input filter. Beam energy was 2.1 MeV. 5000 points recorded at 20 Hz were analyzed in each case. The top, middle, and bottom plots show the rms scatter for each BPM in horizontal vertical, and longitudinal (phase) planes, correspondingly. The phases are expressed in units of degrees of 162.5 MHz.

The scatter in the phases recorded by BPMs decreased significantly as well, as shown in Fig. 6 bottom plot. A numerical comparison of all BPM readings is not applicable since the field amplitudes in the last two bunching cavities were slightly different between two measurements. While it doesn't affect noticeably the transverse dynamics, the energy jitter in the drift space downstream of the MEBT strongly depends on specific bunching cavities' settings. Inside the MEBT ( $Z < 10$  m), the average rms scatter decreased by a factor of 2.5.

Since the decrease of the BPM phase scatter was not originally expected, the phase signals in the data sets used for Fig. 6 were analysed in more detail. The BPM phase signals before installation of the IS HV PS filter showed the frequency spectrum very similar to the one shown in Fig. 2c for the transverse motion, with the same characteristic 1.1 Hz line. Analysis of the first SVD spatial mode indicated that it corresponded to the energy jitter at the exit of the RFQ with rms amplitude of 0.2 keV.

After the filter installation, the 1.1 Hz line disappeared in all BPM signals. The remaining noise was confined to frequencies below 0.2 Hz. The eigenvalues of the first modes were comparable, which indicated that the beam jitter was indistinguishable at the measurement noise.

Response of the BPMs to excitation of the IS HV (before installation of the filter) was recorded as well (Fig. 7). Since the measurement was made again at different settings of the bunching cavities, direct fitting to the beam jitter was not possible. However, conditions at the RFQ exit calculated from the Fig. 7 data agreed with observations in the beam jitter: the response in the initial phase was close to zero, and variation of energy was 3.8 times higher than variation of the IS HV.

We conclude that before installation of the filter a dominant portion of the BPM phase scatter was also related to the noise of IS HV.

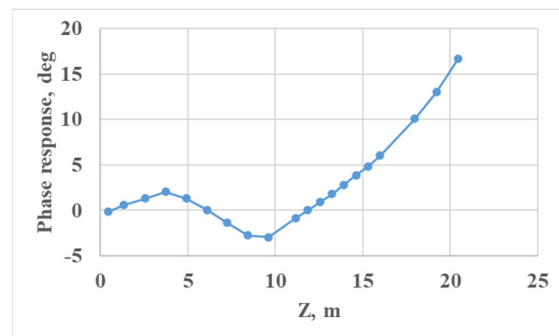


Figure 7: Response of BPM phases to oscillation of the IS HV with 0.2 kV amplitude and 0.125 Hz frequency. 802 points were recorded at 5 Hz. Beam energy was 2.1 MeV.

## CONCLUSION

The scatter in BPM readings at PIP2IT was analysed with SVD and found to be dominated by the beam jitter. To find the source of the jitter, responses of the orbit in the MEBT to variation of parameters in the LEBT and the ion source were measured by applying a small-amplitude si-

nusoidal variation to each parameter and recording the corresponding line in the BPM spectra. Comparison of these orbit responses with the jitter spatial pattern determined that the source of the jitter was the ion source high voltage noise at the level of about 60 V rms. The observation was supported by direct measurements of the high voltage signal. Installation of the low-pass filter at the HV power supply reference signal decreased the rms scatter in BPM position readings by a factor of 2-3. The scatter in BPM phase readings in the MEBT decreased as well by a similar factor.

## ACKNOWLEDGEMENTS

Authors are thankful to the entire PIP2IT team for assistance with the measurements. All data acquisition programs were written by W. Marsh. Discussions with L. Prost and C. Jensen helped to identify the HV power supply reference signal as a likely source of the noise. Support of N. Eddy with BPM measurements is appreciated.

## REFERENCES

[1] P. Derwent *et al.*, “PIP-II Injector Test: Challenges and Status”, in *Proc. 28th Linear Accelerator Conf. (LINAC'16)*, East Lansing, MI, USA, Sep. 2016, pp. 641-645. doi:10.18429/JACoW-LINAC2016-WE1A01

- [2] L. Merminga *et al.*, “The Proton Improvement Plan-II (PIP-II): Design, physics, and technology advances”, invited submission to *Phys. Rev. Accel. Beams* (in preparation), 2021.
- [3] J. Irwin *et al.*, “Model-independent analysis with BPM correlation matrices”, in *Proc. EPAC'98*, Stockholm, Sweden, Jun. 1998, pp. 1644-1646.
- [4] A. Shemyakin *et al.*, “Experimental study of beam dynamics in the PIP-II MEBT prototype”, in *Proc. of HB'18*, Daejeon, Korea, Jun. 2018, pp. 54-59. doi:10.18429/JACoW-HB2018-MOP1WB03
- [5] A. Saini *et al.*, “Beam tests of the PIP-II Injector Test Radio Frequency Quadrupole”, *Nucl. Instrum. Methods Phys. Res., Sect. A*, vol. 978, p. 164368, 2020. doi:10.1016/j.nima.2020.164368
- [6] OptiM, <http://home.fnal.gov/~ostiguy/OptiM/>.
- [7] A. Shemyakin, “Orbit response measurements with oscillating trajectories”, Fermilab, USA, FERMILAB-TM-2763-AD, 2021, <https://arxiv.org/abs/2109.11589>
- [8] X. Yang, V. Smaluk, L. H. Yu, Y. Tian, and K. Ha, “Fast and precise technique for magnet lattice correction via sine-wave excitation of fast correctors”, *Phys. Rev. Accel. Beams*, vol. 20, p. 054001, 2017. doi:10.1103/PhysRevAccelBeams.20.054001
- [9] Glassman catalog, <https://www.vicomtrade.cz/pdf/glassman-catalog.pdf>

# RESONANCE COMPENSATION FOR HIGH INTENSITY AND HIGH BRIGHTNESS BEAMS IN THE CERN PSB

F. Asvesta\*, S. Albright, F. Antoniou, H. Bartosik, C. Bracco, G. P. Di Giovanni,  
 E. H. Maclean, B. Mikulec, T. Prebibaj<sup>1</sup>, E. Renner<sup>2</sup>  
 CERN, Geneva, Switzerland

<sup>1</sup>also at Goethe University, Frankfurt, Germany, <sup>2</sup>also at TU Wien, Vienna, Austria

## Abstract

Resonance studies have been conducted during the recommissioning of the CERN Proton Synchrotron Booster (PSB) following the implementation of the LHC Injectors Upgrade (LIU) project. In particular, resonance identification through so-called loss maps has been applied on all four rings of the PSB, revealing various resonances up to fourth order. In a second step, compensation schemes for the observed resonances were developed using a combination of analytical methods, experimental data and machine learning tools. These resonance compensation schemes have been deployed in operation to minimize losses for reaching high intensity and high brightness, thereby achieving the target brightness for the LHC-type beams.

## INTRODUCTION

After the completion of the LIU project [1], the PSB faces the challenge of achieving the target values of twice the brightness for the LHC-type beams and increased intensity for the fixed target beams of the various physics users, such as ISOLDE [2] and n-TOF [3], as well as possible future users in the scope of the Physics Beyond Colliders (PBC) project [4]. The main limitations for reaching these goals come from space charge effects, which have been mitigated with the increase in injection energy achieved with the new linear accelerator, Linac4 [5], and the H<sup>-</sup> charge exchange injection scheme [6, 7]. However, the  $\beta$ -beating introduced by the injection chicane in the first few ms [8] of the cycle, as well as betatron resonances excited by machine imperfections, still require careful correction for reaching the target beam parameters.

Extended resonance studies were conducted in the pre-LIU era to characterize the resonances, in all PSB rings, at the new injection energy of 160 MeV [9, 10]. The studies, which were used as a preparatory stage for a smoother recommissioning period, revealed several 3<sup>rd</sup> order normal and skew resonances. It should be noted that the four superposed rings did not behave the same in terms of resonances. For example, in Ring 4 only the normal sextupole resonance,  $Q_x + 2Q_y = 13$ , was observed while in Ring 3 all skew and normal 3<sup>rd</sup> order resonances resulted in losses. In addition, the compensation values for the same resonance in different rings, such as the half integer resonance excited in all rings, were different. However, the energy upgrade was only part of the LIU project. The newly installed elements, like the ones

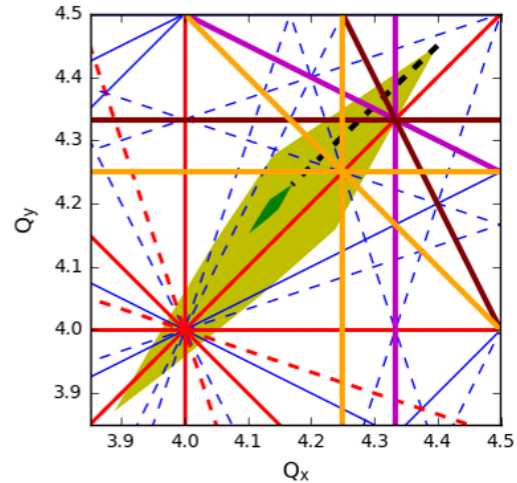


Figure 1: Schematic of the expected incoherent tune spreads at the PSB injection (yellow area) and extraction (green area) for the LHC-type beams. The tunes are varied during the cycle following the dotted black line. Resonance lines up to 4<sup>th</sup> order are plotted, normal in solid and skew in dashed. The non-systematic resonance lines are plotted in blue and the systematic in red. Potentially excited resonances of interest are highlighted in different colors depending on their order, 3<sup>rd</sup> order normal in purple, skew in brown and 4<sup>th</sup> order normal in orange.

needed for the new injection scheme, can have an impact on the excitation of the resonances and hence past studies can only offer an indication of the post-upgrade behaviour. Furthermore, the expected incoherent space charge tune spread at the PSB injection can be, in absolute value, larger than  $|\Delta Q_{x,y}| > 0.5$  for the higher brightness beams [11, 12]. Consequently, the tunes are set to high values at injection, for example  $Q_x = 4.4 / Q_y = 4.45$  for these beams. The tunes are then varied during acceleration to reach the optimized extraction tunes of  $Q_x = 4.17 / Q_y = 4.23$ . Hence, the tune space of interest is large and multiple resonances are crossed during normal operation as shown in Fig. 1. In this respect, complete studies in order to identify and compensate any observed resonances were crucial during the commissioning phase to prepare the operational beams.

## RESONANCE IDENTIFICATION

The resonance studies were one of the priorities of the commissioning period in the PSB, as multiple 2<sup>nd</sup> and 3<sup>rd</sup>

\* foteini.asvesta@cern.ch

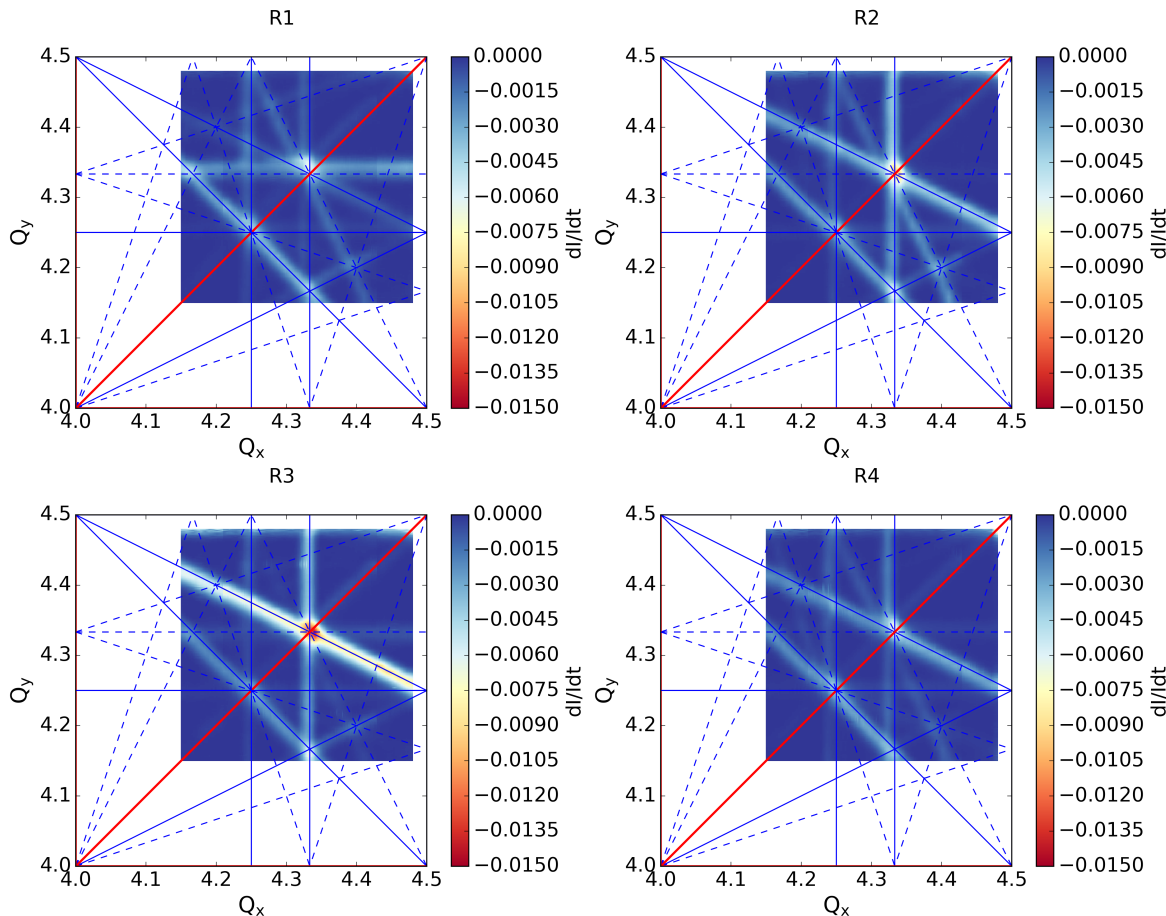


Figure 2: Loss maps resulting from dynamic tune scans in all four rings of the PSB. The transverse tune space is color coded using the loss rate variation. Resonance lines up to 4<sup>th</sup> order are plotted, normal in solid lines and skew in dashed. The non-systematic resonance lines are plotted in blue and the systematic, the coupling resonance in this case, in red.

order resonances were expected to be excited [10]. In order to identify the resonances in the transverse tune space, the dynamic tune scan technique was used to produce the loss maps. In this technique, one of the tunes is kept constant throughout the cycle while the other one is changed dynamically. At the same time, the intensity is recorded and the resonances are revealed through the induced losses. The range of tunes for the scan is 4.15 to 4.48 and the step for the static tune is 0.0085. For the studies, a flat cycle at the injection energy of 160 MeV is used. In this manner, the beam is stored for a long time, 275 ms to 700 ms, and all resonances are studied at the same energy. It should be highlighted that only cycle times after 350 ms are considered to avoid effects coming from the injection process and ensure that the beam parameters are the same at the beginning of each scan. The beam is setup in order to have a small space charge tune spread of  $\Delta Q_{x,y} = -0.035$ , as low brightness beams are the most sensitive in terms of losses to machine driven errors [13].

The dynamic tune scans are conducted in all rings of the PSB and in all directions, i.e. four different scans for each ring. Initially the  $Q_x$  is kept constant while  $Q_y$  varies from max to min following a scan in which it varies from min to

max, the same is repeated keeping  $Q_y$  constant and varying the  $Q_x$ . The different scans are needed as the dynamic tune or the direction of the crossing can have an impact on the observable, i.e. the loss rate. For example, 1D resonances, such as the  $3Q_x = 13$ , can be completely transparent if they are not dynamically crossed, i.e. varying the  $Q_x$  in this case, as on the resonance they create constant losses and not a variation of the loss rate. The direction of the tune sweep can also affect which resonances appears stronger, since the beam degrades during the first crossing of a resonance and subsequent resonance crossings can exhibit a different behavior in terms of loss rate. In the loss maps shown in this paper, the average value for all four scans in each ring is considered.

The resulting loss maps for each ring with the natural excitation of the resonances in the PSB, are shown in Fig. 2. In all rings we can identify resonances up to 4<sup>th</sup> order. In fact, even though the strength of the resonances is not the same in all rings, as deduced from the presented loss rate, all 3<sup>rd</sup> (normal and skew) and 4<sup>th</sup> (normal) order resonances are excited in all rings. It should be noted that this was an unexpected result as the 4<sup>th</sup> order resonances were not observed in the PSB before the LIU upgrade. In addition,

Content from this work may be used under the terms of the CC BY 3.0 licence (© 2021). Any distribution of this work must maintain attribution to the author(s), title of the work, publisher, and DOI

previous studies had shown that different resonances were excited in different rings. In the recent results, the only ring that exhibits a different behaviour is Ring 1 as the dominating errors seem to be the ones exciting the 3<sup>rd</sup> order skew resonances,  $3Q_y = 13$  and  $2Q_x + Q_y = 13$ , and not the 3<sup>rd</sup> order normal ones,  $3Q_x = 13$  and  $Q_x + 2Q_y = 13$ , as in the other rings. The strongest resonance in terms of losses is the  $Q_x + 2Q_y = 13$  in Ring 3. This resonance is observed inducing less losses in the other rings. Finally, the half integer resonance was not included in the scan as the full beam is lost once the 4.5 tune is approached in either plane.

## RESONANCE COMPENSATION

The naturally excited 2<sup>nd</sup> and 3<sup>rd</sup> order resonances in the PSB can be compensated using the available correctors as demonstrated in the past [10, 14]. Even though 4<sup>th</sup> order resonances had not been previously observed, the PSB is equipped with octupole correctors that could act on the observed resonances. To compensate the resonances, a technique based on both analytical tools (Resonance Driving Terms (RDT) analysis using PTC [15] in MADX [16]) and experimental data (intensity monitoring while dynamically crossing the resonance and varying the corrector strengths) is used, as described in [10, 13, 17].

### Vertical Half Integer Resonance

The resonance at  $Q_y = 4.5$  is the strongest in the regime of interest for the operation of the PSB. The injection working point for the high brightness beams is  $Q_x = 4.40 / Q_y = 4.45$  as shown in Fig. 1. Past studies had suggested pushing it above the half integer resonance at  $Q_x = 4.43 / Q_y = 4.60$  to improve brightness [9]. As a result, the first compensation studies focused on the  $2Q_y = 9$  resonance. In the past, the half integer resonance was perfectly compensated [10]. Currently only a partial compensation is possible with  $\approx 5\%$  remnant losses during the crossing as seen in Fig. 3 where the natural excitation and the best found configuration are given. It should be noted that this is not correlated to the  $\beta$ -beating induced by the injection chicane, as the resonance is studied long after the injection process has finished. The fact that the half integer is not perfectly compensated is a limitation for the brightness and the high intensity beams

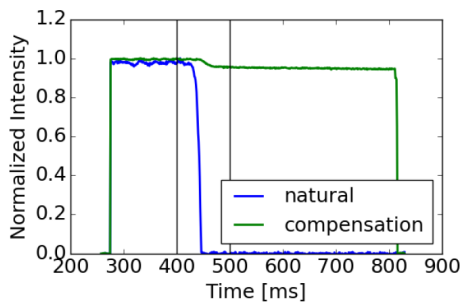


Figure 3: Normalized intensity while crossing the half integer resonance from 400 ms to 500 ms with the natural excitation (blue) and after the compensation (green).

for tunes  $Q_y > 4.5$ . Consequently, all operational beams are currently setup below the  $2Q_y = 9$ .

### High Order Resonances

Nonlinear higher order resonances are compensated following the same procedure. For each resonance the corresponding correction magnets are used, i.e. sextupoles are used for 3<sup>rd</sup> order normal, skew sextupoles for 3<sup>rd</sup> order skew and octupoles for 4<sup>th</sup> order normal resonances. Every time two correctors (orthogonal for the corresponding RDT) are varied and only one resonance is crossed. Like this, the magnet strengths can be used in the MADX PSB model to identify the RDT of the excitation and characterize the resonance.

Resonances of 3<sup>rd</sup> order, both normal and skew, are always fully compensated, however, the 4<sup>th</sup> order resonances could only be partially corrected. Figure 4 shows two representative cases, one of a full compensation of a 3<sup>rd</sup> order normal resonance (left) and one of a partial compensation of a 4<sup>th</sup> order resonance (right). The resonance is fully compensated as a region with practically no losses is identified in Fig. 4 (left). On the other hand, the compensation of the 4<sup>th</sup> resonance cannot be further improved as the correctors are running out of their limits ( $\pm 50$  A) before the losses are completely eliminated in Fig. 4 (right). It is worth noting that in the half integer case discussed previously the limitation for the compensation is not coming from the current as the minimum loss region was fully identified.

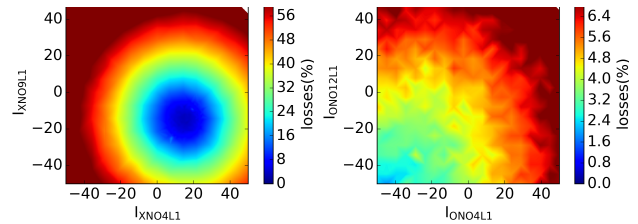


Figure 4: Current configuration of the corresponding correctors to compensate a normal sextupole (left) and normal octupole (right) resonance color coded to the measured losses as the resonance is being crossed.

Given the fact that during normal operation the tune in the PSB changes, as shown in Fig. 1, it is important to investigate global corrector settings that can compensate all resonances of concern at the same time. In this manner, no losses or emittance blow-up should be induced when the resonances are crossed or overlapped due to the space charge induced tune shift. Global settings for the 4<sup>th</sup> order resonances were found experimentally, as all resonances had similar compensation values. It is reminded that, as shown in Fig 4, the compensation for the octupoles is partial. However, for the 3<sup>rd</sup> order resonances, the settings of the correctors were different for each resonance and no global corrections could be found experimentally.

Using in the MADX model the corrector settings found experimentally, the RDT of the error that drives each resonance can be approximated. Calculating the RDTs of each

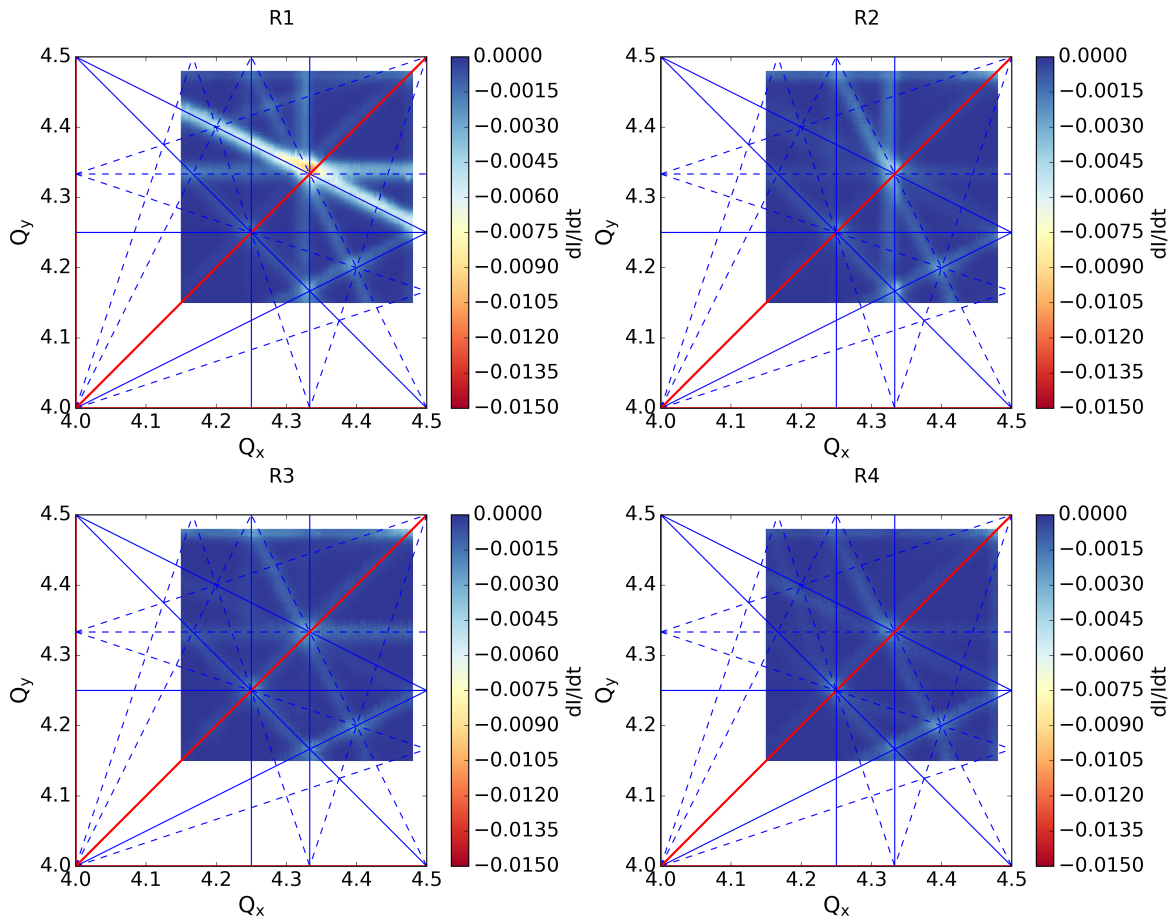


Figure 5: Loss maps resulting from dynamic tune scans in all four rings of the PSB with octupoles and sextupoles for the simultaneous correction of the 3<sup>rd</sup> and 4<sup>th</sup> order normal resonances. Note that in R2 only one of the 3<sup>rd</sup> order normal resonances is compensated. The transverse tune space is color coded using the loss rate variation. Resonance lines up to 4<sup>th</sup> order are plotted as in Fig. 2.

available corrector magnet on the crossing point of the resonances, one could try and characterize the combined effect of each magnet to all considered resonances. For example, performing the RDT analysis at  $Q_{x,y} = 4.33$ , i.e. the cross-

ing point for two 3<sup>rd</sup> order normal resonances  $3Q_x = 13$  and  $Q_x + 2Q_y = 13$ , this response matrix can be devised:

$$\begin{bmatrix} \text{Re}[RDT_{3Q_x}^{sext1}] & \text{Re}[RDT_{3Q_x}^{sext2}] & \text{Re}[RDT_{3Q_x}^{sext3}] & \text{Re}[RDT_{3Q_x}^{sext4}] \\ \text{Im}[RDT_{3Q_x}^{sext1}] & \text{Im}[RDT_{3Q_x}^{sext2}] & \text{Im}[RDT_{3Q_x}^{sext3}] & \text{Im}[RDT_{3Q_x}^{sext4}] \\ \text{Re}[RDT_{Q_x+2Q_y}^{sext1}] & \text{Re}[RDT_{Q_x+2Q_y}^{sext2}] & \text{Re}[RDT_{Q_x+2Q_y}^{sext3}] & \text{Re}[RDT_{Q_x+2Q_y}^{sext4}] \\ \text{Im}[RDT_{Q_x+2Q_y}^{sext1}] & \text{Im}[RDT_{Q_x+2Q_y}^{sext2}] & \text{Im}[RDT_{Q_x+2Q_y}^{sext3}] & \text{Im}[RDT_{Q_x+2Q_y}^{sext4}] \end{bmatrix} \times \begin{bmatrix} F_{k^{sext1}} \\ F_{k^{sext2}} \\ F_{k^{sext3}} \\ F_{k^{sext4}} \end{bmatrix} = \begin{bmatrix} \text{Re}[RDT_{3Q_x}^{meas}] \\ \text{Im}[RDT_{3Q_x}^{meas}] \\ \text{Re}[RDT_{Q_x+2Q_y}^{meas}] \\ \text{Im}[RDT_{Q_x+2Q_y}^{meas}] \end{bmatrix} \quad (1)$$

where, the real and imaginary parts of the measured RDTs and the RDTs from the individual sextupoles can be used to identify the factors  $F_{k^{sext(1,2,3,4)}}$  that are needed in all sextupoles to compensate both resonances at the same time. Note that in order to acquire a global solution using this technique, at least two correctors are needed for each resonance, i.e. 4 in this example. Due to current limitations, the solution for ring 2 could not be used and in ring 1 an extra sextupole magnet, i.e. 5 in total, had to be included. To add this extra magnet, the combined RDT of two sextupoles pow-

ered at the same current was used in Eq. (1). This procedure was followed for the 3<sup>rd</sup> order normal resonance but could not be tested for the skew resonances, as only three skew sextupole correctors are currently connected in all rings.

The global settings for the octupoles and the normal sextupoles are tested experimentally in the machine and the resonance identification studies are repeated. The resulting loss maps with the settings for the compensation of 3<sup>rd</sup> and 4<sup>th</sup> order normal resonances are given in Fig. 5. The 4<sup>th</sup> order resonances seem to be corrected at a satisfactory

Content from this work may be used under the terms of the CC BY 3.0 licence (© 2021). Any distribution of this work must maintain attribution to the author(s), title of the work, publisher, and DOI

level in all rings. On the other hand, the sextupole resonances appear well compensated in rings 2, 3 and 4 (recall that in ring 2 only the setting for the  $Q_x + 2Q_y = 13$  is active), but in ring 1 the situation is quite different. The normal sextupole resonances, which were not very strong naturally as shown in Fig. 2, appear substantially enhanced. This implies a cross talk between the corrector magnets and resonances, other than the ones they are compensating. To investigate this interaction further loss maps compensating the sextupole and octupole resonances alone were performed and are shown in Figs. 6 and 7 respectively. Figure 6 shows that the analytically acquired global compensation values for the sextupole resonances in rings 1, 3 and 4 work as expected and do not affect the other resonances. In the case of octupoles however, (Fig. 7), while the 4<sup>th</sup> order resonances are compensated the 3<sup>rd</sup> order resonances, especially the normal ones, are strongly enhanced in all rings.

### Optimizer Tools

The significant cross talk of the correctors with the resonances and the difficulties in identifying global settings for the skew sextupoles pushed for further optimizations of the compensation schemes. To this end, the tool Generic Optimisation Frontend and Framework (GeOFF) [18], which uses the python implementation of the algorithm for bound constrained optimization without derivatives, pyBOBYQA [19–21], was used to refine the scheme.

The optimization tool significantly reduces the time needed for the corrector current scans as it diminishes the need for a full scan of the parameter space. Consequently, it's possible to use more corrector magnets to improve the compensation of partial corrected resonances as well as in-

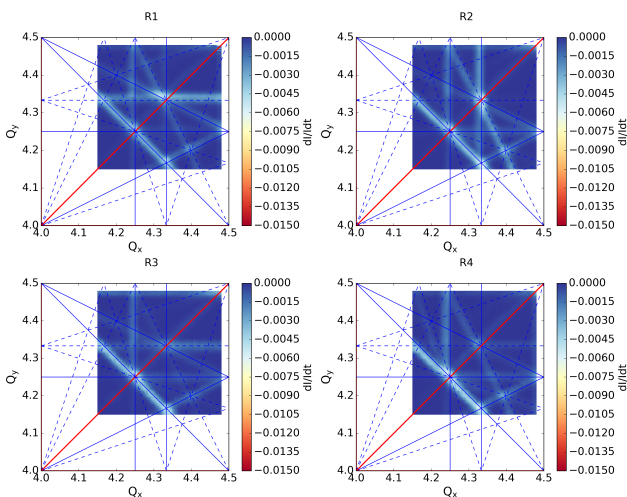


Figure 6: Loss maps resulting from dynamic tune scans in all four rings of the PSB with sextupoles for the compensation of the 3<sup>rd</sup> order normal resonances,  $3Q_x = 13$  and  $Q_x + 2Q_y = 13$ . Note that in R2 only the  $Q_x + 2Q_y = 13$  is compensated as not enough correctors were available. The transverse tune space is color coded using the loss rate variation. Resonance lines up to 4<sup>th</sup> order are plotted as in Fig. 2.

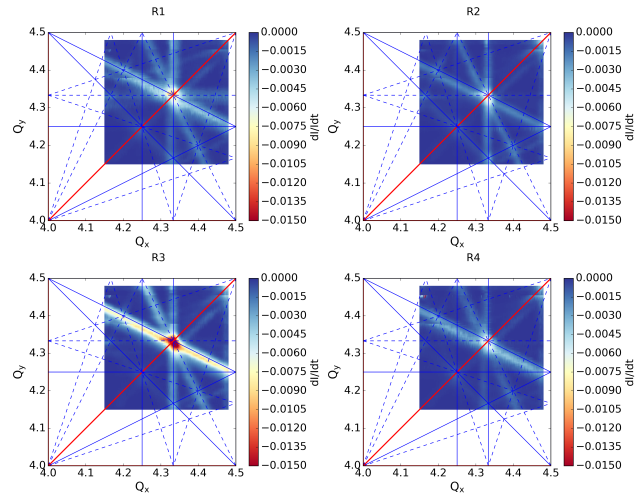


Figure 7: Loss maps resulting from dynamic tune scans in all four rings of the PSB with octupoles for the compensation of the 4<sup>th</sup> order normal resonances,  $4Q_x = 17$ ,  $4Q_y = 17$  and  $2Q_x + 2Q_y = 17$ . The transverse tune space is color coded using the loss rate variation. Resonance lines up to 4<sup>th</sup> order are plotted as in Fig. 2.

vestigate global settings experimentally. As a first step, the resonances were tackled individually. The compensation settings for several resonances appeared different than what was measured at the beginning of the year. It should be noted that these differences are not connected to the new tools used but rather indicate that since the commissioning the errors changed. Furthermore, the 4<sup>th</sup> order compensation was improved using all the available octupoles (four per ring) and global settings for the 3<sup>rd</sup> order skew resonances were found using all skew sextupoles (three per ring). These optimized settings have improved the performance of the machine, contributing to the increased brightness [8]. However, studies are still ongoing to further characterize the resonances and improve the performance exploiting the full potential of the optimizer framework.

## CONCLUSION

Resonance studies were conducted in the PSB during the commissioning period after the upgrade in the frame of the LIU project. The studies revealed resonances up to 4<sup>th</sup> order in all rings, that were observed for the first time. Compensation schemes allowing for global compensation of the resonances were developed through extensive experimental and analytical studies. Refinement of the schemes with optimizer tools provides a better compensation for all resonances and has contributed to higher brightness and intensity for the PSB users.

## ACKNOWLEDGEMENTS

The authors would like to thank the PSB Operations and commissioning teams for their support during the experiments and A. Huschauer, V. Kain and N. Madysa for the optimization tools used during the resonance compensation campaign.

## REFERENCES

- [1] H. Damerau *et al.*, “LHC Injectors Upgrade, Technical Design Report, Vol. I: Protons”, Technical Report, CERN-ACC-2014-0337, Dec 2014.
- [2] B. Jonson and K. Riisager, “The ISOLDE facility”, *Scholarpedia*, vol. 5, no. 7, p. 9742, 2010. doi:10.4249/scholarpedia.9742
- [3] A. Mengoni *et al.*, “Status and perspectives of the neutron time-of-flight facility nTOF at CERN”, *EPJ Web Conf.*, vol. 239, p. 17001, 2020. doi:10.1051/epjconf/202023917001
- [4] J. Jaeckel, M. Lamont, and C. Vallee “The quest for new physics with the Physics Beyond Colliders programme”, *Nat. Phys.*, vol. 16, pp. 393–401. 2020. doi:10.1038/s41567-020-0838-4
- [5] L. Arnaudon *et al.* “Linac4 Technical Design Report”, CERN, Geneva, Switzerland, Rep. CERN-AB-2006-084, 2006
- [6] E. Renner *et al.*, “Beam Commissioning of the New 160 MeV H- Injection System of the CERN PS Booster”, in *Proc. 12th Int. Particle Accelerator Conf. (IPAC'21)*, Campinas, Brazil, May 2021, paper WEPAB210, pp. 3116–3119. doi:10.18429/JACoW-IPAC2021-WEPAB210
- [7] E. H. Maclean *et al.*, “Optics Measurement by Excitation of Betatron Oscillations in the CERN PSB”, in *Proc. 12th Int. Particle Accelerator Conf. (IPAC'21)*, Campinas, Brazil, May 2021, pp. 4078–4081. doi:10.18429/JACoW-IPAC2021-THPAB168
- [8] T. Prebibaj *et al.*, “Injection chicane beta-beating correction for enhancing the brightness of the CERN PSB beams”, presented at HB'2021, Fermilab, Batavia, IL, USA, Oct. 2021, paper MOP18, this conference.
- [9] V. Forte, “Performance of the CERN PSB at 160 MeV with H<sup>-</sup> charge exchange injection”, 2016. <https://cds.cern.ch/record/2194937>
- [10] A. Santamaria Garcia *et al.*, “Identification and Compensation of Betatronic Resonances in the Proton Synchrotron Booster at 160 MeV”, in *Proc. 10th Int. Particle Accelerator Conf. (IPAC'19)*, Melbourne, Australia, May 2019, pp. 1054–1057. doi:10.18429/JACoW-IPAC2019-MOPTS086
- [11] B. Mikulec, A. Findlay, V. Raginel, G. Rumolo, and G. Sterbini, “Tune Spread Studies at Injection Energies for the CERN Proton Synchrotron Booster”, in *Proc. HB2012*, Beijing, China, Sept. 2012, paper MOP249, pp. 175–179.
- [12] E. Benedetto *et al.*, “CERN PS Booster Upgrade and LHC Beams Emittance”, in *Proc. 6th Int. Particle Accelerator Conf. (IPAC'15)*, Richmond, VA, USA, May 2015, pp. 3897–3900. doi:10.18429/JACoW-IPAC2015-THPF088
- [13] F. Asvesta, H. Bartosik, S. Gilardoni, A. Huschauer, S. Machida, Y. Papaphilippou, and R. Wasef, “Identification and characterization of high order incoherent space charge driven structure resonances in the CERN Proton Synchrotron”, in *Phys. Rev. Accel. Beams*, vol. 23, no. 9, 2020, doi:10.1103/PhysRevAccelBeams.23.091001
- [14] P. Urschütz, “Measurement and Compensation of Second and Third Order Resonances at the CERN PS Booster”, in *Proc. 9th European Particle Accelerator Conf. (EPAC'04)*, Lucerne, Switzerland, Jul. 2004, paper WEPLT03, pp. 1918-1920.
- [15] F. Schmidt, E. Forest, and E. McIntosh, “Introduction to the polymorphic tracking code: Fibre bundles, polymorphic Taylor types and ‘Exact tracking’”, CERN-Report *CERN-SL-2002-044-AP. KEK-REPORT-2002-3*, 2002.
- [16] L. Deniau, E. Forest, H. Grote, and F. Schmidt, computer code MAD-X, 2016. <http://madx.web.cern.ch/madx/>
- [17] F. Asvesta, H. Bartosik, A. Huschauer, Y. Papaphilippou, and G. Sterbini, “Resonance Identification Studies at the CERN PS”, in *Proc. 9th Int. Particle Accelerator Conf. (IPAC'18)*, Vancouver, Canada, Apr.-May 2018, pp. 3350–3353. doi:10.18429/JACoW-IPAC2018-THPAK056
- [18] V. Kain and N. Madysa, “Generic Optimisation Frontend and Framework (GeOFF)”. <https://gitlab.cern.ch/vkain/acc-app-optimisation>
- [19] M. Powell, “The BOBYQA Algorithm for Bound Constrained Optimization without Derivatives.” *Technical Report*, Department of Applied Mathematics and Theoretical Physics, 2009.
- [20] C. Cartis, J. Fiala, B. Marteau, and L. Roberts, “Improving the Flexibility and Robustness of Model-Based Derivative-Free Optimization Solvers”, *ACM Transactions on Mathematical Software*, 45:3 (2019), pp. 32:1-32:41. arXiv:1804.00154
- [21] C. Cartis, L. Roberts, and O. Sheridan-Methven, “Escaping local minima with derivative-free methods: a numerical investigation, Optimization” (2021). arXiv:1812.11343

# CHROMATICITY MEASUREMENT USING BEAM TRANSFER FUNCTION IN HIGH ENERGY SYNCHROTRONS

X. Buffat\*, S.V. Furuseh, G. Vicentini, CERN, Geneva, Switzerland

## Abstract

Control of chromaticity is often critical to mitigate collective instabilities in high energy synchrotrons, yet classical measurement methods are of limited use during high intensity operation. We explore the possibility to extract this information from beam transfer function measurements, with the development of a theoretical background that includes the impact of wakefields and by analysis of multi-particle tracking simulations. The investigations show promising results that could improve the operation of the HL-LHC by increasing stability margins.

## INTRODUCTION

Operation with the lowest positive chromaticity is usually advised in high energy hadron synchrotrons (i.e. above transition) to both ensure the self-stabilisation of the rigid bunch mode while maximising the beam lifetime. In machines with a fast cycle, the chromaticity is often set empirically to the lowest value that does not result in instabilities. For machines with a long cycle, such as the Large Hadron Collider, this approach is time consuming. In addition, dynamic effects in superconducting magnets and lengthy beam optics operations may lead to strong variations of the chromaticity requiring dynamic corrections. In the LHC, the chromaticity is corrected through the cycle based on a measurement during a dedicated cycle featuring an energy modulation driven by the RF cavities. Such an energy modulation cannot be used with high intensity beams (i.e. multiple bunches) due to the large amount of beam losses generated. The operation with high intensity beams therefore relies on the corrections done with low intensity beams and the cycle-to-cycle reproducibility of the machine. The design chromaticity for the LHC is 2 units [1]. Figure 1 shows the octupole strength required to stabilise the beams, taking into consideration the residual noise that the beam experiences (dashed lines). We observe that the design chromaticity of 2 units is quite optimal to minimise the strength of the octupole required to stabilise the beams, while avoiding the potential adverse effects on the single particle dynamics that could occur at high chromaticity, e.g. around 20 units. However, this working point is close to the most critical configuration in terms of required octupole strength, i.e. around a chromaticity of 0. The cycle-to-cycle reproducibility is not enough to guarantee a sufficient stability of the chromaticity at the optimal working point. The operational working point was therefore set at 15 units [2], allowing for potential cycle-to-cycle variations in the order of  $\pm 5$  units. Due to this uncertainty, the optimal range of chromaticities, here around 3 units, cannot be exploited. Enabling this opportunity could reduce the

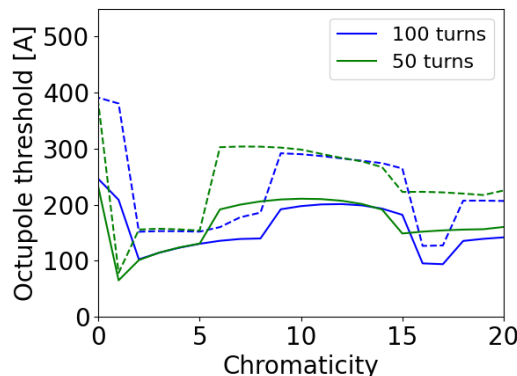


Figure 1: Octupole current required for the stabilisation of the beam in the LHC in the configuration described in Table 1. The solid lines correspond to the octupole threshold obtained neglecting the impact of residual sources of noise on the beam (e.g. [3]), while the dashed lines take into account the destabilising effect of noise [4]. The blue and green curves are labelled with the corresponding damping time of the active feedback.

need for octupole strength by about a factor 2, thus offering significant operational margins, e.g. in terms of control of linear coupling or residual lattice nonlinearities, which need to be compensated with more strength in the arc octupoles to maintain Landau damping [5]. Alternatively, this might also allow for a reduction of the collimator gaps, thus improving the cleaning efficiency.

We observe in Fig. 1 that the width of this range of chromaticities featuring minimal octupole requirement depends on the gain of the transverse damper. In addition, the non-Gaussian modifications of the longitudinal distribution caused by the active blowup during the ramp [6] may significantly narrow down the range of optimal chromaticities [7]. To exploit this optimal working point, we therefore seek a chromaticity measurement technique that features a low level of beam losses, even during high intensity operation, and an accuracy in the order of 1 unit. The Beam Transfer Function (BTF) appears as a good candidate, since it contains information about the chromaticity [8] and it can be measured with a transverse excitation affecting a single bunch among a fully filled machine thanks to fast kickers and pickups. After a brief reminder of important theoretical aspects of the BTF and a description of our numerical model, we shall describe different ways to extract the chromaticity from the BTF measurement, identifying their strengths and shortcomings based on their application to simulation data.

\* xavier.buffat@cern.ch

Table 1: LHC Machine and Beam Parameters

Parameter	Value
Energy [TeV]	7
Bunch intensity [ $10^{11}$ ]	1.8
Norm. trans. emittance [ $\mu\text{m}$ ]	2
$\beta^*$ [m]	1
ATS Telescopic index	1
Frac. horizontal tune	0.31
Frac. vertical tune	0.32
R.m.s bunch length [cm]	8
RF voltage [MV]	12
Synchrotron tune	0.0018
Wakefields model	[9]

### BTF Theory

The BTF is defined as the ratio of the beam oscillation amplitude at a given frequency  $\Omega$  to the external excitation amplitude at that frequency. Following [10], we may write it for a given chromaticity  $Q'$  as:

$$\text{BTF}(\Omega, Q') = \sum_l \mathcal{F}_l(\Omega) w_l(Q'), \quad (1)$$

where we could separate the expression in two integrals that depend on the tune spread and on the chromaticity, respectively. We have

$$\mathcal{F}_l(\Omega) \equiv 2\pi^2 \int_0^\infty \int_0^\infty \frac{J_y \frac{\partial f_0}{\partial J_y}}{\Omega - \omega_0 Q(J_x, J_y) - l\omega_s} dJ_x dJ_y, \quad (2)$$

with  $\omega_0$  the revolution frequency,  $\omega_s$  the synchrotron frequency,  $Q(J_x, J_y)$  the betatron tune as a function of the transverse actions and  $l$  the azimuthal mode number. The unperturbed transverse distribution is given by  $f_0$ . The weights of the azimuthal modes are given by

$$w_l(Q') \equiv 2\pi \int_0^\infty J_l \left( \frac{Q' r_z}{Q_s \beta_z} \right)^2 g_0(r_z) \frac{r_z dr_z}{\beta_z}, \quad (3)$$

with  $Q_s$  the synchrotron tune and  $\beta_z$  the longitudinal  $\beta$  function given by the product of the r.m.s. bunch length and the r.m.s relative momentum spread.  $J_l(\cdot)$  is the Bessel function of the first kind. The longitudinal distribution  $g_0(r_z)$  is expressed as a function of the longitudinal amplitude of oscillation, i.e.  $z = r_z \cos(\Phi)$ .

In the presence of wakefields, the BTF takes a similar form [10]:

$$\text{BTF}_{\text{wake}}(\Omega, Q') = \sum_m \mathcal{F}_{l_m}^{\text{wake}}(\Omega) \tilde{\eta}_m^* \eta_m, \quad (4)$$

with a summation over the modes  $m$  with a corresponding azimuthal number  $l_m$ . We have defined

$$\mathcal{F}_{l_m}^{\text{wake}}(\Omega) \equiv \frac{\mathcal{F}_{l_m}(\Omega)}{1 + 2\Delta\Omega_m \mathcal{F}_{l_m}(\Omega)}, \quad (5)$$

with  $\Delta\Omega_m$  the complex tune shift of mode  $m$ . The corresponding weight depends on the shape of the longitudinal eigenfunction  $m_m(J_z, \phi)$ :

$$\eta_m \equiv \int_0^{2\pi} d\phi \int_0^\infty dJ_z m_m(J_z, \phi) g_0(J_z, \phi), \quad (6)$$

with  $J_z$  and  $\phi$  the longitudinal action angle variables.

### Numerical Model

To evaluate the performance of the various approaches, we numerically generate a set of measurements using macroparticles simulations with the code COMBI [11]. We start by initialising the coordinates of  $10^6$  macroparticles randomly distributed in 6D phase space. The tracking is then performed through a loop over  $10^5$  turns each consisting of the following actions executed sequentially:

- Rotation in transverse and longitudinal phase space based on the respective tunes, including linear detuning with the relative momentum deviation (chromaticity) and linear detuning with the transverse actions. Linear motion is assumed in the longitudinal plane.
- Change of transverse momentum of each of the particles due to the wakefields based on the transverse positions of the particles ahead of it (longitudinal slice model, with 100 slices) and the wakefields' model.
- A change of momentum is applied to all particles in the beam. The value of the kick is changed every turn based on a random number generator and is recorded into a file.
- The average position of the particles in the beam is recorded into a file.

The BTF is obtained as the ratio of the cross power spectral density of the positions and the kicks to the power spectral density of the kicks. They are computed with Welch's algorithm [12].

## BTF WITHOUT WAKEFIELDS

### Sideband Amplitude Ratio

By assuming that the amplitude of a given sideband is affected only by its corresponding term  $l$  in Eq. (1), which means that the betatron tune spread is much smaller than the synchrotron tune, we may write the ratio of the maximum amplitude of the first lower or upper sideband  $l = \pm 1$  to the one of the main mode  $l = 0$ :

$$R_a = \frac{\mathcal{F}_{\pm 1}(\Omega \pm \Omega_s) w_{\pm 1}(Q')}{\mathcal{F}_0(\Omega) w_0(Q')} = \frac{w_{\pm 1}(Q')}{w_0(Q')}. \quad (7)$$

Equation (2) was used to obtain the final expression. The ratio of the amplitude of the first sideband is therefore a powerful tool to assess the chromaticity for low intensity beams

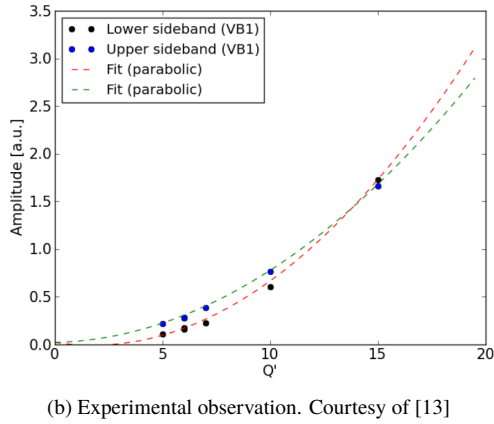
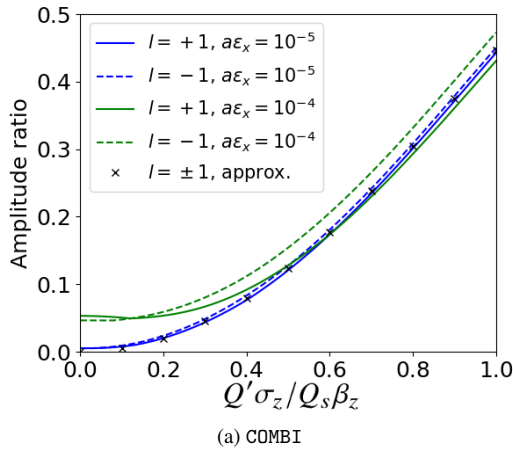


Figure 2: Amplitude ratio obtained analytically (upper plot, black crosses) and numerically for different sidebands  $l$  and detuning. The datasets are labelled by their r.m.s. detuning driven by the direct term  $a \cdot \epsilon_x$  is the geometric transverse emittance. The lower plot shows the result of an experiment at the LHC (dots). Parabolic fits were tried whereas the theory rather suggests Eq. (7).

(i.e. neglecting wakefields). Indeed, by solving Eq. (3) for a Gaussian longitudinal distribution, we have [8]:

$$w_l^G(Q') = e^{-\left(\frac{Q'\sigma_z}{Q_s\beta_z}\right)^2} I_l\left(\left(\frac{Q'\sigma_z}{Q_s\beta_z}\right)^2\right), \quad (8)$$

with  $\sigma_z$  the r.m.s. bunch length and  $I_l(\cdot)$  the modified Bessel functions of the first kind. As shown in Fig. 2, the predicted behaviour is well verified in numerical simulations without wakefields as well as experimentally at the LHC. With a large betatron tune spread (green curves in Fig. 2a) deviations are observed. While the hypothesis used to obtain the simplified expression for the amplitude ratio is no longer valid, the expression for the BTF (Eq. (1)) remains valid. In such configurations where the signals of the sidebands are mixed, it becomes more convenient to use a nonlinear fit approach.

### Nonlinear Fit

In the following we attempt to fit the phase of the BTF obtained with COMBI using Eq. (1). The chromaticity and

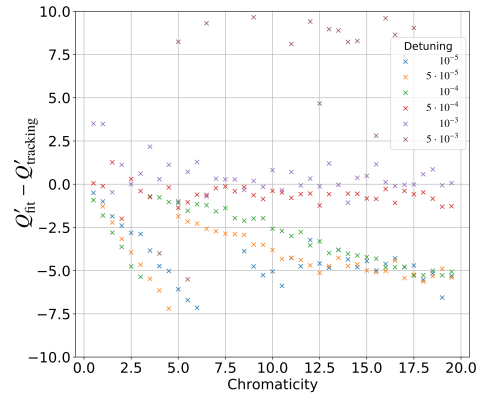


Figure 3: Error on the chromaticity of the fit of simulated tracking data with the analytical formula neglecting wake fields (Eq. (1)). The datasets are labelled with the corresponding r.m.s. tune spread driven by the direct term  $a\epsilon_x$ .

direct linear detuning coefficient were used as Degrees Of Freedom (DOF). To avoid unnecessary DOF, the indirect detuning coefficient was set to -0.7 times the direct one, as expected with the LHC octupoles [14]. The Nelder-Mead algorithm [15] was used to minimise the sum of the absolute differences between the BTF phase from the analytical model and from the numerical data evaluated at 327 frequencies equally spaced in a range that includes the signal of sidebands -2 to 2, inclusive.

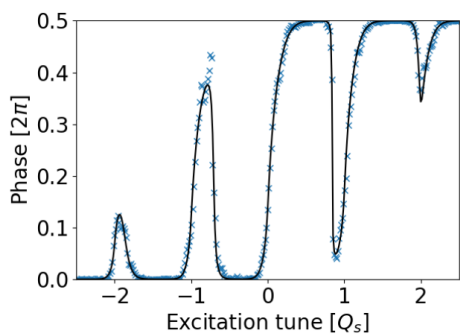
Figure 3 shows the accuracy of the fit for different chromaticities and detunings. Most fits fail for configurations with a low amplitude detuning ( $< 10^{-4}$ ). In such configurations, the BTF is rather sharp at the sidebands and the resolution of the BTF obtained numerically is limited by the number of turns in the tracking simulations. For an intermediate range of detunings ( $< 10^{-3}$  which is comparable to  $Q_s$ ), the accuracy of the fitted chromaticity remains around the unit. Such good fits are illustrated in a configuration where the detuning is significantly smaller than the synchrotron tune (Fig 4a) and comparable to the synchrotron tune (Fig. 4b). The fits tend to fail for large values of detuning, as the signals of the different sidebands overlap due to their broad extend in frequency. A configuration at the limit of the capability of the non-linear fit is shown in Fig. 4c.

The range of detunings for which the nonlinear fit method is accurate seems perfectly suited for an application to the LHC at flat top before collision, for which the r.m.s. detuning is usually smaller than  $Q_s$ . Nevertheless, the goal is to obtain a measurement technique that is compatible with high intensity operation. It is therefore crucial to consider the effect of the wakefields.

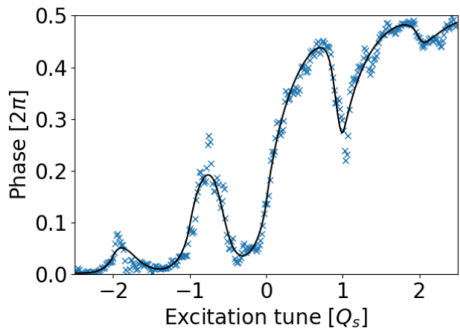
## BTF WITH WAKEFIELDS

### Nonlinear Fit

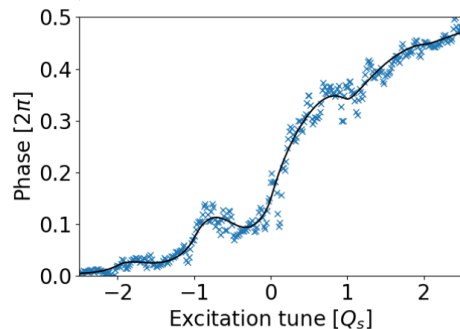
In the presence of wakefields, the BTF is distorted depending on the beam intensity. Such a distortion of the phase is



(a)  $a\epsilon_x = 10^{-4}$



(b)  $a\epsilon_x = 3 \cdot 10^{-4}$



(c)  $a\epsilon_x = 6 \cdot 10^{-4}$

Figure 4: Examples of BTF phases obtained numerically (blue crosses) and the corresponding fit (black lines) for a chromaticity of 15 units and different detunings. The excitation tune is shifted to the betatron tune and expressed in units of the synchrotron tune.

shown in Fig. 5. This distortion affects the sidebands, such that the method based on the amplitude ratio is no longer applicable. In addition, a significant frequency shift of the mode can be observed (here of the mode 0). The nonlinear fit based on Eq. (1), i.e. neglecting the presence of wakefields, cannot adjust to such shifts. The impact on the fit accuracy is shown in Fig. 6a. As previously, only configurations with a low enough tune spread yield a good accuracy, at least with a low intensity. For those good cases, a bias growing with the intensity is observed which can be attributed to the increasing strength of the wakefields.

In order to remove this bias, we rather use Eq. (4) as fitting

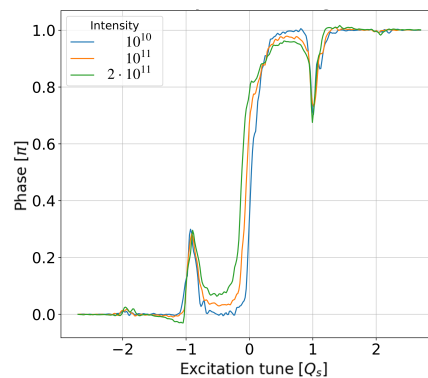


Figure 5: Examples of BTF phases obtained numerically for a chromaticity of 6 units,  $a\epsilon_x = 10^{-4}$  and including wakefields. The excitation tune is shifted to the betatron tune and expressed in units of the synchrotron frequency.

function, adding now one complex tune shift per azimuthal mode number as DOF. The complexity of the fit is thus greatly increased as the number of DOF changed from 2 to 12. As a result, it was observed that Newton based algorithms tended to fail in this configuration, whereas they worked as efficiently as the Nelder-Mead approach for the simpler fit without wakefields. The accuracy of the fit in Fig. 6b shows that the bias observed earlier was indeed removed by this approach, at the expense of a low precision (shown by the larger error bars).

Another attempt was made with a simplified fitting function, still using Eq. (4) but assuming that only the mode 0 is affected by the wakefields, i.e.  $\Delta Q_l = 0$  for  $l \neq 0$ . The number of DOF is thus decreased to 4. The idea of this simplified approach is that the main distortion observed in Fig. 5, i.e. the shift of mode 0, can still be fitted, whereas the more subtle impact on the sidebands is neglected. The accuracy of the fit shown in Fig. 6c shows again a suppression of the bias, yet the precision was not significantly improved.

## NEURAL NETWORK

Finally, we attempt to reconstruct the chromaticity from a BTF using a neural network. In order to train the network a large dataset was generated using COMBI, with 7 intensities ranging from  $10^{10}$  to  $2 \cdot 10^{12}$ , 39 chromaticities ranging from 0.5 to 20, 10 values of r.m.s. detuning arranged logarithmically from  $10^{-6}$  to  $10^{-2}$ . For each simulation, 10 samples were generated by adding random noise to the simulated positions before computing the BTF. The dataset is therefore constituted of 27300 BTF samples. 80% of the samples were used for training, while the remaining 20% were used to measure the accuracy.

Fully connected multilayer neural networks with different depth were tested using Keras [16]. It was found that a four layers network performs well. The input layer is constituted of 327 nodes, corresponding to the BTF phases in a range of frequencies including the sidebands -2 to 2. The two hidden layers each decrease in size by a factor 2 (163 and

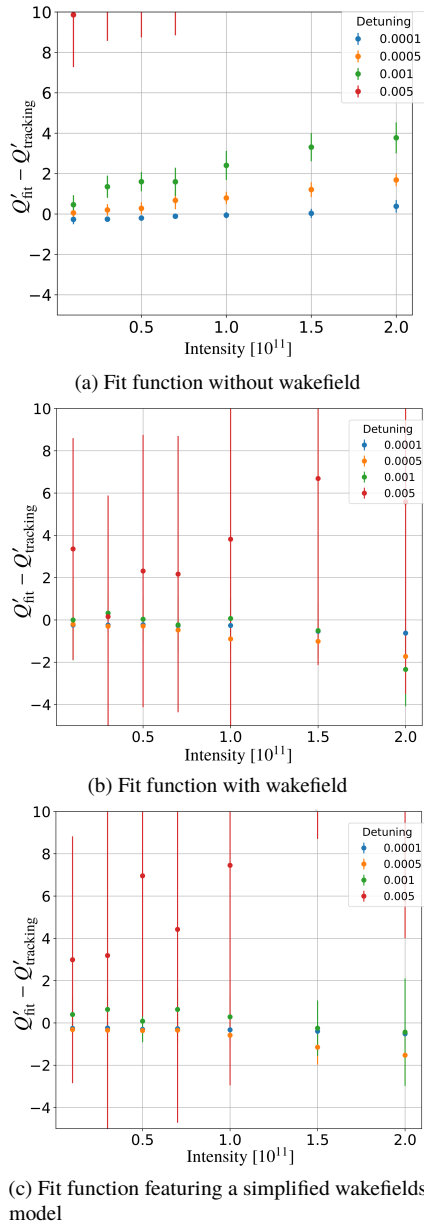


Figure 6: Error on the fitted chromaticity as a function of the beam intensity for different fitting functions. The average and r.m.s. were computed across 39 chromaticities ranging from 0.5 to 20. Each dataset is labelled with the r.m.s. tune spread driven by the direct term  $a\epsilon_x$ .

81 nodes respectively). The output layer is constituted of 3 nodes corresponding to the chromaticity, the direct detuning coefficient and the beam intensity, which were normalised between 0 and 1. The training is done with 100 epochs in batches of 75 samples using the ADAM method [17] with the mean absolute error as loss function. The nodes are activated with a Rectified Linear Unit (ReLU) function.

The accuracy of the chromaticity obtained by the neural network on the testing set is reported in Fig. 7. The accu-

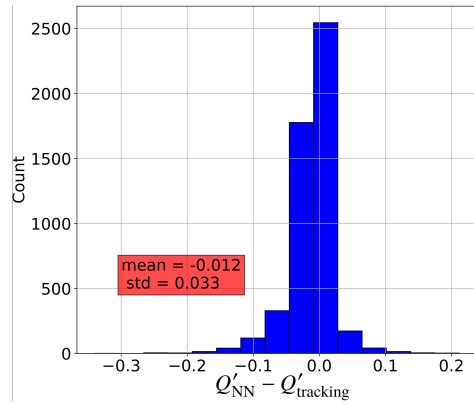


Figure 7: Error on the chromaticity obtained with the neural network.

racy is well below unity in the whole range of parameters on which the network was trained. This method therefore outperforms all the others in terms of accuracy and dynamic range. The need to train the network could become a significant drawback in case the training on simulation data is not sufficient for the network to perform sufficiently well on experimental data.

## CONCLUSION

The pros and cons of the various methods attempted to extract the chromaticity from a BTF can be summarised as follows

- **The amplitude ratio** is by far the simplest method and allows for an accurate measurement of the chromaticity in configurations with a betatron tune spread much lower than the synchrotron tune and in absence of wakefields.
- **Nonlinear fit neglecting wakefields** allows for a better accuracy in configurations featuring a tune spread comparable to the synchrotron tune, yet it still fails for larger tune spread. The presence of wakefields induces a bias in the reconstructed chromaticity.
- **Nonlinear fitting including wakefields** removes the bias induced by the wakefields. Yet the additional DOF tend to deteriorate the resolution.
- **Neural networks** clearly outperforms the other methods in terms of accuracy and dynamic range. The main drawback of this approach lies in the need for training, experimental tests are needed to assess the possibility to use a neural network trained on simulation data.

Both the nonlinear fit including wakefields and the neural networks have the potential to be used at the LHC and HL-LHC to reduce the need for octupole strength, thus motivating experimental tests.

## ACKNOWLEDGEMENTS

This research was supported by the HL-LHC project.

## REFERENCES

- [1] O. Brüning *et al.*, eds., “LHC Design report, Vol. 1 : The LHC Main ring”, CERN, Geneva, Switzerland, 2004. <https://cds.cern.ch/record/782076>
- [2] X. Buffat *et al.*, “Transverse instabilities,” in *Proceedings of the 9th LHC Operations Evian Workshop*, Evian, France, 2019. <https://cds.cern.ch/record/2750298>
- [3] J. Scott Berg and F. Ruggiero, “Landau damping with two-dimensional betatron tune spread”, CERN, Geneva, Switzerland, CERN-SL-AP-96-71-AP, 1996. <https://cds.cern.ch/record/321824>
- [4] S.V. Furusest and X. Buffat, “Loss of transverse Landau damping by noise and wakefield driven diffusion,” *Phys. Rev. Accel. Beams*, vol. 23, p. 114401, 2020. doi:10.1103/PhysRevAccelBeams.23.114401
- [5] X. Buffat *et al.*, “Strategy for Landau damping of head-tail instabilities at top energy in the HL-LHC,” CERN, Geneva, Switzerland, CERN-ACC-NOTE-2020-0059, 2020. <https://cds.cern.ch/record/2745703>
- [6] H. Timko *et al.*, “LHC longitudinal dynamics during Run II,” in *Proceedings of the 9th LHC Operations Evian Workshop*, Evian, France, 2019. <https://cds.cern.ch/record/2750299>
- [7] X. Buffat, “Impact of the longitudinal distribution on the transverse stability at flat top in the LHC,” presented at the 234th Hadron Synchrotron Collective effect section meeting, 10th August 2020, CERN, Geneva, Switzerland. [https://indico.cern.ch/event/942621/contributions/3960847/attachments/2080506/3494417/2020-06\\_SineHoledGaussian-expanded.pdf](https://indico.cern.ch/event/942621/contributions/3960847/attachments/2080506/3494417/2020-06_SineHoledGaussian-expanded.pdf)
- [8] T. Nakamura, “Excitation of betatron oscillation under finite chromaticity,” in *12th Symposium on Accelerator Science and Technology*, Wako, Japan, 1999, p. 534-536. [http://www.spring8.or.jp/pdf/en/ann\\_rep/98/P121-123.pdf](http://www.spring8.or.jp/pdf/en/ann_rep/98/P121-123.pdf)
- [9] N. Mounet and X. Buffat, “Run III: Stability from impedance,” presented at the LHC Run 3 Configuration Working Group, 27th March 2020, CERN, Geneva, Switzerland. [https://indico.cern.ch/event/902528/contributions/3798807/attachments/2010534/3359300/20200327\\_RunIII\\_stability\\_NMounet.pdf](https://indico.cern.ch/event/902528/contributions/3798807/attachments/2010534/3359300/20200327_RunIII_stability_NMounet.pdf)
- [10] S.V. Furusest and X. Buffat, “Vlasov description of the beam response to noise in the presence of wakefields in high-energy synchrotrons: Beam transfer function, diffusion, and loss of Landau damping,” submitted for publication in *Eur. Phys. J. Plus*.
- [11] <https://combi.web.cern.ch/>.
- [12] P. Welch, “The use of the fast Fourier transform for the estimation of power spectra: A method based on time averaging over short, modified periodograms,” *IEEE Trans. Audio Electroacoust.*, vol. 15, pp. 70-73, 1967. doi:10.1109/TAU.1967.1161901
- [13] C. Tambasco *et al.*, “MD 382: Beam Transfer Function and diffusion mechanisms,” CERN, Geneva, Switzerland, CERN-ACC-NOTE-2016-0016, 2016. <http://cds.cern.ch/record/2123854>
- [14] J. Gareyte *et al.*, “Landau damping, dynamic aperture and octupole in LHC,” CERN, Geneva, Switzerland. LHC Project Report 91, 1997. <https://cds.cern.ch/record/321824>
- [15] F. Gao and L. Han, “Implementing the Nelder-Mead simplex algorithm with adaptive parameters,” *Comput. Optim. Appl.*, vol. 51, pp. 259-277, 2012. doi:10.1007/s10589-010-9329-3
- [16] <https://keras.io/>.
- [17] D.P. Kingma and J. Ba, “Adam: A Method for Stochastic Optimization,” arXiv:1412.6980. <https://arxiv.org/abs/1412.6980>

# RECENT PROGRESS ON NONLINEAR BEAM MANIPULATIONS IN CIRCULAR ACCELERATORS

A. Bazzani, F. Capoani<sup>1</sup>, Bologna University and INFN, Bologna, Italy  
 M. Giovannozzi\*, CERN Beams Department, Geneva, Switzerland  
<sup>1</sup>also at CERN Beams Department, Geneva, Switzerland

## Abstract

In recent years, transverse beam splitting by crossing a stable resonance has become the operational means to perform MultiTurn Extraction (MTE) from the CERN PS to the SPS. This method delivers the high-intensity proton beams for fixed-target physics at the SPS. More recently, further novel manipulations have been studied, with the goal of devising new techniques to manipulate transverse beam properties. AC magnetic elements can allow beam splitting to be performed in one of the transverse degrees of freedom. Crossing 2D nonlinear resonances can be used to control the sharing of the transverse emittances. Furthermore, cooling the transverse emittance of an annular beam can be achieved through an AC dipole. These techniques will be presented and discussed in detail, considering future lines of research.

## INTRODUCTION

Nonlinear effects introduce new phenomena in beam physics. In recent years, they have been used extensively to design novel beam manipulations in which the transverse beam distribution is modified in a controlled way for different purposes. This is the case for the beam splitting that is at the heart of the CERN Multiturn Extraction (MTE) [1–4].

The possibility of a controlled manipulation of the phase space by means of an adiabatic change of a parameter opened the road-map to new applications in accelerator and plasma physics [1, 5–9]. In particular, the adiabatic transport performed by means of nonlinear resonance trapping allows manipulation of a charged particle distribution, as to minimize the particle losses during the beam extraction process in a circular accelerator. Furthermore, the control of the beam emittance can be obtained by a similar approach [4, 10, 11]. The experimental procedures [4, 10, 11] require a very precise control of the efficiency of the adiabatic trapping into resonances [12–14], as well as of the phase-space change during the adiabatic transport, when a parametric modulation is introduced by means of an external perturbation. All these processes can be represented by multi-dimensional Hamiltonian systems or symplectic maps [15].

The adiabatic theory for Hamiltonian systems is a key breakthrough towards an understanding of the effects of slow parametric modulation on the dynamics. The concept of adiabatic invariant allows the long-term evolution of the system to be predicted and the fundamental properties of the action variables to be highlighted upon averaging over the fast variables [16, 17]. The theory has been well developed

for systems with one degree of freedom [12, 18–21], but the extension of some analytical results to multi-dimensional systems or to symplectic maps [22] has to cope with the issues generated by the ubiquitous presence of resonances in phase space [23, 24]. For these reasons, such an extension is still an open problem.

The combination of nonlinear effects that do not preserve the linear Courant-Snyder invariant, and adiabatic variation of the system parameters that allow crossing separatrices, opens new regimes that can be used to propose novel beam manipulations, in which essential beam parameters, such as the emittances can be changed in a controlled way.

In this paper, three novel beam manipulations are reviewed, namely beam splitting by means of AC elements [25], sharing of transverse emittances by crossing a nonlinear 2D resonance [26], and cooling of an annular beam distribution [27, 28].

## ADIABATIC THEORY OF SEPARATRIX CROSSING

Phenomena occurring when a Hamiltonian system is slowly modulated have been widely studied in the framework of adiabatic theory [18, 19]. As the modulation of the Hamiltonian changes the shape of the separatrices in phase space, the trajectories can cross separatrices and enter into different stable regions associated with nonlinear resonances. The separatrix crossing can be described in a probabilistic way due to the sensitive dependence on initial conditions, and the crossing probabilities can be computed in the adiabatic limit, like the change of adiabatic invariant due to the crossing [18, 19].

Let us consider a Hamiltonian  $\mathcal{H}(p, q, \lambda = \epsilon t)$ ,  $\epsilon \ll 1$ , where the parameter  $\lambda$  is slowly modulated and whose phase space is sketched in Fig. 1. An initial condition in Region III has a probability to be trapped into Region I or II of phase space given by [18]

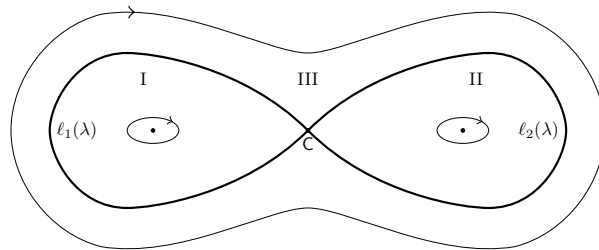


Figure 1: A generic phase-space portrait divided into three regions (I, II, III) by separatrices  $\ell_1(\lambda)$  and  $\ell_2(\lambda)$ .

\* massimo.giovannozzi@cern.ch

$$\mathcal{P}_{\text{III} \rightarrow \text{I}} = \frac{\Theta_{\text{I}}}{\Theta_{\text{I}} + \Theta_{\text{II}}} \quad \mathcal{P}_{\text{III} \rightarrow \text{II}} = 1 - \mathcal{P}_{\text{III} \rightarrow \text{I}}, \quad (1)$$

where

$$\Theta_i = \frac{dA_i}{d\lambda} \Big|_{\tilde{\lambda}} = \oint_{\partial A_i} dt \frac{\partial \mathcal{H}}{\partial \lambda} \Big|_{\tilde{\lambda}} \quad i = \text{I, II}, \quad (2)$$

with  $A_i$  the area of region  $i$ ,  $\partial A_i$  the boundary of region  $i$ , and  $\tilde{\lambda}$  the value of  $\lambda$  when the separatrix is crossed. In case  $\mathcal{P}_{\text{III} \rightarrow i} < 0$ , then  $\mathcal{P}_{\text{III} \rightarrow i} = 0$ , whereas when  $\mathcal{P}_{\text{III} \rightarrow i} > 1$  then  $\mathcal{P}_{\text{III} \rightarrow i} = 1$ .

When a separatrix is crossed, the adiabatic invariant  $J$  changes according to the area difference between the two regions at the crossing time, and just after the crossing into a region of area  $A$ ,  $J = A/(2\pi)$ . This occurs only if the modulation is perfectly adiabatic, i.e.  $\epsilon \ll 1$ , but a correction to the value of the new action can be found following [19].

The adiabatic trapping into resonances has been studied in various works [18, 29] to show the possibility of transport in phase space when some system's parameters are slowly modulated. This phenomenon suggests possible applications in different fields and, in particular, in accelerator physics where MTE has been proposed [1] and successfully made into an operational beam manipulation at the CERN PS [2, 4]. In this case, an extension of the results of adiabatic theory to quasi-integrable area-preserving maps has been considered, and the probability to be captured in a resonance can be computed analogously to those in Eq. (1) [15], when the Poincaré–Birkhoff theorem [30] can be applied to prove the existence of stable islands in phase space. The properties of such resonance islands for polynomial Hénon-like maps [31] have been studied in [32] and the possibility of performing an adiabatic trapping into a resonance by modulating the linear frequency at the elliptic fixed point has been studied [15].

## BEAM SPLITTING USING AC ELEMENTS

### The Model

A new approach can be devised to perform beam splitting by considering a Hénon-like symplectic map of the form

$$\mathcal{M}_{\ell,m} : \begin{pmatrix} q_{n+1} \\ p_{n+1} \end{pmatrix} = R(\omega_0) \times \begin{pmatrix} q_n \\ p_n - \sum_{j>2} k_j q_n^{j-1} - q^{\ell-1} \varepsilon_m \cos \omega n \end{pmatrix}, \quad (3)$$

where  $R(\omega_0)$  is a rotation matrix of an angle  $\omega_0$ ,  $n$  is the iteration number,  $\ell \in \mathbb{N}$ , and the dynamics is perturbed by a modulated kick of amplitude  $\varepsilon_m$  whose frequency  $\omega$  is close to a resonance condition  $\omega = m\omega_0 + \delta$ ,  $\delta \ll 1$ . When  $\ell = 1$ , the fixed point at the origin of the unperturbed system becomes an elliptic periodic orbit of period  $2\pi/\omega$ , and the linear frequencies depend on the perturbation strength, so that they are adiabatically modulated. This is not the case when  $\ell \geq 2$ , which is also interesting for applications.

The Birkhoff Normal Form theory allows a relationship between the map of Eq. (3) and the Hamiltonian [32]

$$\mathcal{H}_{\ell,m}(p, q, t) = \omega_0 \frac{q^2 + p^2}{2} + \sum_{j>2} \hat{k}_j \frac{q^j}{j} + \varepsilon_m \frac{q^\ell}{\ell} \cos \omega t \quad (4)$$

to be established. Note that in [25] the adiabatic theory for the Hamiltonian (4) is used to analyze the results obtained with the map (3) and found in excellent agreement. This observation is essential as it demonstrates that a splitting protocol can be designed based on adiabatic theory for the Hamiltonian (4) and it will be valid, with minor adaptations, also for the map (3).

### Splitting with AC Elements

To study the possibility of beam splitting by means of AC elements, the third-order resonance is selected, but the concepts used can be generalized to any resonance order.

When the system parameters are adiabatically modulated, the trapping of the orbits into the stable islands and the adiabatic transport are possible [18]. To optimize the trapping probability, we propose a protocol divided into two steps. In the first one, the perturbation frequency  $\omega$  is kept constant at a value  $\omega_i < m\omega_0$ , near the  $m$ th-order resonance, while the exciter is slowly switched on, increasing its strength  $\varepsilon_h$  from 0 to the final value  $\varepsilon_{h,f}$ . In the second stage, the exciter strength is kept fixed at  $\varepsilon_{h,f}$ , and the frequency is modulated from  $\omega_i$  to  $\omega_f$ . Both modulations are performed by means of a linear variation in  $N$  time steps. It is essential to mention that, unlike MTE where  $\omega_0$  varies as to cross a resonance, with AC elements the resonance is created between  $\omega_0$  and  $\omega$ , and this is an essential advantage in case the value of  $\omega_0$  is imposed by, e.g. space charge considerations.

An example of the behavior described above is shown in Fig. 2, where the evolution of a set of initial conditions, uniformly distributed on a disk of radius  $R$ , under the dynamics generated by  $\mathcal{H}_{1,3}$ , using the protocol for trapping and transport described above, is shown. The plots show the evolution of an ensemble of initial conditions under the same dynamics generated by  $\mathcal{H}_{1,3}$  and the colors are used to indicate which region the initial conditions are trapped into. The trapping and transport phenomena are clearly visible, thus indicating that the proposed protocol works efficiently. It is worth stressing that no initial condition moves towards very large amplitudes and that there are no particles in between islands, which means that multi-turn extraction would be free of losses also for this type of splitting.

## EMITTANCE SHARING BY CROSSING 2D NONLINEAR RESONANCES

We remark that this idea was inspired by [33], where the analysis of the crossing of a 2D nonlinear resonance was carried out with the goal of quantifying the emittance growth due to a fast resonance crossing. This process is sometimes unavoidable in many high-power accelerators,

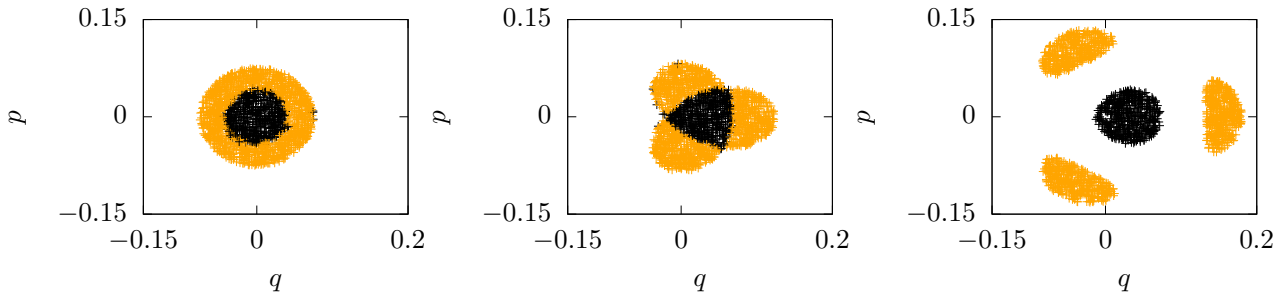


Figure 2: Evolution of an ensemble of particles in phase space with the colors used to identify in which region each initial condition has been trapped into (core, black, and islands, orange) for the Hamiltonian model (4) with  $\ell = 1$ ,  $m = 3$  at the beginning of the process (left column), at the end of the  $\varepsilon_h$  variation (mid column) and at the end of the frequency variation (right column). Parameters:  $k_3 = 1$ ,  $\omega_0/(2\pi) = 0.17133$ ,  $\omega_i = 2.995 \omega_0$ ,  $\omega_f = 2.983 \omega_0$ ,  $\varepsilon_{h,f} = 0.28$ .

such as isochronous cyclotrons, non-scaling fixed field alternating gradients, and other low-energy accelerators.

### The Model

Using the action-angle variables and averaging procedures, transverse motion in a circular accelerator close to a  $(m, n)$  resonance (with  $m, n \in \mathbb{N}$ ) is described by the Hamiltonian

$$\mathcal{H}(\phi_x, J_x, \phi_y, J_y) = \omega_x J_x + \omega_y J_y + \alpha_{xx} J_x^2 + \alpha_{yy} J_y^2 + 2\alpha_{xy} J_x J_y + G J_x^{m/2} J_y^{n/2} \cos(m\phi_x - n\phi_y), \quad (5)$$

the resonance condition being  $m\omega_x - n\omega_y \approx 0$ , and  $\alpha_{xx}$ ,  $\alpha_{xy}$ ,  $\alpha_{yy}$  are the amplitude-detuning parameters.

The canonical transformation (see [16, p. 410])

$$J_x = mJ_1 \quad \phi_1 = m\phi_x - n\phi_y \quad (6)$$

$$J_y = J_2 - nJ_1 \quad \phi_2 = \phi_y \quad (7)$$

transforms the Hamiltonian into

$$\mathcal{H}(\phi_1, J_1) = \delta J_1 + \alpha_{11} J_1^2 + \alpha_{12} J_1 J_2 + G(mJ_1)^{\frac{m}{2}} \times (J_2 - nJ_1)^{\frac{n}{2}} \cos \phi_1 + \left( \omega_y J_2 + \alpha_{22} J_2^2 \right) \quad (8)$$

where  $\delta = m\omega_x - n\omega_y$  is the resonance-distance parameter and  $\alpha_{11}$ ,  $\alpha_{12}$ ,  $\alpha_{22}$  are functions of  $\alpha_{xx}$ ,  $\alpha_{xy}$ ,  $\alpha_{yy}$ . Note that the Hamiltonian (8) does not depend on  $\phi_2$ , hence  $J_2$  is a constant of motion and the last term in (8) can be neglected. Furthermore,  $J_2$ , which is a constant parameter, induces a shift of the resonance condition, which will not be met when  $\delta = 0$ , but rather when  $\delta + \alpha_{12} J_2 = 0$ .

The phase-space topology of the Hamiltonian (8) depends on  $m, n$ , but some elements are common. The condition  $J_y > 0$  constrains the motion to  $J_1 < J_2/n$ , the *allowed disk*. When unstable fixed points lie on the border of this disk, it is possible to draw a separatrix that joins them, the *coupling arc*.

### Emittance Sharing

Let us consider a process where a particle evolves under the Hamiltonian (5), while either  $\omega_x$  or  $\omega_y$  is changed with

time to cross the  $(m, n)$  resonance. This means varying  $\delta$  from a situation where  $\delta + \alpha_{12} J_2 \gg 0$  to one where  $\delta + \alpha_{12} J_2 \ll 0$ . The variation of  $\delta$  changes the position of a separatrix that then sweeps the allowed disk inside which particles are constrained to move.

A particle starts evolving, far from resonance, with an initial action  $J_{1,i} = J_{x,i}/m$ . Its orbit, being far from the resonance, will be close to a circle of area  $2\pi J_1$ . This area, being the adiabatic invariant, is conserved when  $\delta$  is slowly varied. As  $\delta$  is decreased, the separatrix reduces the region in which the particle is moving, dividing the allowed disk in two (the two regions will be equal on resonance). When the area of the initial region is equal to  $2\pi J_1$ , according to separatrix crossing theory [18], the particle crosses the coupling arc entering the other region of the allowed disk, with an action corresponding to  $2\pi$  times the area of the arrival region at the jump time.

Since the allowed disk has an area  $2\pi J_2/n$ , the resulting action will be

$$J_{1,f} = \frac{J_2}{n} - J_{1,i} \quad (9)$$

and, going back to the  $x$  and  $y$  actions

$$J_{x,f} = mJ_{1,f} = m \left( \frac{J_{y,i} + nJ_{x,i}/m}{n} - \frac{J_{x,i}}{m} \right) = \frac{m}{n} J_{y,i} \quad (10)$$

and

$$J_{y,f} = \frac{n}{m} J_{x,i}. \quad (11)$$

As  $\delta$  continues to decrease, the area where the particle orbits increases. At the end of the resonance crossing process, far from resonance, the particle will orbit on a circle around the origin at the new action.

As the  $x$  and  $y$  emittances are the averages of  $J_x$  and  $J_y$ , at the end of the process an *emittance sharing* between the two directions occurs, keeping the product  $J_x J_y$  constant. An example for the  $m = 1, n = 2$  case is given in Fig. 3.

It is worth stressing that the picture described here holds in all cases with no hyperbolic fixed points inside the allowed disk. Otherwise, the situation becomes much more involved, as separatrices, linked with the hyperbolic fixed points, appear, partitioning the phase space into more regions. A different analysis is required in that case [26].

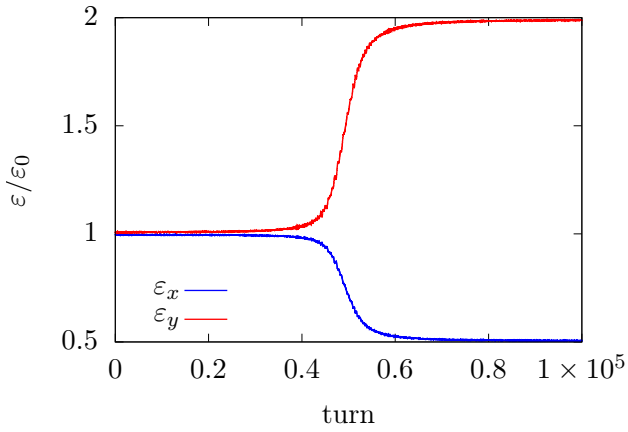


Figure 3: Example of the emittance evolution during the resonance-crossing process for the  $m = 1, n = 2$  case.

## COOLING OF AN ANNULAR BEAM

### The Model

The generic Hamiltonian (4) can be recast by using the unperturbed ( $\varepsilon = 0$ ) action-angle coordinates  $(\phi, J)$  in the form

$$\mathcal{H}(\phi, J) = \omega_0 J + \frac{\Omega_2}{2} J^2 + \varepsilon \sqrt{2J} \cos \phi \cos \omega t, \quad (12)$$

where we introduce the detuning term  $\Omega_2 = O(k_3^2)$ .

Several transformations can then be applied [27, 28], which include moving to a rotating-frame reference, using the angle  $\gamma = \phi - \omega t$ , and averaging the perturbation term over the fast variable  $\omega t$ , to obtain the Hamiltonian of the slow dynamics that, after re-scaling of the action, reads

$$\mathcal{H}(\gamma, J) = 4J^2 - 2\lambda J + \mu \sqrt{2J} \cos \gamma, \quad (13)$$

where the parameters  $\lambda, \mu$  are defined as

$$\lambda = \frac{4}{\Omega_2}(\omega - \omega_0), \quad \mu = \frac{4\varepsilon}{\Omega_2}, \quad (14)$$

and can be changed upon acting on  $\varepsilon$  and  $\omega$ . The Hamiltonian (13) is well-known [18, 29] and can be written

$$\mathcal{H}(X, Y) = (X^2 + Y^2)^2 - \lambda(X^2 + Y^2) + \mu X, \quad (15)$$

upon using the co-ordinates  $X = \sqrt{2J} \cos \gamma, Y = \sqrt{2J} \sin \gamma$ .

Its phase space can be analyzed and the existence and position of the fixed points can be determined analytically [27, 28]. The separatrix divides the phase space in three regions, as shown in Fig. 4, whose areas  $A_i$  are computed analytically [27, 28], which is essential for designing cooling protocols.

### Cooling Protocols

The idea at the heart of the cooling protocol is based on a careful control of the time variation of the size of the phase-space regions  $G_1$  and  $G_2$  so to trap particles in an annular beam distribution and then reduce the value of their action

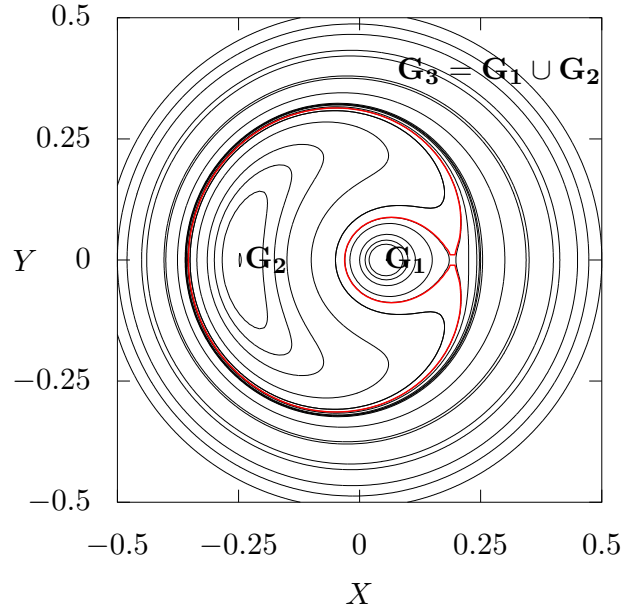


Figure 4: Phase-space portrait of the Hamiltonian (15) with  $\lambda = 0.1, \mu = 0.01$ . The red line represents the separatrix.

at the end of the trapping and transport processes. This can be carried out by using the theory outlined in the previous section, and the details can be found in [27, 28].

At first, an initial condition from an annular-shape distribution evolves in the outer region with an initial action  $J_0$ , and  $\lambda$  and  $\mu$  are slowly varied. At time  $t^*$ ,  $\lambda = \lambda^*, \mu = \mu^*$ , and  $A_3 = 2\pi J_0$ , and according to adiabatic separatrix-crossing theory [16, 18], having defined  $\xi = \frac{dA_i/dt}{dA_3/dt}$  then

$$P_i = \xi \text{ if } \xi \in ]0, 1[, \quad P_i = 0 \text{ if } \xi < 0, \quad P_i = 1 \text{ if } \xi > 1, \quad (16)$$

and the orbit is trapped in the region  $G_i$  ( $i = 1, 2$ ) with probability  $P_i$ , and an action value after trapping of  $A_i/2\pi$ . Given a distribution of initial conditions with action  $J \in [J_0 - \Delta, J_0 + \Delta]$ , the expected value of their final action after trapping, if  $\Delta$  is sufficiently small, is  $\langle J \rangle_f = (A_1 P_1 + A_2 P_2)/2\pi \leq J_0$ , which means that the separatrix-crossing process reduces the emittance of the annular distribution.

To optimize the cooling process, two protocols have been considered: one consists in trapping all particles in  $G_1$ , the other in trapping all particles in  $G_2$ . For both processes, the trapping phase is followed by the adiabatic transport obtained by moving the resonance island toward the origin of the phase space.

The two approaches are presented and discussed in detail in [28]. Here we report an example of the evolution of the annular distribution in Fig. 5. The evolution of the distribution, the optimized variation of the parameters  $\lambda$  and  $\mu$ , and the projected distribution of the actions are shown. The cooling of the initial action distribution is clearly visible, both in the phase-space plots and in the action projection. The color code used to identify the action values provides an indication of a certain level of mixing that occurs during

the trapping phase. Indeed, at the end of the cooling process, the ordering of the colors used to identify action values is only approximately respected and in the outer zone of the action distribution all colors are represented.

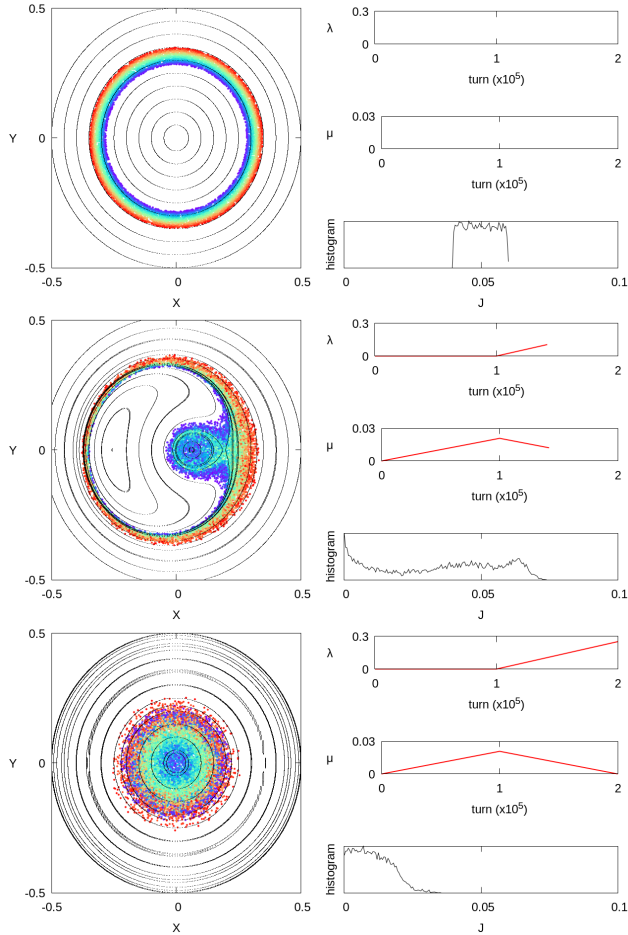


Figure 5: Example of the cooling protocol based on trapping in  $G_1$ , showing the evolution of the beam distribution, its projection, and the parameters  $\lambda, \mu$ .

Finally, in Fig. 6, the performance of the proposed cooling approach is shown as a function of the special parameter values  $\lambda^*$  and  $\mu^*$  that characterize the two types of protocols. The plots report the results of numerical simulations as well as those of theoretical estimates. The agreement is clearly visible and the possibility of achieving very high values of cooling is also evident. The disagreement is due to a lack of adiabaticity for large  $\mu^*$  [28].

## CONCLUSIONS AND OUTLOOK

The developments and recent results of novel beam manipulations based on nonlinear beam dynamics have been reviewed in this paper. The precursor has been beam splitting that is used to perform multiturn extraction in the CERN PS and it allows controlling the emittance in the horizontal plane and stretching the beam beyond the length of the ring circumference.

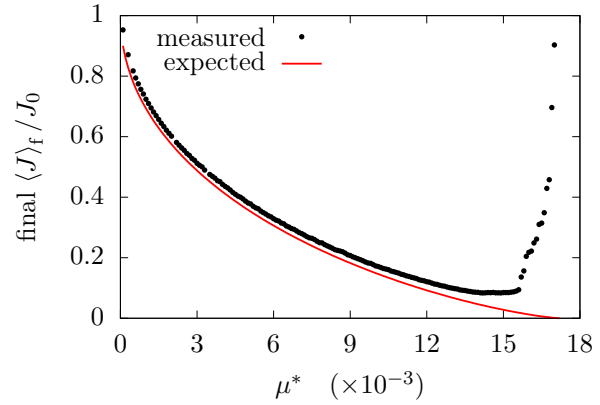


Figure 6: Expected and simulated cooling ratio for trapping in  $G_1$  as a function of  $\mu^*$ . Initial distribution is an annulus at  $J_0 = 0.05$ . The Hamiltonian of Eq. (4) has been used, with  $\hat{k}_3 = 1, \omega_0 = 0.414 \times 2\pi, \Omega_2 = -0.3196$ .

The first generalization of this technique consists in performing beam splitting by means of AC elements. The most natural approach is the use of an AC dipole, but high-order magnets could also be considered. This approach aims at providing the same type of manipulation as the standard beam splitting with, however, a major advantage: the resonance condition is created between the ring tune and the frequency of the AC element. Therefore, even if the tune would be constrained, e.g. by space charge considerations, thus preventing to cross a resonance, beam splitting could still be performed by setting the frequency of the AC element to the appropriate resonant value and then changing it to cross the resonance.

Extending the type of nonlinear manipulation to the crossing of 2D resonances allows entering a new regime, in which the emittance values in both transverse planes are affected and not only that in a single plane. This implies that the redistribution of the values of the transverse emittances is a feasible option.

Finally, the cooling of an annular beam distribution by means of an AC dipole has been successfully studied. Two protocols have been considered, both featuring excellent properties in terms of cooling performance, as well as in terms of the range of amplitudes that can be cooled. Note that the annular beam distribution considered in this study is an excellent model for the beam halo. Therefore, this could be the basis for future applications to halo manipulation, possibly including experimental tests at the LHC.

In the near future, it is planned to pursue these studies using realistic ring lattices in view of experimental tests of the proposed nonlinear manipulations.

## REFERENCES

- [1] R. Cappi and M. Giovannozzi, “Novel method for multiturn extraction: Trapping charged particles in islands of phase space,” *Phys. Rev. Lett.*, vol. 88, p. 104801, 2002. doi:10.1103/PhysRevLett.88.104801

- [2] J. Borburgh *et al.*, “First implementation of transversely split proton beams in the CERN Proton Synchrotron for the fixed-target physics programme,” *EPL*, vol. 113, no. 3, p. 34001, 2016. doi:10.1209/0295-5075/113/34001
- [3] S. Abernethy *et al.*, “Operational performance of the CERN injector complex with transversely split beams,” *Phys. Rev. Accel. Beams*, vol. 20, p. 014001, 2017. doi:10.1103/PhysRevAccelBeams.20.014001
- [4] A. Huschauer *et al.*, “Transverse beam splitting made operational: Key features of the multiturn extraction at the CERN Proton Synchrotron,” *Phys. Rev. Accel. Beams*, vol. 20, p. 061001, 2017. doi:10.1103/PhysRevAccelBeams.20.061001
- [5] A. Neishtadt, “Jumps in the adiabatic invariant on crossing the separatrix and the origin of the 3:1 Kirkwood gap,” *Sov. Phys. Dokl.*, vol. 32, p. 571, 1987.
- [6] S. Sridhart and J. Touma, “Adiabatic evolution and capture into resonance: vertical heating of a growing stellar disc,” *Mon. Not. R Astron. Soc.*, vol. 279, p. 1263, 1996.
- [7] V. Chirikov, “Particle confinement and adiabatic invariance,” *Proc. Royal Soc. London A*, vol. 413, p. 145, 1987.
- [8] D. Escande, “Contributions of plasma physics to chaos and nonlinear dynamics,” *Plasma Physics and Controlled Fusion*, vol. 58, no. 11, p. 113001, 2016. doi:10.1088/0741-3335/58/11/113001
- [9] R. Cappi and M. Giovannozzi, “Multiturn extraction and injection by means of adiabatic capture in stable islands of phase space,” *Phys. Rev. ST Accel. Beams*, vol. 7, p. 024001, 2004. doi:10.1103/PhysRevSTAB.7.024001
- [10] S. Gilardoni *et al.*, “Experimental evidence of adiabatic splitting of charged particle beams using stable islands of transverse phase space,” *Phys. Rev. ST Accel. Beams*, vol. 9, p. 104001, 2006. doi:10.1103/PhysRevSTAB.9.104001
- [11] A. Franchi, S. Gilardoni, and M. Giovannozzi, “Progresses in the studies of adiabatic splitting of charged particle beams by crossing nonlinear resonances,” *Phys. Rev. ST Accel. Beams*, vol. 12, p. 014001, 2009. doi:10.1103/PhysRevSTAB.12.014001
- [12] A. Neishtadt, “Capture into resonance and scattering on resonances in two-frequency systems,” *Proceedings of the Steklov Institute of Mathematics*, vol. 250, p. 183, 2005.
- [13] A. Neishtadt, A. A. Vasiliev, and A. Itin, “Captures into resonance and scattering on resonance in dynamics of a charged relativistic particle in magnetic field and electrostatic wave,” *Physica D*, vol. 141, p. 281, 2000.
- [14] A. N. Vasil’ev and M. A. Guzev, “Particle capture by a slowly varying potential,” *Theor. Math. Phys.*, vol. 68, p. 907, 1986.
- [15] A. Bazzani, C. Frye, M. Giovannozzi, and C. Hernalsteens, “Analysis of adiabatic trapping for quasi-integrable area-preserving maps,” *Phys. Rev. E*, vol. 89, p. 042915, 2014. doi:10.1103/PhysRevE.89.042915
- [16] V. Arnol’d, V. Kozlov, and A. Neishtadt, *Mathematical aspects of classical and celestial mechanics. Dynamical systems III; 3rd rev. version*, ser. Encyclopaedia of mathematical sciences, Heidelberg: Springer, 2006.
- [17] B. V. Chirikov and V. V. Vechevslavov, “Adiabatic Invariance and Separatrix: Single Separatrix Crossing,” *Journal of Experimental and Theoretical Physics*, vol. 90-3, p. 562, 2000.
- [18] A. Neishtadt, “Passage through a separatrix in a resonance problem with a slowly-varying parameter,” *Journal of Applied Mathematics and Mechanics*, vol. 39, no. 4, pp. 594 — 605, 1975. doi:10.1016/0021-8928(75)90060-X
- [19] A. Neishtadt, “Change of an adiabatic invariant at a separatrix,” *Fiz. Plasmy*, vol. 12, p. 992, 1986.
- [20] A. Neishtadt, “Scattering by resonances,” *Celestial Mechanics and Dynamical Astronomy*, vol. 65, p. 1, 1997.
- [21] D. Vainchtein and I. Mezić, “Capture into Resonance: A Method for Efficient Control,” *Phys. Rev. Lett.*, vol. 93, p. 084301, 2004.
- [22] A. Bazzani, F. Brini, and G. Turchetti, “Diffusion of the Adiabatic Invariant for Modulated Symplectic Maps,” *AIP Conf. Proc.*, vol. 395, p. 129, 1997. doi:10.1063/1.52959
- [23] V. I. Arnol’d, “On the behavior of adiabatic invariants under a slow periodic change of the Hamiltonian function,” *Doklady*, vol. 142, p. 758, 1962.
- [24] V. I. Arnol’d, “Conditions of the applicability and an estimate of the mistake of the averaging method for systems, which goes through the resonances during the evolution process,” *Doklady*, vol. 161, p. 9, 1965.
- [25] A. Bazzani, F. Capoani, and M. Giovannozzi, “Analysis of adiabatic trapping phenomena for quasi-integrable area-preserving maps in the presence of time-dependent excitors,” in preparation.
- [26] A. Bazzani, F. Capoani, and M. Giovannozzi, “Manipulations of transverse invariants in 2D Hamiltonian systems,” in preparation.
- [27] F. Capoani, A. Bazzani, M. Giovannozzi, and R. Tomás García, “Cooling of an Annular Beam by Using Nonlinear Effects”, in *Proc. IPAC’21*, Campinas, Brazil, May 2021, pp. 1968–1971. doi:10.18429/JACoW-IPAC2021-TUPAB231
- [28] A. Bazzani, F. Capoani, M. Giovannozzi, and R. Tomás, “Nonlinear cooling of an annular beam distribution,” in preparation.
- [29] A. Neishtadt, A. Vasil’ev, and A. Artem’ev, “Capture into resonance and escape from it in a forced nonlinear

pendulum,” *Regular and Chaotic Dynamics*, vol. 18, no. 6, pp. 686–696, 2013.

- [30] V. I. Arnold and A. Avez, *Problèmes Ergodiques de la Mécanique Classique*, Paris: Gauthier-Villars, 1967.
- [31] M. Hénon, “Numerical study of quadratic area-preserving mappings,” *Q. Appl. Math.*, vol. 27, p. 291, 1969.
- [32] A. Bazzani, G. Servizi, E. Todesco, and G. Turchetti, *A normal form approach to the theory of nonlinear betatronic motion*, ser. CERN Yellow Reports: Monographs, CERN, Geneva, Switzerland, 1994. doi:10.5170/CERN-1994-002
- [33] S. Y. Lee, K. Y. Ng, H. Liu, and H. C. Chao, “Evolution of beam distribution in crossing a Walkinshaw resonance,” *Phys. Rev. Lett.*, vol. 110, p. 094801, 2013. doi:10.1103/PhysRevLett.110.094801

# HL-LHC BEAM DYNAMICS WITH HOLLOW ELECTRON LENSES

P. D. Hermes\*, R. Bruce, R. De Maria, M. Giovannozzi, A. Mereghetti<sup>†</sup>, D. Mirarchi, S. Redaelli  
 CERN Beams Department, Geneva, Switzerland

G. Stancari

Fermi National Accelerator Laboratory, Batavia, Illinois, USA

## Abstract

Each of the two proton beams in the High-Luminosity Large Hadron Collider (HL-LHC) will carry a total energy of 700 MJ. One concern for machine protection is the energy stored in the transverse beam halo, estimated to potentially reach up to 5% of the total stored energy. Several failure scenarios could drive this halo into the collimators, potentially causing damage and therefore severely affecting operational efficiency. Hollow Electron Lenses (HEL) were integrated in the HL-LHC baseline to mitigate this risk by depleting the tails in a controlled way. A hollow-shaped electron beam runs co-axially with the hadron beam over about 3 m, such that halo particles at large amplitudes become unstable, while core particles ideally remain undisturbed. Residual fields from electron beam asymmetries can, however, induce emittance growth of the beam core. Various options for the pulsing of the HEL are considered and are compared using two figures of merit: halo depletion efficiency and core emittance growth. This contribution presents simulations for these two effects with different HEL pulsing modes using updated HL-LHC optics, that was optimized at the location of the lenses.

## INTRODUCTION

Small fractions of the large stored beam energy in HL-LHC [1] can potentially cause severe damage to the machine hardware and negatively impact the operational efficiency, if they are lost in an uncontrolled way. The Large Hadron Collider (LHC) [2] is already equipped with a sophisticated, multi-stage collimation system [3–5] to intercept particles at large betatron or momentum offsets before they are lost in the sensitive LHC hardware. The highly-populated beam halo poses additional concerns that the upgraded HL-LHC collimation system [6] might not be able to cope with.

Assuming that up to 5% of the stored beam energy can be located in the halo of the circulating proton beams [7, 8], some of the failure scenarios that may occur in HL-LHC [9, 10] put at risk the integrity of the collimation system itself, with potentially severe consequences for the scientific programme. Most notably, for the context of this work, machine safety is endangered by sudden orbit shifts which would steer the highly populated beam halo into the primary collimators, that are closest to the circulating beams. Overall, the collimation system must work safely, also with sudden orbit shifts in the order of  $2\sigma$  (with  $\sigma$  being the RMS beam size).

\* pascal.hermes@cern.ch

<sup>†</sup> Currently at Fondazione CNAO, Strada Campeggi 53, 27100 Pavia, Italy

Hollow electron lenses (HEL) have recently been added to the upgrade baseline of the HL-LHC [6] to mitigate effects of highly-populated beam halo through an active control of its halo population. This paper reviews the key parameters of the HELs and gives a status update of the beam dynamics simulations for the halo depletion efficiency and the impact of residual fields on the emittance of the beam core.

## HOLLOW ELECTRON LENSES FOR HL-LHC COLLIMATOR

### Hollow Electron Beam Parameters

The HEL [11] is a device that can actively remove particles at large transverse amplitudes, and thus deplete the halo in a controlled way. For this purpose, a hollow-shaped electron beam (see Fig. 1) is created and guided through a magnetic system in which the hadron and electron beams run co-axially over a certain length. The electron beam distribution is characterized by an inner and outer radius  $r_1$  and  $r_2$ , respectively. Hadron particles moving through the HEL with a transverse amplitude smaller than  $r_1$  are ideally unaffected, because the net electric and magnetic fields generated by the surrounding electron current yield zero. Hadrons with larger amplitudes than  $r_1$  are subject to electric and magnetic fields which change their transverse momentum. This kick  $\theta(r)$  is a function of the radius  $r = \sqrt{x^2 + y^2}$  of the particle and can be quantified as follows

$$\theta(r) = f(r) \theta_{\max} \left( \frac{r_2}{r} \right), \quad (1)$$

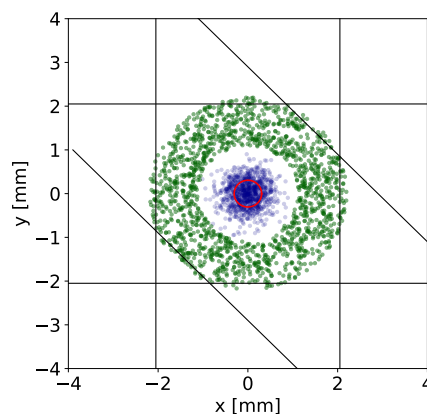


Figure 1: Transverse distribution of the hollow electron beam (green) and the hadron beam (blue) at the HEL. The black lines indicate the cut generated by the primary collimators. The red circle corresponds to one RMS beam size.

where  $f(r)$  is an amplitude-dependent shape function corresponding to the fraction of the total electron current enclosed by a cylinder of radius  $r$ :

$$f(r) = \begin{cases} 0 & r < r_1 \\ \frac{r^2 - r_1^2}{r_2^2 - r_1^2} & r_1 \leq r \leq r_2 \\ 1 & r > r_2 \end{cases} . \quad (2)$$

While HELs can be used for all types of hadron beams that can be stored in HL-LHC, it is crucial for the operation of proton beams, which is why the following description will refer to protons instead of hadrons in general. All parameters of the HEL other than the inner and outer radii are subsumed in the maximum scattering angle  $\theta_{\max}$  given by

$$\theta_{\max} = \frac{1}{4\pi\epsilon_0 c^2} \frac{2L I_e (1 \pm \beta_e \beta_p)}{(B\rho)_p \beta_e \beta_p r_2} , \quad (3)$$

where  $L$  is the active length of the HEL,  $I_e$  is the total electron-beam current,  $\beta_e$  and  $\beta_p$  are relativistic  $\beta$ -factor of the electrons and protons, respectively, and  $(B\rho)_p$  is the magnetic rigidity of the proton beam. It is noteworthy that the transverse kick experienced by a particle increases linearly with the HEL length and the electron beam current. Furthermore, the two possible signs that can be taken by the  $\pm$  in the numerator correspond to the electrons moving in the same direction as the proton beam (-) or in the opposite one (+). Maximising  $\theta_{\max}$  can obviously be reached by letting the electron beam move in the opposite direction with respect to the proton beam and by maximizing  $L$  and  $I_e$ .

With realistic electron beam parameters, values for  $\theta_{\max}$  are typically in the order of some 0.1  $\mu\text{rad}$  for 7 TeV proton beams. Several passages through the HEL are therefore required, before a particle is eventually lost in the collimators. The HEL thus induces a comparably slow transverse diffusion, which also ensures that the machine hardware is not endangered by a rapid beam loss created by the HEL itself.

For machine protection purposes, it is also important to keep the possibility to detect orbit drifts with the beam loss monitors at the HL-LHC collimators early enough to trigger a beam dump. For this purpose, a small fraction of the beam halo must be preserved and it is foreseen to leave several bunches of the proton beam unaffected by the HEL. For these so-called witness bunches, the electron beam is always switched off.

### Residual Effects on the Beam Core

In the previous section, it was assumed that all particles at  $r < r_1$  are not subject to a change of transverse momentum due to the electron lens. This applies to the idealized model of a perfectly symmetric electron beam. In reality, a residual field will act also on particles in the beam core, due to asymmetries in the transverse distribution of electrons. In the design specifications of the HEL [12], it is defined that the residual fields acting on particles in the beam core must not exceed a level that introduces a transverse dipole kick of

$$\Delta\theta_{\text{core}} = 1 \text{ nrad} . \quad (4)$$

A proton beam moving through the electron lens without the electron beam being present will receive no kick.

### Pulsing of the HEL

Operating the HEL at constant current (i.e. the same electron current is applied at every turn for the non-witness bunches) is not expected to deliver sufficient depletion of the beam halo. Better efficiency of the halo depletion can potentially be reached by using turn dependent pulsing schemes. The following schemes have been studied [13]:

**Constant-current mode:** HEL is switched on at every turn with the same current  $I_e$ .

**Pulsed mode  $P_i^j$ :** HEL is switched on for  $i$  turns with constant current  $I_e$  and switched off for  $j$  turns.

**Random mode  $R_p$ :** HEL is switched on and off randomly at every turn with a certain probability  $p$  to be switched on and  $1 - p$  to be switched off. If the HEL is switched on, the current is always equal to a constant value  $I_e$ .

### Beam Dynamics Measures of HEL Performance

We measure the depletion performance of the HEL in terms of the percentage of depleted halo after a given period of time. The target depletion fraction is specified as removing 90% of the transverse halo within 5 minutes of HEL operation. Previous studies demonstrated that the operation of the HEL is the most efficient, i.e. the beam halo is removed fastest, if the electron beam is randomly switched on and off at every turn [11, 13]. This observation is expected, given the broad spectrum of frequencies that this mode of operation covers and it would be ideal for a perfect-HEL scenario with no residual field in the area  $r < r_1$ . In reality, this condition is not achievable and any residual component can perturb the proton beam dynamics.

In general, the non-symmetries of the electron beam introduce all orders of electromagnetic fields. The effect of the lowest order (dipolar) field is studied here. Studies with the effect of higher order field components are currently ongoing. Considering a residual kick  $\theta_{\text{core}}$ , the operation in the random mode introduces random dipolar noise to the particles in the beam core. Such a noise diffuses particles from the beam core to larger amplitudes and thus increases the RMS beam emittance, with detrimental effects on the collider's luminosity. This undesired effect is quantified in terms of the emittance change  $\Delta\epsilon$  per unit time.

## UPDATED OPTICS AT THE HEL

In the current phase of preparing the implementation of the HL-LHC, the envisaged beam optics for HL-LHC are regularly updated, based on revised requirements and new knowledge gathered via simulations and LHC operation. The current optics version (referred to as V1.4, compared to the previous version V1.3) integrates optimised local optical

functions at the HEL location in order to obtain larger beam sizes and round optics, i.e. same  $\beta$ -functions in  $x$  and  $y$  [11]. Table 1 shows a comparison between the previous optics V1.3 and the updated optics V1.4, illustrating that the  $\beta$ -function increases by 42% in  $x$  and 32% in  $y$ .

Table 1: Optical functions at the location of the HEL for B1 of HL-LHC in Version 1.3 and the newer version 1.4, optimized at the location of the HEL.

Optics Version	V1.3	V1.4
$\beta_x$ (m)	197.5	280.0
$\beta_y$ (m)	211.9	280.0
$\alpha_x$	0.98	0.64
$\alpha_y$	-0.13	-0.25
$D_{x/y}$ (m)	0	0

The larger  $\beta$ -functions allow using a larger electron beam with the same normalized proton beam size. With larger electron beam size, the stability of the electron beam is increased and the tolerances for the device are more relaxed. On the other hand, it is expected that the effect of emittance growth due to the residual dipole field increases. Moreover, the efficiency of halo depletion in the different pulsing patterns can be affected by the change of machine optics. The studies presented in [11], carried out for V1.3, are therefore compared to a new set of simulations for V1.4 in the following sections.

## SIMULATIONS OF HEL PERFORMANCE

For the comparison of the HEL performance with different optics, we use the same beam parameters and setup of non-linear elements as in the study presented in [13]. The most important key parameters are summarized in Table 2. Note that beam-beam interactions are not taken into account to assess the HEL performance, since it is intended to be operated after the acceleration ramp. This configuration is more challenging because it is expected that the non-linearities from beam-beam interactions would make the depletion more efficient. The  $\beta^*$  simulated corresponds to the operational configuration with squeezed but separated beams, right before collision. This was chosen for comparability to previous studies [13] and simulations with the configuration right after the acceleration ramp are going to be performed in the future.

As a case study, we take  $r_1 = 5\sigma$  and  $r_2 = 10\sigma$ , using an electron current of 5 A with electrons of 10 keV and a HEL length of  $L = 3$  m. Note that for the asymmetric  $\beta$ -functions in V1.3 the inner radius corresponds to  $5\sigma$  in the horizontal plane, only. The residual kick deemed to have an effect on the beam core is  $\theta_{\text{core}} = 1$  nrad in the vertical direction (where stronger asymmetries are expected from electron beam dynamics simulations [14]). It corresponds to the maximum residual field defined in the HEL design specifications.

While the simulations presented in [13] were carried out with SixTrack [15–17], the halo depletion simulations presented here were obtained by means of the new simulation tool XSuite, a development based on SixTrackLib [18, 19]. Both tools provide second-order symplectic tracking, taking into account multipole errors in the various magnetic elements of the ring. The emittance-growth simulations presented here were both carried out with SixTrack. Due to the long times needed for the tracking simulations, the emittance growth simulations were performed for only 2 million turns in HL-LHC (corresponding to almost 3 minutes in the collider) and the depletion simulations were limited to 60 s in the collider for constant current and random excitations. Pulsed operation was simulated 400 times for each optics with different periodicities, which is why we limited the simulated time in the collider to 10 s.

### HEL Performance for Halo Depletion

We define the circulating halo  $n_{\text{halo}}$  as the amount of particles circulating at amplitudes between the inner radius of the electron beam in the HEL and the primary collimator (TCP) half gap at  $6.7\sigma$ . We distinguish between the beam halo without HEL,  $n_{\text{halo}}^0$ , and the beam halo with the HEL for a given pulsing pattern,  $n_{\text{halo}}^{\text{HEL}}$ , and we define the depletion fraction  $\mathcal{R}_d$  as

$$\mathcal{R}_d = 1 - \frac{n_{\text{halo}}^{\text{HEL}}}{n_{\text{halo}}^0}. \quad (5)$$

The initial distribution used for all simulations was sampled as a double Gaussian composed of one Gaussian with sigma equal to  $1\sigma$  contributing 65% to the total, and another one with sigma equal to  $2\sigma$  contributing 35%, to imitate the over-populated tails observed in the machine [20]. Each simulation considers 30000 initial particles.

**Constant current mode** The depletion fraction in the operation of the HEL with the constant-current pulsing mode, shown in Fig. 2 differ approximately by a factor of two, but are at low levels for both optics studied. After one minute of operation in constant current mode, approximately 1.4% of the halo has been depleted in HL-LHC V1.4, compared to 2.8% in V1.3. The difference is potentially related to

Table 2: Simulation parameters used in the numerical simulations.  $Q'$  corresponds to the chromaticity,  $I_{\text{oct}}$  to the current powering the Landau octupoles, the TCP half gap is the half gap of the primary collimators.

Parameter	Value
Beam	B1
$\beta^*$ (IR1/IR5)	15 cm
$Q'$	15
$I_{\text{oct}}$	-300 A
TCP half gap	$6.7\sigma$

Content from this work may be used under the terms of the CC BY 3.0 licence (© 2021). Any distribution of this work must maintain attribution to the author(s), title of the work, publisher, and DOI

the smaller kick the particles receive with the larger relative electron beam size in the updated optics version.

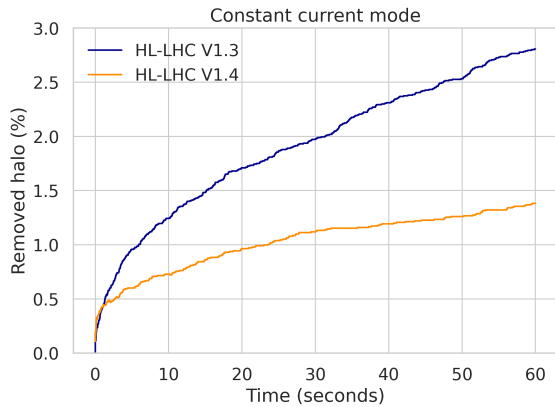


Figure 2: Halo depletion rate in the constant current mode for HL-LHC V1.3 and HL-LHC V1.4.

**Random mode** The simulated depletion efficiency in random mode is compared in Fig. 3. Note the change of scale compared to Fig. 2. In both cases the depletion is significantly more efficient than with the constant-current mode. The level of depletion reached after one minute of operation is 68% for HL-LHC Version 1.3 and 62% for HL-LHC version 1.4. The probability of switching the HEL on or off is 50% at each turn for both optics. While the final depletion fraction achieved is slightly different for the two cases, the depletion curve with time shows a similar shape.

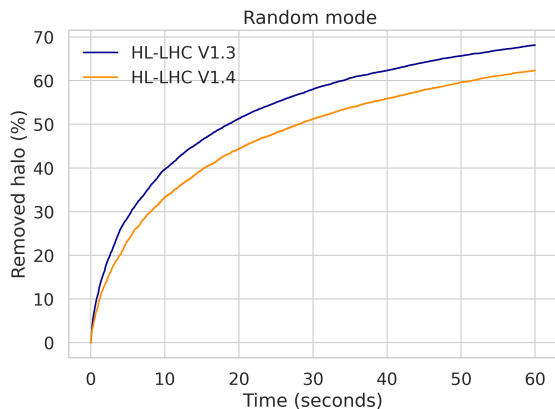


Figure 3: Comparison of the depletion efficiency in random mode for HL-LHC V1.3 and HL-LHC V1.4.

**Pulsed mode** The HEL operation in pulsed mode is simulated over a grid of  $20 \times 20$ , probing all possible combinations of the number of turns on and off between 1 and 20. The total number of turns simulated corresponds to 10 s in HL-LHC. The result is illustrated in Fig. 4. The most remarkable feature in both figures is the clear and distinct periodicity  $T = i$  (turns ON) +  $j$  (turns OFF) for which the depletion efficiency is maximized. For HL-LHC V1.3, this

periodicity is  $T = 23$  turns, for HL-LHC V1.4 it is  $T = 24$  turns. Furthermore, in both cases additional lines at higher harmonics are visible. For example, for HL-LHC V1.4, clear areas of increased depletion efficiency can be identified at  $T = 12$ , half of the most efficient periodicity, and also at  $T = 20$ , at 5/6 of the most efficient periodicity. For the periodicity of 23, the second harmonic cannot be simulated because it does not correspond to an integer. However, we see clear and distinct lines in the proximity at  $T = 13$  and  $T = 11$ . Another difference is the depletion fraction achieved over 10 s. For HL-LHC V1.3, the highest depletion fraction achieved is 20% with  $T = 23$ . For HL-LHC V1.4, the highest depletion fraction is 34% with  $T = 24$ .

These findings altogether indicate that the peaks of depletion in the pulsed operation are caused by a resonant effect from the interaction of particles with the HEL. With the update of the optics, the resonant periodicity has moved from  $T = 23$  to  $T = 24$ . Further studies, outside of the scope of this contribution, showed a large variation of the peak depletion rate in pulsed operation with octupole current. This is in line with the hypothesis that the difference in the peak depletion rate and the resonance periodicity between the two optics can potentially be drawn back to a change of the shape of the phase space area taking into account the non-linearities. Current studies attempting to further explain this resonant behavior are ongoing.

### Assessment of Effects on the Core

Emittance growth is studied for the random mode, which was found to be the most critical operational mode in [13]. The results for both optics versions are shown in Fig. 5. The initial distribution as a single Gaussian with an initial emittance of  $2.5 \mu\text{m rad}$ . The number of tracked particles is set to 30000 and the RMS emittance is inferred from the observed distribution of particles every second. We also show the rolling mean over five data points, corresponding to 5 s, to average over the fluctuating data. To estimate the difference in emittance growth for the two scenarios, we perform a linear regression on the calculated emittances (not on the rolling mean) over time for both cases. In view of the induced emittance growth, it is envisaged to operate the HEL with this pulsing over only five minutes, corresponding to approximately 3.4 million turns. The simulated results of the emittance growth over five minutes, inferred from the linear regressions, are listed in Table 3.

The growth rate simulated for V1.4 is approximately 28% larger than for V1.3 (the change of vertical  $\beta$ -function is 33%). While the pulsing of the electron lens was random with a probability of being switched on/off of 50% in both cases, the precise sequence of turns at which the lens was switched on or off was different in the two simulation cases. This difference, however, should average out over time and should not be significant for a simulation over two million turns. If we take into account that the growth of the emittance can be attenuated by a factor of approximately 15 with the transverse damper system (ADT) [21, 22], the total emittance

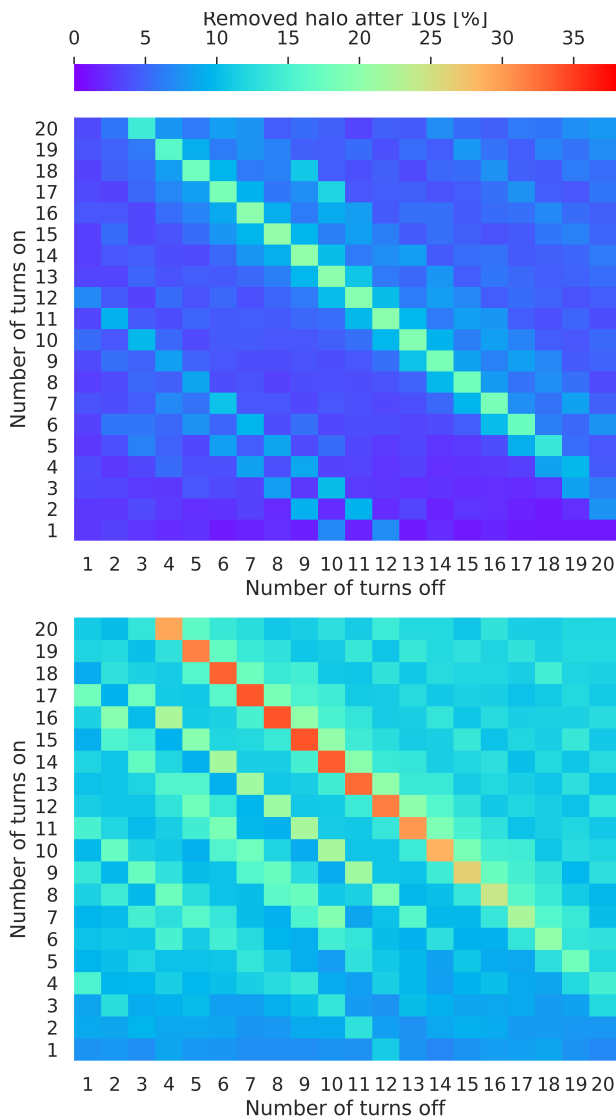


Figure 4: Depletion efficiency over 10s of operation of the HEL in pulsed mode. The vertical axis corresponds to  $i$ , the horizontal axis to  $j$ . Top: HL-LHC V1.3, bottom: V1.4.

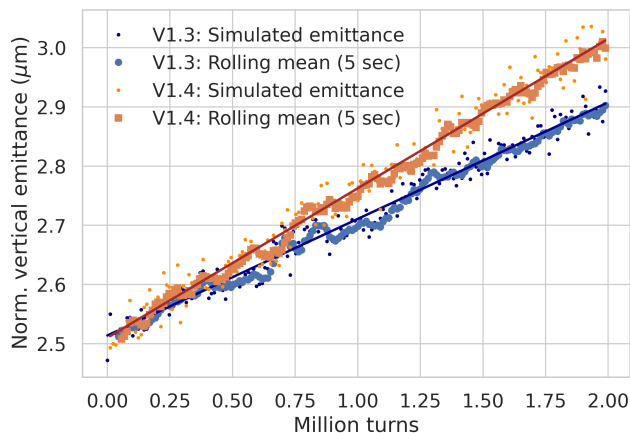


Figure 5: Simulated emittance evolution with a residual vertical dipole kick of 1 nrad for both optics versions, without considering the attenuating effect from the ADT.

growth after five minutes of operation is in the order of 0.04 to 0.06  $\mu\text{m rad}$  for the two optics studied, as listed in Table 3. We deem both as tolerable, considering that it is a onetime effect per fill. Note also, that the studied scenario assumes the HEL to be operated at the maximum current. With lower electron beam currents, the residual dipole kick and the emittance growth will be lower than presented above.

Table 3: Simulated vertical emittance growth for HL-LHC optics V1.3 and V1.4 assuming a residual kick of 1 nrad, operating the HEL with random pulsing over 5 minutes, with and without effect from the ADT. It is assumed that the ADT attenuates the emittance growth by a factor of 15.

Optics	$\Delta\epsilon_y$ ( $\mu\text{m rad}$ ) in 5 minutes	
	Without ADT	With ADT
V1.3	0.65	0.04
V1.4	0.85	0.06

## CONCLUSIONS

Hollow electron lenses are crucial building blocks for the safe and successful operation of the HL-LHC. The key performance indicator for the beam dynamics with HELs is the depletion efficiency. At the same time, the beam-core emittance growth due to residual dipole fields must be minimized. The studies presented in this paper have illustrated that the efficiency of depletion in the relevant modes, without beam-beam interaction, is similar for the two optics considered: the previous HL-LHC baseline and a new version optimized for the HEL. While the efficiency in constant current mode is insufficient to meet the requirements with separated beams with both optics versions, operation in the random mode delivers a promising depletion fraction. Depletion patterns observed in pulsed operation for both optics versions show the same qualitative key features, but at different pulsing periodicity. This behaviour may be caused by a change in the shape of the phase space and is currently under investigation. Further studies are ongoing to assess the impact of beam-beam interactions on the halo depletion efficiency of HELs. The emittance growth induced by the random mode is slightly larger in V1.4 than in V1.3, which can be qualitatively explained by the larger local  $\beta$ -functions. It can be reduced with the ADT to a sufficiently low level in both cases. Overall, the results let us conclude that the update of optics, motivated by better electron beam stability, symmetry between the two transverse planes and relaxed requirements for tolerances on electron and hadron beams, allows us to maintain similar depletion efficiencies for the relevant operational modes without inducing a strong deterioration in terms of emittance growth.

## ACKNOWLEDGMENTS

The authors would like to express their gratitude for the support from the HL-LHC project. We thank G. Iadarola for his support in setting up the XSuite environment.

## REFERENCES

- [1] G. Apollinari *et al.*, “High-Luminosity Large Hadron Collider (HL-LHC): Technical Design Report V. 0.1,” 2017, doi:10.23731/CYRM-2017-004
- [2] O. S. Brüning *et al.*, “LHC design report v.1 : The LHC main ring,” *CERN-2004-003-V1*, 2004.
- [3] R. W. Assmann *et al.*, “The Final Collimation System for the LHC,” in *Proc. 10th European Particle Accelerator Conf. (EPAC’06)*, Edinburgh, UK, 2006, pp. 986–988, <https://jacow.org/e06/papers/tuodfi01.pdf>
- [4] R.W. Assmann, “Collimators and Beam Absorbers for Cleaning and Machine Protection,” in *Proceedings of the LHC Project Workshop - Chamonix XIV*, Chamonix, France, 2005, pp. 261–267, <https://cds.cern.ch/record/987838>
- [5] R. Bruce *et al.*, “Simulations and measurements of beam loss patterns at the CERN Large Hadron Collider,” *Phys. Rev. ST Accel. Beams*, vol. 17, p. 081004, 8 2014, doi:10.1103/PhysRevSTAB.17.081004
- [6] S. Redaelli *et al.*, “High-Luminosity Large Hadron Collider (HL-LHC): Technical design report, Chapter 5: Collimation System,” 2020, doi:10.23731/CYRM-2020-0010.87
- [7] G. Valentino *et al.*, “Beam diffusion measurements using collimator scans in the LHC,” *Phys. Rev. ST Accel. Beams*, vol. 16, p. 021003, 2 2013, doi:10.1103/PhysRevSTAB.16.021003
- [8] A. Gorzawski *et al.*, “Probing LHC halo dynamics using collimator loss rates at 6.5 TeV,” *Phys. Rev. Accel. Beams*, vol. 23, p. 044802, 2020, doi:10.1103/PhysRevAccelBeams.23.044802
- [9] R. Appleby *et al.*, “Report from the review panel,” *Review of the needs for a hollow electron lens for the HL-LHC*, CERN, Geneva, Switzerland, 2016, <https://indico.cern.ch/event/567839/overview>
- [10] B. Lindstrom *et al.*, “Fast failures in the LHC and the future high luminosity LHC,” *Phys. Rev. Accel. Beams*, vol. 23, p. 081001, 8 2020, doi:10.1103/PhysRevAccelBeams.23.081001
- [11] S. Redaelli *et al.*, “Hollow electron lenses for beam collimation at the High-Luminosity Large Hadron Collider (HL-LHC),” *J. Instrum.*, vol. 16, no. 03, P03042, 2021, doi:10.1088/1748-0221/16/03/p03042
- [12] R. Bruce *et al.*, “Functional and operational conditions of the Hollow Electron Lenses (HEL) at HL-LHC,” *CERN EDMS 2514085*, 2021.
- [13] D. Mirarchi *et al.*, “Nonlinear dynamics of proton beams with hollow electron lens in the CERN High-Luminosity LHC,” *Submitted to European Physical Journal Plus*, 2021.
- [14] A. Mereghetti, “Status of Simulations and Required Inputs,” 2019, Presentation at the 122nd Collimation Upgrade Specification Meeting, ColUSM, 22/11/2019, CERN, Switzerland.
- [15] *Sixtrack web site*, <https://sixtrack.web.cern.ch/SixTrack/>
- [16] R. De Maria *et al.*, “SixTrack Version 5: Status and New Developments,” in *Proc. IPAC’19*, Melbourne, Australia, 2019, pp. 3200–3203, doi:10.18429/JACoW-IPAC2019-WEPTS043
- [17] R. Bruce *et al.*, “Status of SixTrack with collimation,” in *Proceedings of the ICFA Mini-Workshop on Tracking for Collimation*, CERN, Geneva, Switzerland, 2018, p. 10, doi:10.23732/CYRCP-2018-002.1
- [18] G. Iadarola *et al.*, *Xsuite website*, <https://xsuite.readthedocs.io/en/latest/>
- [19] R. D. Maria *et al.*, “SixTrack Project: Status, Runtime Environment, and New Developments,” in *Proc. ICAP’18*, Key West, FL, USA, 2019, pp. 172–178, doi:10.18429/JACoW-ICAP2018-TUPAF02
- [20] P. Racano *et al.*, “Review of halo measurements at LHC with collimator scans,” Presentation at the HL-LHC Collaboration Meeting, 15-18 October 2018, Geneva, Switzerland.
- [21] W. Hofle *et al.*, “LHC Transverse Feedback System and its Hardware Commissioning,” in *Proc. EPAC’08*, Genoa, Italy, 2008, pp. 3266–3268, <https://jacow.org/e08/papers/thpc121.pdf>
- [22] X. Buffat *et al.*, “Modeling of the emittance growth due to decoherence in collision at the Large Hadron Collider,” *Phys. Rev. Accel. Beams*, vol. 23, p. 021002, 2020, doi:10.1103/PhysRevAccelBeams.23.021002

# CLOSED FORM FORMULAS FOR THE INDIRECT SPACE CHARGE WAKE FUNCTION OF AXISYMMETRIC STRUCTURES

N. Mounet\*, C. Zannini, E. Dadiani<sup>1</sup>, E. Métral, CERN, Geneva, Switzerland  
 A. Rahemtulla<sup>2</sup>, EPFL, Lausanne, Switzerland

<sup>1</sup>now at Carnegie Mellon University, Pennsylvania, USA, and Tbilisi State University, Georgia  
<sup>2</sup>now at ETHZ, Zurich, Switzerland

## Abstract

Indirect space charge contributes significantly to the impedance of non-ultrarelativistic machines such as the LEIR, PSB and PS at CERN. While general expressions exist in frequency domain for the beam coupling impedance, the time domain wake function is typically obtained numerically, thanks to an inverse Fourier transform. An analytical expression for the indirect space charge wake function, including the time dependence as a function of particle velocity, is nevertheless highly desirable to improve the accuracy of time domain beam dynamics simulations of coherent instabilities. In this work, a general formula for the indirect space charge wake function is derived from the residue theorem. Moreover, simple approximated expressions reproducing the time and velocity dependence are also provided, which can even be corrected to recover an exact formula, thanks to a numerical factor computed once for all. The expressions obtained are successfully benchmarked with a purely numerical approach based on the Fourier transform.

## INTRODUCTION

In high intensity synchrotrons, electromagnetic fields created by the beam passage through its interaction with its surroundings, is one of the main collective effect that can limit the performance of the machine, potentially leading to detrimental consequences such as heat load, emittance growth or, in the most dramatic cases, beam instabilities. Its role was pointed out as early as in 1965 in the seminal work of Laslett et al [1], and the concept of beam coupling impedance introduced slightly later by Sessler and Vaccaro [2]. The impedance, defined as the Fourier transform of the integrated force, felt by a witness (trailing) charge as a consequence of the interaction of a source (leading) charge with a certain accelerator equipment, normalised to the excitation, proved to be a very useful descriptor of the magnitude of such effects in a given machine. In particular, it can be efficiently used in Vlasov equation solvers to compute and predict instabilities.

Over the past fifty years many analytical formulas have been derived to provide such impedances, in particular in the case of a smooth, axisymmetric structure such as a vacuum pipe, made of one or several layers of materials in the radial direction [3–15]. On the other hand, the equivalent time domain quantity, namely the wake function [16]<sup>1</sup>, remains elusive, at least in the form of analytic formulas: for

cylindrical resistive geometries one can mention the famous thick-wall formula [5], its extension to non-ultrarelativistic beams [17], as well as a thin-wall formula [18].

As a matter of fact, even the simplest case of a perfectly conductive, cylindrical beam pipe, often called the indirect space charge (ISC) impedance, although well-known in frequency domain [8] still lacks a formula for its wake function—one can mention the ultrarelativistic expression by Chao [5], which is of limited practical interest as it is expressed as a Dirac delta function in the longitudinal coordinate along the bunch  $z$ . A more general wake function formula would nevertheless be useful when performing macroparticle simulations. In particular, in low-energy machines, the ISC is strong and its broad-band nature makes it very peaked close to  $z = 0$  (the position of the source particle creating the wake), which in turn requires a very fine discretization along  $z$ , leading to time-consuming simulations. A simple analytical formula would therefore be highly beneficial to macroparticle simulations.

The ISC impedance is traditionally separated from the direct space charge (i.e. the impedance in free space), the latter being fundamentally of non-linear nature. In an axisymmetric structure, the longitudinal and transverse dipolar ISC impedances can be expressed respectively as [8]:

$$Z_{\parallel}(\omega) = \frac{i\omega\mu_0 L}{2\pi\beta^2\gamma^2} \frac{K_0\left(\frac{kb}{\gamma}\right)}{I_0\left(\frac{kb}{\gamma}\right)}, Z_{\perp}^{dip}(\omega) = \frac{ik^2 Z_0 L}{4\pi\beta\gamma^4} \frac{K_1\left(\frac{kb}{\gamma}\right)}{I_1\left(\frac{kb}{\gamma}\right)}, \quad (1)$$

with  $i$  the imaginary unit,  $b$  the radius of the pipe,  $L$  its length,  $\omega > 0$  the angular frequency (in rad/s),  $\mu_0$  the vacuum permeability,  $Z_0 = \mu_0 c$  the free space impedance,  $c$  the speed of light in vacuum,  $v = \beta c$  the beam velocity,  $\gamma$  the relativistic mass factor,  $k \equiv \omega/v$  the wave number, and  $I_0$ ,  $I_1$ ,  $K_0$  and  $K_1$  modified Bessel functions of the first and second kinds. Note that SI units are used throughout these proceedings.

In the following sections we will provide expressions for the ISC wake functions, defined as Fourier integrals:

$$W_{\parallel}(z) = \frac{1}{2\pi} \int_{-\infty}^{\infty} d\omega e^{i\omega \frac{z}{v}} Z_{\parallel}(\omega), \quad (2)$$

$$W_{\perp}^{dip}(z) = -\frac{i}{2\pi} \int_{-\infty}^{+\infty} d\omega e^{i\omega \frac{z}{v}} Z_{\perp}^{dip}(\omega). \quad (3)$$

\* nicolas.mounet@cern.ch

<sup>1</sup> The wake function should not to be confused with the so-called wake potential that represents the convolution of the wake function by the

longitudinal bunch distribution. In early works (and in particular in Ref. [16]), the wake function was actually often called "wake potential".

We will provide first an exact formalism to compute the ISC wake functions in the longitudinal and transverse planes. Then, a numerical method will be briefly described and used to benchmark the obtained formulas. This will be followed by the description of a simplified approach in the transverse case, providing a more handy formula that can even be corrected to recover exact results. Finally, we will give our concluding remarks.

## EXACT ANALYTICAL APPROACH

In this section we first outline the formalism used to compute Fourier integrals, before applying it to the specific case of the ISC.

### Computation of Fourier Integrals With the Residue Theorem

Given a function  $f(\omega)$  defined in the complex plane, its Fourier integral at a time  $\tau > 0$  can be expressed as

$$\begin{aligned} \int_{-\infty}^{\infty} e^{i\omega\tau} f(\omega) d\omega &= \lim_{R \rightarrow \infty} \int_{-R}^R e^{i\omega\tau} f(\omega) d\omega \\ &= \lim_{R \rightarrow \infty} \left( \oint_{C_1+C_2} e^{i\omega\tau} f(\omega) d\omega \right. \\ &\quad \left. - \int_{C_2} e^{i\omega\tau} f(\omega) d\omega \right), \end{aligned} \quad (4)$$

with  $C_1$  the path along the real axis going from  $-R$  to  $R$ , and  $C_2$  the counter-clockwise half-circle from  $R$  to  $-R$ , in the positive imaginary part of the complex plane, as illustrated in Fig. 1. By virtue of Jordan's lemma, the second integral vanishes when  $R$  goes to infinity, as long as the maximum of  $f$  on the half-circle  $C_2$  goes to zero at the limit in  $R$ , in other words when

$$\lim_{R \rightarrow \infty} \left[ \max_{0 \leq \theta \leq \pi} f(Re^{i\theta}) \right] = 0. \quad (5)$$

In Eq. (4), the integral on the closed contour  $C_1 + C_2$  can be

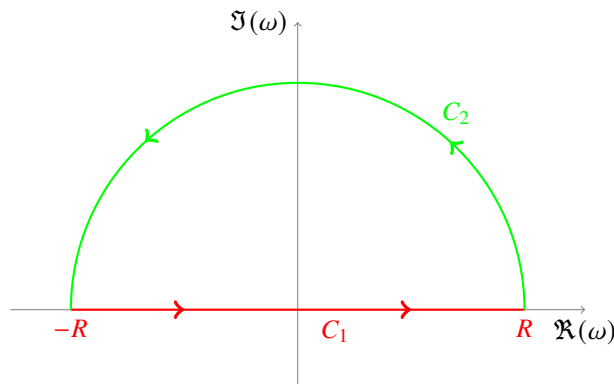


Figure 1: Sketch of the integration path in the complex plane. Arrows indicate the direction of integration.

expressed using Cauchy's residue theorem when  $f$  is meromorphic on the upper complex half plane (i.e. holomorphic

except for a set of isolated points). Assuming also that all the singularities of  $f$  are simple poles, we get

$$\int_{-\infty}^{\infty} e^{i\omega\tau} f(\omega) d\omega = 2\pi i \sum_k e^{i\omega_k\tau} \text{Res}[f, \omega_k], \quad (6)$$

where  $\text{Res}[f, \omega_k]$  is the value of the residue of  $f$  at the pole  $\omega_k$ , and the sum runs over all poles in the upper half-plane.

Note that when  $\tau < 0$ , the same reasoning can be performed using instead a half-circle contour lying in the lower half-plane of  $\mathbb{C}$ , but since the direction of integration of  $C_1 + C_2$  becomes clockwise, a minus sign appears in front of the residue sum in Eq. (6).

### Case of the ISC

The longitudinal and transverse ISC impedances are defined by Eq. (1) for  $\omega \geq 0$ . For  $\omega < 0$ , the impedances are obtained from the following symmetry relations (which ensure that the wake functions remain real quantities)

$$Z_{\parallel}(\omega) = Z_{\parallel}(-\omega)^*, \quad Z_{\perp}^{dip}(\omega) = -Z_{\perp}^{dip}(-\omega)^*, \quad (7)$$

where  $Z^*$  indicates the complex conjugate of  $Z$ .

These relations do not give the same results as Eq. (1), had the latter be applied to a negative  $\omega$ , because these expressions do not obey to the same symmetry relations. In particular, in the left half-plane the modified Bessel functions  $K_m$  ( $m = 0$  or  $1$ ) are obtained from their values on the right half-plane by analytic continuation [19], and a branch cut appears, which has to remain out of the integration contour—we choose it along the negative imaginary semi-axis when  $z > 0$  and the positive one for  $z < 0$ . From these considerations we can write, for  $\Re(x) < 0$ :

$$\begin{aligned} K_0(x) &= K_0(-x) - \text{sgn}(z) i\pi I_0(-x), & I_0(x) &= I_0(-x), \\ K_1(x) &= -K_1(-x) - \text{sgn}(z) i\pi I_1(-x), & I_1(x) &= -I_1(-x), \end{aligned} \quad (8)$$

where  $\text{sgn}(z)$  denotes the sign of  $z$ . Therefore, for  $\omega < 0$  the longitudinal and transverse ISC can be expressed respectively as

$$Z_{\parallel}(\omega) = iA\omega \frac{K_0\left(\frac{kb}{\gamma}\right)}{I_0\left(\frac{kb}{\gamma}\right)} - \text{sgn}(z)\pi A\omega, \quad (9)$$

$$Z_{\perp}^{dip}(\omega) = iB\omega^2 \frac{K_1\left(\frac{kb}{\gamma}\right)}{I_1\left(\frac{kb}{\gamma}\right)} + \text{sgn}(z)\pi B\omega^2, \quad (10)$$

with  $A \equiv \frac{\mu_0 L}{2\pi\beta^2\gamma^2}$  and  $B \equiv \frac{Z_0 L}{4\pi\beta^3 c^2 \gamma^4}$ . Hence, for the longitudinal wake function we get, with the additional term of Eq. (9):

$$\begin{aligned} W_{\parallel}(z) &= \frac{iA}{2\pi} \int_{-\infty}^{\infty} d\omega e^{i\omega \frac{z}{v}} \frac{K_0\left(\frac{kb}{\gamma}\right)}{I_0\left(\frac{kb}{\gamma}\right)} \\ &\quad - \frac{\text{sgn}(z)A}{2} \int_{-\infty}^0 d\omega e^{i\omega \frac{z}{v}} \omega. \end{aligned}$$

The function  $f$  defined by  $f(\omega) = \omega \frac{K_0\left(\frac{kb}{\gamma}\right)}{I_0\left(\frac{kb}{\gamma}\right)}$  fulfils Jordan's condition from Eq. (5) in the upper-right quadrant (from the asymptotic expansion of the Bessel functions [19]), but not in the upper-left quadrant. Using again Eq. (8), the corresponding first term of  $f$  does fulfil Jordan's condition but not the term proportional to  $\omega$ , leading to an integral over a quarter circle along  $C_2$  which remains non-zero. The latter can be combined with the semi-infinite integral above:

$$\begin{aligned} \lim_{R \rightarrow \infty} \left( \int_{\text{sgn}(z)iR}^{-R} d\omega e^{i\omega \frac{z}{v}} \omega \right) + \int_{-\infty}^0 d\omega e^{i\omega \frac{z}{v}} \omega \\ = \int_{\text{sgn}(z)i\infty}^0 d\omega e^{i\omega \frac{z}{v}} \omega = \frac{v^2}{z^2}, \end{aligned}$$

applying the residue theorem to the function  $\omega \rightarrow \omega e^{i\omega \frac{z}{v}}$  which exhibits no pole. Using then Eq. (6) we finally obtain

$$W_{\parallel}(z) = -A \text{sgn}(z) \sum_k e^{i\omega_k \frac{z}{v}} \text{Res}[f, \omega_k] - \frac{\text{sgn}(z) A v^2}{2z^2}. \quad (11)$$

The function  $f$  is meromorphic except for the branch cut of  $K_0$ , which touches the contour of integration only at  $\omega = 0$ , but can be bypassed by modifying slightly the contour around the origin thanks to a half-circle of vanishing radius. The corresponding contribution to the integral vanishes as well, as  $\omega = 0$  is not a singularity of  $f$ , which can be readily seen by noticing that [19]  $f(\omega) \sim -\omega \ln(\omega) \rightarrow \omega \rightarrow 0$ .

The poles of  $f$  are given by the zeros of  $I_0$ , which are all simple [19] and correspond to the real zeros  $j_{0,k} > 0$  of  $J_0$  (Bessel function of the first kind) through

$$\begin{aligned} \omega_k = \frac{ij_{0,k}\gamma v}{b} \quad \text{for } z > 0 \text{ (poles in upper half-plane),} \\ \omega_k = \frac{-ij_{0,k}\gamma v}{b} \quad \text{for } z < 0 \text{ (poles in lower half-plane),} \end{aligned} \quad (12)$$

from  $I_0(x) = J_0(ix)$ . Since the poles are simple, the residue at  $\omega_k$  can be obtained from L'Hôpital's rule:

$$\begin{aligned} \text{Res}[f, \omega_k] &= \frac{\text{sgn}(z) i j_{0,k} \gamma v}{b} \frac{K_0(\text{sgn}(z) i j_{0,k})}{\frac{b}{\gamma v} I_0'(\text{sgn}(z) i j_{0,k})} \\ &= \frac{j_{0,k} \gamma^2 v^2}{b^2} \frac{K_0(\text{sgn}(z) i j_{0,k})}{J_1(j_{0,k})}, \end{aligned} \quad (13)$$

where we have used that  $I_0'(\pm ix) = I_1(\pm ix) = \pm i J_1(x)$  [19]. Combining Eqs. (11), (12) and (13) we get the total longitudinal wake:

$$\begin{aligned} W_{\parallel}(z) &= -\frac{\text{sgn}(z)L}{4\pi\epsilon_0\gamma^2} \frac{1}{z^2} \\ &\quad - \frac{\text{sgn}(z)L}{2\pi\epsilon_0 b^2} \sum_{k=1}^{\infty} e^{-\frac{j_{0,k}\gamma|z|}{b}} \frac{j_{0,k} K_0(\text{sgn}(z) i j_{0,k})}{J_1(j_{0,k})}. \end{aligned} \quad (14)$$

with  $\epsilon_0 \equiv \frac{1}{\mu_0 c^2}$  the vacuum permittivity.

In transverse, a very similar reasoning (in particular regarding the additional integral from the partly unfulfilled Jordan's condition) gives

$$W_{\perp}^{dip}(z) = iB \sum_k e^{i\omega_k \frac{z}{v}} \text{Res}[g, \omega_k] + \frac{\text{sgn}(z) B v^3}{z^3}, \quad (15)$$

with  $g$  the function defined by  $g(\omega) = \omega^2 \frac{K_1\left(\frac{kb}{\gamma}\right)}{I_1\left(\frac{kb}{\gamma}\right)}$ . As  $f$  defined above,  $g$  does not have a singularity in 0 but a well-defined limit  $\frac{2v^2\gamma^2}{b^2}$ , and exhibits a set of simple poles obtained from the zeros  $j_{1,k} > 0$  of  $J_1$  (using the relation  $I_1(x) = -iJ_1(ix)$ ):

$$\omega_k = \frac{i \text{sgn}(z) j_{1,k} \gamma v}{b}. \quad (16)$$

The residue sum is then obtained again from L'Hôpital's rule, and the total transverse wake reads

$$\begin{aligned} W_{\perp}^{dip}(z) &= \frac{\text{sgn}(z)L}{4\pi\epsilon_0\gamma^4} \frac{1}{z^3} \\ &\quad - \frac{i \text{sgn}(z)L}{2\pi\epsilon_0\gamma b^3} \sum_{k=1}^{\infty} e^{-\frac{j_{1,k}\gamma|z|}{b}} \frac{j_{1,k}^2 K_1(\text{sgn}(z) i j_{1,k})}{J_0(j_{1,k}) - J_2(j_{1,k})}, \end{aligned} \quad (17)$$

where we used  $2I_1'(\pm ix) = J_0(x) - J_2(x)$ .

## NUMERICAL BENCHMARK

To compute wake functions when analytical formulas cannot be found, one typically resorts to a numerical integration, using discrete, fast Fourier transforms. In the case of smooth, slowly decaying beam coupling impedances, this can lead to the need of a large number of points, difficult or even impossible to handle [15], related to the number of decades to be meshed with evenly-spaced frequencies.

Another approach is preferred here: we use an uneven frequency sampling, combined with an exact integration of a linear interpolation of the impedance, over each sub-interval. The latter aspect was inspired by a method first found by Filon in 1928 [20], and extended later in various works [21–25]. The full method we use here is extensively described in Ref. [15].

We consider a Fourier integral of the form

$$I(\tau) = \int_{\omega_{min}}^{\infty} d\omega e^{i\omega\tau} f(\omega). \quad (18)$$

Wake functions given by Eqs. (2) or (3) can be easily cast into this semi-infinite form (with  $\omega_{min} = 0$ ), using the symmetry properties of the impedances given in Eq. (7).

We first set  $\omega_{max}$  high enough for the  $f$  function to be small and decaying for  $\omega > \omega_{max}$ , and we cut the interval  $[\omega_{min}, \omega_{max}]$  into several sub-intervals, not necessarily equidistant, delimited by the angular frequencies  $\omega_j$  with  $j$  from 0 to  $N$  ( $\omega_0 = \omega_{min}$  and  $\omega_N = \omega_{max}$ ). Then

$$f(\omega) \approx p_j(\omega) \quad \text{for } \omega_j \leq \omega \leq \omega_{j+1}, \quad (19)$$

where  $p_j$  is the interpolating (linear) polynomial on the interval  $[\omega_j, \omega_{j+1}]$ . The integral  $I(\tau)$  is then obtained from

$$I(\tau) = \sum_{j=0}^{N-1} \int_{\omega_j}^{\omega_{j+1}} d\omega e^{i\omega\tau} f(\omega) + \int_{\omega_{max}}^{\infty} d\omega e^{i\omega\tau} f(\omega). \quad (20)$$

The second integral is approximated by assuming that  $f(\omega) \approx f(\omega_{max})$  for  $\omega > \omega_{max}$ , while the first one is computed using Filon's method on each sub-interval:

$$\begin{aligned} I(\tau) &\approx \sum_{j=0}^{N-1} \int_{\omega_j}^{\omega_{j+1}} d\omega e^{i\omega\tau} p_j(\omega) + e^{i\omega_{max}\tau} \frac{if(\omega_{max})}{\tau} \\ &\approx \sum_{j=0}^{N-1} \Delta_j \left[ f(\omega_j) e^{i\omega_{j+1}\tau} \Lambda(-\Delta_j\tau) \right. \\ &\quad \left. + f(\omega_{j+1}) e^{i\omega_j\tau} \Lambda(\Delta_j\tau) \right] + e^{i\omega_{max}\tau} \frac{if(\omega_{max})}{\tau}, \end{aligned} \quad (21)$$

with  $\Delta_j \equiv \omega_{j+1} - \omega_j$  and  $\Lambda$  defined by

$$\Lambda(x) = -\frac{ie^{ix}}{x} + \frac{e^{ix} - 1}{x^2}. \quad (22)$$

Note that the Taylor expansion of  $\Lambda$  is often useful to compute values for small arguments:

$$\Lambda(x) = \sum_{n=0}^{\infty} \frac{1}{n+2} \frac{(ix)^n}{n!}. \quad (23)$$

Extensions of the method with cubic interpolation, or using a higher order Taylor expansion of  $f$  for  $\omega > \omega_{max}$ , are described in Ref. [15]. An automatic refinement procedure to achieve convergence vs. frequency sampling, was also implemented and used for various kinds of impedances.

The numerical approach just outlined is compared to the exact formulas derived above in Figs. 2 and 3, which reveals the excellent agreement between the two methods.

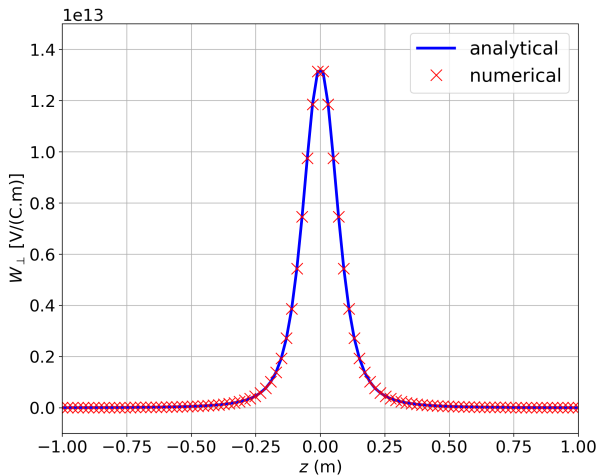


Figure 2: Comparison between the exact transverse ISC wake function from Eq. (17) (solid blue line) and the numerical approach (red crosses) ( $L = 1$  m,  $b = 0.08$  m,  $\gamma = 1.05$ ).

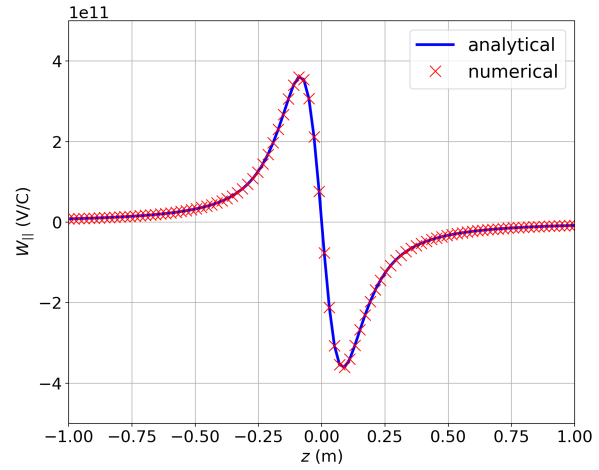


Figure 3: Comparison between the exact longitudinal ISC wake function from Eq. (14) (solid blue line) and the numerical approach (red crosses) ( $L = 1$  m,  $b = 0.08$  m,  $\gamma = 1.05$ ).

## SIMPLIFIED EXPRESSION FOR THE TRANSVERSE WAKE

In this section an approximated formula for the transverse ISC is presented. We will then recover the exact result with a simple correction scheme.

### Approximate Formula

To approximate the transverse ISC impedance given in Eq. (1), one could use the approximation for small arguments of both modified Bessel function, namely  $K_1(x) \approx 1/x$  and  $I_1(x) \approx x/2$  [19]. This would lead to an expression without dependency on frequency, which would be useless to compute the ISC wake function. A useful expression can rather be obtained using solely the approximation for a small argument of the modified Bessel function  $I_1$ . In this case the transverse impedance can be rewritten as follows:

$$Z_{\perp}^{dip}(\omega) \approx \frac{ikZ_0L K_1\left(\frac{kb}{\gamma}\right)}{2\pi b\beta\gamma^3}. \quad (24)$$

The Fourier transform of Eq. (24) can be performed analytically, which gives a useful approximation of the transverse ISC wake function:

$$W_{\perp}^{dip}(z) \approx \frac{Z_0L}{4\pi\beta\gamma^4 \left(z^2 + \frac{b^2}{\gamma^2}\right)^{3/2}}. \quad (25)$$

In Fig. 4, a comparison is performed between the approximated wake function and the exact analytical formula from the previous section, showing that the approximated formula describes, with a reasonable degree of accuracy, the dependency of the transverse wake function with the relativistic factor.

Note that an improved formula can be obtained by combining the approximation for a small argument of the modified Bessel function  $I_1$  with the approximation  $I_1(x) \approx \frac{1}{2K_1(x)}$  [26].

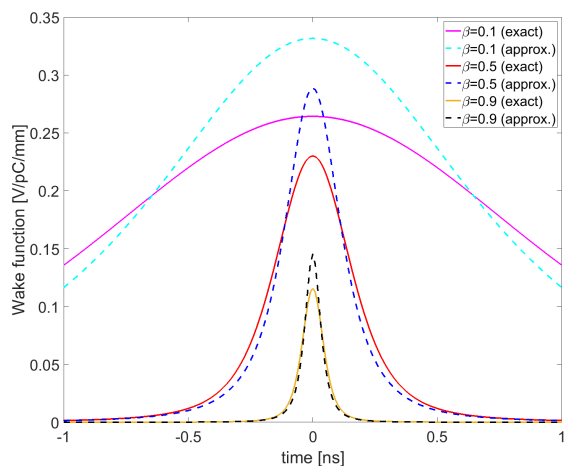


Figure 4: Comparison between the approximated wake function formula from Eq. (25) (dashed lines) and the exact one from Eq. (17) (full lines), for a chamber with radius  $b = 0.03$  m and length  $L = 1$  m, for various values of the relativistic factor  $\beta$ .

### Correcting Factor

The ratio between the exact and the approximated formulas (which we will call hereafter the "discrepancy function") turns out to depend only on  $\tau a$  with  $a = b/(v\gamma)$  and  $\tau = z/v$ . A graphical representation of this function for two different values of  $a$  is displayed in Fig. 5.

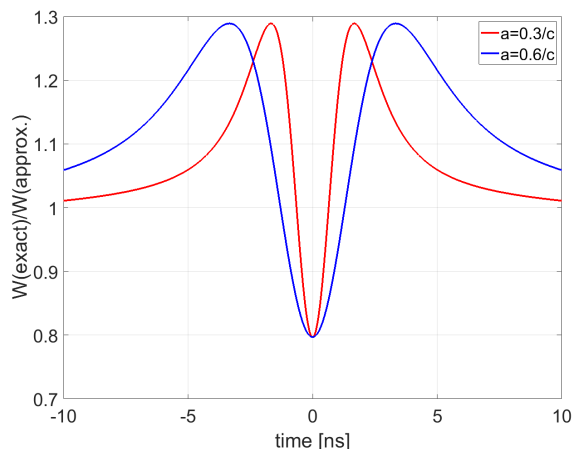


Figure 5: Discrepancy function between the exact and approximated formulas (Eqs. (17) and (25) respectively), for two different values of  $a = b/(v\gamma)$ .

Using this peculiarity we can obtain an exact formula for the ISC wake function, which will require the computation of a single reference discrepancy function. The generalized, corrected formula using the discrepancy function can be written as follows:

$$W_{\perp}^{dip}(\tau) = F(\tau_n) \frac{Z_0 L}{2\pi c^2 \beta^3 \gamma^4 (\tau^2 + a^2)^{3/2}}, \quad (26)$$

where  $F(\tau_n)$  is the discrepancy function with  $\tau_n = \tau a_{ref}/a$  and  $a_{ref} = b_{ref}/(c\beta_{ref}\gamma_{ref})$ . Therefore, computing once for all  $F(\tau_n)$ , it is possible to scale appropriately  $W_{\perp}^{dip}$  for any value of  $a$ . The equation has been successfully benchmarked with the exact approach for various values of the relativistic factor  $\beta$  (see Fig. 6).

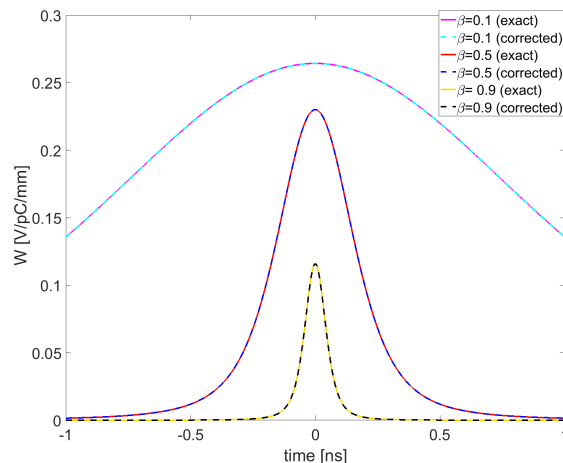


Figure 6: Comparison between the corrected wake function formula from Eq. (26) (dashed lines) and the exact one from Eq. (17) (full lines) for various values of the relativistic factor  $\beta$ .

## CONCLUSION

General formulas for the indirect longitudinal and transverse space charge wake functions have been obtained from an exact analytical approach. Moreover, a simpler expression reproducing the time and velocity dependence has been found for the transverse wake, and can even be corrected to recover an exact formula, thanks to a numerical function that can be calculated once for all. The expressions obtained have been successfully benchmarked with a purely numerical approach based on an uneven frequency sampling and a Filon-like method to compute the Fourier integral.

## ACKNOWLEDGEMENTS

The authors would like to thank Xavier Buffat, Stéphane Fartoukh, Tatiana Pieloni, Giovanni Rumolo and Maximilian Shaughnessy.

## REFERENCES

- [1] L. J. Laslett, V. K. Neil, and A. M. Sessler, "Transverse Resistive Instabilities of Intense Coasting Beams in Particle Accelerators," *Rev. Sci. Instrum.*, vol. 36, pp. 436–448, 4 1965, doi:10.1063/1.1719595
- [2] A. M. Sessler and V. G. Vaccaro, "Longitudinal instabilities of azimuthally uniform beams in circular vacuum chambers with walls of arbitrary electrical properties," 1967, CERN ISR-RF/67-2, <https://cds.cern.ch/record/275815/files/CERN-67-02.pdf>

- [3] B. Zotter, “Transverse Oscillations of a Relativistic Particle Beam in a Laminated Vacuum Chamber,” 1969, CERN ISR/69-15.
- [4] F.J. Sacherer, “Transverse bunched beam instabilities - theory,” in *9th International Conference on High Energy Accelerators (HEACC’74), Stanford, California, USA, 1974*, pp. 347–351, <http://cds.cern.ch/record/322645>
- [5] A. W. Chao, *Physics of Collective Beams Instabilities in High Energy Accelerators*. John Wiley and Sons, 1993.
- [6] E. Keil and B. Zotter, “The impedance of layered vacuum chambers,” in *6th European Particle Accelerator Conference (EPAC’98), Stockholm, Sweden, 1998*, pp. 963–965, <https://jacow.org/e98/PAPERS/THP06B.PDF>
- [7] B. Zotter and S. Kheifeits, *Impedances and Wakes in High-Energy Particle Accelerators*. World Scientific, 1998, doi: 10.1142/3068
- [8] R. L. Gluckstern, “Analytic methods for calculating coupling impedances,” 2000, Report No. CERN-2000-011, doi:10.5170/CERN-2000-011
- [9] A. Burov and V. Lebedev, “Transverse Resistive Wall Impedance for Multi-layer Round Chambers,” in *Proc. 8th European Particle Accelerator Conf. (EPAC’02), Paris, France, 2002*, paper WEPRI021, pp. 1452–1454.
- [10] B. Zotter, “New Results on the Impedance of Resistive Metal Walls of Finite Thickness,” 2005, Report No. CERN-AB-2005-043, <http://cds.cern.ch/record/877819>
- [11] N. Wang and Q. Qin, “Resistive-wall impedance of two-layer tube,” *Phys. Rev. ST Accel. Beams*, vol. 10, no. 111003, 2007, doi:10.1103/PhysRevSTAB.10.111003
- [12] M. Ivanyan, E. Laziev, V. Tsakanov, A. Vardanyan, S. Heifets, and A. Tsakanian, “Multilayer tube impedance and external radiation,” *Phys. Rev. ST Accel. Beams*, vol. 11, no. 084001, 2008, doi:10.1103/PhysRevSTAB.11.084001
- [13] H. Hahn, “Matrix Solution of Coupling Impedance in Multi-Layer Circular Cylindrical Structures,” in *Proc. 23rd Particle Accelerator Conf. (PAC’09), Vancouver, Canada, 2009*, paper TH5PFP082, pp. 3395–3397.
- [14] F. Roncarolo *et al.*, “Comparison between Laboratory Measurements, Simulations and Analytical Predictions of the Transverse Wall Impedance at Low Frequencies,” *Phys. Rev. ST Accel. Beams*, vol. 12, no. 084401, 2009, doi:10.1103/PhysRevSTAB.12.084401
- [15] N. Mounet, “The LHC transverse coupled-bunch instability,” PhD thesis 5305, EPFL, 2012.
- [16] K. L. F. Bane, P. B. Wilson, and T. Weiland, “Wake fields and wake field acceleration,” 1984, Report No. SLAC-PUB-3528, [https://inis.iaea.org/collection/NCLCollectionStore/\\_Public/16/066/16066475.pdf](https://inis.iaea.org/collection/NCLCollectionStore/_Public/16/066/16066475.pdf)
- [17] F. Zimmermann and K. Oide, “Resistive-Wall Wake and Impedance for Nonultrarelativistic Beams,” *Phys. Rev. ST Accel. Beams*, vol. 7, p. 044201, 4 2004, doi:10.1103/PhysRevSTAB.7.044201
- [18] A. Koschik, “Simulation of Transverse Multi-Bunch Instabilities of Proton Beams in LHC,” PhD thesis, Ph.D. dissertation, Tech. Univ. Graz, 2004.
- [19] M. Abramowitz and I. A. Stegun, Eds., *Handbook of Mathematical Functions With Formulas, Graphs, and Mathematical Tables*. US Dep. of Commerce, National Bureau of Standards, 1972, Tenth Printing, with corrections, [https://www.iopb.res.in/~somen/abramowitz\\_and\\_stegun/toc.htm](https://www.iopb.res.in/~somen/abramowitz_and_stegun/toc.htm)
- [20] L. N. G. Filon, “On a Quadrature Formula for Trigonometric Integrals,” *Proc. Roy. Soc. Edinburgh*, vol. 49, pp. 38–47, 1928, doi:10.1017/S0370164600026262
- [21] E. O. Tuck, “A Simple “Filon-Trapezoidal” Rule,” *Math. Comp.*, vol. 21, pp. 239–241, 1967, doi:10.1090/S0025-5718-67-99892-4
- [22] G. Pantis, “The Evaluation of Integrals with Oscillatory Integrands,” *J. Comp. Phys.*, vol. 17, pp. 229–233, 1975, doi:10.1016/0021-9991(75)90038-8
- [23] W. H. Press, S. A. Teukolsky, W. T. Vetterling, and B. P. Flannery, *Numerical recipes in C*, 2nd. Cambridge University Press, 1999.
- [24] A. Iserles and S. Norsett, “Efficient quadrature of highly oscillatory integrals using derivatives,” *Proc. Roy. Soc. A*, vol. 461, pp. 1383–1399, 2005, doi:10.1098/rspa.2004.1401
- [25] D. Huybrechs and S. Vandewalle, “On the Evaluation of Highly Oscillatory Integrals by Analytic Continuation,” *SIAM J. Numer. Anal.*, vol. 44, pp. 1026–1048, 2005, Report No. TW431, Dep. Comp. Science, K.U.Leuven, doi:10.1137/050636814
- [26] C. Zannini, “Approximated formula for the indirect space charge wake function,” 2019, <https://indico.cern.ch/event/844487/>

# CONTROLLED LONGITUDINAL EMITTANCE BLOW-UP FOR HIGH INTENSITY BEAMS IN THE CERN SPS

D. Quartullo\*, H. Damerou, I. Karpov, G. Papotti,  
E. Shaposhnikova, C. Zisou, CERN, Meyrin, Switzerland

## Abstract

Controlled longitudinal emittance blow-up will be required to longitudinally stabilise the beams for the High-Luminosity LHC in the SPS. Bandwidth-limited noise is injected at synchrotron frequency sidebands of the RF voltage of the main accelerating system through the beam phase loop. The setup of the blow-up parameters is complicated by bunch-by-bunch differences in their phase, shape, and intensity, as well as by the interplay with the fourth harmonic Landau RF system and transient beam loading in the main RF system. During previous runs, an optimisation of the blow-up had to be repeated manually at every intensity step up, requiring hours of precious machine time. With the higher beam intensity, the difficulties will be exacerbated, with bunch-by-bunch differences becoming even more important. We look at the extent of the impact of intensity effects on the controlled longitudinal blow-up by means of macro-particle tracking, as well as analytical calculations, and we derive criteria for quantifying its effectiveness. These studies are relevant to identify the parameters and observables which become key to the operational setup and exploitation of the blow-up.

## INTRODUCTION

The “High Luminosity LHC” (HL-LHC) proton beams in the SPS will require stabilization in the longitudinal plane [1–3]. A fourth harmonic 800 MHz RF system in combination with the 200 MHz accelerating one will increase the synchrotron frequency spread inside the bunch enhancing Landau damping [4], whereas controlled blow-up will increase the bunch longitudinal emittance in a controlled way [5]. Both methods will be required to cope with coupled-bunch instabilities along the ramp and at flat-top.

Controlled emittance blow-up is achieved in the SPS by injecting bandwidth-limited phase noise into the phase-loop of the main RF system [6], as done also in the CERN PSB and LHC [7–10]. Phase noise should diffuse just the particles situated in the bunch core, since affecting the tails could lead to particle losses. Emittance blow-up should occur along the SPS ramp, so that particles driven out of the buckets are lost in the SPS, and are not transferred to the LHC.

The noise-generation algorithm produces digital, band-limited phase noise samples. Since the frequency band should cover the synchrotron frequencies of the particles situated in the bunch core, it must follow the changes of synchrotron frequencies during the ramp. The noise generation algorithm receives the required frequency band as input and produces phase noise with the desired spectral properties.

\* danilo.quartullo@cern.ch

One main remaining issue is the determination of the optimal frequency band. A dedicated algorithm has been developed for this purpose. The frequency band is obtained by designing the emittance increase during blow-up and by making use of accurately computed synchrotron-frequency distributions, which include collective effects.

Longitudinal beam dynamics simulations of the SPS cycle are important to validate the effectiveness of the computed frequency bands. One batch of 72 bunches was tracked including the full SPS impedance model, beam loops and emittance blow-up. Simulations were then compared with beam measurements during the SPS cycle. The computed frequency bands provided useful input to set the phase-noise parameters with beam.

In this paper we describe the implementation of emittance blow-up in operation. Then, the procedure for the determination of the phase-noise frequency band is explained in detail. Results from beam dynamics simulations are reported and compared with first beam measurements.

## IMPLEMENTATION OF THE PHASE-NOISE ALGORITHM

The HL-LHC beam requirements drove the LHC Injector Upgrade Project [11], which, at the SPS, foresaw a complete renovation of the RF system, including a rearrangement of the 200 MHz accelerating structures, and a redesign of the Low Level controls (LLRF, [12]), based on the MicroTCA platform, and featuring a restructuring of the beam control loops. The controlled emittance blow-up was operational for LHC-type beams in previous runs (2010-2018) [6], and had to be re-implemented in the new LLRF system. The addition of the noise in the phase loop is now done in the new, digital LLRF, but the previous algorithm for the preparation of the noise pattern and the high level controls are maintained.

The noise algorithm [13] creates an excitation spectrum that follows the varying frequency spectrum during the energy ramp, and that is band-limited, with very low leakage. The noise frequency bands are calculated in the SPS high level controls (LHC Software Architecture, LSA), and sent to the C++ code that prepares the noise pattern. The central synchrotron frequency  $f_{s0}$  in double-RF system without intensity effects is automatically calculated in LSA. The low and high band-limits are obtained by multiplying the calculated  $f_{s0}$  by two knobs, so to scale them easily.

## DETERMINATION OF THE PHASE-NOISE FREQUENCY BAND

A first algorithm for the determination of the frequency band has been developed. It does not require particle track-

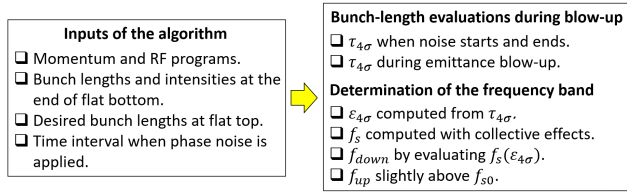


Figure 1: Scheme of the algorithm for the determination of the phase-noise frequency band.

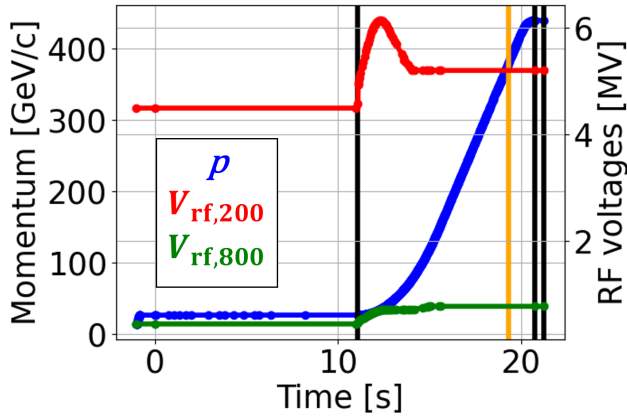


Figure 2: Momentum program (blue), main (red) and fourth (green) harmonic RF programs for the SPS HiRadMat cycle during scrubbing in August 2021. The black lines mark the start of the ramp (11.10 s), the end of the ramp (20.77 s) and the extraction time (21.27 s). The orange line corresponds to the momentum of 380 GeV/c.

ing, but it exploits the generation of distributions matched to the RF bucket with intensity effects to evaluate the bunch lengths and emittances during the blow-up. A scheme of the algorithm structure is shown in Fig. 1.

### Inputs of the Algorithm

The algorithm takes as inputs the momentum and RF programs, the bunch lengths and intensities at the end of the flat-bottom, the desired bunch lengths at flat-top after emittance blow-up, as well as the cycle times when phase noise should start and end.

Figure 2 shows the momentum program of the SPS HiRadMat cycle, together with the programs of the main and fourth harmonic RF systems during scrubbing (with limited RF voltage) in August 2021. The HiRadMat cycle accelerates up to 4 batches of 72 bunches from flat bottom (26 GeV/c) to flat-top (440 GeV/c). Bunch rotation is applied in the CERN PS at flat-top in order to reduce the length of the bunches and make them fit into the SPS RF buckets.

The program of the main RF system in Fig. 2 provides 4.5 MV and 5.2 MV at flat bottom and top, respectively. The voltage bump allows a constant bucket area in that time interval. The fourth harmonic RF system increases the synchrotron frequency spread inside the bunch, enhancing Landau damping. In Fig. 2, the voltage ratio between the two RF systems is 10% at flat bottom, it increases linearly during

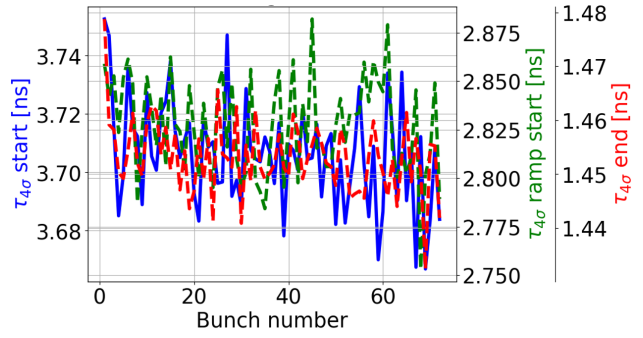


Figure 3: Simulated bunch lengths along the batch at SPS injection (blue), after 0.5 s of flat bottom (green) and at extraction (red). The BLoND simulations used the programs shown in Fig. 2 and started from realistic rotated PS bunch distributions. Emittance blow-up was not applied.

the first part of acceleration and remains at 15% until extraction. The phase between the RF systems is programmed for bunch-shortening mode (BSM) [4].

The bunch intensities and lengths at the end of the flat-bottom were obtained by performing macro-particle simulations. One batch of 72 bunches was simulated for 0.5 s at flat bottom, using the CERN BLoND code [14]. Simulations included the full SPS impedance model and started from realistic bunch distributions, with an intensity of  $1.2 \cdot 10^{11}$  ppb and which were obtained by performing simulations of bunch rotation at PS flat-top with collective effects.

The effect of the One Turn Delay Feedback (OTFB) for beam loading compensation was added in simulations by reducing the shunt impedances of the RF fundamental modes by -26 dB. An accurate model of the beam-based phase, synchro and frequency loops was used in simulations.

The obtained bunch lengths at injection (blue) and after 0.5 s of flat bottom (green) are reported in Fig. 3, where  $\tau_4 = \sqrt{2} \tau_{FWHM} / \sqrt{\ln 2}$  is the convention used in the SPS to compute bunch lengths,  $\tau_{FWHM}$  being the Full Width at Half Maximum of the bunch profile. The bunch lengths at injection in Fig. 3 are within  $3.71 \pm 0.04$  ns, whereas those at the ramp start are  $\tau_{4,rs} = 2.83 \pm 0.08$  ns.

The desired bunch length  $\tau_{4,d}$  at extraction after having applied emittance blow-up should satisfy the cycle-dependent beam requirements and should be large enough to ensure beam stability. Typical values of desired  $\tau_{4,d}$  are between 1.6 ns and 2.0 ns. Without emittance blow-up and for low intensities, the bunch lengths  $\tau_{4,ex}$  at extraction vary usually between 1.45 ns and 1.65 ns (see e.g. Fig. 3, red). Above  $1.6 \cdot 10^{11}$  ppb, a single LHC batch without blow-up is expected to become unstable during the SPS ramp.

The last input parameter for the algorithm is the time interval when phase noise is applied. Concerning the HiRadMat cycle, the starting time of phase noise was set to  $t_s = 15$  s, when the bucket area starts to increase, which reduces particle losses when phase noise is applied.

In general, long time intervals with phase noise are desirable, since they allow more possibilities in the design

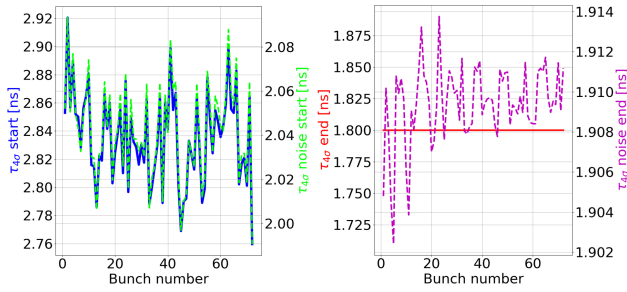


Figure 4: Bunch lengths along the batch at cycle times  $t_s$  (green) and  $t_e$  (magenta), obtained from the algorithm for frequency band determination using the momentum and voltage programs shown in Fig. 2. The bunch lengths at the end of the flat-bottom (blue) and the desired bunch lengths at extraction (red) are input parameters to the algorithm.

of the blow-up manipulation and allow also a slower, and therefore more controlled, bunch-length increase. However, emittance blow-up at the flat-top could lead to transfer to the LHC of particles pushed outside of the SPS buckets by the phase noise. In addition, a transverse scraping starting at 380 GeV/c is foreseen for the HL-LHC beams and, to limit losses, phase noise should stop before this scraping begins. Since a momentum of 380 GeV/c corresponds to the cycle time of 19.3 s (Fig. 2, orange line), the end of phase noise was set to  $t_e = 19$  s, leaving 300 ms of margin.

### Bunch-length Evaluations During the Blow-up

The first step performed by the algorithm is to estimate the bunch lengths at  $t_s$  and  $t_e$ . Since the different  $\tau_{4,rs}$  at ramp start are known, we can generate a matched distribution for each bunch and compute the corresponding full emittance  $\epsilon_f$ . Assuming that  $\epsilon_f$  is preserved until phase noise starts, the  $\epsilon_f$  values are used to generate matched distributions and to compute the bunch lengths at  $t_s$ . This procedure of double matching is also applied to find the bunch lengths at  $t_e$ . Then, for each bunch, the computed  $\tau_{4,s}$  and  $\tau_{4,e}$  are linearly interpolated to obtain the design  $\tau_4$  during the blow-up.

Figure 4 shows an example of bunch lengths at  $t_s$  and  $t_e$  computed with the algorithm, assuming  $\tau_{4,d} = 1.8$  ns. The variations of  $\tau_4$  along the batch are similar at times  $t_{rs}$  and  $t_s$ . The values are  $\tau_{4,rs} = 2.84 \pm 0.08$  ns,  $\tau_{4,s} = 2.04 \pm 0.05$  ns and  $\tau_{4,e} = 1.91 \pm 0.01$  ns.

The generated bunch distributions are binomial. Since it is not easy to foresee the profile shapes at  $t_s$  and  $t_e$ , it is important that the bunch lengths at these times do not significantly depend on the exponent  $\mu$  of the binomial distribution. This occurs for a relatively large range of  $\mu$  values, as shown in the example in Fig. 5, where the FWHM bunch lengths at  $t_e$  differ by just 1% when  $\mu$  varies between 0.5 and 2.5.

### Determination of the Frequency Bands

At a given time between  $t_s$  and  $t_e$ , and for each bunch, a matched distribution with the interpolated  $\tau_4$  is generated. The emittance  $\epsilon_4$  corresponding to  $\tau_4$  is then computed.

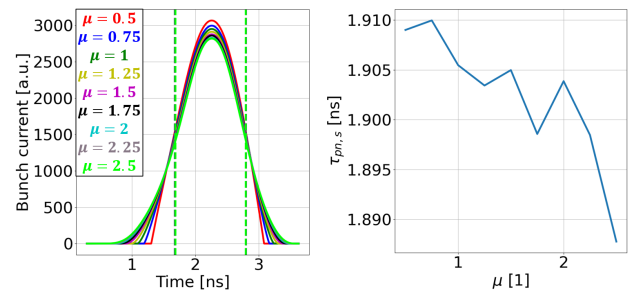


Figure 5: Left: bunch profiles obtained from binomial distributions matched in phase space at time  $t_e$  with different  $\mu$ . The profiles refer to the first bunch of the batch, assuming  $\tau_{4,d} = 1.8$  ns. The dashed lines determine  $\tau_{FWHM}$ . Right:  $\tau_{FWHM}$  corresponding to the profiles on the left.

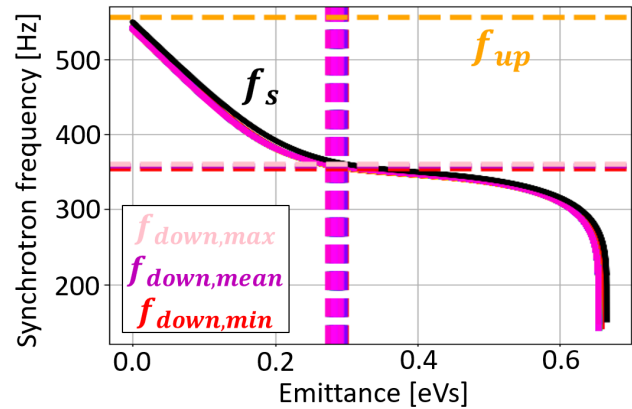


Figure 6: Synchrotron frequency distributions at  $t_s$  without (black) and with (other colours) collective effects for 72 bunches with intensity  $1.2 \cdot 10^{11}$  ppb. The peak voltages of the main and fourth harmonic RF systems are 5.2 MV and 0.78 MV respectively, the phase is programmed for BSM. The vertical lines mark the  $\epsilon_4$  emittances of the 72 bunches (Fig. 7, left). The horizontal lines indicate the maximum, mean, minimum of the  $f_{down}$  values (Fig. 7, right), and the frequency-band upper limit, which is set slightly above  $f_{s0}$ .

Thereafter, for each bunch, the synchrotron frequency distribution including collective effects is evaluated (Fig. 6), this allows to determine  $f_{down}$  (Fig. 7, right) as the frequency corresponding to  $\epsilon_4$  (Fig. 7, left). In general, larger emittances correspond to lower  $f_{down}$  values, although the increase of  $f_{down}$  along the first 20 bunches in Fig. 7 (right) is mostly due to collective effects which change the shapes of the synchrotron frequency distributions.

Since only one value of  $f_{down}$  can be chosen for all the bunches at a given time, the maximum, mean and minimum of the  $f_{down}$  values were considered, as shown in Figs. 6 and 7 (right). The minimum  $f_{down}$  targets at least  $\epsilon_4$  for each bunch. If the target emittance is larger than  $\epsilon_4$ , then bunches could be affected also in the tails, especially when  $\epsilon_4$  is close to the inflection point of the synchrotron frequency distribution (see e.g. Fig. 6). Selecting the maximum  $f_{down}$  allows targeting at most  $\epsilon_4$  for each bunch, with some bunches not

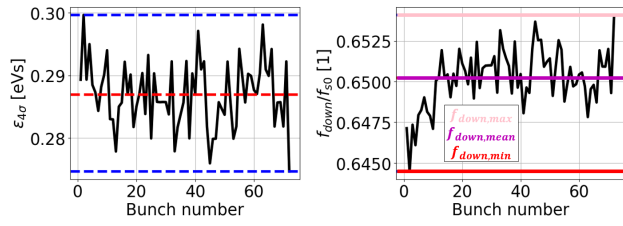


Figure 7: Emittance  $\epsilon_4$  (left) and normalized  $f_{\text{down}}$  (right) along the batch at time  $t_s$ . The emittances are obtained from the bunch lengths at  $t_s$  (Fig. 4, left, green line).

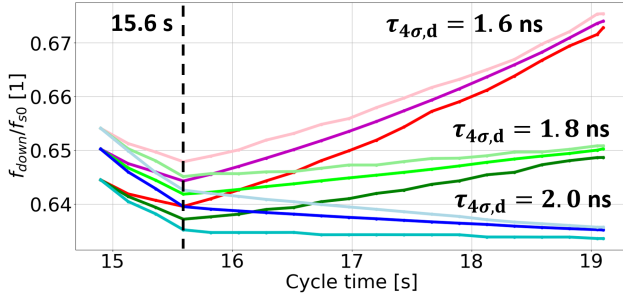


Figure 8: Minimum, mean and maximum normalized  $f_{\text{down}}$  along the blow-up time interval when  $\tau_{4,d} = 1.6$  ns (red colours), 1.8 ns (green) and 2.0 ns (blue). The considered cycle is shown in Fig. 2.

diffused by phase noise as desired. As a compromise, the mean of the  $f_{\text{down}}$  values has been chosen.

The bunch distributions generated during the blow-up are binomial and, similarly to what is described above, changing  $\mu$  did not significantly affect the determination of  $f_{\text{down}}$ .

The upper limit  $f_{\text{up}}$  of the frequency band was set slightly above  $f_{s0}$  (Fig. 6, orange). Indeed, for the present SPS impedance model, the synchrotron frequency distributions of the bunches are always lower than the distribution without collective effects, as shown for instance in Fig. 6, where the 72 distributions (almost superposed) are slightly below  $f_s$ .

The generic procedure described here to determine  $f_{\text{down}}$  at a given time is then repeated for a user-defined set of times during the blow-up time interval. Figure 8 shows the minimum, mean and maximum  $f_{\text{down}}$  along the cycle, when  $\tau_{4,d} = 1.6$  ns, 1.8 ns and 2.0 ns. The lower  $f_{\text{down}}$  values occur when  $\tau_{4,d} = 2.0$  ns, since lower synchrotron frequencies correspond to larger emittances and bunch lengths at the end of the blow-up, and therefore at extraction.

The curves in Fig. 8 change slope at 15.6 s, which is the time when the momentum ramp in Fig. 2 changes from parabolic to linear. Since the RF systems are in BSM and since the main RF voltage is constant above 14 s, this is also the time when the synchronous phase becomes constant.

## MACRO-PARTICLE SIMULATIONS

Macro-particle simulations of the SPS cycle shown in Fig. 2 started at 10.6 s with 72 rotated PS bunches and ended at extraction. Simulations included collective effects,

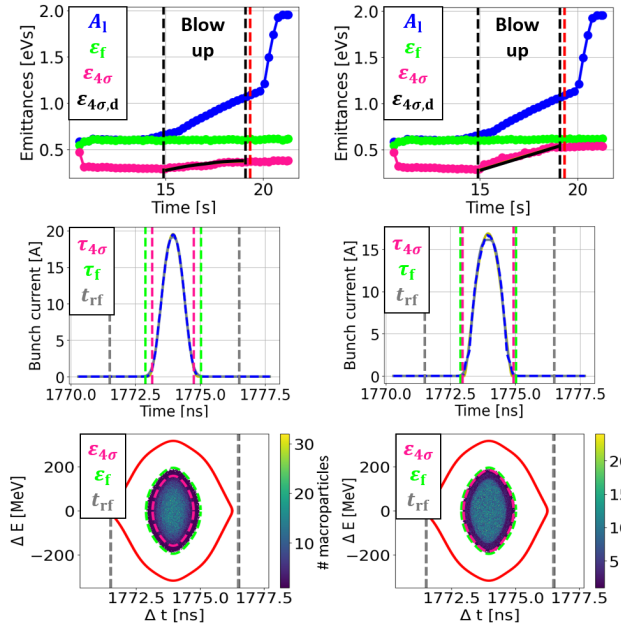


Figure 9: Simulated emittance evolutions (top), profiles at extraction (middle) and corresponding distributions in phase space (bottom) for the bunch 72 when  $\tau_{4,d} = 1.6$  ns (left) and  $\tau_{4,d} = 2.0$  ns (right). The blue and black curves (top) represent respectively the acceptance and design-emittance evolutions, the vertical red lines (top) mark the momentum of 380 GeV/c. The full and  $4\sigma$  emittances/bunch lengths are in green and pink, respectively.

beam loops and emittance blow-up. The algorithm described above has been executed to obtain the frequency bands for desired extracted bunch lengths of 1.6 ns, 1.8 ns and 2.0 ns.

Figure 9 shows the emittance evolutions, profiles at extractions and corresponding distributions of the last bunch, when  $\tau_{4,d} = 1.6$  ns and  $\tau_{4,d} = 2.0$  ns. For each simulation, the phase-noise rms  $\sigma_n$  was kept constant during the blow-up. We found that  $\sigma_n = 5$  mrad and  $\sigma_n = 14$  mrad were the optimal values for  $\tau_{4,d} = 1.6$  ns and  $\tau_{4,d} = 2.0$  ns, respectively. Using these phase noise amplitudes, the evolution of  $\epsilon_4$  followed the design  $\epsilon_{4,d}$  curves (Fig. 9, top) very well. As desired, the full emittances remained constant along the cycle, indicating that phase noise targets just the bunch core. This allows to have a loss free blow-up.

Figure 9 also shows that the extracted distributions and profiles of the last bunch do not present any structure which could degrade the quality of the extracted beam. We just observe that, when  $\tau_{4,d} = 2.0$  ns, the bunch distribution has a low density stripe in the outer part, and the bunch profile is almost parabolic, with the exception of the tails. This indicates that the bunch core could be targeted even more, and indeed  $\sigma_n = 20$  mrad would remove the low density stripe in the bunch distribution, although the extracted bunch length would be slightly larger than the desired one.

The observations done here for the last bunch remain valid also for the other bunches. In particular, no bunch showed any sign of quality degradation at extraction. As expected,

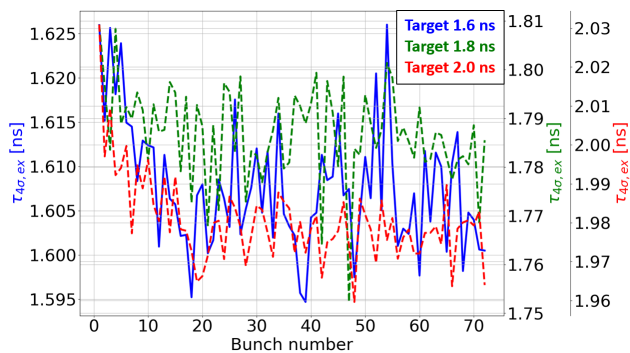


Figure 10: Simulated extracted bunch lengths along the batch when  $\tau_{4,d} = 1.6$  ns (blue), 1.8 ns (green), 2.0 ns (red). The extracted profile and distribution of the last bunch when  $\tau_{4,d} = 1.6$  ns and 2.0 ns are shown in Fig. 9.

the  $\tau_{4,ex}$  values differed along the batch. These spreads should remain small, mostly for HL-LHC beams. Figure 10 shows that  $\tau_{4,ex} = 1.61 \pm 0.02$  ns,  $1.79 \pm 0.04$  ns,  $1.98 \pm 0.05$  ns when  $\tau_{4,d} = 1.6$  ns, 1.8 ns and 2.0 ns, respectively. The maximum spread is 4%, which would be satisfying if found also at the intensity of HL-LHC beams.

## COMPARISON TO BEAM MEASUREMENTS

Simulations were compared with first beam measurements of one batch of 72 bunches accelerated either without or with emittance blow-up. When phase noise was included, we set  $f_{down} = 0.64f_{s0}$  ratio during the blow-up. Although this setting was an approximation of the results shown in Fig. 8, the goal was to verify that a constant  $f_{down}/f_{s0}$  can still provide stable beams and the desired  $\tau_{4,d} = 1.65$  ns during measurements. A constant  $f_{down}/f_{s0}$  would greatly simplify the phase noise setup in operation.

Figure 11 shows the minimum, mean and maximum bunch lengths along the batch as a function of the cycle time, in simulations and measurements. Without emittance blow-up (Fig. 11, top), the bunch lengths are slightly lower in simulations than in measurements, mostly for cycle times above 14 s. At flat-top, the bunch lengths are  $1.57 \pm 0.09$  ns and  $1.49 \pm 0.08$  ns in measurements and simulations, respectively.

When phase noise is applied (Fig. 11, bottom), the agreements in bunch lengths between measurements and simulations are better, both during the cycle and at flat-top. The final bunch lengths are  $1.65 \pm 0.12$  ns and  $1.65 \pm 0.07$  ns in measurements and simulations, respectively.

Although more studies are needed to explain the discrepancies without phase noise, which can be due to other noise sources present in the SPS, these first comparisons between measurements and simulations show that emittance blow-up works as desired, even with a constant normalized  $f_{down}$ .

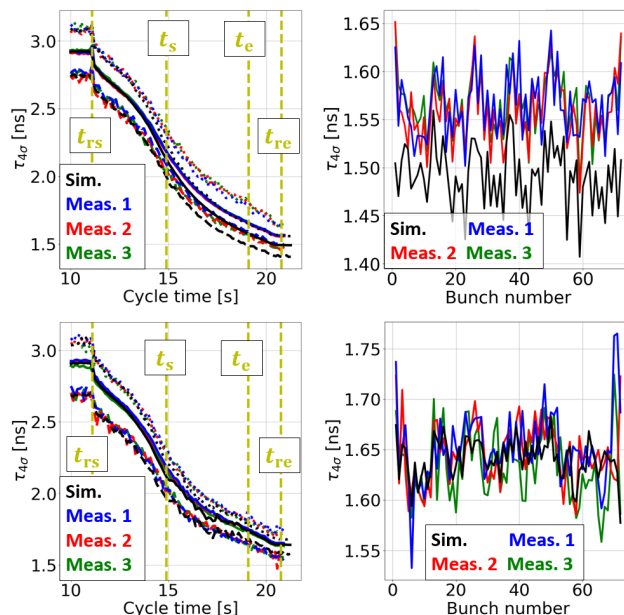


Figure 11: Left: minimum (dashed lines), mean (continuous) and maximum (dotted) bunch lengths along the cycle in simulations (black) and measurements (other colours), without (top) and with (bottom) applying phase noise between  $t_s$  and  $t_e$ . The ramp starts at  $t_{rs}$  and ends at  $t_{re}$ . Right: the corresponding final bunch lengths along the batch.

## CONCLUSIONS

Controlled longitudinal emittance blow-up with bandwidth-limited phase noise is one of the major ingredients to guarantee the longitudinal stability of proton beams for the HL-LHC in the SPS.

In this paper we described an algorithm for the determination of the phase-noise frequency band. This algorithm computes the design emittance evolutions for each bunch during blow-up and determines the frequency bands using the synchrotron frequency distributions with collective effects. We showed that the optimal frequency band can change significantly according to the desired extracted bunch length.

The computed frequency bands were used in realistic macro-particle simulations of one batch of 72 bunches through the SPS cycle. It was possible to obtain different desired bunch lengths at extraction, as well as high quality extracted distributions and bunch profiles.

Results from simulations were compared with beam measurements. We found slight disagreements in bunch length when phase noise was not applied. With a proper choice of the phase noise amplitude, it was possible to obtain good agreements in bunch length when emittance blow-up was present. We showed that an approximation of the optimal frequency band can still provide the desired bunch lengths at extraction, both in measurements and simulations.

## ACKNOWLEDGEMENTS

We thank B. Bielawski who developed the interfaces for an efficient use of the noise algorithm in measurements and

simulations. The simulated PS bunches were kindly provided by A. Lasheen. We also thank the SPS operation team who provided precious support during beam measurements.

## REFERENCES

- [1] E. N. Shaposhnikova *et al.*, “Removing Known SPS Intensity Limitations for High Luminosity LHC Goals”, in *Proc. 7th Int. Particle Accelerator Conf. (IPAC’16)*, Busan, Korea, May 2016, pp. 989–991. doi:10.18429/JACoW-IPAC2016-MOPOY058
- [2] J. Repond, “Possible Mitigations of Longitudinal Intensity Limitations for HL-LHC Beam in the CERN SPS”, Ph.D. thesis, LPAP, EPFL, Lausanne, France, 2019.
- [3] J. Repond, M. Schwarz, and E. Shaposhnikova, “Mitigation of intensity limitation in the CERN SPS using a double RF system,” *International Journal of Modern Physics A*, vol. 34, p. 1942036, 2019. doi:10.1142/S0217751X19420363
- [4] T. Bohl, T. Linnecar, E. Shaposhnikova, and J. Tueckmantel, “Study of Different Operating Modes of the 4th RF Harmonic Landau Damping System in the CERN SPS”, in *Proc. 6th European Particle Accelerator Conf. (EPAC’98)*, Stockholm, Sweden, Jun. 1998, paper THP09A, p. 978.
- [5] T. Toyama, “Uniform bunch formation by RF voltage modulation with a band-limited white signal,” *Nuclear Instruments and Methods in Physics Research Section A: Accelerators, Spectrometers, Detectors and Associated Equipment*, vol. 447, no. 3, p. 317, 2000. doi:10.1016/S0168-9002(99)01312-1
- [6] G. Papotti *et al.*, “Study of Controlled Longitudinal Emittance Blow-up for High Intensity LHC Beams in the CERN SPS,” *Conf. Proc. C*, vol. 0806233, p. 1676, 2008.
- [7] S. Albright and D. Quartullo, “Time varying RF phase noise for longitudinal emittance blow-up,” *J. Phys.: Conf. Ser.*, vol. 1350, p. 012144, 2019. doi:10.1088/1742-6596/1350/1/012144
- [8] D. Quartullo, E. Shaposhnikova, and H. Timko, “Controlled longitudinal emittance blow-up using band-limited phase noise in CERN PSB,” *J. Phys.: Conf. Ser.*, vol. 874, p. 012066, 2017. doi:10.1088/1742-6596/874/1/012066
- [9] P. Baudreghien and T. Mastoridis, “Longitudinal emittance blow-up in the large hadron collider,” *Nuclear Instruments and Methods in Physics Research Section A: Accelerators, Spectrometers, Detectors and Associated Equipment*, vol. 726, p. 181, 2013. doi:10.1016/j.nima.2013.05.060
- [10] H. Timko, P. Baudreghien, E. N. Shaposhnikova, and T. Mastoridis, “Studies on Controlled RF Noise for the LHC”, in *Proc. 54th ICFA Advanced Beam Dynamics Workshop on High-Intensity and High-Brightness Hadron Beams (HB’14)*, East Lansing, MI, USA, Nov. 2014, paper THO4LR03, pp. 414–418.
- [11] K. Hanke *et al.*, “The LHC Injectors Upgrade (LIU) Project at CERN: Proton Injector Chain”, in *Proc. 8th Int. Particle Accelerator Conf. (IPAC’17)*, Copenhagen, Denmark, May 2017, pp. 3335–3338. doi:10.18429/JACoW-IPAC2017-WEPVA036
- [12] G. Hagemann *et al.*, “The CERN SPS Low Level RF upgrade Project”, in *Proc. 10th Int. Particle Accelerator Conf. (IPAC’19)*, Melbourne, Australia, May 2019, pp. 4005–4008. doi:10.18429/JACoW-IPAC2019-THPRB082
- [13] J. T. ckmantel, “Digital Generation of Noise-Signals with Arbitrary Constant or Time-Varying Spectra (A noise generation software package and its application),” Tech. Rep. LHC-PROJECT-Report-1055, CERN, Geneva, 2008.
- [14] “CERN BLoND Code.” <http://blond.web.cern.ch/>.

# UNDERSTANDING OF THE CERN-SPS HORIZONTAL INSTABILITY WITH MULTIPLE BUNCHES

C. Zannini\*, H. Bartosik, M. Carlà<sup>1</sup>, L. Carver<sup>2</sup>, K. Li, E. Métral, G. Rumolo, B. Salvant, M. Schenk  
CERN, 1211 Geneva, Switzerland  
<sup>1</sup>now at ALBA, Barcelona, Spain  
<sup>2</sup>now at ESRF, Grenoble, France

## Abstract

At the end of 2018, an instability with multiple bunches has been consistently observed during high intensity studies at the CERN-SPS. This instability could be a significant limitation to achieve the bunch intensity expected after the LHC Injector Upgrade (LIU). Therefore, a deep understanding of the phenomena is essential to identify the best mitigation strategy. Extensive simulation studies have been performed to explore the consistency of the current SPS model, give a possible interpretation of the instability mechanism and outline some possible cures.

## INTRODUCTION

Major modifications of the CERN-SPS took place during the Long Shutdown 2 (LS2) in the framework of the LHC injectors upgrade project (LIU) [1–3]. In particular, the RF system has been modified with the aim of providing the necessary RF power for compensation of beam loading, which was limiting the acceleration of LHC beams to an intensity of about  $1.3 \times 10^{11}$  protons per bunch (ppb) before the upgrade. The LIU upgrades of the RF system, together with the longitudinal impedance reduction, are expected to enable the acceleration of the future LHC beams to reach the target intensity of  $2.3 \times 10^{11}$  ppb at the CERN-SPS extraction. While such high intensity beams could not be accelerated before the upgrade, they could already be studied at injection energy. After a short description of measurement observations this paper summarises the simulation studies performed to build an understanding of the horizontal instability experienced at injection energy with high intensity LHC beams.

## INSTABILITY MEASUREMENTS

During the 2015 scrubbing campaign with high intensity LHC beams (about  $2.0 \times 10^{11}$  ppb), a horizontal instability affecting the third and fourth batch of trains of 72 bunches was observed. Stabilization was possible with high chromaticity and octupoles.

Since 2017, an increased transverse damper gain at high frequency was available, but high chromaticity was still needed to stabilise the beam. If the chromaticity is not high enough, the unstable bunches exhibit head-tail motion as revealed by measurements with the SPS head-tail monitor. In particular, oscillation patterns of mode 1 were observed for horizontal normalised chromaticity ( $\xi = Q'/Q$ ) settings

of  $0.1 \leq \xi_H \leq 0.3$  and mode 2 for  $0.3 \leq \xi_H \leq 0.5$ . A mode 3 pattern has also been observed for  $\xi_H \approx 0.5$ .

At the end of 2018, dedicated measurements were performed to further characterise the instability and test some possible cures. Four batches of 48 bunches were used for these studies. No instability was observed for lower number of batches and bunch intensity up to  $2.0 \times 10^{11}$  ppb. The horizontal chromaticity was kept high (normalised chromaticity of  $\xi_H \approx 0.5$ ) for the injection of the first three batches but lowered to  $\xi_H \approx 0.05$  just before the injection of the fourth batch while the transverse damper was on during the entire cycle. The octupoles were adjusted in order to compensate the horizontal detuning with amplitude due to residual non-linearities of the machine (setting of  $k_{LOF} = -0.2 \text{ m}^{-4}$ ).

With the operational batch spacing of 200 ns the intensity threshold of the instability was found to be  $1.8 \times 10^{11}$  ppb. Figure 1 (top) shows an example of the intensity evolution along the SPS injection plateau for two different chromaticity settings. Instability starts from the last batch and extends to the other batches for lower chromaticity. Bunches in the last batch exhibit significant losses in the top plot, while for lower chromaticity (bottom plot), the instability clearly extends to the second and third batch. The growth times associated to this instability are in the order of 100 turns, as observed from the head-tail monitor acquisitions or from the turn-by-turn data of the transverse damper pickups. However, their exact value strongly depends on the damper settings. The damper, which does not have enough bandwidth to suppress the mode 1-2 head-tail instability, can, however, significantly modify the growth rates of the instability. Depending on damper settings, a variation of the instability growth rates up to a factor of three has been observed. The instability growth rates versus chromaticity have been measured and will be compared with the mode expectations in the next section.

The effect of batch spacing on the instability was also studied by varying the gap between batches in steps of 50 ns. Fewer bunches are affected by the instability when increasing the batch spacing and no instability was observed for a batch spacing larger than 500 ns.

Finally, measurements of the stability limit as a function of chromaticity and octupole settings were performed. As before, four batches of 48 bunches were injected, where the chromaticity was kept high for the injection of the first three batches and then lowered just before the injection of the fourth batch. Figure 2 shows the obtained stability limits for an intensity of about  $1.8 \times 10^{11}$  ppb at injection. Positive

\* carlo.zannini@cern.ch

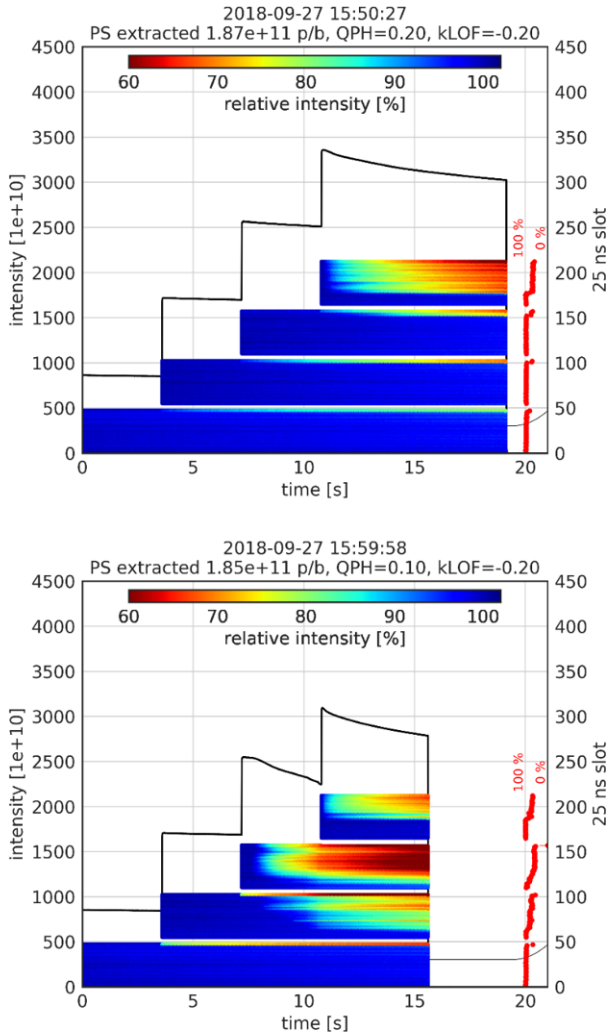


Figure 1: Intensity evolution along the SPS flat bottom for  $\xi_H = 0.2$  (top) and  $\xi_H = 0.1$  (bottom). In both cases, the black line indicates the total intensity and the colour indicates the relative bunch intensity. The bunch slots are indicated on the scale on the right.

values of the octupole knob are not shown as they resulted in worse beam stability.

As expected, the instability becomes more critical with higher intensity. Thus, higher octupole strength and/or higher chromaticity is needed to stabilize the beam. Stabilization was tested up to  $2.1 \times 10^{11}$  ppb. Therefore, there is a large range of unexplored intensities to reach the target LIU intensity of  $2.6 \times 10^{11}$  ppb at injection energy. A good understanding of the instability is fundamental during the intensity rump-up in order to put in place the appropriate stabilization strategy in the unexplored range of intensities.

## UNDERSTANDING OF THE INSTABILITY

A theoretical analysis based on the Sacherer theory [4] has been performed to build a qualitative understanding of

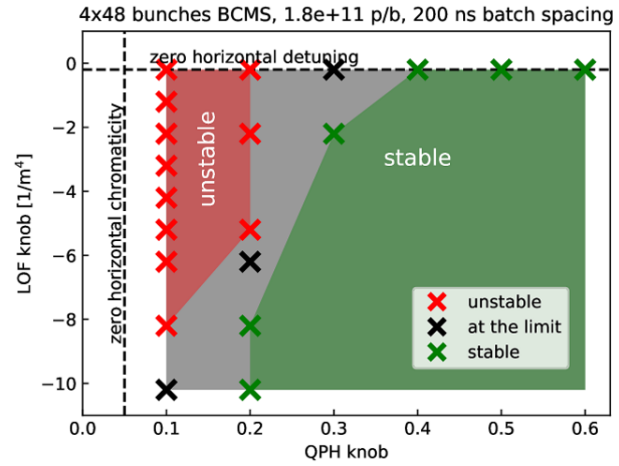


Figure 2: Measured horizontal beam stability for different chromaticity and octupole settings, where the QPH knob controls the normalised horizontal chromaticity  $\xi_H$  and the LOF knob controls the normalised octupole strength. The values for zero chromaticity and no amplitude detuning are indicated by dashed lines. The markers indicate unstable (red), stable (green) and settings where some shots were stable and some unstable (black) as obtained from about 5 shots per setting.

the instability, with an advanced macro-particle simulation model used for more quantitative analysis.

## Analysis with Sacherer Theory

The effect on beam dynamics can be qualitatively assessed using the concept of effective impedance. For bunched beams the impedance is sampled at an infinite number of discrete frequencies given by the mode spectrum. An "effective coupling impedance" can then be defined as the sum over the product of the coupling impedance and the normalized spectral density. The "effective coupling impedance" is required for the calculation of both longitudinal and transverse complex tune shifts of bunched beam and can be defined in the transverse plane as [5–7]:

$$(Z_{\perp})_{\text{eff}} = \frac{\sum_{p=-\infty}^{p=\infty} Z_{\perp}(\omega' + \omega_{\beta}) h_l(\omega' + \omega_{\beta} - \omega_{\xi})}{\sum_{p=-\infty}^{p=\infty} h_l(\omega' + \omega_{\beta} - \omega_{\xi})}. \quad (1)$$

Here  $h_l(\omega)$  is the power spectral density,  $\omega_{\beta}$  is the betatron angular frequency,  $\omega_{\xi}$  is the chromatic frequency shift and  $\omega' = \omega_0 p + l\omega_s$  where  $\omega_0$  is the revolution angular frequency,  $\omega_s$  is the synchrotron frequency and  $l$  determines the type of oscillations (the case  $l = 0$  describes the mode 0 head-tail instability). For a Gaussian bunch,  $h_l(\omega)$  can be written as:

$$h_l(\omega) = \left(\frac{\omega\sigma_z}{c}\right)^{2l} e^{-\frac{\omega^2\sigma_z^2}{c^2}}, \quad (2)$$

where  $\sigma_z$  is the standard deviation of the Gaussian bunch profile (root mean square (RMS) bunch-length) and  $c$  is the speed of light in vacuum. The real and the imaginary parts of the "effective impedance" give the growth rate and the frequency shift of the mode under consideration, respectively [7–10]. If the real part of  $(Z_{\perp})_{\text{eff}}$  is negative, the beam can become unstable. The real part of the transverse impedance is an odd function of frequency. Therefore, for the mode  $l = 0$ , simply assuming that the impedance is positive for positive frequencies leads to the conclusion that this mode would be stable for positive spectral shift and unstable for negative spectral shift (see Fig. 3). The situation is different if we consider higher mode numbers. For a given chromatic shift the sign of the effective impedance depends on the impedance type. Therefore, no general rule for stability criteria can be given for these modes.

Figure 4 for example shows an illustrative view of the mode  $l = 1$  together with the SPS resistive wall impedance (decreasing with frequency) and the SPS ferrite loaded kicker impedance (increasing with frequency). For the resistive wall impedance and for  $\xi < |\xi_{\text{max}}|$  ( $\xi_{\text{max}}$  is defined as the chromaticity value at which the first sign inversion of the growth rate occurs) the mode  $l = 1$  is destabilizing for positive chromaticity and stabilizing for negative chromaticity, the situation is exactly reversed in the case of the impedance of ferrite loaded kickers, which is increasing with frequency up to almost 1 GHz. The overall effect of different impedance contributions depends on the weight of stabilizing and destabilizing effects. An impedance increasing with frequency has a stabilizing effect for mode  $l = 1$  and  $\xi > 0$ . Reducing this kind of impedance makes the situation worse.

A first attempt to understand the nature and the possible impedance source of the instability was performed by using the SPS impedance model [11]. This model was successfully adopted in the past years to benchmark several single bunch beam observations (instability growth rate of mode 0 versus chromaticity [11], tune shift versus intensity and Transverse Mode Coupling Instability (TMCI) behaviour [12]).

The effect of the elements included in the model has been studied and it was found that the combination of kickers and wall impedance is responsible for the observed instability [13].

The expected growth rates as a function of the chromaticity are shown in Fig. 5 for the different modes. The results are in good agreement with the measured intra-bunch motion versus chromaticity [14] discussed in the previous section. This is a strong indication about the nature of the instability, which is considered to be a head-tail instability requiring multiple bunches to be strong enough to be observed in the machine.

### Macro-Particle Simulations

The analysis with Sacherer theory allowed the possible nature of the instability and the impedance sources to be identified. However, the development of a macro-particle model for multi-bunch simulations including the actual beam pattern, the feedback system, the detuning impedance and

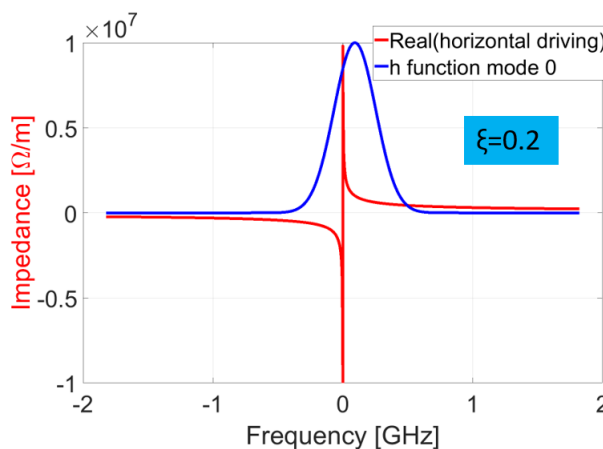


Figure 3: SPS wall impedance model (red) and power spectral density for the mode  $l = 0$  in arbitrary units for a chromaticity  $\xi = 0.2$  (blue) at injection energy for the Q20 optics.

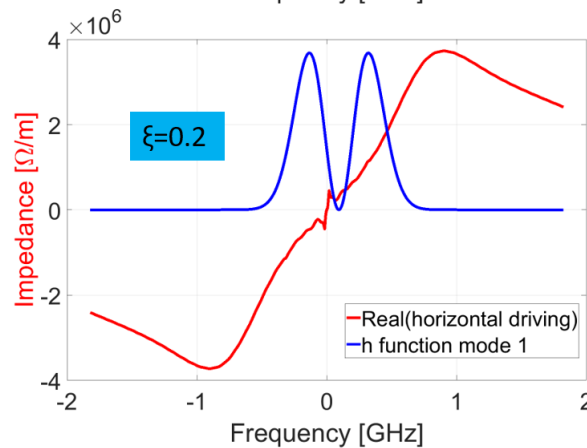
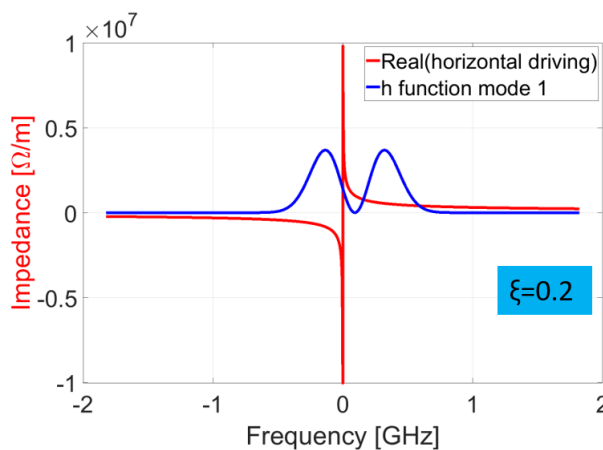


Figure 4: Power spectral density for the mode  $l = 1$  in arbitrary units for a chromaticity  $\xi = 0.2$  (blue) together with the SPS wall impedance model (top) and the SPS kickers without serigraphy (bottom) at injection energy for the Q20 optics.

the effect of nonlinear chromaticity, octupoles and nonlinear synchrotron motion is essential to perform quantitative com-

Content from this work may be used under the terms of the CC BY 3.0 licence (© 2021). Any distribution of this work must maintain attribution to the author(s), title of the work, publisher, and DOI

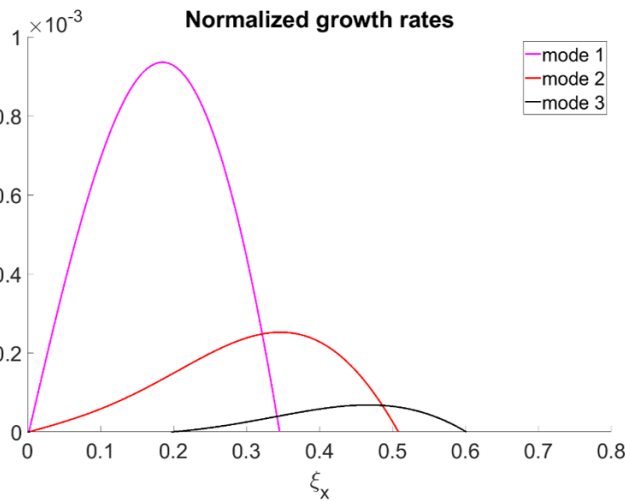


Figure 5: Normalized horizontal instability growth rates as function of the horizontal chromaticity of the head-tail mode 1 in magenta, mode 2 in red and mode 3 in black. The growth rates have been computed by using the Sacherer theory with Gaussian bunches for the SPS impedance model at injection energy for the Q20 optics.

comparisons with the measurements. These studies allow the level of accuracy of the model to be qualified, when used to investigate some possible cures of the instability in the unexplored range of intensities. The macro-particle simulations were performed with the multi-bunch version of PyHEADTAIL [15]. The SPS wake model, which is the main input of these simulations, has been successfully benchmarked in past years with single bunch measurements. However, the 10 ns single bunch model is not appropriate for multi-bunch simulations. A big effort has been devoted to the development of a model more appropriate for multi-bunch studies. In particular, the wall wake has been computed up to 1 ms allowing to take into account a wake memory of 43 turns, and the kicker wake has been computed over 1  $\mu$ s in order to consider all the relevant range of the wake before it vanishes.

The coupled-bunch wake model, including kickers and wall impedance, was then used to benchmark the observation of the SPS horizontal instability with the multi-bunch version of PyHEADTAIL. The simulation considers the exact beam pattern used in measurements ( $4 \times 48$  bunches with 25 ns bunch spacing and a batch gap of 200 ns). An initial Gaussian distribution with  $\sigma_z = 0.23$  m is used. A nonlinear model is used for chromaticity (up to the third order) and synchrotron motion. The double SPS RF system is also taken into account and an ideal bunch-by-bunch damper with damping time of 30 turns is included. The initial transverse emittance of the beam is set to 2.5  $\mu$ m.

The simulations can reproduce the main instability observations such as the bunch intensity threshold (see Fig. 6) and the growth rate versus chromaticity for optimized damper settings (see Fig. 7). The behavior with chromaticity and octupoles of Fig. 2 is also reproduced (see Fig. 8).

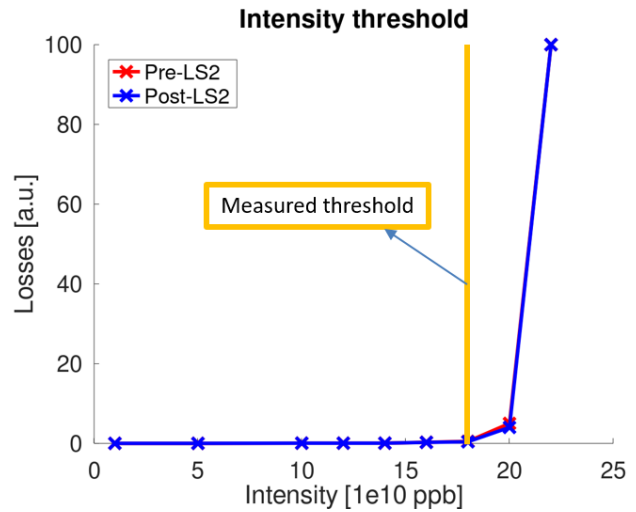


Figure 6: Losses versus intensity. Measured intensity threshold of the instability is represented with the orange line. Both pre-LS2 case (representing the situation during 2018 measurements) and post-LS2 case are displayed, but these two curves are almost indistinguishable as the upgrades of the machine are not expected to change the transverse impedance significantly.

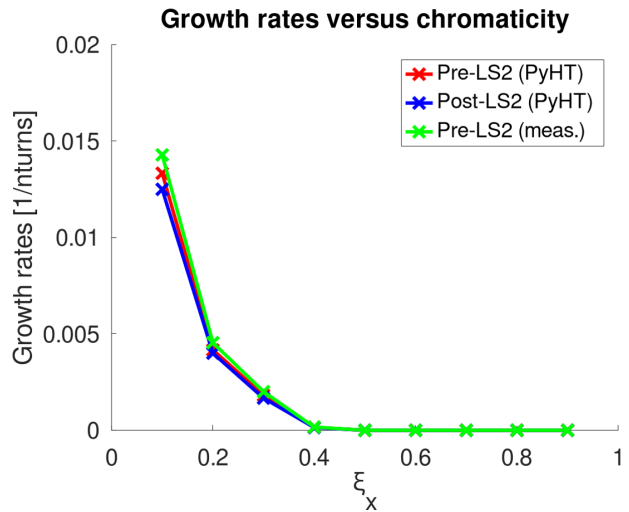


Figure 7: Growth rates as function of the horizontal chromaticity of the instability for a bunch intensity of  $2.0 \times 10^{11}$  ppb. Pre-LS2 and post-LS2 cases have been computed with PyHEADTAIL simulations and compared with the measured values obtained with optimized damper settings.

## PREDICTION FOR THE LIU BEAM

The model used in the PyHEADTAIL multi-bunch simulations has reproduced the behaviour of the instability with a high degree of accuracy [16]. The remarkable agreement in the behaviour versus chromaticity and octupoles gave us confidence to use the simulation model to investigate possible stabilization strategies for the nominal LIU beam ( $4 \times 72$  bunches with  $2.6 \times 10^{11}$  ppb at injection) using chromaticity and octupole knobs.

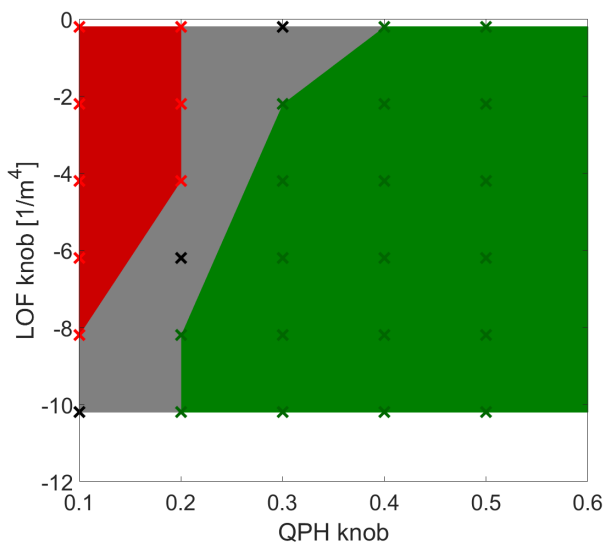


Figure 8: Horizontal beam stability for different chromaticity and octupole settings as obtained from PyHEADTAIL simulations with bunch intensity of  $1.8 \times 10^{11}$  ppb, where the QPH knob controls the normalised horizontal chromaticity  $\xi_H$  and the LOF knob controls the normalised octupole strength. The markers indicate unstable (red), stable (green) and settings where there are no significant losses but exponential growth of the amplitude is visible (black). These points could be reasonably assumed to be at the limit of stability.

The simulations are summarized in the stability map displayed in Fig. 9. A simulation point is assumed to be stable if over 10000 SPS turns there is no exponential amplitude growth, emittance blow-up is below 10% and losses are below 1%. Stable points are represented in green and unstable points in magenta. Using these points the unstable area is depicted in red. Stability without octupoles is expected for  $\xi_H \geq 0.7$ . With octupoles for  $|kLOF| < 10$  stabilization is expected for  $\xi_H \geq 0.5$ . Beam lifetime and quality for the explored operational settings still need to be investigated.

The backup mitigation strategy is the deployment of a wide band feedback system [17]. A prototype of such a system has been demonstrated to be effective in the SPS in the vertical plane against TMCI. Efficiency for the horizontal instability with multiple-bunches needs to be verified in simulation. In order to be able to install the system in the horizontal plane during LS3, dedicated studies need to be launched by 2023. An alternative mitigation strategy could consist in the introduction of an ad-hoc impedance to have a stabilizing effect for the head-tail mode 1-2 horizontal instability [18].

## CONCLUSION

The SPS horizontal instability could be a serious limitation to inject the nominal LIU beam ( $4 \times 72$  bunches with  $N=2.6 \times 10^{11}$  ppb). The impedance mechanism driving the

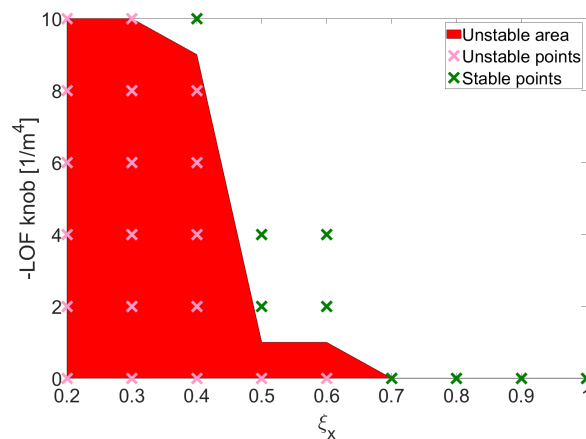


Figure 9: Stability map at injection energy for the nominal LIU beam ( $4 \times 72$  bunches with  $N=2.6 \times 10^{11}$  ppb). Stable points are represented in green and unstable points in magenta. Using these points the unstable area is depicted in red. A simulation point is considered to be stable if over 10000 SPS turns there is no exponential amplitude growth, emittance blow-up is below 10% and losses are below 1%.

instability has been identified by using Sacherer theory. A more detailed simulation model including the actual filling scheme, damper, detuning impedance and nonlinearities can reproduce intensity threshold and growth rate versus chromaticity as well as the behaviour of the instability for different settings of octupoles and chromaticity.

The simulation model was used to identify a possible stabilization strategy. The simulations predict stabilization of nominal LIU beam for  $\xi_H \geq 0.7$  without octupoles and  $\xi_H \geq 0.5$  with octupoles. Beam lifetime and quality for the explored settings still need to be investigated.

## ACKNOWLEDGMENTS

The authors would like to thank V. Kain and the Operation teams for the continuous support. A special thanks to G. Kotzian and W. Hofle for the optimization of damper settings during measurements, T. Levens for the support with the Head-Tail monitor application and J. Kompulla for the development of the PyHEADTAIL multi-bunch version.

## REFERENCES

- [1] K. Hanke *et al.*, “The LHC Injectors Upgrade (LIU) Project at CERN: Proton Injector Chain”, in *Proc. 8th Int. Particle Accelerator Conf. (IPAC’17)*, Copenhagen, Denmark, May 2017, pp. 3335–3338. doi:10.18429/JACoW-IPAC2017-WEPVA036
- [2] H. Bartosik *et al.*, “The LHC Injectors Upgrade (LIU) Project at CERN: Ion Injector Chain”, in *Proc. 8th Int. Particle Accelerator Conf. (IPAC’17)*, Copenhagen, Denmark, May 2017, pp. 2089–2092. doi:10.18429/JACoW-IPAC2017-TUPVA020
- [3] H. Damerau *et al.*, “LHC Injectors Upgrade, Technical Design Report”. CERN, Geneva, Switzerland, Rep. Dec. 2014.

- [4] F. J. Sacherer, “Transverse resistive-wall instabilities of the bunched beam in the SPS,” CERN, Geneva, Switzerland, Rep. CERN-SI-NOTE-BR-72-1, May 1972.
- [5] B. W. Zotter, “The effective coupling impedance for instabilities of Gaussian bunches,” CERN, Geneva, Switzerland, Rep. CERN-ISR-TH-80-03, 1980.
- [6] B. W. Zotter, “The effective coupling impedance for bunched beam instabilities,” CERN, Geneva, Switzerland, Rep. CERN-ISR-TH-78-16, 1978.
- [7] A. W. Chao, *Physics of collective beam instabilities in high energy accelerators*. New York, NY, USA: Wiley, 1993.
- [8] B. W. Zotter, “Collective effects: General description,” CERN, Geneva, Switzerland, Rep. CERN-85-19-V-2, pp. 415–431, 1984.
- [9] J. L. Laclare, “Introduction to coherent instabilities: Coasting beam case,” CERN, Geneva, Switzerland, Rep. CERN-85-19-V-2, pp. 377–414, 1985.
- [10] J. L. Laclare, “Bunched beam coherent instabilities,” CERN, Geneva, Switzerland, Rep. CERN-87-03-V-1, pp. 264–326, 1987.
- [11] C. Zannini, H. Bartosik, G. Iadarola, G. Rumolo, and B. Salvant, “Benchmarking the CERN-SPS Transverse Impedance Model with Measured Headtail Growth Rates”, in *Proc. 6th Int. Particle Accelerator Conf. (IPAC’15)*, Richmond, VA, USA, May 2015, pp. 402–405. doi:10.18429/JACoW-IPAC2015-MOPJE049
- [12] H. Bartosik, G. Iadarola, Y. Papaphilippou, G. Rumolo, B. Salvant, and C. Zannini, “TMCI Thresholds for LHC Single Bunches in the CERN-SPS and Comparison with Simulations”, in *Proc. 5th Int. Particle Accelerator Conf. (IPAC’14)*, Dresden, Germany, Jun. 2014, pp. 1407–1409. doi:10.18429/JACoW-IPAC2014-TUPME026
- [13] C. Zannini *et al.*, “CERN-SPS horizontal instability: impedance model expectations,” Presented at the HSC section meeting, Sep. 2018, <https://indico.cern.ch/event/752791/>.
- [14] C. Zannini *et al.*, “The SPS transverse instability at injection,” Presented at the HSC section meeting, Aug. 2019, <https://indico.cern.ch/event/940765/>.
- [15] M. Schenk, “PyHEADTAIL multi-bunch tutorial,” Presented at the HSC section meeting, Jan. 2019, <https://indico.cern.ch/event/791774/>.
- [16] C. Zannini *et al.*, “The SPS bunch-by-bunch tune shifts,” Presented at the HSC section meeting, Apr. 2021, <https://indico.cern.ch/event/129732/>.
- [17] J. M. Cesaratto *et al.*, “SPS Wideband Transverse Feedback Kicker: Design Report,” CERN, Geneva, Switzerland, Rep. CERN-ACC-NOTE-2013-0047, 2013.
- [18] C. Zannini *et al.*, “Low impedance design with example of kickers (including cables) and potential of metamaterials,” in *Proc. of the ICFA mini-Workshop on Mitigation of Coherent Beam Instabilities in Particle Accelerators (MCBI 2019)*, pp. 167–174, CERN Yellow Reports, Sep. 2020. doi:10.23732/CYRCP-2020-009.167

# INFLUENCE OF TRANSVERSE MOTION ON LONGITUDINAL SPACE CHARGE IN THE CERN PS

A. Laut\*, A. Lasheen, CERN, Geneva, Switzerland

## Abstract

Particles in an intense bunch experience longitudinal self-fields due to space charge. This effect, conveniently described by geometric factors dependent on a particle's transverse position, beam size, and beam pipe aperture, is usually incorporated into longitudinal particle tracking on a per-turn basis. The influence of transverse betatron motion on longitudinal space charge forces is, however, usually neglected in pure longitudinal tracking codes. A dedicated tracking code was developed to characterize the CERN PS such that an effective geometric factor of a given particle could be derived from its transverse emittance, betatron phase advance, and momentum spread. The effective geometry factor is then estimated per particle by interpolation without the need for full transverse tracking and incorporated into the longitudinal tracker BLonD. The paper evaluates this effect under conditions representative of the PS, where space charge is dominant at low energy and progressively becomes negligible along the acceleration ramp. The synchrotron frequency distribution is modified and the filamentation rate is moreover increased, which could suggest a stabilizing space charge phenomenon.

## INTRODUCTION

In the Proton Synchrotron (PS) at CERN, longitudinal space charge, defined in Eq. (1) as a beam coupling impedance, dominates other impedance sources at injection where protons are accelerated from a mildly relativist kinetic energy of  $E_k = 2$  GeV to a highly relativistic  $E_k = 26$  GeV. Proportional to the vacuum impedance  $Z_0$ , a geometry factor  $g$ , and inversely proportional with  $\beta\gamma^2$  [1].

$$\frac{Z}{n} = -j \frac{Z_0}{\beta\gamma^2} g \quad (1)$$

The space charge geometry factor  $g$  describes the longitudinal self fields based on the beam size and aperture [2]. For a particle within a long round beam of uniform transverse density, the geometry factor is often expressed by

$$g = \frac{1}{2} + \ln \frac{b}{a} - \frac{1}{2} \frac{r^2}{a^2}, \quad (2)$$

where  $a$  describes the beam radius,  $b$  describes the radius of a conductive aperture, and  $r$  describes the particle's radial offset.

Throughout the PS, longitudinal space charge impedance and other purely reactive impedance sources with constant  $Z/n$  induce wakefield voltages  $V_W$  given by Eq. (3)

$$V_W = -\frac{i}{\omega_s} \frac{Z}{n} \frac{d\lambda}{d\tau}, \quad (3)$$

\* alexander.laut@cern.ch

where  $n = f/f_s$ ,  $f_s$  being the revolution frequency of the synchronous particle, the time coordinate  $\tau = t - t_s$  being relative to the synchronous particle, and  $d\lambda/d\tau$  being the derivative of  $\lambda(\tau)$  the longitudinal bunch profile. Because of the large range of longitudinal space charge observed in the PS throughout the acceleration ramp (Fig. 1), the induced wakefield voltage will have a strong and varying influence on the longitudinal dynamics, potentially influencing longitudinal beam stability [3]. To reproduce these effects in simulation, it is important to accurately model space charge in the PS.

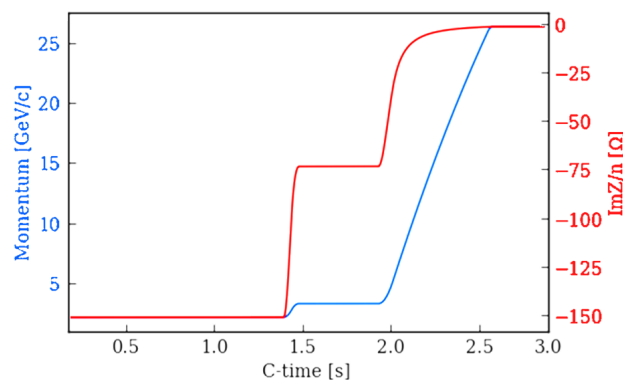


Figure 1: Space charge impedance  $\text{Im}Z/n$  in the PS which dominates until it is compensated at higher momentum by the inductive impedance of the PS aperture of about  $20 \Omega$  [4].

The LHC Injectors Upgrade (LIU) project at CERN [5, 6] aims to increase the total intensity of the injectors for both proton and ion beams to reach the requirements for High-Luminosity LHC (HL-LHC) [7]. At flat bottom where particle energies are lower, beam brightness is limited by space charge effects. In the transverse plane, charges within a bunch will repel each other, limiting the minimum transverse emittance. In the longitudinal plane, the self-fields of a bunch will be defocusing below transition energy, and focusing above. As a pure reactive impedance, longitudinal space charge will also influence Landau damping and overall beam stability.

As illustrated in Fig. 2, a bunch can spontaneously break up shortly after transition crossing due to high frequency impedance sources. Longitudinal space charge being a focusing force after transition, and being a function of  $d\lambda/d\tau$ , will amplify the modulation induced by wakefields.

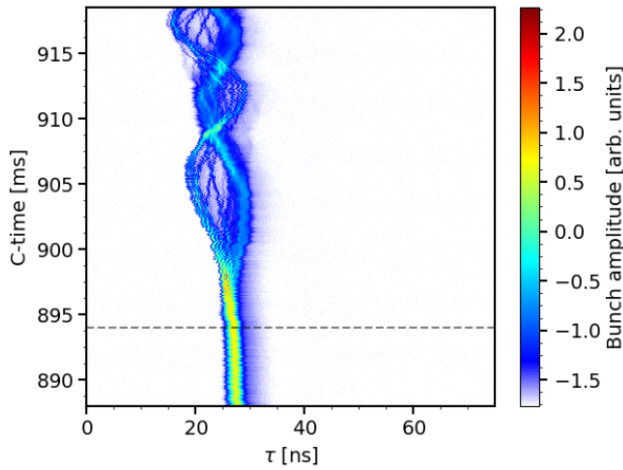


Figure 2: Micro-Bunch Instabilities occurring in protons after crossing transition in the PS.

The instability described above was studied using the tracking code BLoND [8], benchmarked first in comparison with a stable bunch. Modeling space charge as an impedance accurately reproduces the bunch oscillations after transition crossing as seen in Fig. 3. However, the predicted space charge impedance must be reduced by 30% to match the oscillation amplitude as observed in experiment [9].

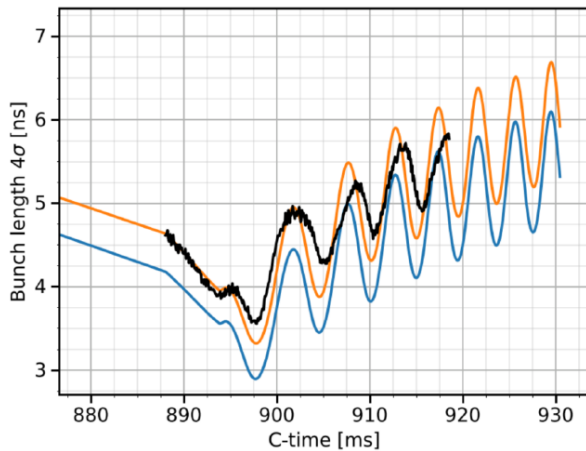


Figure 3: Validation of BLoND space charge model with bunch length oscillations after transition. Reducing impact of space charge by 30% in simulation (blue) improves the match with experimental measurements (black). Bunch lengthening due to the acquisition system’s transfer function is simulated in orange.

Another key parameter for longitudinal space charge is the bunch length. For the LHC-type beam in the PS, the beam undergoes a sequence of RF manipulations including batch compression, merging and splitting (the corresponding momentum and RF during the cycle are shown in Fig. 4), leading to an important variation in bunch length of almost two orders of magnitude from injection to extraction. This also translates into a momentum spread which, through dis-

person, will influence the transverse beam size, which is relevant for studies.

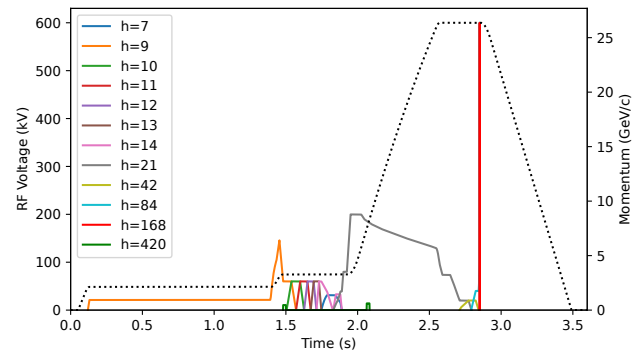


Figure 4: Voltage programs at RF harmonics  $h$  and particle momentum are plotted against time during a cycle in the PS.

Conventional longitudinal tracking codes neglect the radial dependency of the geometry factor  $g$  by assuming all particles are traveling along the center of the beam where space charge is strongest. Realistically, particles with large transverse emittance or momentum spread will have betatron trajectories further from the center of the beam and experience, on average, less space charge. This is also a particularly poor approximation during transition crossing where momentum spread is high. Naturally, the effects of transverse motion on longitudinal space charge are of key interest for describing the current discrepancy observed between simulation and experiment.

### SYNCHROTRON FREQUENCY SHIFT WITH SPACE CHARGE

The equations of motion describing the longitudinal phase space evolution of particles accelerated in a synchrotron can be described by

$$\dot{\tau} = \frac{\eta}{\beta_s^2 E_s} w \quad \dot{w} = \frac{q}{T_s} V(\tau),$$

where  $w$  describes the discrete energy gain, relative to that of the synchronous particle, about one turn. The revolution period of the synchronous particle is  $T_s$  and the slippage factor derived from the transverse optics is given by  $\eta = 1/\gamma_t^2 - 1/\gamma^2$ . Subscripted coordinates specify the synchronous particle.

Particles affected by a linear generalized voltage source  $V(\tau)$  follow elliptical trajectories in longitudinal phase space described by the synchrotron frequency

$$\Omega^2 = -\frac{\eta}{\beta_s^2 E_s} \frac{q}{T_s} V'(\tau), \quad (4)$$

where  $V'(\tau) = \frac{d}{d\tau} V(\tau)$ . In the case of a sinusoidal RF waveform given by peak voltage  $V_g$ , particles will experience a voltage gradient describable by

$$V'_{RF}(\tau) = h\omega_s V_g \cos \varphi,$$

where  $\varphi$  is the RF phase such that  $\varphi = h\omega_s(\tau + t_s)$  where  $h$  is RF harmonic and  $\omega_s$  is the angular revolution frequency of the synchronous particle. For particles oscillating in the center of the bunch with small phase space amplitudes ( $\varphi \approx \varphi_s$ ), the synchronous synchrotron frequency is defined by

$$\Omega_s^2 = -\frac{\eta}{\beta_s^2 E_s} \frac{qV_g}{T_s} h\omega_s \cos \varphi_s.$$

In a non-accelerating bucket, particles with larger oscillation amplitudes  $\hat{\varphi} = h\omega_s \hat{\tau}$  will experience a nonlinear RF gradient and accordingly the normalized synchrotron tune  $\mu$  is given by

$$\mu = \Omega/\Omega_s = \frac{\pi}{2K(\sin \hat{\varphi}/2)} \approx 1 - \frac{\hat{\varphi}^2}{16} + \mathcal{O}(\hat{\varphi}^4),$$

where  $K(m)$  is the complete elliptic integral of the first kind. The net effect of this tune spread is that particles at larger oscillation amplitudes will lag behind the synchrotron particle in terms of  $(\tau, w)$  longitudinal phase space at varying rates. Accordingly, a bunch whose phase space distribution widths ( $\sigma_\tau$  and  $\sigma_w$ ) are not matched, will filament and expand as illustrated in Fig. 5.

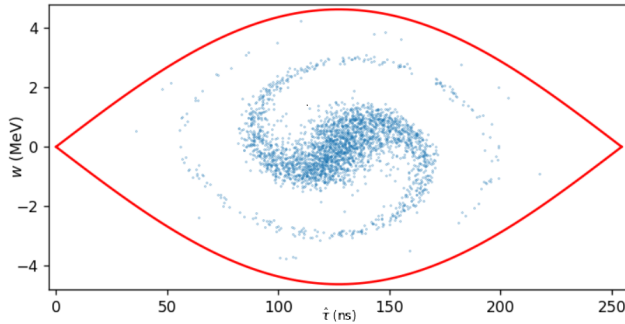


Figure 5: Filamentation due to tune spread of single-particle motion within a separatrix (red) indicating stable motion.

This filamentation induces bunch length oscillations that continue until eventually reaching an equilibrium. The synchrotron frequency spread also contributes as a stabilizing mechanism against longitudinal perturbations through Landau damping.

The effects of space charge induced voltage and RF voltage kicks can be combined such that the net voltage gradient is given by  $V'(\tau) = V'_{RF}(\tau) + V'_{SC}(\tau)$  and

$$V'_{SC}(\tau) = \frac{g}{\omega_s} \frac{Z_0}{\beta_s \gamma_s^2} \frac{d^2 \lambda}{d\tau^2}.$$

As the synchrotron frequency scales according to  $\Omega^2 \propto V'(\tau)$ , the normalized space charges tune shift is given by

$$\mu = \sqrt{1 + \frac{V'_{SC}}{V'_{RF}}}. \quad (5)$$

In the case of a Gaussian longitudinal bunch profile, the space charge tune shift is most significant for small oscillation amplitudes where the space charge gradient is the highest.

## TRANSVERSE EFFECTS

Particles tracked through transverse optics described by beta function  $\beta(s)$  and dispersion function  $D(s)$ , will follow trajectories given by

$$u(s) = \sqrt{\beta(s)\epsilon} \cos(\mu(s) + \mu_0) + D(s)\delta$$

where  $u(s)$  is the particle's transverse offset at longitudinal position  $s$ ,  $\epsilon$  is a single particle's transverse emittance, the momentum spread is given by  $\delta = (p - p_s)/p_s$ , and the betatron phase advance is given by

$$\mu(s) = \int_0^s \frac{ds'}{\beta(s')}.$$

For a matched distribution, the statistical beam width along the ring is given by

$$\sigma_u^2(s) = \beta(s)\sigma_\epsilon + D(s)^2\sigma_\delta^2$$

where  $\sigma_\delta$  and  $\sigma_\epsilon$  describe the transverse bunch RMS momentum spread and emittance respectively.

The transverse optics of the PS (Fig. 6) are quasi-periodic and can be succinctly described by the Fourier series

$$\beta(\theta) \approx \sum_k \beta_k e^{ik\theta} \quad \text{and} \quad D(\theta) \approx \sum_k D_k e^{ik\theta}$$

whose primary coefficients are defined in Table 1.

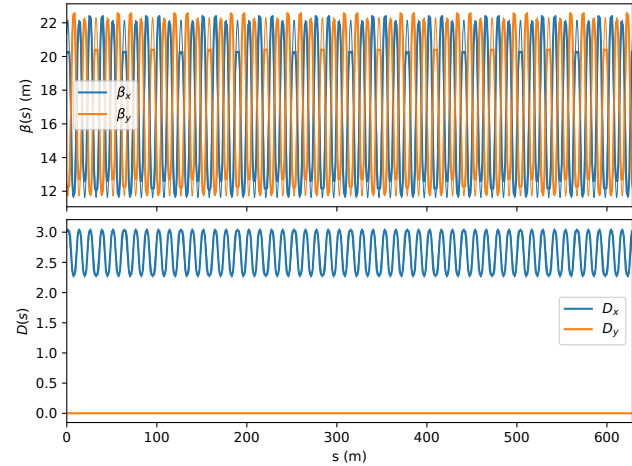


Figure 6: PS transverse optics, expressible as Fourier sum.

Table 1: Main Fourier coefficients of PS optics

k	$\beta_x$	$\beta_y$	$D_x$	$D_y$
0	16.89	17.01	2.66	0
50	4.43-2.84i	-4.46+2.86i	0.34+0.22i	0

Approximating further that the beta and dispersion functions are constant throughout the PS such that  $D(s) \approx D_0$  and  $\beta(s) \approx \beta_0$ , the effective transverse position for a particle, defined by properties  $X \in \{\delta, \epsilon_x, \epsilon_y, \mu_x, \mu_y\}$ , is given by

$$\overline{r^2}(X) = \overline{x^2} + \overline{y^2} \approx \frac{\beta_0}{2} (\epsilon_x + \epsilon_y) + D^2 \delta^2.$$

Content from this work may be used under the terms of the CC BY 3.0 licence (© 2021). Any distribution of this work must maintain attribution to the author(s), title of the work, publisher, and DOI

Because the betatron tune is typically high, the effects of transverse phase advance  $\mu_x, \mu_y$  will average out and can be largely neglected. Similarly, the effective beam size can be approximated by  $a^2 = 4\sigma_x\sigma_y$ , the geometric mean of horizontal and vertical beam size dimensions. Essentially constant throughout the ring, the beam size is given by properties  $Y \in \{\sigma_\epsilon, \sigma_\delta\}$  such that

$$\bar{a}(Y) \approx 2\sqrt{(\beta_0\sigma_\epsilon + D_0^2\sigma_\delta^2)(\beta_0\sigma_\epsilon)}.$$

The averaged geometry factor  $\bar{g}$  for an arbitrary particle  $X$  within a uniform transverse distribution  $Y$  is therefore approximated by

$$\bar{g}(X, Y) \approx \frac{1}{2} + \ln \frac{b}{\bar{a}(Y)} - \frac{1}{2} \frac{r^2(X)}{\bar{a}^2(Y)}.$$

Because  $\bar{g} \propto -r^2$  and  $r^2 \propto \epsilon \propto \delta^2$ , it can be shown that the nominal synchrotron tune shift described by Eq. (5), is reduced for particles whose transverse emittance or momentum spread is large.

The aforementioned relationships with the effective geometry factor  $\bar{g}$ , particle properties  $X$ , and beam properties  $Y$  were numerically verified by transverse tracking. Depicted in Fig. 7, a matched transverse distribution whose emittance is given by a Rayleigh distribution  $\epsilon \sim R^2(\sqrt{\sigma_\epsilon})$ , and uniformly distributed phase advance  $\mu \sim U(-\pi, \pi)$ , was tracked once through the PS ring with respect to the aperture radius  $b$  and beam width  $a$ .

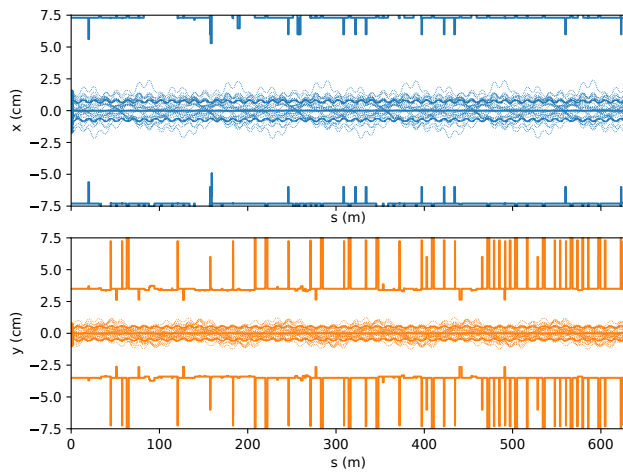


Figure 7: Horizontal (blue) and vertical (orange) trajectories for a matched transverse distribution are tracked through the PS aperture to compute each particle's incurred space charge geometry factor.

A meshed grid of particle properties  $X$  was tracked with respect to beam properties  $Y$  to generate a response matrix for  $\bar{g} = \bar{g}(X, Y)$ . Given  $Y$ , it was confirmed numerically that  $\bar{g} \propto \delta^2$  (Fig. 8), that  $\bar{g} \propto \epsilon$  (Fig. 9) where particle momentum spread is low, and that the dependence of  $\bar{g}$  on transverse phase advance is broadly sinusoidal (Fig. 10).

**MOP13**

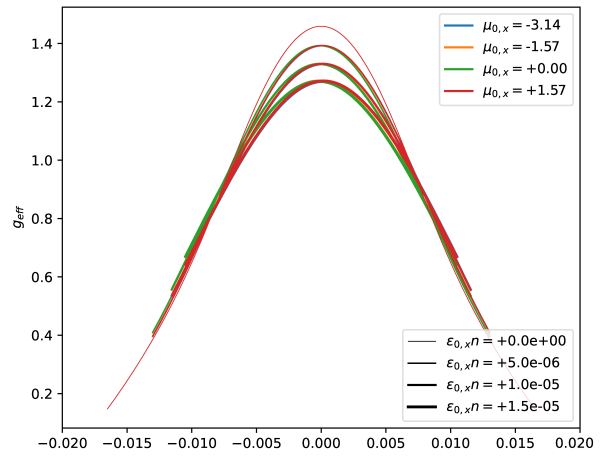


Figure 8: The effective geometry factor  $\bar{g}$  scales with  $\delta^2$  and linearly with emittance  $\epsilon_x$  (line thickness).

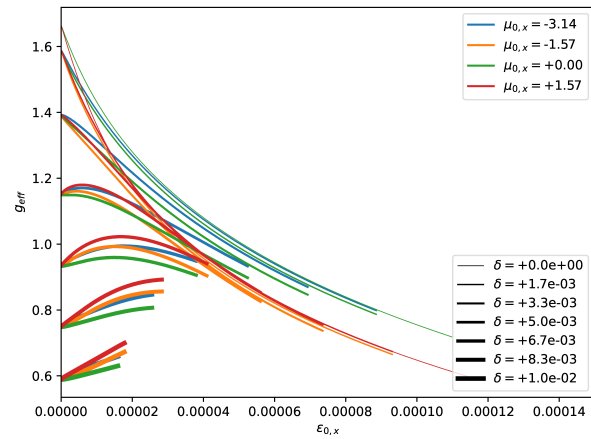


Figure 9: The geometry factor  $\bar{g}$  scales linearly with emittance  $\epsilon_x$  where momentum spread  $\delta$  (line thickness) is low. The domain  $X$  is limited by the aperture radius  $b$ .

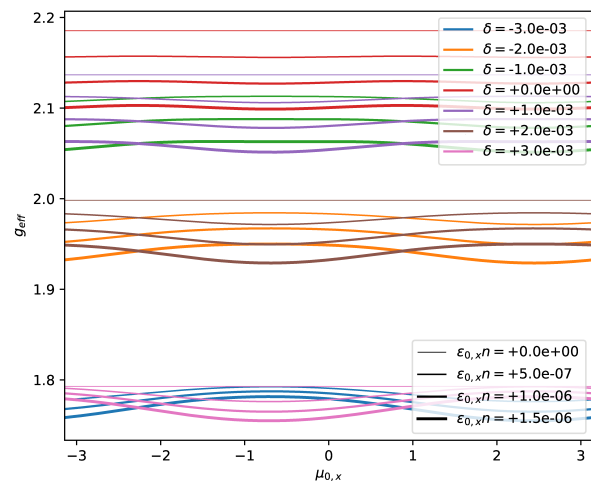


Figure 10: The geometry factor  $\bar{g}$  is sinusoidally dependent on phase advance  $\mu_x$ , however this is dominated by momentum spread  $\delta$  (color) and transverse emittance  $\epsilon_x$  (thickness).

## SIMULATION RESULTS

The Beam Longitudinal Dynamics code (BLonD) has been developed at CERN to track the evolution of an ensemble of particles with intensity effects in synchrotrons [8]. By default, the code incorporates the effects of complex RF harmonic systems by means of RF energy kicks. Each turn, an RF gap of voltage  $V_g$  at harmonic  $h$  will discretely increment a particle's relative kinetic energy change  $w$  given by

$$w = qV(\tau) = q(V_{RF} + V_W), \quad (6)$$

where  $V_{RF} = qV_g(\sin\phi - \sin\phi_s)$  and  $V_W$  is given by Eq. (3) where, in general, space charge can be combined with other impedance sources.

Of the particle properties  $X$  relevant for estimating the geometry factor  $\bar{g}$ , used in Eq. (6), momentum spread  $\delta$  is evaluated once per turn. Because transverse emittance  $\epsilon_x, \epsilon_y$  is assumed to be preserved and phase advance deemed inconsequential, the particle properties follow that

$$X_i(\delta_i, \epsilon_x, \epsilon_y) \rightarrow X_{i+1}(\delta_{i+1}, \epsilon_x, \epsilon_y),$$

where  $i$  indicates the turn number. The tracked beam size  $\bar{a}$ , the momentum spread variance  $\sigma_\delta^2$  can also be evaluated once per turn such that

$$Y_i(\sigma_{\delta,i}, \sigma_\epsilon) \rightarrow Y_{i+1}(\sigma_{\delta,i+1}, \sigma_\epsilon).$$

The evolution of  $\bar{g}_i(X_i, Y_i)$  required to derive  $V_W$  due to space charge was implemented in BLonD. Representative of the PS at flat bottom, a gaussian bunch of length  $4\sigma_\tau = 120$  ns and transverse emittance  $\sigma_\epsilon = 1 \times 10^{-6}$  was tracked against a 22 kV RF voltage source at harmonic 9. The bunch intensity was exaggerated at  $N = 2 \times 10^{12}$  protons to better demonstrate intensity effects.

A particle's synchrotron frequency is computed by taking the FFT of it's tracked phase evolution over time. As depicted in Fig. 11, the nominal synchrotron frequency shift due to space charge is reduced by varying amounts when incorporating transverse motion through the effective geometry factor  $\bar{g}$ . This variance in synchrotron frequency of particles with similar oscillation amplitudes  $\hat{\tau}$  could be described as a "blurring" of synchrotron frequency tune.

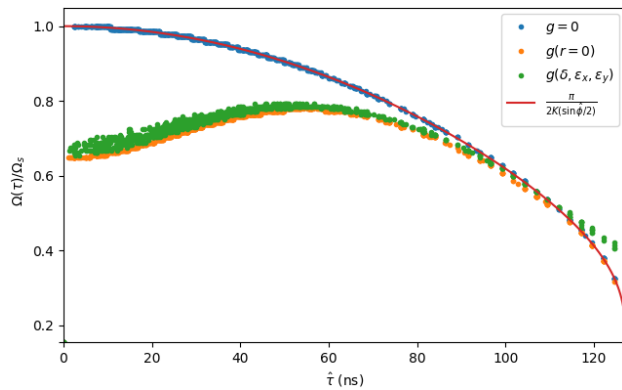


Figure 11: Tune spread (blue), shift (orange) and blur (green) for a long round beam with a uniform transverse distribution and Gaussian longitudinal profile.

In this example, particles tracked in longitudinal phase space will circulate around the bunch center at varying rates independent of oscillation amplitude. The phenomena of filamentation present due to synchrotron frequency spread is seen to be systematically increased and "blurred" when incorporating transverse effects (Fig. 12), suggesting an otherwise overlooked stabilizing phenomenon.

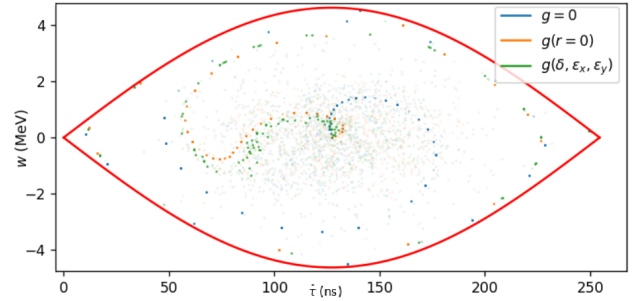


Figure 12: Selected particles, emphasized among a matched distribution, are shown to filament about the bucket center within the separatrix (red) due to tune spread (blue). The effect of space charge tune shift (orange) is observed to be "blurred" when incorporating transverse motion (green).

## CONCLUSIONS

It has been demonstrated that particles at a given longitudinal position will experience varying levels of longitudinal space charge according to an individual particles transverse emittance and momentum spread. Particles with off-axis trajectories will experience less space charge, reducing the space charge tune shift or conversely, increasing the synchrotron frequency. This observed spread in synchrotron frequency may further increase the bulk longitudinal filamentation rate, normally produced by the non-linearities of an accelerating RF voltage alone, which could also contribute to overall beam stability.

Further work might involve designing bunch length oscillation experiments to observe variations in the synchrotron frequency [10] as a function of the transverse beam parameters. Additionally, the description of the effective geometry factor could be further refined by incorporating elliptical geometries, more closely approximating that of the real PS aperture.

## ACKNOWLEDGMENTS

We would like to thank the BLonD development team for discussions and optimizations of the code, A. Huschauer for his development of the PS optics model, and H. Damerau for his advice and guidance.

## REFERENCES

- [1] S. Y. Lee, *Accelerator physics 2nd ed.*, Singapore: World Scientific, 2004.
- [2] M. Ferrario, M. Migliorati, and L. Palumbo, "Space charge effects," CERN, Geneva, Switzerland, CERN-2014-009, pp. 331-356, 2013. doi:10.5170/CERN-2014-009.331

- [3] H. Damerau, A. Lasheen, and M. Migliorati, “Observation and damping of longitudinal coupled-bunch oscillations in the CERN PS,” presented at the ICFA Mini-Workshop “Impedances and Beam Instabilities in Particle Accelerators”, 2018, p. 33. doi:10.23732/CYRCP-2018-001.33
- [4] M. Migliorati, S. Persichelli, H. Damerau, S. Gilardoni, S. Hancock, and L. Palumbo, “Beam-wall interaction in the CERN Proton Synchrotron for the LHC upgrade,” *Phys. Rev. ST Accel. Beams*, vol. 16, p. 031001, 2013. doi:10.1103/PhysRevSTAB.16.031001
- [5] H. Damerau, A. Funken, R. Garoby, S. Gilardoni, B. Goddard, K. Hanke, A. Lombardi, D. Manglunki, M. Meddahi, B. Mikulec, G. Rumolo, E. Shaposhnikova, M. Vretenar, and J. Coupard, “LHC Injectors Upgrade, Technical Design Report,” CERN, Geneva, Switzerland, Tech. Rep. CERN-ACC-2014-0337, 2014. <https://cds.cern.ch/record/1976692>
- [6] J. Coupard, H. Damerau, A. Funken, R. Garoby, S. Gilardoni, B. Goddard, K. Hanke, D. Manglunki, M. Meddahi, G. Rumolo, R. Scrivens, and E. Chapochnikova, “LHC Injectors Upgrade, Technical Design Report,” CERN, Geneva, Switzerland, Tech. Rep. CERN-ACC-2016-0041, 2016. <https://cds.cern.ch/record/2153863>
- [7] O. Aberle *et al.*, “High-Luminosity Large Hadron Collider (HL-LHC): Technical design report”, CERN Yellow Reports: Monographs, CERN, Geneva, Switzerland, CERN-2020-010, 2020. <https://cds.cern.ch/record/2749422>
- [8] “CERN beam longitudinal dynamics code BLonD,” <https://blond.web.cern.ch/>.
- [9] A. Lasheen, H. Damerau, A. Huschauer, and B. K. Popovic, “Longitudinal Microwave Instability Study at Transition Crossing with Ion Beams in the CERN PS”, in *Proc. 12th Int. Particle Accelerator Conf. (IPAC’21)*, Campinas, Brazil, May 2021, pp. 3197–3200. doi:10.18429/JACoW-IPAC2021-WEPAB243
- [10] A. Lasheen, “Longitudinal space charge in the SPS,” CERN, Geneva, Switzerland, Tech. Rep. CERN-ACC-NOTE-2016-0074, 2016. <https://cds.cern.ch/record/2238995>

# THE PS BOOSTER ALIGNMENT CAMPAIGN AND A NEW TUNE CONTROL IMPLEMENTATION AFTER THE LHC INJECTORS UPGRADE AT CERN

F. Antoniou\*, F. Asvesta, H. Bartosik, J-F. Comblin, G. P. Di Giovanni, M. Hostettler, A. Huschauer, B. Mikulec, J. M. Nonglaton, T. Prebibaj<sup>1</sup>, CERN, Geneva, Switzerland  
<sup>1</sup>also at Goethe University, Frankfurt, Germany

## Abstract

The CERN PS Booster (PSB) has gone through major upgrades during the Long Shutdown 2 (LS2) and the recommissioning with beam started in December 2020. Two of the aspects leading to improved operation will be described in this paper: a new tune control implementation; and a full re-alignment campaign. The operation of the PSB requires a large range of working points to be accessible, with a dynamic change of tunes along the acceleration cycle. Before LS2, the PSB tune control was based on an analytical approach assuming linear magnet transfer functions. As part of the LIU project, the PSB main power supply was upgraded to raise the extraction energy from 1.4 GeV to 2 GeV, in order to improve the brightness reach of the downstream machines. A new tune control implementation was necessary to take into account saturation effects of the bending magnets and the reconfiguration of the main circuits, as well as the additional complexity of the new H<sup>-</sup> charge exchange injection. The first part of the paper describes the implementation of the new tune control and its experimental verification and optimization. The second part describes the results of the PSB alignment campaign after LS2, giving emphasis to the method developed to perform a combined closed orbit correction through quadrupole alignments.

## THE NEW PSB TUNE CONTROL

The operation of the PSB requires a large range of working points to be accessible, with a dynamic change of tunes along the acceleration cycle. Pre-LS2, the tune control implementation in the PSB was based on an analytical approach, which assumed linear magnet transfer functions [1]. This approach was proven to give a good agreement between the programmed and the measured machine tune with maximum discrepancies between the two of about  $\Delta Q \approx 0.01$ .

After LS2, the production of the high brightness LHC beams required a raise in the the PSB extraction energy from 1.4 GeV to 2 GeV in order to mitigate space charge effects in the PS. Therefore, the main power supply of the PSB was upgraded as part of the LIU project. Due to the higher operation energies, the main bending magnets of the PSB now operate in their saturation regime. To take into account the increased complexity due to the reconfiguration of the main circuits and the saturation effects of the bending magnets, as well as the additional impact of the new H<sup>-</sup> charge exchange injection [2], a new tune control scheme

was implemented during LS2. This new implementation consists of three main modules:

1. The Q-editor application to set the tune functions along the cycle for each of the four rings of the PSB individually.
2. A make rule “Q → K” for determining the required quadrupole strengths (K) based on the requested tunes (Q). This is using the analytical description of the PSB lattice already employed pre-LS2.
3. A make rule for the translation from the required quadrupole strengths (K) to the respective power supply current (I), as well as the sharing of the power supply current among the different current circuits. This requires as input the calibration curves for the various magnets, taking into account the saturation at high currents and the differences between the magnet transfer functions for inner and outer rings.

## The PSB Main Magnet Circuits

The configuration of the main magnet circuits of the PSB after LS2 is shown in Fig. 1 [3, 4]. It consists of:

- Two dipole circuits: one circuit common for all the bending magnets of the external rings (BR14) and all the 128 QFO focusing quadrupoles for all four rings. The current in this circuit will be denoted as  $I_{b,ext}$ . The other dipole circuit is common for all the bending magnets of the internal rings (BR23) and all the 64 QDE

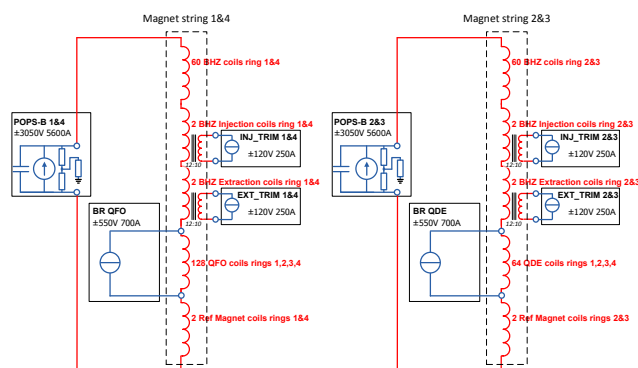


Figure 1: Main PSB power converter circuits after the LIU upgrade [3, 4].

\* fanouria.antoniou@cern.ch

defocusing quadrupoles for all four rings, with the corresponding current denoted as  $I_{b,int}$ .

- Additional trim power converters for the dipoles in the injection and extraction regions to compensate for differences in the calibration curves of these special magnets, that may arise from the modified yoke required for injection/extraction. These trims are individual for each of these magnets and for inner and outer rings.
- Trim power supplies for the QFO and QDE magnets, common for all the four rings, used for the base tune control. The current going through the QFO trim converters will be denoted as  $I_f$ , while the one going through the QDE trim converters as  $I_d$ .
- Q-strip circuits on the focusing (QCF circuit) and defocusing quadrupoles (QCD circuits) with separate circuits for each ring, which can be used for ring-by-ring tune adjustments. The current going through these circuits will be denoted as  $\Delta I_f$  and  $\Delta I_d$ , respectively.
- For the compensation of the beta-beat induced by the injection chicane, there will be two additional fast power supplies for the Q-strips on magnets QDE3 and QDE14 per ring to allow for optics corrections for each ring individually. The Q-strip windings on these magnets are not part of the main Q-strip circuits (QCF and QCD).

### Calibration Curves from Magnetic Measurements

With the new extraction energy in the PSB (2 GeV), the main bending magnets now operate in their saturation regime. As the bending magnets share a common circuit with the quadrupoles, the calibration curves are an important input for the tune control implementation.

During LS2, detailed magnetic measurements were performed for the PSB main bending magnets and the special injection and extraction magnets [5–7]. The following fit function was applied to the measured data for defining the calibration curves of the three types of main magnets for all rings, as proposed in [8]:

$$Bdl = Bdl_{rem} + kI_b \left( 1 - \left( \frac{I_b}{I_0} \right)^n \right), \quad (1)$$

where  $Bdl_{rem}$  is the remnant field at zero current and  $I_b$  the current going through the bending magnets. The parameters  $k$ ,  $I_0$  and  $n$  are defined through a fitting routine. The remnant field is based on magnetic measurements [9].

Figure 2 shows the difference between the measured and fitted integrated field as a function of the excitation current for the main dipoles of Ring 1 (top) and Ring 2 (bottom). The results corresponding to a linear fit are shown in blue, while the ones corresponding to the non-linear fit (Eq. (1)) in orange. The deviation from the linear fit at high currents is due to the saturation of the magnets, which is more pronounced for the external (1 and 4) than the internal (2 and 3) rings. This observation is similar for all rings and for the different types of bending magnets. The fit coefficients of

Eq. (1) are summarized in Table 1 for all types of bending magnets.

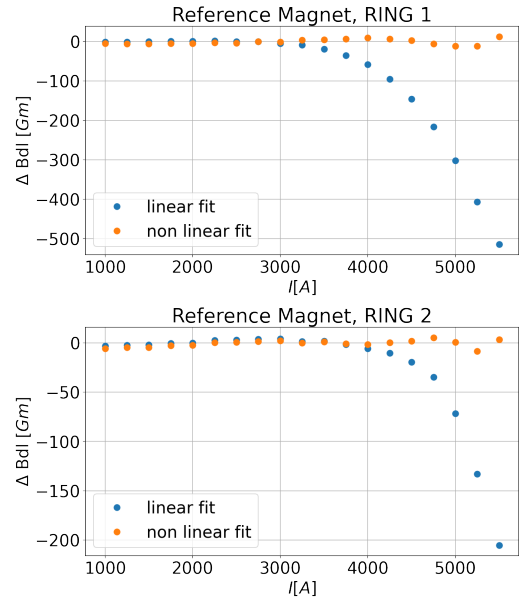


Figure 2: Difference between measured and fitted integrated field as a function of excitation current for the main bending magnets of Ring 1 (top) and Ring 2 (bottom).

Table 1: Fit Coefficients for the Calibration Curves of the PSB Bending Magnets

Dipole type	$I_0$	$k$	$n$
Main (BR23)	8.4911e+3	3.4817e-4	10.3555
Main (BR14)	1.0609e+4	3.4870e-4	5.4973
Special inj. (BR23)	1.6855e+4	3.4824e-4	5.3194
Special inj. (BR14)	1.0014e+4	3.4800e-4	6.1358
Special ext. (BR23)	1.4347e+4	3.4817e-4	5.9844
Special ext. (BR14)	1.0031e+4	3.4815e-4	6.1280

Magnetic measurements were also performed for the focusing (QFO) and defocusing (QDE) quadrupole magnets. A linear fit of the data was applied, as the quadrupoles still operate in their linear regime up to the new extraction energy of 2 GeV.

In the new tune control implementation, the measured calibration curves are taken into account both for the main bending and the quadrupole magnets. The quadrupole strengths as a function of the power supply currents can be written in the more general form:

$$K_{f,i} = \frac{C_{f,i}/L_f}{B\rho} \times (I_{b,ext} + I_f + 0.5 \cdot \Delta I_{f,i}), \quad (2)$$

$$K_{d,i} = \frac{C_{d,i}/L_d}{B\rho} \times (I_{b,int} + I_d + 0.5 \cdot \Delta I_{d,i}),$$

where the index  $i$  refers to the ring number.  $I_{b,int}$  and  $I_{b,ext}$  are the currents in the main circuits passing from the internal ( $i = 2, 3$ ) and external ( $i = 1, 4$ ) rings respectively.  $C_{f,i}$  and  $C_{d,i}$  are the calibration factors of the focusing and

defocusing quadrupoles.  $I_f$  and  $I_d$  are the currents in the trim power supply circuits going through the focusing and defocusing quadrupoles respectively, and they are common for all rings. The factor 0.5 for the currents of the Q-strip power converters  $\Delta I_{f,d}$  is due to the fact that the main coils of the quadrupoles have twice the number of turns compared to the trim coils of the Q-strip circuits. The total current needed from the quadrupole power supplies for achieving the required strengths is obtained by inversion of Eq. (2).

To increase the tuning range in case different tune functions are programmed for each ring, the currents in the QFO and QDE trim power supply circuits common to all rings are chosen as:

$$\begin{aligned} I_f &= \left( \min(I_{f,i})_{i=1-4} + \max(I_{f,i})_{i=1-4} \right) / 2, \\ I_d &= \left( \min(I_{d,i})_{i=1-4} + \max(I_{d,i})_{i=1-4} \right) / 2, \end{aligned} \quad (3)$$

where the max and min is computed among all the rings. The currents  $I_f$  and  $I_d$  will be clamped to the maximum available from the corresponding quadrupole trim power converters.

In the case that ring-by-ring tune adjustments are needed, i.e. if the tune functions per ring are not all the same, the currents in the Q-strips ( $\Delta I_{d,i}$  and  $\Delta I_{f,i}$ ) are used to provide the extra correction on the focusing or defocusing strengths ( $\Delta K_{f,i}$  and  $\Delta K_{d,i}$ ), based again on inversion of Eq. (2).

### Commissioning of the New PSB Tune Control

The new PSB tune control implementation was tested already in the first part of the beam commissioning period. The first checks for the validation of the implementation were done by applying relative tune changes through the tune control application. The measured tune followed the relative changes very well, demonstrating that the new tune control was correctly implemented.

Comparing the absolute values of the set and measured tunes though, showed an increased difference between these values, as well as tune oscillations along the cycle. This initial tune difference as a function of the cycle time is shown in blue in Fig. 3, for R1 (left) and R2 (right). The behavior of R3 and R4 is similar to the ones of R2 and R1 respectively. The observed tune oscillations along the cycle are well correlated with the behavior of the error of the non-linear fit applied over the magnetic measurements, for the computation of the calibration curves [10]. The maximum tune discrepancy goes up to -0.015 in the horizontal plane.

During LS2, the PSB was equipped with a B-train system which distributes the values from a real time B-field measurement, for the accurate measurement and control of the magnetic field in the dipoles. A new calibration curve was thus computed based on the B-train data and the measured excitation currents applied to the tune control. The results are shown in orange in Fig. 3. The tune difference in this case is smaller for R1 and similar in magnitude but opposite in sign for R2. The tune oscillations along the cycle are correlated with the error of the fit, as in the previous case. To avoid these oscillations, a Butterworth filter was applied for smoothing the B-train data and an interpolation between the

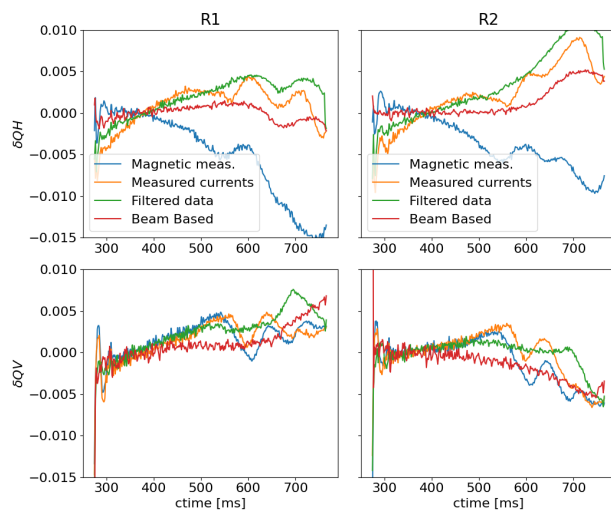


Figure 3: Difference between the set and measured tune as a function of the cycle time, for different calibration curves.

data points was used in the tune control application instead of the fit function. The impact of this calibration curve on the tunes is shown in green in Fig. 3. Indeed, by using the filtered data instead of a fit function, the tune oscillations along the cycle are eliminated.

The observed discrepancies between the set and measured tunes in all rings and in both planes indicate that the magnetic field actually seen by the beam is different both from the original magnetic measurements and the B-train measurements. One possible source that could explain these discrepancies is a time shift between the B-field and excitation current measurements, which can eventually explain an increased tune divergence along the cycle. In an attempt to correct these effects and flatten the tunes along the cycle, simultaneously for all rings, a beam based tune response approach was finally employed. In each time step, the  $\delta K_{f/d,i}$  which corresponds to the measured  $\delta Q$  is calculated, based on MAD-X [11] simulations. Assuming that this  $\delta K_{f/d,i}$  comes only from the calibration curve error, the correction over the smoothed calibration curve was computed based on Eq. (2). The results of these corrected calibration curves are shown in red in Fig. 3. This method led to a better flattening of the tune error for cycle times up to 600 ms. Although, an increase in the tune difference is observed after this time, the maximum discrepancy remains always below  $5 \times 10^{-3}$ . Investigations are ongoing for further simultaneous flattening of the tune error along the cycle, for all 4 rings and both planes.

## THE PS BOOSTER RE-ALIGNMENT CAMPAIGN

The PSB consists of four superposed rings, with the elements sharing the same physical support, as shown in Fig. 4. A tilt of one element would therefore lead to a different horizontal displacement (and thus closed orbit) of the beam for each ring.



Figure 4: The PSB quadrupole stack.

The basic optics cell of the PSB consists of: bending1-QF1-QD-QF2-bending2. Sixteen Beam Position Monitors (BPM) are available in the PSB for orbit measurements, with one BPM available per section which can measure in either plane (H or V). The pickups are installed in between the first focusing quadrupole (QF) and the defocusing quadrupole (QD).

### The PSB Alignment Tool

An alignment tool which takes into account simultaneously the four PSB rings has been developed. The tool follows a very similar approach to the one proposed for the orbit correction in the PSB in 2008 [12]. The minimization procedure is based on the ideal response matrix  $\vec{R}$ , which relates the orbit change at the BPMs ( $\Delta\vec{x}_0, \Delta\vec{y}_0$ ) with the horizontal and vertical displacements of the quadrupoles ( $\Delta\vec{x}, \Delta\vec{y}$ ):

$$\begin{pmatrix} \Delta\vec{x}_0 \\ \Delta\vec{y}_0 \end{pmatrix} = \vec{R} \cdot \begin{pmatrix} \Delta\vec{x} \\ \Delta\vec{y} \end{pmatrix}. \quad (4)$$

As the PSB quadrupoles share the same physical support for all four rings, the quadrupole displacements can not be separately assigned ring-by-ring. The elements of the vectors of the ring-by-ring displacements ( $\Delta\vec{x}_{xi}, \Delta\vec{y}_{yi}$ ) depend linearly on three sets of parameters: the horizontal and vertical displacements and the tilt angles of the quadrupole supports ( $\vec{\alpha}, \Delta\vec{x}, \Delta\vec{y}$ ). Assuming that R3 is the reference ring (the quadrupole supports can be tilted around R3) and with  $\Delta L$  being the vertical distance between two rings (0.36 m), the vector of the ring-by-ring displacements can be written as:

$$\begin{pmatrix} \Delta\vec{x}_1 \\ \Delta\vec{y}_1 \\ \Delta\vec{x}_2 \\ \Delta\vec{y}_2 \\ \Delta\vec{x}_3 \\ \Delta\vec{y}_3 \\ \Delta\vec{x}_4 \\ \Delta\vec{y}_4 \end{pmatrix} = \begin{pmatrix} -2\vec{I} & \vec{I} & \vec{0} \\ \vec{0} & \vec{0} & \vec{I} \\ -\vec{I} & \vec{I} & \vec{0} \\ \vec{0} & \vec{0} & \vec{I} \\ \vec{0} & \vec{I} & \vec{0} \\ \vec{0} & \vec{0} & \vec{I} \\ \vec{I} & \vec{I} & \vec{0} \\ \vec{0} & \vec{0} & \vec{I} \end{pmatrix} \cdot \begin{pmatrix} \Delta L \cdot \vec{\alpha} \\ \Delta x \\ \Delta y \end{pmatrix} = \vec{K} \cdot \begin{pmatrix} \Delta L \cdot \vec{\alpha} \\ \Delta x \\ \Delta y \end{pmatrix}, \quad (5)$$

where  $\vec{I}$  and  $\vec{0}$  the unitary and zero square matrices. Combining (4) and (5), the generalized inversion of the matrix  $\vec{R} \cdot \vec{K}$  is carried out using the Singular Value Decomposition

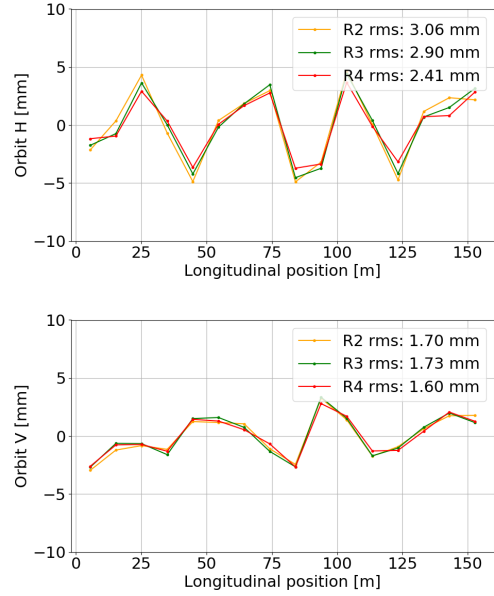


Figure 5: Measured orbits in R2, R3 and R4 in December 2020, before the machine re-alignment.

(SVD) technique and the vector of the required corrections will be given by:

$$\begin{pmatrix} \Delta L \cdot \vec{\alpha} \\ \Delta x \\ \Delta y \end{pmatrix} = -(\vec{R} \cdot \vec{K})^{-1} \cdot \begin{pmatrix} \Delta\vec{x}_{o1} \\ \Delta\vec{y}_{o1} \\ \Delta\vec{x}_{o2} \\ \Delta\vec{y}_{o2} \\ \Delta\vec{x}_{o3} \\ \Delta\vec{y}_{o3} \\ \Delta\vec{x}_{o4} \\ \Delta\vec{y}_{o4} \end{pmatrix} \quad (6)$$

The orbit correction calculation routine is based on the equations described above and was applied in a MICADO-like algorithm [13].

### Re-alignment Campaign after LS2

During LS2, the PSB went through major hardware changes. It was therefore decided to base the realignment proposal on a new orbit measurement campaign, during the PSB recommissioning period after LS2.

The new orbit measurement campaign was performed during the first days of the PSB beam recommissioning period, in December 2020. During this period, the BPM system was available only in R2, R3 and R4. Data were acquired for a flat 160 MeV cycle and a tune working point of  $(Q_H, Q_V) = (4.41, 4.23)$ . Figure 5 shows the rms orbit for R2, R3 and R4 in the horizontal (top) and vertical (bottom) planes. The orbit pattern is very similar to measurements performed in 2018, as expected since the upgrades applied during LS2 should not have an impact on the orbit.

To determine a set of efficient re-alignments for the simultaneous reduction of the bare orbits in all the four PSB

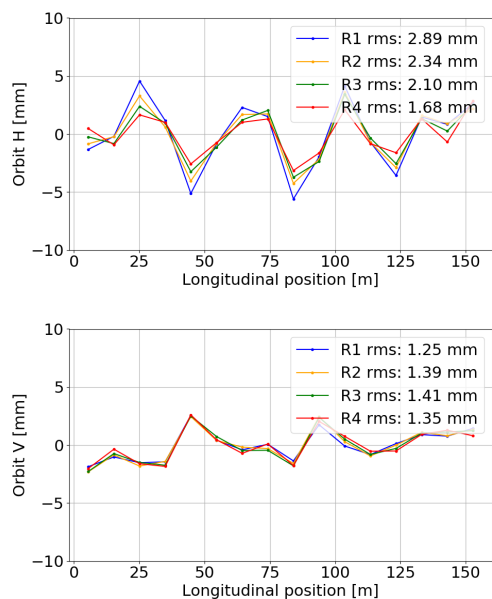


Figure 6: Measured orbits in R1, R2, R3 and R4 in February 2021, after the machine re-alignment.

rings, the horizontal and vertical displacement as well as roll angles of all quadrupoles were considered as potential correction knobs. A horizontal displacement of QDE7 by +1.12 mm and a vertical displacement of QDE13 by +0.19 mm were proposed and finally applied in the machine during the Christmas stop. The measured orbits after the re-alignment are presented in Fig. 6, for the horizontal (top) and vertical (bottom) planes, respectively. A reduction of the orbit was achieved in both planes, following nicely the tool predictions for all rings.

Even though the expected reduction of the orbit was achieved, an important ring-to-ring variation was still observed in the horizontal plane, pointing to possibly one or more roll angle misalignments in the machine.

As mentioned earlier, two special magnets are installed in the injection and extraction regions of each ring. The trim currents to compensate for differences with the main dipoles of the rings are computed based on the calibration curves from magnetic measurements. While for the initial orbit measurement campaign the correction functions for these special magnets were on, the uncertainty on the calibration curves from magnetic measurements led to the decision of switching off this correction for the bare orbit measurements.

The tool was then used to propose one or more re-alignment of elements that would minimize the ring-by-ring horizontal bare orbit differences. Based on this, a tilt of QFO31 by  $d\psi = 1.58$  mrad was proposed and finally applied in the machine during the Technical Stop of April 2021. Figure 7 shows the measured orbits before (top) and after (bottom) the alignment of QFO31 quadrupole. Indeed, this new alignment resulted in very similar orbits in all four rings, as predicted by the tool. The final minimization of the horizontal orbits was performed by using the trim circuits on the special injection and extraction magnets of each ring.

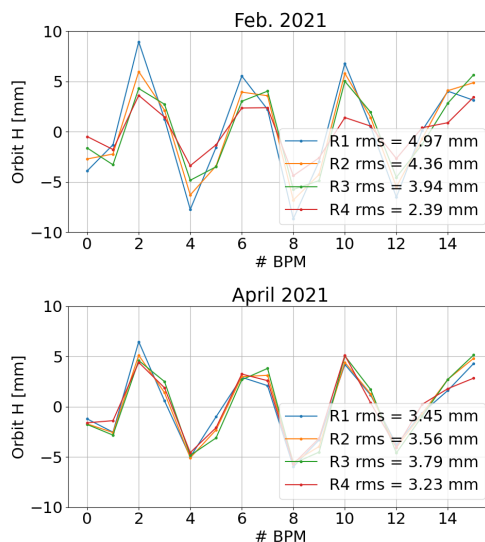


Figure 7: Orbit measurements before (top) and after (bottom) after the second machine re-alignment.

## CONCLUSION

The PS Booster came back into operation in December 2020, after a long shutdown period of two years, where major upgrades were applied to the machine. Two of the aspects leading to improved machine operation were discussed in this paper. A new tune control implementation, which takes into account the reconfiguration of the power supply circuits, the saturation of the main magnets and the increased complexity of the new  $H^-$  injection that was put in place during LS2 and commissioned during the recommissioning period. A successful implementation was demonstrated from the beginning, while a refinement of the calibration curves was required for full optimisation. Currently, the maximum difference between the set and measured tunes is of the order of  $5e-3$ . Further studies are ongoing to identify the source of this discrepancy. In the second part of the paper, the two re-alignment campaigns which took place in 2021 were presented. A minimization of the machine bare orbit was achieved, together with a minimization of the ring-to-ring orbit differences.

## ACKNOWLEDGEMENTS

The authors would like to thank the PSB Operations and commissioning teams for their support during the experiments. We would also like to thank A. Beaumont, A. Newborough and C. Petrone for all their input concerning the magnetic measurements.

## REFERENCES

- [1] J-M. Nonglaton and J-L. Sanchez Alvarez, "PSB Q-strips matrix reloaded", 2003, unpublished.
- [2] E. Renner *et al.*, "Beam Commissioning of the New 160 MeV  $H^-$  Injection System of the CERN PS Booster", in *Proc. 12th Int. Particle Accelerator Conf. (IPAC'21)*, Campinas,

- Brazil, May 2021, pp. 3116–3119. doi:10.18429/JACoW-IPAC2021-WEPAB210
- [3] A. Harle, “Power converters for quadrupole trim in the frameworks of the LIU-PSB project”, EDMS 1971638.
  - [4] L. De Mallac, “Power converters for Qstrip magnets in the framework of the LIU-PSB project”, EDMS 1537264.
  - [5] A. Parrella, J. Vella Wallbank, C. Petrone, R. Chritin, and M. Buzio, “Magnetic measurement results of the magnet PXMBHGC4WP-01000001 for the LIU-PSB project”, EDMS 2397540.
  - [6] A. Parrella, J. Vella Wallbank, C. Petrone, R. Chritin, and M. Buzio, “Magnetic measurement results of the magnet PXMBHGE4WP-CR000003 for the LIU-PSB project”, EDMS 2213120.
  - [7] A. Parrella, J. Vella Wallbank, C. Petrone, R. Chritin, and M. Buzio, “Magnetic measurement results of the magnet PXMBHGD4WP-CR000002 for the LIU-PSB project”, EDMS 2213024.
  - [8] S. Albright, “PS Booster Magnetic Cycles to 1.4 and 2 GeV after LS2”, EDMS 1770413.
  - [9] A. Parrella, J. Vella Wallbank, C. Petrone, R. Chritin, and M. Buzio, “Magnetic measurement results of the magnet PXMBHGC4WP-01000031 for the LIU-PSB project”, EDMS 2332909.
  - [10] F. Antoniou *et al.*, “PSB beam commissioning: Orbits and tunes”, Presentation at ABP Injectors Working Group Meeting, CERN, Geneva, Switzerland, Mar. 2021. <https://indico.cern.ch/event/1013880/contributions/4255843/>
  - [11] L. Deniau, E. Forest, H. Grote and F. Schmidt, computer code MAD-X, 2016. <http://madx.web.cern.ch/madx/>
  - [12] M. Chanel, B. Mikulec, G. Rumolo, R. Tomas, “PS Booster Orbit Correction”, CERN-AB-2008-034 (ABP), unpublished.
  - [13] B. Autin, Y. Marti, “Closed orbit correction of A.G.machines using a small number of magnets”, CERN, Geneva, Switzerland, CERN-ISR-MA-73-17, Mar. 1973.

# THRESHOLD FOR LOSS OF LONGITUDINAL LANDAU DAMPING IN DOUBLE HARMONIC RF SYSTEMS

L. Intelisano\*<sup>1</sup>, H. Damerou, I. Karpov, CERN, Geneva, Switzerland  
<sup>1</sup>Sapienza Università di Roma, Rome, Italy

## Abstract

Landau damping is a natural stabilization mechanism to mitigate coherent beam instabilities in the longitudinal phase space plane. In a single RF system, binomial particle distributions with a constant inductive impedance above transition (or capacitive below) would lead to a vanishing threshold for the loss of Landau damping (LLD), which can be avoided by introducing an upper cutoff frequency to the impedance. This work aims at expanding the recent loss of Landau damping studies to the common case of double harmonic RF systems. Special attention has been paid to the configuration in the SPS with a higher harmonic RF system at four times the fundamental RF frequency, and with both RF systems in counter-phase (bunch shortening mode). Refined analytical estimates for the synchrotron frequency distribution allowed to extend the analytical expression for the loss of Landau damping threshold. The results are compared with semi-analytical calculations using the MELODY code, as well as with macroparticle simulations in BLoND.

## INTRODUCTION

Landau damping [1] provides beam stability to a wide variety of working high beam intensity accelerators. In general, loss of Landau damping (LLD) occurs when the frequency of the coherent bunch oscillations moves outside the incoherent band. In the longitudinal plane, this natural stabilization mechanism is achieved by means of the synchrotron frequency spread which is caused by the nonlinearities of the RF fields. Synchrotron frequency spread, can be enhanced by using multiple RF systems. In particular, higher harmonic RF systems are operated in many accelerators either to change the bunch shape (even split it) or to increase the synchrotron frequency spread inside the bunch, as shown in Fig. 1. In this work we focused mainly on the Super Proton Synchrotron (SPS) configuration namely a 4<sup>th</sup> harmonic RF system (higher harmonic RF system at four times the fundamental RF frequency) and the case above transition energy. For such double harmonic RF systems, the total voltage seen by the particles is defined as:

$$V_{RF}(\phi) = V_0 [\sin(\phi + \phi_{s0}) + r \sin(n\phi + n\phi_{s0} + \Phi_2)], \quad (1)$$

where  $V_0$ ,  $r$  and  $\phi_{s0}$  are respectively the voltage magnitudes of the main harmonic RF system, the voltage ratio between the higher harmonic and the fundamental harmonic RF system, and the phase of the synchronous particle. As far as  $\phi$ ,  $n$  and  $\Phi_2$  are concerned, they represent the phase offset with respect to the synchronous particle, the harmonic number

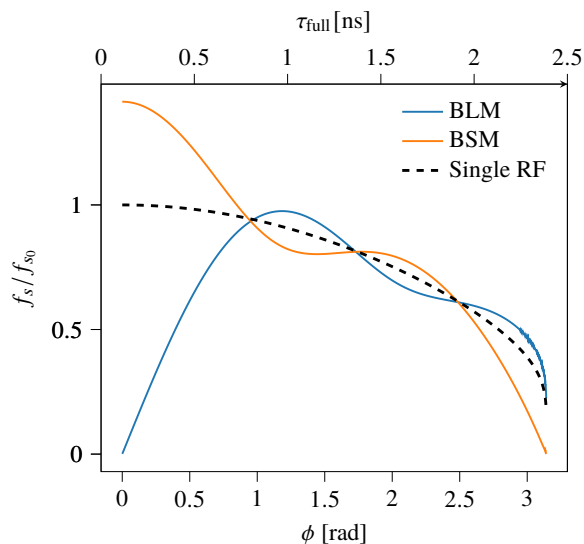


Figure 1: Synchrotron frequency spread normalized to the small-amplitude synchrotron frequency in a single RF system as a function of the maximum phase deviation of the particle. Two different operating modes for the 4<sup>th</sup> harmonic RF system are plotted, for the BSM (orange) and the BLM (blue) with  $r = 0.25$ . The curves are compared with the conventional single RF system case (black dashed line). The axis top concerning the full bunch length  $\tau_{full}$  aims to be a reference for Fig 2.

ratio and the relative phase between the two RF systems. Depending on the relative  $\Phi_2$ , two operating modes are defined; in particular in the case of two RF systems in phase, bunches would get shorter with respect to the single RF system case. This operating mode is called bunch shortening mode (BSM). On the other hand, in the case of both RF systems in counter-phase, one refers to the bunch lengthening operating mode (BLM).

Recent studies [2] prove that for a single RF system, binomial family of particle distributions with a constant inductive impedance  $\text{Im}Z/k$  above transition energy, leads to a vanishing LLD threshold. However, this is avoidable by introducing an upper cutoff frequency  $f_c$  to the impedance. In the present work, an analytical expression of the LLD threshold in BSM, above transition energy, will be derived. Furthermore, its results will be compared with semi-analytical calculations, using the MELODY code [3], and macroparticle simulations in BLoND [4]. Moreover, we will study the LLD by analyzing the offset evolution of the bunch after a rigid-dipole perturbation.

\* leandro.intelisano@cern.ch

## BUNCH SHORTENING MODE ABOVE TRANSITION ENERGY

In this section, we will focus mainly on the LLD in BSM above transition energy. For convenience, the whole analysis is performed with the set of variables  $(\mathcal{E}, \psi)$  for the description of the longitudinal beam dynamics, which correspond respectively to the energy and phase of the synchrotron oscillations.

$$\begin{aligned} \mathcal{E} &= \frac{\dot{\phi}^2}{2\omega_{s0}^2} + U_t(\phi) \\ \psi &= \text{sgn}(\eta\Delta E) \frac{\omega_s(\mathcal{E})}{\sqrt{2}\omega_{s0}} \int_{\phi_{\max}}^{\phi} \frac{d\phi'}{\sqrt{\mathcal{E} - U_t(\phi')}} \end{aligned} \quad (2)$$

where  $\Delta E$  and  $\omega_{s0}$  are the energy offset with respect to the synchronous particle and the angular frequency of small amplitude synchrotron oscillations in single RF,  $\eta = 1/\gamma_{tr}^2 - 1/\gamma^2$  is the slip factor, and  $\gamma_{tr}$  is the Lorentz factor at transition energy. In general, the total potential  $U_t$  is related to the sum voltage Eq. (1) in the following way:

$$U_t(\phi) = \frac{1}{V_0 \cos \phi_{s0}} \int_{\Delta\phi_s}^{\phi} [V_t(\phi') - V_0 \sin \phi_{s0}] d\phi'. \quad (3)$$

The synchronous phase shift  $\Delta\phi_s$  due to intensity effects must satisfy the relation  $V_0 \sin(\phi_{s0}) = V_{RF}(\Delta\phi_s) + V_{\text{ind}}(\Delta\phi_s)$ , where  $V_{\text{ind}}(\Delta\phi_s)$  is the induced voltage.

This work is mainly based on considering particle distribution of a binomial family

$$g(\mathcal{E}) = \left(1 - \frac{\mathcal{E}}{\mathcal{E}_{\max}}\right)^{\mu}, \quad (4)$$

which, depending on  $\mu$ , covers most of the realistic bunch distributions in proton synchrotrons.

### Analytical Equation of the LLD Threshold

In order to derive an analytical expression of the LLD threshold in BSM for the dipole mode, we will follow a similar procedure as in Ref. [2]. The procedure consists of solving the Lebedev equation [5] in presence of a constant inductive impedance  $\text{Im}Z/k = \text{const}$ . We can define the LLD threshold as the point at which the coherent mode frequency  $\Omega$  equals the maximum incoherent frequency; in other words  $\Omega = \max[\omega_s(\mathcal{E})]$ . The general LLD threshold for a binomial distribution can be derived starting equation [2]:

$$\zeta_{\text{th}} = -h \left[ \sum_{k=-\infty}^{\infty} G_{kk}(\Omega) \frac{Z_k(\Omega)/k}{\text{Im}Z/k} \right]^{-1}, \quad (5)$$

where  $G_{kk}(\Omega)$ ,  $h$  and  $\zeta$  represent respectively beam transfer matrices [6], the harmonic number and the dimensionless intensity parameter:

$$\zeta \triangleq -\frac{qN_p h^2 \omega_0 Z_{\text{norm}}}{V \cos \phi_{s0}}. \quad (6)$$

The impedance  $Z_{\text{norm}}$  is an arbitrary normalization factor in units of Ohm.

An analytical expression for the synchrotron frequency spread, as a function of the energy of synchrotron oscillations, can be derived from the oscillation period shown on the right hand side of the second equation (2). Thus, since  $\omega_s(\mathcal{E}) = 2\pi/T_s(\mathcal{E})$ , for short bunches, we obtain [7]:

$$\frac{\omega_s(\mathcal{E})}{\omega_{s0}} = \sqrt{1+nr} \left(1 - \frac{1+nr^3}{(1+nr)^2} \frac{\mathcal{E}}{8}\right). \quad (7)$$

Therefore, considering the first azimuthal mode (dipole mode;  $m = 1$ ), LLD in BSM occurs when  $\Omega = \omega_s(0)$ ; where for Eq. (7)  $\omega_s(0) = \omega_{s0} \sqrt{1+nr}$ . Furthermore, considering only the dipole mode, the matrix  $G_{kk}(\Omega)$  can be written as:

$$G_{kk}(\Omega) = -i \frac{\omega_{s0}}{\pi A_N} \int_0^{\mathcal{E}_{\max}} \frac{dg(\mathcal{E})}{d\mathcal{E}} \frac{|I_{1k}(\mathcal{E})|^2}{\Omega - \omega_s(\mathcal{E})} d\mathcal{E}, \quad (8)$$

with the normalization factor

$$A_N = \omega_{s0} \int_0^{\mathcal{E}_{\max}} \frac{g(\mathcal{E})}{\omega_s(\mathcal{E})} d\mathcal{E}. \quad (9)$$

As far as the function  $I_{mk}$  [5] is concerned, it is expressed as

$$I_{1k}(\mathcal{E}) = \frac{1}{2\pi} \int_{-\pi}^{\pi} e^{i\frac{k}{h}\phi(\mathcal{E},\psi) - i\psi} d\psi. \quad (10)$$

In the case of small amplitude, the integral can be reduced to the Bessel function of the first kind:

$$I_{1k}(\mathcal{E}) \approx iJ_1 \left( \frac{k}{h} \sqrt{\frac{2}{1+nr}} \mathcal{E} \right). \quad (11)$$

Equations (8) can be evaluated analytically and used to deduce the threshold Eq. (10) for the BSM case. However, for  $\text{Im}Z/k = \text{const}$ , it leads to a vanishing threshold  $\zeta_{\text{th}} = 0$ . Hence, in order to avoid this zero LLD threshold, we considered a finite cutoff frequency  $f_c$  to the impedance, obtaining:

$$\zeta_{\text{th}} \approx \frac{1+nr^3}{(1+nr)^{1/2}} \frac{\pi \phi_{\max}^5 h}{32\mu(\mu+1)\chi(k_{\max}\phi_{\max}/h, \mu)}; \quad (12)$$

where  $\phi_{\max}$  represents the maximum phase deviation or, equivalently, the bunch length in radians (full bunch length  $\tau_{\text{full}} = [\phi_{\max}(\mathcal{E}) - \phi_{\min}(\mathcal{E})]/\omega_{RF}$ ). The function  $\chi(y, \mu)$ , is related to the generalized hypergeometric function, according to:

$$\chi(y, \mu) = y \left[ 1 - {}_2F_3 \left( \frac{1}{2}, \frac{1}{2}; \frac{3}{2}, 2, \mu; -\frac{y^2}{1+nr} \right) \right]. \quad (13)$$

Analysing Eq. (12), we can notice that the LLD threshold depends on the voltage ratio and the order  $n$  of the harmonic RF system. In the case of switching off the second RF system ( $r = 0$ ), Eq. (12) simplifies to the LLD threshold for the single RF system case [2]. In Fig. 2 we compared the LLD

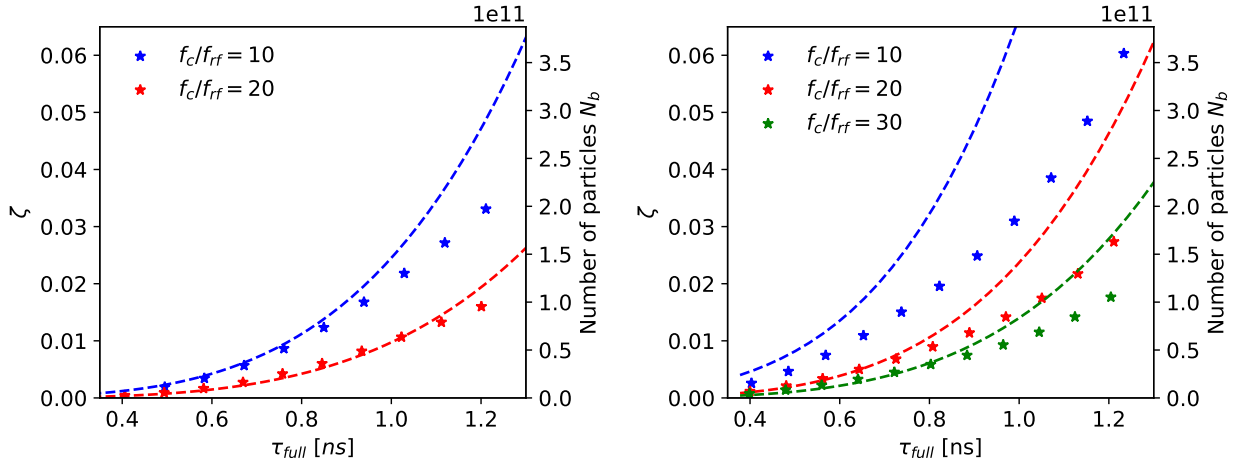


Figure 2: The LLD threshold, for the 2<sup>nd</sup> (left;  $n = 2$ ) and for the 4<sup>th</sup> (right;  $n = 4$ ) harmonic RF system case, as a function of the full bunch length. The thresholds, using MELODY for different impedance cutoff frequencies, are calculated. The analytical predictions are shown as dashed lines and computed based on  $Z_{\text{norm}} = 0.07$  Ohm,  $r = 0.25$  and  $\mu = 2$ .

thresholds, as a function of the full bunch length, for different cutoff frequencies. On the left figure, we can observe that the 2<sup>nd</sup> harmonic case (Fig. 2, left) is in good agreement with the exact solution computed with MELODY for the two different cutoff frequencies. On the other hand, the 4<sup>th</sup> harmonic case (Fig. 2, right) shows that the agreement is less good when decreasing the cutoff frequency. This is due to the fact that the threshold Eq. (12) does not hold for high intensities. Furthermore, we can observe that the LLD threshold depends inversely on the frequency cutoff, which is consistent with the case of the single RF system above transition energy [2].

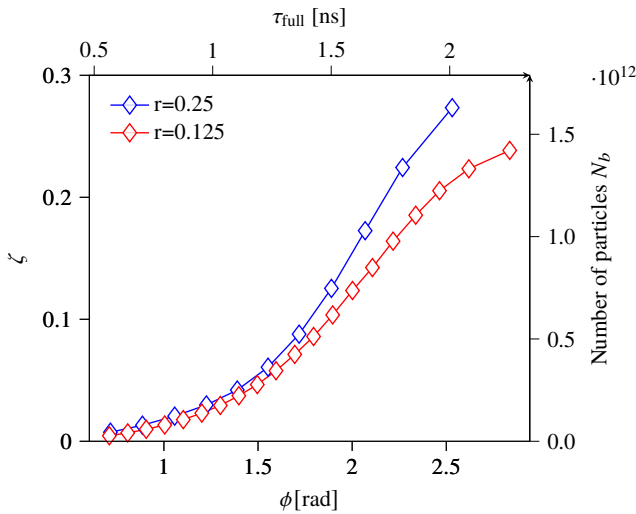


Figure 3: The LLD threshold as a function of the bunch length. The thresholds are computed for the voltage ratio  $r = 0.25$  (blue) and  $r = 0.125$  (red) by considering  $Z_{\text{norm}} = 0.07$  Ohm with a cutoff at  $f_c = 4$  GHz and  $\mu=2$ .

Figure 3 shows that for even longer bunch length, the LLD threshold preserves its monotonic behaviour. This is in contradiction with what has been observed in Ref. [8] which observed a decrease of the LLD threshold along the portion for which the derivative of the frequency distribution is positive (Fig. 1). However, it must be pointed out that in Ref. [8] a different definition of LLD threshold, based on kick, has been used. Moreover, note in Fig. 3 that we could not study the LLD damping beyond a certain intensity. In fact, since the induced voltage of an inductive impedance has a defocusing behaviour on the total potential well, the bunch intensity is limited by the bucket acceptance. In that case, the LLD damping threshold goes to infinity.

### Comparison with Simulations

In this subsection, the results of MELODY were compared with macroparticle simulations performed in BLonD. As an example, we used the LHC parameters, listed in Table 1, to simplify the comparison with the results presented in Ref. [2]. In particular, since azimuthal modes are represented by particular frequencies emerging from the incoherent oscillation band, we looked at the spectrum of the mean value of the bunch position. A bunch with  $10^6$  macroparticles was generated, matched with intensity effects and then tracked for  $10^6$  turns (in order to have a good frequency resolution of the spectrum and to cover a sufficient number of synchrotron oscillations). Finally, fast Fourier transform of the bunch mean values of the bunch position have been performed to move in the frequency domain.

In Fig. 4, the normalized mode frequencies for different intensities were reported, using both MELODY and BLonD. The comparison was performed considering a constant inductive impedance  $Z_{\text{norm}} = 0.07$  Ohm and a cutoff frequency  $f_c = 4$  GHz. The computation was repeated for different bunch lengths, in order to cover the most interesting region

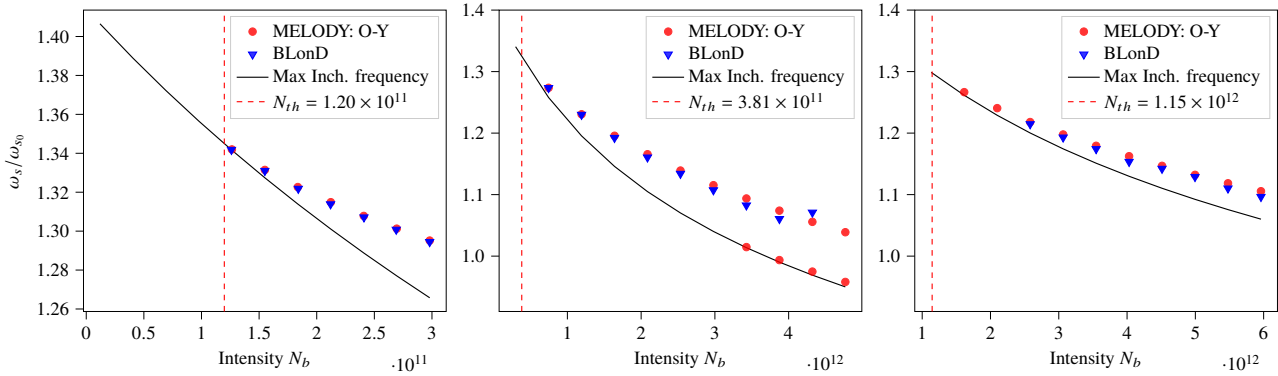


Figure 4: The real part of the normalized mode frequency was found from MELODY, by means of the Oide-Yokoya (O-Y) method [9], and from macroparticle simulations (BLonD) as a function of bunch intensity. The comparison was performed considering a constant inductive impedance with  $\text{Im}Z/k = 0.07 \Omega$  and frequency cutoff  $f_c = 4 \text{ GHz}$ . Results for three different bunch lengths,  $\phi_{\text{max}} = 1.0 \text{ rad}$  (left),  $\phi_{\text{max}} = 1.5 \text{ rad}$  (centre) and  $\phi_{\text{max}} = 2.0 \text{ rad}$  (right), have been reported to scan different parts of the frequency distribution (Fig.1).

of the synchrotron frequency distribution (Fig.1). A good agreement between macroparticle simulations and semianalytical calculations has been observed, and as expected, coherent dipole modes emerging from the maximum incoherent frequency (black line) can be noticed. Since at the LLD threshold the frequency of the coherent mode equals the maximum incoherent frequency, the modes close to the threshold cannot be discriminated properly from the incoherent band. This explains the missing data for  $\phi_{\text{max}} = 2.0$  and in the case of the second emerged mode for  $\phi_{\text{max}} = 1.5$ .

Table 1: Machine Parameters [10]

Parameter	Values
Circumference	26658.86 m
Main harmonic number, $h$	35640
Main RF frequency, $f_{\text{RF}}$	400.79 MHz
Beam energy $E_0$	0.45 TeV
Main RF voltage $V_0$	6 MV
Normalization factor, $Z_{\text{norm}}$	0.07 Ohm

### Beam Response to a Dipole Kick

Observation of the beam response to a kick is a common way to study LLD in either measurements or simulations. In order to simulate a rigid-dipole kick, an instant shift of the bunch position by 1 degree has been introduced at the beginning of the macroparticle simulation. Afterwards, the bunch evolution, up to  $5 \times 10^4$  turns, has been tracked turn by turn. For simulations, the same parameters in Table 1 and  $10^6$  macroparticles have been applied. We want to point out that considering a constant inductive impedance with a truncation at  $f_c$ , leads to a ringing behaviour of the induced voltage in front and after the bunch. However, since no blow-up was observed, it should not have much impact on the bunch evolution.

Figure 5 shows that, after an initial offset, the bunch position evolution for  $\phi_{\text{max}} = 1.0$  (left) and  $\phi_{\text{max}} = 1.5$  (cen-

tre), with intensities below the LLD thresholds, are quickly damped as predicted. Instead, for larger bunch lengths, in this case for  $\phi_{\text{max}} = 2.0$ , Figure 5 indicates a counter-intuitive behavior.

We used an analysis based on expansion of the initial perturbation on a basis of van Kampen modes [11, 12] as in Ref. [2]. We observe that at low intensity the damping time can be very long. At higher intensities, the initial damping becomes faster, but the residual oscillation amplitude remains small. The detailed analysis will be presented in an upcoming publication.

## CONCLUSION

Landau Damping plays a significant role in beam stabilization. In this work, we focused on the LLD studies for the double harmonic RF system. In particular, special attention has been paid to the 4<sup>th</sup> harmonic RF system, in BSM. Starting from a constant inductive impedance, with a certain upper cutoff frequency, an analytical expression of the LLD damping for the binomial distribution has been derived. This expression agrees with the semianalytical code MELODY showing a good agreement for both 2<sup>nd</sup> and 4<sup>th</sup> harmonic cases. However, we observed a significant loss of accuracy for  $f_c/f_{\text{RF}} < 10$  due to the fact that the threshold equation is not applicable for high intensities. Furthermore, MELODY confirmed that the LLD threshold depends inversely on cut-off frequency of the impedance, as observed in the past for single RF systems, and it remains monotonic even for longer bunches length. A comparison between semianalytical calculation and simulation has been set up, showing a very good agreement between the two approaches.

We moved on to evaluate the beam response to a rigid-dipole kick and observing the behaviour of Landau damping under this condition. Particle tracking simulations show that bunches below the threshold are quickly damped as predicted. Exceptions for long bunches have been observed, for which, counterintuitively, bunches with higher intensity

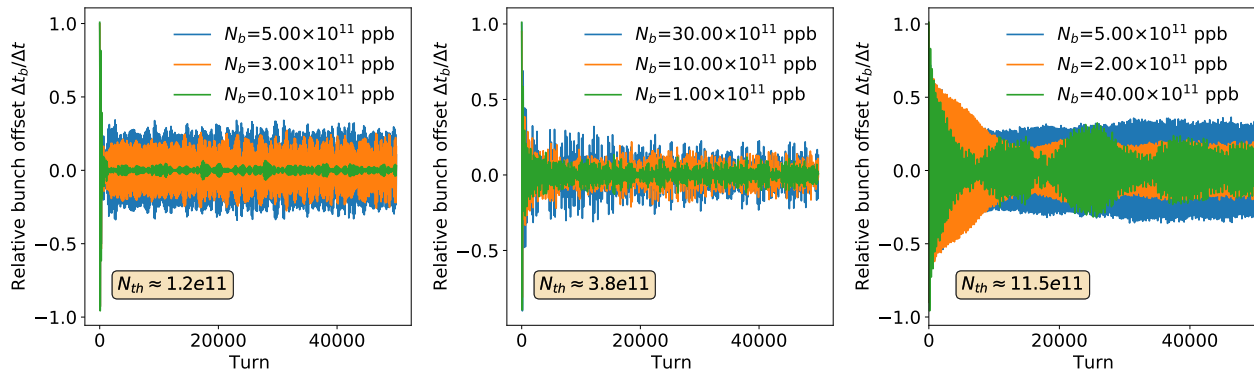


Figure 5: Simulated bunch offset evolution at different intensities, after an initial dipole kick of one degree, with an inductive impedance of  $Z_{\text{norm}} = 0.07 \Omega$  and  $f_c = 4$  GHz. Three different bunch lengths, respectively for  $\phi_{\text{max}} = 1.0$  rad (left),  $\phi_{\text{max}} = 1.5$  rad (centre) and  $\phi_{\text{max}} = 2.0$  rad (right) have been considered. For this latter case,  $10^7$  macroparticles (instead of  $10^6$ ) have been chosen to avoid high statistical noise. In all three cases, the respective LLD thresholds in the box have also been reported.

than the LLD threshold, are damped more than those below the threshold. This behavior can be understood by expanding the perturbations on the basis of van Kampen modes.

## REFERENCES

- [1] L. D. Landau, “On the vibrations of the electronic plasma”, *J. Phys. (Moscow)*, vol. 10, p. 25, 1946.
- [2] I. Karpov, T. Argyropoulos, and E. Shaposhnikova, “Thresholds for loss of Landau damping in longitudinal plane”, *Phys. Rev. Accel. Beams*, vol. 24, p. 011002, 2021. doi:10.1103/PhysRevAccelBeams.24.011002
- [3] I. Karpov, “Matrix equations for longitudinal beam dynamics (MELODY) code”, <https://gitlab.cern.ch/ikarpov/melody/>.
- [4] CERN beam longitudinal dynamics code BLonD, <http://blond.web.cern.ch/>.
- [5] A. N. Lebedev, “Coherent synchrotron oscillations in the presence of a space charge”, *Soviet Atomic Energy*, vol. 25, p. 851, 1968. doi:10.1007/BF01121037
- [6] E. Shaposhnikova, “Bunched beam transfer matrices in single and double rf systems”, Technical Report No. CERN-SL-94-19-RF, CERN, Geneva, Switzerland, 1994.
- [7] P. Bramham, S. Hansen, A. Hofmann and P. Peschardt, “Active Landau Cavity on the 4th Harmonic of the RF Frequency”, ISR Performance Report, CERN, Geneva, Switzerland, 1977.
- [8] A. Theodoros, “Longitudinal beam instabilities in a double RF system”, Ph.D. Thesis, Natl. Tech. U., Athens, 2015.
- [9] K. Oide and K. Yokoya, “Longitudinal single bunch instability in electron storage rings”, Technical Report, No. KEK-Preprint-90, KEK, Tsukuba, Japan, 1990.
- [10] O. Brüning *et al.*, LHC Design Report Vol.1: The LHC main ring, CERN, Geneva, Switzerland, Tech. Rep. CERN-2004-003-V-1, Jun.2004.
- [11] N. G. van Kampen, “On the theory of stationary waves in plasmas”, *Physica (Utrecht)*, vol. 21, p. 949, 1955. doi:10.1016/S0031-8914(55)93068-8
- [12] N. G. van Kampen, “The dispersion equation for plasma waves”, *Physica (Utrecht)*, vol. 23, p. 641, 1957. doi:10.1016/S0031-8914(57)93718-7

# NEW ANALYTICAL CRITERIA FOR LOSS OF LANDAU DAMPING IN LONGITUDINAL PLANE

I. Karpov\*, T. Argyropoulos, E. Shaposhnikova, CERN, Geneva, Switzerland  
 S. Nese, University of Bergen, Bergen, Norway

## Abstract

Landau damping is a very important stabilization mechanism of beams in circular hadron accelerators. In the longitudinal plane, Landau damping is lost when the coherent mode is outside of the incoherent synchrotron frequency spread. In this paper, the threshold for loss of Landau damping (LLD) for constant inductive impedance  $\text{Im}Z/k$  is derived using the Lebedev matrix equation (1968). The results are confirmed by direct numerical solutions of the Lebedev equation and using the Oide-Yokoya method (1990). For more realistic impedance models of the ring, new definitions of an effective impedance and the corresponding cutoff frequency are introduced which allow using the same analytic expression for the LLD threshold. We also demonstrate that this threshold is significantly overestimated by the Sacherer formalism based on the previous definition of an effective impedance using the eigenfunctions of the coherent modes.

## INTRODUCTION

The loss of Landau damping [1] has been observed in operations of different accelerators (Tevatron [2], RHIC [3], SPS [4] and LHC [5]) and has been studied for many years using different approaches [6–16]. A general way to analyze beam stability is to solve the Vlasov equation linearized for a small perturbation of a stationary particle distribution function. The first self-consistent system of equations suitable for the eigenvalue analysis of longitudinal beam stability was proposed by Lebedev in 1968 [6]. In the recent paper [17], we derived an analytic expression for the LLD threshold in the presence of the constant reactive impedance  $\text{Im}Z/k$  using the Lebedev equation. It agrees with the LLD threshold determined numerically by solving the two matrix equations: the Lebedev matrix equation and the Oide-Yokoya equation [18]. In this paper, we present the derivation of the LLD threshold which based on a novel method to compute an effective impedance with an effective cutoff frequency. This allows to evaluate the LLD threshold for complicated impedance models (like the one of the CERN SPS).

## MAIN EQUATIONS AND DEFINITIONS

We consider the case of a single RF system, for the sake of simplicity, while the derivations can be adapted to other RF waveforms. The Lebedev equation can be written using variables  $(\mathcal{E}, \psi)$ , which correspond respectively to the

energy and phase of the synchrotron oscillations,

$$\mathcal{E} = \frac{\phi^2}{2\omega_{s0}^2} + U_t(\phi), \quad (1)$$

$$\psi = \text{sgn}(\eta \Delta E) \frac{\omega_s(\mathcal{E})}{\sqrt{2}\omega_{s0}} \int_{\phi_{\max}}^{\phi} \frac{d\phi'}{\sqrt{\mathcal{E} - U_t(\phi')}}. \quad (2)$$

Here,  $\Delta E$  and  $\phi$  are respectively the energy and phase deviations of the particle from the synchronous particle,  $\eta = 1/\gamma_{\text{tr}}^2 - 1/\gamma^2$  is the slip factor,  $\gamma_{\text{tr}}$  is the Lorentz factor at transition energy, and  $f_{s0} = \omega_{s0}/2\pi$  is the frequency of small-amplitude synchrotron oscillations in a bare RF potential. The total potential can be obtained from the sum voltage  $V_t$

$$U_t(\phi) = \frac{1}{V_0 \cos \phi_{s0}} \int_{\Delta\phi_s}^{\phi} [V_t(\phi') - V_0 \sin \phi_{s0}] d\phi', \quad (3)$$

where  $V_0$  is the RF voltage amplitude, and  $\phi_{s0}$  is the synchronous phase. The synchronous phase shift due to intensity effects  $\Delta\phi_s$  satisfies the relation  $V_0 \sin \phi_{s0} = V_0 \sin(\phi_{s0} + \Delta\phi_s) + V_{\text{ind}}(\Delta\phi_s)$ , where  $V_{\text{ind}}$  is the induced voltage. In practice,  $U_t$  can be obtained for an arbitrary impedance model thanks to an iterative procedure [15]. Then it can be used to compute the synchrotron frequency as a function of the energy of synchrotron oscillations  $\omega_s(\mathcal{E}) = 2\pi/T_s(\mathcal{E})$  in Eq. (2) from the period of oscillations including intensity effects.

Below we will consider particle distributions belonging to a binomial family  $g(\mathcal{E}) = (1 - \mathcal{E}/\mathcal{E}_{\max})^\mu$ . For a finite  $\mu$ , which is usually the case for proton bunches, a full length  $\tau_{\text{full}}$  is defined as

$$\tau_{\text{full}} = [\phi_{\max}(\mathcal{E}_{\max}) - \phi_{\min}(\mathcal{E}_{\max})] / \omega_{\text{RF}}. \quad (4)$$

## Lebedev Equation

Using the variable and notations described above, an infinite system of equations for harmonics of the line density perturbation  $\tilde{\lambda}$  at frequency  $\Omega$  [6], can be written as

$$\tilde{\lambda}_p(\Omega) = -\frac{\zeta}{h} \sum_{k=-\infty}^{\infty} G_{pk}(\Omega) \frac{Z_k(\Omega)/k}{Z_{\text{norm}}} \tilde{\lambda}_k(\Omega), \quad (5)$$

which we refer to as the Lebedev equation. Here,  $\zeta$  is the dimensionless *intensity* parameter,

$$\zeta = -\frac{qN_p h^2 \omega_0 Z_{\text{norm}}}{V_0 \cos \phi_{s0}}, \quad (6)$$

$Z_{\text{norm}}$  is the impedance normalization factor in units of Ohms, which can be arbitrarily chosen (see also Table 1). The

\* ivan.karpov@cern.ch

elements  $G_{pk}$ , called beam transfer matrices [19] are

$$G_{pk}(\Omega) = -i \frac{\omega_{s0}}{\pi A_N} \times \sum_{m=1}^{\infty} \int_0^{\xi_{\max}} \frac{dg(\xi)}{d\xi} \frac{I_{mk}(\xi) I_{mp}^*(\xi) \omega_s(\xi)}{\Omega^2/m^2 - \omega_s^2(\xi)} d\xi \quad (7)$$

where  $p$  and  $k$  are the revolution frequency harmonics,  $m$  is the azimuthal mode number ( $m = 1$ : dipole mode,  $m = 2$ : quadrupole mode, etc.), the normalization factor for the distribution function is

$$A_N = \omega_{s0} \int_0^{\xi_{\max}} \frac{g(\xi)}{\omega_s(\xi)} d\xi, \quad (8)$$

and

$$I_{mk}(\xi) = \frac{1}{2\pi} \int_{-\pi}^{\pi} \exp \left[ i \frac{k}{h} \phi(\xi, \psi) - im\psi \right] d\psi, \quad (9)$$

with  $h$  the harmonic number. Note that the elements  $G_{pk}$  depend on intensity parameter  $\zeta$  as they are found after the stationary problem is solved.

The solution of Lebedev equation for particular  $\Omega$  and  $\zeta$  exists if the determinant of the following matrix is zero

$$D(\Omega, \zeta) = \det \left[ \delta_{pk} + \frac{\zeta}{h} G_{pk}(\Omega) \frac{Z_k(\Omega)/k}{Z_{\text{norm}}} \right] = 0. \quad (10)$$

Below we will show how this criterion can be used to determine the LLD threshold.

### Threshold of Loss of Landau Damping

In this subsection, we will derive the LLD thresholds in a general case for the binomial family of particle distributions and dominating inductive impedance above transition energy  $\eta \text{Im}Z/k > 0$  (or space charge below transition).

Analyzing solutions of the dispersion integral obtained from the Vlasov equation for an infinite plasma, N. G. van Kampen [20, 21] found that they have continuous and discrete parts. In application to longitudinal beam dynamics, at low intensities ( $\zeta \approx 0$ ), all van Kampen modes remain within the continuous spectrum,  $\Omega = m\omega_s(\xi)$ . Landau damping results then from the phase mixing of these modes which do not represent the collective motion of the particles. Above the threshold the discrete van Kampen modes emerge from the continuous spectrum, implying that Landau damping is lost [9].

For the dipole mode ( $m = 1$ ), the LLD threshold  $\zeta_{\text{th}}$  is reached when there is a coherent mode whose frequency  $\Omega$  equals the maximum incoherent frequency  $\hat{\omega}_s = \max[\omega_s(\xi)]$ , i.e.,  $\Omega = \hat{\omega}_s$ . This implies that for any infinitesimally small increase of intensity this mode will move outside the incoherent frequency band. At low intensities, the synchrotron frequency distribution in a single RF system is a monotonic function of the energy of synchrotron oscillations  $\xi$ . Assuming that still holds at the LLD threshold for a dipole mode  $m = 1$ , we can search for a value of the parameter  $\zeta$ , at which  $\Omega = \hat{\omega}_s = \omega_s(0)$  is a solution of Eq. (5). Since, as follows from definition (9),  $I_{mk}(0) = 0$ ,

the integral (7) defining the elements  $G_{pk}$  converges for all  $p$  and  $k$ .

The solution of the Lebedev equation can be found thanks to the following property of the matrix

$$\det [\exp(\varepsilon X)] = \exp[\varepsilon \text{tr}(X)], \quad (11)$$

where  $\text{tr}(X)$  is the trace of an arbitrary square matrix  $X$ , and  $\varepsilon$  is the small parameter  $\varepsilon \ll 1$ , which will be defined later. Consider that  $X$  also depends on  $\varepsilon$ ,  $X(\varepsilon) = X(0) + \varepsilon(dX/d\varepsilon)(0) + \dots$ , expansion up to the first order of  $\varepsilon$  yields,

$$\det [I + \varepsilon X(\varepsilon)] = \det (\exp \{ \ln [I + \varepsilon X(\varepsilon)] \}) \\ = \exp (\text{tr} \{ \ln [I + \varepsilon X(\varepsilon)] \}) \approx 1 + \varepsilon \text{tr} [X(0)], \quad (12)$$

with the identity matrix  $I$ . Thus, we get a general expression for the LLD threshold from Eq. (10)

$$\zeta_{\text{th}} = -h \left[ \sum_{k=-\infty}^{\infty} G_{kk}(\Omega) \frac{Z_k(\Omega)/k}{\text{Im}Z/k} \right]^{-1}. \quad (13)$$

Naturally, the parameter  $\varepsilon \propto \zeta$ . Its dependence on the bunch length will be deduced below. Thus,  $G_{kk}$  needs to be evaluated at zero intensity, as inclusion of potential well distortion will already result in keeping a higher-order term of the parameter  $\varepsilon$ .

In the present work, the elements  $G_{kk}$  are calculated analytically for short bunches in a single RF system, while similar derivations for the double RF system can be found in [22]. Keeping only one element of the sum over azimuthal harmonics ( $m = 1$ ), from Eq. (7) we can obtain  $G_{kk}$  at the LLD threshold ( $\Omega = \omega_{s0}$ )

$$G_{kk} \approx i \frac{16\mu(\mu+1)}{\pi \phi_{\max}^4} \left[ 1 - {}_1F_2 \left( \frac{1}{2}; 2, \mu; -y^2 \right) \right], \quad (14)$$

where  ${}_pF_q(a_1, \dots, a_p; b_1, \dots, b_q; z)$  is the generalized Hypergeometric function with  $y = k\phi_{\max}/h$ , and  $\phi_{\max}$  corresponds to a half bunch length expressed in radians. These matrix elements can be presented as a combination of Bessel functions for the particular values of  $\mu$ . For example, in the case of  $\mu = 1/2$ ,  $\mu = 1$ , and  $\mu = 2$ , one obtains  $G_{kk} \propto [1 - J_1(2y)/y]$ ,  $G_{kk} \propto [1 - J_0^2(y) - J_1^2(y)]$ , and  $G_{kk} \propto [1/2 - J_0^2(y) - J_1^2(y) + J_0(y)J_1(y)/y]$ , respectively. As  $G_{kk} \propto 1/\phi_{\max}^4$ , we can now define the small parameter

$$\varepsilon = \zeta/\phi_{\max}^4$$

and check the validity of expansion (12) later by comparison with exact semi-analytic calculations.

For the case of the inductive impedance  $Z_k = ikZ_{\text{norm}}$ , the sum in Eq. (13) can also be analytically evaluated by approximating it with an integral

$$\frac{1}{h} \sum_{k=-\infty}^{\infty} G_{kk}(\Omega) \frac{Z_k(\Omega)/k}{Z_{\text{norm}}} \approx \frac{i}{h} \int_{-\infty}^{\infty} G_{kk}(\Omega) dk \rightarrow \infty,$$

which diverges for  $\mu > 0$ . This can be easily seen from the asymptotic behavior of the elements  $G_{kk}$  as they saturate at

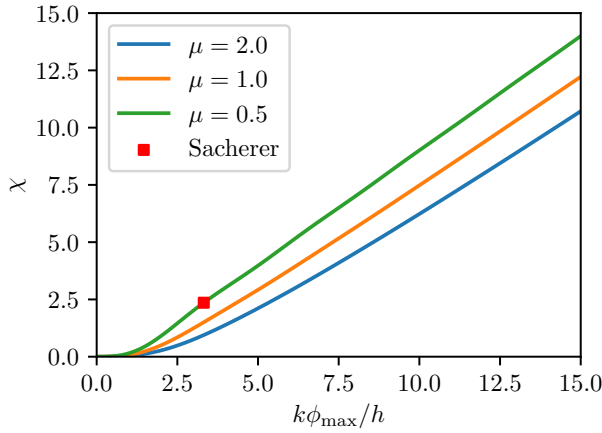


Figure 1: Examples of the function  $\chi(k\phi_{\max}/h, \mu)$  defined by Eq. (17) for three different distribution functions from the binomial family ( $\mu = 0.5, 1,$  and  $2$ ). The values  $k\phi_{\max}/h$ , for which the LLD thresholds corresponds to that used in Sacherer [7] criterion, is shown with a square.

a constant value for larger  $k$ . Once we have truncated the sum at arbitrary  $k_{\max}$ , the LLD threshold becomes

$$\zeta_{\text{th}} = \frac{\pi \phi_{\max}^5}{32\mu(\mu+1)\chi(k_{\max}\phi_{\max}/h, \mu)}, \quad (15)$$

or in terms of intensity

$$N_{p,\text{th}} = -\frac{\pi V_0 \cos \phi_{s0} \phi_{\max}^5}{32qh^2 \omega_0 \mu(\mu+1)\chi(k_{\max}\phi_{\max}/h, \mu)Z_{\text{norm}}}, \quad (16)$$

where we introduced the function

$$\chi(y, \mu) = y \left[ 1 - {}_2F_3 \left( \frac{1}{2}, \frac{1}{2}; \frac{3}{2}, 2, \mu; -y^2 \right) \right]. \quad (17)$$

Examples of this function for different  $\mu$  values are shown in Fig. 1.

For  $\mu = 1/2$ , the Sacherer formalism proposes the LLD threshold which can be written in our notations [23]

$$\zeta_{\text{th,S}} = \phi_{\max}^5 / 18. \quad (18)$$

It can be recovered from Eq. (15) for  $y_{\max} \approx 3.32$  (see also Fig. 1). This means that for a given bunch length the commonly used criteria Eq. (18) is accurate only for the special choice of the cutoff frequency  $f_c \approx 1/\tau_{\text{full}}$ . Based on this, for space charge below transition energy with a rather high cutoff frequency, the LLD threshold will be significantly overestimated for bunches with  $\tau_{\text{full}} \gg 1/f_c$ . Instead, our criteria Eq. (15) gives a simplified expression

$$\zeta_{\text{th}} \approx \frac{\pi \phi_{\max}^4 h}{32\mu(\mu+1)k_{\max}}, \quad (19)$$

since the generalized Hypergeometric function  ${}_2F_3$  approaches zero for  $y \rightarrow \infty$ . One can see that the threshold is inversely proportional to the cutoff frequency, and the fifth power in the dependence on the bunch length is replaced by the fourth.

Table 1: The Machine and RF Parameters of the LHC at Injection Energy and of the SPS at Extraction Energy [25]

Parameter	Units	LHC	SPS
Circumference, $C$	m	26658.86	6911.55
Harmonic number, $h$		35640	4620
Transition gamma, $\gamma_{\text{tr}}$		55.76	17.95
RF frequency, $f_{\text{RF}}$	MHz	400.79	200.39
Beam energy, $E_0$	TeV	0.45	0.45
RF voltage, $V_0$	MV	6	7.2
Norm. factor, $Z_{\text{norm}}$	Ohm	0.07	1

## COMPARISON WITH MELODY CODE

The analytic threshold according to Eq. (15) can be compared with semi-analytical results obtained using code MELODY (Matrix Equations for LOngitudinal beam DYnamics calculations) [24] in applications to the LHC and SPS. The main accelerator parameters are listed in Table 1. In calculations based on the Lebedev equation (5), the determinant  $D(\hat{\omega}_s, \zeta)$  is numerically evaluated for different  $\zeta$  changed iteratively until condition Eq. (10) is satisfied.

In the Oide-Yokoya method [18], the Vlasov equation is converted into a matrix equation and its eigenvalues are calculated as a function of the intensity parameter  $\zeta$ . To find the threshold, the difference between the maximum eigenfrequency and the maximum incoherent frequency is evaluated. The threshold corresponds to the intensity where the difference vanishes (see details in [17]).

### Inductive Impedance

Here we will first show the results for the truncated inductive impedance  $Z_k = ikZ_{\text{norm}}$  for  $|k| < k_{\max}$  and  $Z_k = 0$  elsewhere. Figure 2 shows the LLD threshold as a function of the full bunch length calculated for two different cutoff frequencies using analytic equation (15) and code MELODY. One can see that numerical results obtained using the Oide-Yokoya method and the Lebedev equation agree, with the maximum 2% relative error in the covered bunch-length range. They are close to the analytic expression (15), while, as expected, there is some discrepancy for larger bunch lengths since the analytic threshold was derived in short-bunch approximation while still taking the synchrotron frequency spread into account. We also observe that the dependence on the bunch length is even slightly weaker than the fourth power. The dependence on the cutoff frequency can be also seen in Fig. 2 and results, for two values of the unperturbed bunch length with increasing cutoff frequencies, in Fig. 3. It confirms the vanishing of the LLD threshold for  $f_c \rightarrow \infty$ .

### Effective Impedance

Above we discussed the results for a truncated inductive impedance, while in reality the impedance could be a much more complicated function of frequency. An example of

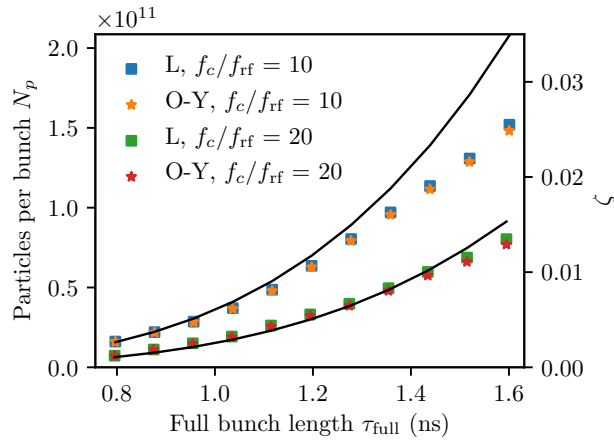


Figure 2: The LLD intensity threshold as a function of the full bunch length  $\tau_{\text{full}}$  calculated using the Lebedev equation (5) and the Oide-Yokoya method for different cutoff frequencies ( $f_c = k_{\text{max}}f_0$ ) of the inductive impedance. The analytic predictions from Eq. (15) are plotted as solid lines. Case of  $\eta > 0$  and other parameters are  $Z_{\text{norm}} = 0.07$  Ohm,  $V_0 = 6$  MV, and  $\mu = 2$ . The corresponding intensity parameter  $\zeta$  is shown on the second vertical axis.

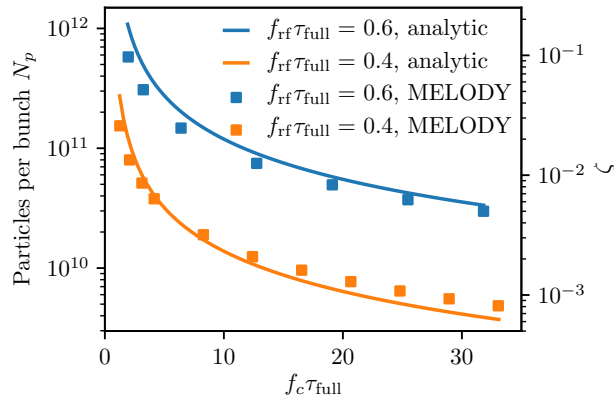


Figure 3: LLD intensity threshold in the logarithmic scale as a function of the cutoff frequency of a reactive impedance  $f_c = k_{\text{max}}f_0$  (multiplied by the full bunch length  $\tau_{\text{full}}$ ) for two different values of  $\tau_{\text{full}}$ . The analytic predictions from Eq. (15) are shown as solid lines and the results of semi-analytic calculations using MELODY as squares. Parameters as in Fig. 2. The corresponding intensity parameter  $\zeta$  is shown on the second vertical axis.

the SPS impedance model [26] is shown in Fig. 4. We aim to comprise the frequency dependence of a particular impedance model in just two numbers:  $(\text{Im}Z/k)_{\text{eff}}$ , the equivalent (effective) value of the inductive impedance and  $k_{\text{eff}}$ , the corresponding effective cutoff frequency. In Ref. [17] we proposed the following definition of the effective impedance

$$(\text{Im}Z/k)_{\text{eff}} = \frac{\sum_{k=-k_{\text{eff}}}^{k_{\text{eff}}} G_{kk} \text{Im}(Z_k/k)}{\sum_{k=-k_{\text{eff}}}^{k_{\text{eff}}} G_{kk}}, \quad (20)$$

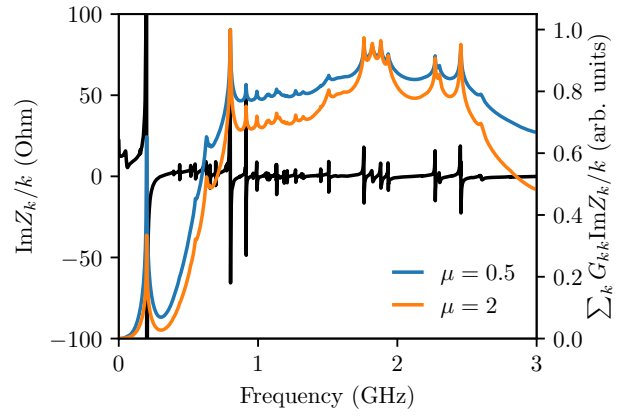


Figure 4: The present SPS reactive impedance model  $\text{Im}Z/k$  (black curve) after the impedance reduction campaign during the 2<sup>nd</sup> Long Shutdown (LS2) 2019-2020. The values of the cumulative sum used for calculation of the effective impedance (20) are shown as blue ( $\mu = 0.5$ ) and orange ( $\mu = 2$ ) curves ( $\phi_{\text{max}} = 2$ ).

while  $k_{\text{eff}}$  was chosen such that  $\text{Im}Z_k/k < 0$  for  $k > k_{\text{eff}}$ . Then the LLD threshold can be written as

$$\zeta_{\text{th}} = \frac{\pi \phi_{\text{max}}^5}{32 \mu (\mu + 1) \chi(k_{\text{eff}} \phi_{\text{max}}/h, \mu)} \frac{Z_{\text{norm}}}{(\text{Im}Z/k)_{\text{eff}}}, \quad (21)$$

and in terms of intensity one gets

$$N_{p,\text{th}} = - \frac{\pi V_0 \cos \phi_{s0} \phi_{\text{max}}^5}{32 q h^2 \omega_0 \mu (\mu + 1) \chi(k_{\text{eff}} \phi_{\text{max}}/h, \mu) (\text{Im}Z/k)_{\text{eff}}}. \quad (22)$$

This formula was successfully verified for the case of a single broadband resonator impedance with quality factor  $Q = 1$  and different values of the resonant frequency  $f_r$ .

In the recent study [27], further investigations were done for the impedance defined as a sum of broadband and narrowband resonator impedance models

$$Z_k = \frac{R}{1 + iQ \left( \frac{kf_0}{f_r} - \frac{f_r}{kf_0} \right)} + \frac{R_2}{1 + iQ_2 \left( \frac{kf_0}{f_{r,2}} - \frac{f_{r,2}}{kf_0} \right)} \quad (23)$$

with shunt impedances  $R = Z_{\text{norm}} Q f_r / f_0$ , and  $R_2 = Z_{\text{norm}} Q_2 f_{r,2} / f_0$ , respectively. To study the impact of the impedance of the resonance structure with the resonant frequency below the cutoff frequency of the main broadband impedance, the systematic analysis of different cases with various  $Q_2 \in [1, 1000]$  and  $f_{r,2} \in (0, f_r)$  was performed. As the result, a new definition of the effective cutoff frequency was suggested

$$k_{\text{eff}} = \arg \max \sum_{k'=0}^k G_{k'k'} \text{Im}(Z_{k'}/k'), \quad (24)$$

which corresponds to a value of  $k$  for which the maximum of the cumulative sum is reached. For a single broadband resonator both old and new methods give the same effective cutoff frequency. For the SPS impedance model the cumulative sum of expression Eq. (24) is presented in Fig. 4,

which reaches the maximum value at  $k_{\text{eff}}f_0 \approx 0.8$  GHz (for  $\phi_{\text{max}} \approx 1$ ). In Fig. 5, the analytic prediction (21) for a smooth distribution with  $\mu = 2$  is compared with the full semi-analytic calculations using MELODY. The maximum error is about 40% for long bunches which is only slightly larger than for the case of a simple constant inductive impedance  $\text{Im}Z/k = Z_{\text{norm}}$  (see Fig. 2).

It is worth to compare this new definition of the effective impedance with the one based on the Sacherer formalism  $(\text{Im}Z/k)_{\text{eff,S}}$ . This formalism requires to find a set of orthogonal coherent modes for a given distribution. Then, the effective impedance is computed as a sum of their power spectral harmonics multiplied by  $\text{Im}Z_k/k$ . For parabolic bunches ( $\mu = 0.5$ ) and dipole mode one gets [23]

$$(\text{Im}Z/k)_{\text{eff,S}} = \sum_{k=-\infty}^{\infty} \frac{J_{3/2}^2(k\phi_{\text{max}}/h)}{|k\phi_{\text{max}}/h|} \text{Im}(Z_k/k) / \sum_{k=-\infty}^{\infty} \frac{J_{3/2}^2(k\phi_{\text{max}}/h)}{|k\phi_{\text{max}}/h|}, \quad (25)$$

so that the LLD threshold is  $\zeta_{\text{th,S}} = \phi_{\text{max}}^5/18 \times Z_{\text{norm}}/(\text{Im}Z/k)_{\text{eff,S}}$ . As expected for very short bunches Sacherer criterion agrees with threshold (21) and MELODY results, while for longer bunches it significantly overestimates the LLD threshold (see Fig. 5). However, we also see a non-monotonic behavior of the LLD threshold obtained using MELODY for this particle distribution. This can be understood from the fact that distribution with  $\mu = 0.5$  has abrupt tails which affect the synchrotron frequency  $\omega_s(\mathcal{E})$  as a function of the synchrotron oscillation energy via potential well distortion and its derivative  $d\omega_s(\mathcal{E})/d\mathcal{E}$  can become a non-monotonic function. This was also observed for a simplified impedance model (23), where the discrepancy between MELODY and analytic predictions was due to potential well distortion [27]. If this type of distribution is expected in operation, we suggest firstly to estimate the LLD threshold using Eq. (21) and then to check the presence of non-monotonic behavior of the derivative of the synchrotron frequency as a function of the synchrotron oscillation energy.

## CONCLUSION

Loss of Landau damping (LLD) in the longitudinal plane can be an important performance limitation of existing and future synchrotrons. In the present paper, the analytic expression for the LLD threshold of the dipole oscillations is discussed for the case of a single RF system and a particle distribution of the binomial family.

The new analysis shows that the LLD threshold is zero for a constant inductive impedance  $\text{Im}Z/k$  above transition (the LHC case) or capacitive (space charge) below. Once a finite cutoff frequency is introduced, the threshold becomes inversely proportional to the cutoff frequency  $f_c$  for  $f_c \gg 1/\tau_{\text{full}}$  ( $\tau_{\text{full}}$  is the full bunch length). We have confirmed this dependence by solving the Lebedev matrix equation semi-analytically as well as using the Oide-Yokoya method, also showing that both numerical methods agree

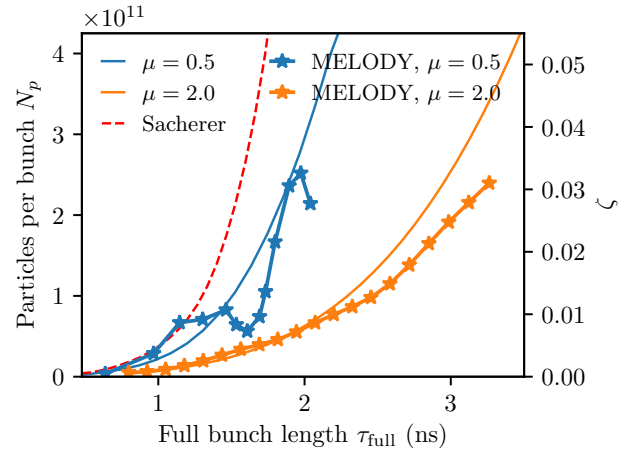


Figure 5: The LLD threshold as a function of bunch length for the SPS impedance model (Fig. 4). The stars connected with lines are calculated by MELODY. The lines are the prediction from the analytical formula (21). The red curve is LLD threshold calculated using Sacherer effective impedance (25). Case of  $\eta > 0$  and other parameters are  $Z_{\text{norm}} = 1$  Ohm,  $V_0 = 7.2$  MV. The corresponding intensity parameter  $\zeta$  is shown on the second vertical axis.

extremely well. The commonly used dependence of the LLD threshold on the bunch length to the fifth power is justified only in the low cutoff-frequency limit ( $f_c \leq 1/\tau_{\text{full}}$ ). The LLD threshold obtained by the Sacherer approach can be reproduced only when  $f_c \approx 1/\tau_{\text{full}}$ . The dependence of the threshold on the bunch length changes to the power of four for the case of a higher cutoff frequency ( $f_c \gg 1/\tau_{\text{full}}$ ).

We introduced a new definition of the effective impedance and the corresponding cutoff frequency to estimate the LLD threshold of more complicated impedance models. It does not require finding a set of the orthogonal modes which is essential for the Sacherer formalism. For the case of a smooth particle distribution function ( $\mu = 2$ ) and the impedance model of the CERN SPS the agreement of analytic expression with full semi-analytic calculations is very good. For parabolic bunches ( $\mu = 0.5$ ), the deviations are larger due to impact of potential well distortion. We also have shown that the Sacherer definition of the effective impedance can significantly overestimate the LLD threshold, especially for the bunch lengths  $\tau_{\text{full}} > 1/f_c$ .

## ACKNOWLEDGEMENTS

We thank Alexey Burov for useful discussions and comments.

## REFERENCES

- [1] L. D. Landau, "On the vibrations of the electronic plasma," *J. Phys. (USSR)* 10, vol. 25, no. 2, p. 574, 1946.
- [2] R. Moore, V. I. Balbekov, A. Jansson, V. A. Lebedev, K. Y. Ng, V. D. Shiltsev, and C. Y. Tan, "Longitudinal

- bunch dynamics in the Tevatron,” in *Proc. 20th Particle Accelerator Conf. (PAC’03)*, Portland, Oregon, USA, May 2003, paper TPPB066, pp. 1751–1753.
- [3] M. Blaskiewicz, J. M. Brennan, P. Cameron, W. Fischer, J. Wei, A. Luque, and H. Schamel, “Longitudinal solitons in RHIC,” in *Proc. 20th Particle Accelerator Conf. (PAC’03)*, Portland, OR, USA, May 2003, paper RPPB008, pp. 3029–3031. doi:10.1109/PAC.2003.1289803
- [4] E. N. Shaposhnikova, “Cures for beam instabilities in the CERN SPS and their limitations”, in *Proc. 39th ICFA Advanced Beam Dynamics Workshop on High-Intensity and High-Brightness Hadron Beams (HB’06)*, Tsukuba, Japan, May-Jun. 2006, paper TUBX05, pp. 153–155.
- [5] E. Shaposhnikova, T. Argyropoulos, T. Bohl, C. Bhat, P. Baudrenghien, A. Butterworth, T. Mastoridis, J. Muller, G. Papotti, J. Tuckmantel, and W. V. Del-solaro, “Loss of Landau Damping in the LHC”, in *Proc. 2nd Int. Particle Accelerator Conf. (IPAC’11)*, San Sebastian, Spain, Sep. 2011, paper MOPC057, pp. 211–214.
- [6] A. N. Lebedev, “Coherent synchrotron oscillations in the presence of a space charge,” *Atomic Energy*, vol. 25, no. 2, pp. 851–856, 6 1968. doi:10.1007/BF01121037
- [7] F. J. Sacherer, “A longitudinal stability criterion for bunched beams,” *IEEE Transactions on Nuclear Science*, vol. 20, no. 3, pp. 825–829, 1973. doi:10.1109/TNS.1973.4327254
- [8] G. Besnier, “Stabilité des oscillations longitudinales d’un faisceau groupe se propageant dans une chambre a vide d’impedance reactive,” *Nuclear Instruments and Methods*, vol. 164, no. 2, pp. 235–245, 1979. doi:10.1016/0029-554X(79)90241-6
- [9] Y. H. Chin, K. Satoh, and K. Yokoya, “Instability of a bunched beam with synchrotron frequency spread,” *Particle Accelerators*, vol. 13, pp. 45–66, 1983.
- [10] E. Keil and W. Schnell, “Concerning longitudinal stability in the ISR,” CERN, Geneva, Switzerland, Tech. Rep. CERN-ISR-TH-RF-69-48, 7 1969.
- [11] V. I. Balbekov and S. V. Ivanov, “The influence of chamber inductance on the threshold of longitudinal bunched beam instability,” in *Proc. 2nd European Particle Accelerator Conf. (EPAC’90)*, Nice, France, Jun. 1990, pp. 1566–1569.
- [12] A. Hofmann and F. Pedersen, “Bunches with local elliptic energy distributions,” *IEEE Transactions on Nuclear Science*, vol. 26, no. 3, pp. 3526–3528, 6 1979. doi:10.1109/TNS.1979.4330088
- [13] O. Boine-Frankenheim and T. Shukla, “Space charge effects in bunches for different rf wave forms,” *Phys. Rev. ST Accel. Beams*, vol. 8, p. 034201, 3 2005. doi:10.1103/PhysRevSTAB.8.034201
- [14] O. Boine-Frankenheim and O. Chorniy, “Stability of coherent synchrotron oscillations with space charge,” *Phys. Rev. ST Accel. Beams*, vol. 10, p. 104202, 10 2007. doi:10.1103/PhysRevSTAB.10.104202
- [15] A. Burov, “Van Kampen Modes for Bunch Longitudinal Motion”, in *Proc. 46th ICFA Advanced Beam Dynamics Workshop on High-Intensity and High-Brightness Hadron Beams (HB’10)*, Morschach, Switzerland, Sep.-Oct. 2010, paper TUO1C03, pp. 358–362.
- [16] A. Burov, “Dancing Bunches as van Kampen Modes”, in *Proc. 24th Particle Accelerator Conf. (PAC’11)*, New York, NY, USA, Mar.-Apr. 2011, paper MOODS4, pp. 94–96.
- [17] I. Karpov, T. Argyropoulos, and E. Shaposhnikova, “Thresholds for loss of landau damping in longitudinal plane,” *Phys. Rev. Accel. Beams*, vol. 24, p. 011002, 1 2021. doi:10.1103/PhysRevAccelBeams.24.011002
- [18] K. Oide and K. Yokoya, “Longitudinal single bunch instability in electron storage rings,” KEK, Tech. Rep. KEK-Preprint-90-10, 1990.
- [19] E. Shaposhnikova, “Bunched beam transfer matrices in single and double rf systems,” CERN, Geneva, Switzerland, Tech. Rep. CERN-SL-94-19-RF, 8 1994.
- [20] N. G. Van Kampen, “On the theory of stationary waves in plasmas,” *Physica*, vol. 21, no. 6, pp. 949–963, 1955. doi:10.1016/S0031-8914
- [21] N. G. Van Kampen, “The dispersion equation for plasma waves,” *Physica*, vol. 23, no. 6, pp. 641–650, 1957. doi:10.1016/S0031-8914
- [22] L. Intelisano, H. Damerau, and I. Karpov, “Threshold for Loss of Longitudinal Landau Damping in Double Harmonic RF Systems,” presented at 64th ICFA Advanced Beam Dynamics Workshop on High-Intensity and High-Brightness Hadron Beams, Batavia, IL, USA, 2021, this conference.
- [23] K. Y. Ng, *Physics of Intensity Dependent Beam Instabilities*. World Scientific, Singapore, 2006. doi:10.1142/5835
- [24] I. Karpov, matrix Equations for LOngitudinal beam DYnamics (MELODY) code, <https://gitlab.cern.ch/ikarpov/melody/>.
- [25] O. Brüning, P. Collier, P. Lebrun, S. Myers, R. Ostojic, J. Poole, and P. Proudlock, “LHC design report vol.1: The LHC main ring,” CERN, Geneva, Switzerland, Tech. Rep. CERN-2004-003-V-1, 6 2004. doi:10.5170/CERN-2004-003-V-1
- [26] CERN SPS Longitudinal Impedance Model, <https://gitlab.cern.ch/longitudinal-impedance/SPS/>.
- [27] S. Nese, “Effective impedance for the threshold of loss of Landau damping,” CERN, Geneva, Switzerland, Tech. Rep. CERN-STUDENTS-Note-2021-214, 2021.

# END-TO-END LONGITUDINAL SIMULATIONS IN THE CERN PS

A. Lasheen\*, H. Damerou, K. Iliakis, CERN, Geneva, Switzerland

## Abstract

In the context of the LHC Injector Upgrade (LIU) project, the main longitudinal limitations in the CERN PS are coupled bunch instabilities and uncontrolled emittance blow-up leading to losses at injection into the downstream accelerator, the SPS. To complement beam measurements, particle tracking simulations are an important tool to study these limitations. However, to avoid excessive runtime, simulations are usually targeting only a fraction of the cycle assuming that bunches are initially matched to the RF bucket. This ignores all initial perturbations that could seed an instability. Simulations were therefore performed along the full PS cycle by using the BLonD tracking code optimized with advanced parallelization schemes. They include beam manipulations with several RF harmonics (batch compression, merging, splittings), controlled emittance blow-up, a model of the beam coupling impedance covering a wide frequency range, as well as beam and cavity feedbacks. A large number of macroparticles is required as well as arrays to store beam induced voltage spanning several revolutions to account for long range wakefields.

## INTRODUCTION

The main target of the High Luminosity (HL)-LHC project is to increase the luminosity for collisions by an order of magnitude [1]. This objective relies on an increased beam brightness from the injectors, which were upgraded in the framework of the LHC Injector Upgrade (LIU) project [2]. The beam intensity shall be doubled. However, at high beam current, limitations arise due to collective effects such as beam instabilities or uncontrolled emittance blow-up.

In the PS, the two main longitudinal limitations to reach the target of  $N_b = 2.6 \times 10^{11}$  protons per bunch (p/b) at extraction are coupled bunch instabilities along the ramp (dipolar and quadrupolar) as well as uncontrolled longitudinal emittance blow-up due to high frequency cavity impedance [3, 4]. The longitudinal emittance should be kept at the nominal value of  $\epsilon_l = 0.35$  eVs at extraction to fit in the rf bucket of the SPS, the final stage in the LHC injector chain. Therefore, extensive studies were conducted to find means to mitigate beam instabilities.

An essential tool for beam instability studies are macroparticle simulations. Previously the simulations were done targeting only a specific instance in the cycle to keep the runtime reasonable (hours to couple of days). An example is the study of dipolar coupled bunch instabilities where simulations were initially performed at constant beam energy [5]. The initial particle distribution then needs to be assumed as matched to the initial RF bucket or with an arbitrary mismatch. In reality mismatches accumulate all along the

cycle and can seed the onset of an instability. They should therefore be taken into account to better reproduce the instability threshold. For example, coupled bunch instabilities start after transition crossing where an initial perturbation is expected, while simulations were originally started with matched conditions during the ramp.

Several studies could benefit from tracking simulations covering a complete cycle. An example is the operation with a higher harmonic RF cavity as Landau RF system to damp instabilities [6]. The present option consists of using the narrow-band 40 MHz cavity along the ramp. However, due to the limited bandwidth of the system, the complete acceleration ramp cannot be covered in such an operation mode. Tracking simulations covering the whole ramp, including transition crossing, were hence needed to evaluate the necessity of a dedicated Landau RF system.

Another aspect is the generation of particles at large amplitude in the longitudinal phase space (referred to as "longitudinal halo"), beyond the 0.35 eVs amplitude at extraction which are lost at SPS injection. The generation of halo can occur at several stages during the cycle and may accumulate. The optimization of the bunch rotation prior to extraction then requires a good knowledge of the halo. A simulation covering the whole cycle is needed to evaluate the impact of each stage in the cycle in terms of halo generation.

In this paper, the particle tracking code BLonD was extended in order to take into account several aspects such as a dynamic beam coupling impedance model, the influence of feedback systems, as well as a complete representation of the cycle including all processes and RF manipulations. The simulation is then compared to measurements. Finally, the computing performances are detailed.

## MODELING THE COMPLETE ACCELERATION CYCLE

Beams with various longitudinal parameters can be generated in the PS. In the context of this paper, the so-called BCMS-type beam (Batch Compression Merging Splitting) produced for the LHC is considered [7]. The complete momentum and RF voltage programs are shown in Fig. 1. In this configuration, 8 bunches are injected from the PS Booster in two consecutive injections spaced by 1.2 s. The beam is then accelerated to an intermediate energy plateau where RF manipulations are performed. The beam is thereafter accelerated to the top energy, passing through transition crossing. The beam is then split again four times and non-adiabatically shortened before extraction to fit in the 5 ns SPS RF bucket (bunch rotation). Along the cycle, the longitudinal emittance is adjusted by applying controlled blow-up [8].

The complete program was simulated using the BLonD tracking code [9] including all the RF manipulations and controlled blow-ups, with the same voltage programs as

\* alexandre.lasheen@cern.ch

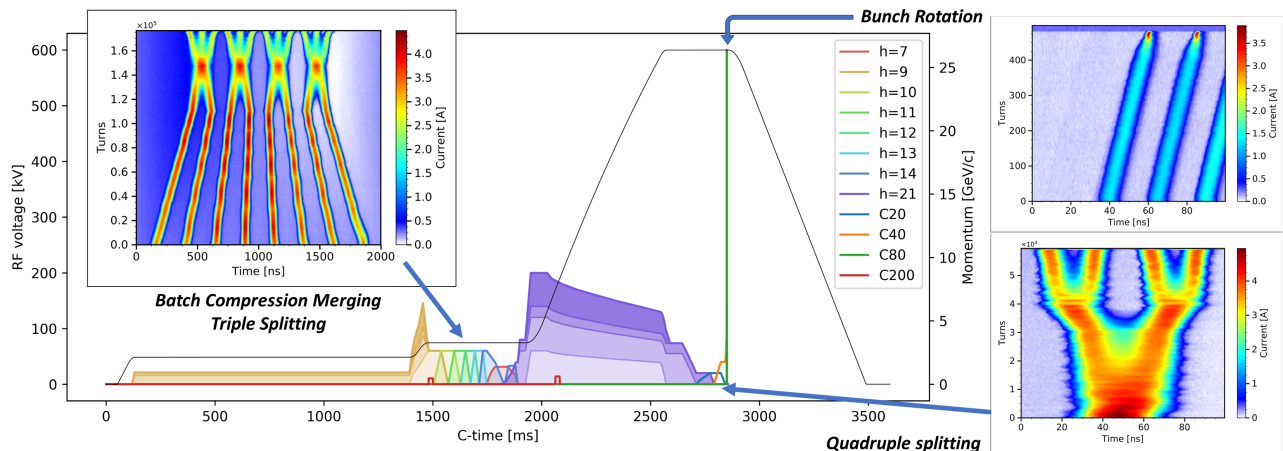


Figure 1: The momentum (black) and RF voltage program (colored) for the BCMS cycle. The RF harmonics  $h = 7$  to  $21$  (10 MHz) are handled by tunable ferrite loaded cavities while the higher harmonics  $h = 42$  (20 MHz),  $h = 84$  (40 MHz) and  $h = 168$  (80 MHz) are generated by fixed frequency RF systems. For each manipulation the evolution of the bunch profiles is shown.

set in the machine. A transition jump scheme is present in the PS [10]. In the simulation the evolution of  $\gamma_t$  was computed using the MAD-X code [11] and is included in the longitudinal simulation.

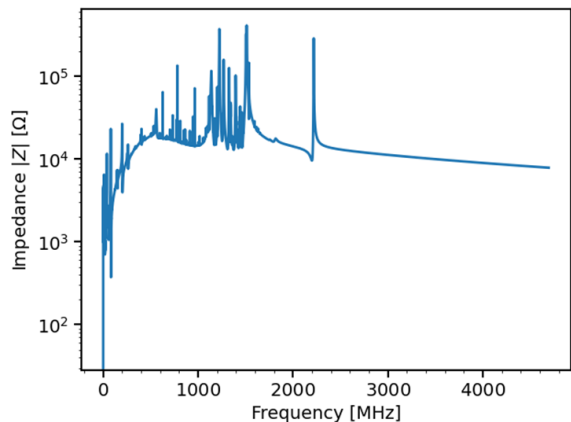


Figure 2: The PS impedance model. The contribution of vacuum equipment is visible at high frequency while the broadband component is due to the kickers.

The next step consisted of including intensity effects. The present PS beam coupling impedance model [12] used for simulations is the product of many years of development, and it now includes the impedance of the RF systems, injection and extraction elements (kickers, septa), vacuum equipment (flanges, pumping manifolds, sector valves), beam instrumentation, resistive wall impedance and longitudinal space charge. The impedance of the various elements are modeled using resonator functions or by passing the complete impedance table as obtained from electromagnetic simulations. While the model is continuously updated, the most important contributions are expected to be well represented. The absolute impedance model  $|Z| (f)$  is displayed in Fig. 2.

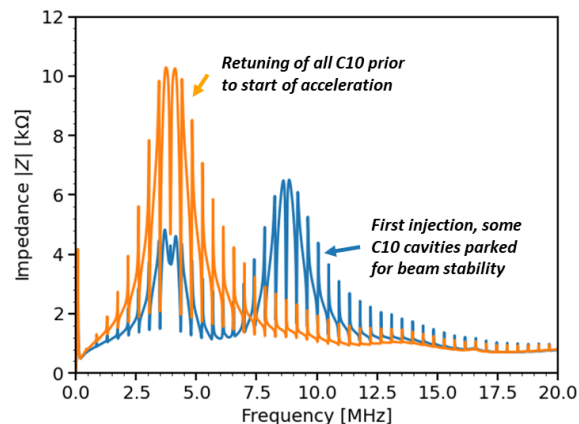


Figure 3: The impedance of the ten C10 cavities on the flat bottom energy and after second injection when accelerating to the intermediate plateau. The impedance is reduced by the OTDFB at revolution frequency harmonics except on the central frequency of the cavity when in use.

The impedance of the RF cavities require a specific treatment. Indeed, some of the cavities are tuned as the beam is accelerated and RF manipulations performed. The example for the accelerating tunable ferrite-loaded cavities (C10) is shown in Fig. 3. The impedance on the 1.2 s injection plateau is compared with the impedance at the start of acceleration. Additionally, each RF cavity is equipped with feedback systems to reduce beam loading. In the case of the C10 cavities, the impedance is reduced at multiples of the revolution frequency by a One Turn Delay Feedback (OTDFB) [13]. The parameters of the notches also need to be updated in simulations to follow the revolution frequency sweep. In the present implementation, the cavity impedance is treated in frequency domain and represented by

$$Z_{fb}(\omega) = \frac{Z_c(\omega)}{1 + Z_c(\omega) GH(\omega) e^{j\omega\Delta t}}, \quad (1)$$

Content from this work may be used under the terms of the CC BY 3.0 licence (© 2021). Any distribution of this work must maintain attribution to the author(s), title of the work, publisher, and DOI

where  $Z_c$  is the cavity impedance including direct feedback obtained from beam based measurements [14],  $H(\omega)$  the transfer function of the OTDFB comb filter centered at revolution frequency harmonics,  $\Delta t$  the loop delay and  $G$  the feedback gain.

For narrowband impedance sources or long delay cavity feedback systems, the decay of the induced voltage can span over many revolution periods. In order to include transient effects with non-stationary beams, a multi-turn induced voltage algorithm was included in BLonD. An example is presented in Fig. 4. The algorithm relies on computing the induced voltage as a large array covering many turns, sufficient to have a complete decay of the signal (150 turns in the present simulation). The second half of the array is set to zero to avoid unphysical artefacts due to the circular convolution (75 effective turns). The induced voltage at a given turn is computed from a circular convolution of the beam current multiplied to the impedance, using Fast Fourier Transforms (FFTs). The contribution from the previous turns, kept in the memory, is then added to the induced voltage to get the total induced voltage. Note that the present treatment of cavity feedback systems by a direct modification of the transfer function do not include potential power limitations. This would require to decompose the signal processing chain.

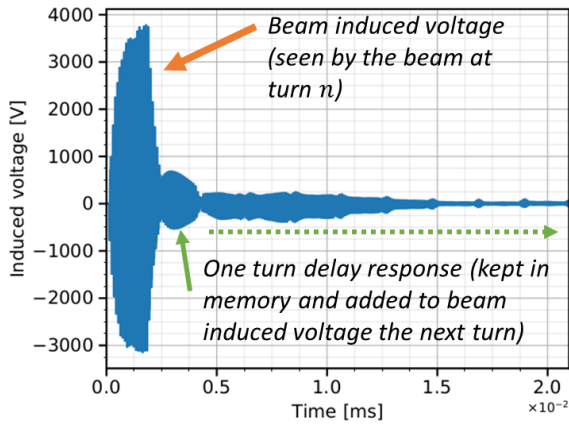


Figure 4: The induced voltage of the C10 cavities including OTDFB on a time period covering ten turns. The impulse response of the feedback is kept in the memory and added to the following simulated turns.

Another intensity effect to consider is longitudinal space charge, which is dominant at low energy in the PS and gradually becomes negligible during acceleration. The evolution of space charge treated as a pure reactive impedance is shown in Fig. 5. The present treatment uses the classical representation of longitudinal space charge with

$$\left(\frac{Z}{n}\right)_{sc} = -j \frac{Z_0}{\beta\gamma^2} g, \quad (2)$$

where  $n = \omega/\omega_0$  is the ratio to the revolution frequency  $\omega_0$ ,  $Z_0$  is the vacuum impedance,  $\beta, \gamma$  are the relativistic velocity and mass factors that evolve during the ramp, and  $g$  a geometric factor depending on the transverse beam size

and the aperture geometry. The value of  $(Z/n)_{sc}$  is updated each turn during the simulation accounting for the evolution of the beam energy and transverse size (via transverse emittance and momentum spread  $\delta$ ). A more advanced model of longitudinal space charge including the influence of the motion of single particles in the transverse plane for the PS is presently developed in [15].

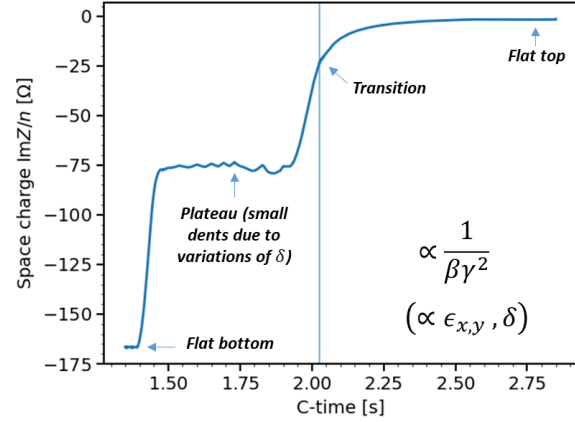


Figure 5: Longitudinal space charge impedance along the cycle, including the variations in energy and transverse beam size. The optics is assumed to remain unchanged during acceleration.

Finally, simplified beam control loops were also included in the simulation using the BLonD implementation as baseline [16]. The beam is accelerated using a phase loop to mitigate zero mode bunch phase oscillations, while the slow drifts in orbit (and consequently in RF frequency) are reduced by a radial loop. The gains were adjusted empirically to obtain stable beam loops and implemented as simple proportional and integrator corrections with

$$\Delta\omega_{PL,i} = -g_{PL}\Delta\phi_i, \quad (3)$$

$$\Delta\omega_{RL,i} = \Delta\omega_{RL,i-1} - \text{sgn}(\eta) g_{RL} \left(\frac{\Delta R}{R}\right)_i, \quad (4)$$

where the loop corrections on the RF frequency  $\Delta\omega$  are summed and applied each turn  $i$ , resulting in a variation in RF phase at the next turn  $i + 1$ . The beam phase error  $\Delta\phi$  is obtained by a convolution with the instantaneous RF waveform (including its variation in frequency each turn), while the orbit error  $\Delta R$  is obtained by taking the mean macro-particle offset in energy with respect to the design energy, converted into an orbit via the momentum compaction factor. The gains  $g_{PL}, g_{RL}$  were adjusted to keep the phase loop action in a time scale much smaller than the one of the radial loop (respectively few  $\mu\text{s}$  versus ms). The sign of the radial loop correction is flipped at transition crossing with the sign of the phase slippage factor  $\eta$ . An extraction synchronization loop was also included at top energy like in the machine, in the same form as the phase loop Eq. (3). In this case however the phase is compared with a signal at fixed frequency corresponding to the expected  $h = 1$ . The radial loop is disabled once the synchronization loop

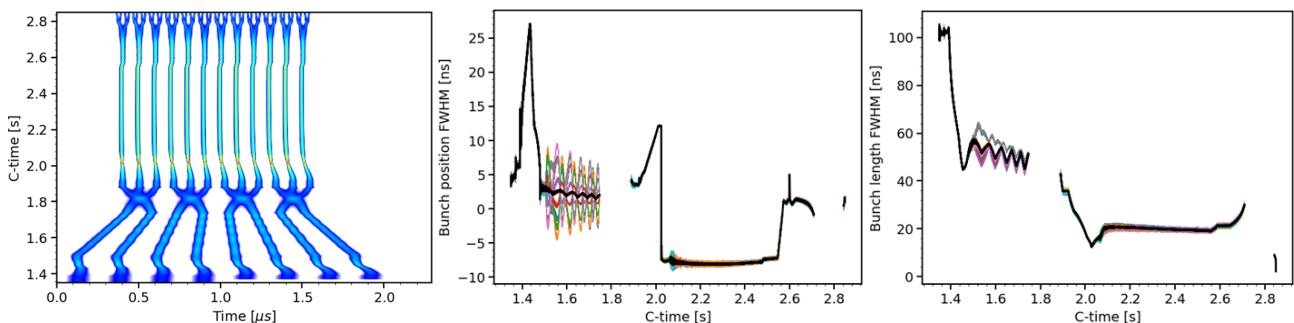


Figure 6: The complete simulated BCMS cycle. The beam profile (left) is shown all along the cycle, including both injections, acceleration to the intermediate plateau, batch compression, merging, splitting, acceleration, transition crossing, controlled emittance blow-up, double splittings, bunch rotation. The bunch-by-bunch position (or phase, middle) and length (right) is analyzed to monitor the evolution of the bunch parameters and identify potential instabilities (colored traces are bunch-by-bunch, black is average). Bunch length and position are not computed during the splittings leading to the blank areas in the corresponding plots.

is enabled. The present model of the beam control loops implies that the phase and radial loops are DC-coupled and act upon the same bandwidth, which is not the case in the machine (AC-coupled phase loop). Although sufficient in simulations, a more realistic implementation is necessary to fully reproduce the dynamic behavior, for instance close to transition crossing.

### SIMULATED CYCLE AND COMPARISON WITH MEASUREMENTS

The elements described in the previous section were assembled to perform a complete simulation including the full RF program, intensity effects as well as feedback systems. The result is detailed in Fig. 6. The beam profile as it would be measured by a Wall Current Monitor is saved regularly along the simulation to monitor its evolution. The RF manipulations introduced in Fig. 1 are well reproduced. Note that the relative phase of the RF systems were adjusted to

minimize the bunch-by-bunch spread in intensity and longitudinal emittance at extraction, just as it is done in real operation. To do so, the simulation parameters such as the longitudinal distribution are saved at each stage of the simulated cycle to optimize sequentially the parameters of the RF manipulations. This is necessary as transient beam loading will induce phase shifts as a function of the beam intensity.

For each simulated beam profile, the bunch positions and lengths are obtained from the Full Width Half Maximum (FWHM). They can then be compared with measurements or used to identify the onset of an instability. The bunch positions (Fig. 6, middle) are expressed with respect to zero crossing of the RF waveform. Hence, the obtained curve follows the synchronous phase evolution along the cycle, with a phase jump at transition crossing. Note that due to beam loading the mean position is shifted due to the resistive impedance (synchronous phase shift). The glitch at the cycle time about 2.6 s is due to the synchronization

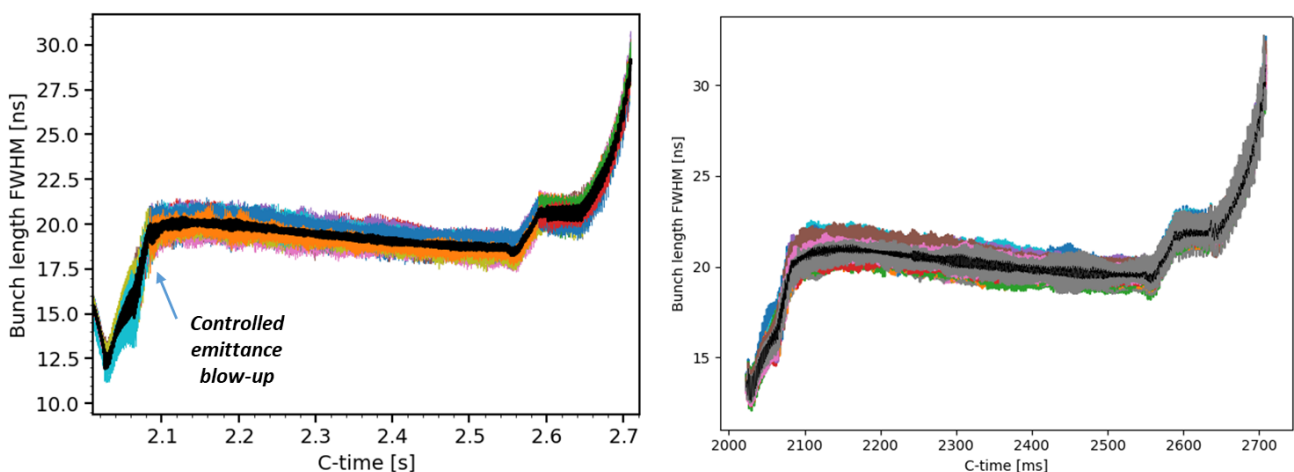


Figure 7: Simulated (left) and measured (right) bunch lengths along the acceleration ramp starting right before transition crossing until the double splittings at flat top energy. The bunch-by-bunch lengths are represented in colors while the mean value is shown in black.

loop. The bunch lengths along the cycle are displayed in the right plot in Fig. 6. The variation of the bunch length  $\tau_l$  from injection to extraction covers almost 2 orders of magnitude. This is an essential parameter regarding intensity effects (e.g. space charge induced voltage scales with  $1/\tau_l^3$ ). Additionally, this is also important for numerical noise and the choice of the number of macroparticles which impacts the simulation runtime. The numerical noise is increased for longer bunches with a fixed number of macroparticles and bin size for the induced voltage calculation.

The simulated and measured bunch length evolution are compared in Fig. 7. To reach this agreement, the RF voltage used for controlled emittance blow-up had to be increased by about a factor two with respect to the expected value. Although the effective RF voltage in the 200 MHz cavities is not known precisely, further investigations are ongoing to find the source of the discrepancy. Nonetheless, after adjusting the voltage applied for the blow-up, the evolution of the bunch length along the ramp until the last splittings is in excellent agreement with the measurements. After bunch rotation, the bunch length at extraction is about 4 ns which is also in perfect agreement with the expectations in real operation. Overall, the measurements for a stable beam are well reproduced in simulations.

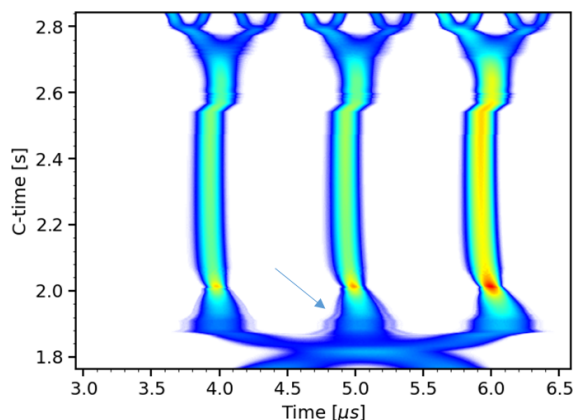


Figure 8: Example of beam profile evolution including a mismatch during the handover between the phase loop from  $h = 7$  to  $h = 21$  after the triple splitting. It generates particles at large amplitude in the RF bucket which are preserved all along the acceleration cycle and kept until top energy.

The benchmark of the model should be completed to calibrate gains of the feedback systems and identify possibly missing impedance sources. Nonetheless, simulations already provide interesting features to analyze, comparable to real operation. An example is presented in Fig. 8. During RF manipulations, the phase discrimination for the phase loop needs to be switched when changing the main RF harmonic. In the context of the triple splitting, the phase loop is handed over from the RF harmonic  $h = 7$  to  $h = 21$ . The initial offset at  $h = 21$  needs then to be adjusted to start with zero phase loop error, minimizing the transient of the loop. However, an error in the phase loop offset can lead to beam oscillations that will be quickly damped but nonetheless

contribute to populate particles at large amplitude in the RF bucket. As shown in Fig. 8 these particles will be kept until the flat top, and eventually contribute to the losses at SPS injection. The present acquisition systems make the measurement of the longitudinal halo generation along the cycle very difficult. This effect can now be studied in simulation by adding all potential sources of halo generation.

To make the simulation possible in a reasonable time frame, the BLoND simulation code was optimized and parallelized combining OpenMP and MPI [17, 18]. The example from the previous section was made sampling the complete impedance model up to 5 GHz, using 480 M macroparticles to have sufficiently low numerical noise for the induced voltage calculation. The runtime was of the order of 2.5 days using 4 MPI nodes with 20 cores each and could be further reduced increasing the number of nodes. The repartition for the different numerical routines is listed in the table below.

Numerical routine	Runtime %
Induced voltage FFTs	50%
Tracking (including beam loops)	20%
Beam profile update	13%
Space charge update	7%
Impedance update	5%
Other (plots...)	5%

The present bottleneck in computing time is the induced voltage calculation due to the FFTs with large numbers of points. Although several approaches could be considered to reduce this runtime (e.g. time domain modeling of the feedback systems, adapting bin size depending to the bunch length to neglect very high frequency impedance sources), it appears that the present level of optimization is sufficient to cover a frequency range including all possible resonances and yet keep the simulation runtime in the order of days.

## CONCLUSIONS

The complete BCMS cycle of the PS was modeled including RF manipulations, intensity effects (impedance model and space charge) as well as feedback systems (cavity and beam loops). The initial results show that the main features of the cycle are well reproduced and are comparable to the observations. A complete benchmark campaign is needed to adjust the parameters that were set empirically such as the feedback gains. The model can then be used to simulate beam instabilities and include remaining items such as the coupled-bunch feedback. The optimization of the BLoND code through large scale parallelization allows the simulation of the full cycle while keeping the runtime in the order of days. This opens the door to instability studies including all sources of initial perturbations, low and high frequency impedance sources and tracking of the longitudinal halo along the cycle.

## ACKNOWLEDGMENTS

The authors would like to thank the BLoND developer team, as well as all contributors to the PS impedance model.

## REFERENCES

- [1] “High-Luminosity Large Hadron Collider (HL-LHC): Technical design report,” Tech. Rep. CERN-2020-010, Geneva, 2020.
- [2] J. Coupard, H. Damerau, A. Funken, R. Garoby, S. Gilardoni, B. Goddard, K. Hanke, A. Lombardi, D. Manglunki, M. Meddahi, B. Mikulec, G. Rumolo, E. Shaposhnikova, and M. Vretenar, “LHC Injectors Upgrade, Technical Design Report,” Tech. Rep. CERN-ACC-2014-0337, 2014.
- [3] H. Damerau, S. Hancock, C. Rossi, E. Shaposhnikova, J. Tuckmantel, J.-L. Vallet, and M. Mehler, “Longitudinal Coupled-Bunch Instabilities in the CERN PS”, in *Proc. 22nd Particle Accelerator Conf. (PAC’07)*, Albuquerque, NM, USA, Jun. 2007, paper FRPMN069, pp. 4180–4182.
- [4] H. Damerau and L. Ventura, “Longitudinal coupled-bunch instability studies in the PS,” in *Injector MD Days 2017*, no. CERN-Proceedings-2017-002, pp. 59–62, 2017.
- [5] L. Ventura, “Studies of Longitudinal Coupled-Bunch Instabilities in the LHC Injectors Chain”, Ph.D. thesis, Rome U., Rome, Italy, 2017.
- [6] H. Damerau, A. Lasheen, and E. N. Shaposhnikova, “Higher-Harmonic RF System for Landau Damping in the CERN PS”, in *Proc. 9th Int. Particle Accelerator Conf. (IPAC’18)*, Vancouver, Canada, Apr.-May 2018, pp. 728–731. doi:10.18429/JACoW-IPAC2018-TUPAF026
- [7] H. Damerau, H. Bartosik, R. Garoby, S. Gilardoni, S. Hancock, B. Mikulec, Y. Papaphilippou, G. Rumolo, E. Shaposhnikova, and R. Tomas, “LIU: exploring alternative ideas,” in *RLIUP: Review of LHC and Injector Upgrade Plans*, pp. 127–137, 2014.
- [8] H. Damerau, M. Morvillo, E. N. Shaposhnikova, J. Tuckmantel, and J.-L. Vallet, “Controlled Longitudinal Emittance Blow-up in the CERN PS”, in *Proc. 22nd Particle Accelerator Conf. (PAC’07)*, Albuquerque, NM, USA, Jun. 2007, paper FRPMN070, pp. 4186–4188.
- [9] “CERN Beam Longitudinal Dynamics code BLonD”, <https://blond.web.cern.ch/>
- [10] A. Sørensen, “Crossing The Phase Transition In Strong Focusing Proton synchrotrons,” *Part. Accel.*, vol. 6, pp. 141–165, 1975.
- [11] “MAD - Methodical Accelerator Design”, <http://madx.web.cern.ch/madx/>
- [12] “PS Longitudinal Impedance Model (2019)”, Zenodo, 2020. doi:10.5281/zenodo.4722835
- [13] F. Blas and R. Garoby, “Design and operational results of a “one-turn-delay feedback” for beam loading compensation of the CERN PS ferrite cavities,” Tech. Rep. CERN-PS-91-16-RF, May 1991.
- [14] G. Favia, “Study of the beam-cavity interaction in the CERN PS 10 MHz cavities and investigation of hardware solutions to reduce beam loading,” Ph.D. Thesis, Univ. of Rome, Rome, Italy, 2017.
- [15] A. Laut and A. Lasheen, “Influence of Transverse Motion on Longitudinal Space-Charge in the CERN PS,” this conference.
- [16] H. Timko, J. E. Müller, A. Lasheen, and D. Quartullo, “Benchmarking the Beam Longitudinal Dynamics Code BLonD”, in *Proc. 7th Int. Particle Accelerator Conf. (IPAC’16)*, Busan, Korea, May 2016, pp. 3094–3097. doi:10.18429/JACoW-IPAC2016-WEPOY045
- [17] K. Iliakis, H. Timko, S. Xydis, and D. Soudris, “Blond++: Performance analysis and optimizations for enabling complex, accurate and fast beam dynamics studies,” in *Proceedings of the 18th International Conference on Embedded Computer Systems: Architectures, Modeling, and Simulation, SAMOS ’18*, (New York, NY, USA), p. 123-30, Association for Computing Machinery, 2018.
- [18] K. Iliakis, H. Timko, S. Xydis, and D. Soudris, “Scale-out beam longitudinal dynamics simulations,” in *Proceedings of the 17th ACM International Conference on Computing Frontiers, CF ’20*, (New York, NY, USA), p. 29-38, Association for Computing Machinery, 2020.

# INJECTION CHICANE BETA-BEATING CORRECTION FOR ENHANCING THE BRIGHTNESS OF THE CERN PSB BEAMS

T. Prebibaj\*<sup>1</sup>, S. Albright, F. Antoniou, F. Asvesta, H. Bartosik,  
 C. Bracco, G. P. Di Giovanni, E.H. Maclean, B. Mikulec, E. Renner<sup>2</sup>  
 CERN, Geneva, Switzerland

<sup>1</sup>also at Goethe University, Frankfurt, Germany, <sup>2</sup>also at TU Wien, Vienna, Austria

## Abstract

In the context of the LHC Injectors Upgrade Project (LIU), the Proton Synchrotron Booster (PSB) developed an H<sup>-</sup> charge exchange injection system. The four short rectangular dipoles of the injection chicane induce focusing errors through edge focusing and eddy currents. These errors excite the half-integer resonance  $2Q_y = 9$  and cause a dynamically changing beta-beating in the first milliseconds after injection. Using the beta-beating at the positions of two individually powered quadrupoles, measured with k-modulation, correction functions based on a model response matrix have been calculated and applied. Minimizing the beta-beating at injection allows the machine to be operated with betatron tunes closer to the half-integer resonance and therefore with larger space charge tune spreads. In this contribution the results of the beta-beating compensation studies and the impact on the achievable beam brightness limit of the machine are presented.

## INTRODUCTION

The LHC Injectors recently underwent major upgrades, as part of the LHC Injectors Upgrade (LIU) project [1], with the aim of achieving the high-intensity and high-brightness beams required by the High Luminosity LHC [2]. As part of these upgrades, the PS Booster (PSB) received a new charge exchange injection region, for converting the negative hydrogen ions (H<sup>-</sup>) from Linac4 [3] to protons, at injection.

The main limitation for the beam brightness achievable at the PSB are space charge effects at injection [4]. The Linac4 delivers H<sup>-</sup> at an increased energy of 160 MeV, compared to its predecessor, Linac2, which delivered protons at an energy of 50 MeV. The increase of the PSB injection energy mitigates the space charge effects and allows the beam intensity to be doubled while having similar space charge detuning for the same transverse emittances.

The new PSB charge-exchange injection system [5] consists of a horizontal chicane and a thin carbon stripping foil. A set of four, short, pulsed, dipole chicane magnets (BSWs), creating a maximum horizontal bump of 46 mm, have been installed in a short 2.6 m straight section, located at the first sector of the machine, for each of the four PSB rings (16 independently powered magnets in total). The edge focusing of the rectangular BSWs causes quadrupolar field perturbations in the vertical plane. Furthermore, during the ramp-down of the injection chicane, eddy currents are generated in the

metallic vacuum chamber, which distort the magnetic field seen by the beam. The eddy currents induce a sextupolar field, proportional to the ramp rate of the BSWs [6]. Since the beam enters the magnets with an offset with respect to the center of the BSWs, the sextupolar component leads to feed-down quadrupolar field perturbations. All these focusing errors cause distortion of the vertical  $\beta$  function around the machine.

At injection, the incoherent space charge tune spread can reach values up to  $\Delta Q = -0.5$  [7]. The systematic resonances at the integer tunes  $4Q_{x,y} = 16$  are strongly excited by the space charge potential due the lattice periodicity of 16, in combination with all other random field errors. To avoid beam degradation due to the integer resonances, the machine is operated very close to the vertical half-integer resonance  $2Q_y = 9$ . Operation with working points close to the half-integer resonance strongly enhances the  $\beta$  function distortions, which can eventually lead to beam losses. Studies showed that two of the main defocusing quadrupoles of the machine (QDE3 and QDE14) are optimal for compensating the perturbations caused by the injection chicane and for this reason they have been equipped with additional, individually controlled power supplies [8].

## SIMULATIONS OF THE PSB INJECTION CHICANE OPTICS PERTURBATIONS

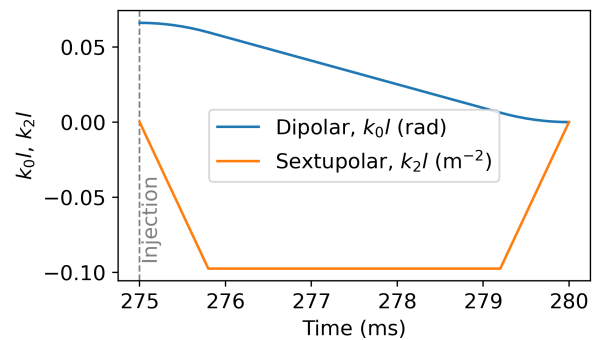


Figure 1: Modelled dipolar (blue) and sextupolar (orange) component of the BSWs.

The edge effects and the sextupolar components generated by eddy currents have been modelled in MAD-X [9] and applied in the PSB lattice. Figure 1 shows the expected dipolar and sextupolar component at one of the BSW magnets. The

\* tirsi.prebibaj@cern.ch

chicane fully collapses 5 ms after the injection, which itself happens 275 ms after the start of the PSB magnetic cycle.

The edge focusing and the feed-down effects induce a  $\beta$ -beating in the vertical plane, which is defined as:

$$\frac{\delta\beta_y}{\beta_y} = \frac{\beta_y - \beta_{y,0}}{\beta_{y,0}}, \quad (1)$$

where  $\beta_{y,0}$  is the nominal  $\beta$ -function around the machine. The injection perturbations change dynamically during the collapse of the chicane, leading to a dynamic change of the vertical  $\beta$ -beating, as shown in the top plot of Fig. 2. Because of that, time dependent compensation strengths are needed to be applied in QDE3 and QDE14 during these 5 ms. At the injection time ( $t = 275$  ms), the chicane is at its maximum amplitude and the perturbation is the strongest with the expected maximum  $\beta$ -beating reaching 45% for a vertical tune of  $Q_y = 4.44$ . For tunes closer to the half-integer resonance, the maximum  $\beta$ -beating can exceed 200%. The tune distortions coming from the injection chicane are of the order of  $3 \cdot 10^{-2}$  for the vertical plane.

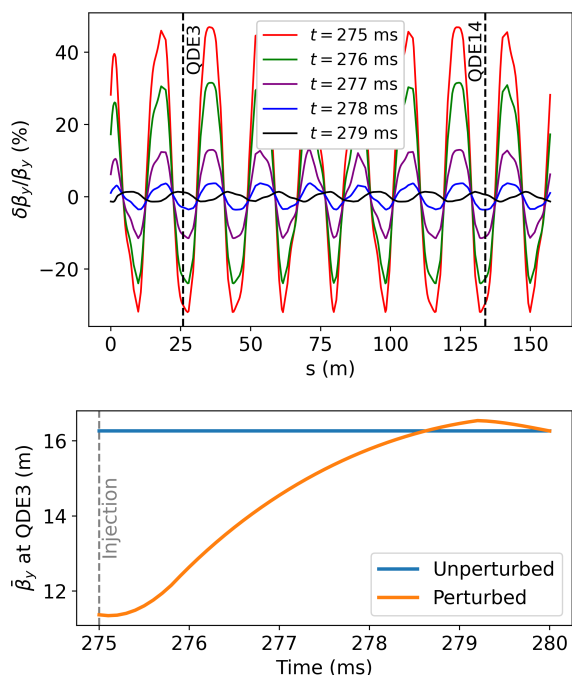


Figure 2: Expected  $\beta$ -beating around the ring for different times in the cycle (top) and optics distortion at the position of QDE3 (bottom).

The bottom plot of Fig. 2 shows a simulation of the expected distortion in the spatial average  $\bar{\beta}_y = \int \beta_y(s) ds$  inside the QDE3 as a function of time. The unperturbed  $\bar{\beta}_y$  (blue line) is 16.26 m. Due to the injection chicane perturbations, the  $\beta$ -function is deformed (orange line). The deformation is similar for the QDE14 magnet. The injection chicane  $\beta$ -beating is compensated by correcting the local  $\beta$  function distortions at the position of these two quadrupoles.

To identify the induced distortion in the  $\beta$ -function at the positions of QDE3 and QDE14, the k-modulation method is

used. This method consists of applying a small quadrupolar kick ( $\delta k$ ) to the beam, and measuring the induced tune shift ( $\delta Q$ ), which depends on the  $\beta$ -function at the position of the quadrupole. In the region close to the half-integer resonance and in first order approximation in  $\delta k$ , this tune shift is given by [10]:

$$\delta Q = \frac{1}{2\pi} \cos^{-1} \left( \cos(2\pi Q_0) + \frac{\bar{\beta} \delta k L}{2} \sin(2\pi Q_0) \right) - Q_0, \quad (2)$$

where  $Q_0$  is the nominal betatron tune,  $L$  is the quadrupole magnetic length and  $\bar{\beta}$  is the spatial average  $\beta$ -function along the quadrupole. Simulations showed that by using k-modulation, the distortion in the  $\beta$ -function at QDE3 and QDE14 can be determined very accurately.

The measured distortions in the  $\beta$ -functions are used to compute the dynamic  $\beta$ -beating correction from a predefined response matrix. This response matrix is generated in MAD-X by installing focusing errors around the injection region of the PSB lattice, to mimic the induced  $\beta$ -beating of the injection chicane, and then by matching the optics using the focusing strength of QDE3 and QDE14. This process is repeated for a wide range of working points and for different focusing errors. The  $\beta$ -functions measured with k-modulation are interpolated to the response matrix to find the optimal configuration for the strengths of QDE3 and QDE14 that will minimize the  $\beta$ -beating. In a similar way, dynamic correction values that are applied to all the PSB focusing and defocusing quadrupoles are also extracted from the response matrix, in order to compensate the tune perturbations due to the injection chicane.

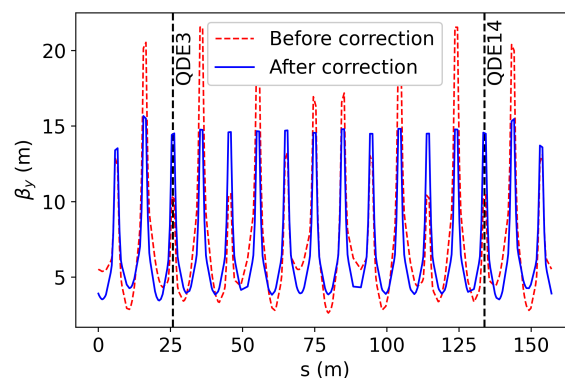


Figure 3: Simulated  $\beta$ -function before and after applying the correction at  $t = 275$  ms for a working point of  $(Q_x, Q_y) = (4.39, 4.44)$ .

A simulation of the k-modulation measurement was performed and the dynamic  $\beta$ -beating correction was calculated and applied to the PSB lattice, with the model injection chicane perturbation. The result was the decrease of the injection chicane  $\beta$ -beating to values less than 1% (RMS). The simulation was repeated for various vertical tunes and the results were equally good, even when including the dynamic tune correction, which slightly degraded the  $\beta$ -beating correction. This showed that, for the case of the PSB, the method

Content from this work may be used under the terms of the CC BY 3.0 licence (© 2021). Any distribution of this work must maintain attribution to the author(s), title of the work, publisher, and DOI

works in principle very well. Figure 3 shows an example simulation of the perturbed and the corrected vertical  $\beta$ -function around ring 3 of the PSB for the working point of  $(Q_x, Q_y) = (4.39, 4.44)$ . With this method, some unavoidable residual  $\beta$ -beating around the injection region is present, which is nevertheless small.

A series of simulation studies followed in order to investigate the robustness of the k-modulation-based correction method, when considering uncertainties that are expected to be present in the actual machine. These include uncertainty in the tune measurement, presence of random focusing errors other than the injection chicane, space charge effects and calibration errors. In all cases, the k-modulation-based correction method managed to maintain the RMS  $\beta$ -beating levels on average below 6 % [11, 12], which was considered acceptable.

### $\beta$ -BEATING MEASUREMENT AND CORRECTION AT THE INJECTION OF THE PSB

During the PSB commissioning after the LIU upgrade, the  $\beta$ -beating was measured at the positions of QDE3 and QDE14 for all rings using the k-modulation technique, with an operational application developed for this purpose [13].

The quadrupole setting was static, in the sense that a single shift in the strength ( $\delta k$ ) was programmed for the full duration of the chicane. The quadrupole strength was changed for QDE3 and QDE14 individually in order to avoid any tune shift dependence on the relative phase advance between the two quadrupoles.

For a particular k-setting, the tune was measured multiple times during the PSB cycle. The tune measurement is performed by exciting the beam with the transverse damper applying a frequency chirp and recording the turn-by-turn data through a Base-Band-tune pickup (BBQ system). By applying a Fast Fourier Transformation to this BPM signal over many turns, the fractional tune of the beam is extracted. Due to the frequency chirp excitation, the minimum number of turns that can be recorded with this method in the PSB is 1024, which corresponds to approximately 1 ms, at injection energy. This limits the tune measurement to only five times during the fall of the injection chicane. Furthermore, during these 1 ms intervals, the  $\beta$ -beating changes considerably, and so the uncertainty in the calculated  $\beta$ -functions is expected to be relatively large.

Multiple cycles with different k-settings are necessary for the  $\beta$ -beating measurement. The PSB is a fast-cycling accelerator with a basic period of 1.2 s. The different cycles are independent from each other and follow a predefined super-cycle which is repeated continuously (pulse-by-pulse modulation). This allowed the use of hundreds of cycles within a reasonable time for collecting the data. The measurement process was automated with the k-modulation application.

Figure 4 shows the reconstruction of the vertical  $\beta$ -functions at QDE3 of ring 3 by fitting the measured  $(\delta k, Q_y)$  pairs with Eq. (2). The different colors correspond to differ-

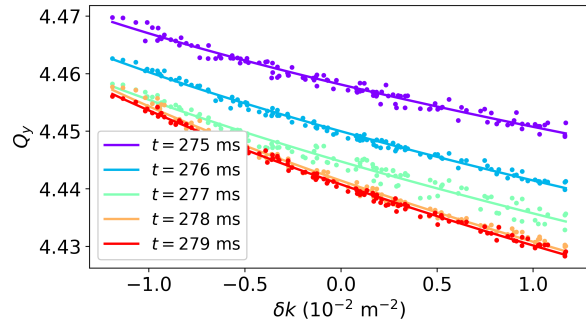


Figure 4: K-modulation data for ring 3 of the PSB. Each color corresponds to a different time of the cycle after injection.

ent times during the fall of the chicane. The fluctuation of the tune measurement is of the order of  $5 \cdot 10^{-3}$ , and thus more than 100 different cycles, i.e. different k-settings, are needed to get a precision in the  $\beta$ -function of less than 0.2 m. The programmed vertical tune is constant at the value of  $Q_y = 4.44$ , but at  $\delta k = 0$  the actual tune is perturbed due to the focusing errors from the injection chicane. Beam losses start to appear for vertical tunes higher than  $Q_y = 4.45$ . The results are similar for the quadrupole QDE14, and all rings.

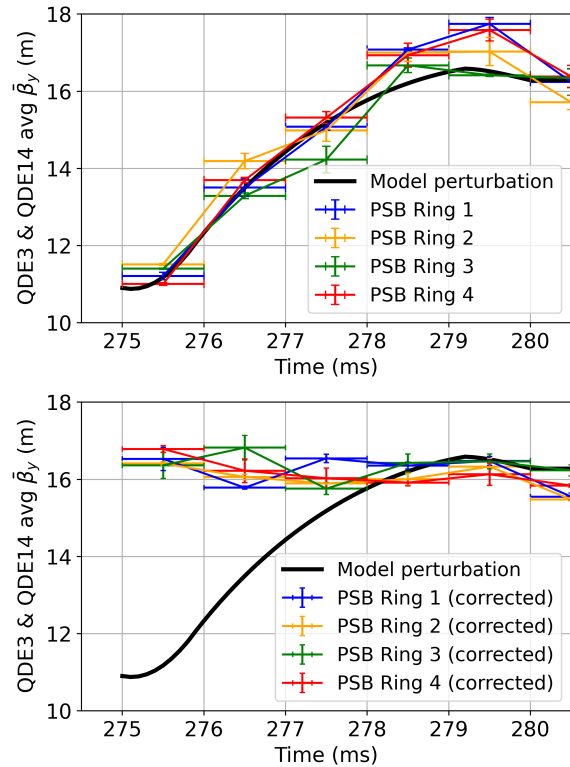


Figure 5: Measured  $\bar{\beta}_y$  values (averaged between QDE3 and QDE14) before (top) and after (bottom) applying the dynamic injection chicane  $\beta$ -beating correction

The top plot of Fig. 5 summarizes the average  $\beta$ -function at the positions of QDE3 and QDE14 for all rings as a function of time for the first 5 ms after injection. The black

line represents the distortion due to the injection chicane perturbations, as expected from the model of Fig. 1 and was extracted from the simulations at the working point of  $(Q_x, Q_y) = (4.39, 4.44)$ , for which the measurements were performed. After  $t = 280$  ms, the chicane is being fully collapsed and so the  $\beta$ -function remains constant and equal to the unperturbed value, which is 16.26 m.

The agreement between the expected and the measured perturbation is excellent, which suggests that there is a good modelling of the injection chicane error sources and the machine lattice. Some ring-to-ring differences are also observed, with the external rings appearing to have larger than expected values for the  $\beta$ -beating between 278 ms and 280 ms where the sextupolar component is more dominant than the edge focusing. This could be caused by stronger eddy currents at the magnets of these rings, but further investigations are needed to confirm this.

The measured  $\beta$ -beating at the locations of QDE3 and QDE14 was then interpolated to the response matrix and the dynamic  $\beta$ -beating correction was calculated and applied to these two quadrupoles. Furthermore, the tune perturbations caused by the injection chicane were also improved by applying additional corrections to all the focusing and defocusing quadrupoles of the PSB.

The  $\beta$ -beating was then once more measured, in a similar way as before, and the result is shown in the bottom plot of Fig. 5. It can be observed that the vertical  $\beta$ -functions are roughly constant, with values very close to the unperturbed value, throughout the entire duration of the chicane decay. This clearly shows the effectiveness of this approach for the minimization of the  $\beta$ -beating around the machine. Another set of measurements was followed in order to calculate and apply a second iteration of correction functions, but this did not give noticeable improvements.

The  $\beta$ -beating correction functions have been calculated for a specific working point. Measurements and simulations show that for small tune changes, the sensitivity of the correction on the exact tune is not significant [14]. Thus, the same dynamic  $\beta$ -beating correction has been used for all vertical tunes up to  $Q_y = 4.47$  and only the tune correction has been adjusted accordingly for each working point. In order to approach even closer to the half-integer resonance and eventually cross it, the injection chicane perturbation must be corrected iteratively, along with the correction of the half-integer resonance excited by error sources other than the injection chicane.

## IMPACT ON BEAM PARAMETERS

The need for the PSB to operate close to the half-integer resonance is due to the fact that the beams at injection energies suffer from a large space charge tune spread. Above a certain intensity, particles from the beam core reach the strong resonances at the integer tunes  $Q_{x,y} = 4.0$  causing an increase in the emittance. By moving the working point further away from the integer, i.e. closer to the half-integer resonance, the emittance increase for the same intensity be-

comes smaller. Thus, larger intensities can be accumulated for the same emittance, resulting in a beam with a higher brightness.

### Intensity

In order to observe the effect of the corrected  $\beta$ -beating, the beam intensity was measured at injection for different vertical betatron tunes. In the PSB, the beam intensity is measured with Beam Current Transformers [15]. Figure 6 shows the beam intensity for different vertical tunes with (green bars) and without (red bars) the  $\beta$ -beating correction. For tunes far from the half-integer resonance, the effect of the correction is insignificant. When approaching the half-integer resonance, if the  $\beta$ -beating is not corrected, more than 25% of the beam intensity is lost at the vertical tune of  $Q_y = 4.46$ , while the beam is completely lost for  $Q_y = 4.47$ . With the correction enabled, the beam fully survives for tunes much closer to the half-integer resonance at  $Q_y = 4.5$ . Up to the present moment, for tunes above  $Q_y = 4.47$  the beam is lost in all cases. The results are similar for higher intensities.

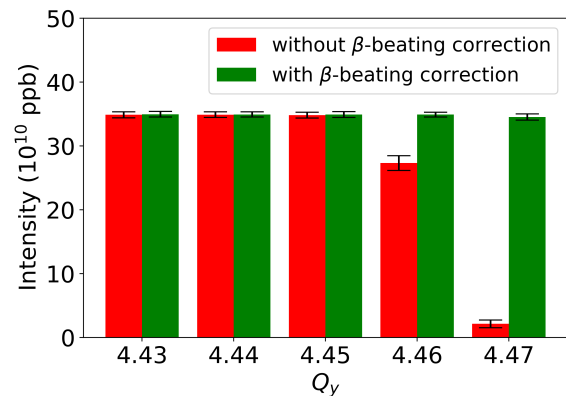


Figure 6: Intensity with (green) and without (red) the injection chicane dynamic  $\beta$ -beating and tune correction applied as a function of the vertical tune.

### Emittance

The emittance was also measured for various vertical tunes at flat-top energy, before extraction. The transverse beam profiles were measured with a wirescanner (WS) [16]. For the calculation of the emittance, the model  $\beta$ -function and the dispersion were assumed, while the momentum spread ( $\delta p/p$ ) was measured using longitudinal tomography [17]. A Gaussian fit was applied to all profiles. The measurements were performed with a beam close to the LIU intensities (approximately  $300 \cdot 10^{10}$  ppb) at which the interaction of the beam with the resonances is enhanced.

Figure 7 shows the horizontal (top) and the vertical (bottom) emittance for three vertical tunes, with and without the  $\beta$ -beating correction enabled. In the horizontal plane, the emittance remains constant between 1.8 to 1.9  $\mu\text{m-rad}$ , as expected. In the vertical plane, the emittance becomes

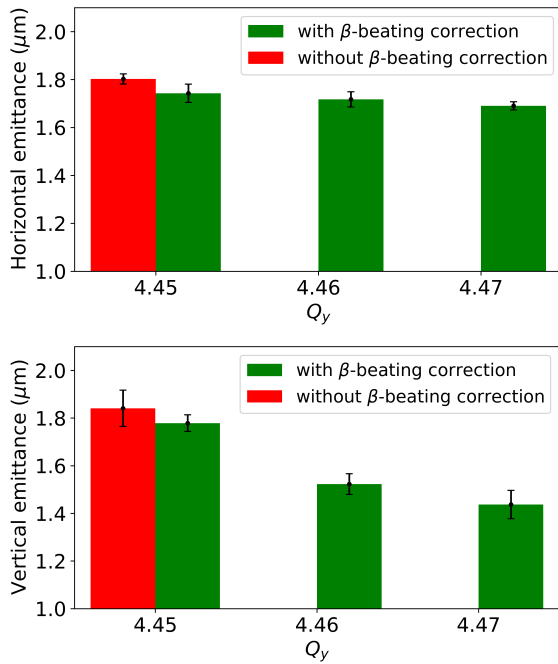


Figure 7: Horizontal (top) and vertical (bottom) emittances as a function of the vertical tune close to extraction ( $t = 770$  ms). The emittances without the  $\beta$ -beating correction are shown only for  $Q_y = 4.45$ , since for the other vertical tunes there are significant losses which distort the profiles.

smaller when moving away from the integer resonance. For this particular intensity, for a tune increase of 0.02, the emittance decreased by approximately  $0.2 \mu\text{m}$ -rad. The effect is less pronounced for lower intensities.

It is important to mention that non-Gaussian overpopulated tails are observed in the vertical beam profiles of the beam and their origin is not yet fully understood.

### Brightness

In the PSB, the figure of merit which characterizes the performance of the LHC beams is the beam brightness, defined as the ratio of the intensity over the emittance.

Figure 8 summarizes recent brightness measurements for different configurations and compares them with the brightness curve before the LIU upgrades (orange), for which at an intensity of  $300 \cdot 10^{10}$  ppb the emittance is approximately  $3.5 \mu\text{m}$ . The data presented in blue were acquired after the LIU upgrades, during the initial phase of the beam commissioning, when the injection chicane  $\beta$ -beating correction, the resonance compensation schemes and the tune evolution were not yet fully optimized. The beam brightness in this initial phase was already very close to the LIU specifications, with an emittance of  $1.8 \mu\text{m}$  for an intensity of  $300 \cdot 10^{10}$  ppb. The latest results, including the injection chicane beta-beating correction, the optimised compensation schemes of the third and fourth order resonances [18], and the working point and tune evolution optimisation, are shown in green. In the latest case, the brightness can exceed

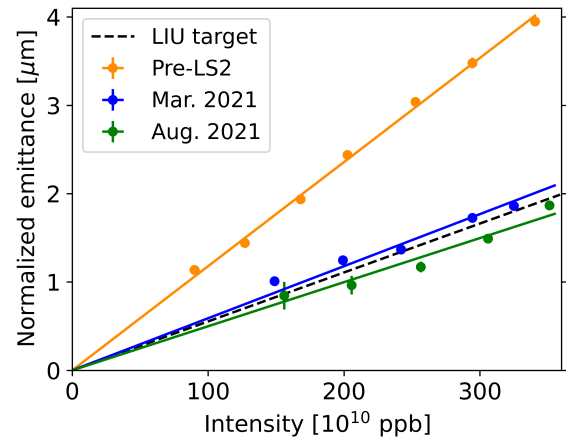


Figure 8: PSB brightness curves in ring 3.

the LIU target (black dashed line), as was expected from the simulations [19]. At an intensity of  $300 \cdot 10^{10}$  ppb, the emittance is smaller by approximately  $0.2 \mu\text{m}$  compared to the data of early 2021.

Although the first results are encouraging, the work to optimize the correction of the focusing perturbations to raise the vertical tune above the half-integer resonance in order to further improve the beam brightness is still ongoing.

## CONCLUSIONS AND OUTLOOK

A strong vertical  $\beta$ -beating is induced by the magnets of the  $\text{H}^-$  injection chicane after the LIU upgrades in the PSB. A method to identify and correct this  $\beta$ -beating was presented. This method consists of using k-modulation to measure the induced optics distortion at the positions of two individually powered quadrupoles and then to interpolate these values to a model-based response matrix. The method was employed during the PSB beam commissioning after the LIU upgrades. The injection chicane  $\beta$ -beating was measured at the expected levels and then corrected using the defocusing quadrupoles QDE3 and QDE14. The correction allowed a stable operation of the beam with working points closer to the half-integer resonance  $2Q_y = 9$ . This mitigated the interaction of the beam with the systematic resonances of the PSB at the integer tunes ( $4Q_x = 16$  and  $4Q_y = 16$ ) through the space charge tune spread, thus reducing the emittance and increasing the brightness of the LHC beams.

Optimization studies are ongoing to address the origin and the evolution of the non-Gaussian tails observed in the vertical beam profiles, the impact of the chromaticity correction and the injection above the half-integer resonance without considerable beam degradation.

## ACKNOWLEDGEMENTS

The authors would like to thank A. Calia, G. Franchetti, A. Huschauer, T. Levens and the PSB Operations and commissioning teams for the continuous support.

## REFERENCES

- [1] J. Coupard (ed.) *et al.*, “LHC Injectors Upgrade, Technical Design Report, Vol. I: Protons”, CERN, Geneva, Switzerland, CERN-ACC-2014-0337, 2014.
- [2] G. Apollinari, *et al.*, “High-Luminosity Large Hadron Collider (HL-LHC): Technical Design Report V. 0.1”, CERN, Geneva, Switzerland, CERN-2017-007-M, 2017. doi:10.23731/CYRM-2017-004
- [3] L. Arnaudon *et al.*, “Linac4 Technical Design Report”, CERN, Geneva, Switzerland, CERN-AB-2006-084, CARE-Note-2006-022HIPPI, 2006.
- [4] E. Benedetto, M. Cieslak-Kowalska, V. Forte and F. Schmidt, “Space Charge Effects and Mitigation in the CERN PS Booster, in View of the Upgrade”, in *Proc. 57th ICFA Advanced Beam Dynamics Workshop on High-Intensity and High-Brightness Hadron Beams (HB’16)*, Malmö, Sweden, Jul. 2016, pp. 517-522. doi:10.18429/JACoW-HB2016-THPM9X01
- [5] W. J. M. Weterings, C. Bracco, L. O. Jorat, M. Meddahi, R. Noulibos, and P. Van Trappen, “The New Injection Region of the CERN PS Booster”, in *Proc. 10th Int. Particle Accelerator Conf. (IPAC’19)*, Melbourne, Australia, May 2019, pp. 2414-2417. doi:10.18429/JACoW-IPAC2019-WEPM039
- [6] E. Benedetto, B. Balhan, J. Borburgh, C. Carli, V. Forte, and M. Martini, “Detailed Magnetic Model Simulations of the H- Injection Chicane Magnets for the CERN PS Booster Upgrade, Including Eddy Currents, and Influence on Beam Dynamics”, in *Proc. 5th Int. Particle Accelerator Conf. (IPAC’14)*, Dresden, Germany, Jun. 2014, pp. 1618-1620. doi:10.18429/JACoW-IPAC2014-TUPRI027
- [7] B. Mikulec, A. Findlay, V. Raginel, G. Rumolo, and G. Sterbini, “Tune Spread Studies at Injection Energies for the CERN Proton Synchrotron Booster”, in *Proc. HB’12*, Beijing, China, Sep. 2012, paper MOP249, pp. 17-21.
- [8] M. Aiba, C. Carli, M. Chanel, B. Goddard, M. Martini, W. Weterings, “Lattice Issues of the CERN PSB with H- Charge Exchange Injection Hardware”, in *Proc. PAC’09*, Vancouver, BC, Canada, May 2009, paper TH6PFP036, pp. 3781-3783.
- [9] MAD - Methodical Accelerator Design, <http://mad.web.cern.ch/mad/>
- [10] P. Thrane, “Measuring  $\beta^*$  in SuperKEKB with K Modulation”, *CERN-Thesis-2018-300*, Dec. 2018, pp. 9-11, <https://cds.cern.ch/record/2652855/>
- [11] T. Prebibaj *et al.*, “Beta-beat correction in the PSB during injection bump decay”, Presentation at ABP Injectors Working Group Meeting, CERN, Geneva, Switzerland, Apr. 2020. <https://indico.cern.ch/event/910642/contributions/3830849>
- [12] T. Prebibaj *et al.*, “Status of the k-modulation application”, Presentation at Injectors Performance Panel Meeting, CERN, Geneva, Switzerland, Nov. 2020. <https://indico.cern.ch/event/975301/contributions/4107125>
- [13] T. Prebibaj *et al.*, “K-modulation application for PSB and PS”, Presentation at Accelerating Python update 2020 Q4 meeting, CERN, Geneva, Switzerland, Dec. 2020. <https://indico.cern.ch/event/974806/contributions/4104882>
- [14] T. Prebibaj *et al.*, “PSB compensation of injection chicane perturbations and impact on beam performance”, Presentation at INC Section meeting, CERN, Geneva, Switzerland, Jul. 2021. <https://indico.cern.ch/event/1056960/contributions/4442064>
- [15] G. Gelato, “Beam current and charge measurements”, in *Beam Instrumentation (Ed. J. Bossler)*, CERN-PE-ED 001-92 p. 185.
- [16] R. Veness *et al.*, “Installation and Test of Pre-series Wire Scanners for the LHC Injector Upgrade Project at CERN”, in *Proc. 8th Int. Particle Accelerator Conf. (IPAC’17)*, Copenhagen, Denmark, May 2017, pp. 412-414, doi:10.18429/JACoW-IPAC2017-MOPAB121
- [17] S. Hancock, “A simple algorithm for longitudinal phase space tomography”, CERN, Geneva, Switzerland, CERN-PS-RF-NOTE-97-06, May 1997. <https://cds.cern.ch/record/1174559>
- [18] F. Asvesta *et al.*, “Resonance Compensation for High Intensity and High Brightness Beams in the CERN PSB”, presented at the 64th ICFA Advanced Beam Dynamics Workshop (HB’21), Fermilab, Batavia, Illinois, USA, Oct. 2021, paper MOP06, this conference.
- [19] F. Asvesta *et al.*, “Production of the LHC multi-bunch beams in the PSB”, Presentation at Injectors Performance Panel meeting, CERN, Geneva, Switzerland, May 2020. <https://indico.cern.ch/event/915909/contributions/3851043>

# OPTIMISED TRANSVERSE PAINTING SCHEMES FOR THE NEW 160 MeV H<sup>-</sup> INJECTION SYSTEM AT CERN

E. Renner\*<sup>1</sup>, S. Albright, F. Antoniou, F. Asvesta, H. Bartosik,  
 C. Bracco, G. P. Di Giovanni, B. Mikulec, T. Prebibaj<sup>2</sup>,  
 F. M. Velotti, CERN, Geneva, Switzerland

<sup>1</sup>also at TU Wien, Vienna, Austria

<sup>2</sup>also at Goethe University, Frankfurt, Germany

## Abstract

A major aspect of the LHC Injectors Upgrade (LIU) project at CERN is the Proton Synchrotron Booster (PSB) connection to the newly built Linac4 and the related installation of a new 160 MeV H<sup>-</sup> charge exchange injection. This contribution presents the first operational experience with the new injection system and its flexibility of applying horizontal phase space painting to tailor different beams to the respective user-defined brightness targets. The presented measurement and multi-particle simulation results focus on the optimisation of the required transverse injection settings to reduce losses when producing high-intensity beams, i.e. for the ISOLDE experiment. In this context, feasibility studies towards applying numerical optimisation algorithms for improving and efficiently adapting the respective injection settings online are presented.

## INTRODUCTION

The PSB is the first synchrotron in the CERN injector complex and consists of four superposed rings. It was upgraded during the Long Shutdown 2 (LS2) in 2019/2020 as part of the LIU project [1], with the aim of doubling the beam brightness for the High Luminosity LHC [2] era. When connecting the new 160 MeV H<sup>-</sup> accelerator Linac4 [3] to the PSB, the injection energy was increased from 50 to 160 MeV and with it the relativistic factor  $\beta_r \gamma_r^2$  by a factor two. A key component of this connection is the newly installed charge exchange injection system [4], which replaces a conventional proton multi-turn injection. The injection process into the PSB is used for tailoring the wide range of transverse beam characteristics as requested by the various users at CERN, covering intensities from  $N_{p^+} = \mathcal{O}(10^{10})$  to  $\mathcal{O}(10^{13})$  protons per ring and normalized transverse emittances from  $\epsilon_{n,rms} < 0.7 \mu\text{m}$  (LHC-like beams) to  $\approx 9\text{--}10 \mu\text{m}$  (high intensity, e.g. for the ISOLDE [5] or nTOF [6] experiment). Prior to the upgrade, the production of the high intensity fixed target beams with  $N_{p^+} = 0.8 - 1 \cdot 10^{13}$  p+ per ring resulted in up to 30 – 40% losses at the injection septum due to the nature of the conventional multi-turn injection. With the new injection system, similar beams can be produced while keeping the losses within a few percent.

The required transverse beam characteristics for each user are customized by defining the programmable field decay of the horizontal injection bump as well as the offset between injected beam and circulating beam orbit during the injection process.

This tailoring of the phase space distribution during injection is referred to as phase-space painting and enables a reduction of the charge density during beam accumulation, particularly when injecting high intensity beams. Consequently, the space charge detuning is reduced and emittance growth due to interaction of the detuned protons with integer resonances mitigated. Adequate painting schemes to produce operational beams with the same parameters as before the upgrade (pre-LS2) were previously defined using multi-particle simulations [1, 7–9]. These have been refined with beam and are now successfully used in operation. However, automatically optimising these programmed transverse painting schemes based on pulse per pulse modulation user requests and beam instrumentation feedback becomes a key aspect to improve operational efficiency, especially considering the perspective of increasing the delivered intensity for selected fixed target beams to  $I > 1 \cdot 10^{13}$  p+ per ring.

This contribution presents simulation and measurement results to assess the impact of applied transverse painting settings on the losses obtained during high intensity beam production, taking an ISOLDE-like beam as an example. Subsequently, we discuss the potential of applying numerical optimisation algorithms to set and adapt the transverse painting functions automatically.

## PSB CHARGE EXCHANGE INJECTION AND PAINTING SETTINGS

The Linac4 H<sup>-</sup> beam features normalised transverse emittances  $\epsilon_{u,n} \approx 0.3 \mu\text{m}$  in both planes  $u = x, y$ . Beam can be accumulated in the PSB over up to  $n_t = 150$  turns, which corresponds to an injection over  $t_{\text{INJ}} = 150 \mu\text{s}$  considering the PSB revolution period at injection energy  $\tau \approx 1 \mu\text{s}$ . For the here presented high intensity beam production studies, a chopping factor of  $CF = 0.6$  is applied to the H<sup>-</sup> beam. This results in an injected intensity of  $I_{\text{INJ/turn}} \approx 1 \cdot 10^{11}$  p+ per PSB turn of beam accumulation [9], based on the present Linac4 peak current of 26 mA. The PSB accelerates beam from 160 MeV to 2 GeV in 530 ms with a 1.2 s repetition rate. In this contribution, we use time in ms relative to the start of the cycle (“C-time”) to refer to time instances. Injection takes place at C275, extraction at C805.

The new injection system is illustrated in Fig. 1. The H<sup>-</sup> beam coming from Linac4 (red in Fig. 1) is injected via a  $\approx 200 \mu\text{g cm}^{-2}$  carbon stripping foil [10–13]. The already circulating beam (blue in Fig. 1) is horizontally deflected towards the foil by a chicane in the injection region [14],

\* elisabeth.renner@cern.ch

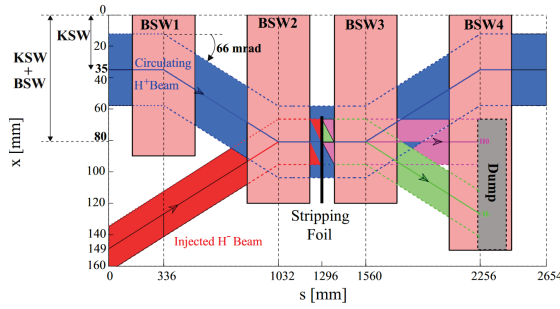


Figure 1: Schematic of the PSB H<sup>-</sup> injection system (KSW: painting kicker magnets, BSW: injection chicane) [1].

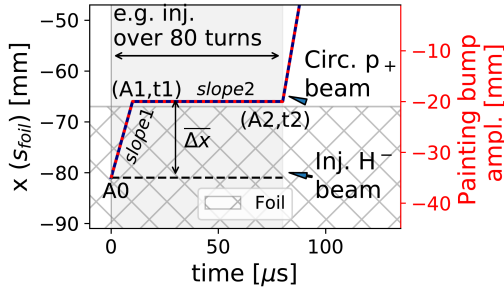


Figure 2: Circulating orbit at the stripping foil during the painting bump decay. Left axis: combined deflection of chicane and painting bump, right: painting bump amplitude.

creating a bump of  $-46$  mm amplitude, and by painting kickers with nominal bump amplitude of  $-35$  mm and variable field decay [15, 16]. The painting kicker field modulation during injection is controlled by piece-wise linear functions. Figure 2 illustrates the time evolution of the closed orbit at the location of the stripping foil, when applying a painting kicker field decay as programmed for example for high intensity beams. The nominal position of the injected beam ( $-81$  mm) is indicated for reference by the dashed line. The maximum bump amplitude  $A_0$  defines the offset of the circulating orbit with respect to the injected beam when injecting the first bunch. The horizontal phase space distribution and the resulting painted beam size is mainly tailored by setting slope 1, which is defined by the amplitude-marker pair  $A_1$  and  $t_1$ . Slope 2 ( $A_2, t_2$ ) controls the subsequent intensity accumulation.  $t_2$  [ $\mu\text{s}$ ] marks the end of the injection process and is set equal to number of PSB revolutions during beam accumulation. The vertical beam size can be tailored by applying a fixed vertical offset  $\Delta y$  [mm] or angle  $\Delta y'$  [mrad] to the injected beam using corrector magnets in the injection line. However, as there is no difference expected between applying an offset or angle, we consider for the following report only the impact of optimising  $\Delta y$  while setting  $\Delta y' = 0$  mrad.

## PHASE SPACE PAINTING FOR HIGH INTENSITY FIXED TARGET BEAMS

In this section, injection painting studies for an ISOLDE-like beam are presented with machine configurations as summarised in Table 1. It has to be noted that machine optimisa-

Table 1: Parameters for Painting Studies on ISOLDE Beams

	Parameter	Unit	Measurement Config.
General	Ring		3
	$I_{\text{INJ}} / n_t$	p+ /	$805 \cdot 10^{10} / 80$
	$dE_{\text{rms,INJ}}$	keV	280
	$Q_x / Q_y$		4.22 / 4.36
Painting	$t_1, t_2$	$\mu\text{s}$	10, 80
	$A_0$	mm	-35
	$A_1$	mm	-26 (-29 to -20)
	$A_2$	mm	as A1
	$\Delta y$	mm	0 (0-6)
Results	$\epsilon_{n,y,\text{RMS}} / \epsilon_{n,y,\text{fit}}$	$\mu\text{m}$	$\approx 5 - 5.5 / \approx 6$
	$\epsilon_{n,x,\text{RMS}} / \epsilon_{n,x,\text{fit}}$	$\mu\text{m}$	$\approx 7.5 - 10.5 / \approx 9 - 14$
	$L_{\text{C805}}$	%	2.6 (2.6-7.5)

tion studies, including resonance compensation and working point optimisations [17], are ongoing. The working conditions presented here are used to commission the transverse painting logic for high intensity beams and develop tools for optimisation, which can be transferable to future machine configurations, as described below.

### Motivation and Constraints

For ISOLDE beams, injection setting optimisation is intended to reduce the losses along the cycle and maximise the beam transfer, not to tailor a specific beam size. Limitations for the extent of the painted transverse emittances of ISOLDE beams are only given by the minimum PSB acceptance. Previous studies estimate maximum allowed normalised  $1\sigma$  emittances of  $\epsilon_{n,x,\text{max}} = 9$  mm mrad [18] and  $\epsilon_{n,y,\text{max}} = 6$  mm mrad [19] in order to fit the beam into the horizontal  $4\sigma_{x,\text{max}}$  and vertical  $2.5\sigma_{y,\text{max}}$  acceptance (recombination part of the extraction line), respectively. A new absorber system comprising a movable and a fixed mask was installed during LS2 to protect those identified bottlenecks [20]. During the here presented measurement campaign, the PSB was operated without the movable mask inserted. The resulting aperture bottleneck generated by the fixed mask features per design an acceptance of  $4\sigma_{x,\text{max}}$  and  $3.5\sigma_{y,\text{max}}$ , assuming a Gaussian transverse distribution [20]. However, it has to be noted that the obtained profiles generally feature strongly under-populated tails and that acceptance limitations are not the dominant cause of losses.

### Simulation and Measurement Set-Up

For this first assessment of different injection painting settings we keep  $t_1, A_0$  and  $t_2$  constant. Vertically, the offset of the injected beam is varied  $\Delta y = 0 - 6$  mm. Horizontally we set  $A_1 = A_2 = -29$  to  $-20$  mm, resulting in a variation of the effective offset between injected beam position and circulating beam orbit during beam accumulation of  $\Delta \bar{x} = 6 - 15$  mm (Fig. 2). As in the previous studies presented in [10], the probed configurations span both extremes: Transverse injection settings resulting in controlled transverse emittance blow up dominated by the applied paint-

ing ( $\Delta y = 6$  mm and  $\Delta \bar{x} = 12 - 15$  mm), and uncontrolled emittance growth due to increased space charge detuning and interaction of the beam core with integer resonances ( $\Delta y = 0 - 3$  mm and  $\Delta \bar{x} = 6$  mm).

The obtained losses throughout the cycle are defined as

$$L_{C805} = \frac{|I_{BI,INJ}| - I_{BR,EXTR}}{|I_{BI,INJ}|} \quad (1)$$

where  $|I_{BI,INJ}|$  is the intensity of the  $H^-$  beam measured in the injection line and  $I_{BR,EXTR}$  the intensity observed with the ring beam current monitor immediately before extraction (C805). Additional losses in the extraction line are not considered in this work. All presented wire-scans are taken at extraction energy close to the end of the cycle (C770) using the newly installed LIU wire-scanners [21]. Measurement of the longitudinal profile and a tomographic reconstruction [22] are used to calculate the momentum spread at extraction time, which was  $\frac{dp}{p} \approx 1.1 \pm 0.06 \cdot 10^{-3}$ .

Comparative multi-particle simulations of the injection process are conducted for the first 5 ms, i.e. up to C280, using PTC-pyOrbit [23]. Foil scattering, optics perturbation due to the injection chicane [24] and a quadrupolar error are included in the simulations.

### Observations in Simulations and Measurements

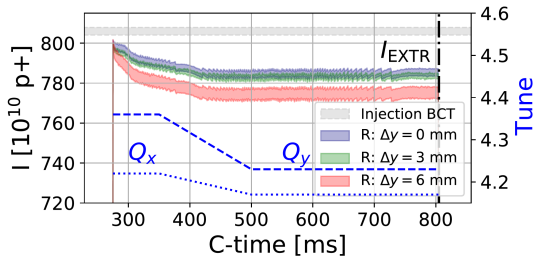


Figure 3: Measured intensity along the cycle ( $1\sigma$  errorbar, injection: C275, extraction: C805) for  $\Delta \bar{x} = 9$  mm and different vertical offsets, compared to the intensity measured in the injection line (grey). The programmed tune evolution (blue) is displayed using the second axis.

Figure 3 displays the characteristic of the measured current along the cycle for a subset of the probed settings. Losses during the injection process itself (C275) mainly due to beam size limitations account for  $L_{C275} \approx 0.6 - 1 \pm 0.1$  %. For the applied settings the majority of the losses are observed up to C450 due to interaction with various resonances [17, 25]. The dependence of the total obtained losses on the probed injection settings is summarised in Fig. 4. For  $\Delta \bar{x} = 6$  mm (space charge dominated blow-up of  $\epsilon_x$ ), the losses decrease when applying a vertical offset  $\Delta y > 0$  mm. On the other hand, for  $\Delta \bar{x} = 9 - 15$  mm (painting dominated blow-up of  $\epsilon_x$ ), the losses increase with increasing  $\Delta y$ . Considering the probed injection settings as displayed in Fig. 4, minimal losses of  $L_{805, \min} \approx 2.6 \pm 0.2$  % are obtained for  $\Delta y = 0$  mm and  $\Delta \bar{x} = 9$  mm. We note, that this considerable dependence of the obtained losses to the applied  $\Delta y$

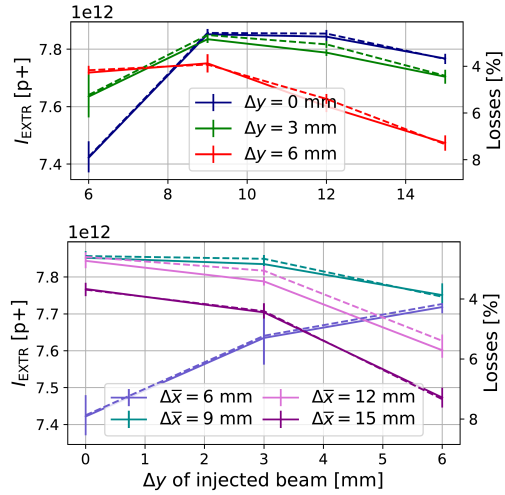


Figure 4: Measured intensity before extraction (solid) for different painting settings. The corresponding losses with respect to the injected intensity are displayed using the second axis (dashed).

is observed despite the resulting vertical emittances being similar in all cases, as illustrated in Fig. 5 (centre and right).

Figure 5 (left) shows the tune footprints as obtained in simulations after 5 ms, i.e. at C280. For cases with increased losses, the footprints show a shift of the vertical tune distribution's peak towards increased  $Q_y$  (blue in Fig. 5a and red in Fig. 5c), indicating an enhanced probability to excitation due to resonance crossing. The vertical profiles measured at C770 are presented in Fig. 5 (centre). The profiles are compared to a Gaussian distribution  $\mathcal{N}(\sigma_y, (\epsilon_{n,y} = 6 \mu\text{m}))$  as this corresponds to the beam size assumed for the aperture limitation described above. The residuals of the obtained distributions with respect to  $\mathcal{N}(\sigma_y, (\epsilon_{n,y} = 6 \mu\text{m}))$  are plotted in Fig. 5 to illustrate the difference in tail population. The presented profiles feature an increased vertical tail population for painting settings with increased losses, mainly visible for  $\Delta \bar{x} = 6$  and 15 mm. However, these results have to be considered with care, as acquired profiles, and particularly the tails, are distorted by the wire-scanner acquisition [26]. As the wire crosses the beam in Fig. 5 from left to right, the left side of the profile ( $y = -10$  to  $-5$  mm) is considered less affected by such scattering distortions.

The presented measurements give first indications towards the optimised injection settings. For the present operational configuration we summarise that it is not beneficial to paint a large transverse emittance at injection in both planes, as the reduced initial tune spread both, horizontally and vertically, results in increased losses during resonance crossing. To profit from the complete painting kicker's flexibility,  $A_0$ ,  $t_1$  and  $t_2$  can additionally be varied to obtain minimised losses. Further, the applied painting function may need to be adapted when changing the operating conditions such as injected intensity, working point, energy spread or resonance compensation. This sensitivity of the optimum injection settings to varying operational conditions makes automatic tuning of injection settings attractive, as discussed below.

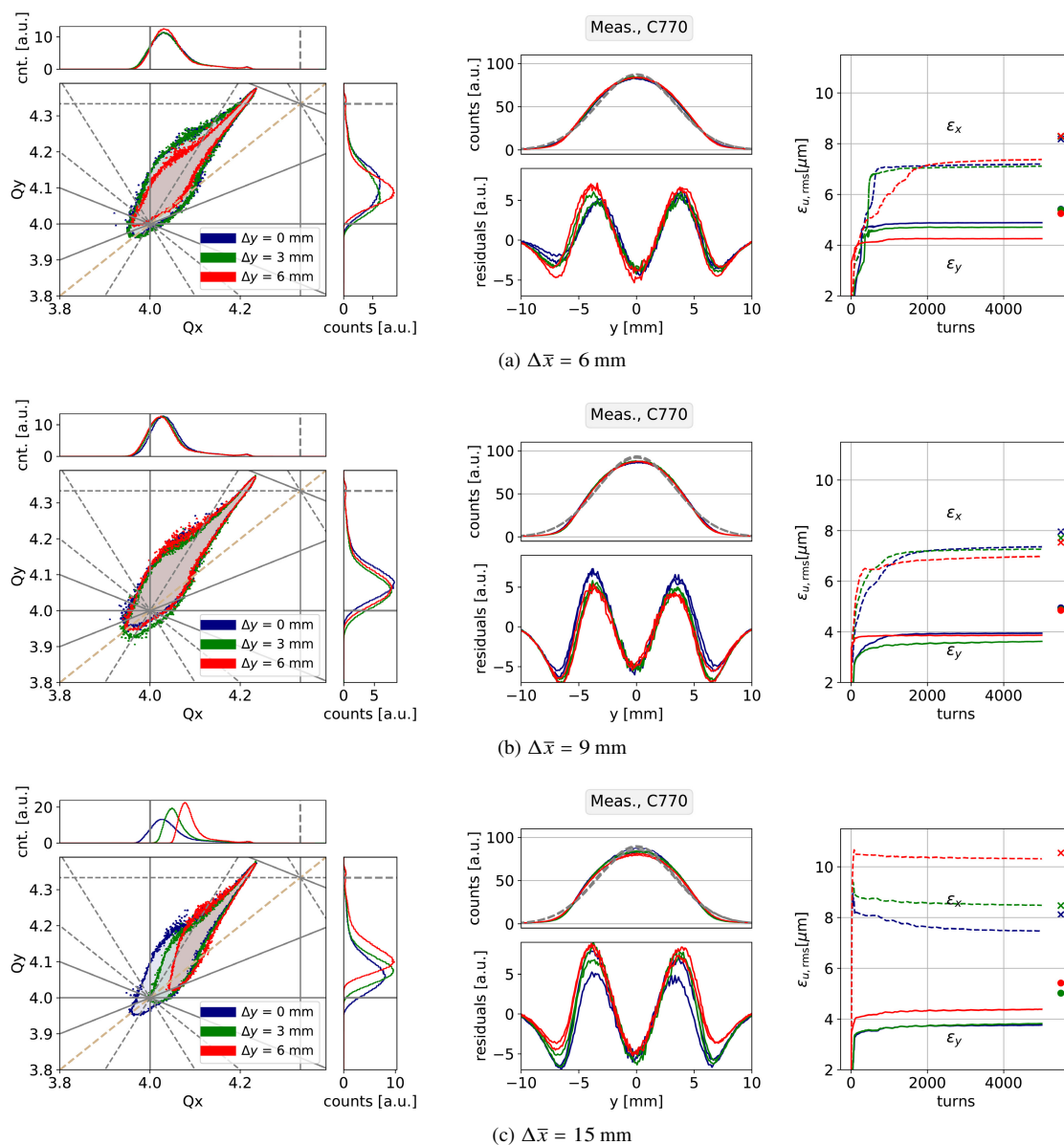


Figure 5: Simulation and measurement results for various painting settings. Left: Tune footprints for C280 obtained from multi-particle simulations for different painting scenarios. Centre: Measured vertical profiles (at C770) for different injection painting scenarios, compared to a Gaussian distribution for  $\epsilon_y = 6 \mu\text{m}$  (grey dashed). Right: Simulated intensity and r.m.s.-emittance evolution up to C280.  $\epsilon_{u,rms}$  measured at C770 are displayed with cross (x) and circle (y) markers.

## TOWARDS APPLYING NUMERICAL OPTIMISATION ALGORITHMS

Numerical optimisation algorithms are increasingly employed within the CERN accelerator complex to enhance operational and commissioning efficiency. During beam commissioning, tools to optimise the transverse injection settings for various users are being developed and probed using the in-house Generic Optimisation Frontend and Framework (GeOFF) [27]. For the above described ISOLDE beams, the optimisation environment allows variation of 5 parameters,  $A_0, t_1, A_1, v_2(t_2, A_2) = \frac{dx}{dt}$  of slope 2 and  $\Delta y$ . We optimise on a loss function as defined in Eq. (1). If required, the loss function can be expanded by including various intensity and

loss measurements in the injection, extraction region and the ring to weight location and temporal occurrence of losses.

Different derivative-free numerical optimisation algorithms have been considered for this problem, i.e. pyBOBYQA [28, 29], Powell [30], COBYLA [31] and Nelder-Mead [32]. Whereas the latter did not converge to a solution within  $\approx 100$  steps, we obtain a reasonable performance of pyBOBYQA, COBYLA and Powell for the first optimisation attempts, which converge to acceptable solutions within 30–100 steps. To state an example, the progress of an optimisation run using pyBOBYQA is displayed in Fig. 6 (left). Data acquired for a fixed machine configuration (ring 3,  $|I_{BL,INJ}| \approx 0.9 \cdot 10^{13}$  p+) over multiple optimisation runs with different algorithms and hyper-parameter settings is used

for analysis of the feature space. The minimum loss surface for selected feature combinations highlights the convex characteristic and the flat minimum of the problem (centre and right in Fig. 6). The steps taken by the optimisation algorithm in this exemplary run are indicated by scatter markers. For this dataset (acquired over multiple optimisation runs), the probed painting bump decays and applied vertical offsets are displayed in Fig. 7, color-coded by the losses obtained when applying the respective settings.

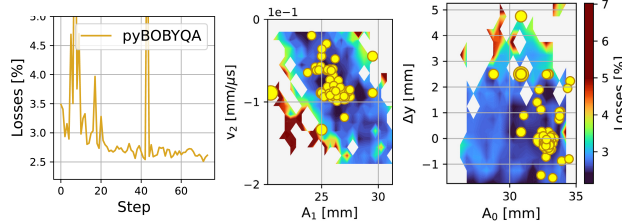


Figure 6: Example for optimisation progress using pyBOBYQA (left) and illustration of optimisation steps in selected feature subspaces (centre, right).

To compare the solutions obtained for different machine configurations (rings, intensities), the settings resulting in minimal losses (blue in Fig. 7) are selected for each scenario and corresponding parameter spans illustrated in Fig. 8. As expected, the optimised loss levels differ for the various operational conditions, for example 2.3% in ring 3 compared to 4% in ring 2 for  $|I_{\text{BLINJ}}| \approx 0.9 \cdot 10^{13} \text{ p+}$ . Still, the characteristic of the optimised injection configurations stays similar. As in the study presented above, the optimised settings converge to  $\Delta y \approx 0 \text{ mm}$ . The horizontal painting converges towards solutions with an amplitude decay  $|A_2| < |A_1|$ , compared to the studies presented above in which we chose  $|A_2| = |A_1|$ . However, considering the flat minimum (Fig. 6), a dependency of this obtained horizontal painting bump decay on the initial conditions has not been excluded so far.

Detailed studies to assess the optimised injection configurations as well as to improve the optimiser performance are ongoing. A surrogate model is trained with a Random Forest Regressor [33] using the presented dataset acquired during the first optimisation runs. This model is used for ongoing studies regarding offline hyper-parameter and loss-function tuning as well as algorithm performance evaluation. The high noise level of the loss function ( $\sigma_{\text{noise}} = 6\%$  of the objective value) as well as the flat minimum prove to be some of the major challenges. Further, keeping the aim in mind to operationally use this tool to efficiently adapt to new operational conditions, the focus when tuning the hyper-parameters is put on providing a high sample efficiency.

## SUMMARY

The new PSB  $\text{H}^-$  injection enables tailoring of the transverse phase space distribution during injection. The impact of transverse painting schemes on losses during high intensity beam production has been assessed with beam and compared to multi-particle simulations. We observe a significant

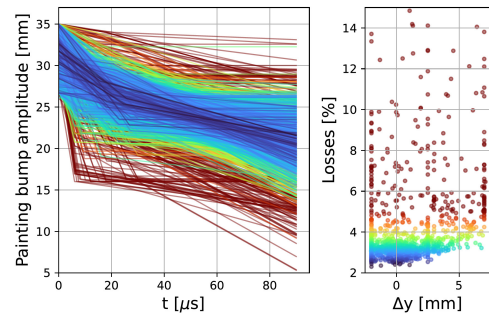


Figure 7: Selection of injection settings obtained in optimiser steps: Horiz. painting bump decay during beam accumulation (left), applied  $\Delta y$  of injected beam (right). Data collected over multiple runs for  $I_{\text{INJ}} = 0.9 \cdot 10^{13} \text{ p+}$ , R3.

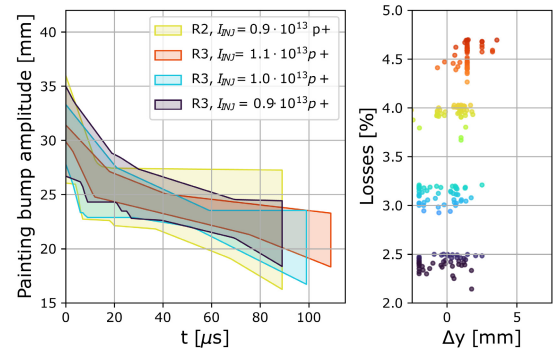


Figure 8: Comparison of the injection settings range as optimised by using diverse numerical optimisation algorithms for different operational conditions.

dependency of the vertical losses obtained during resonance crossing to the applied transverse painting settings and the resulting phase space distribution after injection. Promising results have been obtained when applying numerical optimisation algorithms to efficiently optimise the transverse injection settings to reduce those losses during high intensity beam production. A data driven surrogate model is being used for offline hyper-parameter tuning and feature engineering to improve the optimisation set-up.

## ACKNOWLEDGMENTS

The authors would like to thank all teams involved in the PSB and Linac4 operation, hardware and beam commissioning for their continuous support and input, as well as V. Kain and N. Madysa for development of and support with the Generic Optimisation Frontend and Framework.

## REFERENCES

- [1] J. Coupard *et al.*, “LHC Injectors Upgrade, Technical Design Report, Vol. I: Protons”, CERN, Geneva, Switzerland, Rep. CERN-ACC-2014-0337. 2014.
- [2] G. Apollinari, *et al.*, “High-Luminosity Large Hadron Collider (HL-LHC): Technical Design Report V. 0.1”, CERN-2017-007-M, CERN, Geneva, 2017. doi:10.23731/CYRM-2017-004

- [3] L. Arnaudon *et al.*, “Linac4 Technical Design Report”, CERN, Geneva, Switzerland, Rep. CERN-AB-2006-084, 2006.
- [4] W. J. M. Weterings *et al.*, “The New Injection Region of the CERN PS Booster”, in *Proc. IPAC’19*, Melbourne, Australia, May 2019, pp. 2414–2417. doi:10.18429/JACoW-IPAC2019-WEPMP039
- [5] B. Jonson and K. Riisager, “The ISOLDE facility”, *Scholarpedia*, vol. 5(7), p. 9742, 2010. doi:10.4249/scholarpedia.9742
- [6] A. Mengoni *et al.*, “Status and perspectives of the neutron time-of-flight facility nTOF at CERN”, in *EPJ Web Conf.* 239, 2020. doi:10.1051/epjconf/202023917001
- [7] E. Renner *et al.*, “PSB simulation studies for post LS2 operation”, presented at *4th ICFA Mini-Workshop on Space Charge*, CERN, Geneva, Switzerland, Nov. 2019.
- [8] V. Forte, “Performance of the CERN PSB at 160 MeV with H<sup>-</sup> charge exchange injection”, CERN, Geneva, Switzerland, Rep. CERN-THESIS-2016-063, Jun. 2016.
- [9] V. Forte *et al.*, “Multi-Particle Simulations of the Future CERN PSB Injection Process with Updated Linac4 Beam Performance”, in *Proc. HB’19*, Daejeon, Korea, Jun. 2018, pp. 278–283. doi:10.18429/JACoW-HB2018-WEP2P0007
- [10] E. Renner *et al.*, “Beam Commissioning of the New 160 MeV H<sup>-</sup> Injection System of the CERN PS Booster”, in *Proc. IPAC’21*, Campinas, SP, Brazil, May 2021, pp. 3116–3119. doi:10.18429/JACoW-IPAC2021-WEPAB210
- [11] B. Goddard *et al.*, “Stripping Foil Issues for H- Injection into the CERN PSB at 160 MeV”, in *Proc. IPAC’10*, Kyoto, Japan, May 2010, paper THPEB030, pp. 3951–3953.
- [12] C. Bracco *et al.*, “Commissioning of the Stripping Foil Units for the Upgrade of the PSB H- Injection System”, in *Proc. IPAC’17*, Copenhagen, Denmark, May 2017, pp. 595–598. doi:10.18429/JACoW-IPAC2017-MOPIK041
- [13] C. Bracco *et al.*, “Measurements with the stripping foil test stand in the Linac4 Transfer Line”, in *Proc. INTDS’18*, East Lansing, United States, Oct. 2018, p. 01003. doi:10.1051/epjconf/202022901003
- [14] B. Balhan *et al.*, “Design and Construction of the CERN PS Booster Charge Exchange Injection Chicane Bumpers”, in *Proc. IPAC’18*, Vancouver, Canada, Apr.-May 2018, pp. 2575–2577. doi:10.18429/JACoW-IPAC2018-WEPMF082
- [15] L. M. C. Feliciano *et al.*, “A New Hardware Design for PSB Kicker Magnets (KSW) for the 35 mm Transverse Painting in the Horizontal Plane”, in *Proc. IPAC’15*, Richmond, VA, USA, May 2015, pp. 3890–3892. doi:10.18429/JACoW-IPAC2015-THPF086
- [16] G. Gräwer, “A multi-waveform pulsed current generator for slow kicker magnets”, in *Proc. EPE’19*, Genova, Italy, September 2-5, 2019. doi:10.23919/EPE.2019.8915536
- [17] F. Asvesta *et al.*, “Resonance Compensation for High Intensity and High Brightness Beams in the CERN PSB”, presented at HB’21, virtual, paper MOP06, this conference.
- [18] C. Bracco *et al.*, “PSB injection beam dynamics”, presented at *LIU Day 14*, CERN, Geneva, Switzerland, Apr. 2014. <https://indico.cern.ch/event/299470/contributions/686522/>
- [19] J. Abelleira Fernandez, “Beam Dynamics Study on LIU High Intensity Beams in the BT Line”, CERN EDMS 1537199 v.1.0, CERN, Geneva, Switzerland, Nov. 2015. <https://edms.cern.ch/document/1537199/1.0>
- [20] H. Bartosik, G. P. Di Giovanni, B. Mikulec, and F. Schmidt, “PS Booster Beam Absorber/Scrapper after LS2”, CERN EDMS 1578463 v.2.1, CERN, Geneva, Switzerland, Jan. 2018. <https://edms.cern.ch/document/1578463/2.1>
- [21] R. Veness *et al.*, “Installation and Test of Pre-series Wire Scanners for the LHC Injector Upgrade Project at CERN”, in ICCS, Copenhagen, Denmark, May 2017, pp. 412–414. doi:10.18429/JACoW-IPAC2017-MOPAB121
- [22] S. Hancock, “A simple algorithm for longitudinal phase space tomography”, CERN-PS-RF-NOTE-97-06, CERN, Geneva, May 1997. <https://cds.cern.ch/record/1174559/>
- [23] A. Shishlo *et al.*, “The Particle Accelerator Simulation Code PyORBIT”, in *Proc. ICCS’15*, Reykjavík, Iceland, Jun. 2015, pp. 1272–1281.
- [24] T. Prebaj *et al.*, “Injection chicane beta-beating correction for enhancing the brightness of the CERN PSB beams”, presented at HB’21, virtual, paper MOP18, this conference.
- [25] A. Santamaria Garcia *et al.*, “Identification and Compensation of Betatronic Resonances in the Proton Synchrotron Booster at 160 MeV”, in *Proc. IPAC’19*, Melbourne, Australia, May 2019, pp. 1054–1057. doi:10.18429/JACoW-IPAC2019-MOPTS086
- [26] A. Santamaría García *et al.*, “Systematic Studies of Transverse Emittance Measurements Along the CERN PS Booster Cycle”, in *Proc. IPAC’18*, Vancouver, Canada, Apr.-May 2018, pp. 806–809. doi:10.18429/JACoW-IPAC2018-TUPAF047
- [27] V. Kain and N. Madysa, “Generic Optimisation Frontend and Framework (GeOFF)”, <https://gitlab.cern.ch/vkain/acc-app-optimisation/>
- [28] C. Cartis *et al.*, “Improving the Flexibility and Robustness of Model-Based Derivative-Free Optimization Solvers”, *ACM TOMS*, vol. 45, no. 3, p. 32, Aug. 2019. doi:10.1145/3338517
- [29] C. Cartis *et al.*, “Escaping local minima with local derivative-free methods: a numerical investigation”, *Optimization*, Feb. 2021. doi:10.1080/02331934.2021.1883015
- [30] M. J. D. Powell, “An efficient method for finding the minimum of a function of several variables without calculating derivatives”, *The Computer Journal*, vol. 7, no. 2, pp. 155–162, 1964. doi:10.1093/comjnl/7.2.155.
- [31] M. J. D. Powell, “A direct search optimization method that models the objective and constraint functions by linear interpolation”, in *Advances in Optimization and Numerical Analysis*, vol. 275, p. 51–67, Springer, Dordrecht, 1994. doi:10.1007/978-94-015-8330-5\_4
- [32] John A. Nelder and R. Mead, “A simplex method for function minimization”, in *Computer Journal*, vol. 7, no. 4, p. 308–313, 1965. doi:10.1093/comjnl/7.4.308
- [33] L. Breiman *et al.*, “Random Forests” *Machine Learning*, vol. 45, p. 5–32, 2001. doi:10.1023/A:1010933404324

# SPACE CHARGE RESONANCE ANALYSIS AT THE INTEGER TUNE FOR THE CERN PS

F. Asvesta and F. Schmidt, CERN, Geneva, Switzerland

## Abstract

In the context of the LHC Injectors Upgrade (LIU) project, a series of studies have been performed in order to better understand the beam brightness limitations imposed by resonances and space charge effects.

Space charge simulations using the adaptive space charge solver as implemented in the MAD-X code conducted for the CERN Proton Synchrotron (PS) show that a particle approaching the integer tune of  $Q_x = 6$  demonstrates a resonant behavior. The analysis of the single particle transverse motion reveals the excitation of a second order resonance. The interplay of the space charge effect and the optics perturbation in the regime of the integer tune on this excitation was further investigated. The simulations were complemented with the analysis of the resonance driving terms coming from the space charge potential derived in a classical perturbative approach.

## INTRODUCTION

The space charge is a dominant effect in high brightness low energy machines like the CERN PS. In this respect, multiple studies were conducted in order to understand the limitations for pushing the brightness in the scope of the LHC Injectors Upgrade (LIU) project [1]. Numerous studies, have shown that the available tune space in the PS is limited by both machine error and space charge driven resonances [2–6]. With such a limited transverse tune space, there is a need to better understand the impact of the integer resonance on the beam and investigate the sources of the excitation [7].

Experimental and simulation studies have been performed at the CERN PS to understand space charge effects in conjunction with sextupole non-linearities [3], including tune working points that sample a sextupole resonance but also the integer resonance. The minimum horizontal bare machine tune used in experiments and simulations alike was  $Q_x = 6.039$ , i.e. slightly above the integer while the maximum horizontal incoherent tune spread was  $-0.05$ . For the simulations discussed in this paper the code used is MADX-SC, an extension of the MAD-X Ref. [8] code including a space charge (SC) implementation of the adaptive mode. MADX-SC is presented in more details in Ref. [9] at this workshop.

For the SC studies presented here, the MADX-SC adaptive mode was selected, in which the beam emittances are re-calculated from the particle distribution at each turn in order to adapt the SC kicks accordingly. The analytical solvers allow simulating just a few 1'000 macro-particles and is therefore the only way to reach long periods, e.g. 500'000 turns for the typical CERN PS storage time. However, the

SC force recalculations of the adaptive mode introduces some noise to the beam that needs to be minimized by increasing the number of macro-particles. For the PS simulation we had to increase the number of macro-particles from 1'000 to 2'000 to reduce the noise to an acceptable level [9]. This has to be seen as a compromise between simulation speed and artificial emittance blow-up, although this is much less of a problem than for the Particle In Cell (PIC) simulations [10–12]. It should be noted that MADX-SC also has a self-consistent mode but its much larger noise levels and longer simulation times make it impractical for most applications.

The simulation results will be discussed taking into account the PS complexity concerning matching of the tunes. The PS is a machine with combined function magnets with additional circuits for Pole Face Windings (PFWs). The combined function magnets define the transverse tune space that is accessible for the PS while the PFWs and additional quadrupoles, namely the Low Energy Quadrupoles (LEQs), can be used for fine adjustment of the tunes. The perturbations of the optics, when different combinations of the above elements are used, have an impact on resonance excitation in the presence of the space charge force.

In the first section, the analysis of the resonance structure found in phase space during the simulations will be presented. In the second section, the nature of the excitation of this higher order resonance on the integer tune will be discussed using the calculation of the resonance driving terms coming from the space charge potential and the harmonic analysis of the beam size and hence the beta functions as the integer resonance is approached.

## RESONANCE ISLANDS IN SIMULATIONS

MADX-SC simulations are conducted for a working point close to the integer tune,  $Q_x = 6.039$  and  $Q_y = 6.479$  with the beam parameters shown in Table 1. To this end, a particle distribution of 2'000 macro particles is chosen to minimize numerical noise. A single particle that basically sits in the center of the bunch with very small initial coordinates is added to the 2'000 particle distribution. This special particle can be considered as a probe particle that is influenced by the full beam but itself affects very little the other particles of the bunch. Therefore, this particle is very close to the closed orbit and can be used to determine the maximum SC tune shift by analyzing its turn-by-turn motion.

### *Tune Matching as in the Experiment*

In this section we are using the PFW for a large shift of the working point from the base tunes. The fine-tuning towards the horizontal integer and the vertical half integer

tunes is done via the LEQ families. This is very close to the procedure used in the 2012 PS experiment [3].

Table 1: Beam Characteristics for the Simulations and the Calculation of the RDTs Shown in Fig. 6

Kinetic energy	2 GeV
Intensity [ $1 \times 10^{10}$ ppb]	55
Bunch length (rms) [m]	9.59
Momentum spread $\Delta p/p$ (rms) [ $10^{-3}$ ]	0.95
Hor. normalized emittance, $\epsilon_x^n$ ( $1\sigma$ ) [ $\mu\text{m}$ ]	3.5
Ver. normalized emittance, $\epsilon_y^n$ ( $1\sigma$ ) [ $\mu\text{m}$ ]	2.2
Horizontal tune shift, $\Delta Q_x$	-0.05
Vertical tune shift, $\Delta Q_y$	-0.07

In the following we examine the phase space topology by inspecting the phase space trajectories for individual particles. In particular, particles are launched with different initial horizontal offsets from the closed orbit, while in the vertical and the longitudinal planes the initial conditions were chosen very close to the closed orbit. Different particle trajectories will be shown in different colors. In all phase space plots (Figs. 1 to 5) the coordinates follow the MAD-X convention.

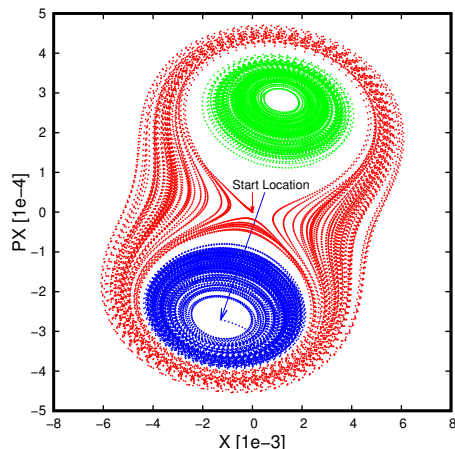


Figure 1: Horizontal Phase Space for three particles: Tiny initial amplitude with chaotic motion (red); Upper Island (green) and Lower Island (blue). Red and blue arrows point to the tiny initial amplitude and the initial coordinates of the lower island respectively.

In Fig. 1 one finds in red the horizontal phase space for a particle launched close to zero amplitude, where the red arrow points to the horizontal starting point. The particles shown in blue and in green are launched with an offset and exhibit the motion inside an “upper” (green) and a “lower” (blue) island. For the lower island the starting locations is indicated by a blue arrow.

In Fig. 2 one finds the corresponding traces in the longitudinal phase space.

At this point a few explanations are needed: in the horizontal plane the zero amplitude has become the unstable fixed point of the second order resonance and the motion

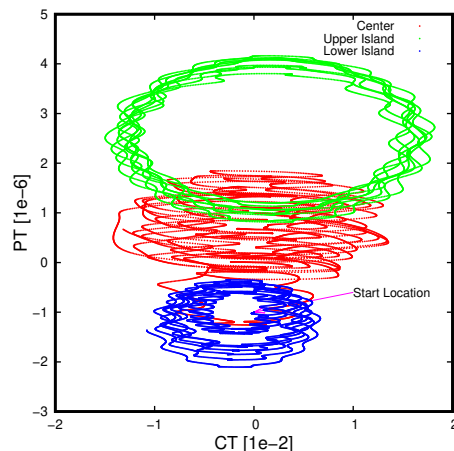


Figure 2: Longitudinal Phase Space for three particles: Tiny initial amplitude with chaotic motion (red); Upper Island (green) and Lower Island (blue). The arrow, magenta for visibility, is pointing to the start location of the Lower Island.

evolves around the separatrix, which by nature is chaotic. On the other hand, the island cases, while existing for at least 10'000 turns are not truly stable, but should be called meta-stable at best. This might happen just due to the fact that other effects like the sextupole non-linearities also drive this or other resonances at the integer; the strong coupling between horizontal and longitudinal phase space due to horizontal dispersion which is further enhanced by SC; or the fact that in the adaptive mode noise is being introduced. The latter is discussed below.

Figures 1 and 2 seem to suggest that one may just zoom into the respective horizontal and longitudinal islands to find the stable island fixed points. In practice, it turns out that it is exceedingly difficult to do just that. Instead it becomes an elaborate search in 4D (apparently it does not depend on the vertical plane). The limitation of this attempt becomes apparent in the 2 figures for the lower island: the starting location in both plots seem to be close to the center of either island, yet this area seems not stably accessible.

In Ref. [13] it had been shown that the four-fold increase of the number of macro-particles leads to the statistical reduction of the noise by a factor of 2. Therefore the upper island simulations have been repeated with a factor 5 increased number of macro-particles (i.e. 10k instead of 2k), since the simulations can still be done reasonably fast. In Fig. 3 one finds that the jittery islands MOP20.images are even more enhanced for the higher number of macro-particles. This does not prove that this kind of noise is unimportant for particle stability but it does seem more likely that the internal non-linear dynamics are causing this meta-stable particle behavior.

We do not show here the vertical phase space since it is not coupled to either of the other two planes.

It needs to be mentioned that in parallel, M. Titze has performed separate studies for his PhD at the PS under slightly different conditions [14]. He did find similar indications of

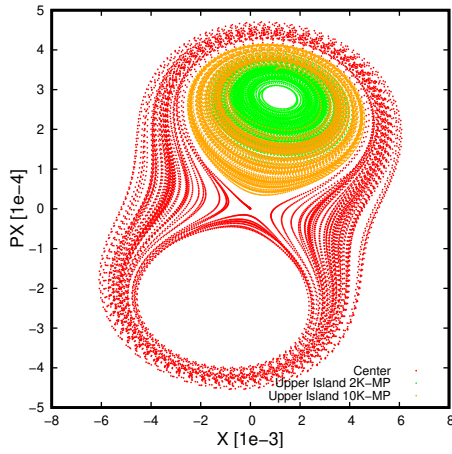


Figure 3: Noise test in Horizontal Phase Space for three particles: Tiny initial amplitude with chaotic motion (red) as in Fig. 1; Upper Island (green) as in Fig. 1. In orange one finds the result for the same initial coordinates of the upper Island but with 5 times larger number of macro-particles.

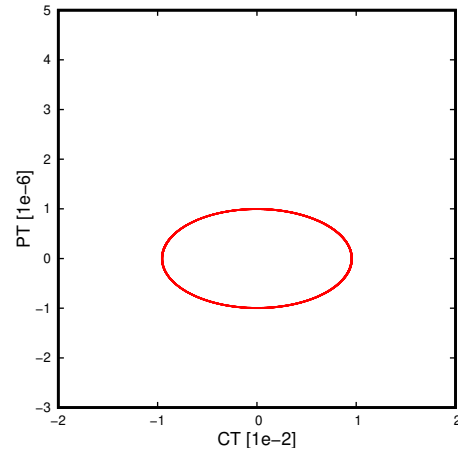


Figure 5: PFW System: Longitudinal Phase Space keeping the same scale as in Fig. 2.

a resonant behavior but did not include a full analysis in his thesis.

### Tune Matching with the PFW System Only

Knowing about the limitations of the LEQ system [7] we have attempted a tune matching with just the PFW system.

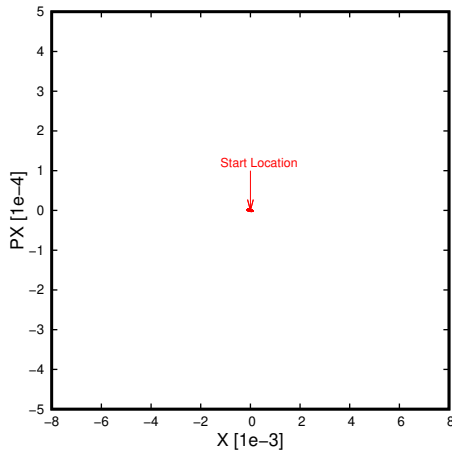


Figure 4: PFW System: Horizontal Phase Space with the red arrow to the tiny initial amplitude, keeping the same scale as in Fig. 1.

In Fig. 4, showing the horizontal plane, the arrow points again to the tiny initial amplitude, but this time the amplitude remains tiny and is hardly visible since we have kept the same scale as in Fig. 1. In Fig. 5 one finds the longitudinal phase space that occupies about the same area in the longitudinal phase as in Fig. 2, but here one can no longer find the jittery motion that is due to the strong coupling with the horizontal plane.

Thus it seems that the use of the LEQs leads to the resonance behavior, presumably due to the interplay of the

quadrupole perturbations with the SC force. In the following we will discuss a SC driving term analysis.

## DRIVING-TERM ANALYSIS

An analysis of the Resonance Driving Terms (RDT) coming from the SC potential, using PySCRDT [15], is conducted to try and explain the mechanism that leads to the excitation of the integer resonance in the machine and in MADX-SC [13] simulations. The optics needed for the calculations are taken from the MAD-X twiss files of the PS lattice in two different configurations: a) When the tunes are matched using PFWs, i.e. windings on all of the main magnets that perfectly preserve the periodicity of the machine, and b) when the LEQs, i.e. dedicated quadrupole magnets that are not preserving the periodicity of 50, are used together with the PFWs to control the tune. In normal machine operation, the tune is always controlled using both LEQs and PFWs [16]. The beam characteristics for the calculation of the RDTs are given in Table 1.

Figure 6 shows the evolution of the RDTs due to the SC potential as the integer resonance is approached either using the PFWs (top) or both PFWs and LEQs (bottom). The RDT amplitudes are calculated using:

$$G_{2,0} = -\frac{K_{sc}}{2\pi} \int_0^C \frac{\beta_x}{\sigma_x \cdot (\sigma_x + \sigma_y)} \cdot e^{j(2\phi_x)} ds \quad (1)$$

where,  $K_{sc} = \frac{r_0 N_b}{\beta^2 \gamma^3 \sqrt{2\pi} \sigma_s}$ ,  $r_0$  is the classical particle radius,  $N_b$  the bunch intensity,  $\beta, \gamma$  the relativistic factors,  $\sigma_{s,x,y}$  the longitudinal and transverse beam sizes accordingly and  $\phi_x$  the horizontal phase advance. In the PFW case, the periodicity of the machine is not perturbed and as a result the resonance is suppressed by the lattice symmetry. On the other hand, when the LEQs are also used the RDT starts increasing in the proximity of the integer tune at  $Q_x = 6$ . However, once the tune reaches values below  $Q_x < 6.01$ , the RDT seems to drop. To understand this behavior the harmonic analysis of the beam size is needed.

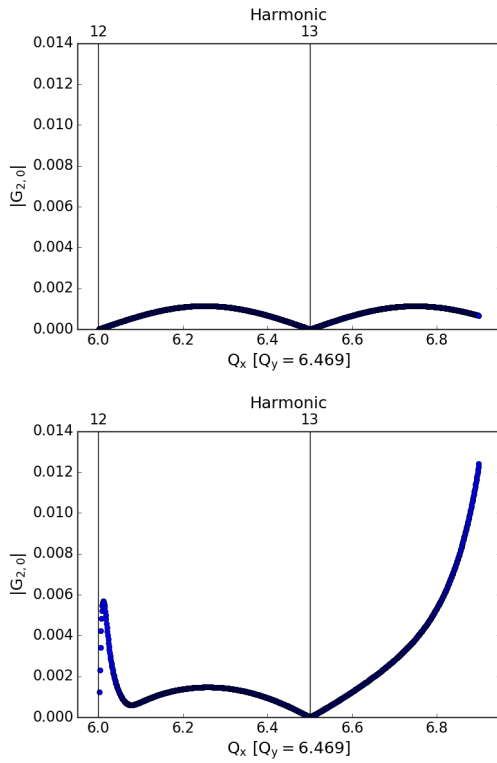


Figure 6: RDT evolution along the horizontal tune  $Q_x$ , when the matching is done using the PFWs (top) and a combination of both PFWs and LEQs (bottom).

The lattice is matched at the nominal working point,  $Q_x = 6.2/Q_y = 6.24$  using the PFWs or the LEQs. The harmonic analysis is presented in Fig. 7 for the different configurations. Using the LEQs, new harmonics are introduced that are suppressed in the fully symmetric lattice. One of the enhanced harmonics is the 12<sup>th</sup> which coincides with the quadrupole resonance at the integer tune  $Q_x = 6$ , i.e. the  $2Q_x = 12$  resonance. These lower order harmonics make it impossible to match the PSB lattice closer to the integer using the LEQs alone.

For the more realistic case of using both PFWs and LEQs, as in the analysis of Fig. 6 (bottom), the harmonic analysis is done at the nominal working point, and closer to the integer resonance as shown in Fig. 8. The combination of both LEQs and PFWs is introducing lower order harmonics but not as many as in the case of LEQs alone. These lower order harmonics, and in particular the harmonic 12, are enhanced substantially as the tune approaches the integer of  $Q_x = 6$ . The harmonic 12 becomes the most important as its amplitude is even larger than the 50<sup>th</sup> harmonic.

In order to understand why the RDT seems to drop when we approach the resonance for  $Q_x < 6.01$  the beam size evolution around the machine is shown in Fig. 9. The beam size is always calculated using the parameters of Table 1. Comparing the beam size for tunes  $Q_x = 6.01$  and  $Q_x = 6.003$  we can see that it has blown up significantly. This means that the SC force, which depends on the beam size,

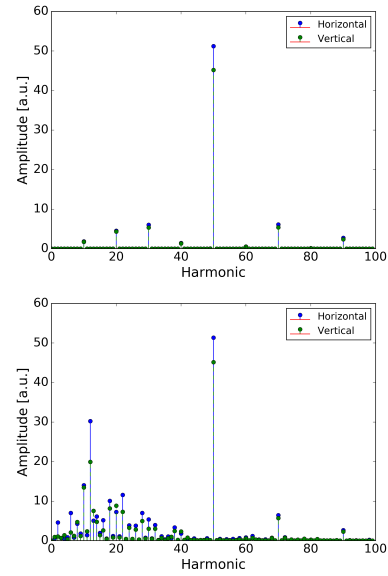


Figure 7: Harmonic analysis of the beam size evolution when the matching is done at  $Q_x = 6.2/Q_y = 6.24$  using the PFWs (top) and LEQs (bottom).

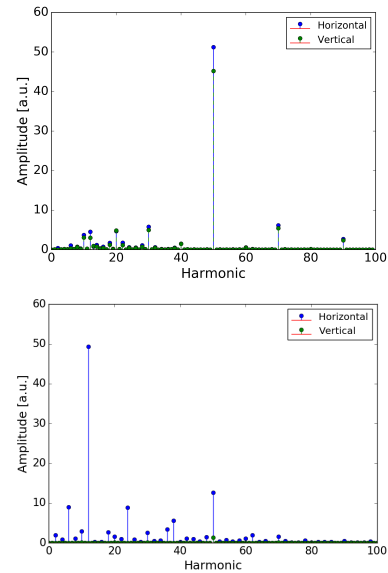


Figure 8: Harmonic analysis of the beam size evolution when the matching is done using both PFWs and LEQs at  $Q_x = 6.2/Q_y = 6.24$  (top) and at  $Q_x = 6.003/Q_y = 6.469$  (bottom).

is significantly reduced. It should be noted that the tune cannot be lowered further when the LEQs and the PFWs are used. Furthermore, the disruption of the optics and the dominance of the 12<sup>th</sup> harmonic can be clearly identified. For completeness the beam size evolution for  $Q_x = 6.001$  when the matching is done using only the PFWs is given. No blow up is observed in this case and the periodicity of 50 is clearly maintained.

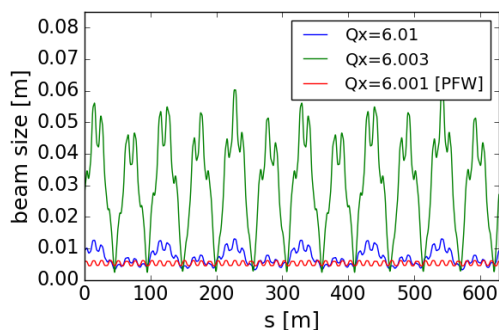


Figure 9: Beam size evolution along the location in the machine while approaching the integer tune. The matching is done using both PFWs and LEQs the  $Q_x = 6.01$  and  $Q_x = 6.003$  cases while for the  $Q_x = 6.001$  only the PFWs are used.

## CONCLUSION

The integer resonance has been studied in the CERN PS in simulations and analytical calculations, in order to better understand the brightness limitation it might impose. The studies revealed that even in the absence of dipole-like errors, which would excite the resonance in 1<sup>st</sup> order, or other random errors in the machine, the resonance can be excited through the disruption of the optics as the integer tune is approached. This disturbance of the machine periodicity leads to 2<sup>nd</sup> order resonance excitation at the integer tune due to space charge.

Further studies may complement what has been described in this report. It would be interesting to analyze the 2<sup>nd</sup> order SC resonance with simulations using PIC codes as no self-consistent analysis has been performed until now. Equally important would be an experimental attempt to approach the PS integer tune without using the LEQs. Moreover, further analysis of the quadrupole RDTs could improve the understanding of the nature of the excitation and quantify the SC contribution.

## ACKNOWLEDGMENTS

The authors would like to thank H. Bartosik for the fruitful discussions.

## REFERENCES

- [1] H. Damerau *et al.*, “LHC Injectors Upgrade, Technical Design Report”, CERN, Geneva, Switzerland, Rep. CERN-ACC-2014-0337, 2014, doi:10.17181/CERN.7NHR.6HGC
- [2] A. Huschauer, “Working point and resonance studies at the CERN Proton Synchrotron,” CERN, Geneva, Switzerland, Rep. CERN-THESIS-2012-212, <http://cds.cern.ch/record/1501943/>.
- [3] G. Franchetti, S. Gilardoni, A. Huschauer, F. Schmidt, and R. Wasef, “Space charge effects on the third order coupled

resonance,” *Phys. Rev. Accel. Beams*, vol. 20, p. 081006, 2017, doi/10.1103/PhysRevAccelBeams.20.081006

- [4] F. Asvesta *et al.*, “Space charge studies in the PS,” *Injector MD Days 2017*, pp. 37–42, 2017, doi:10.23727/CERN-Proceedings-2017-002.37
- [5] R. Wasef, “8th Order Super-Structure Resonance driven by Space Charge,” CERN, Geneva, Switzerland, Rep. CERN-THESIS-2017-455, 2017, <http://cds.cern.ch/record/2670261/>.
- [6] F. Asvesta *et al.*, “Identification and characterization of high order incoherent space charge driven structure resonances in the CERN Proton Synchrotron,” *Phys. Rev. Accel. Beams*, vol. 23, p. 091001, 2020, doi:10.1103/PhysRevAccelBeams.23.091001
- [7] H. Rafique, F. Asvesta, H. Bartosik, A. Huschauer, and M. Kaitatzi, “Approaching the Integer Tune in the Proton Synchrotron to Probe Space Charge at Injection,” Presentation in LIU-PS Beam Dynamics WG meeting #36, 2019, <https://indico.cern.ch/event/857161/>.
- [8] T. Persson, L. Deniau, and G. Roy, “The mad-x program (methodical accelerator design), version 5.07.00,” May 2021, <http://cern.ch/madx/releases/5.07.00/madxguide.pdf>
- [9] A. Latina, S. F. H. Renshall, and Y. Alexahin, “3D symplectic space charge implementation in the latest MAD-X version,” presented at HB’21, Batavia, IL, USA, Oct. 2021, paper MOP21, this conference.
- [10] I. Hofmann and O. Boine-Frankenheim, “Grid dependent noise and entropy growth in anisotropic 3d particle-in-cell simulation of high intensity beams,” *Phys. Rev. ST Accel. Beams*, vol. 17, p. 124201, Dec. 2014, doi:10.1103/PhysRevSTAB.17.124201
- [11] F. Schmidt, “Micro-instability in Space Charge PIC Codes,” Geneva, Switzerland, Apr. 2013, <https://indico.cern.ch/event/221441/>.
- [12] E. Stern, “Synergia Space Charge Benchmarking and Compensation with Electron Lens,” 2nd CERN Space Charge Collaboration Meeting 2018, <https://indico.cern.ch/event/688897/>.
- [13] F. Schmidt and Y. Alexahin, “New SC Algorithm for MAD-X,” CERN, Geneva, Switzerland, Rep. CERN-ACC-2018-0036, 2019, <https://cds.cern.ch/record/2644660/>.
- [14] M. Titze, “Space Charge Modeling at the Integer Resonance for the CERN PS and SPS,” Apr. 2019, <https://edoc.hu-berlin.de/handle/18452/22207/>.
- [15] F. Asvesta and H. Bartosik, “Resonance Driving Terms From Space Charge Potential,” CERN, Geneva, Switzerland, Rep. CERN-ACC-NOTE-2019-0046, 2019, <http://cds.cern.ch/record/2696190/>.
- [16] P. Freyermuth *et al.*, “CERN Proton Synchrotron working point Matrix for extended pole face winding powering scheme,” CERN, Geneva, Switzerland, Rep. CERN-ATS-2010-180, <http://cds.cern.ch/record/1287599/>.

# 3D SYMPLECTIC SPACE CHARGE IMPLEMENTATION IN THE LATEST MAD-X VERSION

A. Latina, F. Schmidt, H. Renshall, CERN, Geneva, Switzerland,  
 Y. Alexahin, FNAL, Batavia, USA

## Abstract

In 2018 as part of a collaboration between CERN and FNAL, the space charge (SC) implementation has been upgraded in a test version of MAD-X. The goal has been to implement the 3D symplectic SC kick together with a number of new features and benchmark it with earlier MADX-SC versions. Emphasis was given to the use of the Sigma Matrix approach that allows to extend MAD-X optics calculations.

In the meantime, significant effort has been made to fully debug and optimize the code and in particular to achieve a speed-up of the simulations by a factor of 2. The code has been ported to the latest MAD-X version, the elaborated set-up procedures have been automated and a user manual has been written.

## INTRODUCTION

In 2010 (see Ref. [1]) V. Kapin and Y. Alexahin from FNAL started to implement the frozen space charge model into MAD-X [2]. One of the authors, F. Schmidt, joined their effort in 2012, establishing a special Fermilab version that we call MADX-SC, that has been presented in Ref. [3]. In the meantime, we have made a thorough cleaning and debugging of the code and have ported it to the latest MAD-X version. A manual has also been provided [4].

MADX-SC features both the frozen SC mode (as requested by BNL [5]) and the adaptive SC mode, the latter means that the SC force is recalculated when the emittances or beam intensity are changing. One can consider this as somewhere in between frozen and the full self-consistent mode, the latter provided in SC Particle-In-Cell (PIC) codes like Py-Orbit [6]. The adaptive mode allows for SC simulations with a few 1,000 macro-particles, and is therefore very fast and the only way to reach long periods, e.g., 500,000 turns for typical CERN PS SC runs. However, these SC force recalculations introduce some noise to the beam that needs to be minimized by increasing the number of macro-particles. For the PS simulation we had to increase the number of macro-particles from 1,000 to 2,000 to reduce the noise to an acceptable level. Nevertheless, this has to be seen as a compromise between simulation speed and artificial emittance growth due to numerical noise, although this is much less of a problem than for the PIC simulations.

This report discusses the physics aspects of MADX-SC in the first chapter, and summarizes the latest code development in the second chapter.

## THE PHYSICS OF THE MADX-SC IMPLEMENTATION

### Symplectic 3D SC Kick

We will concentrate here on the main MADX-SC design principles, further details can be found in Ref. [3].

The SC kick will be automatically symplectic if it is derived from a potential. We assume the bunch charge density to be of the form

$$\rho(x, y, z, t) = \frac{\lambda(z - v_0 t)}{2\pi\sigma_x\sigma_y} \exp\left(-\frac{x^2}{2\sigma_x^2} - \frac{y^2}{2\sigma_y^2}\right), \quad (1)$$

with  $\lambda$  being the line charge density, which should not be necessarily Gaussian but the present implementation is limited to a Gaussian profile.

For a long bunch,  $\sigma_z \gg \max(\sigma_x, \sigma_y)$ , the space-charge potential can be factorized in a similar fashion

$$\phi(x, y, z, t) \cong \lambda(z - v_0 t) \cdot \Phi(x, y), \quad (2)$$

where the two-dimensional potential function  $\Phi$  can be presented in the form [7]<sup>1</sup>

$$\Phi(x, y) = \int_0^1 \left\{ \exp\left(-\frac{x^2 t}{2\sigma_x^2} - \frac{y^2 r^2 t}{2\sigma_y^2[1 + (r^2 - 1)t]}\right) - 1 \right\} \frac{dt}{t\sqrt{1 + (r^2 - 1)t}}, \quad (3)$$

with  $r = \frac{\sigma_y}{\sigma_x}$  for  $\sigma_y < \sigma_x$ . If  $\sigma_y > \sigma_x$  one can use formulas with interchanged  $x$  and  $y$ . Computing all components of a quasi-stationary Maxwellian field from the same potential ensures the symplecticity of the associated kick.

The potential in Eq. (3) is regularized and satisfies the boundary condition

$$\Phi(x, y)|_{x=y=0} = 0. \quad (4)$$

As a future development it can be complemented with a longitudinal wake which is independent of the transverse position (in order not to break the symplecticity).

Note [7] discusses the derivation of Eq. (3) in detail and considers methods of its numerical calculation in cases of small, large, and intermediate values of the transverse displacement, in units of beam sizes. Report [8] presents precision tests for each of these cases.

<sup>1</sup> Gaussian units are used. To convert to SI units the r.h.s. should be divided by  $4\pi\epsilon_0$

Content from this work may be used under the terms of the CC BY 3.0 licence (© 2021). Any distribution of this work must maintain attribution to the author(s), title of the work, publisher, and DOI

Ref. [3] summarizes the main results. For different transverse displacements the evaluation of the potential can be separated into three, mostly distinct regions: Power Series Expansion, Asymptotic Expansion and Numerical Integration.

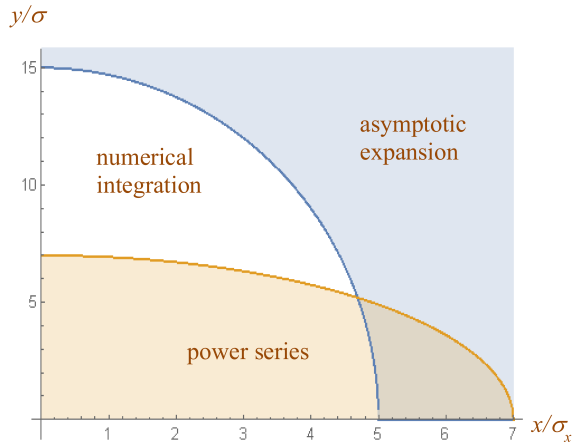


Figure 1: Regions of good precision for power series and asymptotic expansion for aspect ratio  $r = \frac{\sigma_y}{\sigma_x} = \frac{1}{3}$ . For coordinates in the white region the numerical integration has to be used.

In Figure 1 for the region where numerical integration is required one needs to determine the relative error in  $\Phi$  vs. the number of integration steps.

Figure 2 shows the precision of the potential found using the Simpson rule as a function of the number of steps of integration. Errors in  $E_x$  and  $E_y$  are about two orders of magnitude lower.

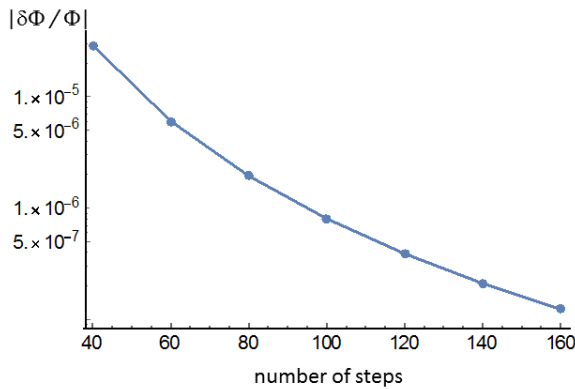


Figure 2: Relative error in  $\Phi$  vs. the number of integration steps.

About 100 grid points in Fig. 2 appear to be sufficient for various cases we have studied.

### Beam Sigma and Optics Calculation without Twiss

The beam sizes should be periodically updated (e.g. every turn) based on the evolving particle distribution. The previ-

ously implemented algorithm (described a posteriori in [9]) requires stable optics using the MAD-X Twiss command: first to find the action variables of the normal modes for each particle at the observation point to determine emittances; and then to calculate the beam sizes with updated emittances at all space-charge elements.

The optics functions can also be updated but, even if the stable periodic solution exists, this significantly slows down the computation.

Another drawback of the old algorithm is the rather soft suppression of the halo particles contribution to the emittance leading to larger beam sizes and weaker space-charge kicks.

A different approach was proposed in [10], which involves the exact Gaussian fit of the particle distribution in terms of the beam  $\Sigma$  matrix and its subsequent propagation from the observation point along the lattice using the transfer matrix  $T$  as

$$\Sigma^{(2)} = T \cdot \Sigma^{(1)} \cdot T^t, \quad (5)$$

where superscript “t” means transposition.

The precision of the fit was checked in [10] for a one-dimensional distribution. Tests with a multi-dimensional distribution revealed problems with spurious coupling, which only slowly decreases with the number of particles and in the case of equal emittances does not decrease at all.

The probable cause of the spurious coupling is the very strong suppression of the contribution of particles with even moderate amplitudes, effectively reducing the number of particles. To alleviate this problem, the fitting algorithm was modified in the way described below.

First of all, we shall show that the fitting formulas in [10] can be obtained from simple considerations valid also for other types of model distribution function. Let  $z_i, i=1, \dots, n$  be the  $n$ -dimensional phase space coordinates and  $W(z_1, \dots, z_n)$  some weight function that we will use for construction of the  $\Sigma$  matrix from a sample of  $N$  particles, while trying to approximate this sample with the model distribution function  $F(z_1, \dots, z_n)$ . In what follows we will denote the  $n$ -tuple  $(z_1, \dots, z_n)$  by  $z$ .

Let  $F(z)$  be the actual normalized beam distribution function. Then, as a consequence of the law of large numbers, we will have for any function  $H(z)$  in the limit of large number of particles  $N \rightarrow \infty$

$$\frac{1}{N} \sum_{k=1}^N H(z^{(k)}) \xrightarrow{N \rightarrow \infty} \int_{\Omega} H(z) F(z) d^n z, \quad (6)$$

with  $\Omega$  being the available phase space.

Now we can define the fitted  $\Sigma$  matrix using weight function  $W(z)$  as

$$\sum_{ij}^{(fit)} = \frac{\frac{1}{N} \sum_{k=1}^N z_i^{(k)} z_j^{(k)} W(z^{(k)})}{\frac{1}{N} \sum_{k=1}^N W(z^{(k)}) - p}, \quad (7)$$

with  $p$  being some parameter. Imposing the requirement that matrix Eq. (7) coincides with the actual  $\Sigma$  matrix in the limit  $N \rightarrow \infty$

$$\sum_{ij}^{(exact)} = \int_{\Omega} z_i z_j F(z) d^n z, \quad (8)$$

we have for non-zero elements  $\Sigma_{ij}^{(exact)}$

$$p = \int_{\Omega} W(z) F(z) d^n z - \frac{1}{\sum_{ij}^{(exact)}} \int_{\Omega} z_i z_j W(z) F(z) d^n z. \quad (9)$$

In the case of Gaussian distribution and weight functions

$$F(\underline{z}) = \frac{1}{(2\pi)^{\frac{n}{2}} \sqrt{\det \Sigma}} \exp[-\frac{1}{2}(\underline{z}, \Sigma^{-1} \underline{z})], \quad (10)$$

$$W(\underline{z}) = \exp[-\alpha(\underline{z}, \Sigma^{-1} \underline{z})],$$

where  $\underline{z}$  are  $n$ -dimensional vectors of displacements from some average values, we obtain

$$p = \frac{2\alpha}{(1+2\alpha)^{\frac{n}{2}+1}}. \quad (11)$$

With  $\alpha = 0, p = 0$  Eq. (7) provides simple r.m.s. values while with  $\alpha = \frac{1}{2}, p = \frac{1}{2^{\frac{n}{2}+1}}$  we retrieve the result of [10].

By adjusting  $\alpha$  we can suppress the contribution of halo particles while not cutting into the beam core. The choice  $\alpha = \frac{1}{4}$  greatly reduced the spurious coupling. It should be noted that with  $\alpha \neq \frac{1}{2}$  this fit does not render the minimum of the integrated squared difference in the phase density of actual particle distribution and the model distribution in this sense is not exact. However, it leads to more practical results.

Since the  $\Sigma$  matrix is not known, Eq. (7) is a non-linear equation which can be solved iteratively. The full set of equations to solve is:

$$\underline{a} = \frac{\sum_{k=1}^N \underline{z}^{(k)} \exp[-\alpha(\underline{z}^{(k)}, \Sigma^{-1} \underline{z}^{(k)})]}{\sum_{k=1}^N \exp[-\alpha(\underline{z}^{(k)}, \Sigma^{-1} \underline{z}^{(k)})]}, \quad \underline{z}^{(k)} = \underline{z}^{(k)} - \underline{a}, \quad (12)$$

$$\sum_{ij} = \frac{\frac{1}{N} \sum_{k=1}^N \zeta_i^{(k)} \zeta_j^{(k)} \exp[-\alpha(\underline{z}^{(k)}, \Sigma^{-1} \underline{z}^{(k)})]}{\frac{1}{N} \sum_{k=1}^N \exp[-\alpha(\underline{z}^{(k)}, \Sigma^{-1} \underline{z}^{(k)})] - \frac{2\alpha}{(1+2\alpha)^{\frac{n}{2}+1}}}. \quad (13)$$

The iterative procedure for Eqs. 12 and 13 has a tendency to overshoot, but the convergence can be improved by the introduction of a damping factor  $0 < d < 1$ :

$$\Sigma_l = d \Sigma_l^{(formula)} + (1-d) \Sigma_{l-1}, \quad (14)$$

where  $l$  is the iteration number. Tests showed that  $d = 0.85$  is close to the optimum.

The  $\Sigma$  matrix propagated along the lattice according to Eq. (5) may contain a free-oscillating part due to e.g. initial mismatch. This gives us the ability to study the effects of interaction of individual particles with coherent (envelope) oscillations, such as halo formation [11] and Landau damping.

With a finite number of macro-particles there are inevitable statistical fluctuations which act as a never ending

pump, increasing beam emittance through this interaction. The obvious remedy, a larger number of macro-particles, defeats our goal of the speed of simulations.

Thus we have to consider two modes of operations: freely propagating  $\Sigma$  and periodic  $\Sigma$ . The first option allows one to study envelope resonances but requires the maximum available number of particles to suppress the statistical noise. The second option is analogous to the existing MAD-X algorithm but more efficiently suppresses the halo contribution to emittances and includes effects of the machine coupling (we plan to add coupling through the space charge forces in the future).

The periodic  $\Sigma$  option requires the existence of a stable optics and it involves computation of the eigen-mode emittances  $\varepsilon_m, m=1,2,3$ , which are imaginary parts of eigenvalues of matrix

$$\Omega = S, \quad (15)$$

with  $S$  being the symplectic unity matrix

$$S = \begin{pmatrix} 0 & 1 \\ -1 & 0 \end{pmatrix} \oplus \begin{pmatrix} 0 & 1 \\ -1 & 0 \end{pmatrix} \oplus \begin{pmatrix} 0 & 1 \\ -1 & 0 \end{pmatrix}. \quad (16)$$

After completing turn  $n-1$ , we obtain the transfer matrix  $T(n-1)$  and the particle distribution at the starting point of turn  $n$ . We use the algorithm as calculated above for  $\Sigma(n)$  but instead of propagating it around machine we use it for computing normal mode emittances  $\varepsilon_m$  from matrix Eq. (15). To build a (quasi-) periodic  $\tilde{\Sigma}(n)$  at the starting point of turn  $n$  we also need the eigenvectors of the 1-turn transfer matrix that has three complex-conjugate pairs of eigenvalues and eigenvectors

$$T \underline{v}_k = \lambda_k \underline{v}_k, \quad \lambda_{2m} = \lambda_{2m-1}^*, \quad \underline{v}_{2m} = \underline{v}_{2m-1}^* \quad (17)$$

where  $m=1,2,3$  is the mode number, asterisk denotes complex conjugation, underscore means 6D vector. We choose the same normalization as used in MAD:

$$(\underline{v}_{2m-1}^*, S \underline{v}_{2m-1}) = 2i, \quad (18)$$

that can be rewritten for real and imaginary parts of the eigenvectors as

$$\begin{aligned} (\underline{v}'_i, S \underline{v}'_j) &= (\underline{v}''_i, S \underline{v}''_j) = 0, \\ (\underline{v}'_{2m-1}, S \underline{v}''_{2m-1}) &= \delta_{mn}, \\ \underline{v}'_i &\equiv \text{Re}(\underline{v}_i), \quad \underline{v}''_i \equiv \text{Im}(\underline{v}_i). \end{aligned} \quad (19)$$

Assuming that the new transfer matrix,  $T(n)$ , will not differ much from  $T(n-1)$ , we can use eigenvectors of  $T(n-1)$  to build  $\tilde{\Sigma}(n)$  according to [12–14]

$$\tilde{\Sigma}_{ik} = \sum_{m=1}^3 \varepsilon_m (\underline{v}'_{2m-1,i} \underline{v}'_{2m-1,k} + \underline{v}''_{2m-1,i} \underline{v}''_{2m-1,k}), \quad (20)$$

where  $v_{m,k}$  means  $k$ -th component of  $m$ -th eigenvector. The eigenvectors can be propagated around the ring for Eq. (20) to be applied at every space-charge kick. Alternatively,  $\tilde{\Sigma}(n)$  can be propagated around the ring using MAD-X sectormaps.

Content from this work may be used under the terms of the CC BY 3.0 licence (© 2021). Any distribution of this work must maintain attribution to the author(s), title of the work, publisher, and DOI

### SC Simulations Predictions

In 2012 a dedicated PS experiment was conducted to study beam stability and emittance blow-up due to SC and sextupole non-linearities. Table 1 shows the relevant parameters from this experiment. The results were published in 2017 [15].

Table 1: Beam Characteristics for the 2012 PS Experiment

Parameter	Value
Intensity [ $1 \times 10^{10}$ ppb]	55
Bunch length (rms) [m]	9.59
$\Delta p/p$ (rms) [ $10^{-3}$ ]	0.95
$\epsilon_x^n$ ( $1\sigma$ ) [ $\mu\text{m}$ ]	3.5
$\epsilon_y^n$ ( $1\sigma$ ) [ $\mu\text{m}$ ]	2.2
Turns in Machine/Simulations	500,000

Using the beam parameters from the 2012 experiment, a first test was done to study the impact of the number of macro-particles on the resulting artificial emittance growth in the simulations. Figure 3 shows that for the PS the turn-by-turn “noise” of the obtained emittance values goes down by roughly a factor of two, which might be expected when raising the number of macro-particles by a factor of four. The long-term blow-up is also largely reduced. The “apparent” reduction of emittance at the beginning seems to be an artifact of the very small number of macro-particles used in the simulations. In the following we have used 2,000 macro-particles, i.e. by a factor 2 more than in the original simulations. Fortunately, we took advantage of the factor of 2 in speed-up due to optimization, but we still need some 4 weeks of CPU on CERN’s PC farms for each run.

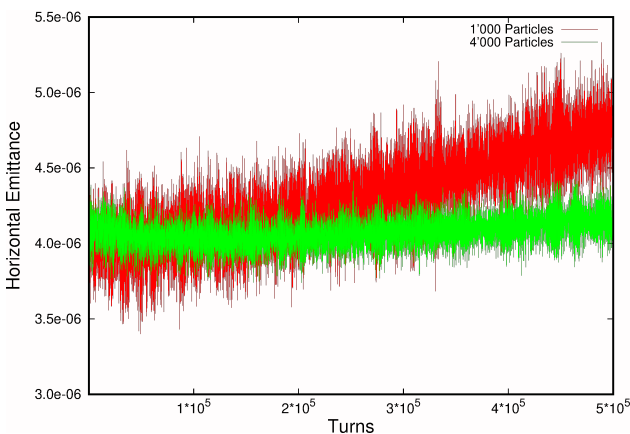


Figure 3: Horizontal emittance evolution versus turn number for the CERN PS for 1,000 and 4,000 macro-particles respectively. Both turn-by-turn noise and long-term emittance growth due to numerical noise decrease with the number of macro-particles, the former by a factor of 2.

The following Figures 4 to 7 show the comparison of the PS experiments with predictions of simulations of a recent MADX-SC version: Fig. 4 shows the horizontal distributions at the start; Fig. 5 the horizontal distributions after 500,000

turns; Fig. 6 the vertical distributions at start, and Fig. 7 the vertical distributions after 500,000 turns.

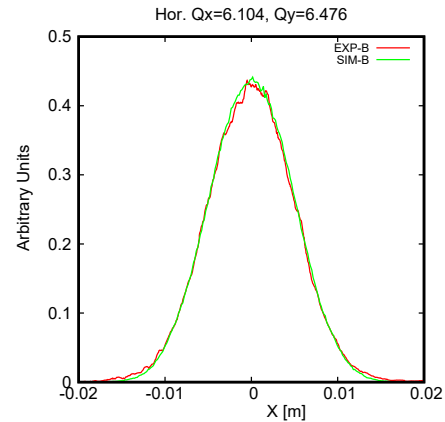


Figure 4: Horizontal Distribution at start, the experimental data are in red, the simulations in green.

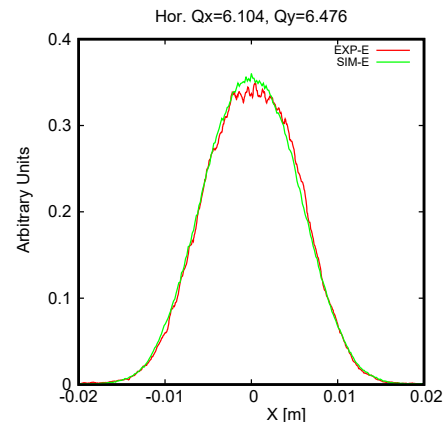


Figure 5: Horizontal Distribution after 500,000 turns, the experimental data are in red, the simulations in green.

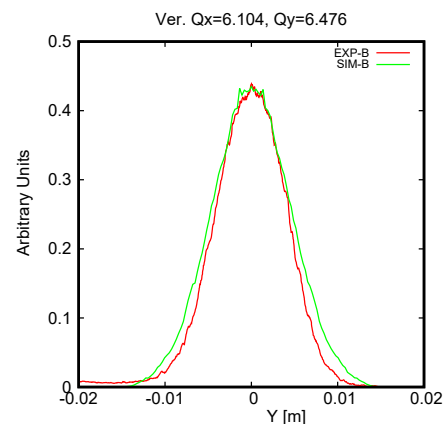


Figure 6: Vertical Distribution at start, the experimental data are in red, the simulations in green.

The two main features of agreement with the experiment are the facts that the broadening of the horizontal profile

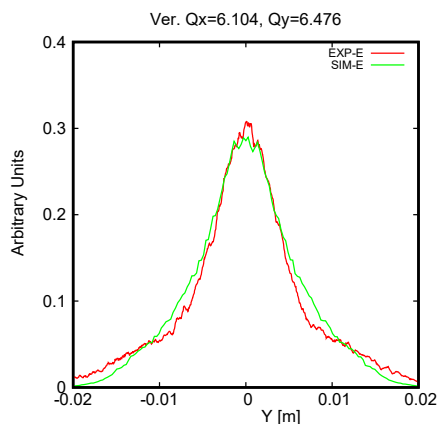


Figure 7: Vertical Distribution after 500,000 turns, the experimental data are in red, the simulations in green.

is well reproduced and the development of vertical tails is almost perfectly followed. Moreover, the obtained results are in very good agreement with previous simulation results reported in [15].

## PORTING TO LATEST MAD-X VERSION

The SC calculation described in this paper was first implemented in the test version of MAD-X at FNAL. In recent years, the official CERN MAD-X version of the code has undergone significant restructuring and consolidation. Among various interventions, the original Fortran 77 code has been partially rewritten to benefit from the latest features offered by the Fortran 90 language. Matrix operations, for instance, that were originally performed with dedicated subroutines have been rewritten to use the native matrix operators provided by F90. In this framework, the SC routines have also been restructured before being updated to include the latest new features introduced in the FNAL test MAD-X version, described in this paper.

A new module was created, containing all the SC- / beam-beam-related routines that in the FNAL MAD-X version were originally hard-coded in the modules TWISS and TRACK. The new space-charge module was provided with a simple interface, consisting of just three functions: Initialize, Update, and Finalize the SC kick, which are directly called from TWISS and TRACK. This restructuring allowed us to improve the overall readability and maintainability of the code, while enabling dedicated optimizations.

Subsequently, the latest features of the SC calculation, described in this paper were introduced, and a work of optimization was carried out to benefit from multi-core parallelism, through OpenMP. A fine tuning of the code and dedicated benchmarks allowed us to optimize the overall performance of the simulation. The work of integrating the new SC routines in the latest official version of MAD-X is being completed, and we expect it to be available from the next MAD-X release, 5.08.00.

Another important issue is the set-up phase that simplifies the lattice, introduces SC kicks in a controlled way and the

adiabatic switching on of the SC kick strength to minimize the problem of unstable optics detected with TWISS, i.e. the attempt to approach the tune working-point as close as possible to integer or half-integer resonances. In the original coding all these tasks were performed with MAD-X macros. This is quite alright concerning the results but for any new user it was exceedingly difficult to adapt a new case to this structure. During the Fermilab visit in 2012 a large number of macros were turned into MAD-X code. Nevertheless, a 3-step expert set-up procedure was still needed for any new case. In 2021, and in conjunction with an upgrade of the manual, we automated these steps in a way such that a typical MAD-X user should now be able to operate the code just with the use of this manual. A bit of fine-tuning is still in progress.

## CONCLUSIONS

This paper summarized the development of the MADX-SC Fermilab code in a collaboration between FNAL and CERN finalized at the end of 2018. In the meantime the code has evolved, as the result of an intense debug and optimization work. In particular, a speed-up of a factor of 2 has been accomplished. The simulation results presented in this paper have been obtained using a more recent version of the code. In parallel, there has been a significant effort to port all changes to the latest MAD-X version. The set-up phase has been simplified and the manual is being updated.

We still have a significant program to extend the scope of the code. In particular, to allow for distributions beyond Gaussian.

## REFERENCES

- [1] V. V. Kapin and Y. Alexahin, “Space Charge Simulation Using MADX with Account of Synchrotron Oscillations”, in *Proc. 22nd Russian Particle Accelerator Conf. (RuPAC’10)*, Protvino, Russia, Sep.-Oct. 2010, paper WEPSB017, pp. 204–206.
- [2] T. Persson, L. Deniau, and G. Roy, “The mad-x program (methodical accelerator design), version 5.07.00.”, May 2021. <http://cern.ch/madx/releases/5.07.00/madxguide.pdf>
- [3] F. Schmidt and Y. Alexahin, “New SC Algorithm for MAD-X,” Oct. 2018, Revised Nov. 2019. <https://cds.cern.ch/record/2644660>
- [4] V. Kapin, A. Latina, H. Renshall, and F. Schmidt, “MADX-SC Flag Description” to be published.
- [5] C. Montag, private communication, Apr. 2014.
- [6] J. Ostiguy and J. Holmes, “PyORBIT: A Python Shell for ORBIT”, in *Proc. 20th Particle Accelerator Conf. (PAC’03)*, Portland, OR, USA, May 2003, paper FPAG018, p. 3503.

- [7] Y. Alexahin, “New Formulae for 3DoF Space Charge Field,” FNAL, Batavia, IL, USA, FNAL Beams-doc-5032-v3, 2017.
- [8] Y. Alexahin, “Progress on 3D space charge kick,” Batavia, IL60510, USA, Mar 2018. <https://indico.cern.ch/event/688897>
- [9] Y. Alexahin, V. Kapin, F. Schmidt, A. Valishev, and R. Wasef, “Adaptive Space Charge Calculations in MADX-SC”, in *Proc. North American Particle Accelerator Conf. (NAPAC’16)*, Chicago, IL, USA, Oct. 2016, pp. 1126–1128. doi:10.18429/JACoW-NAPAC2016-THPOA15
- [10] Y. Alexahin, “Computing Eigen-Emittances from Tracking Data”, in *Proc. North American Particle Accelerator Conf. (NAPAC’16)*, Chicago, IL, USA, Oct. 2016, pp. 1132–1134. doi:10.18429/JACoW-NAPAC2016-THPOA17
- [11] R. L. Gluckstern, “Analytic model for halo formation in high current ion linacs,” *Phys. Rev. Lett.*, vol. 73, pp. 1247–1250, Aug. 1994. doi:10.1103/PhysRevLett.73.1247
- [12] G. Ripken, “Investigations on disturbances in the storage ring caused by the detector field and their corrections (in German),”, DESY, Hamburg, Germany, DESY-R-1-70/5, Jun. 1970.
- [13] L. H. A. Leunissen, F. Schmidt, and G. Ripken, “Six-dimensional beam-beam kick including coupled motion,” *Phys. Rev. ST Accel. Beams*, vol. 3, p. 124002, Dec. 2000. doi:10.1103/PhysRevSTAB.3.124002
- [14] C. Iselin, “The MAD program (methodical accelerator design), version 8.13, physical methods manual,” May 1992.
- [15] G. Franchetti, S. Gilardoni, A. Huschauer, F. Schmidt, and R. Wasef, “Space charge effects on the third order coupled resonance,” *Phys. Rev. Accel. Beams*, vol. 20, p. 081006, Aug 2017. doi:10.1103/PhysRevAccelBeams.20.081006

# A DEDICATED WAKE-BUILDING FEEDBACK SYSTEM TO STUDY SINGLE BUNCH INSTABILITIES IN THE PRESENCE OF STRONG SPACE CHARGE

R. Ainsworth\*, A. Burov, N. Eddy, A. Semenov, Fermilab<sup>†</sup>, Batavia, USA

## Abstract

Recent advances in the theoretical understanding of beam stability in the presence of strong space charge, has suggested a new class of instabilities known as convective instabilities. A novel approach to excite and study these instabilities will be to install a ‘waker’ system, a dedicated wake-building feedback system. The System was installed in the Fermilab Recycler and commissioned during 2021. The first results are presented.

## INTRODUCTION

The transverse mode coupling instability (TMCI) is known to be one of the main intensity limitations for bunch stability in circular machines. For many years, space charge was thought to have a stabilizing effect on TMCI raising the instability threshold to higher intensities. However, recent advances in the theoretical understanding of beam stability in the presence of strong space charge has led to the suggestion of a new class of instabilities, convective instabilities [1–4]. Numerical simulations [5] taking into account space charge also see these instabilities. It is believed these instabilities have been observed [6, 7] before but are often attributed to TMCI.

In order to study these instabilities, a new experimental program making use of Fermilab’s existing accelerator complex is underway. The primary objective of the proposed research will be to characterize these instabilities in the presence of varying space charge and varying wake amplitudes. Usually, the wake amplitudes which drive instabilities are machine dependent and are determined by the impedance of the components installed within the machine. A novel approach to control instabilities will be to install a ‘waker’ system, a dedicated wake-building feedback system.

## WAKER CONCEPT

One of the advantages of simulations, is that the user can vary the wake parameter however they please. If this could be accomplished in actual machine, it would open the door to many exciting studies that could not normally be performed. The waker system is a novel concept which tries to mimic this approach and allow the user to define their own wake.

The system design will be similar to a traditional damper system however, used to excite instabilities rather than damp them. The concept of the system is as follows;

\* rainswor@fnal.gov

<sup>†</sup> Operated by Fermi Research Alliance, LLC under Contract No. De-AC02-07CH11359 with the United States Department of Energy.

- The user defines a wake,  $W(s)$ .
- The system will measure the position and intensity of the bunch at different time slices along the bunch in a single turn given by  $x_j$  and  $q_j$  respectively.
- On the next turn, the system applies multiple kicks along the bunch where the kick size,  $K$  is determined by the convolution of transverse offsets of the upstream time slices with the wake function of the longitudinal position difference

$$K_i \propto \sum_{j=1}^{i-1} x_j q_j W(s_j - s_i) \quad (1)$$

The bandwidth of the system should be much bigger than the inverse bunch length i.e.

$$\Delta\omega \gg 1/\sigma_b \quad (2)$$

For standard operation in the Recycler, the beam is bunched at 53 MHz. A typical bunch length is 2 ns, which would require a bandwidth larger than 500 MHz which would not be feasible to build. However, the beam can be re-bunched to 2.5 MHz which is routinely performed for the Muon program. In this case, a typical 1-sigma bunch length of 30 ns can be expected and so, a bandwidth larger than 30 MHz would be needed. Assuming a full bunch length equivalent to 4-sigma of 120 ns, a 100 MHz system would provide 12 time slices across the bunch and a 200 MHz system would provide 24 time slices. Based on this, the bandwidth of the system will be designed to be at least 100 MHz.

## WAKER SYSTEM

The waker system is installed in the Fermilab Recycler. The main components are as follows:

**Kicker** A 0.5m vertical stripline kicker is used to provide the kicks that mimic a wakefield. The length is chosen based on the frequency response in order to meet a bandwidth of 200 MHz.

**Pickups** Two split plate BPMs are used. Ideally, the two BPMs would be separated by 90° in betatron phase advance. The two signals from these BPMs can be combined with the correct coefficients to control the phase to the kicker. The pickups used are located at 206 and 208 in the Recycler and are separated in phase by 82°.

**Amplifiers** Two amplifiers are used to drive each plate of the kicker. Each amplifier is a R&K-A010K221-6464R which has a broadband frequency range of 10kHz-225MHz. The output power at saturation is 2.5kW from 10kHz - 100MHz and at least 2kW from 100MHz-225MHz. Two RF loads/attenuators are also used.

**Digital Feedback Board** The board is needed to process the signals, apply the wake and output the kick signal to the amplifiers. The current board allows a bandwidth of 100 MHz [8].

## COMMISSIONING

In order to commission the system in, two important parameters need to be determined. The first is time delay needed such that kick is applied at the correct time. The two are the coefficients needed to combined the bpms signals to simulated a pickup signal that is 90° from the kicker. These parameters can be found by using performing an open loop transfer function measurement.

Figure 1 shows a schematic of an open loop BTF measurement. The circuit is broken between the board and the amplifiers. A vector signal analyzer (VSA) sends out a white noise signal in the bandwidth of interest to the kicker. The beam response is then measured by the bpms and sent to the VSA via the board.

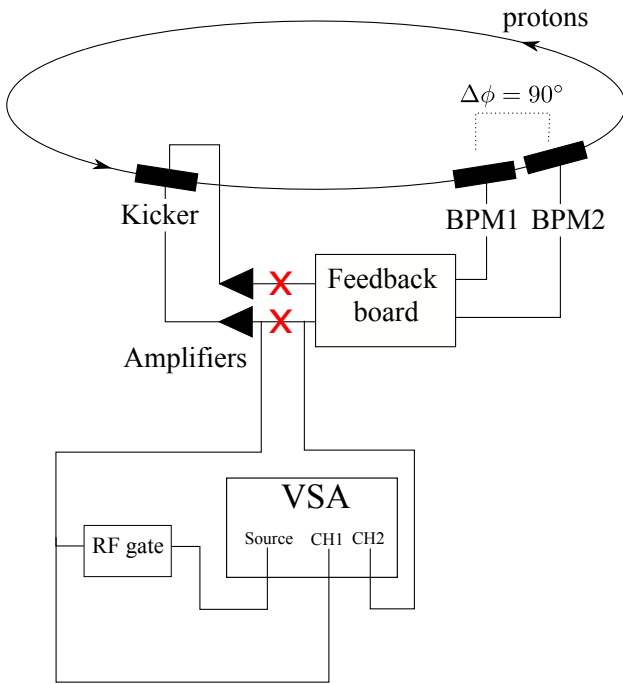


Figure 1: BTF schematic.

If the driving term from kicker is proportional to  $\cos(2\pi\nu f_0 t)$ , then the signal from the detector is proportional to

$$\cos[2\pi\nu f_0(t - t_d) + \vartheta] \cos[2\pi\nu f_0(t - t_d) + \phi] \quad (3)$$

which can be separated into the upper and lower betatron sidebands.

$$\cos[2\pi(n + \nu)f_0(t - t_d) - \vartheta + \phi] \quad (4)$$

$$+ \cos[2\pi(n - \nu)f_0(t - t_d) + \vartheta - \phi] \quad (5)$$

where the phase of the upper and lower sidebands is given by:

$$\theta_{lsb} = \vartheta + \phi - 2\pi f_{lsb} t_d \quad (6)$$

$$\theta_{usb} = \vartheta - \phi - 2\pi f_{usb} t_d \quad (7)$$

From this, the sum and difference of these two phases can let us determine all the information needed to time in the system.

$$\theta_{lsb} - \theta_{usb} = 2\phi + 2\pi(f_{usb} - f_{lsb})t_d \quad (8)$$

$$\theta_{lsb} + \theta_{usb} = 2\vartheta + 2\pi(f_{usb} + f_{lsb})t_d \quad (9)$$

By the measuring the sum of the sideband phases at multiple frequencies, we can find a time delay used by the board that simulates  $t_d = 0$ . Figure 2 shows an example measurement. Once the correct delay is found, the difference phase equals twice the phase advance from the pickup to the kicker. However, the board uses a numerical notch filter i.e. the board is looking at the position difference between revolutions rather than absolute difference. The result of this notch filter is that the upper betatron sidebands phase are flipped 180°. This means that in order to simulate a pickup signal that's 90° from the kicker, the bpm coefficients are chosen such that the phase of upper and lower sidebands are the same.

Once the delay and bpm coefficients were found, the timing was tested by trying to damp and antidamp the beam. This was performed on both 53 MHz bunched beam and 2.5 MHz bunched beam. The next step is to try a wake. A theta (Heaviside step function) wake was used. The initial test was done use moderate intensity and beam fallout was observed. The intrabunch motion was captured using a set of stripline pickups connected to an oscilloscope and is shown in Figure 3. The integrated sum signal from the pickups shows the longitudinal profile. The difference signal is proportional to both position and intensity. The head of the bunch is on the left and tail on the right. The instability appears to show signs of being a convective instability as intrabunch motion seems to be slightly more tail dominated.

Successful excitation of an instability using the waker system meant that instability studies could begin. However, two important measurements needed to be made first. The

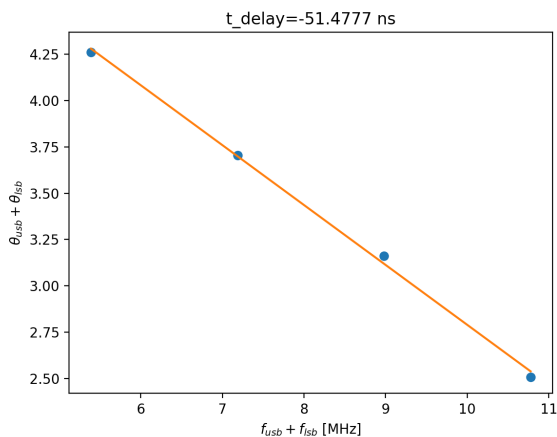


Figure 2: The sum of the upper and lower betatron sideband phases at different frequencies. The gradient is proportional to the time delay.

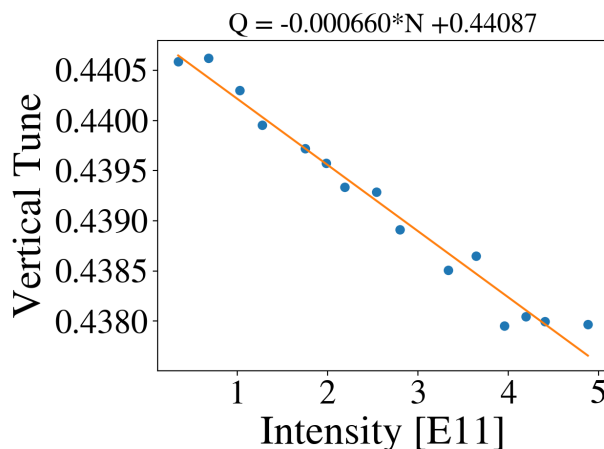


Figure 4: The vertical tune shift due to increasing bunch intensity.

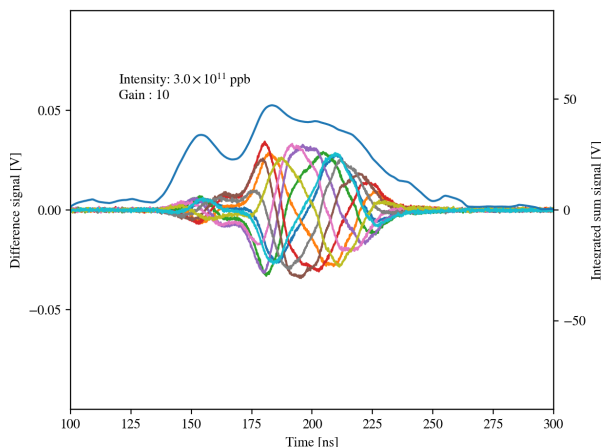


Figure 3: Snapshot of first instability observed using waker system. The integrated sum signal from the pickups shows the longitudinal profile. The difference signal is proportional to both position and intensity.

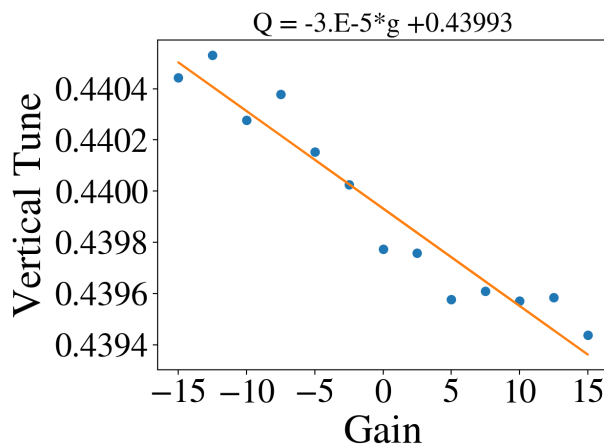


Figure 5: The vertical tune shift as a function of gain of the system. Positive gain results in a negative tune shift i.e. it follows the natural tuneshift of the machine. Note: There is some large uncertainty in the tune measurements but the sign of the slope is believed to be correct.

natural tune shift due to intensity without the waker and the tuneshift caused by the waker itself.

The first measurement needed is to determine the natural tune shift vs intensity for the Fermilab Recycler. The result is shown in Figure 4.

The next measurement is to see how the waker affects the tune shift. Figure 5 shows how the tune varies as the gain is changed well below the intensity threshold. It can be seen that at positive gain, the tune shifts down. i.e. it follows the natural tune shift of the machine. A negative gain results in a positive tune shift. There is some large uncertainty in the tune measurements and so the magnitude of the slope may not be correct however the sign of the slope is believed to be correct.

## INSTABILITY STUDIES

The first study was to find the instability threshold at varying intensities. After the beam was injected and rebunched to 2.5 MHz, the waker system was run for 50000 revolutions. Typical parameters during the study are shown in Table 1. At each intensity, the gain of the waker was gradually increased until an instability was observed. Figure 6 shows instability snapshots at 3 different intensities at the minimum gain needed to cause an instability. It can be seen that as the space charge parameter increases, a strong amplification from the head of the bunch to the tail is observed and looks like a convective instability predicted by [1].

The last measurement was to compare the instability threshold with positive and negative gain. Figure 7 shows the result. It can be seen that significantly more gain is

Content from this work may be used under the terms of the CC BY 3.0 licence (© 2021). Any distribution of this work must maintain attribution to the author(s), title of the work, publisher, and DOI

Table 1: Typical Parameters Used for Instability Measurements in the Fermilab Recycler

Parameter	
$Q_s$	0.0005
$\xi_x, \xi_y$	0.03,-0.15
$\Delta p/p$	0.0005
$\sigma_l$	30 - 40 ns
$\epsilon_{n,95\%}$	15 $\pi$ mm mrad
$\beta$	0.9944
$R$	528 m

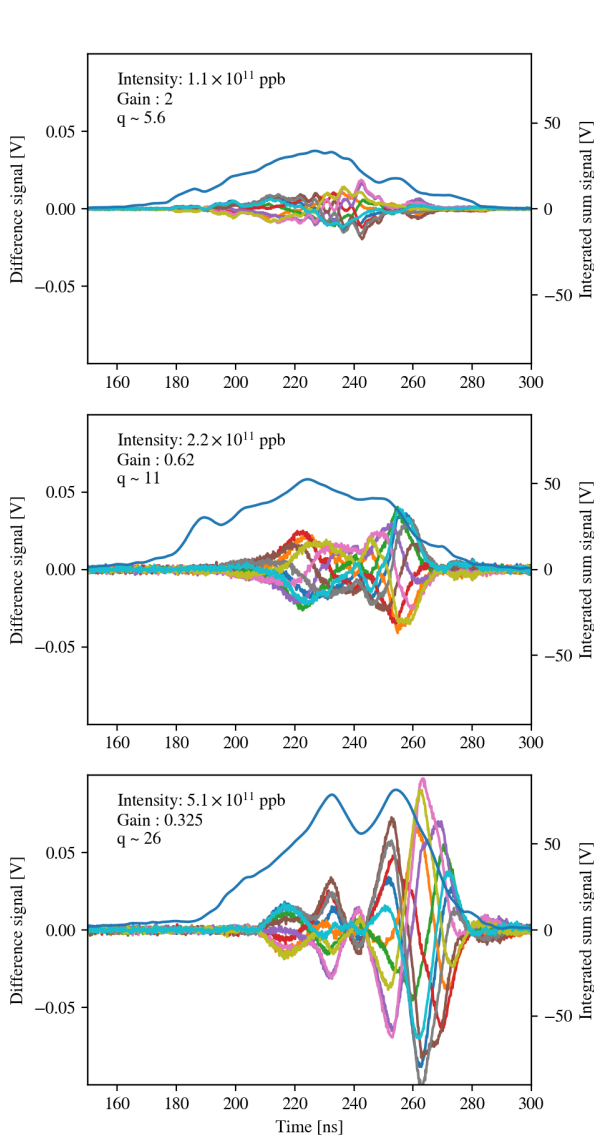


Figure 6: Instability snap-shot taken at three different intensities. The difference signal is proportional to position and intensity. The integrated sum signal shows the longitudinal profile. As the intensity and space charge is increased, huge amplification is observed from the head to the tail.

required when attempting to couple to the +1 mode vs coupling to the -1 mode. One possible reason for this is due to the natural tune shift of the Recycler. At high intensity, the tune has already shifted and so a small amount of gain is needed to push it become unstable. However, large negative gain is needed to result in an instability as the waker needs to counter the natural tune shift. The snapshots also agree well with theoretical predictions. From the theory on convective instabilities, we should expect to see large amplification from the head to the tail when following the natural tuneshift however, the intrabunch motion should be much more symmetric when coupling to the positive modes.

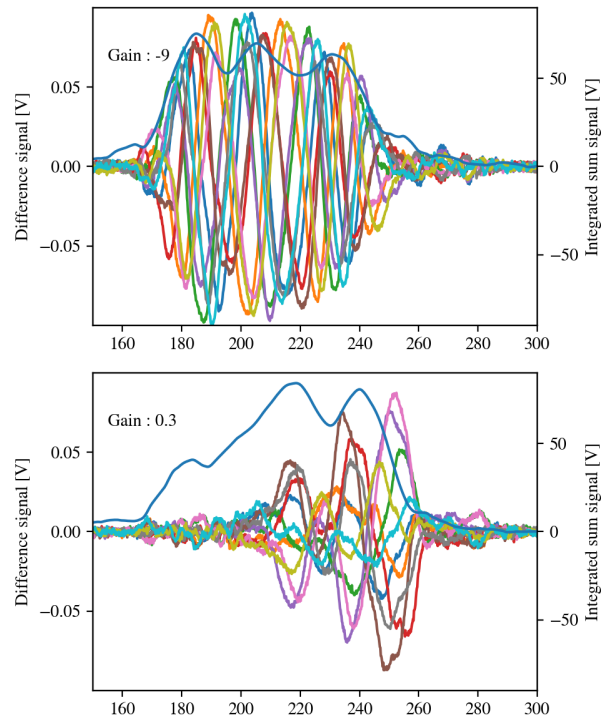


Figure 7: Instability snap-shot taken at three different intensities. The difference signal is proportional to position and intensity. The integrated sum signal shows the longitudinal profile. As the intensity and space charge is increased, huge amplification is observed from the head to the tail.

## SUMMARY

A new hardware system has been commissioned in the Fermilab Recycler to study beam instabilities. It has successfully excited single bunch beam instabilities. As space charge was increased, huge amplification from the head to the tail is observed which agrees well with the theory relating to convective instabilities. The initial measurements show a good qualitative agreement but more studies are needed for a more quantitative agreement. Studies in the Recycler will continue for another 1 to 2 years before the system is move to IOTA. A new digital feedback board is in development

which will increase the bandwidth of the system by a factor of 2.

Work is also ongoing to upgrade the board of the system which will allow the bandwidth to be increased to 200 MHz.

## ACKNOWLEDGMENTS

This manuscript has been authored by Fermi Research Alliance, LLC under Contract No. DE-AC02-07CH11359 with the U.S. Department of Energy, Office of Science, Office of High Energy Physics.

## REFERENCES

- [1] A. Burov, “Convective instabilities of bunched beams with space charge”, *Phys. Rev. Accel. Beams*, vol. 22, p. 034202, 2019. doi:10.1103/PhysRevAccelBeams.22.034202
- [2] A. Burov, “Transverse Microwave Convective Instability at Transition Crossing”, arXiv 1908.02916, 2019.
- [3] A. Burov, “Core-Halo Collective Instabilities”, arXiv 1808.08498, 2018.
- [4] Y. Alexahin, “Vlasov eigenfunction analysis of space-charge and beam-beam effects”, *CERN Yellow Rep. Conf. Proc.*, vol. 9, 2020. doi:10.23732/CYRCP-2020-009.193
- [5] X. Buffat *et al.*, “Description of beam instabilities in synchrotrons with wakefields and space charge forces using the circulant matrix model”, *Phys. Rev. Accel. Beams*, vol. 24, p. 060101, 2021. doi:10.1103/PhysRevAccelBeams.24.060101
- [6] H. Bartosik, “Beam dynamics and optics studies for the LHC injectors upgrade”, Ph.D. thesis, TU Vienna, Vienna, Austria, 2013.
- [7] T. Toyama, “Beam instability issue and feed-back system in the MR of J-PARC”, presented at HB’21, Batavia, IL, USA, Oct. 2021, paper THAC1, this conference.
- [8] N. Eddy, J. L. Crisp, “Transverse Digital Damper System for the Fermilab Anti-Proton Recycler”, *AIP Conf.Proc.*, vol. 868, p. 293, 2006. doi:10.1063/1.2401416

# COUPLED BUNCH INSTABILITIES GROWTH IN THE FERMILAB BOOSTER DURING ACCELERATION CYCLE\*

C. M. Bhat<sup>†</sup> and N. Eddy, Fermilab, Batavia, IL, U.S.A.

## Abstract

Currently, Fermilab Booster accelerates  $\sim 4.5 \cdot 10^{12}$  protons per pulse (ppp) in 81 bunches from 400 MeV to 8 GeV at 15 Hz to provide beam to multiple HEP experiments and is being upgraded to handle higher beam intensity  $> 6.7 \cdot 10^{12}$  ppp at a repetition rate of 20 Hz. In the current mode of operation, we control longitudinal coupled bunch instabilities (LCBI) using combination of passive and active dampers. The issues with LCBI are expected to worsen at higher beam intensities. Here, we would like to investigate at what time in the beam cycle a particular mode is going to originate and how much it contributes at a different time of the acceleration cycle using the collected wall current monitor data from injection to extraction. Also, measure growth rates as a function of beam intensity for some dominant modes. Finally, this paper presents results from the observed LCBI analysis for the highest available beam intensities, unexpected findings, and future plans to mitigate the LCBI at higher beam intensities.

## INTRODUCTION

The Fermilab Booster is one of the oldest RCS in the world which cycles at 15 Hz rate [1-3] and providing 8 GeV beam to HEP programs for the last 50 years. Until 2016 the beam in the Booster was accelerated with low duty factor, e.g., during the early part of the Main Ring fixed target HEP era it provided  $\sim 2 \cdot 10^{12}$  ppp with an average repetition rate slightly more than 0.5 Hz out of 15 Hz and with lower beam brightness. In early 1980s, as we entered the collider era along with fixed target HEP programs, the demand on the beam intensity from the Booster per cycle as well as the beam delivery repetition rate increased. All these periods, the longitudinal coupled bunch instability was troublesome in the Booster and, was being addressed and controlled [4-13]. In 2012, Fermilab entered the intensity frontier era PIP [14, 15] and by the end of this decade it will be in PIP-II era [16]. Currently, we are providing  $> 4.3 \cdot 10^{12}$  ppp at 15 Hz rate from the Booster and,  $> 700$  kW proton beam power on the NuMI neutrino target and at the same time beam to multiple Booster neutrino experiments. Between now and when the PIP-II comes online, we have a near-term goal to increase the beam output power per Booster cycle by about 25%. PIP-II calls for a further increase in beam intensity by  $\sim 50\%$  and a cycle rate of 20 Hz. In this regard the coupled bunch instability needs to be revisited

Since the start of the Booster, the beam has been injected into the Booster without any RF buckets opened. After the

completion of the injection the beam is captured slowly in the RF buckets with harmonic number  $h=84$ . So, it is expected that the bunches are well matched to the RF buckets from the start of their formation with minimal longitudinal instabilities. However, during the acceleration from injection energy to 8 GeV beam encounters transition crossing at  $\gamma=5.47$  with normal transition phase jump and we have observed significant longitudinal emittance growth only after transition energy. This emittance growth is related to longitudinal coupled bunch instability observed after transition crossing [7]. Since then, multiple upgrades were made to add passive [8] and active [4, 9, 11-13] dampers to mitigate LCBI in the beam. In all these cases it was enough to enable the active dampers only after the transition crossing and monitor the coupled bunch instability in the extracted beam using a wall current monitor (WCM) in the 8 GeV transfer line. During PIP-II era, 800 MeV beam will be injected directly into the Booster RF buckets and by the end of the injection process the beam distribution is expected to match well with the RF buckets. Nevertheless, the bunch intensity will be significantly higher than that in the current operation. As a result of this, it is of interest to investigate the evolution of LCBI in Booster for high intensity beam, ahead of PIP-II and develop mitigation strategy.

## ASPECTS OF DIPOLE LCBI

Theory of longitudinal coupled bunch instability and stability criterion are one of the widely discussed subjects in beam physics [17-20]. An application of the theory to study and control the coupled bunch dipole mode instability in the Fermilab Booster was carried out by D.P. McGinnis [4, 5] in early 1990s. Here, we highlight some key aspects of the theory in the context of studies carried out for the intensity upgrade in the Booster.

Circulating bunches of charged particle in a synchrotron give rise to longitudinal as well as transverse wake fields because of machine impedance including higher-order modes of RF cavities. The longitudinal wake field which is not decayed between arrival of consecutive bunches in the ring will be responsible for longitudinal coupling between bunches and is an important source of instability in longitudinal plane. The wake fields can potentially cause both bunch displacement as well as distortion and help growing exponentially during successive passage in the synchrotron. The particles in bunches execute synchrotron oscillations due to RF force. So, the displaced bunches will also experience this additional force in the RF bucket which adds up for further emittance dilution and possibly beam loss during the beam acceleration. There are other sources of bunch oscillations which may not be due to wake field effects. Such exam-

\* Work supported by Fermi Research Alliance, LLC under Contract No. De-AC02-07CH11359 with the United States Department of Energy

<sup>†</sup> cbhat@fnal.gov

ples are energy and phase mismatch during bucket-to-bucket bunch transfer from one accelerator to the other or in the case of space charge dominated beam, immediately after the transition crossing with RF phase jump from  $\phi$  to  $\pi - \phi$ . Such bunch oscillations are generally not considered as longitudinal beam instability. However, they can induce LCBI. In any case, the line densities of such oscillating bunches can be decomposed into two parts viz., stationary distribution and additional charge density oscillating in synchrotron phase space. The oscillation part is approximately sinusoidal standing-wave with  $m$  azimuthal nodes. (these are intra-bunch synchrotron oscillation modes). For example, a single bunch can perform rigid dipole oscillations due to phase mismatch which corresponds to mode  $m=1$  and in the case of RF voltage mismatch one can expect quadrupole oscillations with  $m=2$  (also called breathing mode). A nearly triangular shape distribution of particles in  $(dE, \Delta t)$  phase-space in a RF bucket would lead to sextupole oscillations with  $m=3$  and so on. Sometimes multiple modes can occur at the same time. To drive higher azimuthal modes, longitudinal impedance of higher frequencies is needed. The standard formalism is to transform the bunch displacements into Fourier modes. The modes can be identified by the lines that can be seen in bunch Fourier spectrum [17-20] with

$$f_p = (n + pM)f_0 \pm |m|f_s$$

with  $p = 0, \pm 1, \pm 2, \dots \pm \infty$  and  $|m| = 0, 1, 2, \dots \infty$  (1)

$f_0$  is revolution frequency of the bunches,  $f_s$  is synchrotron frequency,  $M$  is number of bunches, generally same as RF harmonic number  $h$ ,  $n$  is mode number for LCBI. In the presence of LCBI the spectrum consists of additional signal at those rotation harmonics corresponding to  $(n + pM)f_0$  which is characteristic of coupled bunch mode  $n$ .  $p$  represents band number; negative and positive values of  $p$  correspond to lower and upper bands, respectively. As mentioned earlier, a single bunch can perform dipole, quadrupole, and higher ordered mode oscillations. In addition to this, all  $M$  bunches may oscillate with same mode  $m$  and with same amplitude but, with constant phase advance of  $2\pi n/M$  between bunches due to coupling. For  $M$  identical bunches there are  $M$  coupled bunch modes of oscillations and the mode number  $n$  takes the values  $0, 1, 2, \dots, M - 1$ . Generally, a mixture of different oscillation modes  $m$  and  $n$  is observed. Selection of a specific mode of interest for observation or mitigation can be done by a discrete Fourier transform (DFT) or by measuring the beam signal within a limited bandwidth and suppress it as needed. In the current measurements and analysis, we use the former method.

As mentioned earlier, the phase-space distribution  $\psi$  of a bunch can be separated into stationary  $\psi_0$  and small oscillations about the stationary distribution  $\psi_1$  as follows [17-20],

$$\psi(r, \phi, t) = \psi_0(r, \phi) + \psi_1(r, \phi, t)$$

$$= \psi_0(r, \phi) + \sum_{m=1}^{\infty} R_m(r) e^{-im\phi} e^{-i(mf_s + \Delta f_m)t} \quad (2)$$

$\Delta f_m$  is coherent frequency shift [17]. In the above equation the quantities  $r$  and  $\phi$  are radius and angle, respectively, in the longitudinal phase space that have been normalized to make the unperturbed trajectories circular. The variable  $t$  represents location of the test particle [20, chapter 1].  $R_m(r)$  is a function corresponding to  $m$ th azimuthal mode. The distribution functions for other bunches are identical to Eq. (2) except that the modes are multiplied by phase advance of  $2\pi n/M$  per bunch. The complete distribution function for bunches is a superposition of  $M$  function of the type given by Eq. (2). Thus, complete distribution function is given by,

$$\psi(r, \phi, t, k) = \psi_0(r, \phi) + \sum_{n=0}^{M-1} \sum_{m=1}^{\infty} B_n R_p(r) \cdot e^{i2\pi nk/M} \cdot e^{-im\phi} \cdot e^{-i(mf_s + \Delta f_m)t} \quad (3)$$

where  $k$  is the bunch index.  $B_n$  is the relative strength of the various azimuthal modes. As shown in [5], by measuring the average phase error  $\langle \phi_k \rangle$  for  $k$ th bunch and performing DFT one can extract  $B_n$  for each mode. Notice that this method of extraction is exact for dipole modes only, which are dominant modes of LCBI in most of the cases at hand.

We start with measurement of total distribution function  $\psi$ , given by Eq. (3), which is snap-shot single turn line charge distribution data as a function of time for circulating train of  $M$  bunches. This can be obtained using a resistive wall current monitor (WCM) of enough band width and a high-speed oscilloscope which gives enough resolution for each bunch. Selecting the first bunch is somewhat arbitrary if there is no single turn marker like a notch in the beam. If there is notch in the beam, then the first bunch from the notch can be used as a reference bunch. The actual centroid of  $k$ th bunch  $bc_k$  can be determined using a relation like,

$$bc_k^\circ = \frac{\int t \psi_k(t) dt}{\int \psi_k(t) dt} \quad (4)$$

where  $\psi_k(t)$  is distribution function (or WCM data) for  $k$ th bunch. The extent of each bunch is one turn. As we have explained earlier, the relative change in spacing of adjacent bunch centroids is due coupled bunch mode oscillations which is a combination of  $\phi_0$ -unperturbed centroid measured with respect to the RF wave,  $\phi_1$ -linear increase of phase by  $2\pi n/M$  at a given RF frequency,  $\phi_2$ -due to slewing of the RF frequency during beam acceleration, and other negligibly small higher order terms. Thus, the phase can be written as,

$$\langle \phi_k \rangle_{fit} = \phi_0 + \phi_1 k + \phi_2 k^2 + \dots \quad (5)$$

The phase errors  $\Delta \phi_k$  due to the coupled bunch motion are obtained by,

$$\Delta \phi_k = bc_k - \langle \phi_k \rangle_{fit} \quad (6)$$

From Eq. (6) one can extract the mode strengths by Fourier analysis. In the case of Booster with 84 bunches one expects 84 modes of oscillations. The Fourier spectrum obtained

Content from this work may be used under the terms of the CC BY 3.0 licence (© 2021). Any distribution of this work must maintain attribution to the author(s), title of the work, publisher, and DOI

from  $\Delta\phi_k$  on one turn beam data displays 84 lines with each line corresponding to one value of mode number  $n$ . Furthermore, magnitude of mode  $n(= 0 - 41)$  is exactly same as that for  $83 - n$  [20].

## MEASUREMENTS AND DATA ANALYSIS

The distribution function for the circulating beam in the Booster is obtained using a 6 GHz bandwidth wall current monitor (WCM). A Tektronix, TDS7154B Digital Phosphor Oscilloscope of type 1.5 GHz 20 GS/s is used in the Booster to record the WCM data. At the same time, RF waveform data is collected in synchronized with WCM signal. Due to limited memory size of the scope, about 300 traces of data with 67 turn delay which covers entire beam cycle are collected. The RF frequency in the Booster swings from about 37.92 MHz to 52.81 MHz during the beam acceleration from 400 MeV to 8 GeV, correspondingly, the Booster beam revolution varies from 2.22  $\mu$ s to 1.59  $\mu$ s from injection to extraction. The WCM data for each trace spans at least one Booster turn. During the beam cycle 81 buckets out of 84 buckets are populated leaving three buckets empty which are used as kicker gap at the time of beam extraction. A typical mountain range of the WCM data is shown in Fig. 1. The beam between notches in a trace represents total beam in Booster. A Mathcad program is developed to perform the rest of the data analysis following the procedure explained in the previous section.

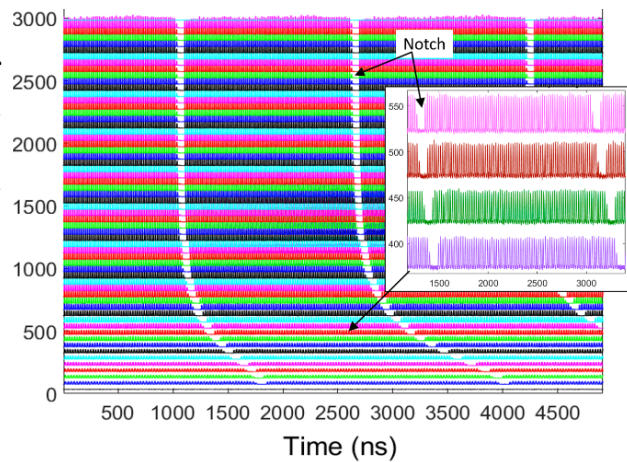


Figure 1: Mountain Range of the Booster WCM data from injection to extraction. The x-axis scale is time around the ring. The scale on the y-axis is also time with 355 turn delay between traces. This large turn delay is selected only for clarity.

Since the beginning of PIP era, we have been upgrading our longitudinal dampers from analogue to digital to suppress LCBI for modes 1, 2, 45 – 53 which have become dominant modes of beam instability. We use all our twenty RF stations to control modes 1 and 2 [21]. During early part of the beam acceleration where time derivative of the frequency is very large, it uses almost all available RF voltage of  $\sim 1$  MV and as beam crosses the transition energy at about

17 ms in the cycle the required RF voltage for further beam acceleration will go down nearly by 10%. A quad damper uses this excess of RF power and is turned on only after the transition crossing. The modes 45 – 53 (same as 30 – 38) damper uses a dedicated 80 MHz broad-band rf cavity [11-13]. One can turn ON and OFF the dampers on individual modes separately. The beam data have been taken under varieties of damper configurations and beam intensities.

### *An Illustration for Extracting LCBI Mode Strength from a Single Turn Data*

Figure 2 illustrates an example of extracting the coupled bunch mode strengths for dipole mode oscillations using single turn WCM data for  $1.8 \cdot 10^{12}$  ppp in Booster with all longitudinal dampers turned OFF. The extent of each bunch in a batch of 81 (84 buckets) is established using the RF waveform as a reference. An example of such RF waveform along with the corresponding WCM data for all 81 bunches is shown in Fig. 2(a). Figures 2(b) and 2(c) are for 81 bunches shown in the form of mountain range and contour plots which helps one to observe coupled bunch motion visually. The reference RF waves used in establishing bunch extents are shown in Fig. 2(d). Extracted bunch centroid as a function of bunch number is shown in Fig. 2(e). The measured phase error according to Eq. (6) in units of RF degrees for each of the bunches and its DFT are shown in Figs. 2(f) and 2(g), respectively.

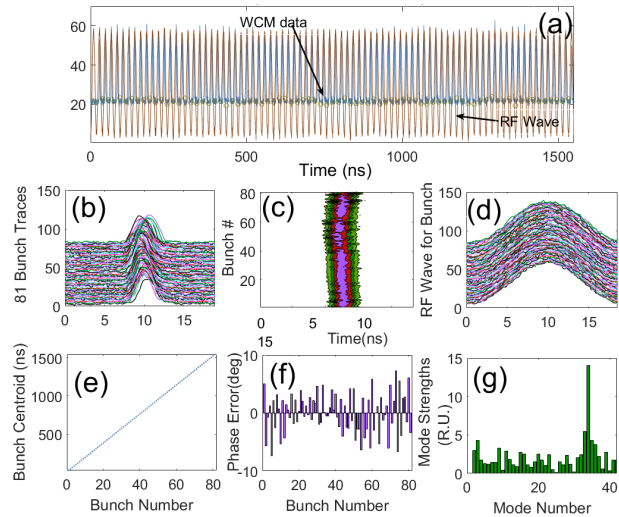


Figure 2: A sample of (a) Line-charge distribution with RF wave. The details on (b) to (g) are explained in the text.

### *LCBI Mode Strengths Through the Beam Cycle and Growth Rate for Some Dominant Modes*

Here we present the LCBI results for various beam intensities in the range from  $1.2 \cdot 10^{12}$  ppp to  $3.6 \cdot 10^{12}$  ppp with longitudinal dampers turned OFF. Figures 3(a) and (b) illustrate LCBI analysis for turn #9581 and turn #19631, slightly below the transition energy (transition energy is around turn

number 9700) and near extraction well above transition energy, respectively, for beam intensity  $3.6 \cdot 10^{12}$  ppp. It is quite clear from Fig. 3(b) mountain range plot (left) that there is significant amount of dilution in longitudinal emittance. Also, we observe considerable amount of beam loss before beam extraction. Before transition to after transition the coupled bunch instability strength differ by more than a factor of twenty for several modes at this intensity.

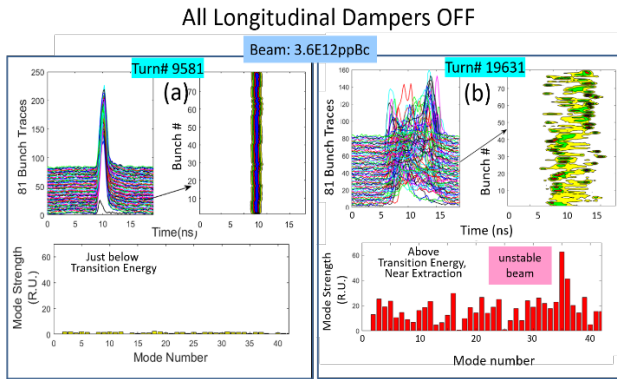


Figure 3: Extraction of Booster dipole LCBI strengths (a) below transition energy and (b) very near the extraction energy (after transition energy).

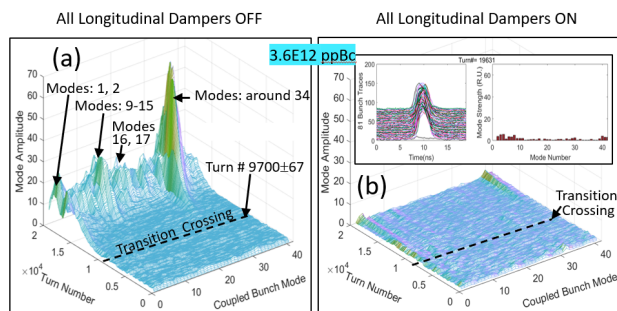


Figure 4: Surface plots for extracted LCBI strengths from injection to extraction in the case of  $3.6 \cdot 10^{12}$  ppp with (a) all longitudinal dampers OFF, (b) all dampers ON. The insets are, respectively, mountain range for all 81 bunches (left) and measured mode strengths with dampers ON (right).

Figures 4(a) and 4(b) illustrates typical surface plots of the measured LCBI strengths from injection to extraction for all modes from 0-41 for beam intensity of  $3.6 \cdot 10^{12}$  ppp with all active longitudinal damper turned OFF and turned ON, respectively. In Fig. 4(a) an approximate turn number corresponding to transition energy during the beam acceleration is also shown just for a comparison of the mode strengths before and after the transition energy. The data shows that below transition crossing very little LCBI is observed for any mode. On the other hand, above transition energy almost all modes showed up with considerable strengths. Among them, modes 1, 2, some modes around 12, 17 and 34 (same as 49) showed up with noticeable strengths.

Figure 5 shows growth rates for some dominant modes as a function of beam intensity. The data shows that modes 33, 34 and 35 (50, 49 and 48), have significantly higher growth rate as compared with others. Further-more, for beam intensities  $> 2 \cdot 10^{12}$  ppp without longitudinal dampers turned ON, we have observed significant longitudinal beam emittance growth as well as noticeable loss during transport to the downstream experimental facilities of the Booster. With all active dampers turned ON (and phased-in), we were able to mitigate LCBI instability as shown in surface plot in Fig. 4(b). The bunches are quite centered as shown in left inset of Fig. 4(b) (compared with similar mountain range of bunches shown in Fig. 3(b) with dampers OFF).

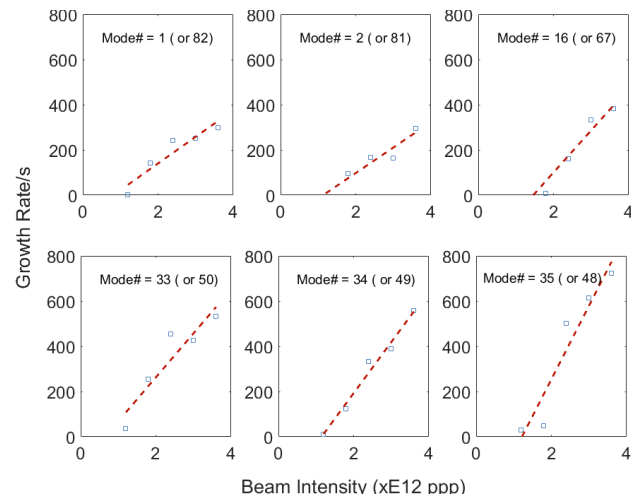


Figure 5: LCBI growth rate as a function of beam intensity for mode 1,2, 16, 33, 34 and 35.

### Operational and Higher Intensity Cases with Dampers Turned ON

The measurements showed that in the current mode of operation the highest beam intensity that can be accelerated in the Booster without any loss pass transition energy is about  $3.6 \cdot 10^{12}$  ppp. For intensities over  $3.6 \cdot 10^{12}$  ppp we must have the digital dampers turned ON and adjust the phase and magnitude as needed to mitigate the LCBI. Figure 6 shows surface plot for measured LCBI strengths for all modes with dampers for  $4.5 \cdot 10^{12}$  ppp which is slightly larger than PIP design beam intensity. The inset Fig. 6(a) illustrates the results from a typical longitudinal emittance measurement after beam capture at 400 MeV (top) and very close to the extraction at 8 GeV (bottom). The measured beam longitudinal emittances  $\epsilon_L$  (95%)  $\sim 0.07 \pm 0.01$  eVs and  $\sim 0.11 \pm 0.01$  eVs, respectively, at the end of the capture and near to the extraction in the Booster. This beam is acceptable by the facilities downstream of the Booster. Studies showed that about 10% smaller emittances can be reached by improving capture process at 400 MeV [22]. Average injection to extraction efficiency was about 94% at these beam intensities. The inset Fig. 6(b) shows a time evolution of LCBI strength for mode #39 (same as mode 44) averaged

Content from this work may be used under the terms of the CC BY 3.0 licence (© 2021). Any distribution of this work must maintain attribution to the author(s), title of the work, publisher, and DOI

over three data samples. This is an indication that this mode could be a concern at higher intensities and needs better damping.

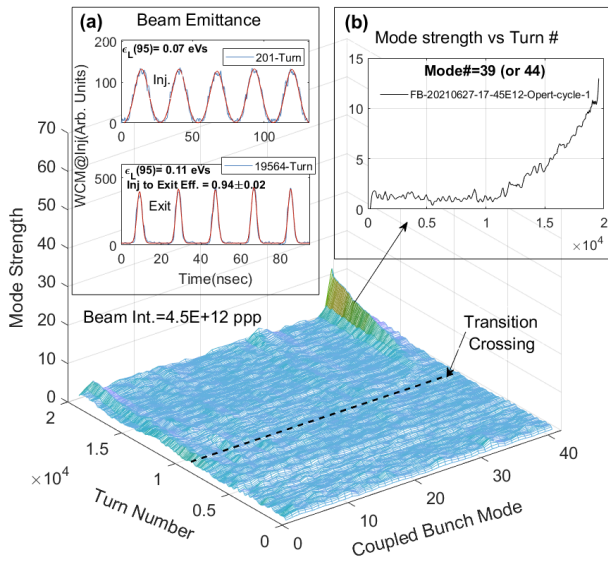


Figure 6: Surface plot showing all modes for the case of  $4.5 \cdot 10^{12}$  ppp at extraction with longitudinal dampers turned ON. The insets (a) and (b) display typical beam emittance measurements and mode strengths for mode 39.

Figure 7(a) shows similar surface plot for the LCBI strengths for all modes for the highest beam intensity studied here. Injection to extraction efficiency for this case was about 92%. Multiple modes started showing up here with non-negligible LCBI strengths. As indicated in Fig. 7(a) and in Fig. 7(b), we also start seeing modes near 28 showing up even before transition crossing. The reasons for the mode strengths going down before transition energy by themselves for the cases shown in Fig. 7(b) is not well understood and is part of our future studies. By optimizing the capture process, we had longitudinal emittances  $\epsilon_L(95\%) \sim 0.06 \pm 0.01$  eVs at the end of beam capture and  $\sim 0.09 \pm 0.01$  eVs near extraction, respectively.

The current study with high intensities  $> 5 \cdot 10^{12}$  ppp clearly shows that a) multiple mode not damped with the existing digital dampers start growing even before the transition energy and b) some of the modes which are damped using existing dampers at beam intensities  $\sim 5 \cdot 10^{12}$  ppp start popping up after the transition crossing. Therefore, for PIP-II era Booster beam intensities  $\sim 6.7 \cdot 10^{12}$  ppp at extraction we need further upgrades to our longitudinal dampers to mitigate modes around 12, 16 and 39 in addition to other modes. In this regard, we are planning to build dedicated longitudinal damper systems including new rf cavities to suppress modes 1, 2 and modes around 16 and 39 in a few years' time. Nevertheless, these problems may not preclude us to achieve our intermediate goal of providing 900 kW beam power on the NuMI neutrino target with the existing longitudinal dampers in Booster.

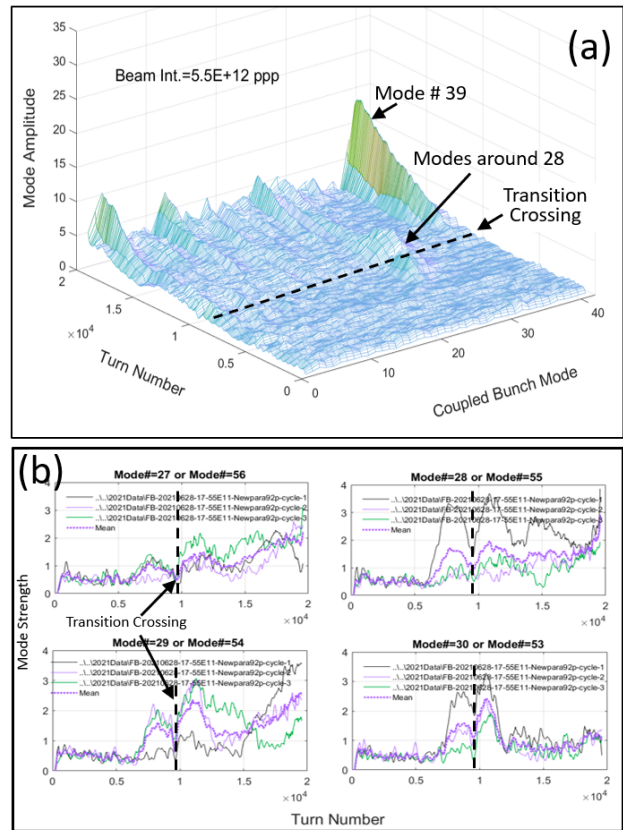


Figure 7: (a) Surface plot showing all modes for the case of  $5.5 \cdot 10^{12}$  ppp at extraction with longitudinal dampers turned ON. (b) Some typical modes, 27-30, showing up even before the transition crossing.

## ACKNOWLEDGEMENTS

We would like to thank W. Pellico, C. Y. Tan and S. J. Chaurize for many discussions. We also would like to thank MCR crew for their help during these measurements.

## REFERENCES

- [1] R. R. Wilson, "The NAL proton synchrotron," in *Proc. 8th International Conference on High-Energy Accelerators (HEACC 1971)*, CERN, Geneva, Switzerland, Sep 1971, pp. 3-13. <https://lss.fnal.gov/conf/C710920/p3.pdf>
- [2] R. Billinge, S. C. Snowdon, and A. van Steenbergen, "The Design of the NAL Booster," *IEEE Transactions on Nuclear Science*, vol. 16, pp. 969-974, 1969. doi:10.1109/TNS.1969.4325419
- [3] Booster Rookie Book, v4.1, April 2009. [https://operations.fnal.gov/rookie\\_books/Booster\\_V4.1.pdf](https://operations.fnal.gov/rookie_books/Booster_V4.1.pdf)
- [4] D. P. McGinnis, "Coupled bunch mode instabilities measurement and control," *AIP Conference Proceedings*, vol. 252, pp. 65-87, 1992. doi:10.1063/1.42127
- [5] D. McGinnis, J. Marker, and V. Bharadwaj, "Coupled Bunch Dipole Mode Measurements of Accelerating Beam in The Fermilab Booster," in *IEEE Particle Accelerator Conference, PAC1991*, San Francisco, CA, USA, pp. 1255-1257, 1991. [https://jacow.org/p91/PDF/PAC1991\\_1255.PDF](https://jacow.org/p91/PDF/PAC1991_1255.PDF)

- [6] K. C. Harkey, V. K. Bharadwaj, and P. L. Colestock, "Studies of Coupled-Bunch Modes in the Fermilab Booster," in *IEEE Particle Accelerator Conference (PAC1991)*, San Francisco, California, pp. 1830-1832, 1991. [https://jacow.org/p91/PDF/PAC1991\\_1830.PDF](https://jacow.org/p91/PDF/PAC1991_1830.PDF)
- [7] K. C. Harkey, "A Study of longitudinal instabilities and emittance growth in the Fermilab Booster synchrotron," Ph.D. Thesis, 1993, unpublished.
- [8] D. Wildman and K. Harkay, "HOM RF Cavity Dampers for Suppressing Coupled Bunch Instabilities in the Fermilab Booster," in *Proc. of the 1993 Particle Accelerator Conference (PAC'93)*, Washington, DC, USA, vol. 5, pp. 3258-3260, 1993. [https://jacow.org/p93/PDF/PAC1993\\_3258.PDF](https://jacow.org/p93/PDF/PAC1993_3258.PDF)
- [9] W. A. Pellico and D. W. Wildman, "Booster's Coupled Bunch Damper Upgrade," in *Proc. of the 2003 Particle Accelerator Conference (PAC2003)*, Portland, OR, USA, paper RPPB077, pp. 3177-3179, 2003. <https://jacow.org/p03/PAPERS/RPPB077.PDF>
- [10] S.A. Bogacz and S. Stahl, "Coupled Bunch Instability in Fermilab Booster - Longitudinal Phase-Space Simulation," in *Proc. EPAC'88*, Rome, Italy, pp. 646-648, 1988. [https://jacow.org/e88/PDF/EPAC1988\\_0646.PDF](https://jacow.org/e88/PDF/EPAC1988_0646.PDF)
- [11] N. Eddy, W. Pellico, A. Semenov, D. C. Voy, and A. M. Waller, "A Longitudinal Digital Mode Damper System for the Fermilab Booster," in *Proc of NAPAC2016*, Chicago, IL, USA, pp. 320-322, 2016. doi:10.18429/JACoW-NAPAC2016-TUPOA17
- [12] N. Eddy, "New Booster Longitudinal Dampers," Beam Doc 8642 (2020), unpublished.
- [13] N. Eddy, "New Longitudinal Damper Status," Beam Doc 9094 (2021), unpublished.
- [14] F. G. Garcia *et al.*, "Proton Improvement Plan Design Handbook", Fermilab-Beams-Doc-4053-v4, 2012.
- [15] W. Pellico *et al.*, "FNAL - The Proton Improvement Plan (PIP)", in *Proc. IPAC'14*, Dresden, Germany, pp. 3409-3411, June 2014. doi:10.18429/JACoW-IPAC2014-THPME075
- [16] "The PIP-II Reference Design Report", 2015. [https://indico.fnal.gov/event/9939/attachments/75550/90629/PIP-II\\_RDR\\_v1.0.pdf](https://indico.fnal.gov/event/9939/attachments/75550/90629/PIP-II_RDR_v1.0.pdf)
- [17] F. J. Sacherer, "A Longitudinal Stability Criterion for Bunched Beams," in *Proc. Particle Accelerator Conference (PAC1973)*, San Francisco, CA, USA, pp. 825-829, March 1973. [https://jacow.org/p73/PDF/PAC1973\\_0825.PDF](https://jacow.org/p73/PDF/PAC1973_0825.PDF)
- [18] F. J. Sacherer, "Methods of Computing Bunched Beam Instabilities," CERN/SI-BR/72-5, September 1972. [https://cds.cern.ch/record/2291670/files/2291670\\_001.pdf](https://cds.cern.ch/record/2291670/files/2291670_001.pdf)
- [19] F. Pedersen and F. Sacherer, "Theory and performance of the longitudinal active damping system for the CERN PS booster," in *Proc. 1977 Particle Accelerator Conference (PAC1977)*, Chicago, IL, USA, pp. 1396-1398, 1977. [https://jacow.org/p77/PDF/PAC1977\\_1396.PDF](https://jacow.org/p77/PDF/PAC1977_1396.PDF)
- [20] K. Y. Ng, *Physics of Intensity Dependent Beam Instabilities*, Singapore: World Scientific Publishing Company, 2006.
- [21] W. Pellico, private communications, 2021.
- [22] C. M. Bhat, S. J. Chaurize, P. Derwent, M. W. Domeier, V. Grzelak, W. Pellico, J. Reid, B. A. Schupbach, C.Y. Tan, and A. K. Triplett, "Recent Improvements in the Beam Capture at Fermilab Booster for High Intensity Operation," presented at HB2021, Fermilab, IL, USA, paper MOP02, this conference.

# STATUS OF LAYOUT STUDIES FOR FIXED-TARGET EXPERIMENTS IN ALICE BASED ON CRYSTAL-ASSISTED HALO SPLITTING\*

M. Patecki<sup>†</sup>, D. Kikoła, Warsaw University of Technology, Faculty of Physics, Warsaw, Poland  
A. Fomin, D. Mirarchi, S. Redaelli, CERN, Geneva, Switzerland

## Abstract

The Large Hadron Collider (LHC) at the European Organization for Nuclear Research (CERN) is the world largest and most powerful particle accelerator colliding beams of protons and lead ions at energies up to 7 TeV and 2.76 TeV, respectively. ALICE is one of the detector experiments optimised for heavy-ion collisions. A fixed-target experiment in ALICE is considered to collide a portion of the beam halo split by means of a bent crystal with an internal target placed a few meters upstream of the detector. Fixed-target collisions offer many physics opportunities related to hadronic matter and the quark-gluon plasma to extend the research potential of the CERN accelerator complex. This paper summarises our progress in preparing the fixed-target layout consisting of crystal assemblies, a target and downstream absorbers. We discuss the conceptual integration of these elements within the LHC ring, impact on ring losses, conditions for a parasitic operation and expected performance in terms of particle flux on target.

## INTRODUCTION

The ALICE fixed-target (ALICE-FT) programme [1] is proposed to extend the research potential of the Large Hadron Collider (LHC) [2] and the ALICE experiment [3]. The concept is based on steering onto a solid internal target a fraction of the proton beam halo split by means of a bent crystal, similar to crystals being developed for beam collimation at the LHC [4–6]. Splitting the beam is performed by exploiting the channeling process occurring inside a bent crystal, resulting in a trajectory deflection equivalent to the geometric bending angle of a crystal body [7]. Such a setup, installed in the proximity of the ALICE detector, would provide the most energetic proton beam ever in the fixed-target mode with centre-of-mass energy per nucleon-nucleon ( $\sqrt{s_{NN}}$ ) of 115 GeV offering a possibility to study the hadronic matter and to provide inputs for cosmic ray physics as summarised by the AFTER@LHC study group [1, 8].

Our proposal of the ALICE-FT layout follows general guidelines on technical feasibility and impact on the LHC accelerator of potential fixed-target experiments provided by the LHC Fixed Target Working Group of the CERN Physics Beyond Colliders forum [9, 10]. We also profit from the preliminary designs reported in [11, 12] and from the design study of an analogous fixed target experiment at the LHC proposed to measure electric and magnetic dipole moments of short-lived baryons [13].

\* This project has received funding from the European Union's Horizon 2020 research and innovation programme.

<sup>†</sup> marcin.patecki@pw.edu.pl

In this report, we summarise the status of the ALICE-FT layout, including conceptual integration of its elements (crystal and target assemblies, downstream absorbers), their impact on ring losses, and expected performance in terms of particle flux on target, taking into account parasitic and dedicated operation modes.

## MACHINE CONFIGURATION

A potential installation of the ALICE-FT setup will coincide with a major LHC upgrade in terms of instantaneous luminosity, commonly referred to as the High-Luminosity LHC (HL-LHC) [14], taking place in the Long Shutdown 3 (2025-2027), to make it ready for Run4 starting in 2027. Some of the expected beam parameters, having a direct impact on the ALICE-FT experiment performance, are given in Table 1. Among beam parameters being a subject of the upgrade, we highlight the total beam current increase nearly by a factor of 2, up to about 1.1 A, leading to more than 0.7 GJ of total beam energy stored in the machine. A highly efficient collimation system is therefore present in the LHC [15] and it will be upgraded for the HL-LHC [16]. Its role is to intercept the beam halo and to protect the cryogenic aperture from beam losses as some tens of mJ/cm<sup>3</sup> deposited in a superconducting magnet can cause an abrupt loss of its superconducting properties, i.e. a magnet quench. The halo splitting scheme is to be embedded into the transverse hierarchy of the betatron collimation system, as shown in Fig. 1, such that the collimation system efficiency is not affected. A fraction of secondary halo particles redirected towards the target can be used for fixed-target collisions instead of disposing them at the absorbers. The present collimation system is organised in a precise multi-stage hierarchy (see Table 2) over two dedicated insertions (IRs): IR3 for momentum cleaning and IR7 for betatron cleaning. Each collimation insertion features a three-stage cleaning

Table 1: Some Parameters of the Future HL-LHC Beams Important for the ALICE-FT Experiment, Referred to as *Standard* in [14]

Beam energy in collision	E	7 TeV
Bunch population	$N_b$	$2.2 \cdot 10^{11}$
Maximum number of bunches	$n_b$	2760
Beam current	I	1.09 A
Transverse normalised emittance	$\epsilon_n$	2.5 $\mu\text{m}$
$\beta^*$ at IP2		10 m
Beam crossing angle at IP2		200 $\mu\text{rad}$

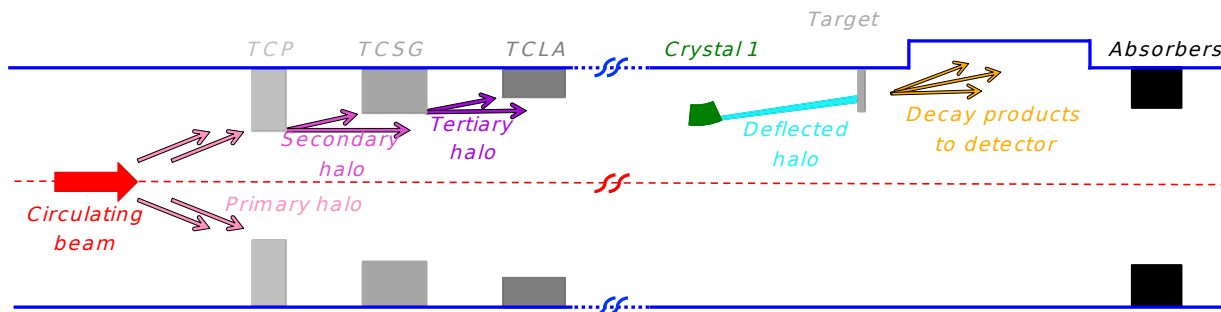


Figure 1: Working principle of the crystal-based fixed-target experiment (right side of the graphics) being embedded into the multi-stage collimation system (left side of the graphics). TCP, TCSG and TCLA stand for primary, secondary and tertiary stage of collimation, respectively. Graphics from [13].

based on primary collimators (TCP), secondary collimators (TCSG) and absorbers (TCLA). In addition, dedicated collimators are present in specific locations of the ring to provide protection of sensitive equipment (e.g. TCTP for the inner triplets), absorption of physics debris (TCL) and beam injection/dump protection (TDI/TCDQ-TCSP). The collimation system undergoes an upgrade, as described in [16], to make it compatible with HL-LHC requirements, but the general working principle will remain the same.

Table 2: HL-LHC Collimation Settings Expressed in Units of RMS Beam Size ( $\sigma$ ), Assuming a Gaussian Beam Distribution and Transverse Normalised Emittance,  $\varepsilon_n = 2.5 \mu\text{m}$

Coll. family	IR	Settings ( $\sigma$ )
TCP/TCSG/TCLA	7	6.7/9.1/12.7
TCP/TCSG/TCLA	3	17.7/21.3/23.7
TCT	1/2/5/8	10.4/43.8/10.4/17.7
TCL	1/5	14.2
TCSP/TCDQ	6	10.1/10.1

## ALICE-FT LAYOUT

A general concept of the ALICE-FT layout is illustrated in Fig. 1. A bent crystal is embedded into the collimation system and intercepts a fraction of the beam halo, which is deflected towards the target based on the crystal channeling process. Collision products are registered by the ALICE detector. Possible losses originating from the crystal+target assembly are intercepted by downstream absorbers. The main goal of the ALICE-FT layout is to provide a number of protons on target ( $N_{\text{pOT}}$ ) high enough to exploit full capabilities of ALICE detector acquisition system, while keeping the losses on superconducting magnets within tolerable limits. At the moment it is not clear if both regular beam-beam collisions and additional fixed-target collisions can be registered by the ALICE detector in parallel. On the other hand ALICE anticipates to reach its luminosity goal for beam-beam proton-proton collisions after one year of data taking in the Run4 [17]. Afterwards, the ALICE detector could be dedicated to fixed-target collisions while the LHC is operated

with proton beams. As estimated in [8], the ALICE detector can handle in the order of  $10^7$  protons on target per second; an exact number depends on the final implementation of the target [18], which is under investigation.

We assume the layout to be operated with the presently planned HL-LHC optics (version 1.5 [19] at the moment), as the overhead would become too large if new optics needs to be commissioned. Similarly, we assume that the ALICE-FT layout will not violate the multi-stage cleaning hierarchy, in particular the crystal will be in the shadow of IR7 primary collimators. As discussed in [13], the relative retraction of the crystal with respect to the IR7 primary collimator should not be smaller than  $0.5 \sigma$  (RMS beam size), mostly to account for optics and orbit errors, but it should be kept as low as possible to maximise the number of protons impacting the target [10]. Similarly to [13], we also assume that, for machine safety reasons, the distance from the deflected beam to the aperture and the distance from the target to main beams should be at least 4 mm. The system is to be installed in the vertical plane in order to avoid issues related to the beam dump system operating in the horizontal plane; otherwise, larger margins on settings would be required. The crossing scheme at IP2 is also in the vertical plane. Furthermore, the main solenoid of ALICE can be operated in two polarities which affect the slope of both beams at IP2. We mark the negative slope of the LHC beam 1 (B1) at IP2 as *negX* and the positive slope as *posX*. Both polarities are covered by our layout, but all the numbers reported in this paper correspond to *negX* scenario as the difference is minor. The ALICE-FT will act on B1 due to ALICE detector geometry. The graphical illustration of the proposed layout, that fulfils all above requirements, is given in Fig. 2.

We consider crystals made of silicon, with 110 bending planes and a bending radius of 80 m, the same as a bending radius of crystals already used in the LHC, following the parametric studies reported in [5] to ensure an optimum crystal channeling performance at LHC top energy, while keeping the nuclear interaction rate as low as possible. The optimum crystal bending angle depends on the ALICE solenoid polarity:  $100 \mu\text{rad}$  for *negX* and  $175 \mu\text{rad}$  for *posX* meaning that, at the moment, we consider an installation of two crystal assemblies next to each other. The longitudinal co-

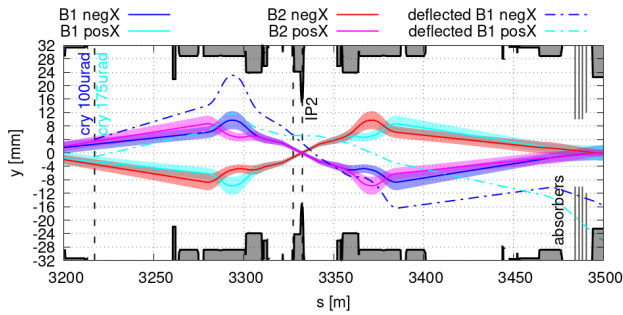


Figure 2: The proposed layout of the ALICE-FT experiment. Both beams (B1 and B2) with their envelopes ( $7.3\sigma$ ) are given with solid lines for both ALICE solenoid polarities. Deflected beams are given in dashed blue lines. Machine aperture is given in black solid lines. Vertical dashed lines mark locations of crystals, target and IP2, respectively. Location of absorbers is marked in the right bottom corner.

ordinate for the crystal installation is 3217.5 m (with 0 at IP1), chosen to maximise the number of protons impacting the crystal due to local phase-space conditions of secondary beam halo [20]. However, preliminary integration considerations indicate that this location will be challenging for the crystal installation, as this region is already crowded with other equipment and complex from the point of view of vacuum systems [21]. Moving the crystal downstream is considered as a possible mitigation method at the cost of reduced system performance due to unfavourable phase advance with respect to the primary collimator at IR7, resulting in a lower number of protons impacting the crystal.

The target assembly is planned to be installed nearly 5 m upstream from IP2 with a target made of either light or heavy material as, e.g. carbon, tungsten of about 5 mm of length. Details on target design studies can be found in [22].

Four absorbers, of the same design as collimators already used in the LHC, are proposed to be installed about 150 m downstream from the IP2. The first three are made of 1 m long carbon-fibre-carbon composite jaws, as the present TCSGs in the LHC, while the last one is made of 1 m long tungsten jaws, as the present TCLAs in the LHC; similarly as in [13]. The difference is that in our study we use a maximum opening of about  $50\sigma$  that still intercepts the channeled beam to keep the absorbers in the shadow of the entire collimation system and therefore to minimise their impact on the regular collimation system and on the machine impedance, instead of searching for minimum gaps that maintain the collimation hierarchy. As will be shown later, we do not experience any issues related to cleaning. The proposed setup of absorbers follows a performance-oriented approach with a potential to reduce the number of required absorbers, based on a detail energy deposition study to be done in the future. An optimisation of absorbers design will be done if it turns out to be needed.

The main parameters of the proposed layout are summarised in Table 3.

Table 3: Main Parameters of the ALICE-FT Layout; Cry Stands for a Crystal and Abs Stands for an Absorber

	position [m]	length [cm]	mat.	half-gap [mm]	bending angle [ $\mu$ rad]
cry <sub>negX</sub>	3217.5	0.8	Si	1.4	100
cry <sub>posX</sub>	3217.5	1.4	Si	1.4	175
target	3327.6	(5,10)	C/W	3.8	—
abs1	3484.4	100	C	9.9	—
abs2	3486.4	100	C	10.3	—
abs3	3488.4	100	C	10.7	—
abs4	3490.4	100	W	12.4	—

### EXPECTED PERFORMANCE

The MAD-X code [23] is used to manage the HL-LHC model, to prepare suitable lattice and optics descriptions used as input to the tracking studies, and to calculate the trajectory of particles experiencing an angular kick equivalent to the crystal bending angle. Detailed evaluation of the layout performance is done using multi-turn particle tracking simulations in SixTrack [24] that allows a symplectic, fully chromatic and 6D tracking along the magnetic lattice of the LHC, including interactions with collimators and bent crystals, and a detailed aperture model of the machine [25]. In our simulations, we use at least two million protons, initially distributed over a narrow ring of radius  $r + dr$  slightly above  $6.7\sigma$  in the normalised transverse vertical position-angle phase space ( $y, y'$ ) which allows an estimation of the number of protons impacting the collimation system (including the crystal and the target of the ALICE-FT layout) as well as the density of protons lost per metre in the aperture with a resolution of 10 cm along the entire ring circumference.

The ALICE-FT experiment must be compatible with the standard physics programme of the LHC, meaning that it cannot add any operational limitations, mostly related to particle losses, which must stay within acceptable limits. This is demonstrated in Fig. 3 where a loss map of the machine including the ALICE-FT system does not contain any abnormal loss spikes comparing to the reference loss map of the machine without the ALICE-FT system. The only new spikes correspond to protons impacting the elements of the ALICE-FT setup.

Loss maps presented in Fig. 3 refer to the case with the crystal at  $7.3\sigma$ , i.e. close to the minimum allowed retraction with respect to the primary collimator in IR7. This is a conservative choice from the cleaning point of view as it corresponds to a larger number of protons impacting the crystal ( $N_{PoC}$ ) and therefore also a larger number of protons impacting the target ( $N_{PoT}$ ) comparing to larger crystal retractions. The dependence of a fraction of the beam halo intercepted by the crystal (PoC) or by the target (PoT) over all protons intercepted by the collimation system on the relative

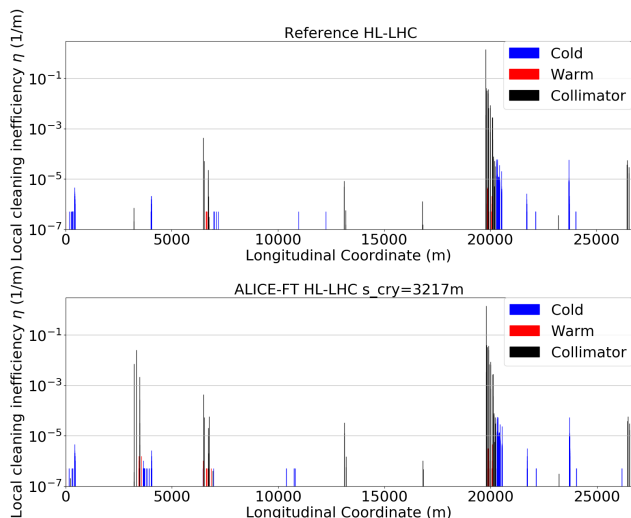


Figure 3: Comparison of loss maps for the machine with (bottom) and without (top) the ALICE-FT system. The local cleaning inefficiency is a measure of the number of protons not intercepted by the collimation system and impacting the machine aperture. The simulation limit of 1 proton lost in the machine aperture corresponds to  $5 \cdot 10^{-7} \text{m}^{-1}$  in a 10 cm longitudinal bin.

crystal retraction is given in Fig. 4. PoT is lower than PoC due to limited angular acceptance of the crystal leading to the channeling process (about  $2.5 \mu\text{rad}$  for 7 TeV protons) and due to crystal channeling efficiency, which is lower than 1.

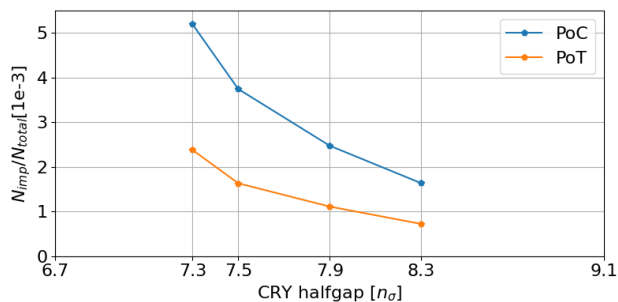


Figure 4: Fraction of beam halo intercepted by the crystal (PoC) and target (PoT) for some values of crystal halfgap expressed in the number of beam sigma. Limits of the horizontal axis correspond to halfgaps of primary and secondary collimators in IR7.

We define a *parasitic* mode of operation as a situation in which the fixed-target collisions at IP2 occur during the regular beam-beam collision mode of the LHC. The  $N_{\text{PoT}}$  scales with the number of protons impacting primary collimators at IR7 (see Eq. (1)), which depends on the beam intensity being a complex function of time, discussed in more detail in [13]. An exponential decrease of the beam intensity is assumed, characterised by the time coefficient  $\tau$  interpreted as a beam lifetime, which depends on beam parameters and machine state. A dominant contribution to the total beam lifetime comes from the beam burn-off due

to collisions ( $\tau_{BO}$ ), while the  $N_{\text{PoT}}$  depends mostly on  $\tau_{coll}$  corresponding to beam core depopulation towards tails that are intercepted by the collimation system. Following the same assumptions as in [13], with  $I_0$  being the initial beam intensity, time coefficients  $\tau_{BO} \approx 20 \text{ h}$  and  $\tau_{coll} \approx 200 \text{ h}$ , the number of protons impacting the target per 10 h long fill ( $T_{\text{fill}}$ ) in 2018 operation conditions can be estimated as:

$$N_{\text{PoT}} = \frac{1}{2} \text{PoT} \int_0^{T_{\text{fill}}} \frac{I_0}{\tau_{coll}} \exp\left(-\frac{t}{\tau_{BO}}\right) \exp\left(-\frac{t}{\tau_{coll}}\right) dt \approx 10^{10}. \quad (1)$$

A more detailed statistical analysis of all 2018 fills of the LHC [26] indicates the  $N_{\text{PoT}}$  to be within the same order of magnitude, with an expected proton flux on target of about  $5 \cdot 10^5 \text{ p/s}$ . This number may grow by a factor of two, to about  $10^6 \text{ p/s}$ , in the HL-LHC operation due to two times larger initial beam intensity, if the remaining parameters are the same, but an exact estimation is difficult to perform at the moment. This is about one order of magnitude lower than ALICE detector data acquisition capabilities, even if the target is extended to 10 mm length [8, 18].

A possible method to increase the proton flux on target is discussed in [26] where a special *dedicated* beam mode is proposed at the end of every LHC fill. The proposal is to extend these fills with several minutes long periods of a special beam excitation mode, during which the transverse beam emittance is increased in a controlled way by using the transverse damper. This allows increasing the number of protons impacting the primary collimators such that the proton flux on target can be increased up to a factor of 10, reaching the maximum capabilities of the ALICE detector acquisition system, see Table 4. The disadvantages of this method are a loss of an integrated luminosity (less than 1 % over a year) by the LHC experiments registering the beam-beam collisions and a larger impact of beam losses on the collimation system (but still within the design limits). Studies are ongoing to assess the feasibility of this method.

Other methods of increasing the proton flux on target, mostly in the *parasitic* mode, are under investigation.

Table 4: Order of magnitude of proton flux on target for *parasitic* and *dedicated* beam modes (estimated according to 2018 operation conditions) compared with expected capabilities of ALICE detector acquisition system. The first two numbers may grow by about a factor of 2 for HL-LHC conditions, due to two times larger initial beam intensity, but an exact estimation is difficult at the moment.

	proton flux on target [p/s]
beam <i>parasitic</i> mode	$5 \cdot 10^5$
beam <i>dedicated</i> mode	$5 \cdot 10^6$
ALICE acquisition system	$10^7$

## CONCLUSIONS AND OUTLOOK

In this report, we summarise the status of layout studies for ALICE fixed-target experiment based on crystal-assisted beam halo splitting. The proposed layout allows for a *parasitic* operation without compromising machine safety. The preliminary estimation of flux of protons on target in the *parasitic* mode indicates a number about one order of magnitude lower (assuming the HL-LHC beam intensity) compared to capabilities of the ALICE detector acquisition system. Its full potential can be exploited by applying a special *dedicated* operation mode based on beam excitation techniques. Integration of the ALICE-FT system will be challenging for both crystal assembly and target assembly and requires further investigation. In case of severe difficulties, some backup solutions are being prepared (e.g. moving the crystal downstream, double-crystal setup), but their detailed description is out of the scope of this report.

## ACKNOWLEDGEMENTS

We would like to acknowledge members of the ALICE Fixed-Target Project meetings [27] and Physics Beyond Colliders Fixed-Target Working Group [28], especially C. Hadjidakis, L. Massacrier and M. Ferro-Luzzi.

## REFERENCES

- [1] F. Galluccio *et al.*, “Physics opportunities for a fixed-target programme in the ALICE experiment”, Apr. 2019, <https://cds.cern.ch/record/2671944>
- [2] O. S. Brüning *et al.*, “LHC Design Report”, CERN, Geneva, Switzerland, Rep. 2004, <http://cds.cern.ch/record/782076>
- [3] K. Aamodt *et al.*, “The ALICE experiment at the CERN LHC. A Large Ion Collider Experiment”, *JINST*, vol. 3, p. S08002, 2008, also published by CERN Geneva in 2010, <https://cds.cern.ch/record/1129812>
- [4] W. Scandale *et al.*, “Observation of channeling for 6500 GeV/c protons in the crystal assisted collimation setup for LHC”, *Phys. Lett. B*, vol. 758, pp. 129–133, 2016. doi:10.1016/j.physletb.2016.07.072
- [5] D. Mirarchi, G. Hall, S. Redaelli, and W. Scandale, “Design and implementation of a crystal collimation test stand at the Large Hadron Collider”, *Eur. Phys. J. C*, vol. 77, no. 6, p. 424, 2017. doi:10.1140/epjc/s10052-017-4985-4
- [6] S. Redaelli *et al.*, “First observation of ion beam channeling in bent crystals at multi-TeV energies”, *Eur. Phys. J. C*, vol. 81, no. 2, p. 142, 2021. doi:10.1140/epjc/s10052-021-08927-x
- [7] A. M. Taratin, “Particle channeling in a bent crystal”, *Phys. Part. Nucl.*, vol. 29, no. 5, pp. 437–462, Sep. 1998.
- [8] C. Hadjidakis *et al.*, “A fixed-target programme at the LHC: Physics case and projected performances for heavy-ion, hadron, spin and astroparticle studies”, *Phys. Rep.*, vol. 911, pp. 1–83, 2021. doi:10.1016/j.physrep.2021.01.002
- [9] Kickoff meeting for the Physics Beyond Collider study, Mar. 2016, <https://indico.cern.ch/event/523655>

- [10] C. Barschel *et al.*, “LHC fixed target experiments”, CERN, Geneva, Switzerland, Rep. Mar. 2019, <https://cds.cern.ch/record/2653780>
- [11] F. Galluccio, “UA9 proposal for beam splitting in IR2”, FTE@LHC and NLOAccess STRONG 2020 joint kick-off meeting, 2019, <https://indico.cern.ch/event/853688/contributions/3620725/>
- [12] A. Fomin, “Updates on IP2 FT layouts”, 21st meeting of the PBC-FT working group, 2020, <https://indico.cern.ch/event/981210/>
- [13] D. Mirarchi, A. Fomin, S. Redaelli, and W. Scandale, “Layouts for fixed-target experiments and dipole moment measurements of short-lived baryons using bent crystals at the LHC”, *The European Physical Journal C*, vol. 80, p. 929, 2020. doi:10.1140/epjc/s10052-020-08466-x
- [14] G. Apollinari *et al.*, “High-Luminosity Large Hadron Collider (HL-LHC): Technical Design Report V. 0.1”, CERN, Geneva, Switzerland, Rep. 2017, <https://cds.cern.ch/record/2284929>
- [15] R. W. Assmann *et al.*, “The final collimation system for the LHC”, Jul. 2006, <http://cds.cern.ch/record/972336>
- [16] O. Aberle *et al.*, “High-Luminosity Large Hadron Collider (HL-LHC): Technical design report”, CERN, Geneva, Switzerland, Rep. 2020, <https://cds.cern.ch/record/2749422>
- [17] “Future high-energy pp programme with ALICE”, Jul. 2020, <https://cds.cern.ch/record/2724925>
- [18] C. Hadjidakis, private communication.
- [19] LHC optics repository, [https://abpdata.web.cern.ch/abpdata/lhc\\_optics\\_web/www/hllhc15/](https://abpdata.web.cern.ch/abpdata/lhc_optics_web/www/hllhc15/)
- [20] M. Patecki, “News on crystal layout studies”, Monthly Regular Fixed-Target Meeting, 2021, <https://indico.cern.ch/event/1074308/>
- [21] J. Sestak, private communication.
- [22] K. Pressard, “Solid target design for ALICE”, Joint workshop GDR-QCD/QCD@short distances and STRONG2020/PARTONS/FTE@LHC/NLOAccess, 2021, <https://indico.i.jclab.in2p3.fr/event/7201/contributions/22534/>
- [23] H. Grote and F. Schmidt, “MAD-X: An Upgrade from MAD8”, CERN, Geneva, Switzerland, Rep. CERN-AB-2003-024-ABP, May 2003, <http://cds.cern.ch/record/618496>
- [24] G. Ripken and F. Schmidt, “A symplectic six-dimensional thin-lens formalism for tracking”, CERN, Geneva, Switzerland, Rep. CERN-SL-95-12, CERN-SL-95-12-AP, DESY-95-063, Apr. 1995, <https://cds.cern.ch/record/281283>
- [25] ICFA Mini-Workshop on Tracking for Collimation in Particle Accelerators, CERN, Geneva, Switzerland, Dec. 2018, <https://cds.cern.ch/record/2646800>
- [26] A. Fomin, D. Mirarchi, and S. Redaelli, “Increasing the statistics of the LHC fixed-target experiments through 1 bunch excitation”, CERN-PBC-Notes, to be published in Oct. 2021.
- [27] ALICE Fixed-Target Project meetings, <https://indico.cern.ch/category/11595/>
- [28] Physics Beyond Colliders Working Group, <https://indico.cern.ch/category/8815/>

# DESIGN AND IMPLEMENTATION OF FAST MACHINE PROTECTION SYSTEM FOR CSNS

P. Zhu\*<sup>1</sup>, D. P. Jin<sup>1</sup>, Y. L. Zhang<sup>1</sup>, Y. C. He<sup>1</sup>, K. J. Xue<sup>1</sup>, X. Wu<sup>1</sup>, L. Wang<sup>1</sup>  
Institute of High Energy Physics, Chinese Academy of Sciences, Beijing, China  
<sup>1</sup>also at Spallation Neutron Source Science Center, Dongguan, China

## Abstract

According to the design concept of high availability, high reliability and high maintainability, CSNS accelerator fast machine protection system (FPS) adopts the distributed architecture based on “high-performance chip (FPGA) + high-speed transmission link (Rocket I/O) + VME”. We self-developed the main logic board with the function of reading and writing via VME, and which is the core and real-time to summary each interlocking signals, then determine and send out the protection action with accurately and stably. Simultaneously, in order to achieve interaction with each device flexible, we also self-customized a variety of interface boards. The permanent and instantaneous protection strategy was researched independently to meet the requirements of improving the efficiency of beam supply under the premise of ensuring operational safety. CSNS accelerator FPS has been put into operation for nearly six years stable and reliable until it is strict and systemic to test the function and performance on line, especially time-consuming, which is one of the important basic conditions for the efficient operation of CSNS accelerator.

## INTRODUCTION

The Chinese Spallation Neutron Source (CSNS) is a large-scale scientific facility, which is mainly composed of an 80 MeV LINAC accelerator (LINAC), a 1.6 GeV Rapid Cycling Synchrotron (RCS), a target station, LINAC to Ring beam transport line (LRBT), RCS to target beam transport line (RTBT), multiple neutron scattering spectrometers and corresponding supporting facilities [1]. CSNS is the first pulsed neutron source facility in developing countries. It is expected to have positive effects in promoting the development of fundamental sciences and technology.

CSNS is based on accelerated high-energy protons, so if equipment failure or other reasons cause the high-energy protons to deviate from the normal orbit, the equipment along the beam, such as Drift Tube LINAC (DTL), may be suffered from graze or permanent damage by continuous beam bombardment because of the strong destructiveness protons. Therefore, it is essential to establish machine protection system to cut off the beam with high reliability in the shortest possible time, and execute the relevant progress in order time accurately. The CSNS accelerator fast machine protection system (FPS) is crucial to be need to meet the special functional requirements, which must have the characteristics of high stability, high reliability, and high speed

under long-term operation. This article will introduce the requirements of system function, the design of architecture and protection strategy, and also the operation status.

## REQUIREMENT

According to the simulations and calculations carefully, if beam abnormality occurs during LINAC accelerator operation, the entire protection action should be completed within 10  $\mu$ s to cut off the beam promptly [2], as shown in Figure 1. Generally, the response time of PLC-based slow protection system (SPS) is on the level of milli-seconds [3], which cannot meet the requirements of the CSNS LINAC accelerator. In view of the overall the urgent and actual requirements of the CSNS accelerator, we decided to design and develop a fast machine protection system (FPS) based on the current high-speed digital electronic technology, and the key purpose of design is to achieve the response time of less than 10  $\mu$ s.

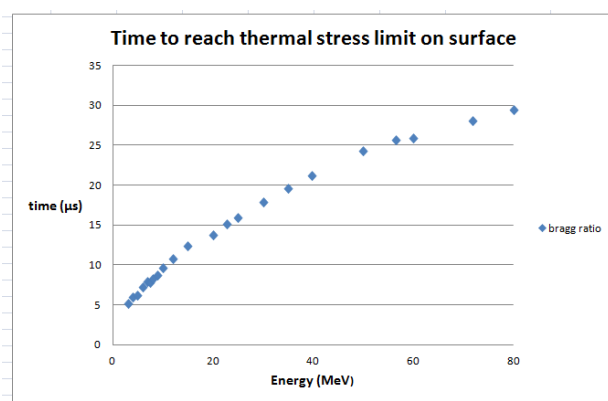


Figure 1: The relationship between the thermal stress limit in the material (copper) and the cumulative beam loss time. ①  $I=15$  mA,  $\sigma_x = \sigma_y = 0.2$  cm,  $J=62$  J/gm (energy density); ② Un-chopped beam, 15 mA; ③ Beam size: 0.2 cm  $\times$  0.1 cm RMS; ④ Hitting the components directly.

## ARCHITECTURE

According to CSNS accelerator physical design and beam research requirements, CSNS accelerator currently has a total of 6 beam targets [4], including: Ion Source (IS), LRBT Beam Dump (L-DUMP), LR Beam Dump (LRDUMP), Injection Beam Dump (I-DUMP), RTBT Beam Dump (R-DUMP) and target station, each beam target corresponds to the beam along the line and related equipment. Therefore, CSNS machine protection system needs to be able to timely

\* zhup@ihep.ac.cn

Content from this work may be used under the terms of the CC BY 3.0 licence (© 2021). Any distribution of this work must maintain attribution to the author(s), title of the work, publisher, and DOI

and accurately update the connected machines and equipment when the beam target is switched. In addition, in order to protect the personal safety of the staff, CSNS accelerator has set up a total of 3 independent radiation protection areas, including: LINAC area, RCS area and target area, as shown in Figure 2.

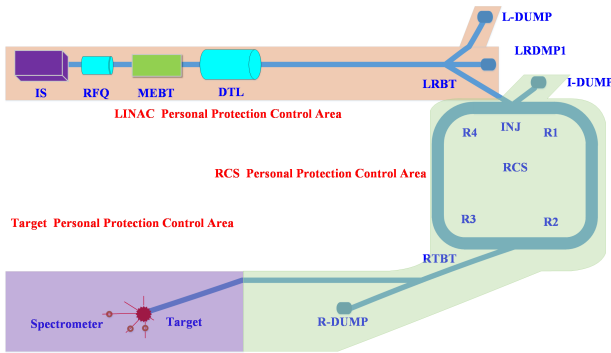


Figure 2: The schematic diagram of signal link.

In order to ensure the safe operation of the CSNS accelerator, we adopted the distributed architecture based on “Run Management System (RMS) + two slow machine protection systems based on PLC (SPS) + fast machine protection systems speed based on high-speed digital technology (FPS)” [5], the interaction of each system is shown in Figure 3, Both SPS and FPS are not only independently responsible for interacting with their respective devices signals, but also interlocking or unlocking with each other by the global reset signal from RMS, which hold a concurrent post that it is responsible for soft interlock, such as that the current beam of radiation frequency quadrupole (RFQ) is lower than pass rate. According to the characteristics of each interlocking signal and in-depth study, CSNS accelerator machine protection has the characteristics of high availability, high scalability and easy maintenance based on both mature commercial technology and the latest high-speed digital technology.

According to the above analysis, the main object of FPS is the DTLs with a small aperture in a vacuum along the beam line. In order to cut off the beam safely and reliably, the most effective method is to control in the early stage of beam rapidly. Therefore, the CSNS FPS mainly involves three systems: the ion source control system, the timing of the ion source extraction power supply and the power of RFQ. Table 1 is the table of input equipment and its distribution, including RFQ, DTL power, global beam loss, SPS and global reset and timing signals. Table 2 is the table of output equipment and its distribution, including the timing of the ion source extraction power supply, the power of RFQ, the beam gate of LINAC LLRF and SPS.

According to the equipment and distribution characteristics, and considering the actual needs of system installation, maintenance and expansion, FPS adopts the distributed architecture “high-performance FPGA chip + high-speed Rocket I/O transmission + VME”, as shown Figure 4. “FPGA +

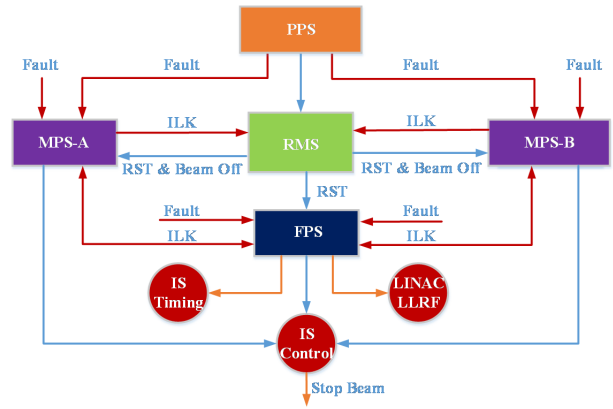


Figure 3: Layout of MPS.

Table 1: Input Signals for FPS

System Station	RF	PI	BI	MPS	RMS	Total
LINAC	8	120	12	4	2	146
LRBT	0	0	28	0	0	28
RCS	0	0	83	0	0	83
RTBT	0	0	50	0	0	50
Total	8	120	173	4	0	307

Rocket I/O” is responsible for signal aggregation, logic processing, signal fan-out, etc. VME is responsible for data readout, line OR for backplane signal, etc., which is designed though user-defined bus. In the light of the functional design, the architecture of FPS is divided into the third layers: collection, summary and preliminary processing, processing and execution. The layers are corresponding to the access sub-station, the summary sub-station and the executive master station respectively. Based on the principle of “minimizing the transmission delay and transmission quality of key inter-locking signals as much as possible”, the executive master station and each summary sub-station are connected by multi-mode optical cables based on high-speed Rocket I/O transmission, and the same as each summary sub-station and each access sub-station.

There, the summary sub-station is illustrated as an example. The summary sub-station is responsible to summary and deal with interlocking signals preliminary and then sent interlock signals to executive master station. Figures 5a, 5b show the architecture of “multiple main logic boards + Rocket I/O + standard 21-slot VME chassis”. The functions of the main logic boards are following: the main logic board of slot 1 is used for reading and writing the self-definition registers by standard VME bus; the main logic boards of other slots except slot 4 are used for receiving the data sent by the collection station based on high-performance FPGA and Rocket I/O. In order to achieving the purpose of “the main logic board can share interlock signals and reduce transmission delay”, it is creative to design that the connection between each main logic board and the VME Backplane is bidirectional, so all main logic boards sent or get the in-

Table 2: Output Signals for FPS

System Station	IS Control	IS Timing	RFQ Power	RF Beam Gate	MPS	Total
LINAC	2	1	1	8	4	16

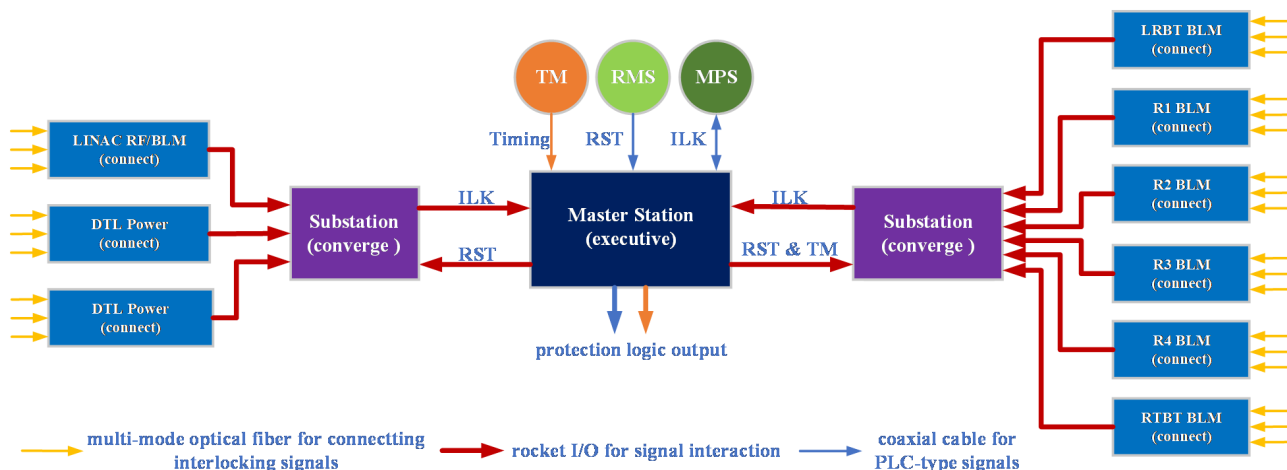
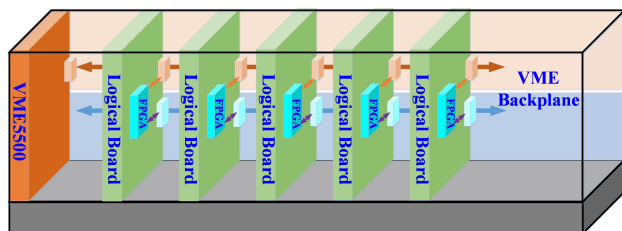


Figure 4: The schematic diagram of signal link.

terlock signals via VME Backplane respectively, which is used the open-collectors to realize the "wire-OR" logic, as shown in Figure 6. the main logic board of slot 4 is used to collect the real-time signals from VME Backplane and send to execution master.



Schroff VME 64x

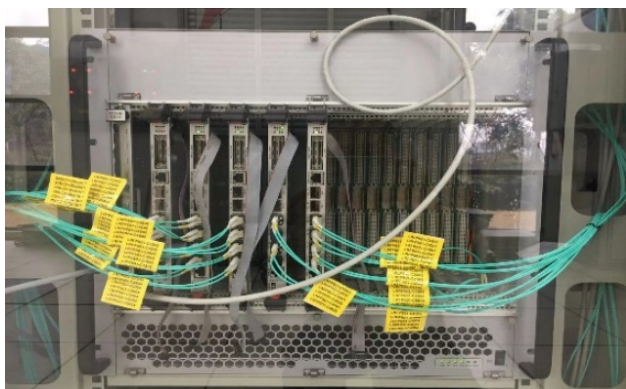


Figure 5: (Top) The schematic diagram of the summary sub-station, (Bottom) The physical map of the summary sub-station.

In order to ensure that the whole transmission link of each node is normal, a heartbeat signal, a width of 100 ns with 1 Hz, is generated at every sending terminal of the trans-

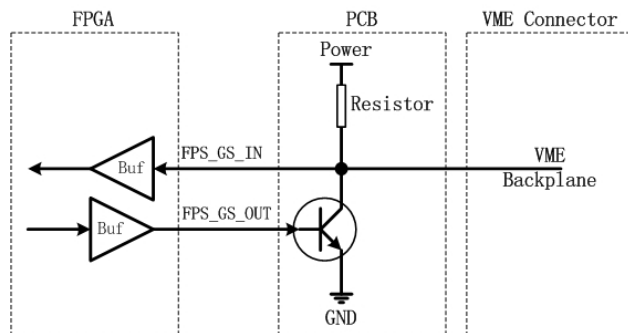


Figure 6: The schematic diagram of logic "OR".

mission link, and each link is used to transmit the heartbeat signal and real-time status signal simultaneously; the heartbeat signal is detected at the receiving terminal in real time, as shown is Figure 7. It is need to stop the beam immediately if an abnormal heartbeat signal is checked.

## PROTECTION STRATEGY

In order to formulate protection strategies, the characteristics of each interlocking signal should be in-depth recognized and analysed.

The signal of CSNS LINAC accelerator DTL power supply system during operation will be unique state, normal or abnormal. Therefore, if the FPS receives the abnormal signal from DTL power supply or SPS, the faults is locked whatever the duration is short or long. Figure 8 is a schematic diagram of the signal processing for DTL power supply.

The signal of beam loss detector can be normal or abnormal, and the duration of the abnormal state is one beam cycle. Therefore, the FPS receives the abnormal signal from

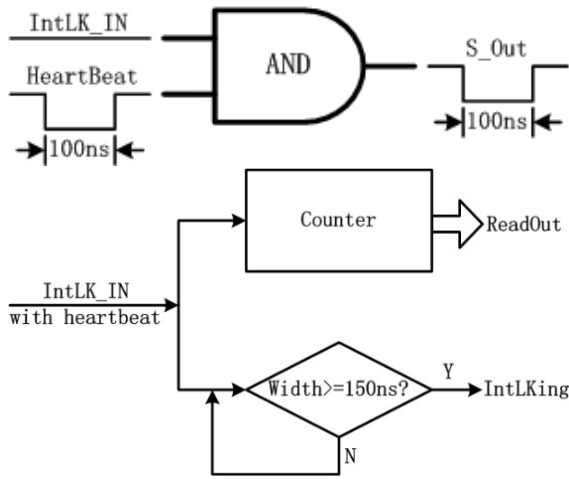


Figure 7: The logic function of heartbeat.

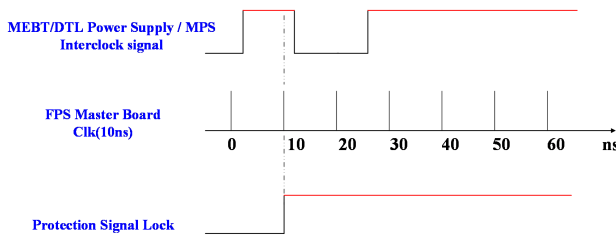


Figure 8: The schematic diagram of the signal processing for DTL power supply.

beam loss detector, it is instantaneous to stop beam. However, it is unacceptable if the abnormal signal is occurrence frequently. According to physics discussion, it is permanent if the number of instantaneous times within 10 seconds is six in LINAC or the number of in-staneous times within 5 seconds is two in RCS. Figure 9 is the schematic diagram of the signal processing for RCS BLM.

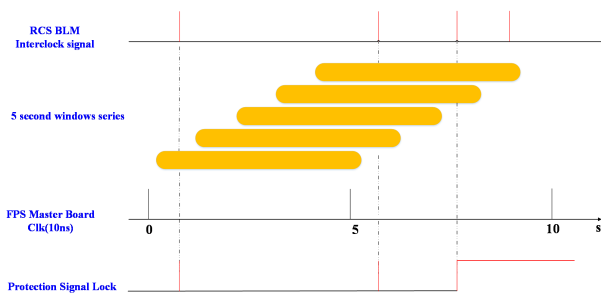


Figure 9: The schematic diagram for RCS BLM signal processing.

According to the characteristics of the interlock signals, the whole faults caused by equipment failures are divided into two categories: transient faults or permanent faults. In order to improve the operation efficiency of the CSNS accelerator, protection strategy is in-depth studied based on ensuring the safe operation. If the fault is transient, the beam should be cut off immediately, and the beam will be sync

recovery automatically after the fault has passed, as shown in Figure 10; on the contrary, the beam should be cut off immediately, and the beam should be recovery manually because of the locked fault. It is indeed that the protection strategy can significantly improve the operation efficiency under ensuring equipment safety. Figure 11 shows the schematic diagram for implementing permanent protection function.

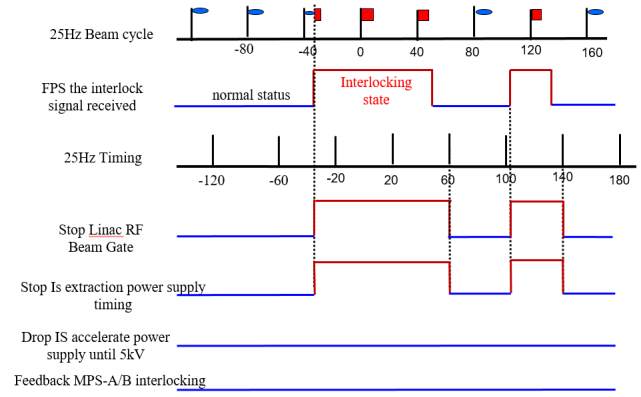


Figure 10: The schematic diagram for instantaneous protection logic.

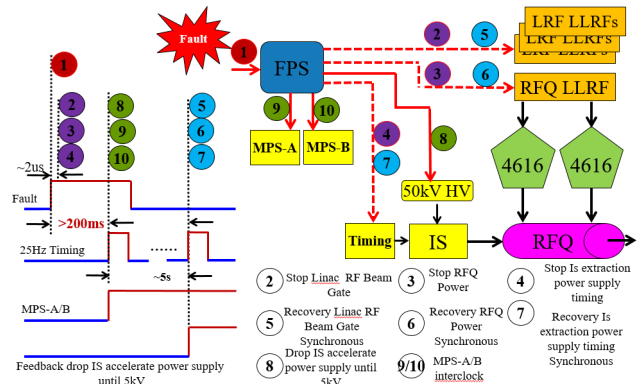


Figure 11: The schematic diagram for implementing permanent protection function.

## TIME CONSUMING

FPS can not put into operation guaranty until the internal and joint testing with related equipment have been carried. The transmission delay of each node in the system has been tested rigorously, as shown in Figure 12; the time consumption for two fast execution shutdown targets is also carried out, as shown in Figure 13. The results of all tests show that the CSNS fast machine protection system can meet the current and subsequent upgrade needs of the accelerator.

- Figure 13 (Top): The progressing is that “get fault signal->judgment->sent out interlock signal->stop the timing of ion source extraction power supply”, the total time is about 1.3 μs, which includes the delay 1.1 μs due to transmission.

Content from this work may be used under the terms of the CC BY 3.0 licence (© 2021). Any distribution of this work must maintain attribution to the author(s), title of the work, publisher, and DOI

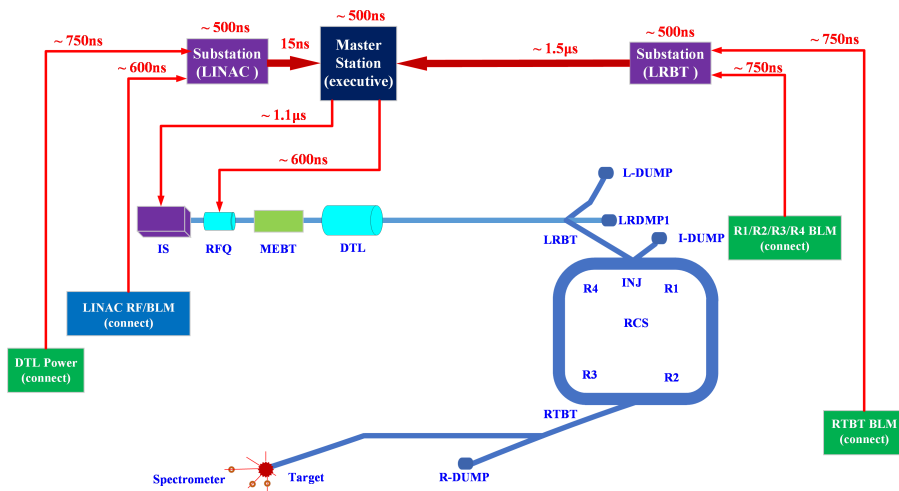


Figure 12: The response time of critical link.

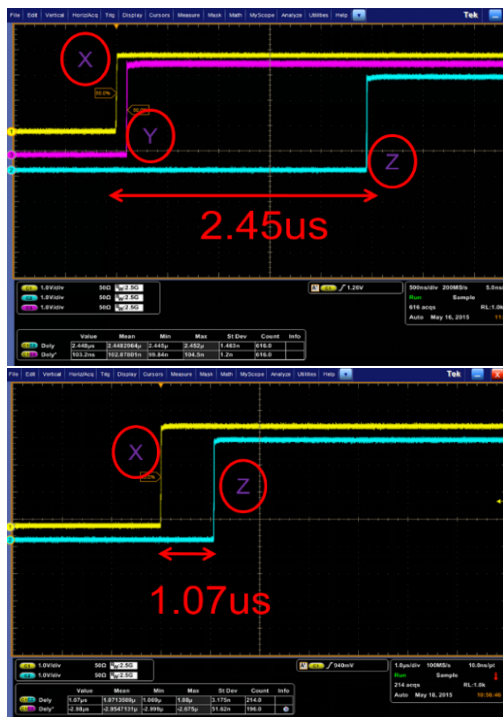


Figure 13: (Top) stop the timing of ion source extraction power supply, (Bottom) cut off the power of RFQ.

- Figure 13 (Bottom): The progressing is that “get fault signal->judgment->sent out interlock signal->cut off the power of RFQ”, the total time is about 1.3 µs, which includes the delay 600 ns due to transmission.

## CONCLUSION

In order to cut off the beam with high reliability in the shortest possible time, and to maintain the relevant state in time to meet the operational safety, we the self-developed

FPS for CSNS accelerator, which has under-gone detailed response time-consuming tests and careful traversal testing.

Since the beginning of installation, commissioning and gradual use in 2015, the FPS of CSNS has been operating stably for nearly six years, safe and reliable, and has been continuously optimized during adjustment and operation, such as adding the beam gate for each BLM and improving the design that all the beam loss signals of RCS are connect to FPS, whose enhance the robustness and high availability. It has been put into operation for nearly six years with stable and reliable, which is one of the important basic conditions for the efficient operation of CSNS accelerator.

## ACKNOWLEDGEMENTS

The authors would like to thank all the leaders, teachers and colleagues of the Accelerator Technology Department.

## REFERENCES

- [1] S. Wang *et al.*, “Introduction to the overall physics design of CSNS accelerators”, *Chinese Physics C*, vol. 33, pp. 1-3, 2009. doi:10.1088/1674-1137/33/S2/001
- [2] H. C. Liu *et al.*, “DTL Construction Status of China Spallation Neutron Source”, *Atomic Energy Science and Technology*, vol. 49(S2), pp. 556-559, 2015.
- [3] M. T. Kang *et al.*, “The Machine Protection System for CSNS”, *Radiation Detection Technology and Methods*, vol. 5, pp. 273-279, 2020. doi:10.1007/s41605-021-00239-8
- [4] Y. L. Zhang *et al.*, “The accelerator control system of CSNS”, *Radiation Detection Technology and Methods*, vol. 4, pp. 478-491, 2020. doi:10.1007/s41605-020-00203-y
- [5] D. P. Jin *et al.*, “Design, Implementation and Setup of the Fast Protection System for CSNS”, in *Proc. 15th Int. Conf. on Accelerator and Large Experimental Physics Control Systems (ICALEPCS’15)*, Melbourne, Australia, Oct. 2015, pp. 543-544. doi:10.18429/JACoW-ICALEPCS2015-TUC3002

# AN OPERATIONALLY INTEGRATED APPROACH TO THE SNS 2.8 MW POWER UPGRADE\*

J. Galambos<sup>†</sup>, on behalf of the PPU team, SNS, Oak Ridge TN, USA

## Abstract

The Spallation Neutron Source (SNS) accelerator consist of a 1 GeV H<sup>-</sup> linac and an accumulator ring producing a 1.4 MW pulsed proton beam which drives a spallation neutron source [1]. The Proton Power Upgrade project will double the power capability from 1.4 to 2.8 MW by increasing the linac beam energy 30% and the beam current about 50%. Equipment upgrades include new superconducting RF cryomodules and supporting RF equipment, upgraded ring equipment, and upgraded high power target systems. An important aspect of the up-grade is a gradual power ramp-up starting in 2022 in which new equipment is installed during maintenance outages as it arrives, and used in subsequent run periods.

## INTRODUCTION

The SNS is a neutron scattering materials science user facility that has been operating since 2006. The neutron flux used to study material structures and properties is proportional to the proton beam power, the history of which is shown in Fig. 1. Beam power has been operating stably at the design level of 1.4 MW since 2018, and SNS has been embarked on a Proton Power Upgrade (PPU) project since 2017 [2, 3]. This project aims to double the beam power capability by increasing the beam energy by 30% and increasing the average beam current by 50%. Of the post-upgrade 2.8 MW proton beam power capability, 2 MW will be provided to the existing First Target Station (STS) at SNS, and additional power will be available to power a new Second Target Station [4], which is a separate ongoing project. The PPU project received approval for long lead procurements in the areas of superconducting cryomodules, RF equipment and RF service building upgrades in the fall of 2019. In fall 2020 the project baseline and the start of construction was approved.

A major consideration of high-power proton accelerators is beam loss, which is discussed in section 2, along with some discussion on operational experience that guides the upgrade. The progress of different PPU technical systems is discussed in section 3. The coordination of the upgrade equipment installation and use with ongoing operations resulting in a gradual power ramp-up is discussed in section 4.

## OPERATIONAL EXPERIENCE

As indicated in Fig. 1, SNS has been operating stably at 1.4 MW for 3 years. Accelerator availability of over 90% and

over 4500 operational hours per year have been sustained over this period. The operational experience garnered since 2006 guides the PPU upgrade choices for 2.8 MW operation [2, 3]. In addition to the equipment needed to provide the higher power, PPU will provide additional beam instrumentation and control in the injection dump area, which is presently has limited diagnostics.

Beam loss was a major consideration in the design of SNS. Beam loss was expected to be less than 1 W/m [5] (or <10<sup>-6</sup> fractional loss for much of the facility) and this is the case. This level of beam loss is beyond what simulation tools accurately predict. But it is possible to scale anticipated post-upgrade beam loss from present observed beam loss levels at ~1 MW operation. This was done for the various sections of the SNS accelerator in Ref. [2], and the increase in beam loss and subsequent activation levels is expected to be smaller about a factor of 2 from presently observed residual activation levels. This increase can be accommodated without major impact on machine operations.

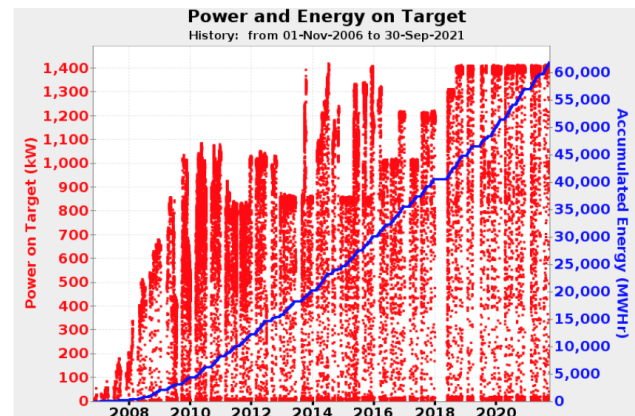


Figure 1: SNS Beam power history.

## UPGRADE STATUS

### Superconducting Linac

Seven new cryomodules will be installed in existing slots in the SNS high energy end of the linac [6]. Over the past year the superconducting RF cavities have been supplied by the vendor and cryomodule production is ramping up at the partner lab, JLab. Equipment procurements are largely in hand, cavities have been jacketed and qualified for the first 3 cryomodule strings, and the first cryomodule cold mass is nearing final assembly. (see Fig. 2). In addition, an 8<sup>th</sup> spare cryomodule has been added to the project scope. The cryomodule production is on schedule for delivery of the initial 2 cryomodules in April 2022.

\* This research used resources at the Spallation Neutron Source, a DOE Office of Science User Facility operated by the Oak Ridge National Laboratory.

<sup>†</sup> jdgalamb@ornl.gov

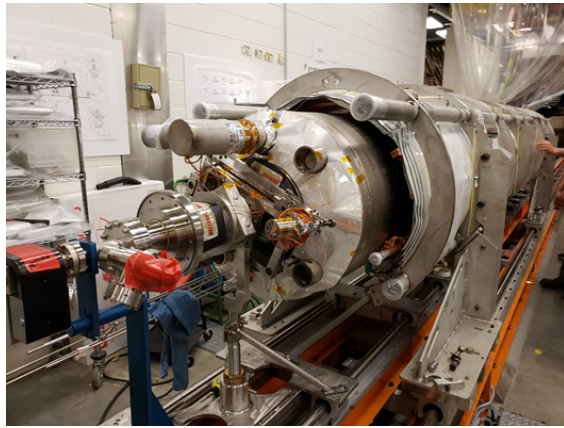


Figure 2: Initial PPU cryomodule cold mass.

### RF Upgrades

The primary RF scope is the addition of new equipment to power the 7 new cryomodules. This includes transmitters, high voltage converter modulators and klystrons. These are all incremental extensions of existing technology implementations at use in SNS, with no fundamentally new developments. Because of this the RF equipment was well positioned for early long lead time procurement in 2019. Figure 3 shows a new klystron for the superconducting linac section delivered to SNS. Upgrades are also being made on the lower energy DTL RF systems to accommodate the higher beam loading post-PPU [7]. Also, the new LLRF systems will accommodate dual pulse flavors to support future interleaving of beam to the STS [8].



Figure 3: New RF klystron at SNS.

### Ring Systems

The primary Ring system upgrades are upgraded injection and extraction magnet systems, and new diagnostics and control elements in the ring injection dump line. Two new chicane magnets and a new septum magnet are being provided for the injection region. We are partnering with

FNAL for the design and fabrication of these critical upgrade elements. Figure 4 shows the final design for the chicane magnets. Also, a safety credited system to prevent exceeding the target power limit is being provided in the beam transport line upstream of the target [9].

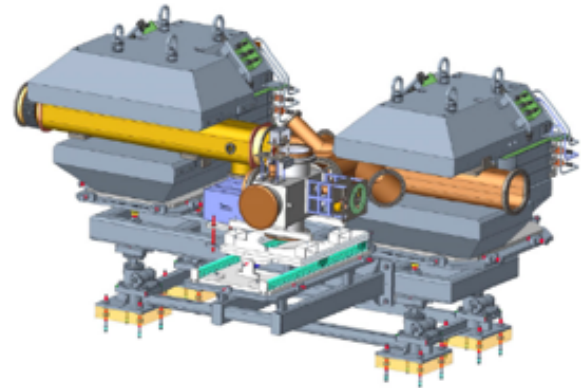


Figure 4: New ring injection chicane design.

### Target System Upgrades

The primary target upgrade is a new target vessel with structure designed to handle the increased loads associated with higher beam intensity [10]. A major demonstrated operational target damage mitigation technique is gas injection to the flowing liquid mercury target material. PPU will provide for increased gas injection capability, new gas bubble generation techniques [11], and more complete gas coverage throughout the target vessel [12, 13]. These target upgrades will be implemented through a series of 2 incremental test targets. Other system upgrades include improvements in the mercury offgas treatment systems and providing a new orthopara hydrogen conversion system for the cryogenic moderator. Figure 5 shows the initial test target ready for installation, with the new gas bubble injection system.



Figure 5: First PPU test target ready for installation.



Figure 6: Klystron gallery installed cooling systems.

### Civil Construction

Construction is complete on the klystron gallery service building alongside the linac that houses the RF equipment powering the new cryomodules. Construction included adding a new pump room, installing HVAC equipment, cooling pipes installation and cable tray installation. Figure 6 shows the klystron gallery in August. Equipment installation activities are ongoing. In addition to the klystron gallery

upgrades, a stub will be added to the transport line from the ring to the first target station.

### POWER RAMP-UP PLAN

PPU will implement the remaining upgrade tasks in coordination with SNS operations. Typically, the SNS operation cycle includes 2-3 extended maintenance outages per year, of ~2-month duration each. PPU will take advantage of these outages for equipment installation in tunnels, electrical tie-ins, shielding modifications etc. Other PPU activities can take place during operation, such as equipment installation in the klystron gallery. Operations has its own sets of constraints on machine maintenance and upgrades. Also considered in PPU planning is the outage schedule for the sister neutron source at ORNL, at the High Flux Isotope Reactor (HFIR). Expected vendor delivery dates for equipment also are an element for outage scheduling. Finally, input was also solicited from the SNS government sponsor. The outage durations include the time required for restart approval with the newly installed equipment. All these impacts were considered in adopting the overall power ramp up schedule shown in Fig. 7. The red bars indicate extended maintenance periods, and the white bars indicate operational run periods. Some PPU project high-level activities in these periods are also indicated. There is one longer than usual (10 month) outage in 2023. Together, the interleaving of outage periods for equipment installation and run periods where the newly installed equipment is used constitutes the planned gradual power ramp-up. This will occur between 2022 and 2024.

The general approach is to use new equipment as soon as it is available. In the target area, we will implement upgrades starting with the first test target in early 2022 that

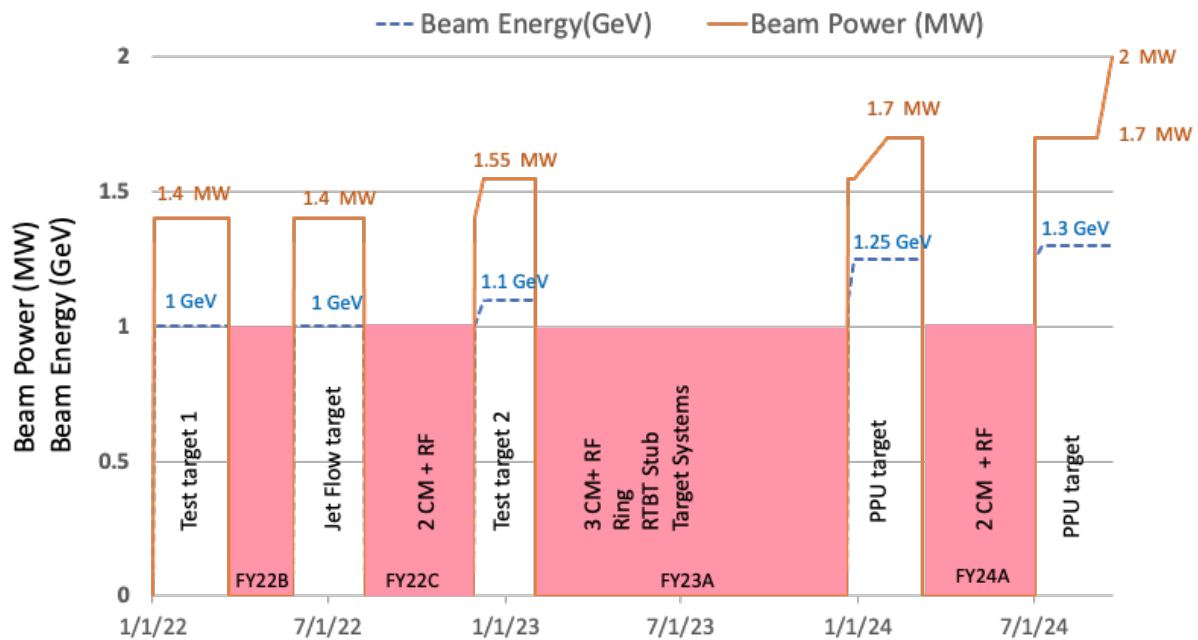


Figure 7: PPU gradual power ramp-up plan, indicating the expected beam energy and beam power increases. (CM+RF=cryomodule and supporting RF equipment installation).

incorporates new gas bubbler injection technology and some of the new structural elements. The final target upgrades will be included in the long outage in 2023, after which higher flow and more complete target coverage gas injection will be possible.

A major component of the planned upgrade is to operate cryomodules starting in the run cycles following their installation. The first 2 cryomodules are planned for installation in mid 2022, and we will increase the beam energy and power by ~10% (to 1.1 GeV and 1.55 MW) coming out of this outage.

The following 10-month extended outage in 2023 is the primary installation period for PPU. Several activities require extended down time and it is important to have these proceed in parallel to minimize overall machine downtime. Two of these extended duration activities are the upgrade to the ring injection area and the addition of a stub in the tunnel from the ring to the existing target station. Including the stub during this period will avoid a future long outage to tie into the future second target station. Coming out of this extended outage in late 2023, 5 of the 7 PPU provided cryomodules should be installed and operation at 1.25 GeV and 1.7 MW is planned. Also, the final PPU target configuration should be operational coming out of this outage.

The maintenance period near the start of 2024 is planned to be close to the normal outage length and the last 2 PPU cryomodules will be installed, after which the full capability to run at the full upgrade energy of 1.3 GeV and power of 2.8 MW will be complete. We plan to initially run at 1.7 MW for 1250 hours to meet a project completion threshold milestone, and then quickly ramp-up to the 2 MW capability of the existing target station. When the new STS is available additional proton beam power will be sent there.

## REFERENCES

- [1] S. Henderson *et al.*, “The Spallation Neutron Source Accelerator System Design”, *Nucl. Instrum. Methods Phys. Res., Sect. A*, vol. 763, p. 610-673, 2014. doi:10.1016/j.nima.2014.03.067
- [2] “Final Design Report, Proton Power Upgrade”, ORNL, Oak Ridge, USA, Rep. ORNL/TM-2020/1570-R0, June 2020. [https://neutrons.ornl.gov/sites/default/files/Final\\_Design\\_Report.pdf](https://neutrons.ornl.gov/sites/default/files/Final_Design_Report.pdf)
- [3] M. Champion *et al.*, “Progress on the Proton Power Upgrade at the Spallation Neutron Source”, in *Proc. 12th Int. Particle Accelerator Conf. (IPAC’21)*, Campinas, Brazil, May 2021, pp. 1876-1879. doi:10.18429/JACoW-IPAC2021-TUPAB199
- [4] Second Target Station Project, <https://neutrons.ornl.gov/sts>
- [5] N. Catalan-Lasheras, S. Cousineau, J. Galambos, N. Holtkamp, D. Raparia, R. Shafer, J. Staples, J. Stovall, E. Tanke, T. Wangler, and J. Wei, “Accelerator physics model of expected beam loss along the SNS accelerator facility during normal operation”, ORNL, Oak Ridge, USA, SNS/AP-Technical Note 07, 2001.
- [6] M. Howell, B. DeGraff, J. Galambos, and S. Kim, “SNS Proton Power Upgrade,” in *Proc. CEC/ICMC 2017*, Madison, WI, USA, Jul. 2017. doi:10.1088/1757-899X/278/1/012185
- [7] J. S. Moss, M. T. Crofford, S. W. Lee, G. D. Toby, and M. E. Middendorf, “The SNS Normal Conducting Linac RF System Design for the Proton Power Upgrade Project”, in *Proc. 12th Int. Particle Acc. Conf. (IPAC’21)*, Campinas, Brazil, May 2021, pp. 4383-4386. doi:10.18429/JACoW-IPAC2021-THPAB296
- [8] M. Crofford *et al.*, “Spallation Neutron Source Proton Power Upgrade Low Level RF Control System Development”, in *Proc. 12th Int. Particle Accelerator Conf. (IPAC’21)*, Campinas, Brazil, May 2021, pp. 3363-3366. doi:10.18429/JACoW-IPAC2021-WEPAB299
- [9] C. Deibele and K. Mahoney, “SNS Credited Beam Power Limit System Preliminary Design,” in *Proc. 12th Int. Particle Acc. Conf. (IPAC’21)*, Campinas, Brazil, May 2021, pp. 2242-2244. doi:10.18429/JACoW-IPAC2021-TUPAB319
- [10] D. Winder, “Evolution of High-Power Spallation Mercury Target at the SNS”, in *Proc. 12th Int. Particle Acc. Conf. (IPAC’21)*, Campinas, Brazil, May 2021, pp. 3735-3739. doi:10.18429/JACoW-IPAC2021-THXC03
- [11] C. Barbier *et al.*, “Bubble Generation in the SNS 2MW Mercury Target”, in *Proc. 12th Int. Particle Acc. Conf. (IPAC’21)*, Campinas, Brazil, May 2021, pp. 3567-3570. doi:10.18429/JACoW-IPAC2021-WEPAB367
- [12] J. Weinmeister, E. Dominguez-Ontiveros, and C. Barbier, “Gas Wall Layer Experiments for SNS Target”, *ASMEJSME-KSME 2019 8th Joint Fluids Engineering Conference, American Society of Mechanical Engineers Digital Collection*, 2019. doi:10.1115/AJKFluids2019-5101
- [13] C. Barbier, E. Dominguez-Ontiveros, and R. Sangrey, “Small Bubbles Generation with Swirl Bubblers for SNS Target”, *Fluids Engineering Division Summer Meeting*, vol. 51579, American Society of Mechanical Engineers, 2018. doi:10.1115/FEDSM2018-83077

# SELF-CONSISTENT LONG-TERM DYNAMICS OF SPACE CHARGE DRIVEN RESONANCES IN 2D AND 3D

Ingo Hofmann and Adrian Oeftiger\*

GSI Helmholtzzentrum für Schwerionenforschung GmbH, Darmstadt, Germany  
Oliver Boine-Frankenheim, Technische Universität Darmstadt, Darmstadt, Germany

## Abstract

Understanding the 3D collective long-term response of beams exposed to resonances is of theoretical interest and essential for advancing high intensity synchrotrons. This study of a hitherto unexplored beam dynamical regime is based on 2D and 3D self-consistent particle-in-cell simulations and on careful analysis using tune spectra and phase space. It shows that in Gaussian-like beams Landau damping suppresses all coherent parametric resonances, which are of higher than second order (the “envelope instability”). Our 3D results are obtained in an exemplary stopband, which includes the second order coherent parametric resonance and a fourth order structural resonance. They show that slow synchrotron oscillation plays a significant role. Moreover, for the early time evolution of emittance growth the interplay of incoherent and coherent resonance response matters, and differentiation between halo and different core regions is essential. In the long-term behaviour we identify a progressive, self-consistent drift of particles towards and across the resonance, which results in effective compression of the initial tune spectrum. However, no visible imprint of the coherent features is left over, which only control the picture during the first one or two synchrotron periods. An intensity limit criterion and an asymptotic formula for long-term rms emittance growth are suggested. Comparison with the commonly used non-self-consistent “frozen space charge” model shows that in 3D this approximation yields a fast and useful orientation, but it is a conservative estimate of the tolerable intensity.

## INTRODUCTION

Beam intensity in operating or future high intensity circular hadron accelerators is limited by space charge effects on resonances [1]. Contrary to low intensity operation, where resonances are single particle phenomena, high intensity requires self-consistent treatment with differentiation between incoherent and coherent resonance effects as well as consideration of Landau damping of nonlinear coherent parametric resonances. Analytical or semi-analytical models of the latter do not exist – in contrast to the rich literature on impedance driven dipole modes –, hence we depend largely on simulation and careful theory-based interpretation.

Long-term space charge effects on synchrotron resonances have been measured in dedicated campaigns (see, for example, Refs. [1–3]). Comparison with simulation models is essential for understanding resonant processes and min-

imizing their effects on beam quality; but so far – for cpu and noise related reasons – only non-self-consistent “frozen space charge models” (FSM) have been employed in these campaigns, which require modeling of  $10^5 \dots 10^6$  machine turns. Such fully self-consistent 3D simulations using large numbers of simulation particles and many turns of synchrotron lattices are quite possible. Examples are long-term studies of the Montague resonance with the IMPACT code [4], or recent work on parametric Landau damping using the SYNERGIA code [5].

Recently, coasting beam 2D studies in relatively short systems (hundreds of cells rather than hundreds of thousands) have been used as basis for conjectures on coherent resonance effects and suggestion of new types of synchrotron resonance charts based on assumed coherent shifts, with partly controversial conclusions (see Ref. [6], also Refs. [7, 8]). The need for *long-term* and self-consistent 3D studies to adequately address these issues becomes obvious.

Historically, Smith [9] first pointed out in the early 1960’s that coherent effects on gradient error resonances should result in higher intensity; followed by Sacherer [10] who extended the concept of coherent shifts to nonlinear resonances in a 1D Vlasov-Poisson study. In the 1990’s, the suggestion by Smith was partly confirmed in relatively short-term simulations by Machida [11]; a Vlasov model presented coherent frequencies in 2D including anisotropy [12], and a review article by Baartman [13] further advocated for the coherent shift concept. The distinction between coherent and incoherent second order resonance effects was studied experimentally in HIMAC [14] and the PSR [15].

In high intensity linear accelerators the theoretically predicted structural space charge resonance effects [16] got verified experimentally by detailed phase space diagnostics [17].

In circular accelerators space charge resonant effects are known to exist; however, distinguishing them from often dominating externally driven resonances and other machine specific effects continues to be a challenging issue for performance optimization of high intensity synchrotrons [18–21]. Besides studies in operating linear accelerators and synchrotrons, compact linear Paul trap devices are also used to explore – experimentally and theoretically – incoherent and coherent resonances in periodic focusing and 2D [22].

For high intensity hadron circular accelerators – different from linear devices – a main beam dynamics challenge is self-consistent and long-term 3D modelling including synchrotron oscillation, which has motivated the present study. As an exemplary case we choose a simple FODO cell for

\* a.oeftiger@gsi.de

transverse periodic focusing and study primarily – with exceptions in 2D – the space charge induced resonances above 90°, the so-called 90° stopband of periodic focusing. It combines a fourth order structure resonance with the second order parametric resonance – the envelope instability – and thus allows studying the interplay of incoherent and coherent resonance.

We proceed with a short theory overview in Section , followed by a detailed 2D simulation analysis of different stopbands, Landau damping and incoherent core resonances in Section . In Section we compare long-term 2D with 3D PIC simulation; Section discusses the “frozen space charge modeling” (FSM) in 2D and 3D, Section discusses possible applications and Section presents conclusions and a brief outlook.

## THEORETICAL BACKGROUND

In circular accelerators it is common practice to describe the effect of space charge in terms of an incoherent footprint on resonance charts, which depends on the distribution function – besides chromatic and other effects not in the focus here. Equally wide-spread is the assumption that resonance analysis should be based on avoiding major resonance lines - defined in the absence of space charge - to intercept with this incoherent footprint. Such a picture cannot adequately account for self-consistent and possibly existing coherent resonant response beyond incoherent behaviour. This Section reviews some basic definitions and notions useful for the further discussion.

In a periodic and linear focusing lattice – ignoring bending – the single particle equation of motion in  $x$  (and similar in  $y, z$ ) along distance  $s$  can be written as

$$x'' + K_x(s)x - \frac{q}{mc^2\beta^2\gamma^3}E_x(x, y, z, s) = 0, \quad (1)$$

where the electric field from space charge is assumed non-linear. For a matched beam it modifies the focusing and includes the space charge contribution from the whole ensemble of particles - also due to coherent effects - subject to self-consistent modeling. It is convenient to describe the FODO focusing by  $k_{xy}$  as single particle transverse phase advance per FODO cell. It includes the space charge shift due to the linear part of the electric field, which reduces the zero-intensity phase advance  $k_{0xy}$ , with a dependence on amplitude due to nonlinear terms in the electric field. As an example, and using the ring-specific nomenclature of “tunes”, the SIS18 at GSI includes  $N = 12$  cells of periodic focusing, and a typical vertical  $k_{0y} = 96^\circ$  amounts to a tune of  $Q_{0y} \equiv Nk_{0xy}/360^\circ = 3.2$ . In the remainder of our discussion the variation of focusing strength per cell is described by phase advances, while “tunes” is kept in general terms.

For simplicity, we restrict the present discussion also to symmetric phase advances and emittances in  $x$  and  $y$ ; machine specific studies relating to a broader range of parameters and lattice configurations are left to future works.

In the remainder of our discussion the usual “tunes” as phase advances per turn are replaced by the phase advances

per cell, thus emphasizing the focus on the stopband around 90° as well as its higher order counterparts at 60° and 45°.

### Incoherent and Coherent Resonance Conditions

As transverse incoherent resonance condition – refraining from coupling – can be written as

$$mk_{xy} = h 360^\circ, \quad (2)$$

which is used here to characterize space charge driven incoherent structure resonances. Here  $m$  is the resonance order and  $h > 1$  describes a possible higher harmonic of the driving lattice structure term (with  $h = 1$  in all following simulation examples). This is equivalent to  $mQ_{xy} = hN$  in circular notation with  $N$  cells per turn. The term *incoherent* is meant to describe the resonance response as single particle behaviour in the presence of a space charge force from an assumed matched beam distribution. It is essential to distinguish the spectral distribution  $k_{xy}$  from  $\bar{k}_{xy}$ , the space charge shifted value of phase advances of an rms-equivalent KV beam. As usual, this shift is described in rms-equivalence as  $\Delta\bar{k}_{xy} \equiv k_{0xy} - \bar{k}_{xy}$ . In 3D bunches  $\Delta\bar{k}_{xy}$  refers to the longitudinal bunch center, i.e. half the maximum phase advance shift for a Gaussian distribution.

This incoherent shift is also used to characterize the strength of coherent effects. For the latter, the distribution as a whole is assumed to deviate from its matched configuration by adopting a coherent mode structure, which induces a specific coherent frequency shift  $F_m$ . The question of whether such coherent effects actually exist for other than KV-distributions will be discussed further below. Assuming their existence, a coherent structure resonance condition can be formally written in the form:

$$m(\bar{k}_{xy} + F_m\Delta\bar{k}_{xy}) = \frac{h}{2}360^\circ, \quad (3)$$

where we use the notation of Ref. [23], which is based on evaluating dispersion relations from the Vlasov model of Ref. [12] (an alternative definition replacing  $\bar{k}_{xy}$  by  $\bar{k}_{0xy}$  is used in Ref. [24], and in analogous manner in Ref. [6]). Note that the corresponding circular notation is again obtained by replacing all  $k$  by  $Q$  and  $360^\circ$  by  $N$ . The resonance order is given by  $m$ , which also describes the order of a coherent mode pattern. The  $F_m$  characterize the extra coherent shift depending on the mode, respectively resonance order, and in general on the ratios of focusing strengths and emittances.  $h$  is an integer as before, but now  $h = 2$  stands for the fundamental lattice harmonic, and higher even numbers for multiples thereof. Of special interest in this study is the case  $h = 1$  (generally all odd numbers). This coherent half-integer – here also called 1:2 – mode describes the parametric resonances to be discussed further on.

### Parametric Resonances

These coherent parametric resonances – as a special case of coherent resonances – have originally been introduced in the 2D Vlasov perturbation analysis of KV distributions in periodic focusing in Ref. [25]. They were called

“180-degree” modes describing their half-integer nature and shown to exist from second to at least sixth order. The more widely used terminology of parametric resonances was later suggested in the 1D Vlasov analysis of a waterbag-type sheet beam of Ref. [26]. Note that the equivalent term “parametric instability” is also applied here. It is equally used for the “Mathieu instability” of particles propagated at 180° phase advance in periodic focusing [27] – the single-particle analogue to the unstable coherent modes considered here.

In both cases the exponential growth is enforced by the periodic focusing force varying at twice the eigenfrequency of the particle, respectively coherent mode. In the coherent parametric case the transverse oscillation mode characterized by the order  $m$  in Eq. (3) determines the oscillation frequency of the coherent part of the electrical field term in Eq. (1), which in turn provides the resonance driving term. The parametric nature of this mechanism materializes through the periodical modulation of the focusing force, which pumps energy into the beam eigenmode and results in exponential growth – as opposed to non-parametric resonances. The term “instability” actually appears justified in view of the fact that initially the driving term of order  $m$ , along with an odd  $h$  in Eq. (3), exists in the electric field term only on the noise level. This is different from the structure space charge resonances with only even  $h$  – for example the  $m=4$  case in Section –, which require the presence of a driving term in the initial (matched) beam. In spite of this physical justification we continue with the widely used terminology “parametric resonance” in the remainder of this paper. Obviously this parametric picture also applies to the  $m=2$  envelope mode starting from initial noise or slight mismatch of the  $h=1$  periodicity; here we keep the notation “envelope instability” as commonly used in accelerator literature.

More recently, the 2D KV Vlasov basis was broadened by generalizing the analysis of Refs. [12, 25] to combine the effects of periodic focusing with different focusing strengths and emittances in the two transverse planes [28].

These and all other Vlasov models of higher than first order (dipole) transverse modes have in common the absence of incoherent tune spread – apparently due to the mathematical difficulties to handle non-KV distributions with tune spreads. As a result, none of these analytical models includes the possibility of Landau damping, and computer simulation is needed. Nonetheless, results from KV-based Vlasov perturbation analysis are a useful tool to interpret simulation results with more realistic beam models.

## SHORT-TERM 2D SIMULATION RESULTS

To elucidate the interplay of incoherent and coherent resonance effects we start from 2D and focus on different stopbands of structure type resonances driven by space charge itself [29]. Magnet driven resonances with space charge are closely related, but left to future studies.

## Simulation of Stopbands

For the 2D simulations we use the TRACEWIN PIC code [30] with 128.000 particles and  $\Delta\bar{k}_{xy}$  kept constant at 12°. Waterbag distributions are compared with (uncorrelated) Gaussian distributions, which are truncated at  $3.4\sigma$  throughout this study. Fig. 1 shows the relative rms emittance growth after 300 FODO cells versus  $k_{0xy}$  for the 90° stopband. The sharp space charge shifted peak for an initial

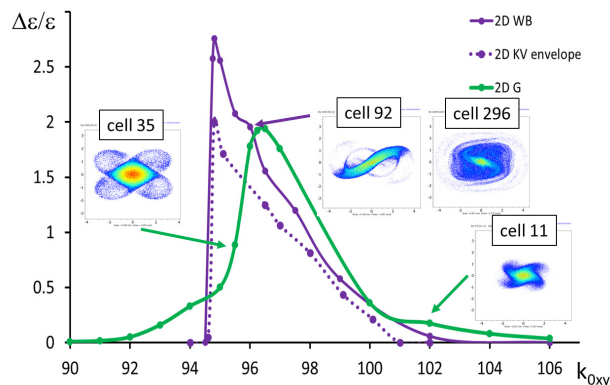


Figure 1: Rms emittance growth versus  $k_{0xy}$  for the stopband above 90° for 2D waterbag and Gaussian distributions after 300 FODO cells. Inserts showing  $x - x'$  phase space at different  $k_{0xy}$  and cells.

waterbag distribution is due to the  $m=2$  parametric resonance – the envelope instability – according to Eq. (3) (see inserts at cell 92 and 296), which coincides with the peak of the same mode obtained by the KV envelope equation. The initial Gaussian case shows a similar though somewhat weaker coherent response. The softer shoulders of the stopband reflect in addition an  $m=4$  incoherent response according to Eq. (2). It is apparently driven by the structure type pseudo-octupole term of the space charge potential as confirmed by the four-fold symmetry in the inserts: at cell 35 for  $k_{0xy} = 95.5^\circ$  at the lower tune side; and a less pronounced one at cell 11 for  $k_{0xy} = 102^\circ$  (equivalent to  $\bar{k}_{xy} = 90^\circ$ ). Note that the absence of emittance growth for  $k_{0xy} < 91^\circ$  is owed to the truncation of Gaussian tails.

The 60° waterbag stopband in Fig. 2 gives a weaker response for the nonlinear  $m=3$  parametric resonance with only 40% emittance growth (insert cell 225). For the Gaussian this mode is entirely absent; instead, a tiny ( $< 0.8\%$ ) rms emittance growth due to a sixth order  $m=6$  incoherent resonance driven by the structure pseudo-dodecapole of the space charge potential is found (insert cell 41). The 45° stopband in Fig. 2 shows the  $m=4$  parametric resonance (insert cell 245), which reaches an rms emittance growth of only 2% for the waterbag and no detectable growth for the Gaussian case.

## Landau Damping of Parametric Resonances

All in all, in 2D we find parametric resonances of second, third and fourth order to exist in the waterbag distribution, but only the second order mode in the Gaussian case. We

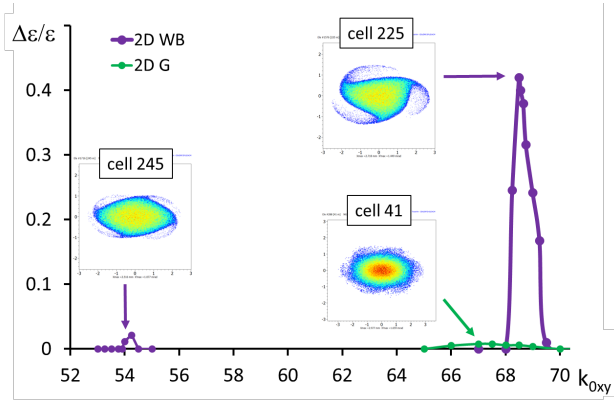


Figure 2: Rms emittance growth versus  $k_{0xy}$  for the stopbands above  $60^\circ$  and  $45^\circ$  for 2D waterbag and Gaussian distributions after 300 FODO cells. Inserts showing  $x - x'$  phase space at different  $k_{0xy}$  and cells.

explain this by Landau damping using the tune spectra extracted from self-consistent TRACEWIN simulations. In Fig. 3 the working point  $k_{0xy} = 90^\circ$  is chosen to obtain resonance-free spectra  $f_0(k_{xy})$  representative for an initial beam situation at arbitrary  $k_{0xy}$ . Particle trajectories over  $2^{14}$  elements (1820 cells with 9 elements per cell) are evaluated for this purpose. The coherent shifts following Eq. (3) (divided by  $m$ ) are determined here from the peaks of response in the waterbag simulations in Figs. 1 and 2, indicated in Fig. 3 by colored lines. They can be compared with the corresponding  $F_m$  obtained analytically from the 2D KV-based Vlasov analysis. For symmetric beams the highest frequency branches yield coherent factors decreasing with increasing  $m$ :  $F_2 = \frac{1}{2}$ ;  $F_3 = \frac{1}{4}$ ;  $F_4 = \frac{3}{16}$  [23]. These theoretical values for the  $F_m$  agree excellently with the waterbag simulations for  $m=2$ , but are about 30% lower for  $m=3, 4$ .

For Landau damping, an overlap in a region with  $\partial f_0 / \partial k_{xy} < 0$  is a necessity, which enables energy transfer from the coherent mode to the incoherent spectrum. For the waterbag beam none of the parametric modes  $m=2, 3, 4$  satisfies this condition. For the Gaussian the  $m=3, 4$  modes

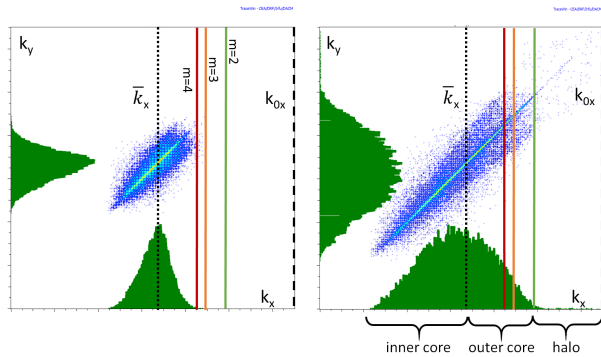


Figure 3: Spectral distributions  $f_0(k_{xy})$  (as unnormalized intensity (per bin of  $k_{xy}$ ) for 2D waterbag (l.h.s.) and Gaussian (r.h.s.) distributions generated for a fixed  $k_{0xy}$ . Also shown are locations of  $\bar{k}_x$  and of the  $m=2, 3, 4$  coherent mode lines (i.e. mode frequencies divided by  $m$ ).

well satisfy it, which explains their suppression in Fig 2. The  $m=2$  envelope instability overlaps only marginally – consistent with its instability. It can be assumed that the trend of decreasing  $F_m$  for higher  $m$  continues beyond  $m=4$ , which is supported by analytical expressions for 1D sheet beams in Ref. [26], and Landau damping should equally be expected.

### Incoherent Core Resonances

It is helpful to divide the spectra in Fig. 3 into three spectral tune regions: an *inner core* with  $\partial f_0 / \partial k_{xy} \geq 0$ ; it transitions to an *outer core* with  $\partial f_0 / \partial k_{xy} < 0$  at  $\bar{k}_{xy}$ ; and a *halo region*, where  $f_0(k_{xy}) = 0$ . For the resonance response it is essential in which tune region the resonance condition (here  $90^\circ$ ) falls. Applied to Fig. 1: for  $k_{0xy}$  from  $90 \dots 95^\circ$  this occurs in the halo region; from  $95 \dots 102^\circ$  in the outer core; and from  $102 \dots 114^\circ$  in the inner core region.

The main characteristic of the Eq. (2) incoherent resonances is their local excitation in the tune spectrum. Their existence even in the beam core is verified in Fig. 4 for a Gaussian distributions and two different working points  $k_{0xy}$ . For  $k_{0xy} = 102^\circ$  the  $4k_x = 360^\circ$  resonance condition (see

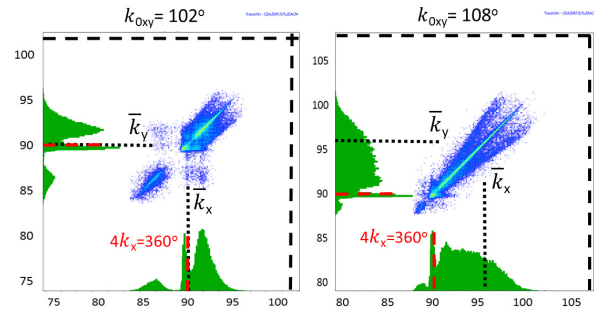


Figure 4: Spectral tune distributions for 2D Gaussian distributions with incoherent 4<sup>th</sup> order resonances in the beam core.

also insert cell 11 in Fig. 1) coincides with  $\bar{k}_{xy}$  – the transition from outer to inner core. The gap opening up in the tune spectrum below  $90^\circ$  indicates a drift of particles towards and across the resonance, which progresses self-consistently due to the resulting density dilution in the inner core. We find an overall minor rms emittance growth of about only 10% over 3000 cells.

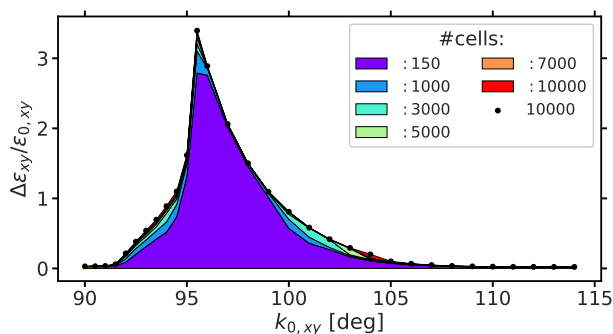
In the inner core region illustrated by the  $k_{0xy} = 108^\circ$  case in Fig. 4 the situation differs. We find again a clear resonance imprint on the tune spectrum, but only negligible rms emittance growth.

### LONG-TERM 2D AND 3D SIMULATION

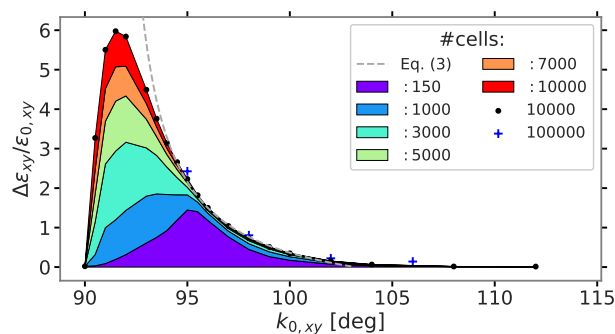
The 2D results shown in Figs. 1 and 2 suggest that parametric resonance only matters for the  $m=2$  mode, e.g. envelope instability in Eq. (3). This resonance occurs in the  $90^\circ$  stopband, which is the reason for focusing on this particular stopband in the following.

The code basis of SixTrackLib [31] and PyHEADTAIL [32] is used to simulate the long-term behaviour with full 3D PIC [33], which also allows 2D simulations for comparison.

This is a preprint — the final version is published with Phys. Rev. Accel. Beams at doi:10.1103/PhysRevAccelBeams.24.024201



(a) Self-consistent 2D PIC simulation.



(b) Self-consistent 3D PIC simulation.

Figure 5: Long-term PIC simulations. Rms emittance growth versus  $k_{0,xy}$  for different total numbers of FODO cells.

The same tools are also used for the FSM calculations in Section . By employing GPU hardware for high-performance computation, a high resolution of 4 million macro-particles were tracked in only a few hours on a 3D grid of transversely  $256 \times 256$  and longitudinally 64 cells, limiting grid heating effects to below permille level over the simulations. In order to focus on transverse space charge effects in a 3D bunch including realistic synchrotron motion time scales, parameters are chosen such that longitudinal space charge is reduced to a negligible level. The bunch length is kept small compared to the RF period such as to remain in the linear synchrotron motion regime.

## 2D Simulation Results

Figure 5a shows the rms emittance evolution for working points above the  $90^\circ$  resonance, with shaded areas relating to the rms emittance value after the indicated number of FODO cells. The purple area corresponds to the early short-term behaviour, which reproduces the same features as observed in TRACEWIN (cf. the green curve in Fig. 1): a peak around  $96^\circ$  is shaped by the coherent response of the space charge shifted envelope instability, with shoulders of incoherent resonance response on both sides.

The following evolution of the rms emittance until 10000 FODO cells reveals limited additional growth for the 2D problem. In particular, the tune region directly above  $90^\circ$  remains at weak emittance growth, where only the halo particles – limited by the truncation of Gaussian tails – are affected by the incoherent resonance. No particles are fed into the resonance once the halo region is depleted. We note that the long-term 2D behaviour of coasting beams is thus mainly characterized by the absence of synchrotron oscillations, which will be contrasted by the next section on 3D dynamics.

## 3D Simulation Results

In elongated 3D bunched beams the additional synchrotron oscillation effect is significant [34, 35]. It leads to a periodical crossing of resonance islands through the orbits, and trapping of particles occurs, if the motion of the island is slow with regard to the period of revolution around the fixed point. As shown in Ref. [35] this is more likely to occur for

smaller synchrotron amplitudes, whereas large amplitudes may result in a sequence of small jumps of the single-particle emittance (“scattering”). The relative importance of trapping or scattering depends on the strength of the resonance and the synchrotron period.

Note that in this Section we assume 3D uncorrelated Gaussian distributions and use the same lattice and other parameters as in 2D simulations. Figure 5b shows the rms emittance evolution at the slowest synchrotron oscillation in our study – a ratio of 1:300 for betatron to synchrotron period. The same contour levels of rms emittance evolution are plotted like in Fig. 5a. As opposed to the latter 2D case, where only effects related to short-term dynamics are observed (the upper edge of the violet 150-cells region almost coincides with the black dotted 10000-cells contour), the 3D case reveals significant long-term dynamics.

In the halo region  $90 \dots 95^\circ$ , the emittance growth due to the fourth-order incoherent resonance is much enhanced due to the synchrotron oscillation. We argue that due to the relatively strong space charge resonance the synchrotron period chosen in our simulation is already slow enough to have a dominant part of particles in the trapping regime. This is supported by the observation that a single synchrotron period (1200 cells) already shows a substantial increase of the rms emittance in Figure 5b. A strong growth is visible already after 150 FODO cells (1/8th synchrotron period). This effect significantly continues with the number of FODO cells, while the peak of the emittance growth curve shifts more and more down towards  $k_{0,xy} = 90^\circ$ .

The transition from halo to the outer core lies in the region around  $90^\circ + \Delta\bar{k}_{xy}/2 \approx 96^\circ$ , where the peak of the envelope instability is encountered in the early evolution (cf. violet area). Eminent coherent motion in phase space as well as in the coherent spectrum is identified, which vanishes after a few 100 turns. At the same time, in all of the outer core (similar to the halo) particles at large transverse amplitudes are found to be driven into a four-fold symmetric island structure: an imprint of the incoherent  $m=4$  resonance in accordance with 2D in 4. In contrast to the halo region, rms emittance growth effectively stops after about 150 turns and the dynamics is largely independent of the synchrotron motion time scale.

The inner core region beyond the point  $k_{0xy} = 102^\circ$  in Fig. 5b, where  $\bar{k}_{xy}$  crosses the  $90^\circ$  resonance from below, is characterised by negligibly small emittance growth. We noted this important result already in the 2D treatment: although tunes are observed to accumulate around the resonance at  $90^\circ$  in the self-consistent simulations, there is little to no net effect on rms emittance growth.

To confirm the long-term behaviour in the outer and inner core region, selected simulation cases have been run for an order of magnitude longer: the blue crosses in Fig. 5b mark the rms emittance growth values after 100000 FODO cells. Apart from a slightly increased rms emittance owing to the inherent noise effects of the PIC method such as grid heating, the blue crosses indeed match the black dots (marking the evolution after 10000 FODO cells). Therefore there is no evidence of additional significant resonance dynamics impacting the *rms emittance* beyond what is described above: the rms emittance growth has well saturated within 10000 turns in both outer and inner core  $k_{0xy}$  regions.

The continuous emittance growth near the resonance  $k_{0xy} = 90^\circ$ , on the other hand, would translate to losing the resonating particles in the halo region in the aperture of a real machine. Exact emittance growth figures beyond the structural behaviour described in the 10000 turns here are thus of less interest.

### 3D Asymptotic Emittance Growth

We use these observations to postulate an approximate long-term asymptote for the emittance evolution in the halo and outer core regions. It is based on the fact that the tune spread of a space charge dominated beam is inversely proportional to its rms emittance. Hence a comparison between the initial and expected final tune spread allows an estimate of the rms emittance growth factor. The final tune spread results from a geometrical argument: for  $\bar{k}_{xy} < 90^\circ$  the self-consistent, progressive drift of particle tunes across  $k_{res} = 90^\circ$  results in a final ‘‘compression’’ of tune space to the available width above resonance,  $k_{0xy} - k_{res}$ . The corresponding initial spread is  $k_{0xy} - \bar{k}$ , which allows to describe the relative growth by the asymptotic formula

$$\left(\frac{\Delta\epsilon}{\epsilon}\right)_{final} \approx \frac{k_{res} - \bar{k}_{xy}}{k_{0xy} - k_{res}} = \frac{\Delta\bar{k}_{xy}}{k_{0xy} - k_{res}} - 1. \quad (4)$$

It is applicable as long as  $k_{res} > \bar{k}_{xy}$ , or  $k_{0xy} < k_{res} + \Delta\bar{k}_{xy}$ ; and no growth in the inner core region with  $k_{res} < \bar{k}_{xy}$  consistent with Section .

A finite stop-band width would shift the effective  $k_{res}$  to slightly above  $90^\circ$ . This margin can be used for an optimum fit to the 10000 cells simulation data of Fig. 5b in the range  $k_{0xy} \geq 95^\circ$ , where saturation is approximately reached. With an effective  $k_{res} = 91.2^\circ$  the resulting hyperbolic asymptote is represented by the dashed gray line in Fig. 5b with a remarkably good match.

Note that the absence of further parameters in Eq. (4) suggests a general applicability to long-term resonance behavior dominated by large space charge tune spreads, also

extending to externally driven resonances and beyond the  $90^\circ$  stopband, which warrants further study. Obviously, in a realistic machine the mechanical aperture would turn the continuous emittance growth for  $k_{0xy} \rightarrow 90^\circ$  into finite beam loss.

A striking insight from the present long-term study is the observed absence of eminent isolated emittance growth peaks relating to coherent resonance conditions, in particular for time scales as relevant for synchrotrons (i.e. beyond 1000 FODO cells).

### Halo vs. Core Dynamics

The difference between the slow incoherent regime in the halo  $k_{0xy}$  region and the fast coherent regime in the outer core  $k_{0xy}$  region can be illustrated using incoherent tune footprints. They are acquired via harmonic analysis over 512 FODO cells.

Figure 6a shows the halo case for  $k_{0xy} = 92^\circ$ : the final tune footprint at 10000 FODO cells is plotted in black. The corresponding black histogram projections indicate that half of the particles have accumulated above the  $k_{res} = 90^\circ$  condition. The incoherent resonance causes a slow drift of particles across the resonant tune and the overall tune spread shrinks. The slow pace becomes apparent when comparing to earlier times in the simulation: the violet histogram corresponds to the situation after 150 FODO cells (like in Fig. 5b) and shows more than 85% of the particles situated below  $90^\circ$ . Some particles are resonating at  $90^\circ$  indicated by the growing peak there. The turquoise histogram corresponds to 3000 FODO cells where a third of the particles have moved above  $90^\circ$ .

Figure 6b depicts the outer core case at  $k_{0xy} = 96^\circ$ . The black tune footprint at 10000 FODO cells indicates that most particles have been reallocated to above the resonance, a mere 6% are left below. In contrast to the previous halo scenario, the now present envelope instability has carried more than 80% of the particles to above the resonance already around 150 FODO cells, as can be seen in the violet histogram. This behaviour is illustrated in the simulation animation published as Ref. [36]. The coherent resonance mechanism does not distinguish transverse amplitudes, particles participate in the pumped mode across all transverse single-particle emittances simultaneously. Correspondingly, both the rms emittance and the individual particle emittances grow at the same time. After the parametric resonance has faded, the remaining particles at the lower end of the tune footprint (at small betatron amplitudes in the centre of the bunch) are slowly transported above  $90^\circ$  via the incoherent resonance mechanism.

The two simulation cases in the incoherent halo region as well as the outer core region with both coherent and incoherent resonance dynamics agree on the asymptotic state: the tune spread shrinks – either at slow or fast pace, respectively – until its lower end is located above the  $k_{res} = 90^\circ$  condition. This observation illustrates the asymptotic behaviour discussed in the previous section.

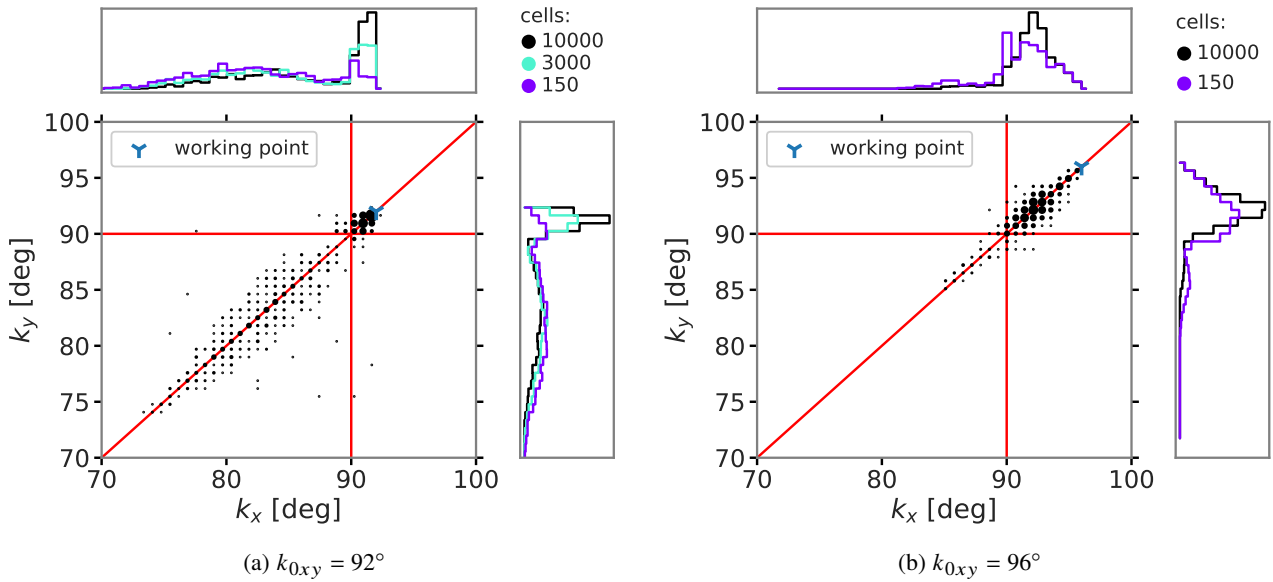


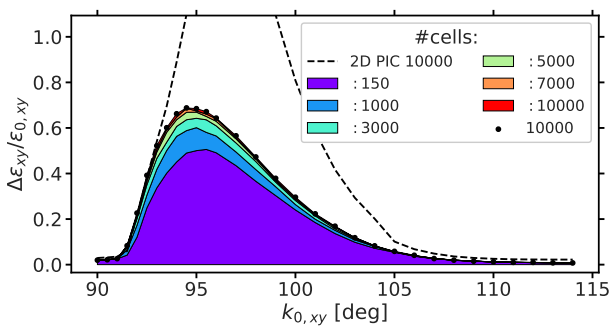
Figure 6: Tune footprints in halo and outer core region for 3D PIC simulation.

### FROZEN SPACE CHARGE SIMULATION

In the last part we compare the previous self-consistent PIC computations to FSM, where the initial Gaussian beam space charge force is kept unchanged and macro-particles are merely treated as test particles not contributing to the space charge force dynamically, for otherwise identical parameters as for PIC in Section . The FSM by definition generates only incoherent response in all regions without self-consistent feedback. It thus allows to single out incoherent effects, where the full PIC simulation includes coherent effects as well as the self-consistent change of the distribution.

#### 2D FSM

Figure 7a presents FSM results for coasting beam conditions. The black dots indicate the emittance growth from the frozen fieldmap treatment in FSM after 10000 FODO cells, which is saturated as there is almost no further emittance growth observed across the final 3000 cells. This result is to be compared with the 2D PIC simulations from Fig. 5a, where the final contour after 10000 FODO cells has been added here as a dashed line for reference.



(a) 2D FSM computation (2D PIC in dashed).

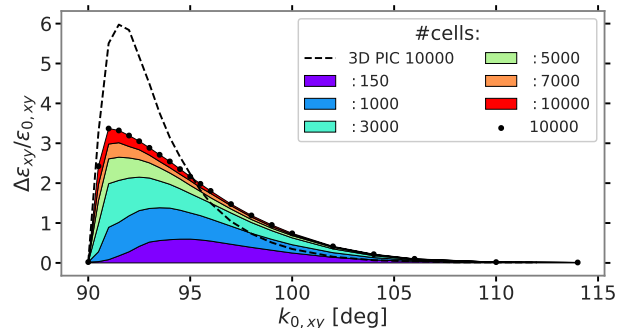
In contrast to the FSM simulation, the self-consistent PIC treatment delivers strongly enhanced emittance growth in a tune interval between  $94^\circ \leq k_{0xy} \leq 105^\circ$ , where the  $m=2$  envelope instability grows significantly. On the other hand, PIC and FSM predicted emittance growth matches very well on the left shoulder close to  $90^\circ$ , where the halo particles increase in amplitude only due to the incoherent fourth-order resonance driven by the octupole component of the space charge field from the resonance-free core.

#### 3D FSM

Figure 7b presents FSM results to be compared with the PIC simulations in Fig. 5b. The PIC simulated 10000 FODO cells curve is included in dashed for reference.

In the halo region, we find reduced rms emittance growth due to the missing self-consistent tune drift towards the resonance in FSM. Over still longer times the dominating periodic resonance crossing effect through synchrotron motion appears to provide FSM results closer to the PIC simulations.

In the outer core region, the absence of coherent effects in the FSM leads to initially slower developing rms emittance



(b) 3D FSM computation (3D PIC in dashed).

Figure 7: Long-term frozen simulations. Rms emittance growth versus  $k_{0xy}$  for different total numbers of FODO cells.

This is a preprint — the final version is published with Phys. Rev. Accel. Beams at doi:10.1103/PhysRevAccelBeams.24.024201

growth. Final saturation, instead, occurs at a non-negligibly higher level due to the non-self-consistent nature of the space charge force in FSM. For synchrotron design applications, we conclude that the FSM tends to underestimate the area of working points with low-level emittance growth compared to PIC.

## DISCUSSION

The results of long-term simulations presented here have a number of implications for the choice of working points and intensity limits. They also shed light on the confidence level of FSM simulations, which are often the dominant simulation tool for evaluating synchrotron beam dynamics experiments.

The findings of Sections and suggest as criterion for negligible rms emittance growth that it is sufficient to keep the rms-equivalent KV tune above the resonance condition – here  $90^\circ$  – instead of the more restrictive “conventional” single particle assumption requiring the complete tune footprint above the resonance. This can be applied, for example, to the SIS18 at GSI with 12 lattice periods and  $k_{0y}$  above  $90^\circ$ , hence  $Q_{0y}$  above 3. From the point of view of the here discussed space charge driven second and fourth order structure resonances, the choice of a vertical  $Q_{0y} = 3.25$  would still allow a maximum incoherent space charge tune spread of  $-0.5$  in the center of a Gaussian beam – twice as large as assumed by the single particle arguments. This would similarly apply to the PS Booster at CERN with its 16 lattice periods.

The 2D comparison between FSM and PIC space charge modelling in Section demonstrates that FSM underestimates emittance growth in the outer core region by a large factor, and by a smaller factor in the inner core region. The large factor is due to the existence of the envelope instability in the  $90^\circ$  stopband.

In 3D though, a long lasting emittance growth effect by this unstable mode is inhibited by synchrotron oscillation, which itself is also modelled by FSM as shown in Section . This qualifies the approximate 3D FSM treatment as a computationally effective tool for conservative identification of emittance conserving working points. On the one hand, the predicted finite emittance growth for resonance affected tune regions with FSM deviates quantitatively from PIC results: according to Fig. 7b FSM underestimates growth in the halo region, but overestimates it in the inner core region (at the very right) by more than a factor two. On the other hand, resonance-free tune regions computed via the fast FSM also remain resonance-free in the PIC case, which qualifies 3D FSM as conservative in all regions.

## CONCLUDING REMARKS

In summary, incoherent effects are found to play a major role in the long-term dynamics of bunches – not only in the beam halo but also in the beam core. Sufficient overlap with the incoherent spectrum in 2D is found to account for Landau damping of the  $m > 2$  parametric resonances. In 3D, synchrotron oscillation is expected to even further en-

hance Landau damping – in analogy to studies of head-tail modes [37–39]. On the other hand, very short synchrotron periods comparable with betatron periods – as typical for near-spherical linac bunches – suppress the resonant mechanism of Landau damping [24, 29].

In the *halo region*, in our example at tunes slightly above  $90^\circ$ , synchrotron motion strongly enhances rms emittance growth due to incoherent resonance. In the adjacent *outer core region*, we stress the importance of the encountered self-consistent interplay between coherent and incoherent effects. Incoherent resonances emerge with particle tunes accumulating at the incoherent resonance condition (in our example  $m=4$ ), and corresponding resonance islands form in phase space.

Our comparison between the 3D self-consistent and frozen treatments demonstrates that the early time evolution of rms emittance growth is largely determined by distribution change and coherent effects. Long-term saturation of rms emittance growth in 3D, however, is qualitatively determined by the compression of the entire incoherent tune footprint into the interval between bare tune and incoherent resonance condition as described by our asymptotic formula.

Thus, over times of long-term bunch storage, we find the overall rms emittance growth response curves in 3D to be smooth. Comparison of Fig. 5a with Fig. 5b confirms that even the strong envelope instability shows no coherent imprint after few thousand cells of 3D simulation (e.g. few synchrotron periods). This suggests that introducing parametric resonance lines to the synchrotron resonance charts introduced in Ref. [6] is relevant only for coasting beams in case of the  $m=2$  envelope instability; furthermore for  $m>2$  parametric resonances and such initial distributions, which are truncated to the extent that Landau damping does not work. Instead, we find the criterion that the  $k_{0xy}$  region with non-negligible emittance growth spans from the resonant  $90^\circ$  to  $90^\circ + \Delta k_{xy}$ , with final rms emittances determined by the tune footprint compression effect.

This study is expected to have an impact on future studies at various accelerators with the goal to extend and test the applicability of our conclusions to (a) higher-order resonances driven by space charge and (b) externally driven resonances in conjunction with space charge.

## REFERENCES

- [1] H. Bartosik, “Challenges in Understanding Space Charge Dynamics”, in *Proc. 61st ICFA Advanced Beam Dynamics Workshop on High-Intensity and High-Brightness Hadron Beams (HB’18)*, Daejeon, Korea, Jun. 2018, pp. 1–7. doi:10.18429/JACoW-HB2018-MOA1PL01
- [2] G. Franchetti *et al.*, “Experiment on space charge driven nonlinear resonance crossing in an ion synchrotron”, *Phys. Rev. ST Accel. Beams*, vol. 13, p. 114203, 2010. doi:10.1103/PhysRevSTAB.13.114203
- [3] G. Franchetti, S. Gilardoni, A. Huschauer, F. Schmidt, and R. Wasef, “Space charge effects on the third order coupled resonance”, *Phys. Rev. Accel. Beams*, vol. 20, p. 081006, 2017. doi:10.1103/PhysRevAccelBeams.20.081006

- [4] J. Qiang, R. D. Ryne, G. Franchetti, I. Hofmann, and E. Métral, “Numerical Simulation Study of the Montague Resonance at the CERN Proton Synchrotron”, in *Proc. 3rd Int. Particle Accelerator Conf. (IPAC’12)*, New Orleans, LA, USA, May 2012, paper WEP011, pp. 2958–2960.
- [5] A. Macridin, A. Burov, E. Stern, J. Amundson, and P. Spentzouris, “Parametric Landau damping of space charge modes”, *Phys. Rev. Accel. Beams*, vol. 21, p. 011004, 2018. doi:10.1103/PhysRevAccelBeams.21.011004
- [6] K. Kojima, H. Okamoto, and Y. Tokashiki, “Empirical condition of betatron resonances with space charge”, *Phys. Rev. Accel. Beams*, vol. 22, p. 074201, 2019. doi:10.1103/PhysRevAccelBeams.22.074201
- [7] I. Hofmann, “Comment on ‘Empirical condition of betatron resonances with space charge’”, *Phys. Rev. Accel. Beams*, vol. 23, p. 028001, 2020. doi:10.1103/PhysRevAccelBeams.23.028001
- [8] K. Kojima, H. Okamoto, and Y. Tokashiki, “Reply to ‘Comment on ‘Empirical condition of betatron resonances with space charge’””, *Phys. Rev. Accel. Beams*, vol. 23, p. 028002, 2020. doi:10.1103/PhysRevAccelBeams.23.028002
- [9] L. Smith, “Effect of gradient errors in the presence of space charge forces”, in *Proc. of the 4th Intern. Conf. on High-Energy Accelerators*, edited by A. A. Kolomenskij and A. B. Kuznetsov, Dubna, USSR, 1963, p. 1232.
- [10] F. J. Sacherer, Ph.D thesis, Lawrence Radiation Laboratory Report No. UCRL-18454, 1968.
- [11] S. Machida, “Space charge effects in low-energy proton synchrotrons”, *Nucl. Instrum. Methods Phys. Res., Sect. A*, vol. 309, pp. 43–59, 1991. doi:10.1016/0168-9002(91)90091-4
- [12] I. Hofmann, “Stability of anisotropic beams with space charge”, *Phys. Rev. E*, vol. 57, p. 4713, 1998. doi:10.1103/PhysRevE.57.4713
- [13] R. Baartman, “Betatron resonances with space charge”, *AIP Conf. Proc.*, vol. 448, p. 56, 1998. doi:10.1063/1.56781
- [14] T. Uesugi, S. Machida, and Y. Mori, “Experimental study of a half-integer resonance with space-charge effects in a synchrotron”, *Phys. Rev. ST Accel. Beams*, vol. 5, p. 044201, 2002. doi:10.1103/PhysRevSTAB.5.044201
- [15] S. Cousineau, J. Holmes, J. Galambos, A. Fedotov, J. Wei, and R. Macek, “Resonant beam behavior studies in the Proton Storage Ring”, *Phys. Rev. ST Accel. Beams*, vol. 6, p. 074202, 2003. doi:10.1103/PhysRevSTAB.6.074202
- [16] D. Jeon, L. Groening, and G. Franchetti, “Fourth order resonance of a high intensity linear accelerator”, *Phys. Rev. ST Accel. Beams*, vol. 12, p. 054204, 2009. doi:10.1103/PhysRevSTAB.12.054204
- [17] L. Groening *et al.*, “Experimental Evidence of the 90° Stop Band in the GSI UNILAC”, *Phys. Rev. Lett.*, vol. 102, p. 234801, 2009. doi:10.1103/PhysRevLett.102.234801
- [18] F. Asvesta, H. Bartosik, A. Huschauer, and Y. Papaphilippou, “Space Charge Driven Resonances in the CERN PS”, in *Proc. 10th Int. Particle Accelerator Conf. (IPAC’19)*, Melbourne, Australia, May 2019, pp. 3216–3219. doi:10.18429/JACoW-IPAC2019-WEPTS047
- [19] V. Kornilov, A. Oeftiger, O. Boine-Frankenheim, V. Chetvertkova, S. Sorge, and P. Spiller, “Beam quality and beam loss predictions with space charge for SIS100”, *Journ. of Instr.*, vol. 15, p. P07020, 2020. doi:10.1088/1748-0221/15/07/P07020
- [20] H. Bartosik, F. Asvesta, A. Huschauer, Y. Papaphilippou, and F. Schmidt, “Space charge induced losses in the CERN injector complex”, *Journ. of Instr.*, vol. 15, p. P07021, 2020. doi:10.1088/1748-0221/15/07/P07021
- [21] H. Hotchi *et al.*, “J-PARC 3-GeV RCS: 1-MW beam operation and beyond”, *Journ. of Instr.*, vol. 15, p. P07022, 2020. doi:10.1088/1748-0221/15/07/P07022
- [22] H. Okamoto, M. Aoki, C. Ichikawa, K. Kojima, T. Kurachi, and Y. Yamane, “Coherent and incoherent space-charge effects in high-intensity hadron rings”, *Journ. of Instr.*, vol. 15, p. P07017, 2020. doi:10.1088/1748-0221/15/07/P07017
- [23] I. Hofmann, *Space Charge Physics for Particle Accelerators*, New York, NY, USA: Springer, 2017, p. 49.
- [24] I. Hofmann and O. Boine-Frankenheim, “Parametric instabilities in 3D periodically focused beams with space charge”, *Phys. Rev. Accel. Beams*, vol. 20, p. 014202, 2017. doi:10.1103/PhysRevAccelBeams.20.014202
- [25] I. Hofmann, L.J. Laslett, L. Smith and I. Haber, “Stability of the Kapchinskij-Vladimirskij (K-V) distribution in long periodic transport systems”, *Part. Accel.*, vol. 13, p. 145, 1983. <http://cds.cern.ch/record/140869>
- [26] H. Okamoto and K. Yokoya, “Parametric resonances in intense one-dimensional beams propagating through a periodic focusing channel”, *Nucl. Instrum. Methods Phys. Res., Sect. A*, vol. 482, p. 51, 2002. doi:10.1016/S0168-9002(01)01684-9
- [27] M. Reiser, *Theory and Design of Charged Particle Beams*, Weinheim, Germany: WILEY-VCH Verlag, 2008, p. 149.
- [28] C. Li and R.A. Jameson, “Structure resonances due to space charge in periodic focusing channels”, *Phys. Rev. Accel. Beams*, vol. 21, p. 024204, 2018. doi:10.1103/PhysRevAccelBeams.21.024204
- [29] I. Hofmann and O. Boine-Frankenheim, “Space-charge structural instabilities and resonances in high-intensity beam”, *Phys. Rev. Lett.*, vol. 115, p. 204802, 2015. doi:10.1103/PhysRevLett.115.204802
- [30] D. Uriot and N. Pichoff, “Status of TraceWin Code”, in *Proc. 6th Int. Particle Accelerator Conf. (IPAC’15)*, Richmond, VA, USA, May 2015, pp. 92–94. doi:10.18429/JACoW-IPAC2015-MOPWA008
- [31] R. De Maria *et al.*, “SixTrack V and runtime environment”, *International Journal of Modern Physics A*, vol. 34, no. 36, p.1942035, 2019. doi:10.1142/S0217751X19420351
- [32] K. S. B. Li *et al.*, “Code Development for Collective Effects”, in *Proc. 57th ICFA Advanced Beam Dynamics Workshop on High-Intensity and High-Brightness Hadron Beams (HB’16)*, Malmö, Sweden, Jul. 2016, pp. 362–367. doi:10.18429/JACoW-HB2016-WEAM3X01
- [33] A. Oeftiger and S. Hegglin, “Space Charge Modules for PyHEADTAIL”, in *Proc. 57th ICFA Advanced Beam Dynamics Workshop on High-Intensity and High-Brightness Hadron Beams (HB’16)*, Malmö, Sweden, Jul. 2016, pp. 124–129. doi:10.18429/JACoW-HB2016-MOPR025

- [34] G. Franchetti and I. Hofmann, “Particle trapping by nonlinear resonances and space charge”, *Nucl. Instrum. Methods Phys. Res., Sect A*, vol. 561, p. 195, 2006. doi:10.1016/j.nima.2006.01.031
- [35] G. Franchetti and I. Hofmann, “Resonance trapping due to space charge and synchrotron motion, in theory, simulations, and experiments”, in *Proc. 39th ICFA Advanced Beam Dynamics Workshop on High-Intensity and High-Brightness Hadron Beams (HB’06)*, Tsukuba, Japan, May-Jun. 2006, paper WEAX01, pp. 167–171.
- [36] A. Oeftiger, “Animation of Space Charge Driven Parametric Resonance in 90 deg Stopband”. doi:10.6084/m9.figshare.13562423.v1
- [37] A. Burov, “Head-tail modes for strong space charge”, *Phys. Rev. ST Accel. Beams*, vol. 12, p. 044202, 2009. doi:10.1103/PhysRevSTAB.12.044202
- [38] V. Balbekov, “Transverse modes of a bunched beam with space charge dominated impedance”, *Phys. Rev. ST Accel. Beams*, vol. 12, p. 124402, 2009. doi:10.1103/PhysRevSTAB.12.124402
- [39] V. Kornilov and O. Boine-Frankenheim, “Head-tail instability and Landau damping in bunches with space charge”, *Phys. Rev. ST Accel. Beams*, vol. 13, p. 114201, 2010. doi:10.1103/PhysRevSTAB.13.114201

# IMPACT OF POWER SUPPLY RIPPLE ON THE BEAM PERFORMANCE OF THE LARGE HADRON COLLIDER AND THE HIGH-LUMINOSITY LHC \*

S. Kostoglou<sup>†</sup>, H. Bartosik, Y. Papaphilippou, G. Sterbini, CERN, Geneva, Switzerland

## Abstract

Harmonics of the mains frequency (50 Hz) have been systematically observed in the form of dipolar excitations in the transverse beam spectrum of the Large Hadron Collider (LHC) since the beginning of its operation. The power supply ripple, consisting of both fundamental and higher frequency components, is proven not to be the result of an artifact of the instrumentation systems with which they are observed. Potential sources of the perturbation have been identified through systematic analysis and experimental studies. Single-particle tracking simulations have been performed including a realistic power supply ripple spectrum, as acquired from experimental observations, to demonstrate the impact of such noise effects on beam performance.

## INTRODUCTION

Since the start of the Large Hadron Collider (LHC) operation, harmonics of the mains power frequency (50 Hz) in the form of dipolar excitations have been perturbing the transverse beam spectrum. Similar observations of power supply ripple, including high-order harmonics, have also been reported in the past by several other accelerators such as the Relativistic Heavy Ion Collider (RHIC) and the Tevatron [1–4]. The presence of such perturbation may degrade the accelerator’s performance by acting as an additional diffusion mechanism through the excitation of specific resonances. Together with the other resonances excited by the lattice non-linear fields and the beam-beam interactions, this effect can prove detrimental to the beam lifetime.

To this end, identifying the origin of the perturbation and applying mitigation measures is of paramount importance, especially for the High-Luminosity LHC (HL-LHC) era where a good understanding and control of all the beam degradation mechanisms is necessary, as unprecedented values of integrated luminosity are envisaged [5]. The present paper summarizes the main findings, which provide evidence that the 50 Hz harmonics correspond to real beam excitations rather than being an artifact of the instrumentation systems. It furthermore presents the dedicated experiments and measurements performed to identify their origin and illustrates the simulation analysis used to evaluate their impact on the beam lifetime. A thorough analysis of the 50 Hz harmonics in the LHC can be found in [6, 7].

\* Research supported by the HL-LHC project.

<sup>†</sup> sofia.kostoglou@cern.ch

## OBSERVATIONS FROM THE LHC

The presence of a series of 50 Hz harmonics in the beam signal has been confirmed with measurements with several independent instruments. One of these instruments is the transverse Observation Box (ADTObsBox) which provides bunch-by-bunch and turn-by-turn calibrated position measurements [8–10]. The high-sampling rate allows the spectrum to be computed in a broad high-frequency range. Thanks to the calibrated metric of the turn-by-turn data used to compute the spectrum, the amplitude of each harmonic can be extracted.

Figure 1 shows the beam spectrum for the horizontal plane of Beam 2 as computed with the data obtained from the ADTObsBox for a frequency range up to 10 kHz. Two regimes of interest are identified: a cluster of 50 Hz harmonics extending up to 3.6 kHz (blue), referred to as the *low-frequency cluster*, and another regime with spectral components around 7-8 kHz (yellow), namely the *high-frequency cluster*. Based on the fact that the LHC revolution frequency, hence the sampling frequency, is not an exact multiple of 50 Hz (11.245 kHz), it can be seen that both clusters consist of 50 Hz harmonics and not aliases that could arise from the sampling of the data. Higher amplitudes of the harmonics in the high-frequency cluster are observed. Similar observations have been collected for both beams and planes.

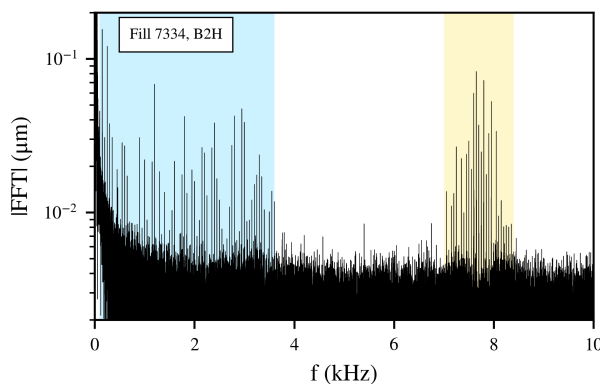


Figure 1: The horizontal spectrum of Beam 2 extending up to 10 kHz using the bunch-by-bunch and turn-by-turn data of the ADTObsBox. The low and high-frequency clusters, both consisting of 50 Hz harmonics, are illustrated with blue and yellow shaded areas, respectively.

Several observations confirm that the observed beam excitation is not an artifact of the instrumentation system. First, the harmonics are visible in several unrelated instruments and a comparison between the spectra before and after the

dump of the beam shows that they are visible only in the presence of the beam, which is a first indication that they do not emerge from instrumentation noise.

Secondly, modifications in the beam or machine configuration, such as changes in the betatron phase advance, tune and beam energy have a direct impact on the amplitude evolution of the harmonics on the beam. Specifically, Fig. 2 depicts the response of the  $h=12$  harmonic ( $\approx 600$  Hz) when the horizontal betatron phase advance between Interaction Point (IP) 1 and 5 is modified within a range of  $\pm 20$  degrees while maintaining a constant tune. The current of the quadrupole trimming the phase scan is shown (red) together with the amplitude evolution of the 600 Hz line (black). The clear correlation between the betatron phase and the amplitude of the harmonics confirms that this harmonic is not caused by an instrumental effect.

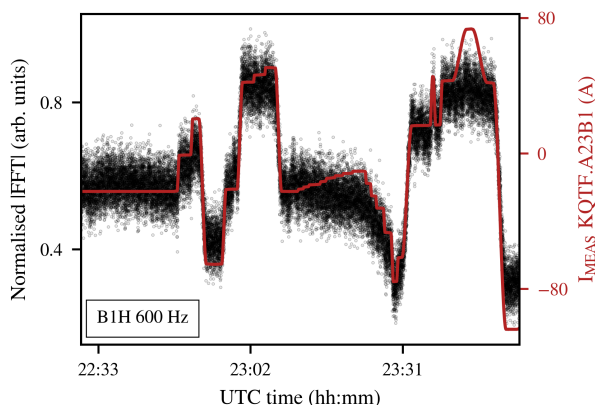


Figure 2: The amplitude evolution of the  $h=12$  harmonic observed on the beam spectrum (black) when changing the phase advance between IP1 and IP5, as indicated by the change of quadrupole current (red), while the tune is kept constant.

As a complement to the amplitude-based observations, the phases of the 50 Hz reveal additional information concerning their nature. Figure 3 presents the dephasing of a high-order harmonic ( $h=156$ ) as a function of the train number in the accelerator for two pickups, Q7 (blue) and Q9 (green). The two pickups are located at a relatively close distance with respect to each other so that no other noise perturbation is likely to be present in between them (e.g. no main dipole magnets). The phase difference between the signal of the two pickups ( $\Delta\phi=113.78$  degrees) is in agreement with the betatron phase advance for the collision optics ( $\Delta\mu=110$  degrees). Similar observations were collected for the majority of the 50 Hz harmonics. All the previous observations confirm that the 50 Hz harmonics are a feature seen by the beam and not an artifact of the instrumentation system.

The 50 Hz harmonics are visible in both beams, all beam modes and all fills. Changes in the betatron tune do not impact their frequency, which reveals the dipolar nature of the source, as the presence of quadrupolar field errors would lead to the appearance of sidebands around the tune. Further-

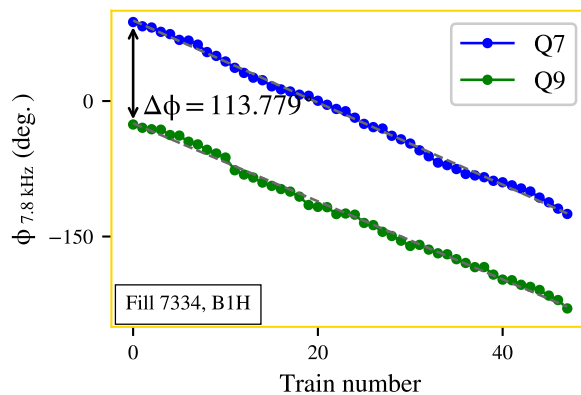


Figure 3: The dephasing of the  $h=156$  harmonic as a function of the train number, hence the bunch position in the beam, for two closely separated pickups Q7 (blue) and Q9 (green). The phase difference of the ripple between the two pickups ( $\Delta\phi=110$  degrees) matches the betatron phase advance.

more, Fig. 4 illustrates a comparison between the horizontal (magenta) and vertical (cyan) spectra of Beam 1 (left) and Beam 2 (right). A comparison of the amplitudes, normalized to the beam size, shows that the harmonics mainly impact the horizontal plane, an effect that is compatible with a dipole field error, while the attenuated perturbation in the vertical plane appears to be the result of transverse coupling. The maximum amplitude of the perturbation in the horizontal plane corresponds to  $10^{-3} \sigma$ . An asymmetry in the amplitudes of the 50 Hz between Beam 1 and 2 is systematically observed, with Beam 1 being more impacted by a factor of two.

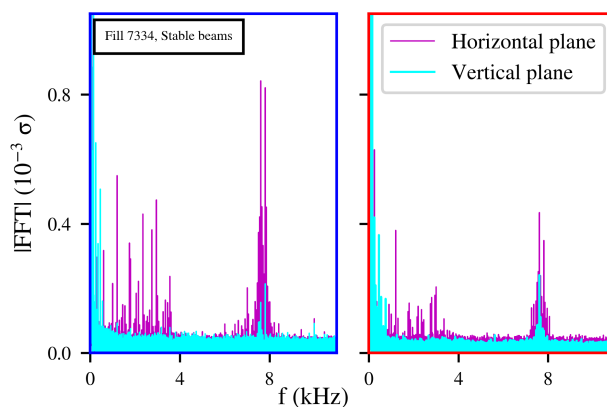


Figure 4: The spectrum in the horizontal (magenta) and vertical (cyan) plane at collisions for Beam 1 (left) and 2 (right), normalized to the beam size.

## DEDICATED EXPERIMENTS AND MEASUREMENTS

All the parasitic observations collected during the operation of the accelerator revealed the dipolar nature of the

Content from this work may be used under the terms of the CC BY 3.0 licence (© 2021). Any distribution of this work must maintain attribution to the author(s), title of the work, publisher, and DOI

source. To determine the exact origin of the perturbation, simple modifications to the configuration of the eight Silicon Controlled Rectifier (SCR) power supplies of the main LHC dipoles were applied. In particular, the active filters of the main dipole power supplies, responsible for the attenuation of the 50 Hz harmonics ripple, were enabled and disabled sector-by-sector during dedicated experiments [11–13]. At the same time, measurements of the beam’s spectrum were collected and analyzed.

Figure 5 presents the amplitude evolution of the  $h=12$  harmonic (top) in Beam 1 (blue) and 2 (red) when the active filters are switched on and off. The status of the active filters is also depicted (bottom) color-coded with the sector number. The abrupt changes in the amplitude of the 600 Hz line when the filter status is changed provides evidence that the eight power supplies of the main dipoles contribute to the perturbation and the ripple is, thus, propagating across the whole accelerator. This correlation is established for all the harmonics in the low-frequency range ( $<3.6$  kHz). However, no clear impact was observed in the harmonics of the high-frequency cluster during these tests. It must be noted that the active filters cover a lower range of harmonics and they do not act on the high-frequency part of the spectrum. In addition, although common power supplies are used for Beam 1 and 2, a different behavior is observed between the two beams when the status of the active filters is modified due to their different betatronic phase advance along the arcs with respect to the observation point.

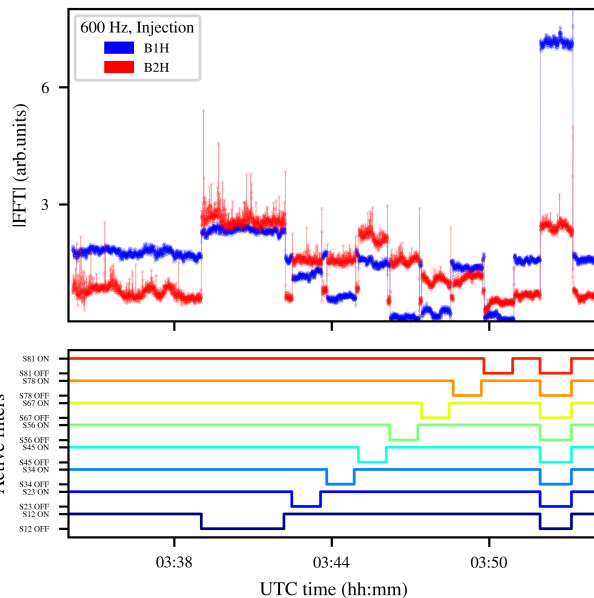


Figure 5: Amplitude evolution of 600 Hz line (top) in Beam 1 (blue) and 2 (red) during the experiments with the active filters of the main dipole power supplies. The status of the eight active filters, color-coded with the sector number, is also illustrated (bottom).

Concerning the high-frequency cluster, the exact origin has yet to be identified, although many similarities are observed with the low-frequency cluster. The importance of

identifying its origin lies in the fact that the high-frequency cluster components are expected to have a more important impact on the beam performance as indicated by the simulations reported in the next section. Possible ripple sources such as the Uninterruptible Power Supply (UPS) system are currently being investigated.

Preliminary measurements in a spare LHC UPS system were performed to identify whether the UPS output voltage spectrum is a possible source of the high-frequency cluster. Figure 6 presents the UPS output voltage spectrum in the normal mode of operation (blue), i.e. a configuration similar to the one used during operation with beam. The environmental and instrumentation noise was also measured (black). A zoomed view of the spectrum (light blue box) shows that the UPS voltage spectrum consists of several 50 Hz harmonics around the switching frequency of the inverter and its first harmonic (4 and 8 kHz, respectively). Therefore, the UPS spectrum contains 50 Hz harmonics in a regime that corresponds to the high-frequency cluster observed on the beam spectrum and further studies reveal that they depict a similar signature to the one observed on the beam. However, additional studies are necessary in the next LHC Run (from 2022) to determine whether there is a correlation between the UPS and the high-frequency cluster and to identify the exact coupling mechanism of the noise to the beam.

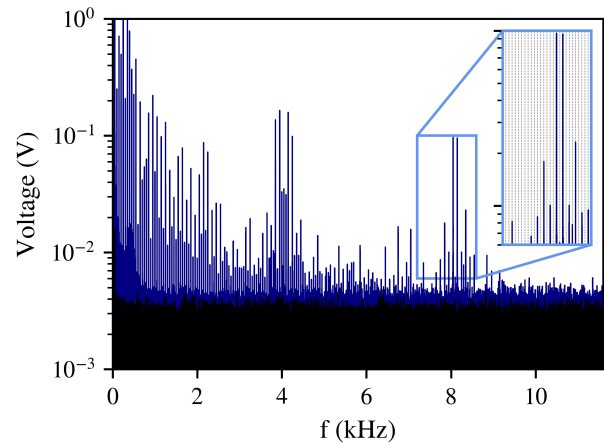


Figure 6: The UPS output voltage spectrum in normal operation (blue) and due to environmental noise (black). A zoomed window (light blue box) depicts the harmonics present in the UPS spectrum coinciding with multiples of 50 Hz (gray lines).

## IMPACT ON THE BEAM PERFORMANCE

Tracking simulations are performed to evaluate the impact of the 50 Hz harmonics in terms of tune diffusion and beam lifetime. Using the single-particle element-by-element tracking code SixTrack [14, 15], a distribution of particles is tracked in the LHC lattice including strong non-linearities, such as head-on and long-range beam-beam interactions. The simulated conditions correspond to the start of colli-

Table 1: The LHC parameters at Top Energy Used in the Tracking Simulation That Correspond to the Start of Collisions

Parameters (unit)	LHC (values)
Beam energy (TeV)	6.5
Bunch spacing (ns)	25
RMS bunch length (cm)	7.5
Bunch population (protons)	$1.25 \times 10^{11}$
Normalized emittance ( $\mu\text{m rad}$ )	2.0
Chromaticity	15
Octupole current (A)	550
IP1/5 Half crossing angle ( $\mu\text{rad}$ )	160
IP1/5 $\beta^*$ (cm)	30
Relative momentum deviation $\delta p/p$	$27 \times 10^{-5}$

sions. Table 1 presents a summary of the most important parameters.

A modulated dipole is used to simulate the power supply ripple spectrum including the 40 largest 50 Hz harmonics from both the low and high-frequency clusters. The applied kick at each frequency is selected such that the offsets observed experimentally in the transverse beam spectrum are reproduced in the simulations. Based on the observations of the previous section, the power supply ripple is distributed across the whole LHC ring. An accurate representation of the power supply ripple propagation across all the LHC dipoles requires a model of the transfer function for all the frequencies present in the spectrum. However, an accurate model of the LHC dipoles as a transmission line for such high frequencies is not available at the moment. Therefore, a simplified model is used where all the noise sources are lumped in a single location and the power supply ripple spectrum observed experimentally is reproduced.

Frequency Map Analysis (FMA) [16–19] is used to depict the increase of tune diffusion due to the power supply ripple. A distribution of particles is tracked for a specific number of turns ( $10^4$ ) and the turn-by-turn data are divided into two-time intervals. The tune of each particle is computed at each time interval and the variation of the tune between these two-time intervals defines the tune diffusion.

Figure 7 illustrates the frequency maps (left panel) and the initial configuration space (right panel) in the absence (top) and in the presence of the 50 Hz harmonics (bottom), color-coded with the logarithm of the tune diffusion. The resonances excited due to the non-linear fields such as beam-beam interactions and magnet non-linearities are depicted in gray. Including the dipolar perturbations, the strength of some of the resonances is enhanced, while additional resonances are excited in a location equal to the excitation frequency (green) or its alias (purple) in the horizontal plane. The increase of tune diffusion in the configuration space illustrates that both the core and the tails of the distribution are affected.

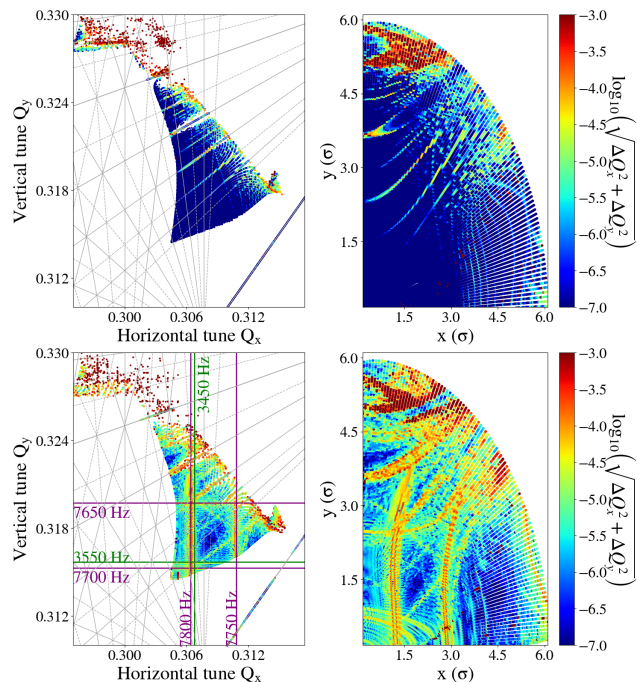


Figure 7: Frequency map (left panel) and initial configuration space (right panel) in the absence of power supply ripple (top) and including a realistic 50 Hz spectrum (bottom). The color-code illustrates the tune diffusion, the nominal resonances and the additional resonances excited due to power supply ripple are also presented (gray and purple/green, respectively).

To compute the degradation of the beam lifetime due to the power supply ripple, simulations with realistic beam distributions are performed. Experimental observations indicate that the tails of the LHC bunch profiles have overpopulated and underpopulated tails in the transverse and longitudinal plane, respectively, compared to a normal Gaussian distribution. For an accurate description of the simulated bunch profiles, a weight is assigned in the post-processing depending on the amplitude of each particle as derived by the Probability Density Function (PDF) of a q-Gaussian distribution with  $q=0.88$  and 1.15 for the longitudinal and transverse plane, respectively [20, 21].

Figure 8 presents the intensity evolution for a duration of  $10^6$  turns, corresponding to 90 seconds of LHC operation, in the absence of power supply ripple (black) compared to the cases when including the spectrum of Beam 1 (blue) and 2 (red). As the amplitudes of the 50 Hz harmonics observed in Beam 2 are lower by approximately a factor of two compared to Beam 1, an asymmetry between the lifetime of the two beams is observed. To quantify this effect, a fit of the intensity evolution in each case is applied. Starting from a beam lifetime of 28.4 h, the lifetime is reduced to 22.3 and 27.4 for Beam 1 and 2, respectively. Additional studies show that the main contributor to the reduction of the beam intensity is the high-frequency cluster. An asymmetry between the lifetime of the two beams has been observed

during the whole duration of Run2 and the simulations indicate that, amongst other mechanisms, the 50 Hz harmonics can contribute to this effect.

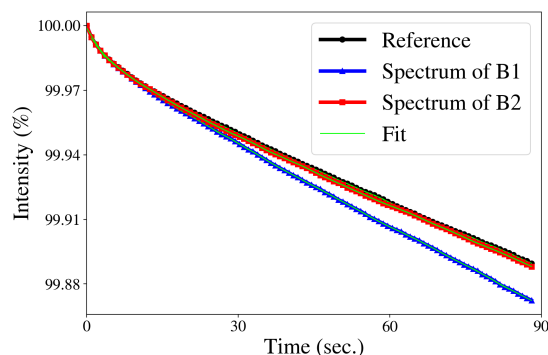


Figure 8: Intensity evolution in the absence of noise (black), including the power supply ripple spectrum observed in Beam 1 (blue) and 2 (red) and the fit used to compute the beam lifetime (green).

## SUMMARY

The present paper summarized the main findings concerning the 50 Hz harmonics that have been observed across several unrelated instruments in the transverse LHC beam spectrum since its commissioning. Two regimes of interest have been identified in frequency domain, namely the low-frequency cluster extending up to 3.6 kHz and the high-frequency cluster located around 7-8 kHz. Both regimes correspond to actual beam oscillations and the possibility of an instrumentation artifact has been excluded based on several beam observations. Both regimes consist of 50 Hz harmonics and not alias frequencies.

By changing the status of their active filters and observing the impact on the beam, it was shown that the eight SCR power supplies of the main dipoles are the origin of the low-frequency cluster. It is the first time that such a correlation has been demonstrated in the LHC. Concerning the high-frequency cluster, the exact underlying mechanism has not been clearly identified and other systems are currently being investigated such as the UPS and the transverse damper.

Single-particle tracking simulations including realistic power supply ripple spectra as acquired by experimental observations indicate that the presence of the harmonics results in increased tune diffusion and eventually to the degradation of the beam lifetime. It was found that the high-frequency cluster is the main contributor and that the asymmetry in the power supply ripple spectrum of Beam 1 and 2 can contribute to the lifetime asymmetry observed in operation. It must be noted that a simplified model was used where all the noise sources were lumped in a single location and further studies are needed for an accurate model of the ripple transfer function across the LHC ring.

Based on the observations collected in Run2, the 50 Hz harmonics are also expected to be present in the future operation of the accelerator. Additional studies and measurements

during the next operation of the accelerator will provide more insight into the present research and the possibility of identifying and applying mitigation measures for their suppression.

## REFERENCES

- [1] P. Cameron, M. Gasior, R. Jones, and C. Tan, “The effects and possible origins of mains ripple in the vicinity of the betatron spectrum”, Brookhaven National Lab.(BNL), Upton, NY (United States), Tech. Rep., 2005.
- [2] P. Cameron, M. Gasior, R. Jones, and C. Tang, “Observations of direct excitation of the betatron spectrum by mains harmonics in RHIC”, Brookhaven National Laboratory (BNL) Relativistic Heavy Ion Collider, Tech. Rep., 2006.
- [3] C.-Y. Tan, “Novel Tune Diagnostics for the Tevatron”, in *Proc. 21st Particle Accelerator Conf. (PAC’05)*, Knoxville, TN, USA, May 2005, paper TOAD002, pp. 140–144.
- [4] V. Shiltsev, G. Stancari, and A. Valishev, “Ambient betatron motion and its excitation by “ghost lines” in Tevatron,” *Journal of Instrumentation*, vol. 6, no. 08, p. P08002, 2011. doi:10.1088/1748-0221/6/08/p08002
- [5] G. Apollinari *et al.*, “High-Luminosity Large Hadron Collider (HL-LHC),” *CERN Yellow Rep. Monogr.*, vol. 4, pp. 1–516, 2017. doi:10.23731/CYRM-2017-004
- [6] S. Kostoglou, G. Arduini, Y. Papaphilippou, G. Sterbini, and L. Intelisano, “Origin of the 50 hz harmonics in the transverse beam spectrum of the large hadron collider,” *Phys. Rev. Accel. Beams*, vol. 24, p. 034001, 2021. doi:10.1103/PhysRevAccelBeams.24.034001
- [7] S. Kostoglou, G. Arduini, Y. Papaphilippou, G. Sterbini, and L. Intelisano, “Impact of the 50 hz harmonics on the beam evolution of the large hadron collider,” *Phys. Rev. Accel. Beams*, vol. 24, p. 034002, 2021. doi:10.1103/PhysRevAccelBeams.24.034002
- [8] L. R. Carver *et al.*, “Usage of the Transverse Damper Observation Box for High Sampling Rate Transverse Position Data in the LHC”, in *Proc. 8th Int. Particle Accelerator Conf. (IPAC’17)*, Copenhagen, Denmark, May 2017, pp. 389–392. doi:10.18429/JACoW-IPAC2017-MOPAB113
- [9] M. Ojeda Sandońs *et al.*, “Processing High-Bandwidth Bunch-by-Bunch Observation Data from the RF and Transverse Damper Systems of the LHC”, in *Proc. 15th Int. Conf. on Accelerator and Large Experimental*

- Physics Control Systems (ICALEPCS'15)*, Melbourne, Australia, Oct. 2015, pp. 841–844. doi:10.18429/JACoW-ICALEPCS2015-WEPGF062
- [10] M. Söderri, G. Kotzian, M. Ojeda Sandoń, and D. Valuch, “Online Bunch by Bunch Transverse Instability Detection in LHC”, in *Proc. 8th Int. Particle Accelerator Conf. (IPAC'17)*, Copenhagen, Denmark, May 2017, pp. 397–399. doi:10.18429/JACoW-IPAC2017-MOPAB117
- [11] A. Verweij *et al.*, “Performance of the Main Dipole Magnet Circuits of the LHC during Commissioning”, in *Proc. 11th European Particle Accelerator Conf. (EPAC'08)*, Genoa, Italy, Jun. 2008, paper WEPD029, pp. 2473–2475.
- [12] O. S. Brüning, P. Collier, P. Lebrun, S. Myers, R. Ostojic, J. Poole, and P. Proudlock, “Power converter system,” in *LHC Design Report*, ser. CERN Yellow Reports: Monographs, Geneva: CERN, 2004, pp. 275–307. <https://cds.cern.ch/record/782076>
- [13] J.-P. Burnet, “Test results of RPTE LHC thyristor rectifier with active filter,” 2019, unpublished.
- [14] SixTrack, <http://sixtrack.web.cern.ch/SixTrack/>, 2019, accessed: 2019-11-26.
- [15] R. De Maria *et al.*, “SixTrack Project: Status, Runtime Environment, and New Developments”, in *Proc. 13th International Computational Accelerator Physics Conference (ICAP'18)*, Key West, Florida, USA, Oct. 2018, pp. 172–178. doi:10.18429/JACoW-ICAP2018-TUPAF02
- [16] Y. Papaphilippou, “Detecting chaos in particle accelerators through the frequency map analysis method,” *Chaos: An Interdisciplinary Journal of Nonlinear Science*, vol. 24, no. 2, p. 024412, 2014. doi:10.1063/1.4884495
- [17] J. Laskar, “Introduction to frequency map analysis,” in *Hamiltonian systems with three or more degrees of freedom*, Springer, 1999, pp. 134–150.
- [18] J. Laskar, “Frequency map analysis and particle accelerators,” in *Proc. 20th Particle Accelerator Conf. (PAC'03)*, Portland, OR, USA, May 2003, paper WOAB001, pp. 378–382.
- [19] J. Laskar, “Application of frequency map analysis,” in *The Chaotic Universe: Proceedings of the Second ICRA Network Workshop*, Rome, Pescara, Italy, 1-5 February 1999, vol. 10, World Scientific, 2000, p. 115.
- [20] S. Papadopoulou, F. Antoniou, T. Argyropoulos, M. Fitterer, M. Hostettler, and Y. Papaphilippou, “Modelling and measurements of bunch profiles at the LHC,” *Journal of Physics: Conference Series*, vol. 874, p. 012008, 2017. doi:10.1088/1742-6596/874/1/012008
- [21] S. Papadopoulou, F. Antoniou, T. Argyropoulos, M. Hostettler, Y. Papaphilippou, and G. Trad, “Impact of non-gaussian beam profiles in the performance of hadron colliders,” 2018. arXiv:1806.07317[physics.acc-ph]

# OPERATIONAL EXPERIENCE WITH NANOCRYSTALLINE INJECTION FOILS AT SNS

N.J. Evans\*, Oak Ridge National Laboratory, Oak Ridge, USA

## Abstract

The Spallation Neutron Source (SNS) uses 300-400  $\mu\text{g}/\text{cm}^2$  nanocrystalline diamond foils grown in-house at the Center for Nanophase Materials Sciences to facilitate charge exchange injection (CEI) from the 1 GeV H- linac into the 248 m circumference accumulation ring. These foils have performed exceptionally well with lifetimes of thousands of MW-hrs. This contribution shares some experience with the operation of these foils during 1.4 MW operation, and discusses current operational concerns including injection related losses, foil conditioning, deformation, and sublimation due to high temperatures. The implications for the SNS Proton Power Upgrade are also discussed.

## INTRODUCTION

The Spallation Neutron Source is a 1.0 GeV short-pulse accelerator that operates at 60 Hz to produce an average power on target of 1.4 MW. Linac pulses are approximately 1 ms long, and are compressed by roughly a factor of 1000 in the accumulator ring. Injection into the ring is achieved via charge exchange injection using approximately 30x17mm, 300-400  $\mu\text{g}/\text{cm}^2$  thick nanocrystalline diamond foils grown on a Silicon substrate, a portion of which serves as a 'handle' for mounting. Figure 1 shows the various parts of the foil, including the conditioned corner on the bottom left. Foils are mounted at a 30° angle relative to injected and recirculating beams which increases the effective thickness determining stripping efficiency. The optimal foil thickness balances stripping efficiency, foil heating, beam scattering, and mechanical stability which can contribute to the stability of losses, and power to the injection dump. A foil changer mechanism, or 'chainsaw', allows the installation of up to 12 foils which are changed roughly once per year. In a typical year between 4 and 6 foils will be used and replaced, with one conditioned foil often left in to accommodate high-power target studies done immediately upon start up.

Early in the design of SNS the survivability of foils at the high average power of SNS operation was a major concern. Although there were problems with charge exchange injection at high power, the worst fears about foil failure have not been realized, and many issues discussed previously have been mitigated [1], [2]. After several years of routine operation at the SNS design power of 1.4 MW the foils have

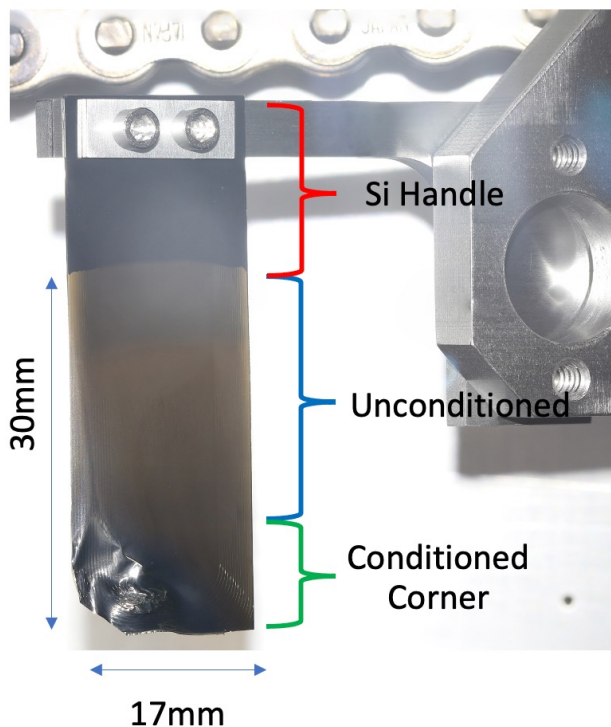


Figure 1: A used, mounted foil.

performed exceptionally well, with the best foils lasting an entire run cycle of 2500 MW-hrs or more.

The Proton Power Upgrade will increase the power capability of the SNS accelerator from 1.4 MW to 2.8 MW by increasing kinetic energy from 1.0 GeV to 1.3 GeV, and the charge per pulse from 24  $\mu\text{C}$  to 33  $\mu\text{C}$  by increasing the peak current in the linac. The 60 Hz repetition rate, and number of accumulated turns will remain the same. However, the actual power at which the accelerator will operate will be staged over several years as the First Target Station(FTS) will only be capable of handling 2.0 MW, with the remaining power eventually destined for the Second Target Station(STS). Key parameters affecting the foils are summarized in Table 1, where SNS refers to current operation, PPU/FTS the first stage of operation to the first target station after the completion of PPU, and STS the 2.8 MW era currently planned for the early 2030's. These upgrades have renewed interest in the limits of nanocrystalline foils for high power charge exchange injection.

Currently the primary challenges for operation are: beam loss, foil conditioning time, foil deformation, and foil sublimation. With the exception of foil sublimation, these are mainly an annoyance to operation, but do not represent single-point failures. Foil sublimation due to heating, how-

\* nhe@ornl.gov

\* ORNL is managed by UT-Battelle, LLC, under Contract No. DE-AC05-00OR22725 with the U.S. Department of Energy. The United States Government retains, and the publisher, by accepting the article for publication, acknowledges that the United States Government retains a nonexclusive, paid-up, irrevocable, world-wide license to publish or reproduce the published form of this manuscript, or allow others to do so, for United States Government purposes.

Table 1: Key SNS Upgrade Parameters

	SNS	PPU/FTS	STS
Charge( $\mu\text{C}$ )	24	25	33
Energy(GeV)	1.0	1.3	1.3
Power(MW)	1.4	2.0	2.8
Rep Rate(Hz)	60	60	60

ever, does represent a possible single-point failure for increased power. The following sections will describe these concerns and their effect on operations.

## BEAM LOSS

Beam loss induced activation is one of the primary concerns in high power accelerators, and the interaction of injected beam with stripping media represents an unavoidable source of beam loss. The ring injection region represents the highest loss, and residual activation by roughly an order of magnitude, and is the only section of the machine that does not meet the 1 W/m loss design specification. Even under ideal conditions, simulations show losses in this region to be on the order of a part in  $10^{-5}$ , about an order of magnitude above the 1 W/m limit.

Beam loss is grouped into two categories: first turn losses, and recirculating beam hits. Without considering exotic stripping methods (e.g. laser-assisted charge exchange injection) a certain fraction of first turn losses (due to coulomb, and nuclear scattering of the injected protons with the stripping medium) are intrinsic to the process of charge exchange injection and represent a lower limit on losses for a given stripping medium. In the current painting scheme each injected particle hits the foil between 4 and 5 times, based on realistic ORBIT simulations of the entire injection process. Recirculating beam hits can be minimized, but currently there is no scheme to maintain the required phase space distribution while eliminating recirculating hits entirely.

Losses and stripping efficiency, increase with foil thickness. However, Mike Plum noticed in 2015 [3] a distinct lack of correlation between foil thickness and losses. Archived data for operating powers above 1.35 MW over the last several years shown in Fig. 2 clearly demonstrates this. Of course, we are not suggesting that the foil thickness is not related to losses, this seems to be a consequence of operational procedure.

Operators are instructed to keep the current to the dump constant at 1 mA ( $\approx 60$  kW) despite the dump limit of 150 kW, partly out of concern for the longevity of the dump window. As foils become thicker stripping efficiency is increased and the beam is moved closer to the edge of the foil to maintain constant dump power, and the waste beam consists of a larger proportion of H- beam. Moving the beam toward the edge of the foil also reduces the number of recirculating beam hits. Our current hypothesis is that the reduction in losses from recirculating hits the increase in losses due to the thicker foil, but this has not been definitively established.

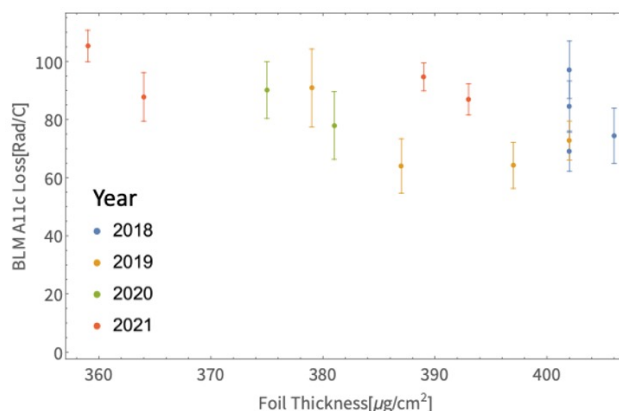


Figure 2: Beam loss at a representative loss monitor vs. foil thickness for operation above 1.35 MW.

## FOIL CONDITIONING

Nano-crystalline diamond foils used for CEI discolor, deform, and change composition when subjected to high temperatures. This process known as 'graphitization' was investigated by Barrowclough using an electron beam to heat foils to similar temperatures as those expected in the SNS [4]. The emissivity of the graphitized regions has been measured to be about 0.85 compared to 0.17 for unexposed foils. Because of the higher emissivity, more energy can be deposited in the foil while maintaining a favorable temperature. (Though there is no hard limit, for temperatures above 2000 K we expect foil lifetimes to decrease as described in the following section.)

Figure 3 illustrates the beam power ramp used during operation to graphitize the region of the foil that will be subjected to full power. This process is called 'conditioning'. A one hour rep-rate ramp up to 400 kW which allows the vacuum systems time to clear any products of outgassing from the foil, then a roughly 12 hour ramp up to 850 kW in steps of 40 kW/hr during which the foil is moved at each step to position the injected beam on one of the two  $45^\circ$  angles at the edge of the foil that sits in the beam, and finally a ramp up to 1.4 MW in steps of 20 kW/hr during which the foil is not moved.

This procedure was developed conservatively based on knowledge gleaned from the foil test stand, and has not been optimized. We know from test stand experiments that the actual process of graphitization is very quick once foils reach temperatures of  $\approx 1500$  K [4], but the variability of the beam position on the foil because of deformation, beam jitter, or operator tuning means large areas must be conditioned for use at high power. While tests using a conditioning ramp almost twice as fast have been successful, a new procedure has not been implemented for routine operation.

## FOIL DEFORMATION

During conditioning the density of the material changes causing deformation of foils. This deformation is unpredictable and can cause the foil to curl, pucker, tear or distort

Content from this work may be used under the terms of the CC BY 3.0 licence (© 2021). Any distribution of this work must maintain attribution to the author(s), title of the work, publisher, and DOI

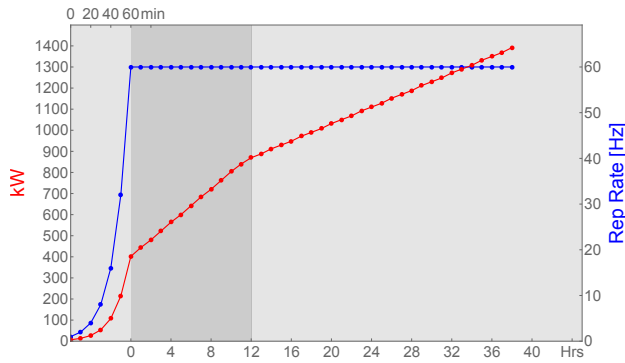


Figure 3: Current conditioning schedule.

in ways that adversely affect operation. Figure 4 shows a small area that has been graphitized using a 30 keV electron gun that simulates the heat load of the SNS ion beam on the foil test stand [5]. The graphitized region is at the center of the image with sub-mm puckering around the edge of the beam spot where the change in density distorts the foil. Larger scale deformation can also be seen as creases in the foil not subjected to beam, a new foil would be very flat by comparison.

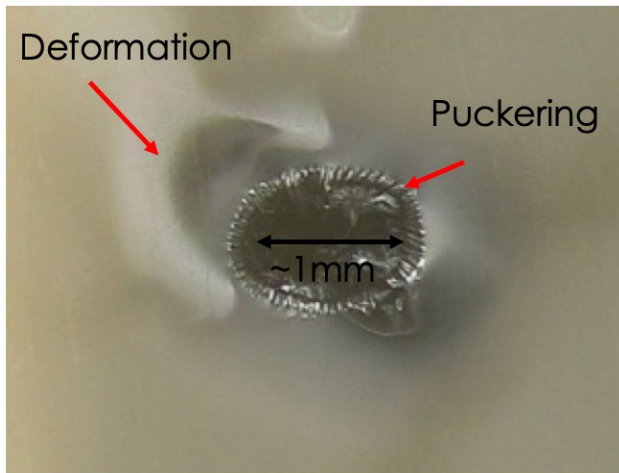


Figure 4: A small region graphitized on the foil test stand.

Figure 5 shows two foils after conditioning, and operation in the SNS. The foil on the right has significantly more distortion along the perimeter which can cause a change in the makeup of the waste beam, requiring operators to move the foil to maintain constant power. Additionally, the twisting and puckering which is particularly evident in the left foil can change the effective thickness of the foil which can also lead to changes in the stripping efficiency, losses, and heating.

The random nature of this deformation means a foil may be fully conditioned and still be unsuitable for operation. One solution to this problem may be to pre-condition foils using an electron beam similar to the one on the foil test stand mentioned above to better control the distortion, or just to reject poorly conditioned foils before they are used

for operation. Because conditioned foils are very fragile, this would likely have to be done in the tunnel with an in-situ electron gun, and would require a redesign of the foil changer.



Figure 5: Two foils after conditioning demonstrating the unpredictable deformation.

Foils can also experience tears, which tend to form at the interface of the Si handle and the free foil. Figure 6 shows the result of a massive tear in foil #3111 during operation that formed sometime between Feb. 7-8, 2020. An outline of the extent of the foil has been added to the image taken from the online video foil monitor on the top left. The beam spot can be seen as a bright circle in the lower left corner of the foil. On Feb 8<sup>th</sup>, 2020 operators noticed another bright feature, but no difference in performance. The foil was left in for another 10 days without incident. Only after post-mortem images were taken was the source of the bright spot appreciated. The tear that formed appears to have been contained by the fine-scale U-shaped corrugations, details of which are described elsewhere [6]. This foil was run for 2967 MW·hrs.

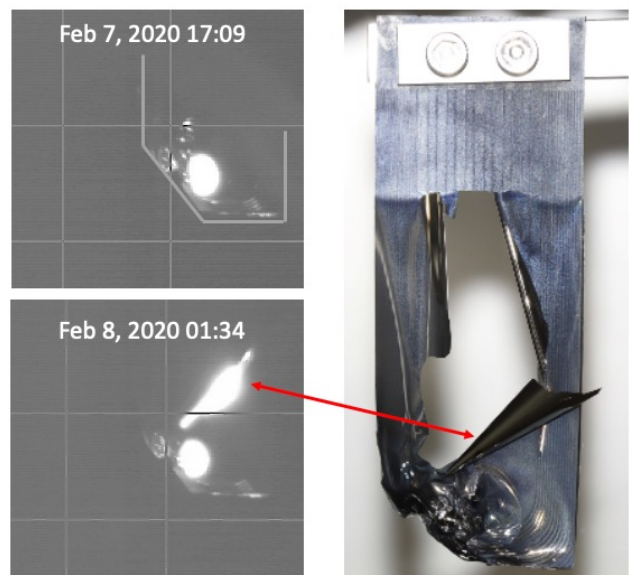


Figure 6: Foil exhibiting a large tear during operation. Foil outline has been added on top left image.

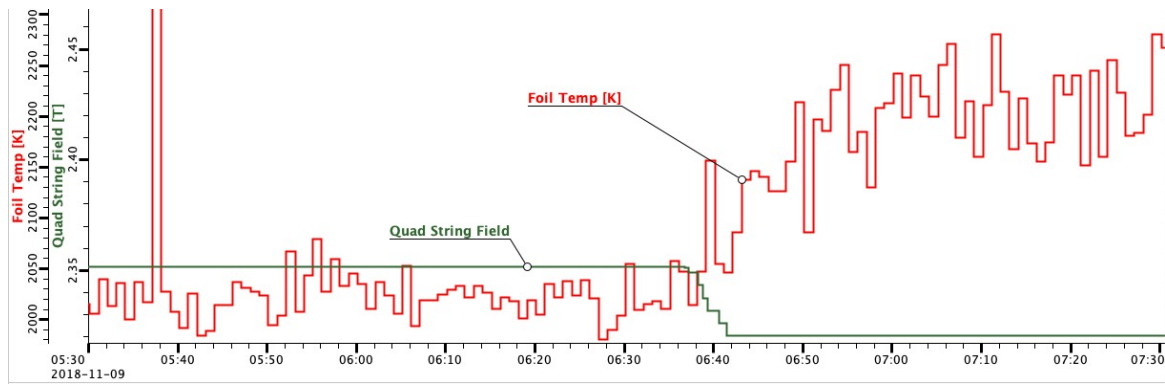


Figure 7: HEBT quad field and foil temperature during quad tuning.

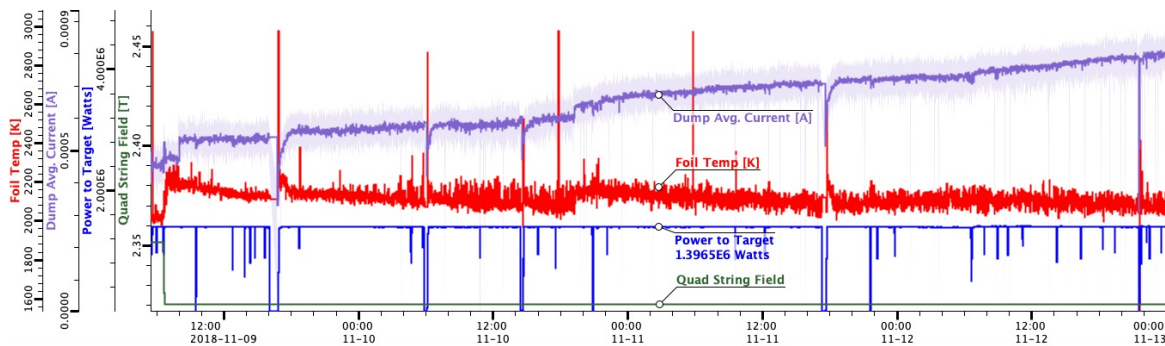


Figure 8: Injection dump current, foil temperature, power to target, and quad field immediately after tuning event in Fig. 7.

## FOIL SUBLIMATION

Of the concerns presented here, foil sublimation is potentially the most disruptive, representing the possibility of a single-point failure at high power. As mentioned in the previous sections, radiative cooling dominates and is proportional to the emissivity of the material, near 0.9 after foil conditioning. Even so, at high power the temperature of the foil can get very high, leading to sublimation of the foil. As the foil sublimates it thins and the stripping efficiency declines. This process can be fast enough that the foil is effectively destroyed as the beam burns a hole in the material. Approaching this limit of catastrophic failure, however, the sublimation rate can be much slower and still detrimental to operation. Once the stripping efficiency drops below 90% at 1.4 MW, or 95% at 2.8 MW the foil would need to be retired as the waste beam would necessarily exceed the 150 kW limit of the injection dump. If this situation were to occur with a frequency of 1 week, SNS would spend roughly 25% of its operational time conditioning new foils with the current conditioning ramp. (A key reason the foil conditioning time itself is under investigation, despite long foil lifetimes.)

A prototype foil pyrometer [7] provides a real-time measurement of the foil temperature, allowing us to correlate suspected thinning with temperature. Upgrades to this system are being implemented now that will make it easier to use as part of routine operation. Figure 7 shows data from operations as a quad string in the High Energy Beam Transport (HEBT) line just upstream of the foil is being tuned to

reduce losses, squeezing the beam on the foil and increasing the temperature by about 180 K to just over 2200 K. Figure 8 shows the foil temperature slowly decreasing and the dump current slowly increasing over the next several days with constant beam power to the target. While this is circumstantial evidence for foil thinning, the temperature range is consistent with slow sublimation, and this observation was accompanied by counter-intuitive behavior of the dump current in response to foil position adjustments consistent with thinning, e.g. moving the foil to position the injected spot closer to the edge of the foil decreased dump current.

## FOILS AND SNS UPGRADE PLANS

Noting that current operation sometimes puts foils near the failure point would seem to bode poorly for SNS upgrade plans, but there are several mitigating factors to consider.

First, the foils currently used in operation are thicker than is strictly required because the mechanical stability offered by thicker foils means less tuning of the foil position to maintain desirable dump power, and the lack of correlation between foil thickness and losses means there is no pressure to reduce foil thickness. In the future, the temperature of the foils will provide additional constraints.

Second, for the PPU-FTS case shown in Table 1, the beam current will not increase significantly, and while an  $\approx 8\%$  thicker foil would be required to maintain the same stripping efficiency at 1.3 GeV the foils we currently use are thick enough for operation at 1.3 GeV. In addition, the stopping

power in graphite decreases by about 5% for both protons and electrons [8], which means the energy deposition should decrease if the foil thickness is not changed.

Finally, the spot size on the foil is much smaller than the design - horizontal and vertical beta functions as small as 3.93 m, 2.97 m with emittances of 0.29 mm-mrad, 0.33 mm-mrad have been calculated at the foil using wire-scans upstream and loss-tuned production optics, compared to 10.44 m and 12.12 m, and 0.3 mm-mrad design values, giving a beam density about 3× design. No constraints are imposed on the beam size today. We plan to use feedback from the pyrometer as an additional constraint on optics tuning in the injection region once it is reliable enough for routine operation, and if necessary magnet interlocks to restrict changes to the beam size on the foil after machine set up prior to a run, similar to the protection of the mercury target.

In the STS era, beam current will increase by about 50%, which we believe can be easily compensated by increasing the beam size closer to design values once gains from reduced foil thickness have been exhausted. We are currently working to understand the tuning pressures that lead operators to reduce the beam size on the foil and address them through other means, such as beam collimation in the HEBT line.

Combining data from operations shown here, and foil test stand data in preparation for publication, we are confident that with design beam sizes at the foil, nanocrystalline foils should easily survive above 4-5 MW for a 1.3 GeV SNS. Higher powers may be possible.

## CONCLUSION

Experience over the last several years at the design energy of 1.4 MW has shown that the nanocrystalline diamond foils used for charge exchange injection at the SNS perform exceptionally well. Typical foil lifetimes are measured in thousands of MW·hrs. Still some problems cause operational headaches, notably beam losses related to interaction with the foils - for which a clear correlation with foil thickness is surprisingly absent, a disruptively long 'conditioning'

procedure that requires continuous operator intervention, and possible foil sublimation.

## ACKNOWLEDGEMENTS

I would like to thank all of my colleagues at the SNS, CNMS, and the University of Tennessee, Knoxville. I would especially like to thank Charles Peters for many helpful discussions about operating the SNS.

## REFERENCES

- [1] M. Plum, "H- Charge Exchange Injection Issues at High Power," in *Proc. HB'16*, Malmö, Sweden, July 2016, pp. 304–309. doi:10.18429/JACoW-HB2016-TUPM6X01
- [2] M. A. Plum, S. M. Cousineau, J. Galambos, S. H. Kim, P. Ladd, C. F. Luck, C. C. Peters, Y. Polsky, R. W. Shaw and R. J. Macek, *et al.* "Stripper foil failure modes and cures at the Oak Ridge Spallation Neutron Source," *Phys. Rev. ST Accel. Beams*, vol. 14, p. 030102, 2011. doi:10.1103/PhysRevSTAB.14.030102
- [3] M. Plum, Internal Presentation.
- [4] E. Barrowclough, "Analysis of Primary Stripper Foils at the Spallation Neutron Source by an Electron Beam Foil Test Stand", Ph.D. diss., University of Tennessee, 2017. [https://trace.tennessee.edu/utk\\_graddiss/4732](https://trace.tennessee.edu/utk_graddiss/4732)
- [5] R. Shaw, D. Bontrager, M. Plum, L. Wilson, C. Feigerle and C. Luck, "An Electron Beam SNS Foil Test Stand", in *Proc. 23rd Particle Accelerator Conf. (PAC'09)*, Vancouver, Canada, May 2009, paper TU6RFP042, pp. 1638–1640.
- [6] R. W. Shaw, V. A. Davis, R. N. Potter, L. L. Wilson, C. S. Feigerle, M. E. Peretich and C. J. Liaw, "Corrugated Thin Diamond Foils for SNS H- Injection Stripping", in *Proc. 21st Particle Accelerator Conf. (PAC'05)*, Knoxville, TN, USA, May 2005, paper RPPE030, pp. 2152–2154.
- [7] W. Blokland, N.J. Evans, C.F. Luck, and A. Rakhman, "Injection Foil Temperature Measurements at the SNS Accelerator", in *Proc. HB'18*, Daejeon, Korea, June 2018, pp. 104–109, doi:10.18429/JACoW-HB2018-TUP2WE01
- [8] ESTAR, PSTAR Databases, <https://physics.nist.gov/PhysRefData/Star/Text/intro.html>

# TEST OF MACHINE LEARNING AT THE CERN LINAC4

V. Kain\*, N. Bruchon, S. Hirlander, N. Madysa,  
 I. Vojskovic, P. Skowronski, CERN, Geneva, Switzerland  
 G. Valentino, University of Malta, Msida, Malta

## Abstract

The CERN H<sup>-</sup> linear accelerator, LINAC4, served as a test bed for advanced algorithms during the CERN Long Shutdown 2 in the years 2019/20. One of the main goals was to show that reinforcement learning with all its benefits can be used as a replacement for numerical optimization and as a complement to classical control in the accelerator control context. Many of the algorithms used were prepared beforehand at the electron line of the AWAKE facility to make the best use of the limited time available at LINAC4. An overview of the algorithms and concepts tested at LINAC4 and AWAKE will be given and the results discussed.

## INTRODUCTION AND MOTIVATION

The CERN accelerators generally use a modular control system to deal with the resulting complexity of hundreds or thousands of tuneable parameters. Low level hardware parameters are combined into higher level accelerator physics parameters defined by simulation results. For correction and tuning, low-level feedback systems are available, together with high-level physics algorithms to correct beam parameters based on observables from instrumentation. With this hierarchical approach large facilities like the LHC can be exploited efficiently.

There are still many processes at CERN's accelerators, however, that require additional control functionality. In the lower energy accelerators, models are often not available online or cannot be inverted to be used in algorithms. Sometimes instrumentation that could be used as input for model-based correction is simply lacking. Examples include optimisation of electron cooling without electron beam diagnostics, setting up of multi-turn injection in 6 phase-space dimensions and optimisation of longitudinal emittance blow-up with intensity effects. In recent years numerical optimisers, sometimes combined with machine learning techniques, have led to many improvements and successful implementations in some of these areas, from automated alignment of various devices with beam to optimising different parameters in FELs, see for example [1–6].

For a certain class of optimisation problems, the methods of Reinforcement Learning (RL) can bring further advantages. With RL the exploration time that numerical optimisers inevitably need at every deployment is reduced to a minimum - to one iteration in the best case. In 2019 most of the CERN accelerators were in shutdown to be upgraded as part of the LHC Injector Upgrade project [7]. The new linear accelerator LINAC4 and the proton-driven plasma wakefield test facility AWAKE [8] were, however, operated for part

of the year. Taking advantage of recent rapid developments in deep machine learning and RL algorithms, the authors successfully implemented sample-efficient model-free RL for CERN accelerator parameter control and demonstrated its use online for trajectory correction both at the AWAKE facility and at LINAC4. The results were published in [9]. In 2020, trajectory correction with model-based RL could be demonstrated in addition.

This paper is organized as follows. A brief introduction is given to Reinforcement Learning in the domain of accelerator control following [9]. In the experimental section, the problem statements and results of the tests on trajectory correction both for the AWAKE 18 MeV electron beamline and the 160 MeV LINAC4 are given. A short summary of the main outcome of [9] is followed by new results using model-based reinforcement learning. The next steps and potential for wider application are covered in the discussion and conclusion part.

## REINFORCEMENT LEARNING FOR ACCELERATOR CONTROL

The optimisation and control of particle accelerators is a sequential decision making problem, which can be solved using RL if meaningful state information is available. In the RL paradigm, Fig. 1, a software Agent interacts with an environment, acquiring the state and deciding actions to move from one state to another, in order to maximise a cumulative reward [10]. The Agent decides which action to take given the current state by following a policy. The goal is to learn the optimal policy for the problem.

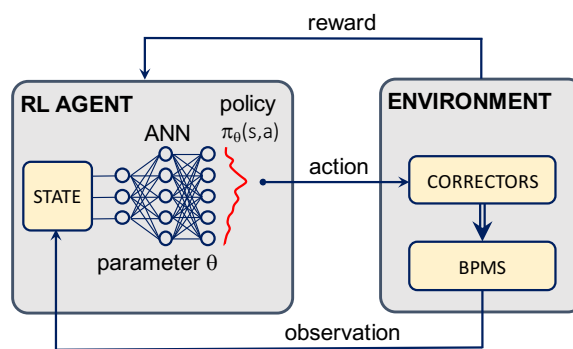


Figure 1: The RL paradigm as applied to particle accelerator control, showing the example of trajectory correction.

Reinforcement Learning algorithms can be divided into two main classes: model-free and model-based. Model-free control assumes no *a priori* model of the environment, learning the system dynamics implicitly from interacting with

\* verena.kain@cern.ch

the environment, and can be further sub-divided. Policy Optimisation methods consist of policy gradient or actor-critic methods which are more suitable for continuous action spaces. These methods attempt to learn the policy directly using gradient descent. Q-Learning methods seek to find the best action to take given the current state, i.e. the action that maximises the  $Q$ -function, and are specifically suitable for discrete action spaces.

The  $Q$ -function in RL is a measure of the overall expected (discounted) reward assuming the Agent in state  $s$  performs action  $a$  and then continues until the end of the episode following a stationary policy  $\pi$ .  $\pi(a|s)$  assigns a probability to action  $a$  for a given state  $s$ . The  $Q$ -function and its parametric approximation  $Q^\pi(s, a|\theta^Q)$  ( $\theta^Q$  are network parameters), are given as:

$$Q^\pi(s, a) = \mathbb{E} \left[ \sum_{i=0}^N \gamma^i r(s_i, a_i) \mid \pi, s_0 = s, a_0 = a \right], \quad (1)$$

$$Q^\pi(s, a) \approx Q^\pi(s, a|\theta^Q). \quad (2)$$

$N$  is the number of states from state  $s = s_i$  till the terminal state,  $\gamma \in [0, 1]$  is a discount factor and  $r(s, a) \in \mathbb{R}$  is the reward the agent receives after performing action  $a$  in state  $s$ .

Within the class of model-free algorithms, policy gradient algorithms are generally less sample-efficient than  $Q$ -learning ones and, as *on-policy* methods, cannot take advantage of experience replay [10].

For accelerator applications a continuous action space is usually required. This can be a serious limitation for  $Q$ -learning, due to the need to perform the non-trivial maximisation of the  $Q$ -function with respect to continuous  $a$ . It can however be overcome by assuming a specific algebraic form of the  $Q$ -function, such that  $Q(a, s)$  is straightforward to optimise with respect to the action. This approach is applied in the Normalised Advantage Function (NAF) algorithm [11].

In model-based methods, the control method uses a predictive model of the environment dynamics to guide the choice of next action. Establishing a reliable enough model is clearly critical to success. Several sub-divisions of this class of RL algorithms exist, including Analytic Gradient Computation methods such as LQR [12], Sampling-Based Planning [13] and Model-Based Data Generation methods such as Sutton's original Dyna [14] and related algorithms using Bayesian methods (e.g. model ensemble techniques) to capture the uncertainty of the model and avoid model bias. An overview of the various algorithms is provided in [15].

For most real-world applications, where the state-space is large, the  $Q$ -function or the policy need to be approximated using e.g. neural networks. Advances in the use of deep learning to train such models in the RL paradigm have led to a range of algorithms such as Deep Q-Network (DQN) [16], Deep Deterministic Policy Gradient (DDPG) [17] and Normalized Advantage Function (NAF) [11].

The results in this paper were obtained with the very sample-efficient NAF algorithm, iLQR as well as the DDPG

variant TD3 [18] as part of Dyna-style model-based Reinforcement Learning.

## Operational Deployment

The CERN accelerator control system offers a python package (pyjapc [19]) to communicate directly with the hardware systems or with the high-level control system for parameters like deflection angle or tune.

For the problem description (environment), the generic OpenAI Gym framework [20] was chosen, to enforce standardisation and allow easy switching between different control problems or Agents. The OpenAI Gym environment python class provides an interface between RL agent and optimisation problem and is used by many available RL algorithm implementations. Gym environments contain all the control problem specific code - the interaction with the machine or simulation for setting the action, reading or calculating observation data as well as calculating or measuring reward.

## RL AGENT FOR AWAKE TRAJECTORY CORRECTION

The first RL Agents were trained for trajectory correction on the AWAKE electron line with the goal that the trained Agents correct the line with a similar efficiency as the response matrix based SVD algorithm that is usually used in the control room, i.e. correction to a similar RMS as SVD within ideally 1 iteration.

The AWAKE electrons are generated in a 5 MV RF gun, accelerated to 18 MeV and then transported through a beam line of 12 m to the AWAKE plasma cell. A vertical step of 1 m and 60° bend bring the electron beam parallel to the proton beam shortly before the plasma cell. The trajectory is controlled with 11 horizontal and 11 vertical steering dipoles according to the measurements of 11 beam position monitors (BPMs). The BPM electronic read out is at 10 Hz and acquisition through the CERN middleware at 1 Hz.

The electron transfer line with all of its equipment is modelled in MAD-X [21]. The MAD-X model was used to prepare a simulated OpenAI Gym environment with the purpose to test various RL algorithms offline and define the hyper-parameters for the chosen algorithm for optimum sample efficiency.

## Experiment Results from AWAKE RL Tests

The first successful online training of a NAF Agent on trajectory steering in the horizontal plane was obtained on November 22, 2019. The training for 11 degrees of freedom (DOF) took roughly 30 minutes, corresponding to about 350 iterations. At each start of an episode the correctors were reset to the initial setting before the training. A random  $\Delta$  setting was then sampled from a Gaussian distribution with  $\sigma = 300 \mu\text{rad}$  for each corrector and added to the initial setting, leading to maximum 7 mm RMS (a factor 2-3 above the normal trajectory distortions caused by drifts and

different initial conditions). The maximum step a corrector could do per iteration was set  $\pm 300 \mu\text{rad}$ .

The objective of the training was twofold: to maximise the reward from each initial condition, and to maximise the reward in the shortest possible time. Figure 2 shows the evolution of the 200 episode online training. The upper plot gives the length of the episodes in number of iterations as training evolves, while the lower plot shows the initial reward (i.e. negative RMS) at the beginning of the episode (green line) as well as the final reward achieved (blue line) at the end of each episode. For a successful termination of the episode, the final reward had to be above the target (dashed red line).

At the beginning of the training, the Agent could not correct the line to an RMS below 2 mm, despite many iterations. Instead, the trajectory deteriorated further. After about 15 episodes it had learned to successfully correct the trajectory within 1-2 iterations to mostly even below 1 mm RMS starting from any initial condition.

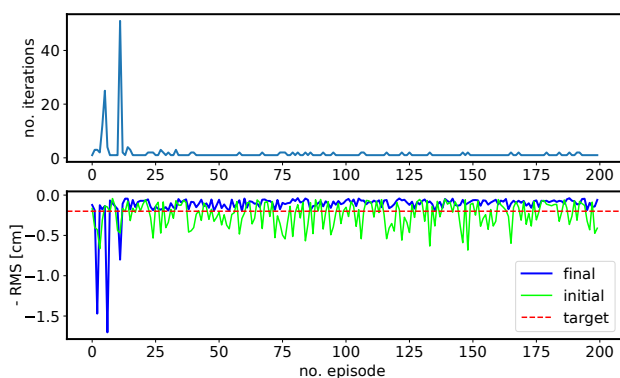


Figure 2: Online training of NAF Agent of AWAKE electron line trajectory steering in the horizontal plane. In the upper plot the number of iterations per episode is given. The lower plot shows the initial and final negative RMS value for each episode. The target negative RMS value is indicated in red.

## RL AGENT FOR LINAC4 TRAJECTORY CORRECTION

Training the AWAKE RL Agent for trajectory correction was a test case for algorithm development, since classical optics model-based steering algorithms are available for the AWAKE 18 MeV beamline. The CERN LINACs, on the other hand, did not have online models at the moment of the first RL experiments. RL and numerical optimisation could be obvious and inexpensive solutions to many typical LINAC tuning problems. The 160 MeV LINAC4 provides  $H^-$  to the upgraded CERN proton chain through charge exchange injection into the PS Booster [22]. LINAC4 had its final commissioning run at the end of 2019, where some time was also allocated to test various advanced algorithms for different control problems. Also, an RL Agent using the NAF algorithm was trained for trajectory steering in the LINAC exploiting the experience with AWAKE.

LINAC4 accelerates  $H^-$  from 3 MeV after source and RFQ to 160 MeV. The Medium Energy Beam Transport (MEBT) after the RFQ is followed by a conventional Drift Tube Linac (DTL) of about 20 m that accelerates the ions to 50 MeV, then to 100 MeV in 23 m by a Cell-coupled Drift Tube LINAC (CCDTL) and finally to 160 MeV by a  $\pi$ -mode structure (PIMS). The total length of the LINAC up to the start of the transfer line to the PSB is roughly 75 m. The pulse repetition rate is 0.83 Hz. The trajectory in the MEBT is fine tuned for optimising chopping efficiency and should not be modified during general trajectory optimisation. In addition there are no BPMs available in the MEBT as observable for an RL Agent.

The LINAC4 Gym environment comprised state information from 17 BPMs and actions possible on 16 correctors, through DTL, CCDTL, PIMS and start of the transfer line in the horizontal plane (the allocated accelerator development time was not sufficient to also train for the vertical plane). The LINAC4 trajectory steering OpenAI Gym environment had to respect the machine protection constraints and finalise episodes in case of violation, reset to safe settings as well as to deal with various hardware limitations (e.g. the power supplies of the steering dipoles cannot regulate for  $|I| < 0.1 \text{ A}$ ).

### Experimental Results from LINAC4 RL Tests

LINAC4 had 8 weeks of final commissioning run in 2019. On November 27, half a day was allocated to training and testing the NAF Agent. The training is shown in Fig. 3. The total number of episodes was set to 90 (taking in total about 300 iterations).

After about 25 episodes (or the equivalent of about 125 iterations), the Agent had learned to correct the trajectory to below 1 mm RMS within a maximum of 3 iterations each time.

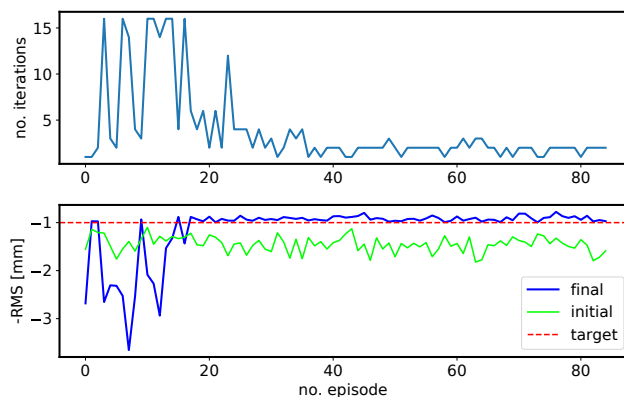


Figure 3: Online training of NAF Agent on LINAC4 trajectory steering in horizontal plane. The maximum allowable RMS was limited to 3 mm due to machine protection reasons. The target for the training was set to reach 1 mm RMS.

Content from this work may be used under the terms of the CC BY 3.0 licence (© 2021). Any distribution of this work must maintain attribution to the author(s), title of the work, publisher, and DOI

## MORE SAMPLE-EFFICIENCY WITH RL

Another important application of RL will result from training RL Agents on simulation and then exploiting the Agent with or without additional short training on the accelerator. The obvious advantage of this approach, if possible, is that in this case the algorithm does not have to be restricted to be a very sample-efficient one, as accelerator time for training is either zero or limited. To test this principle of offline training, another NAF Agent was trained - this time on the simulated AWAKE trajectory correction environment. This Agent was then used on the accelerator in operational configuration as trajectory correction algorithm. As expected, the results - maximum 2 iterations for correction to well below 2 mm RMS for each episode - were as good as with the online trained Agent. Figure 4 shows the results.

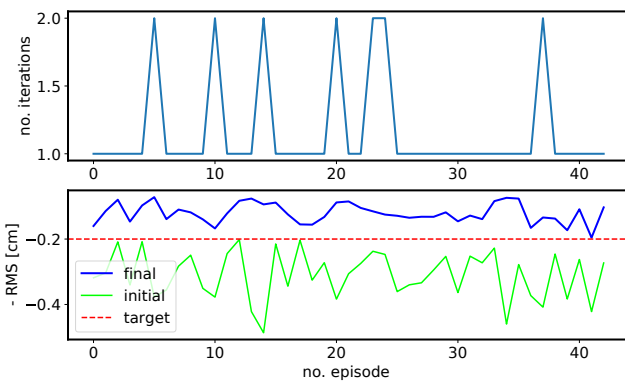


Figure 4: Validation on accelerator of Agent that was trained on simulation. The Agent corrects the trajectory to better than 2 mm RMS within 1-2 iterations.

## Experiments with Model-based Reinforcement Learning

Model-based RL is a promising alternative to overcome the sample efficiency limitation. Sutton's Dyna-style algorithm uses supervised learning for explicitly learning the dynamics model and then trains a model-free RL Agent (TD3 in our case) on the learned model instead of the real environment. Improving the model and agent training are interleaved until reaching a termination criterion. The Dyna algorithm deployed for AWAKE trajectory correction (see Algorithm 1) uses a simple fully connected artificial neural network  $s_{t+1} = f(s_t, a_t)$  for the dynamics model, avoiding the additional complexity with uncertainty-aware models as used in other model-based RL algorithms (e.g. [23]). This approach was sufficient due to the short horizon and the beforehand reduced stochasticity of the problem.

Algorithm 1 was used with the AWAKE trajectory steering online environment and led indeed to a significant reduction of required data samples to train the Agent. Figure 5 shows the number of data samples for 6 consecutive trainings. The median number of required data samples was  $N_{data} \approx 80$  compared to  $N_{data} \approx 300$  for the model-free case.

**Algorithm 1** The OpenAi Gym environment  $env_{model}$  contains the neural network for the data-driven dynamics model and the methods to train this model.  $N_{init}$  data samples are collected with random policy at the beginning. Agent training and dynamics model learning is repeated maximum  $N_{dyna}$  times. After each agent training, the agent is tested on the real environment according to some performance criterion. In case of successful test, the training is stopped.

```

env_model = env_model(env_real, s_0)
td3 = TD3(env_model)
fill initial buffer  $\mathcal{D}$  with  $N_{init}$  samples
env_model.train_model()
for  $N_{dyna}$  do
    td3.learn( $N_{td3}$ )
    test on env_real with td3.predict(s)
    add validation data to  $\mathcal{D}$ ;
    if test OK then
        break
    end if
    env_model.train_model()
end for
    
```

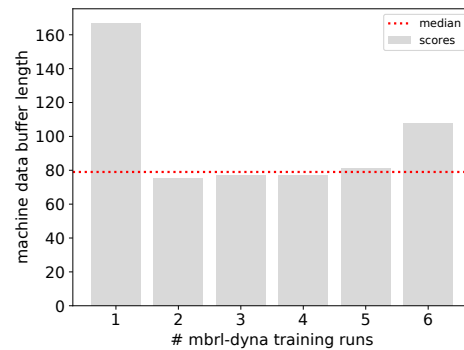


Figure 5: Required number of data samples before obtaining a sufficiently well trained agent using Dyna-style model-based RL following algorithm 1 on the online AWAKE trajectory correction environment.

Another approach of using explicit dynamics models involves model-predictive control algorithms. Instead of training a model-free Agent on the data-driven dynamics model and iterating between model learning and Agent training, the surrogate dynamics model could be used as input to a model-predictive control algorithm like iLQR [12]. The successful deployment of this approach is shown in Fig. 6.

## DISCUSSION AND CONCLUSION

The experience with the AWAKE and LINAC4 RL Agent deployment has proved that the question of sample efficiency for RL can be addressed for real accelerator control problems. The training with algorithms such as NAF, TD3 and in particular model-based RL is sample-efficient enough to allow for deployment in the control room. It still requires more iterations than a numerical optimisation algorithm,

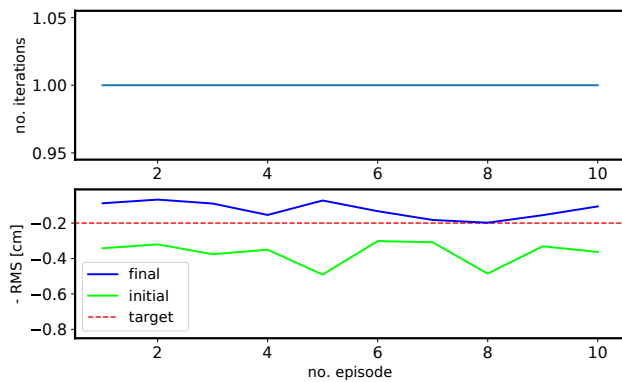


Figure 6: Running iLQR to correct the horizontal trajectory of the AWAKE electron line on a dynamics model trained with 200 data points for various initial trajectories. The problem is solved within 1 step each time.

but after training it out-performs numerical optimisers. The resulting product is a control algorithm like SVD, but in the case of RL without the requirement of a linear response.

The standardisation of the environment description using OpenAI Gym proved a big advantage, allowing rapid switching between simulated and online training, and between Agents.

In addition to studying new algorithms, infrastructure and frameworks will have to be deployed in the control system to easily make use of advanced algorithms and machine learning. At CERN, a generic optimisation framework for the control room was provided, including centrally stored neural networks as well as registering environments and algorithms for common use.

## REFERENCES

- [1] A. Edelen, N. Neveu, M. Frey, Y. Huber, C. Mayes, and A. Adelmann, “Machine learning for orders of magnitude speedup in multiobjective optimization of particle accelerator systems”, *Phys. Rev. Accel. Beams*, vol 23, p. 044601, 2020. doi:10.1103/PhysRevAccelBeams.23.044601
- [2] G. Azzopardi, A. Muscat, G. Valentino, S. Redaelli, B. Salvachua, “Operational results of LHC collimator alignment using machine learning”, *Proc. IPAC’19*, Melbourne, Australia, pp. 1208–1211, 2019. “Operational Results of LHC Collimator Alignment Using Machine Learning”, in *Proc. IPAC’19*, Melbourne, Australia, May 2019, pp. 1208–1211. doi:10.18429/JACoW-IPAC2019-TUZZPLM1
- [3] S. Hirlander, M. Fraser, B. Goddard, V. Kain, J. Prieto, L. Stoel, M. Szakaly, F. Velotti, “Automatisation of the SPS ElectroStatic Septa Alignment”, in *Proc. IPAC’19*, Melbourne, Australia, May 2019, pp. 4001–4004. doi:10.18429/JACoW-IPAC2019-THPRB080
- [4] J. Duris *et al.*, “Bayesian Optimization of a Free-Electron Laser”, *Phys. Rev. Lett.*, vol. 124, p. 124801. doi:10.1103/PhysRevLett.124.124801
- [5] A. Hanuka *et al.*, “Online tuning and light source control using a physics-informed Gaussian process Adi”, <https://arxiv.org/abs/1911.01538/>.
- [6] M. McIntire *et al.*, “Sparse Gaussian Processes for Bayesian Optimization”, <https://www-cs.stanford.edu/~ermon/papers/sparse-gp-uai.pdf/>.
- [7] E. Shaposhnikova *et al.*, “LHC Injectors Upgrade (LIU) Project at CERN”, in *Proc. IPAC’16*, Busan, Korea, May 2016, pp. 992–995. doi:10.18429/JACoW-IPAC2016-MOPOY059
- [8] E. Adli, A. Ahuja, O. Apsimon, R. Apsimon, A.-M. Bachmann, D. Barrientos, F. Batsch, J. Bauche, V. B. Olsen, M. Bernardini *et al.*, “Acceleration of electrons in the plasma wakefield of a proton bunch,” *Nature*, vol 561, pp. 363–367, 2018. doi:10.1038/s41586-018-0485-4)
- [9] V. Kain, S. Hirlander, B. Goddard, F. Velotti, G. Zevi Della Porta, N. Bruchon, G. Valentino, “Sample-efficient reinforcement learning for CERN accelerator control”, *Phys. Rev. Accel. Beams*, vol 23, p. 124801, 2020. doi:10.1103/PhysRevAccelBeams.23.124801
- [10] R. Sutton, A. Barto, “Introduction to Reinforcement Learning”, MIT Press, Cambridge, MA, USA, 2018.
- [11] S. Gu, T. Lillicrap, I. Sutskever, S. Levine, “Continuous Deep Q-Learning with Model-based Acceleration”, in *Proc. 33rd International Conference on Machine Learning*, New York, NY, USA, 2016, pp. 2829–2838.
- [12] H. Kwakernaak, R. Sivan, “Linear Optimal Control Systems”, Wiley-Interscience, 1972.
- [13] A. Nagabandi, G. Kahn, R. S. Fearing, S. Levine, “Neural Network Dynamics for Model-Based Deep Reinforcement Learning with Model-Free Fine-Tuning”, arXiv:1708.02596, 2017.
- [14] R. Sutton, “Dyna, an integrated architecture for learning, planning, and reacting”, *AAAI Spring Symposium*, pp. 151–155, 1991. doi:10.1145/122344.122377
- [15] T. Wang *et al.*, “Benchmarking Model-Based Reinforcement Learning”, <https://arxiv.org/abs/1907.02057v1>, 2019.
- [16] V. Mnih *et al.*, “Human-level control through deep reinforcement learning”, *Nature*, vol. 518, pp. 529–533, 2015. doi:10.1038/nature14236
- [17] T. Lillicrap *et al.*, “Continuous control with deep reinforcement learning”, in *Proc. ICLR*, 2016. <https://arxiv.org/abs/1509.02971/>.
- [18] S. Fujimoto, H. van Hoof, D. Meger, “Addressing Function Approximation Error in Actor-Critic Methods”, arXiv:1802.09477, 2018.
- [19] “pyjapc”, available at <https://pypi.org/project/pyjapc/>.
- [20] <http://gym.openai.com/>.
- [21] MAD-X documentation and source code available at <https://mad.web.cern.ch/mad/>.
- [22] G. Bellodi, “Linac4 Commissioning Status and Challenges to Nominal Operation”, in *Proc. HB’18*, Daejeon, Korea, Jun. 2018, pp. 14–19. doi:10.18429/JACoW-HB2018-MOA1PL03
- [23] S. Hirlander and N. Bruchon, “Model-free and Bayesian Ensembling Model-based Deep Reinforcement Learning for Particle Accelerator Control Demonstrated on the FERMI FEL”, <https://arxiv.org/abs/2012.09737/>.

# MYRRHA-MINERVA INJECTOR STATUS AND COMMISSIONING\*

A. Gatera<sup>†</sup>, J. Belmans, S. Boussa, F. Davin, W. De Cock, V. De Florio, F. Doucet, L. Perez, F. Pompon, A. Ponton, D. Vandeplassche, E. Verhagen, SCK CEN, Mol, Belgium  
 F. Bouly, E. Froidefond, A. Plaçais, LPSC, CNRS-IN2P3/UJF/INPG, Grenoble, France  
 M. Ben Abdillah, C. Joly, L. Perrot, CNRS/IN2P3/IJClab, Université Paris-Saclay, Orsay, France  
 H. Podlech, IAP, Goethe-University, Frankfurt a. M., Germany  
 C. Zhang, GSI Helmholtz Center for Heavy Ion Research, Darmstadt, Germany  
 J. Tamura, Japan Atomic Energy Agency (JAEA/J-PARC) J-PARC Center, Japan

## Abstract

The MYRRHA project [1] at SCK CEN, Belgium, aims at coupling a 600 MeV proton accelerator to a subcritical fission core operating at a thermal power of 60 MW. The nominal proton beam for this ADS has an intensity of 4 mA and is delivered in a quasi-CW mode. MYRRHA's linac is designed to be fault tolerant thanks to redundancy implemented in parallel at low energy and serially in the superconducting linac. Phase 1 of the project, named MINERVA, will realise a 100 MeV, 4 mA superconducting linac with the mission of demonstrating the ADS requirements in terms of reliability and of fault tolerance. As part of the reliability optimisation program the integrated prototyping of the MINERVA injector is ongoing at SCK CEN in Louvain-la-Neuve, Belgium. The injector test stand aims at testing sequentially all the elements composing the front-end of the injector. This contribution will highlight the beam dynamics choices in MINERVA's injector and their impact on ongoing commissioning activities.

## INTRODUCTION

The MYRRHA Accelerator is a 600 MeV proton linear accelerator part of a flexible irradiation facility being created by SCK CEN in Belgium as a test-bed for transmutation and as a fast-spectrum facility for material and fuel developments.

a highly modular medium-and-high energy section (a so-called main linac) connecting a series of independently controlled accelerating superconducting cavities. Figure 1 depicts the accelerator and its two sections.

When compared with other accelerators of the same class [3], a major distinctive character of this system is given by its considerably harder reliability requirements: in MYRRHA, beam trips of a duration exceeding 3 seconds are considered as a system failure leading to a plant shutdown. In terms of MTBF, this corresponds to requiring a mean time between consecutive failures of at least 250 hours during the system's operative cycle (90 days). A common strategy to meet reliability requirements is given by fault-tolerance, namely the systematic adoption of provisions to compensate for unexpected deviations of the system state originating inside or outside of the system's boundaries. Given the complexity of our linac system, two fault-tolerance design patterns have been selected in function of the characteristics of the section they shall be applied to:

- In the low-energy section, hot spares shall be used as a form of parallel redundancy: two equivalent 16.6 MeV injectors with fast switching capabilities [4] shall be put in place.
- In the main linac section, the availability of similarly structured cavities shall be capitalized so as to realize a serial redundancy strategy, with the functions of failing cavities to be compensated by their four nearest neighbors [5].

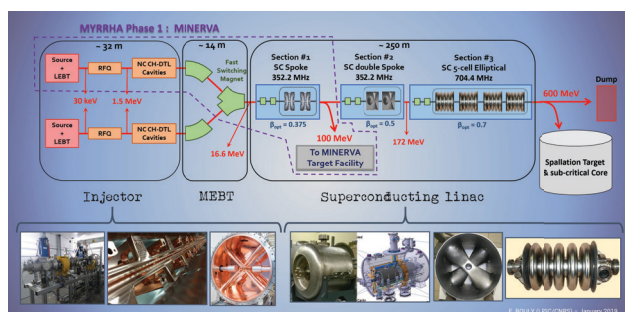


Figure 1: Accelerator scheme for the 100 MeV (MINERVA) and 600 MeV (MYRRHA ADS) phases [2].

This ADS consists of a low energy section (injector or Linac front-end) characterized by low beam velocity and

The MYRRHA project is scheduled to proceed in stages, with a first accelerator only based on a single injector connected to a superconducting section and an extraction line to a set of target facilities. In the first MYRRHA stage, MINERVA, the main linac shall be based on single-spoke cavities and reach 100 MeV. In a second stage, the accelerator shall be extended with double-spoke and elliptical cavities up to a full-fledged 600 MeV configuration. A final stage will see the accelerator connected to a subcritical nuclear reactor.

## THE INJECTOR TEST STAND

The MINERVA injector accelerates the beam up to 16.6 MeV. Its front-end is composed of an ECR proton source, a 2.6 m long LEBT (low energy beam transport line) [6] and a four-rod RFQ accelerating the beam to

\* Part of this work supported by the European Commission Framework Programme H2020, MYRTE project nr. 662186  
<sup>†</sup> angelique.gatera@sckcen.be

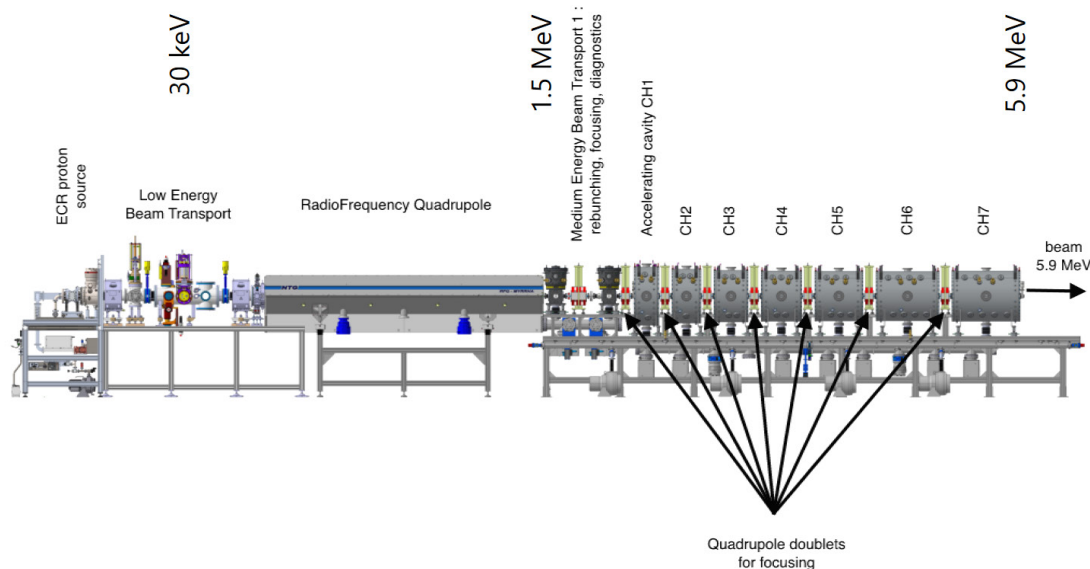


Figure 2: The injector test stand for MINERVA's front-end linac from the ECR source to the 7th accelerating cavity (up to 5.9 MeV).

1.5 MeV [7]. After the RFQ comes a small matching section with quarter wave resonators, called MEBT1, followed by a series of normal conducting CH cavities [8].

The front-end and the first seven CH cavities are being installed and tested on a dedicated test stand in Louvain-la-Neuve, Belgium, on the Cyclotron Resources Center (CRC) site. Today we have installed and are currently testing up to MEBT1 (see Fig. 2). We started by recommissioning the LEBT that had already been installed and commissioned at LPSC in Grenoble, France [6]. The two main objectives of the recommissioning have been (1) the study of the beam matching from the LEBT to the RFQ and its transmission, and (2) the study of space charge compensation transients, achieved by observing in detail the effects of enhanced space charge compensation when injecting gas into the LEBT.

For a defined current at the source exit, one can demonstrate by scanning through combinations of the two solenoids, that RFQ beam transmission is better optimised when argon is injected into the LEBT. Transmission maps without and with argon are shown in Fig. 3 where it is clear that transmission at high current is improved. Previously [9], we also measured that adding argon allowed smaller steady-state emittance to be achieved. But that said, gas addition improves neither the transmission at nominal current nor the current rise-time at the RFQ exit. Therefore, unless there is a need for high beam current (>5 mA), the added value of injecting argon is limited.

### RFQ BEAM COMMISSIONING

The first stage of RFQ beam commissioning, including full power commissioning, was carried out in 2020. As presented in Ref. [9], all the measured performances were according to expectations and no problems were encountered when pushing duty cycle to CW. The RFQ transmission at theoretical optimal power (110 kW or 44 kV) was 95 %, which could be increased to 98 % at 125 kW (48 kV). In

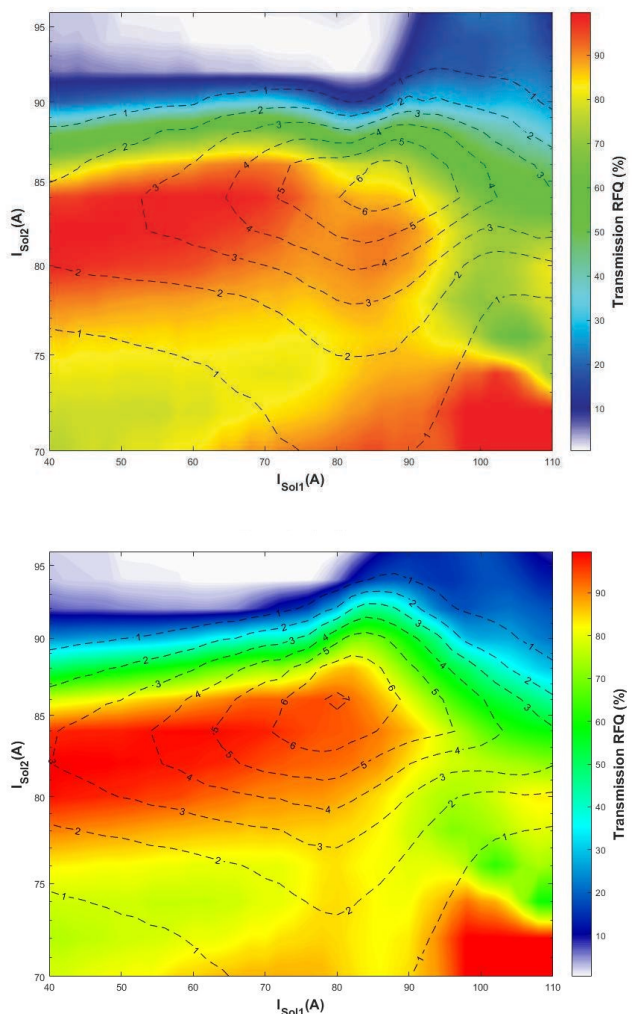


Figure 3: RFQ transmission maps with RFQ output isocurrent curves when scanning the solenoids in the LEBT for residual gas (top picture) / injected argon (bottom picture) in the LEBT.

the last months, we found out that running the RFQ also improved the transmission performances. We can now reach 98.9 % transmission at 4 mA around our new nominal RF power: 120 kW (46.5 kV).

The second stage of commissioning, carried out from Mid-2021, had as main objective the measurement of beam energy at the RFQ exit by time of flight (ToF).

### The Time of Flight Method

The bunch's time of flight between two beam phase pick-up systems (BPM or phase probe) can be estimated based on the phase shift measured at both detectors assuming that the number of RF buckets between the two is well known and that the phase offset due to cables and electronics is well calibrated [10]. If the bucket number is not known, a third pick-up is needed to determine it.

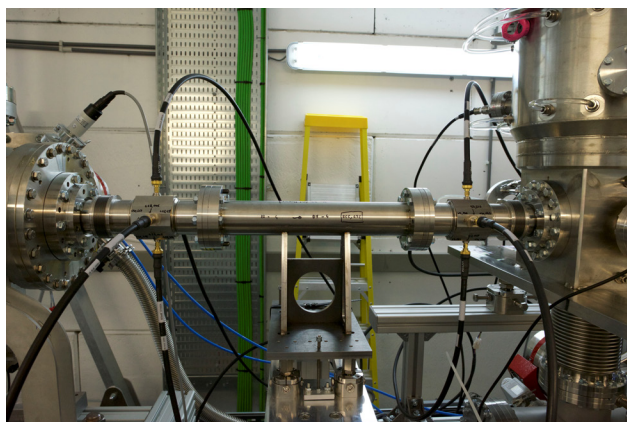


Figure 4: Setup for ToF measurement between two BPM.

The setup in Fig. 4 is composed of two BPM (at black cables location) developed for MYRRHA during the MYRTE project [11]. It is installed at the end of MEBT1, after the second quarter wave rebuncher (see Fig. 2). A third BPM placed between the two rebuncher cavities has been used for bucket count verification.

### RFQ Energy Measurement

The ToF setup described in the previous section was used for RFQ energy measurement with both bunching cavities switched off and detuned.

The measured output energy shows small fluctuations with respect to the RF power level inside the RFQ as can be seen from Fig. 5. These fluctuations are believed to come from synchrotron oscillations due to input energy mismatch. Below 90 kW, the beam bunching is not complete and the phase measurement shows more and more statistical variations until the system becomes unable of locking the phase.

The measured reference energy at nominal power (120 kW) is  $1.494 \pm 0.003$  MeV. The uncertainty margin covers statistical uncertainties and phase and distance errors from both BPMS. The obtained result is fairly close to the expected 1.5 MeV and is fully in the acceptance range of the downstream cavities.

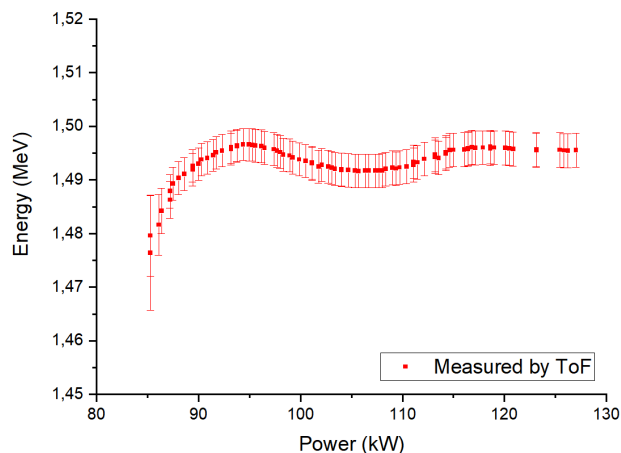


Figure 5: RFQ output energy with respect to RF power inside the RFQ.

It was previously demonstrated in equivalent installations that the oscillation in function of RF power is sensitive to the RFQ input energy [12]. In an effort to minimise the oscillation, we attempted an input energy scan by changing the source platform voltage.

As can be seen from the results in Fig. 6, increasing the platform voltage from 30.0 kV to 30.4 kV improves slightly energy stability. No improvement was observed passed 30.4 kV. Being the energy stability at 30.0 kV already good (only  $\pm 4$  keV variation), improving it to  $\pm 3$  keV variation does not seem as an improvement worth pursuing. The final decision on source platform voltage optimisation will have to wait for emittance measurements.

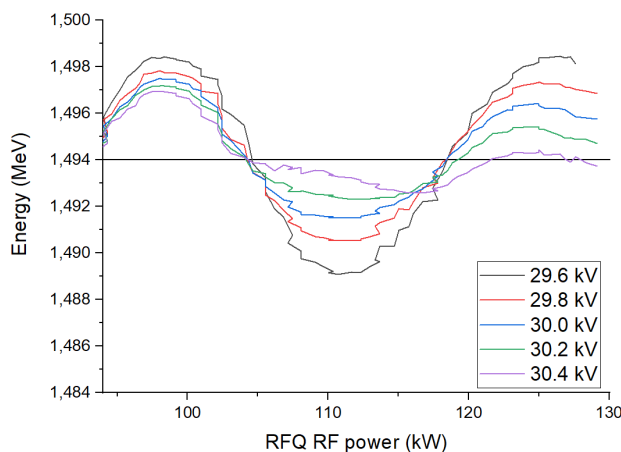


Figure 6: Fluctuations due to synchrotron oscillation for different RFQ input energy defined by the source platform voltage.

We have in the same measurement campaign tried to test RFQ energy stability both in time and for different input beam currents. The energy variation in time was better than 1 keV over an hour of measurement and across different measurements (for the same LEBT and RFQ setpoints). Our next step is to install diagnostics to measure the longitudinal

emittance. This should also help to conclude on the source platform voltage choice.

## MEBT1 TUNING

MEBT1, for first medium energy transport line, is the first matching section right after the RFQ. Its main goal is to match the beam into the longitudinal acceptance of the CH section linac. It is composed of two quarter wave rebunchers (QWR1 and QWR2) and one quadrupole triplet as shown in Fig. 7.

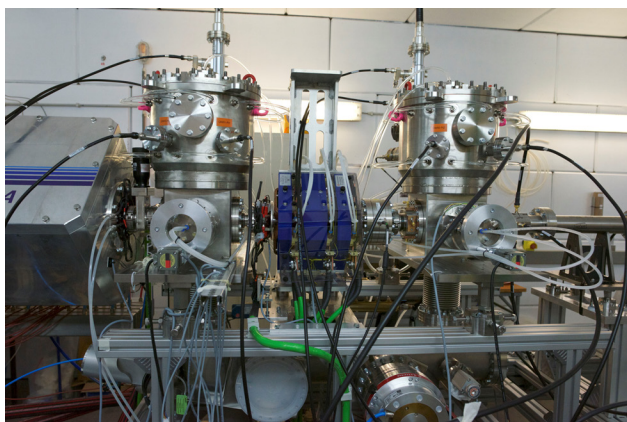


Figure 7: MEBT1 composed of two quarter wave rebunchers and one quadrupole triplet as currently installed at the injector test stand.

The full RF conditioning of QWR1 and QWR2 was done in less than a day each. For these cavities, we use the same type of solid state amplifiers as for the RFQ [13] and dedicated in-house cavity tuners and LLRF systems on RFSoc FPGA [14].

The tuning of MEBT1 was done in two steps. First, the triplet was fine tuned around its beam dynamics determined setpoints in order to optimize beam transmission through MEBT1.

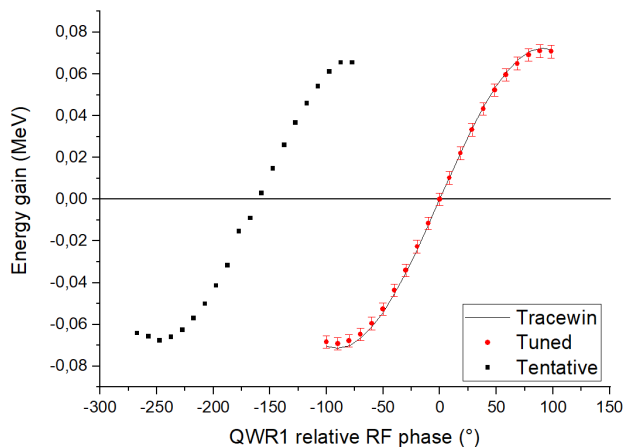


Figure 8: Measured relative phase versus energy gain before (tentative) and after tuning a quarter wave rebuncher to match Tracewin simulation.

Then, the rebunchers were tuned in phase and amplitude using the same ToF setup as for energy measurement. They were tuned so as to match an energy variation pattern simulated by the Tracewin code [15] with very good agreement as shown in Fig. 8.

Based on the good agreement between measurements and simulations, we are confident that the beam has the right characteristics for entering the first accelerating CH cavity. We should soon receive diagnostics that will allow us to confirm this with transverse emittance and bunch shape measurements.

## CONCLUSION

In the last months, we have achieved the measurement of RFQ beam energy and tuning of our first RF cavities using a ToF setup composed of two BPM. A third independent BPM was used for bunch count or energy range confirmation.

The measured RFQ energy is 1.494 MeV which is in the acceptance range. Added to almost 99 % transmission at nominal current and good behavior in CW mode, the RFQ has so far performed very well through all the milestones.

We are currently preparing the transverse emittance and bunch shape test bench. The diagnostics to be used are expected on site by the end of the year and the measurements are planned for the first quarter of 2022.

## REFERENCES

- [1] D. De Bruyn, H. Ait Abderrahim, P. Baeten and J. Verpoorten, “The Belgian MYRRHA ADS project: recent developments and future perspectives”, 10th annual International Conference on Sustainable Development through Nuclear Research and Education (NUCLEAR-2017), Pitesti, Roumania, May 2017, p. 344.
- [2] F. Bouly *et al.*, “Superconducting LINAC Design Upgrade in View of the 100 MeV MYRRHA Phase I”, in *Proc. IPAC’19*, Melbourne, Australia, May 2019, pp. 837–840. doi: 10.18429/JACoW-IPAC2019-MOPTS003
- [3] D. Vandeplassche and L. Medeiros-Romao, “Accelerator Driven Systems”, in *Proc. IPAC’12*, New Orleans, LA, USA, May 2012, paper MOYAP01, pp. 6–10.
- [4] E. Froidefond *et al.*, “Study and Design of a Fast Switching Magnet for the MYRRHA Project”, in *Proc. IPAC’21*, Campinas, Brazil, May 2021, pp. 2356–2359. doi: 10.18429/JACoW-IPAC2021-TUPAB361
- [5] F. Bouly, “Method Development for Cavity Failure Compensation in a Superconducting Linac”, in *Proc. IPAC’21*, Campinas, Brazil, May 2021, pp. 647–650. doi: 10.18429/JACoW-IPAC2021-MOPAB191
- [6] F. Bouly *et al.*, “Commissioning of the MYRRHA Low Energy Beam Transport Line and Space Charge Compensation Experiments”, in *Proc. IPAC’17*, Copenhagen, Denmark, May 2017, pp. 1226–1229. doi: 10.18429/JACoW-IPAC2017-TUOBA2
- [7] C. Zhang, H. Podlech, “New Reference Design of the European ADS RFQ Accelerator for MYRRHA”, in *Proc. IPAC’14*, Dresden, Germany, Jun. 2014, pp. 3223–3225. doi: 10.18429/JACoW-IPAC2014-THPME008

- 64<sup>th</sup> ICFA ABDW on High-Intensity and High-Brightness Hadron Beams  
 ISBN: 978-3-95450-225-7 ISSN: 2673-5571 HB2021, Batavia, IL, USA JACoW Publishing  
 doi:10.18429/JACoW-HB2021-WEBC3
- [8] K Kümpel *et al.*, “Current Status of the MYRRHA Cavities”, in *Proc. IPAC’19*, Melbourne, Australia, May 2019, pp. 892–894. doi:10.18429/JACoW-IPAC2019-MOPTS022
- [9] A. Gatera *et al.*, “Minerva (MYRRHA Phase 1) RFQ Beam Commissioning”, in *Proc. IPAC’21*, Campinas, Brazil, May 2021, pp. 675–678. doi:10.18429/JACoW-IPAC2021-MOPAB205
- [10] M. Bozzolan, “BPM Time of Flight Measurements for Setting-up the RF Cavities of the CERN Linac4”, in *Proc. LINAC’18*, Beijing, China, Sep. 2018, pp. 879–881. doi:10.18429/JACoW-LINAC2018-THPO084
- [11] M. Ben Abdillah *et al.*, “Development of a Low-beta BPM for MYRTE Project”, in *Proc. IBIC’19*, Malmö, Sweden, Sep. 2019, pp. 504–507. doi:10.18429/JACoW-IBIC2019-WEPP002
- [12] A.K Orduz *et al.*, “Beam Commissioning SPIRAL2”, in *Proc. IPAC’21*, Campinas, Brazil, May 2021, pp. 2540–2543. doi:10.18429/JACoW-IPAC2021-WEXB05
- [13] D. Vandeplasseche *et al.*, “Integrated Prototyping in View of the 100 MeV Linac for Myrrha Phase 1”, in *Proc. IPAC’18*, Vancouver, Canada, Apr.-May 2018, pp. 661–664. doi:10.18429/JACoW-IPAC2018-TUPAF003
- [14] <https://www.xilinx.com/products/silicon-devices/soc/rfsoc.html/>.
- [15] D. Uriot and N. Pichoff, “Status of TraceWin Code”, in *Proc. IPAC’15*, Richmond, VA, USA, May 2015, pp. 92–94. doi:10.18429/JACoW-IPAC2015-MOPWA008

Content from this work may be used under the terms of the CC BY 3.0 licence (© 2021). Any distribution of this work must maintain attribution to the author(s), title of the work, publisher, and DOI

# STUDY ON THE INJECTION BEAM COMMISSIONING AND PAINTING METHOD FOR CSNS/RCS\*

Ming-Yang Huang<sup>1,2,3,#</sup>, Sheng Wang<sup>1,2,3</sup>, Shou-Yan Xu<sup>1,2</sup>

<sup>1</sup>Institute of High Energy Physics, Chinese Academy of Sciences (CAS), Beijing, China

<sup>2</sup>Spallation Neutron Source Science Center (SNSSC), Dongguan, China

<sup>3</sup>University of Chinese Academy of Sciences, Beijing, China

## Abstract

In this paper, firstly, the beam commissioning of the injection system for CSNS/RCS will be studied, including: timing adjustment of the injection pulse powers, injection beam parameter matching, calibration of the injection painting bumps, measurement of the painting distribution, injection method adjustment, application of the main stripping foil, optimization of the injection beam loss and radiation dose, etc. Secondly, the painting methods for the CSNS/RCS will be studied, including: the fixed-point injection method, anti-correlated painting method and correlated painting method. The results of the beam commissioning will be compared with the simulation results. Combining with other precise optimizations, the beam power on the target has successfully reached the design value of 100kW and the stable operation of the accelerator has been achieved.

## INTRODUCTION

The China Spallation Neutron Source (CSNS) is a high power proton accelerator-based facility [1, 2]. It consists of an 80 MeV H<sup>-</sup> Linac, a 1.6 GeV rapid cycling synchrotron (RCS), two beam transport lines, a target station, and several instruments. The RCS accumulates the injection beam, accelerates the beam to the design energy of 1.6 GeV and extracts the high energy beam to the target. Its repetition rate is 25 Hz. The design goal of the beam power on the target is 100 kW [3] which had been achieved in Feb. 2020. Figure 1 shows the layout of the CSNS.

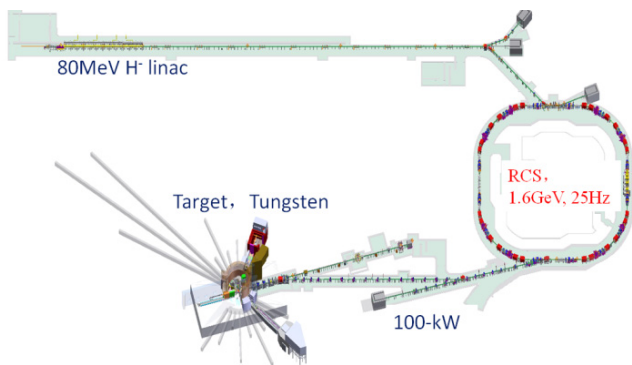


Figure 1: Layout of the CSNS.

\*Work supported by National Natural Science Foundation of China (Project Nos. 12075134 and U1832210)

#huangmy@ihep.ac.cn

Since 2016, the CSNS had begun the accelerator beam commissioning. Figure 2 shows the historical curve of the beam power on the target. It can be seen that: in Nov. 2017, the first 10 kW beam power on the target had been operated for a short while; in Mar. 2018, the beam power over 20 kW had been achieved in the test operation; in Jan. 2019, the beam power was gradually increased to over 50 kW with well controlled beam loss; in Sep. 2019, the beam power in user operation was increased to 80 kW step by step; in Feb. 2020, the beam power was increased to 100 kW to achieve the design goal; in Oct. 2021, the beam power had exceeded 120 kW.

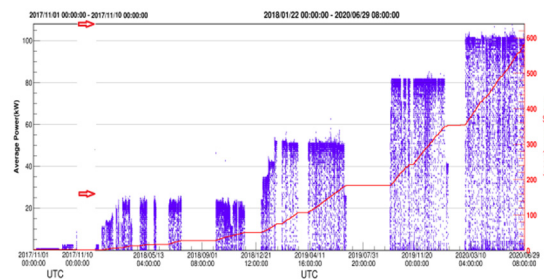


Figure 2: Historical curve of the CSNS beam power.

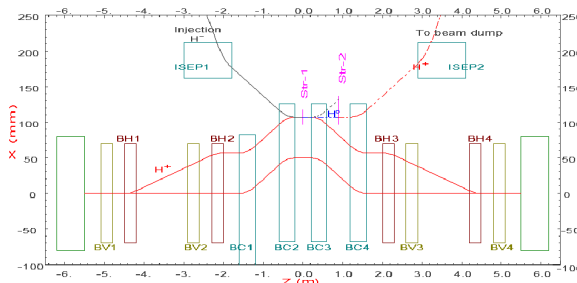


Figure 3: Layout of the CSNS injection system.

The injection system is the core component of the accelerator and the injection beam loss is one of the decisive factors that limit whether the RCS can operate at the high beam power [4]. In order to reduce the beam loss, a combination of the H<sup>-</sup> stripping and phase space painting method is used to accumulate a high intensity beam in the RCS [5]. Figure 3 shows the layout of the CSNS injection system. There are three kinds of orbit bumps: a horizontal bump generated by four dipole magnets (BH1-BH4) for painting in the horizontal plane; a vertical bump (BV1-BV4) for painting in the vertical plane; a fixed horizontal bump (BC1-BC4) in the middle for an additional closed-orbit shift of 60 mm. There are two carbon stripping foils: a main stripping foil and a secondary stripping foil. Their materials are both HBC.

Content from this work may be used under the terms of the CC BY 3.0 licence (© 2021). Any distribution of this work must maintain attribution to the author(s), title of the work, publisher, and DOI

For the CSNS [6], the anti-correlated painting method is adopted as the design scheme for the injection system.

In this paper, the beam commissioning of the injection system and painting methods for the CSNS/RCS will be studied in detail. The results of the beam commissioning will be compared with the simulation results. Combining with other precise optimizations, the beam power on the target has successfully reached the design value of 100 kW and the stable operation of the accelerator has been achieved.

## BEAM COMMISSIONING OF THE INJECTION SYSTEM

In this section, the results and problems of the beam commissioning for the CSNS injection system will be studied, including: timing adjustment of the injection pulse powers, injection beam parameter matching, calibration of the injection painting bumps, measurement of the painting distribution, injection method adjustment, application of the main stripping foil, optimization of the injection beam loss and radiation dose, etc. After the above optimizations, the injection beam loss has been well controlled and the injection efficiency has been over 99%.

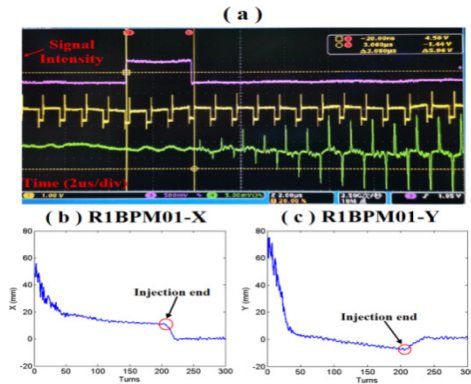


Figure 4: The timing adjustment of the injection pulse powers.

### Timing Adjustment of the Injection Pulse Powers

The timing adjustment of the pulse power supply (injection timing adjustment) is very important for the injection beam commissioning. For the CSNS, a new method for precisely adjusting the injection timing have been proposed. Firstly, the standard injection timing signal (T0), the RCS frequency timing signal, and the circulating beam signal can be obtained from a special beam position monitor (R1BPM01) by using the oscilloscope. Then, the timing relationship between the circulating beam and standard injection timing can be given. By using the R1BPM01, the turn-by-turn (TBT) position data of the circulating beam can be measured, and the timing relationship between the pulse power supply and the injection standard timing can be given. By comparing these two timing relationships, the timing relationship between the circulating beam and the pulse power supply can be obtained. As a result, the injection

WEDC1

timing can be accurately adjusted. Figure 4 shows the timing adjustment of the injection pulse powers.

### Injection Beam Parameters Matching

A mismatch between the injection beam and circulating beam can result in large beam loss and an undesirable transverse emittance growth. There are three aspects which should be considered in the injection beam parameters matching: twiss parameters, beam orbit, and dispersion function.

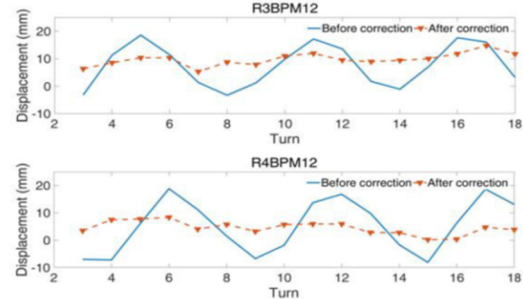


Figure 5: The detected betatron oscillation at two different BPMs before and after the correction for the injection beam.

For the CSNS/RCS, during the beam commissioning, the requirement of the injection twiss parameters matching and dispersion function matching were easy to satisfy. Therefore, we focused on the methods of the orbit matching between the injection beam and circulating beam. After the machine study, a new method based on multi-turn injection and Fourier fitting was developed to match the injection beam orbit [7]. Figure 5 shows the detected betatron oscillation at two different BPMs before and after the correction for the injection beam. The machine study results show that the mismatch of injection parameters can be well depressed by using this new method.

### Calibration of the Injection Painting Bumps

In order to control and optimize the phase space painting results, the positions and ranges of the horizontal and vertical painting need to be adjusted accurately. Therefore, in the early stage of the beam commissioning, the calibration of the injection painting bump sizes were very important and need to be done as soon as possible.

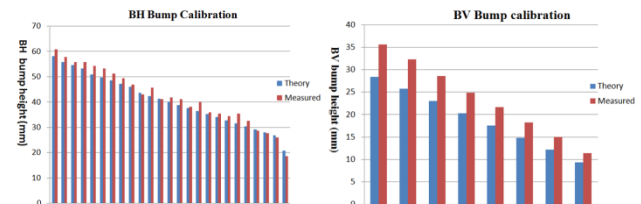


Figure 6: Comparison of the measured and theoretical values of the BH and BV bump sizes.

After the calibration of the injection painting bumps, Fig. 6 shows the comparison of the measured and theoretical values of the BH and BV bump sizes. It can be found that: for the horizontal bump, the calibration error is smaller than 4 mm which is caused by the system errors

and measurement errors of the two BPMs; for the vertical bump, the difference between the theoretical and measured values is large which is mainly caused by the BC edge focusing effect.

The BC edge focusing effect mainly affects the four-fold symmetry of the RCS, the BV bump height, and causes the disclose of the BV bump. From the simulation results by using the code Py-ORBIT [8], in the current working point mode, the BC edge focusing effect causes about 30% variation of the BV bump, as shown in Fig. 7.

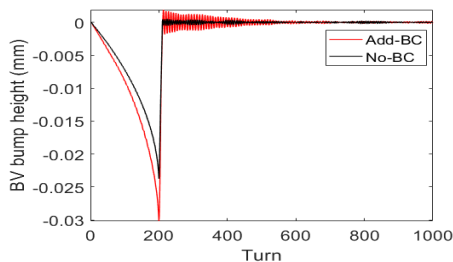


Figure 7: BV bump height with and without the BC edge focusing effect.

### Measurement of the Painting Distribution

In order to better adjust and optimize the painting method, the painting distribution needs to be measured. With the fast extraction scheme, after the injection painting completed, the circulating beam can be extracted quickly and the transverse beam distribution can be measured by a multi-wire scanner (MWS) on the beam transport line from the RCS to the target (RTBT). Therefore, the transverse beam sizes and beam distribution after the injection painting completed can be obtained. Figure 8 shows the RCS direct-current current transformer (DCCT) display for the fast extraction scheme and the transverse beam distribution measured by a multi-wire scanner on the RTBT.

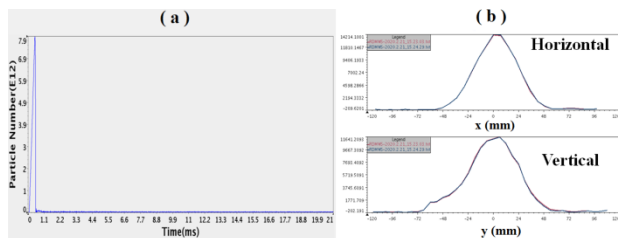


Figure 8: (a) RCS DCCT display for the fast extraction scheme; (b) the transverse beam distribution measured by a multi-wire scanner on the RTBT.

### Injection Method Adjustment

In the early stage of beam commissioning, since the precise position of the injection point was unknown and the injection beam power was relatively small, in order to inject the Linac beam into the RCS as soon as possible, the fixed-point injection method was selected. Latter, in order to increase the beam power and reduce the beam loss, the phase space painting in the horizontal plane was used. Finally, the phase space painting in both horizontal and vertical planes was used, and the painting ranges and

painting curves were studied and optimized.

When the beam power on the target was less than 80 kW, after the detailed optimization, the anti-correlated painting method can meet the requirements for the stable operation of the accelerator. However, when the beam power on the target exceeded 80 kW, the beam loss was very large. A new method was proposed to perform the correlated painting method. By using this new correlated painting method, the beam loss and the beam distribution were much better. Then, the beam power on the target has reached the design value of 100 kW.

### Application of the Main Stripping Foil

During the beam commissioning of the injection system, the main stripping foil was optimized: the material of HBC and the thickness of 0.44  $\mu\text{m}$  were used for the main stripping foil; the double-layer foil was instead of the single-layer foil to reduce the injection beam loss; after detailed measurement, at the design beam power of 100 kW, the service life of the main stripping foil was only 1.5 months; if overused, the stripping foil would be severely deformed.

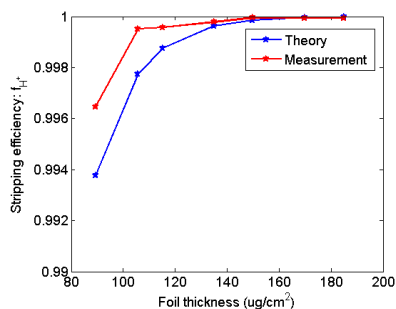


Figure 9: Measured and theoretical stripping efficiencies.

In order to control the injection beam loss, the measurement of the stripping efficiency is very important [9, 10]. During the beam commissioning, a method to measure the stripping efficiency [4] was proposed and applied. By using this method, the stripping efficiencies for different foil thicknesses were measured. Figure 9 shows the comparison of the measured and theoretical stripping efficiencies. It can be found that there is a little difference between the theoretical and actual measured results. This difference is mainly caused by the measurement errors of the stripping foil thickness and INDCT. For the CSNS, the stripping efficiency of the main stripping foil is greater than 99.7% at present.

### Injection Beam Loss and Radiation Dose

The injection beam loss is the main source of the RCS beam loss which is one of the decisive factors that limit whether the RCS can operate at the high beam power. There are several main sources of the injection beam loss, including: injection parameter mismatch; low stripping efficiency; stripping foil scattering; unstripped H<sup>-</sup> beam loss; stripped electrons. After in-depth machine study, three solutions to reduce the injection beam loss have been found. Firstly, the injection beam parameters

Content from this work may be used under the terms of the CC BY 3.0 licence (© 2021). Any distribution of this work must maintain attribution to the author(s), title of the work, publisher, and DOI

matching should be more accurately. Secondly, the painting ranges and painting curves should be optimized more accurately. Thirdly, the thickness, structure and material of the main stripping foil should be optimized.

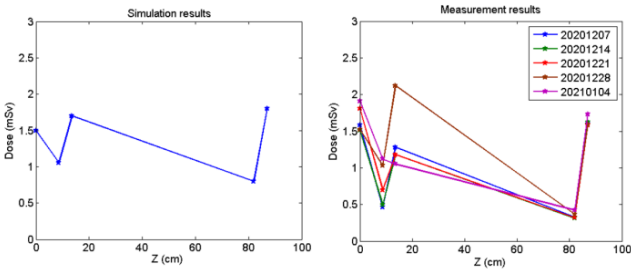


Figure 10: Simulation and measurement results of the residual doses in the injection region.

By using the codes FLUKA [11] and ORBIT [12], the beam transport and particle scattering of the main stripping foil can be simulated. After week by week measurement, the residual doses in the injection region can be obtained. Figure 10 shows the simulation and measurement results of the residual doses in the injection region. It can be seen that, from the simulation results, the maximum residual dose caused by the foil scattering is less than 2 mSv. By comparing the simulation results and measurement results, it can be confirmed that the particle scattering of the main stripping foil is the most important source of the residual doses in the injection region.

### STUDY ON THE PAINTING METHOD

During the beam commissioning, different injection methods were used in different periods. In the early stage, since the precise position of the injection point was unknown and the beam power was relatively small, the fixed-point injection was selected. When the beam power on the target was less than 80 kW, the anti-correlated painting method of the design scheme can meet the requirements for the stable operation of the accelerator. When the beam power on the target exceeded 80 kW, the beam loss was very large. A new method was proposed to perform the correlated painting method. By using this new method, the beam power on the target has reached the design value of 100 kW.

#### Fixed-point Injection

The fixed-point injection method means the Linac beam injected into the ring at a fixed point. Figure 11 shows the schematic of the RCS acceptance ellipse and injection beam in the fixed-pointing injection process. It can be seen that the relative position of the injection beam and circular beam is unchanged during the injection process. In the early stage of beam commissioning, since the precise relative position of the injection beam and circular beam was unknown and the injection beam power was very small, in order to inject the beam into RCS as soon as possible, the fixed-point injection method was selected.

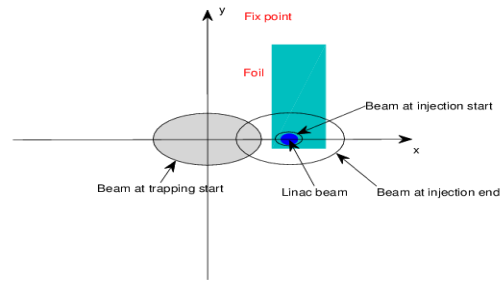


Figure 11: Schematic of the RCS acceptance ellipse and injection beam in the fixed-point injection process.

While the fixed-point injection method was used, there was a sudden beam loss which cannot be removed during the injection process. Figure 12 shows the RCS DCCT display while the fixed-point injection was used. It can be found that there was sudden beam loss during the injection process no matter the matching of the injection beam and circulating beam. The machine study shows that the sudden beam loss increases with the off-center position between the circulating beam and injection beam.

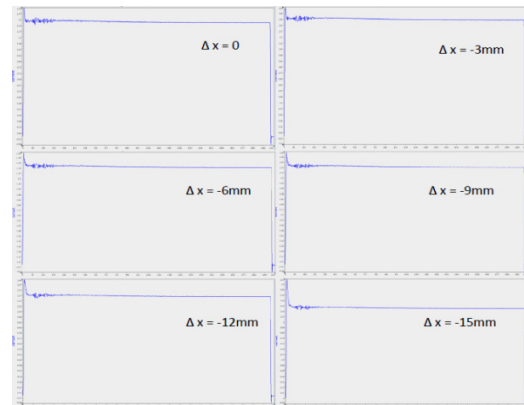


Figure 12: RCS DCCT displays while the fixed-point injection was used.  $\Delta x$  is the off-center position between the circular beam and injection beam.

#### Anti-correlated Painting Method

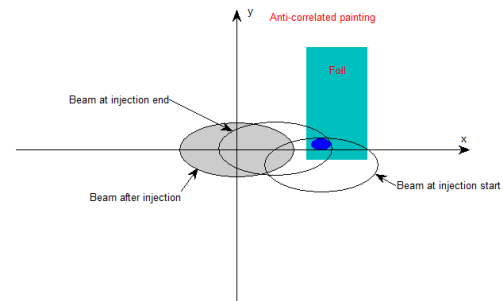


Figure 13: Schematic of the RCS acceptance ellipse and injection beam in the injection process for the anti-correlated painting method.

The anti-correlated painting method is adopted as the design scheme for the CSNS injection system. In the injection process, the circulating beam is painted from the center to the border in the horizontal plane and from the border to the center in the vertical plane. The injection

point locates in the lower left corner of the main stripping foil to reduce the traversal times. Figure 13 shows the schematic of the RCS acceptance ellipse and injection beam in the injection process.

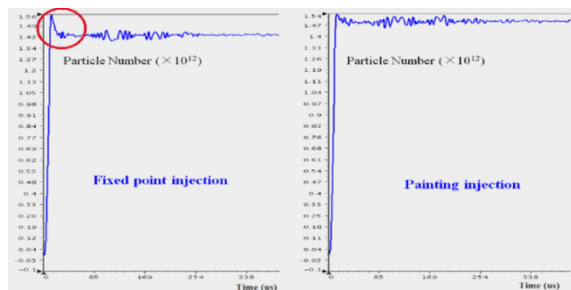


Figure 14: RCS DCCT displays when the fixed-point injection and painting injection were used.

In the above section, it can be found that when the fixed-point injection method was used, there was a sudden beam loss in the injection process. By using the transverse phase space painting instead of the fixed-point injection, the sudden beam loss in the injection process was gone. Figure 14 shows the RCS DCCT display when the fixed-point injection and painting injection were used. It can be found that, with the transverse phase space painting, the sudden beam loss was gone and the injection efficiency was improved.

With the anti-correlated painting method of the design scheme, after the injection beam parameters matching, stripping foil optimization, phase space painting optimization, and injection beam loss adjustment, the injection beam loss has been well controlled and the injection efficiency has been over 99%. Combined with other aspects of the beam commissioning, the beam power on the target has exceeded 50 kW and achieved the stable operation.

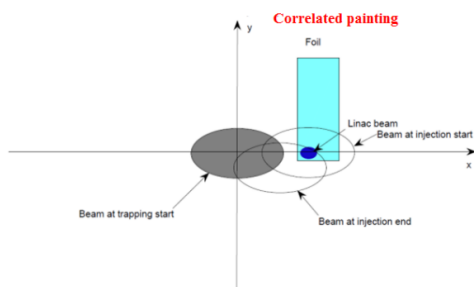


Figure 15: Schematic of the RCS acceptance ellipse and injection beam in the injection process for the correlated painting method.

### Correlated Painting Method

When the beam power on the target exceeded 80 kW, the beam loss was very large. In order to reduce the beam loss and increase the beam power on the target, after in-depth machine study, a new method was proposed to perform the correlated painting method [13]. By using the rising edge of the vertical pulse current curve instead of the falling edge for painting in the vertical plane, the correlated painting scheme can be carried out. Figure 15

shows the schematic of the RCS acceptance ellipse and injection beam in the injection process. Figure 16 shows the BH and BV pulse current curves for the anti-correlated painting scheme and correlated painting scheme.

By using the correlated painting method, the beam loss of the RCS was greatly reduced, the painting distribution was much better, and the beam intensity in vertical phase space was effectively mitigated. Then, the beam power on the target has reached the design value of 100 kW.

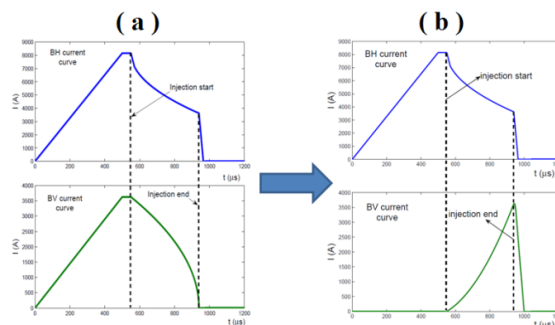


Figure 16: BH and BV pulse current curves for the anti-correlated painting scheme (a) and correlated painting scheme (b).

## CONCLUSIONS

Firstly, the beam commissioning of the injection system for the CSNS/RCS was studied and discussed, including: timing adjustment of the injection pulse powers, injection beam parameter matching, calibration of the injection painting bumps, measurement of the painting distribution, injection method adjustment, application of the main stripping foil, optimization of the injection beam loss and radiation dose, etc. Secondly, the injection painting methods were studied, including: the fixed-point injection method, anti-correlated painting method and correlated painting method.

Compared to the simulation results of the design scheme, the transverse beam distribution, transverse coupling effect and beam loss of the actual anti-correlated painting were somewhat different. In order to reduce the beam loss and increase the beam power on the target, a new method was proposed to perform the correlated painting method for CSNS/RCS. By using the correlated painting method, the beam loss and the beam distribution were much better. Then, the beam power on the target has reached the design value of 100 kW.

## ACKNOWLEDGMENTS

The authors would like to thank other CSNS colleagues for the discussions and consultations. M.Y. Huang also want to thank Yoshiro Irie of KEK for helpful discussions.

## REFERENCES

- [1] S. Wang *et al.*, "Introduction to the overall physics design of CSNS accelerators", *Chinese Physics C*, vol. 33, pp. 1-3, 2009. doi: 10.1088/1674-1137/33/s2/001

- [2] CSNS Project Team, “China Spallation Neutron Source Feasibility Research Report”, Chinese Academy of Sciences, 2009 (in Chinese).
- [3] J. Wei *et al.*, “China Spallation Neutron Source - an overview of application prospects”, *Chinese Physics C*, vol. 33, pp. 1033-1042, 2009.  
 doi:10.1088/1674-1137/33/11/021
- [4] M. Y. Huang, S. Wang, S. Y. Xu, “Beam loss and the stripping efficiency measurement for CSNS injection system”, *Journal of Physics: Conference Series*, vol. 1350, p. 012107, 2019.  
 doi:10.1088/1742-6596/1350/1/012107
- [5] M. Y. Huang *et al.*, “Effects of injection beam parameters and foil scattering for CSNS/RCS”, *Chinese Physics C*, vol. 37, p. 067001, 2013.  
 doi:10.1088/1674-1137/37/6/067001
- [6] M. Y. Huang *et al.*, “Study on the anti-correlated painting injection scheme for the Rapid Cycling Synchrotron of the China Spallation Neutron Source”, *Nuclear Inst. and Methods in Physics Research A*, vol. 1007, p. 165408, 2021. doi:10.1016/j.nima.2021.165408
- [7] X. H. Lu, M. Y. Huang, S. Wang, “Injection orbit matching for a rapid cycling synchrotron”, *Physical Review Accelerators and Beams*, vol. 21, p. 062802, 2018.  
 doi:10.1103/PhysRevAccelBeams.21.062802
- [8] A. Shishlo, S. Cousineau, J. Holmes, T. Gorlov, “The Particle Accelerator Simulation Code PyORBIT”, *Procedia Computer Science*, vol. 51, pp. 1272-1281, 2015.  
 doi: 10.1016/j.procs.2015.05.312
- [9] P. K. Saha *et al.*, “State of the art online monitoring system for the waste beam in the rapid cycling synchrotron of the Japan Proton Accelerator Research Complex”, *Physical Review Special Topics-Accelerators and Beams*, vol. 14, p. 072801, 2011.  
 doi:10.1103/PhysRevSTAB.14.072801
- [10] P. K. Saha *et al.*, “Measurement of 181 MeV H<sup>-</sup> ions stripping cross-sections by carbon stripper foil”, *Nuclear Inst. and Methods in Physics Research A*, vol. 776, pp. 87-93, 2015. doi:10.1016/j.nima.2014.12.068
- [11] A. Ferrari *et al.*, “FLUKA: multi-particle transport code”, Geneva, Switzerland, Rep. CERN-2005-010, Oct. 2005.
- [12] J. Gabambos *et al.*, “ORBIT User’s Manual”, SNS/ORNL/AP Technical Note 011, 1999.
- [13] M. Y. Huang *et al.*, “A new method to perform the correlated painting based on the machine structure of anti-correlated painting”, in preparing.

# ACCELERATION OF THE HIGH CURRENT DEUTERON BEAM THROUGH THE IFMIF-EVEDA RFQ: CONFIRMATION OF THE DESIGN BEAM DYNAMICS PERFORMANCES

L. Bellan<sup>†</sup>, L. Antoniazzi, M. Comunian, E. Fagotti, F. Grespan, M. Montis, , M. Giacchini, A. Palmieri, M. Poggi, F. Scantamburlo, A. Pisent INFN-LNL, Legnaro, Italy  
 B. Bolzon, N. Chauvin, J. Marroncle, CEA-IRFU, Gif-sur-Yvette, France  
 T. Akagi, K. Masuda, K. Kondo, M. Sugimoto, QST, Aomori, Japan  
 P. Cara, IFMIF/EVEDA Project Team, Aomori, Japan  
 D. Jimenez-Rey, I.Podadera, CIEMAT, Madrid, Spain  
 I. Moya, H. Dzitko, C. Yann, F4E, Garching, Germany

## Abstract

The Linear IFMIF Prototype Accelerator (LIPAc) is a high intensity D<sup>+</sup> linear accelerator; demonstrator of the International Fusion Material Irradiation Facility (IFMIF). In summer 2019 the IFMIF/EVEDA Radio Frequency Quadrupole (RFQ) accelerated its nominal 125 mA deuteron (D<sup>+</sup>) beam current up to 5 MeV, with >90% transmission for pulses of 1 ms at 1 Hz, reaching its nominal beam dynamics goal. The paper presents the benchmark simulations and measurements performed to characterize the as-built RFQ performances, in the low and high perveance regime. In this framework, the commissioning strategy with a particular focus on the reciprocal effects of the low-medium energy transfers lines and the RFQ is also discussed. In the last part of the paper, the future commissioning outlooks are briefly introduced.

## INTRODUCTION

The accelerator setup of LIPAc [1] for the pulse commissioning of the RFQ was composed by the ECR high intensity deuteron ion source [2], the Radio-Frequency Quadrupole [3] and the Medium Energy Transfer Line [4] coupled with a diagnostic plate [5]. The line was terminated with a temporary low power beam dump, with a maximum sustainable DC of 0.1%. First D<sup>+</sup> injection was possible in March 2019, then we reached in July 132 kV-2.5 ms-20 Hz and in July 24th we achieved a 125 mA D<sup>+</sup> current at 1 ms/1 Hz out the RFQ, with transmission>90%. In order to identify the RFQ performances, it was important to separate the effects on the transmission of the preceding and subsequent parts of the accelerator.

## THE RFQ

The Radio Frequency Quadrupole is a 4-vane 9.8 m CW accelerator which accelerates 125 mA positive deuteron beam from 100 keV up to 5 MeV. The maximum Kilpatrick at its nominal file is 1.76. During the RF conditioning at LNL, 1.94 value was reached in the CW regime for 5 hours with the third section of the RFQ. At the state of the art, at the Rokkasho site, in Japan, we reached 1.85 value during pulse conditioning, and we are under high D.C. conditioning of the whole assembly. [6].

<sup>†</sup> luca.bellan@lnl.infn.it

Some design parameters of the RFQ are shown in Fig. 1. The details are reported in reference [7]. However, it is worth re-calling some features that are relevant for this paper:

- The generalized perveance of the nominal beam, from the low energy up to the high section of the accelerator ranges from 10<sup>-3</sup> to 10<sup>-5</sup>.
- The tune depression from the shaper is roughly constant,  $\frac{\sigma_t}{\sigma_{0,t}} = 0.5$  and  $\frac{\sigma_l}{\sigma_{0,l}} = 0.4$
- The input/output beam normalized rms emittance are 0.25/0.26 mm mrad for the transverse plane while the longitudinal rms emittance is 0.2 MeV deg.

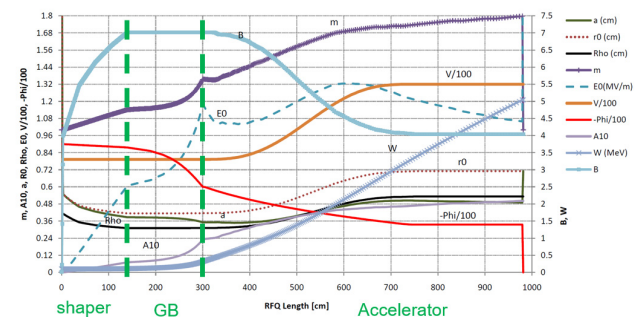


Figure 1: Design parameters of the IFMIF/EVEDA RFQ.

During the Critical Design review, in order to decrease the input beam requirements from the Low Energy Transfer Beam (LEBT) section, easing the beam matching to the RFQ focusing channel, it was decided to decrease the RFQ focusing factor B defined by Eq. (1) smoothly, after the RMS (Radial Matching Section) up to the shaper end, following the undepressed longitudinal phase advance of the RFQ.

$$B = \frac{qV\lambda^2}{mc^2r_0^2} \quad (1)$$

The net effect is a drop of the input beam convergence requirements. In particular

- the rms value of the X' decreases from 43 mrad down to 24 mrad.
- the transmission of the accelerated particles drops from the previous design 95% down to 93.7%.

Content from this work may be used under the terms of the CC BY 3.0 licence (© 2021). Any distribution of this work must maintain attribution to the author(s), title of the work, publisher, and DOI

The transmission was estimated considering a 4D Gaussian distributed beam, truncated at  $4\sigma$ , with an input current of 130 mA, with a 0.25 mm mrad rms normalized transverse emittance. The software used for the RFQ modelling was TOUTATIS [8]: its ability to change the voltage and the vane profile was a key feature for the implementation of the as-built RFQ model. Other parameters of the RFQ can be found in Table 1.

Table 1: Main RFQ Parameters

Input/output Energy	0.1-5	MeV
Duty cycle	cw	
Dueteron beam current	125	mA
Operating Frequency	175	MHz
Length ( $5.7\lambda$ )	9.78	m
Vg (min-max)	79-132	kV
R0 (min-max) $\rho/R0=0.75$	0.4135-0.7102	cm
Total Stored Energy	6.63	J
Cavity RF power dissipation	550	kW
Maximum dissipated power	86	kW/m
Power density (average-max)	3.5-60	kW/cm <sup>2</sup>
$Q_0/Q_{sf}=0.82$	13200	
Shunt impedance( $\langle V^2 \rangle$ )/ $L/P_d$	201	K $\Omega$ -m
Frequency tuning	Water temp.	
N cells ( $\beta\lambda/2$ )	489	

### As-built RFQ

In order to further improve the precision of our simulations with respect the experiments, we implemented the mechanical errors of the RFQ modules and the bead pull measurements after tuning [9]. In this case, the beam transmission further decreases of about 2%, while the transverse and longitudinal emittances increase. Table 2 summarizes the new values of the transmission and emittance increase

Table 2: Mechanical and Bead Pull Errors on Beam Transmissions and Emittances

Parameters	Values
$\Delta\epsilon_{rms,t,n}/\epsilon_{rms,t,n}$	+3%
$\Delta\epsilon_{rms,l}/\epsilon_{rms,l}$	+8%
$\Delta Tr./Tr$	-2% (i.e., 91.8%)

The as-built RFQ was implemented in all the simulations involved during the commissioning and beam characterization.

### Criteria for Larger than 90% of Transmission

The beam coming from the high intensity ion source is not in an equilibrium distribution: its phase-space distribution is hardly comparable with a well-known stationary

phase space distributions or even to the most common design-used distributions, such as the waterbag, gaussian and KV. It more often shows the characteristics of hollow and halo distribution. In order to decrease the dependence of the RFQ design with respect the particle distribution, we performed the RFQ design following the evolution of the equivalent beam rms quantities (relying on the Sacharor equivalent principle) [3]. We used the same philosophy for evaluating the input beam requirements from the LEPT: for any beam current  $I_b$ , exists a maximum rms normalized transverse emittance  $\epsilon_{Gaussian,rms,t,n}$  of the equivalent Gaussian beam that allows to transmit > 90%, with rms matched conditions. If the current is negligible the  $\epsilon_{Gaussian,t,n}$  (total emittance) becomes comparable with the well-known geometric acceptance A, in particular

$$\epsilon_{Gaussian,t,n} = 4 \epsilon_{Gaussian,rms,t,n} = 1.1$$

The larger acceptance of the lower current beam results in the possibility to allow a larger mismatch with lower current beam. As an example, for 7 mA proton beam the acceptable mismatch [10] increases up to 220%. These two last considerations were extensively used for the probe beam (low current low emittance beam) first commissioning.

## THE INJECTOR

The injector, an the ECR (Electron Cyclotron Resonance) ion source, consists of a 2.45 GHz RF power source with two coils magnetic structure. The nominal CW beam extracted consists of 140 mA D+ at 100 kV. For commissioning purposes, the source can also extract tens of mA of H+ at 50 kV and can work in pulse mode. From the beam dynamics point of view, these beams are characterized by a high perveance beam transport: the general perveance (un-compensated) ranges from  $5 \times 10^{-4}$  for the probe up to  $5 \times 10^{-3}$  nominal beam. In order to preserve the beam quality from the ion source up to the RFQ injection point (the LEPT), two magnetic solenoids and two repellers, one in the extraction and one at the RFQ entrance, are used in order to allow the space-charge compensation to take place.

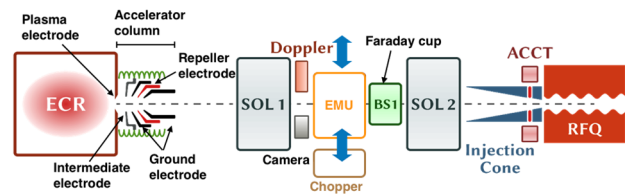


Figure 2: Sketch of the IFMIF/EVEDA injector.

The solenoids need to be tuned in order to match the output beam characteristics from the source exit to the RFQ input, while the steerers (integrated into the solenoids) set to 0 the first order moments of the beam at injection point. A permanent diagnostic box was installed between the two solenoids.

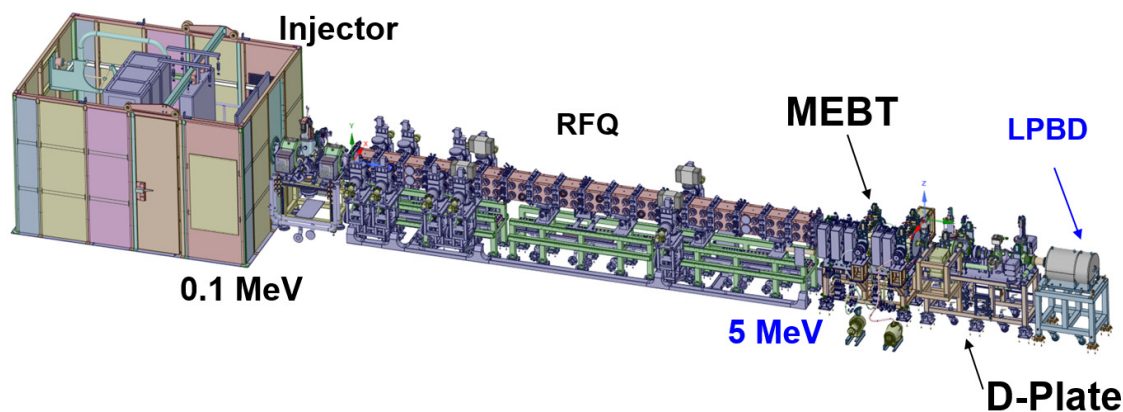


Figure 3: Sketch of the accelerator during RFQ pulsed commissioning.

During the injector commissioning a second diagnostic box in place of the RFQ was used. Figure 2 shows the sketch of the injector in its nominal configuration (see Fig. 3 for the sketch of whole setup). For this configuration the source is equipped with a diagnostic box between the two solenoids which contains an Allison type emittance-meter, the Doppler shift spectrometers and CCD camera. The aim of the ion source, from the RFQ point of view, is to produce a 125 mA  $D^+$  with an  $\epsilon_{rms,t,n} < 0.3$  mm mrad (at RFQ in-injection), the  $\epsilon_{Gaussian,rms,t,n}$  for 125 mA. It is difficult to measure the phase spaces at the RFQ injection point, since the envelopes are small and the power density high. Therefore, the input beam emittance and Twiss must be estimated via the combination of appropriate beam dynamics models [11] and the measurements

spect the RFQ injection point are shown. The major reasons of the emittance increase were identified, confirmed by the simulations [15], due to the solenoid aberrations and uncompensated space-charge fields. The beam considered in Fig. 4 is an 85 mA proton beam at 50 keV. The emittance shows the higher values near the matched positions, in the left high part of the plot. Therefore, in order to be sure to not lowering the emittance quality at the RFQ input while changing the solenoids for the matching procedure, we developed a criterion that helps up to evaluate the injector working point without the second diagnostic box:

- we choose a specific value of the first solenoid that correspond to a beam parallel transport between the solenoids.
- we measure the emittance for various injector configurations.

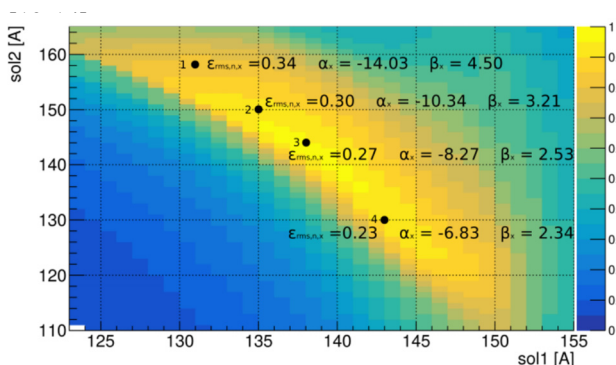


Figure 4: 85 mA proton beam at 50 keV measured transmission plot, during injector commissioning, with a second diagnostic box in place of the RFQ. Superimposed to the plot, the measured emittances are shown, after 300 mm from the injection point.

In particular, the estimation of the emittance growth along the LEBT is very important for the characterization of the emittance at RFQ input. During the injector commissioning we found out that the emittance had a trend with respect the solenoids values of the LEBT. Fig. 4 shows the measured solenoids scan plot of the transmission through the injection cone up to the end of second diagnostic box that was placed in place of the RFQ. Superimposed to that plot the measured emittance values after 300 mm with re-

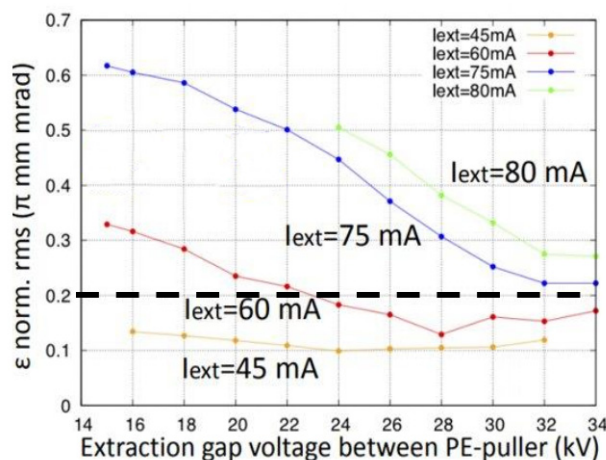


Figure 5: Example of several source tunings: the emittance is measured between the two solenoids with respect the puller voltage. The black dotted line shows the criterion limit for injecting into the RFQ.

If  $\epsilon_{rms,t,n} < 0.2$  mm mrad, then the margin for the emittance growth was considered safe for injecting the beam into the RFQ. Fig. 5 shows an example of the application of such criteria for several proton beam extractions. The software used during the RFQ beam commissioning are,

Content from this work may be used under the terms of the CC BY 3.0 licence (© 2021). Any distribution of this work must maintain attribution to the author(s), title of the work, publisher, and DOI

for the extraction, IBSIMU [16], while WARP [17] and Tracewin [18] for the LEBT transport.

### THE MEBT

The MEBT (Medium Energy Beam Transfer) line of 2.3 m length, composed by 5 magnetic quadrupoles, for the transverse matching to the SRF, and 2 bunchers, for the longitudinal matching. The beam generalized perveance is, for the nominal beam,  $10^{-5}$ . Fig. 6 shows the sketch of the MEBT. The MEBT is equipped also with two scrapers positioned between the first three quadrupoles, as well as with BPMs for the beam phase and TOF measurements along the line and current monitors.

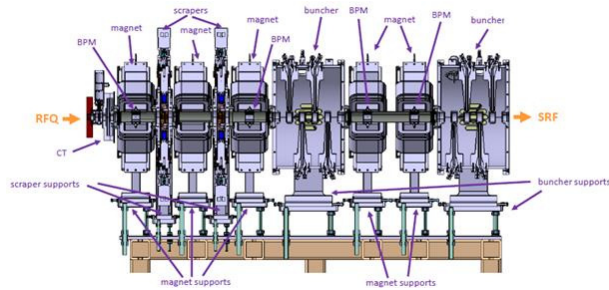


Figure 6: Sketch of the optics element of the MEBT and its diagnostics.

The diagnostic plate was attached after the MEBT. The diagnostic plate implements a system for the emittance measurements through the method of slits and grids. The method was further improved thanks to the usage of a magnetic steerers. The details are presented in reference [19]. Beside the diagnostics, the beam dynamics of the MEBT includes another hindered attribute: it can separate, through the strong chromatism effects, the not accelerated particles (i.e. the particles that are not captured by the separatrix) and the residual contaminants presents at the RFQ injection point that survived within the RFQ channel. (see Fig. 3).

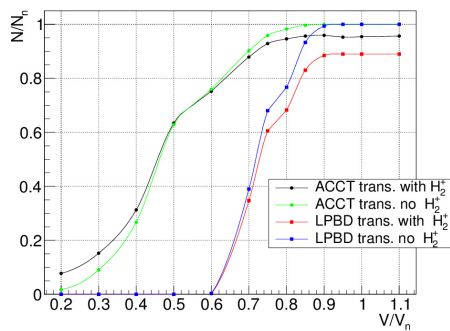


Figure 7: Transmission curve for 13 mA extracted current proton beam with 61.5% proton fraction, in case the simulations take (or not) into account the  $H_2^+$

This effect is very important because it can bias the measurement of the voltage calibration curve of the RFQ: as a matter of fact, the experimental transmission is given by  $I_{LPBD}/I_{LEBT}$ . Therefore, it depends on the value of  $I_{LEBT}$ , which generally also measure the residual compo-

nent of contaminants that reaches the injection cone. Figure 7 shows a simulation on voltage calibration curve performed considering a low perveance beam (13 mA extracted proton beam current with 61.5% proton fraction). It is possible to see that the curve depends on including or not the contaminants contribute to  $I_{LEBT}$ . This may cause a down estimation of the current, which can be significant ( $> 10\%$ ).

### PROTON RESULTS

The proton results presented here considers the low and half beam perveance. During the probe beam commissioning (low perveance), thanks to the presence of a permanent magnet we could measure the effect of contaminants onto the transmission, foresee by the simulations. Fig. 8 shows the combined effect of the steerers and the permanent magnet onto the transmission and current at the LPBD.

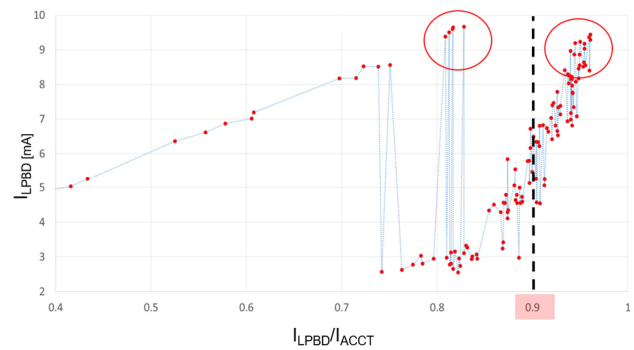


Figure 8: the plot shows some record of the current vs transmission in the RFQ for a low perveance beam of 10 mA proton beam, during the operation of an automatic steerer scan routine. The two regions of maximum currents are encircled. The 90% transmission level is shown.

Two regions are shown (with red circles) which present similar currents at the LPBD but corresponding to a not negligible different transmissions (82% and 98%). This was due to the contaminants, that were able, in one case, to be lost before the current monitor position in LEBT. After the first set of measurement of the probe beam, we increase the current up to roughly half perveance.

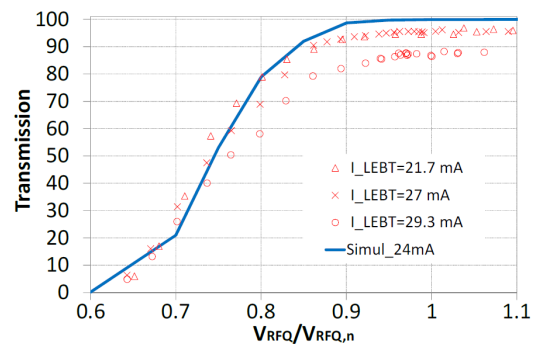


Figure 9: voltage calibration curve with several current points and simulated curve at 24 mA.

Figure 9 shows the voltage calibration curve with different currents at the LEBT ACCT. For comparison a simulation with 24 mA is also reported. It is worth to notice the

measurement referring to 29.3 mA: its lower transmission, below 90%, was explained by the fact that its emittance was not compliant with  $\epsilon_{rms,t,n} < 0.2$  mm mrad criterion. Another important measurement was the transverse emittance after the RFQ [19]. We took some systematic data varying the LEBT solenoids and the voltage of the RFQ. We obtained satisfying benchmarking results, for the half proton beam, as shown in Fig. 10.

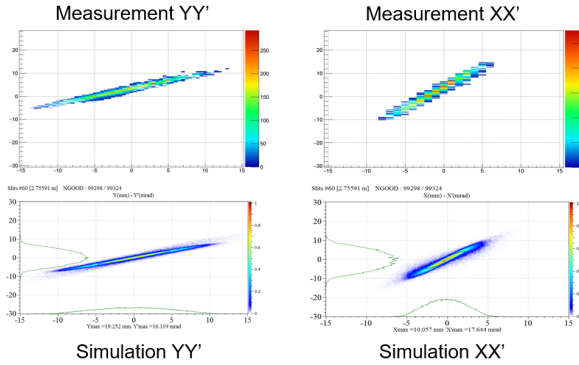


Figure 10: voltage calibration curve with several current points and simulated curve at 24 mA.

The larger simulated/measured relative differences on the rms emittances for the scan up to now performed is 16%. We obtained 13% on the betatron's and 10% on the  $\alpha$ .

## DEUTERON RESULTS

This chapter presents the results of the RFQ beam dynamics performances at nominal perveance (125 mA accelerated beam, 0.1% D.C., 1 ms beam pulse [20]). Unlucky, the chopper was not functioning during this measurement shifts, and therefore we could not measure the transverse emittance at the exit of the RFQ and the profiles.

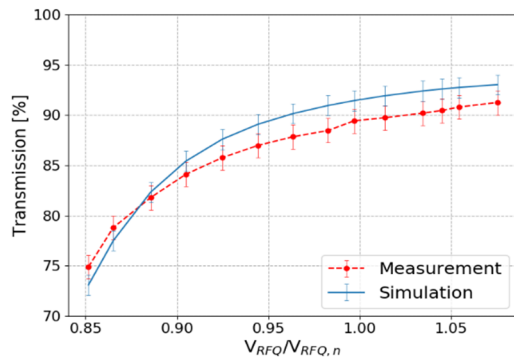


Figure 11: Voltage calibration curve of 136 mA deuteron beam. The simulation considers the effect of the contaminants. The data refer to the accelerated particle only.

These measurements will be performed in the future campaign. Fig. 11 shows the measurements and the simulation of the voltage calibration curve performed with 125 mA deuteron beam accelerated through the RFQ. During the same shift we measured the energy of the accelerated particles with the BPMs positioned after the RFQ (see Fig. 12). The results were in agreement with the neutron

production on the LPBD and on the MEBT scrapers due to the reaction  $^{27}\text{Al}(d,n)$  [21]

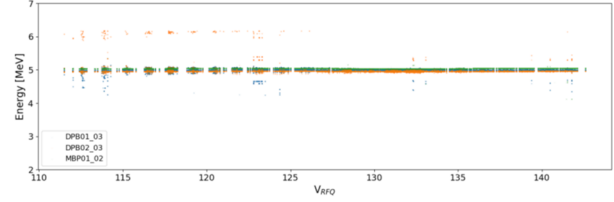


Figure 12: Energy measurement with respect the RFQ voltage.

Another interesting measurement performed with the BPMs [22] allowed us to measure the oscillations of the beam barycentre energy after the RFQ with respect the RFQ voltage. It turned out that we can connect such oscillations of the barycentre to the voltage offset of  $\pm 1$  kV of the 100 kV platform (see Fig. 13). A dedicated experiment is foreseen in the next campaign

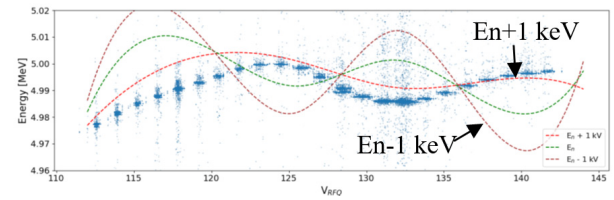


Figure 13: Energy measurement with respect the RFQ voltage. Simulation curves with different beam input energy (corresponding to  $V_{ext}/e$ ) are shown.

## CONCLUSIONS

The RFQ beam dynamics have been tested for two main regimes: the half and nominal perveance beams. The emittance at half perveance and the transmissions on both nominal and low current beams of the accelerated particles resulted compatible to the simulations. Table 3 summarizes the results for nominal beam perveance.

Table 3: Summary of the results on the 125 mA accelerated deuteron beam @  $V/V_n=1$ . The emittances are in mm mrad.

Beam dist.	$\epsilon_{rms,t,n}$	$\epsilon_{99\%,t,n}$	Transm.
Experimental	/	/	89.7 $\pm$ 1.2
Sim. D <sup>+</sup> and D <sub>2</sub> <sup>+</sup>	/	/	91.5 $\pm$ 1.0
Sim. D <sup>+</sup>	0.2	3.7	92.5 $\pm$ 1.0
4D Gauss.	0.25	2.2	91.8 (as-b.), 93.7(design)

## ACKNOWLEDGEMENTS

The present work was performed in the framework of the Broader Approach Agreement. The authors gratefully acknowledge the support of their home institutions and research funders for this work. Views and opinions expressed herein do not necessarily reflect those of QST, Fusion for Energy, or of the authors' home institutions or research funders.

## REFERENCES

- [1] P. Cara *et al.*, “IFMIF/EVEDA Project: Achievements and Outlooks beyond 2020”, presented at FEC’20, 650, unpublished.
- [2] R. Gobin *et al.*, “Final Design of the IFMIF Injector at CEA/Saclay”, in *Proc. IPAC’13*, Shanghai, China, May 2013, paper THPWO003, pp. 3758-3760.
- [3] A. Pisent *et al.*, “IFMIF-EVEDA RFQ Design”, in *Proc. EPAC’08*, Genoa, Italy, June 2008, paper THPP078, pp. 3542-3544.
- [4] I. Podadera *et al.*, “The Medium Energy Beam Transport Line (MEBT) of IFMIF/EVEDA LIPAc”, in *Proc. IPAC’11*, San Sebastian, Spain, Sep. 2011, paper WEPS058, pp. 2628-2630.
- [5] J. Marroncle *et al.*, “IFMIF-LIPAc Diagnostics and its Challenges”, in *Proc. IBIC’12*, Tsukuba, Japan, Oct. 2012, paper WECC01, pp. 557-565.
- [6] E. Fagotti *et al.*, “Beam Commissioning of the IFMIF/EVEDA very high power RFQ”, in *Proc. IPAC’18*, Vancouver, Canada, May 2018, pp. 2902-2907.  
doi:10.18429/JACoW-IPAC18-THXGBF2
- [7] M. Comunian and A. Pisent, “Beam Dynamics Redesign of IFMIF-EVEDA RFQ for a Larger Input Beam Acceptance”, in *Proc. IPAC’11*, San Sebastian, Spain, Sep. 2011, paper MOPS031, pp. 670-672.
- [8] R. Douperrier, “TOUTATIS: A radio frequency quadrupole code”, *Phys. Rev. Accel. Beams*, vol 3, p.124201, Dec. 2000.  
doi:10.1103/PhysRevSTAB.3.124201
- [9] A. Palmieri *et al.*, “Tuning the IFMIF 5MeV RFQ Accelerator”, in *Proc. LINAC’16*, East Lansing, MI, USA, Sep. 2016, pp. 969-971.  
doi:10.18429/JACoW-LINAC2016-THPLR049
- [10] T. P. Wangler, “RF Linear Accelerators”, in *Physics Textbook*, John Wiley & Sons, Ltd, 2008  
doi:10.1002/9783527623426
- [11] L. Bellan *et al.*, “Extraction and low energy beam transport models used for the IFMIF/EVEDA RFQ commissioning”, presented in ICIS’21, 25, unpublished.
- [12] N. Chauvin *et al.*, “Deuteron beam commissioning of the linear IFMIF prototype accelerator ion source and low energy beam transport”, *Nucl. Fusion*, vol. 59, p.106001, August 2019. doi:10.1088/1741-4326/ab1c88
- [13] T. Akagi *et al.*, “Commissioning of high current H<sup>+</sup>/D<sup>+</sup> ion beams for the prototype accelerator of the International Fusion Materials Irradiation Facility”, *Rev. Sci. Instrum.*, vol. 91, p.023321, February 2020.  
doi:10.1063/1.5129598
- [14] B. Bolzon *et al.*, “Intermediate Commissioning Results of the 70 mA/50 keV H<sup>+</sup> and 140 mA/100 keV D<sup>+</sup> ECR Injector of IFMIF/LIPAc”, in *Proc. IPAC’16*, Busan, Korea, May 2016, pp. 2625-2627.  
doi:10.18429/JACoW-IPAC2016-WEPMY033
- [15] L. Bellan *et al.*, “Source and LEBT Beam Preparation for IFMIF-EVEDA RFQ”, in *Proc. LINAC’16*, East Lansing, MI, USA, Sep. 2016, pp. 420-423.  
doi:10.18429/JACoW-LINAC2016-TUPRC005
- [16] T. Kalvas *et al.*, “IBSIMU: A three-dimensional simulation software for charged particle optics”, *Rev. Sci. Instrum.*, vol 81, p. 02B703, February 2010.  
doi:10.1063/1.3258608
- [17] D.P. Grote and A. Freidman, “The WARP Code: Modeling High Intensity Ion Beams”, *AIP Conf. Proc.*, vol. 749, p.55-58, March 2016. doi:10.1063/1.1893366
- [18] <http://irfu.cea.fr/en/Phocsa/Page/index.php?id=780>
- [19] J. Marroncle *et al.*, “Transverse emittance in 2.5 MeV proton beam on LIPAc, IFMIF’s Prototype”, in *Proc. IBIC’19*, Malmö, Sweden, September 2019, pp. 288-293.  
doi:10.18429/JACoW-IBIC2019-TUPP006
- [20] F. Grespan *et al.*, “IFMIF/EVEDA RFQ Beam Commissioning at Nominal 125 mA Deuteron Beam in Pulsed Mode”, presented at the IPAC’20, Caen, France, May 2020, paper TUVIR11. doi:10.18429/JACoW-IPAC2020-TUVIR11
- [21] K. Kondo *et al.*, “Neutron production measurement in the 125-mA 5-MeV deuteron beam commissioning of Linear IFMIF Prototype Accelerator (LIPAc) RFQ”, *Nucl. Fusion*. September 2021, accepted manuscript.  
doi:10.1088/1741-4326/ac233c
- [22] I. Podadera *et al.*, “Beam commissioning of beam position and phase monitors for LIPAc”, in *Proc. IBIC’19*, Malmö, Sweden, September 2019, pp. 534-538.  
doi:10.18429/JACoW-IBIC2019-WEPP013

## STATUS OF FRIB COMMISSIONING\*

P.N. Ostroumov<sup>†</sup>, F. Casagrande, K. Fukushima, M. Ikegami, T. Kanemura, S. Kim,  
S. Lidia, G. Machicoane, T. Maruta, D. Morris, A.S. Plastun, J. Popielarski,  
J. Wei, T. Xu, T. Zhang, Q. Zhao, S. Zhao,

Facility for Rare Isotopes Beams, Michigan State University, East Lansing, MI 48824, USA

### Abstract

The Facility for Rare Isotope Beams (FRIB), a major nuclear physics facility for research with fast, stopped, and reaccelerated rare isotope beams, is approaching the commencement of user operation in 2022 as planned. The readiness of the linear accelerator for the production of rare isotopes was verified by the acceleration of Xenon-124 and Krypton-86 heavy ion beams to 212 MeV/u using all 46 cryomodules with 324 superconducting cavities. Several key technologies were successfully developed and implemented for the world's highest energy continuous wave heavy ion beams, such as full-scale cryogenics and superconducting radiofrequency resonator system, stripping heavy ions with a thin liquid lithium film flowing in an ultrahigh vacuum environment, and simultaneous acceleration of multiple-charge-state heavy-ion beams. These technologies are required to achieve ultimate FRIB beam energies beyond 200 MeV/u and beam power up to 400 kW. High intensity pulsed beams capable in delivering 200-kW beams to the target in CW mode were studied in the first segment of the linac.

### INTRODUCTION

The FRIB includes a high-power superconducting driver accelerator, an isotope production target, and a fragment separator. The layout of the FRIB is shown in Fig. 1. The FRIB driver linac will provide stable nuclei accelerated to 200 MeV/u for the heaviest uranium ions and higher energies for lighter ions with 400 kW power on the target [1]. The progress with the FRIB linac construction, development, and testing was reported in previous HB workshops, see for example, [2-5]. The 400-kW ion beams will be delivered to a thin fragmentation target which is followed by a large-acceptance high-resolution fragment separator (FS). The FRIB FS will be capable to capture large-emittance rare isotope beams resulting from production reactions, i.e., angular acceptance is  $\pm 40$  mrad in both transverse directions and momentum acceptance is  $\pm 5\%$ . The maximum magnetic rigidity of the fragment separator can reach 8 T·m. While many isotopes will be studied in the in-flight experiments, FRIB will use upgraded National Superconducting Cyclotron Laboratory (NSCL) facilities to prepare and re-accelerate stopped isotopes up to 12 MeV/u.

In a continuous wave (CW) superconducting (SC) linac, the 400-kW beams can be achieved with a low beam current, below 1 emA. Therefore, the space charge effects are

mostly negligible in the linac except the ion source and the Low Energy Beam Transport (LEBT). Although the performance of Electron Cyclotron Resonance Ion Sources (ECRIS) has been significantly improved in the past decades, they cannot produce sufficient intensities of the heaviest ions, in order to reach 400 kW on target in a single charge state. To achieve 400 kW power on the target for the heaviest ion beams, multiple charge states of the same ion species are accelerated simultaneously. Particularly, in the case of uranium, two charge states ( $U^{33+}$  and  $U^{34+}$ ) will be accelerated before the stripping and five charge states after the stripping at 17 MeV/u. Also, multiple-charge-state acceleration after the stripper dramatically reduces the total power of unwanted charge states dumped in the first folding segment. Therefore, the multiple-charge-state acceleration will be used for all ion species with a mass above  $\sim 60$ .

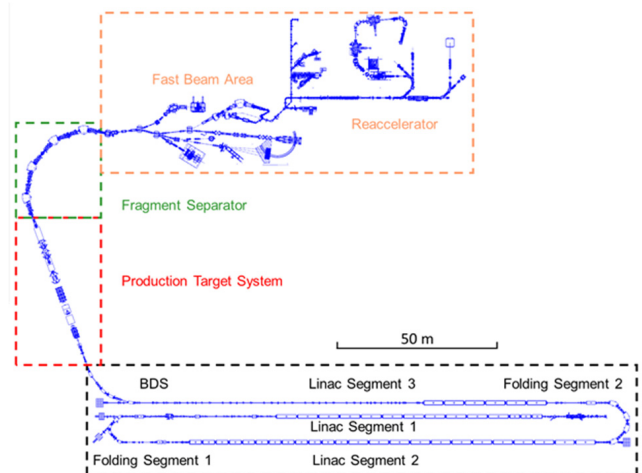


Figure 1: Layout of the FRIB driver accelerator, target, fragment separator, re-accelerator and existing infrastructure. The driver linac consists of three straight segments, Linac Segment 1 (LS1), Linac Segment 2 (LS2), Linac Segment 3 (LS3) and two folding segments, Folding Segment 1 (FS1) and Folding Segment 2 (FS2).

The staged beam commissioning was adopted for the FRIB. The beam commissioning started in 2017 with the Front End (FE) and continued until April 2021. All this time, the installation of the accelerator equipment has been taking place. The current state of the tunnel is shown in Fig. 2. Each stage of the beam commissioning took less than two weeks. The results of each stage were reported in multiple journal papers [6-9]. In this paper, we report the results of the recent commissioning progress. The Kr and Xe beams were accelerated to 212 MeV/u and delivered to

\* Work supported by the U.S. Department of Energy Office of Science under Cooperative Agreement DE-SC0000661, the State of Michigan and Michigan State University.

<sup>†</sup> ostroumov@frib.msu.edu

the beam dump at the linac's end using all 46 cryomodules with 324 superconducting cavities [10].



Figure 2: FRIB tunnel after the completion of installation.

## FRONT END STATUS

A significant experience has been gained with the operation and tuning of the FE for various ion beam species. The tuning procedure of the FE for any ion beam species from scratch has been developed. Currently, there is a library of settings for about ten different ion beam species. It should be noted that the FRIB LEBT, unlike many other LEBTs elsewhere, is designed and built to extract and accelerate all ion beam components produced in the ECRIS to their final energies. The energy of the ions of interest is 12 keV/u. The accelerated beam components are separated and selected after the first 90° bending magnet. The charge selection segment as well as the whole FRIB LEBT can provide the no-loss achromatic transport of dual-charge-state heavy ion beams.

We noticed, however, that if the ECRIS is cold started to produce the same ion species that were used previously, there is a slight deviation of the beam phase space parameters after the charge state selection. The most sensitive parameter is a 6D vector of the beam position in the phase space downstream of the RFQ. The ECRIS itself has many parameters that are hidden or fluctuating during the operation. Therefore, the parameters of multi-component ion beams extracted from the ECRIS are also changing. To better understand the beam dynamics of the multi-component ion beams, we have developed a 3D computer model of the ECRIS and beam transport line. The extraction of the ion beams from the ion source is simulated using particle tracking in the CST Particle Studio [11] and TRACK code [12], taking into account the 3D fields of the ECRIS and assuming that the plasma is neutral. After the extraction, the multi-component ion beam is simulated in TRACK, including 2D space charge particle-in-cell (PIC) calculations and charge neutralization. The neutralization factor and the plasma temperature were adjusted in the computer model to fit the Allison scanner emittance measurements of the

beam after the charge selector. Figure 3 shows the simulated and measured beam images after selecting a particular charge state of the xenon beam. The tuned model reproduces beam images well. The model can reproduce the phase space plots from the Allison scanner as well.

The focusing distance in the transport channel downstream of the ECR is a function of the charge-to-mass ratio. If the transport system is slightly misaligned, the 4D beam position of the ions of interest in the multi-component ion beam depends on the space-charge forces. It results in a change of the 6D beam position vector downstream of the RFQ. The beam energy and phase after the RFQ are sensitive to the beam transverse misalignment in the multi-harmonic buncher and the first accelerating cells of the RFQ. There is a correlation of the 6D beam vector downstream of the RFQ with the total ECRIS platform drain current even if the current of the ion of interest remains unchanged.

Currently, we are developing Machine Learning (ML) algorithms for the quick tuning of LEBT to maintain the beam vector in the MEFT close to the reference tune. The ECRIS-LEBT simulations and measurements will be used for the training of the ML algorithm.

## AUTO-START OF RESONATORS

FRIB consists of 324 SC and 8 Room Temperature (RT) resonators operating at five different frequencies. The stable operation of resonators is provided by the FRIB-developed digital Low-Level RF (LLRF) [13]. The operational experience shows that the peak-to-peak errors of the amplitudes and phases of RF fields are within  $\pm 0.2\%$  and  $\pm 0.1^\circ$  which are an order of magnitude less than the original specification. From the early stage of installation and RF conditioning of resonators, it was realized that the resonators could be taken to the nominal accelerating gradients by computer programs. The auto-start procedure programmed at the Input-Output Control (IOC) level reduces the resonator turn-on time to about 40 seconds and excludes possible human error. A typical sequence of events during the auto-start for a half-wave resonator (HWR) is shown in Fig. 4. Most HWRs experience multipacting after a warm up event and require conditioning. Now, this multipacting conditioning is also automated.

The auto-start procedure is especially beneficial for the high availability of the RFQ operating in CW mode since occasional sparking can occur, and fast recovery is required. The RFQ recovery from occasional sparks takes 3 seconds for the amplitude and 30 seconds for the phase. The cold start of the RFQ requires up to 45 minutes to the highest power level due to using of the cooling water flow for the frequency tuning.

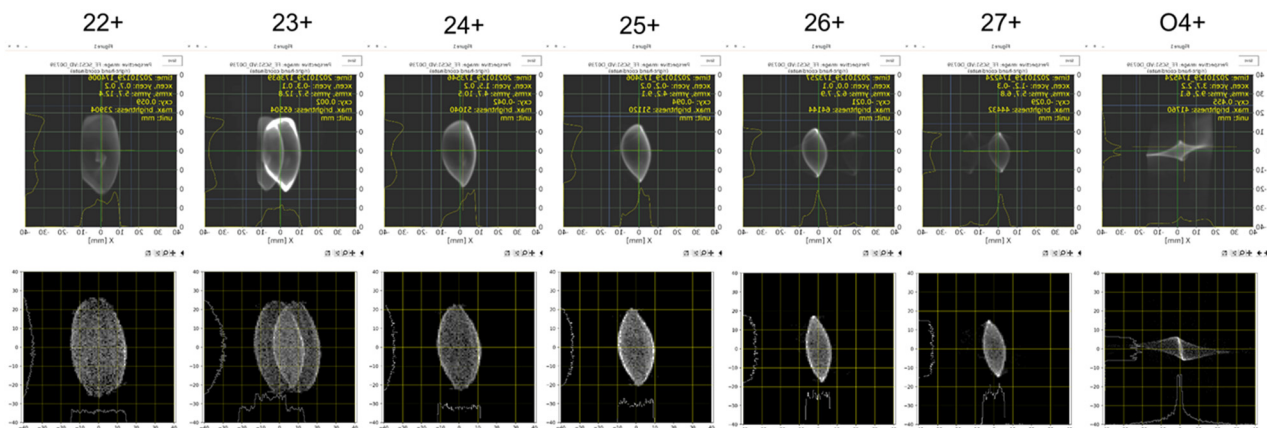


Figure 3: The measured (top) and simulated (bottom) xenon beam images and profiles on the viewer after the selection of particular charge state shown above the images.

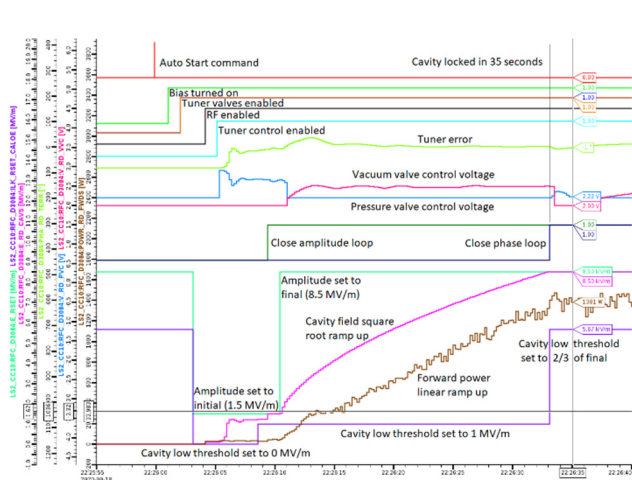


Figure 4: Time sequence of the RF, resonator and tuner events during the auto-start procedure.

## MODEL BASED BEAM STEERING CORRECTION

There are 144 Beam Position and Phase Monitors (BPM) and 127 correctors distributed along the linac. The orbit response matrix (ORM) method was applied previously for the beam steering correction in the first segment of the linac [7]. This method was based on the measured response matrix elements. This method works well but takes too much time for the measurements. Therefore, we have decided to use a response matrix calculated with the computer model of the linac. This approach also works well, and it is much faster. The model-based ORM method works best if it is applied to short sections of the linac containing 6-8 correctors and a slightly larger number of BPMs. In most cases, the second iteration is not required if the beam alignment goal is  $\pm 0.5$  mm. The second iteration may be necessary for longer linac sections due to misalignment of the beam optics devices and minor hysteresis in the superconducting (SC) dipole coils. Figure 5 shows the beam offset in horizontal and vertical directions in each BPM along the entire linac after completing of the  $^{86}\text{Kr}^{34+}$  beam acceleration to 212 MeV/u.

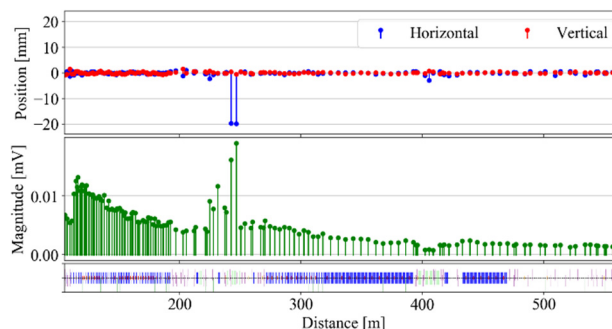


Figure 5: BPM readings along the linac after the completion of the  $^{86}\text{Kr}^{34+}$  beam steering correction. The large signals from the FS1 BPMs is related to the fact that the  $180^\circ$ -bend was intentionally tuned for charge state 33.5+.

## PHASE SCAN PROCEDURES

The phase scan procedure was applied to determine synchronous phases for SC resonators and bunchers. This procedure constitutes the measurement of the beam-induced signal in downstream BPMs as a function of the resonator RF field phase as described in ref. [7,8]. Since the auto-start of resonators became available, the phase scan procedure is also automated and can be applied to many cavities without human intervention. The phasing of short sections of the linac is alternated with the model-based beam steering correction to align beam with the accelerator axis.

The experiments with rare isotope beams are limited in time, just about a week or less. The FRIB linac should provide various primary beams at different energies, and shortening the accelerator setup time is critical to meet the requirements of the FRIB Users community. Using an automated phase scan procedure reduces the tuning time, but setting up a new velocity profile in the entire linac requires at least 15 hours.

Recently we developed and tested a model-based instant phase setting of the linac segments 1, 2, and 3. The coordinates of the resonators along the linac are well known from the alignment survey, and RF field distributions are available from the CST models. The accelerator model can calculate the optimal phase setting of all resonators for the required energy of the given ion species if the calibration data

Content from this work may be used under the terms of the CC BY 3.0 licence (© 2021). Any distribution of this work must maintain attribution to the author(s), title of the work, publisher, and DOI

is provided. The field level in the resonator is calibrated with the beam. The phase calibration data is generated using the standard phase scan procedure with the beam of known energy for each resonator and BPM. As a result of such calibration, a static phase shift in each RF line and BPM cable can be determined with respect to the RF reference clock. The model-based instant phase setting was applied to 88  $\beta_{opt} = 0.085$  quarter wave resonators (QWRs) in the Linac Segment 1. The calibration data was collected during the phase scan to set up 17 MeV/u  $^{86}\text{Kr}^{17+}$  beam. Then, the instant setting was applied in the same section to accelerate  $^{86}\text{Kr}^{17+}$  beam to 20 MeV/u. The instant phase setting procedure resulted in the same beam energy as in the case of the standard phase scan procedure. The synchronous phase difference in the cavities obtained by two phase setting methods is plotted in Fig. 6.

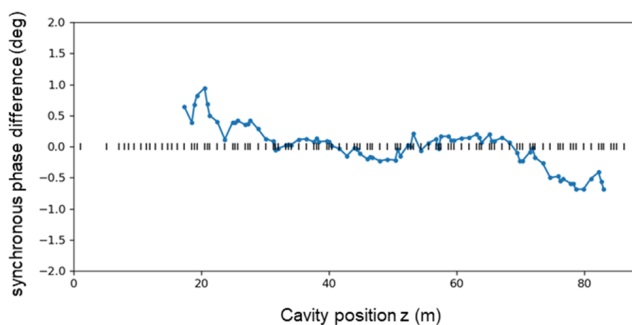


Figure 6: Synchronous phase difference between the standard phase scan procedure and instant phase setting in the LS1.

## LIQUID LITHIUM STRIPPER TESTING WITH BEAM

To achieve the design heavy ion beam energies above 200 MeV/u and beam power up to 400 kW, the FRIB linac requires a stripper at an intermediate energy of 17 MeV/u. The solid metal foils used previously for stripping heavy ions are easily damaged at the beam intensities required for the FRIB primary beams on the fragmentation target. To overcome the existing technical limitations associated with the stripping of high intensity heavy ion beams, FRIB developed and commissioned a liquid lithium stripper [14]. The charge stripper is based on molten liquid lithium film with a thickness of  $\sim 10\text{-}20\ \mu\text{m}$ , flowing at  $\sim 60\ \text{m/s}$  in the ultra-high vacuum environment. We experimentally confirmed that the windowless liquid lithium thin film could be used as a charge stripper by successfully running  $^{124}\text{Xe}^{26+}$ ,  $^{36}\text{Ar}^{10+}$ , and  $^{238}\text{U}^{36+}$  beams through the charge stripper. Figure 7 shows the charge state distributions of xenon and uranium beams after the liquid lithium stripper. The average charge state after the stripper was compared with the ETACHA4 [15] simulations. We found that the average charge state of xenon beam is  $\sim 2.6\%$  higher than ETACHA prediction, while the uranium average charge state is lower by  $0.7\%$  for incident beam energies of 17 MeV/u and 20 MeV/u.

## COMMISSIONING OF THE ENTIRE LINAC

On April 25, 2021, the FRIB accelerator became the highest energy continuous wave linear accelerator in the world after acceleration of  $^{86}\text{Kr}$  ion beam to 212 MeV per nucleon (MeV/u), achieving 100-percent beam transmission in less than three hours on the first attempt. Later, the  $^{124}\text{Xe}$  ion beam was accelerated to the same energy of 212 MeV/u. All 46 cryomodules with a total of 324 superconducting cavities were powered for the acceleration of ion beams. Successful beam commissioning of the FRIB linac validates operation of all accelerator systems per design specifications, including:

- FRIB's helium refrigeration system and cryogenic distribution system,
- All linac superconducting radiofrequency cryomodules and superconducting magnets operating at cryogenic temperatures below 4.5K,
- All linac normal conducting electromagnetic devices,
- Lithium and carbon charge strippers co-existing for enhanced availability.

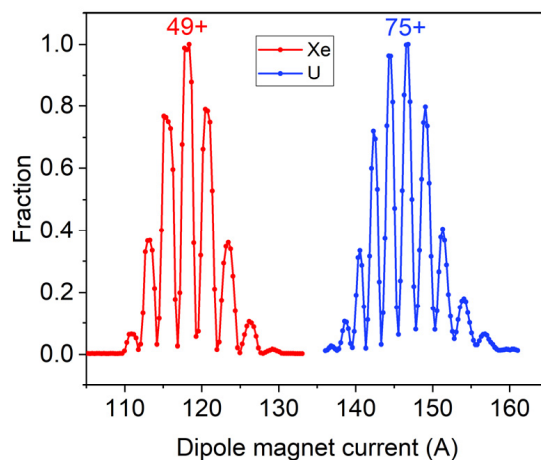


Figure 7: Xenon (red) and uranium (blue) charge state distributions after the liquid lithium stripper. The thickness is  $1.05\ \text{mg/cm}^2$  for the xenon and  $1.40\ \text{mg/cm}^2$  for uranium beams.

## CONCLUSION

The FRIB linac beam commissioning is complete, and various primary beams are available for rare isotope production for nuclear physics experiments. The beam commissioning of the fragment separator is scheduled for January 2022. The first Program Advisory Committee approved 34 experiments with nine different primary ion beams to be started in early 2022.

## ACKNOWLEDGEMENTS

The authors are grateful to the entire FRIB team for supporting the beam commissioning and achieving the project goals.

## REFERENCES

- [1] J. Wei *et al.*, “Advances of the FRIB project”, *International Journal of Modern Physics E*, vol. 28, no. 3, p. 1930003, 2019. doi:10.1142/S0218301319300030
- [2] Q. Zhao *et al.*, “FRIB Accelerator Beam Dynamics design and Challenges”, in *Proc. 54th ICFA Advanced Beam Dynamics Workshop on High-Intensity and High-Brightness Hadron Beams (HB'12)* Beijing, China, Sep. 2012, paper WEO3B01, pp. 404-408.
- [3] J. Wei *et al.*, “Accelerator Challenges of Hadron Linacs and the Facility for Rare Isotope Beams - Extending High Beam Power from Protons to Heavy Ions”, in *Proc. 54th ICFA Advanced Beam Dynamics Workshop on High-Intensity and High-Brightness Hadron Beams (HB'16)*, East-Lansing, MI, USA, paper MOZLR07, pp. 12-17.
- [4] M. Ikegami *et al.*, “Accelerator Physics Challenges in FRIB Driver Linac”, in *Proc. 57th ICFA Advanced Beam Dynamics Workshop on High-Intensity and High-Brightness Hadron Beams (HB'16)*, Malmö, Sweden, July 2016, paper MOPM1P80, pp. 27-30.  
doi:10.18429/JACoW-HB2016-MOPM1P80
- [5] Z. Liu *et al.*, “Collimation Design and Beam Loss Detection at FRIB”, in *Proc. 57th ICFA Advanced Beam Dynamics Workshop on High-Intensity and High-Brightness Hadron Beams (HB'16)*, Malmö, Sweden, July 2016, paper WEPM8X01, pp. 400-403.  
doi:10.18429/JACoW-HB2016-WEPM8X01.
- [6] E. Pozdeyev *et al.*, “FRIB Front End Construction and Commissioning”, in *Proc. 9th International Particle Accelerator Conference (IPAC'18)*, Vancouver, BC, Canada, April 2018, pp. 58-62.  
doi:10.18429/JACoW-IPAC2018-M0ZGBF1
- [7] P.N. Ostroumov *et al.*, “Beam commissioning in the first superconducting segment of the Facility for Rare Isotope Beams”. *Phys. Rev. Accel. Beams*, vol. 22, p. 080101, Aug. 2019. doi:10.1103/PhysRevAccelBeams.22.080101
- [8] P.N. Ostroumov, M. Hausmann, K. Fukushima, T. Maruta, A.S. Plastun, M. Portillo, J. Wei, T. Zhang, Q. Zhao, “Heavy ion beam physics at Facility for Rare Isotope Beams”, *Journal of Instrumentation*, vol. 15, p. P12034, 2020.  
doi: 10.1088/1748-0221/15/12/p12034.
- [9] P. N. Ostroumov, K. Fukushima, T. Maruta, A. S. Plastun, J. Wei, T. Zhang, and Q. Zhao, “First Simultaneous Acceleration of Multiple Charge States of Heavy Ion Beams in a Large-Scale Superconducting Linear Accelerator”, *Phys. Rev. Lett.*, vol. 126, p. 114801, 2021.  
doi:10.1103/PhysRevLett.126.114801
- [10] T. Xu *et al.*, “Completion of FRIB Superconducting Linac and Phased Beam Commissioning”, presented at SRF'21, East Lansing, MI, USA, Jun.28-Jul. 2, 2021, paper MOO-FAV10, to be published.
- [11] CST Studio Suite, <http://www.cst.com/>.
- [12] P.N. Ostroumov, V.N. Aseev and B. Mustapha, “TRACK – a code for beam dynamics simulations in accelerators and transport lines with 3D electric and magnetic fields”, 2007. [https://www.phy.anl.gov/atlas/TRACK/Trackv39/Manuals/tv39\\_man\\_index.html](https://www.phy.anl.gov/atlas/TRACK/Trackv39/Manuals/tv39_man_index.html)
- [13] S. Zhao *et al.*, “The LLRF Control Design and Validation at FRIB”, in *Proc. NA-PAC'19*, Lansing, MI, USA, Sep. 2019, pp. 667-669.  
doi:10.18429/JACoW-NAPAC2019-WEPLM03
- [14] T. Kanemura, J. Gao, R. Madendorp, F. Marti, Y. Momozaki, M.J. LaVere, “Progress of Liquid Lithium Stripper for FRIB”, in *Proc. NA-PAC'19*, Lansing, MI, USA., Sep. 2019, p. 636.  
doi:10.18429/JACoW-NAPAC2019-WEYBB4
- [15] E. Lamour *et al.*, “Extension of charge-state-distribution calculations for ion-solid collisions towards low velocities and many-electron ions”, *Physical Review A*, vol. 92, p. 042703, 2015. doi:10.1103/PhysRevA.92.042703

# BEAM INSTABILITY ISSUE AND TRANSVERSE FEEDBACK SYSTEM IN THE MR OF J-PARC\*

T. Toyama<sup>†1</sup>, A. Kobayashi<sup>1</sup>, T. Nakamura<sup>1</sup>, M. Okada<sup>1</sup>, Y. Shobuda<sup>2</sup> and M. Tobiyama<sup>3</sup>,  
 Accelerator division, J-PARC Center, <sup>1</sup>KEK / <sup>2</sup>JAEA, Tokai, Ibaraki, Japan  
<sup>3</sup>Accelerator division, KEK, Tsukuba, Ibaraki, Japan

## Abstract

In the J-PARC MR, according to the beam power upgrade over 100 kW, beam losses due to transverse collective beam instabilities had started to appear. We had introduced "bunch-by-bunch feedback" system in 2010. Continuing beam power upgrade over 250 kW again caused the transverse instabilities. We introduced "intra-bunch feedback" system in 2014. This has been suppressing those instabilities very effectively. But further beam power upgrade over 500 kW (2.6E+14 ppp, 8 bunches) needs upgrade of "intra-bunch feedback" system. The current understanding of the transverse instabilities in the MR and the effect of the feedback system are presented from the view points of simplified simulation without the space charge effect and measurements. We are upgrading the system in two steps. The first step is "time-interleaved sampling and kicking" with two feedback systems. The second step is getting the sampling rate twice as much as the current rate, ~110 MHz. Details are explained using simulation.

## INTRODUCTION

Figure 1 is the layout of the accelerators in J-PARC. The Main Ring (MR) accelerates 8 proton bunches from 3 GeV to 30 GeV [1]. Figure 2 shows beam power history from January 2010 to April 2021. We have two acceleration modes, a slow extraction mode and a fast extraction mode. In the slow extraction mode (Fig. 3, [2]), the beam power is about 64 kW, the beam intensity is 7E+13 protons in a current MR cycling time 5.2 seconds. In the fast extraction mode (Fig. 4), the beam power is about 500 kW, the beam intensity is 2.6E+14 protons in a current MR cycling time 2.48 seconds

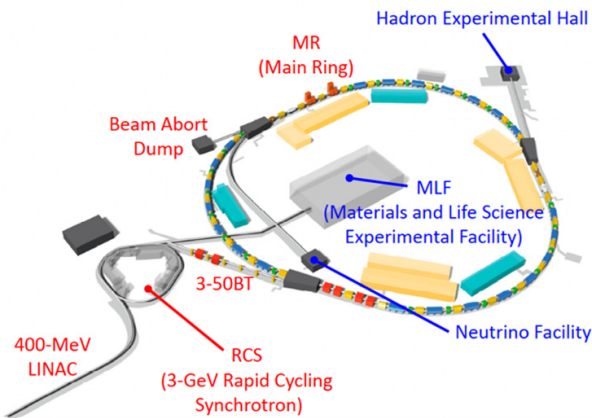


Figure 1: Schematic layout of J-PARC accelerators and experimental facilities.

<sup>†</sup> takeshi.toyama@kek.jp

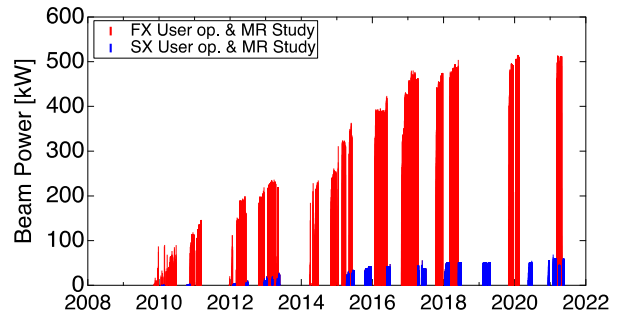


Figure 2: Beam power history of the MR.

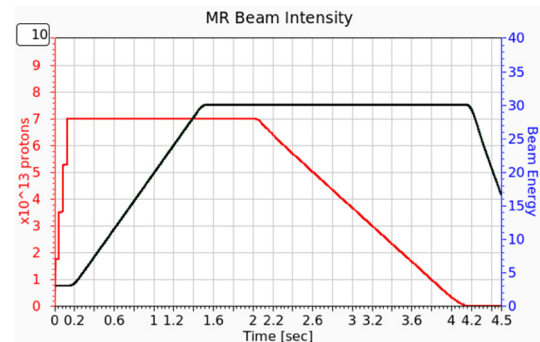


Figure 3: Slow extraction.

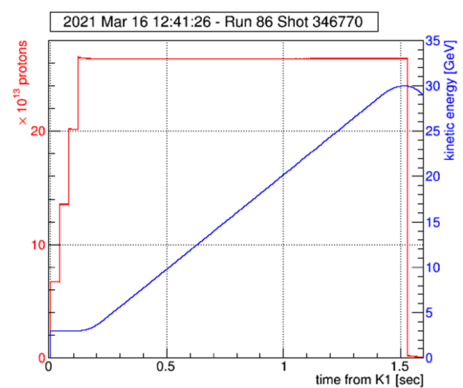


Figure 4: Fast extraction.

## PRESENT OBSERVATIONS IN THE MR

### SX Mode

In the SX mode, a bunch-by-bunch feedback system is sufficient to suppress instabilities. Limiting factor to increase the SX beam power is the beam instabilities in debunching process at the 30 GeV flat top [2]. In debunching process at the 30 GeV flat top, longitudinal microwave instability occurs, then electron cloud build-up, transverse

Content from this work may be used under the terms of the CC BY 3.0 licence (© 2021). Any distribution of this work must maintain attribution to the author(s), title of the work, publisher, and DOI

instability, vacuum pressure-rise and beam loss occur at the same time.

The example of an electron cloud event and related topics are also presented by Tomizawa [2] in this workshop. Causality of the phenomena, i.e. the electron cloud build-up and transverse instability, are not yet clear because there are a few events without electron cloud signal. The beam power is set as high as possible with several countermeasure, such as RF manipulations. Current operation is a result of compromise between user requirement for higher beam power and effectiveness of the countermeasure.

### FX Mode

In the FX mode, transverse (horizontal/vertical) intra-bunch feedback system is an essential ingredient. Another essential ingredient is horizontal and vertical chromaticities. Figure 5 shows the operating point and estimated incoherent tune spread [1].

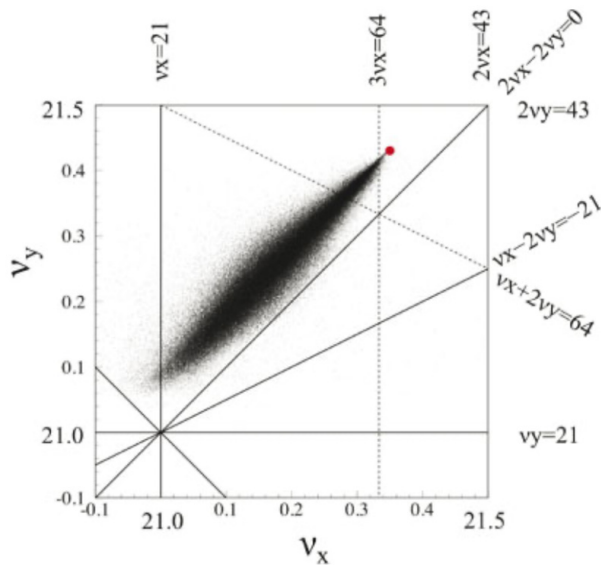


Figure 5: Incoherent tune spread in the MR.

## TRANSVERSE INTRA-BUNCH FEEDBACK

Figure 6 is the block diagram of the intra-bunch feedback system in the J-PARC MR [3]. The signal detected with the stripline BPM is fed to the iGp12H [4], a processing circuit, then amplified and fed to the kicker. The system bandwidth is determined by the processing clock of 64 multiple of the RF frequency, that is, 107 - 110 MHz. Simplified signal flow is shown in Fig. 7. Beam bunch is coloured with black. The intra-bunch position is sampled with the processing clock, filtered with FPGA, amplified, then fed to the corresponding position in the bunch, but one-turns later. The four-turns signals are processed at each feedback cycle.

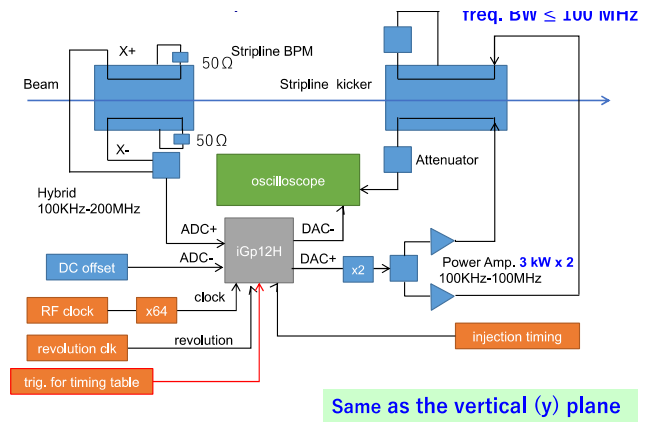


Figure 6: Block diagram of the transverse intra-bunch feedback system in the J-PARC MR.

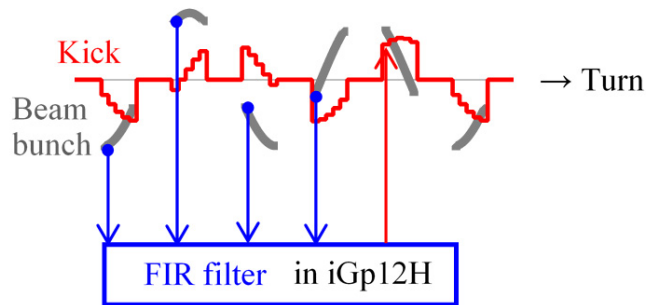


Figure 7: Simplified signal flow. Signal flow from blue dots to a red arrow tip is one feedback loop. This kind of process is performed in each bunch slice.

## STABILITY OF THE MR BEAM

Using this feedback system, several dedicated beam experiments were performed. We can store the bunches with the transverse intra-bunch feedback on and keep them stable without instabilities. When we switched off the feedback of a desired plane at a desired timing, the beam becomes unstable.

### Vertical Instability

Examples are shown as spectrograms of transverse oscillation in Figs. 8 and 9. Single bunch case is in Figs. 8 and 3 bunches case in Fig. 9. Chromaticities are nearly zero. Precise values are  $v_x = \Delta v_x / (\Delta p/p) = 0.56$  and  $v_y = -0.37$ . The feedback is switched off at the timing indicated by dashed lines in the figures. First unstable motion occurred in the vertical plane.

We examined the effect of space charge with changing the bunching factor from 0.3 to 0.17. The results (Figs. 10 and 11) are that a beam with smaller bunching factor, i.e. larger peak current case, is more stable.

Content from this work may be used under the terms of the CC BY 3.0 licence (© 2021). Any distribution of this work must maintain attribution to the author(s), title of the work, publisher, and DOI

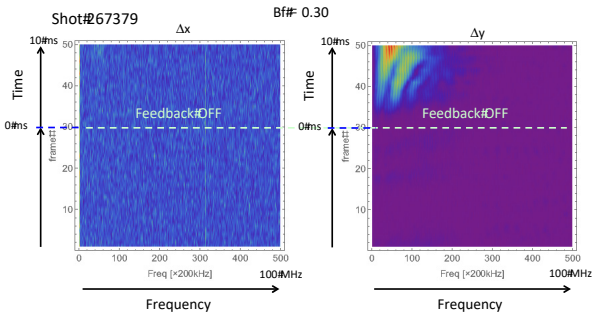


Figure 8: Stability of the single bunch with the number of protons,  $7e+12$ .

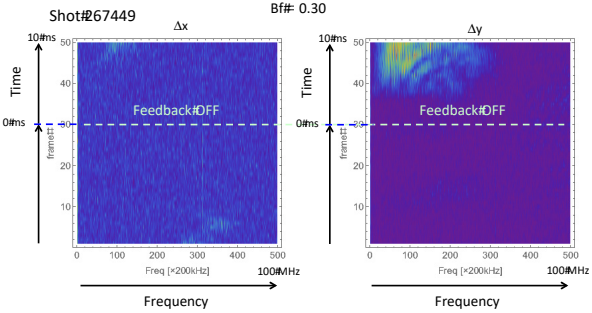


Figure 9: Stability of the three bunches stored symmetrically in the MR with the total number of protons,  $2.8e+13$ .

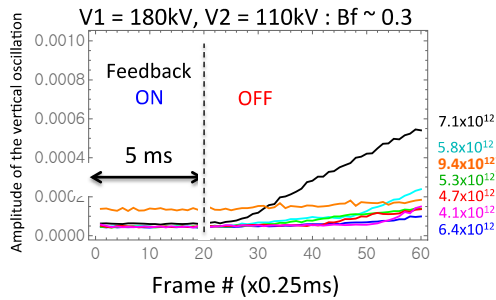


Figure 10: Vertical instability with single bunch,  $B_f \sim 0.3$ .

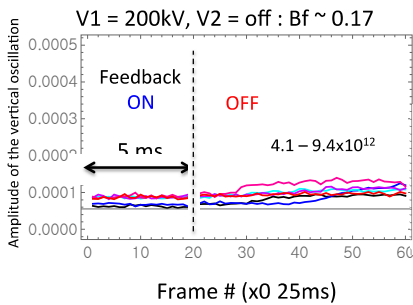


Figure 11: Vertical instability with single bunch,  $B_f \sim 0.17$ .

Closer look into the intra-bunch motion shows at the larger bunching factor 0.3, the mode seems 1, and growing steadily (Fig. 12). On the other hand, at the smaller bunching factor 0.17, the mode seems higher, and the instability grows and damps (Fig. 13).

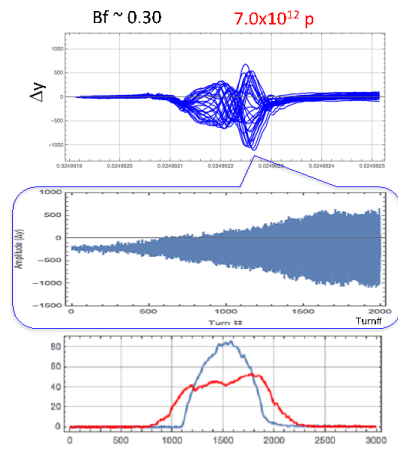


Figure 12: Intra-bunch motion with  $B_f \sim 0.3$ . Top plot shows an overlap of vertical intra-bunch position signals. Middle plot shows the growth of the maximum amplitude timing. Bottom plot shows longitudinal bunch profiles at injection (indigo line) and equilibrium (red line).

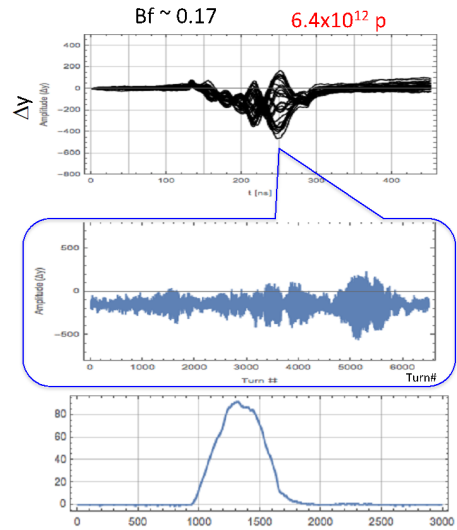


Figure 13: Intra-bunch motion with  $B_f \sim 0.17$ . The meaning of the plots is the same as Fig. 12.

With three bunches stored symmetrically in the ring, same tendency was observed. The growth rate with  $B_f \sim 0.3$  increases as the bunch intensity gets larger as shown in Fig. 14. When  $B_f \sim 0.17$ , the beam is stable even at the highest intensity in the case of  $B_f \sim 0.3$  (Fig. 15).

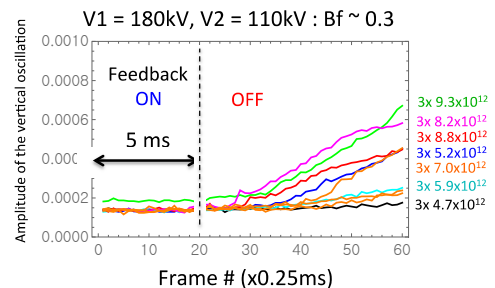


Figure 14: Vertical instability with 3 bunches,  $B_f \sim 0.3$ .

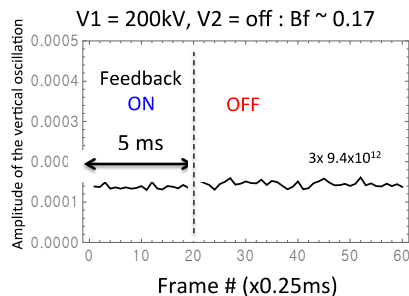


Figure 15: Vertical instability with 3 bunches,  $B_f \sim 0.17$ .

Chromaticity effects is summarized in [5]. The internal oscillation mode is 0 in a slightly positive chromaticity, while in a slightly negative chromaticity, the mode is more than 1, as the theory predicts. In a positive chromaticity clear coupled bunch oscillation was observed.

### Horizontal Instability

With the parameters of a routine operation of 500 kW beam power, we measured growth rates at several intensities, with switching only the horizontal feedback off after 8 bunches were stored in the MR. After feedback is switched off, the horizontal instability occurs (Fig. 16), then the beam touches the vacuum chamber, and beam loss occurs (Fig. 17). The aim was rather getting practical information for the operation.

The result is plotted in Fig. 18 with blue dots and dashed line. The maximum growth rate in the case of nearly full corrected chromaticity is indicated with red dashed line. The growth rate scatters even at the same intensity. The reason is not yet clear. The present operation is at almost a limit of feedback ability, that is, with any optimization attempts almost no stable operation has been achieved at higher beam power. Damping ability should be strengthened almost 50 % more to reach the beam power of 1.3 MW.

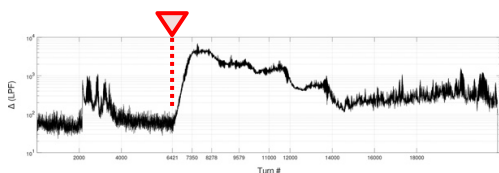


Figure 16: Example of the growth rate. Indicated with the red dashed line.

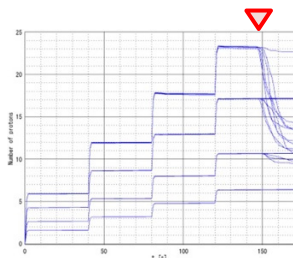


Figure 17: Beam intensity variation. Several shots are overlapped. At the timing indicated with the red triangle beam losses start. Growth rates are estimated using data before this loss timing.

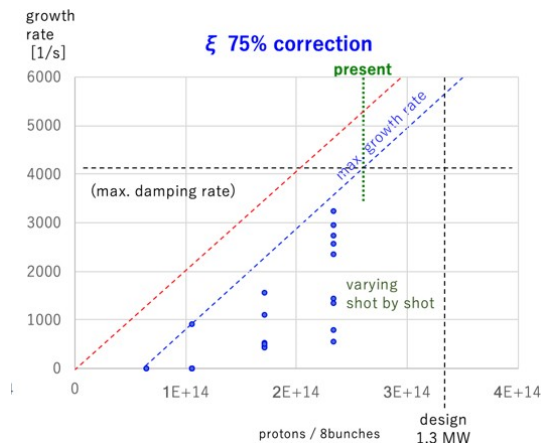


Figure 18: Growth rates with 8 bunches. A red dashed line indicates maximum growth rates with about ten shots in the case of 95% chromaticity correction. Blue dots and dashed lines indicate in the case of 75% chromaticity correction.

## SIMULATION

We simulated the instability discretizing with a triangular distribution [6]. Plots in Fig. 19 are wake potentials of the resistive wall (a left plot) and the FX kickers (a right plot). Main purpose of this simulation is examining the stability of the feedback system.

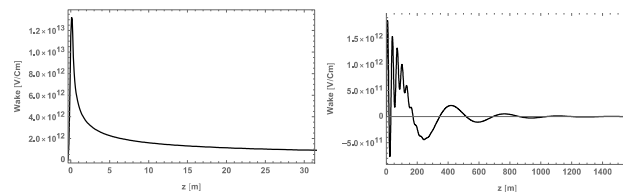


Figure 19: Wake potentials used in the simulation.

Figure 20 is an example of the simulation at the chromaticity -1. The simulation starts with uniform dipole injection error. This mode is stabilized, then mode 1 intra-bunch motion occurs.

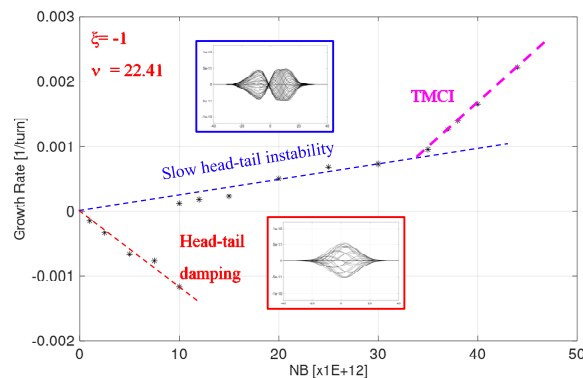


Figure 20: Simulated instability.

With several rates of processing clock, beam stabilities are calculated with the intra-bunch feedback. In this case the chromaticity was set to zero. Raising the rates of the processing clock makes the beam more stable (Fig. 21). This direction is the goal of upgrade plans.

Content from this work may be used under the terms of the CC BY 3.0 licence (© 2021). Any distribution of this work must maintain attribution to the author(s), title of the work, publisher, and DOI

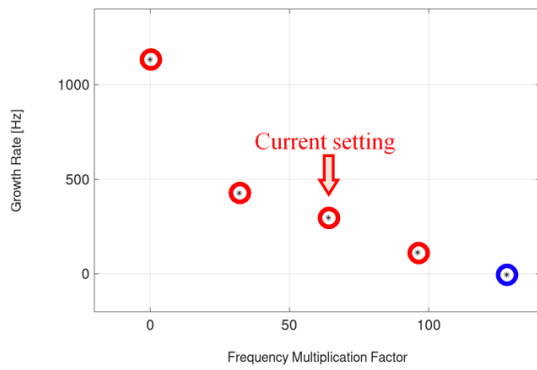


Figure 21: Growth rate variation with various processing clock rates. Clock rate is a multiplication factor times  $f_{RF}$ , 1.67 – 1.72 MHz.

Examining the intra-bunch oscillation, stabilizing occurs at certain positions and in other positions bunch becomes unstable (Fig. 22). This is because the optimum feedback is only possible at the sampling time and motion at the other timing is not optimum. In a measurement, similar signals are obtained (Fig. 23).

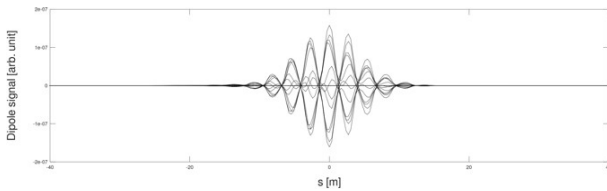


Figure 22: Simulated dipole signals, overlap of 13 turns with the processing clock of 64 multiple of  $f_{RF}$ .

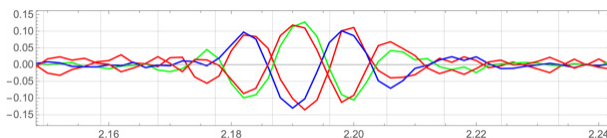


Figure 23: Measured dipole signals, overlap of 3 turns, suggesting stable and unstable points along the bunch caused by the processing clock.

Then we came up with the following idea. Fortunately, we have two feedback systems (Fig. 24) due to a historical reason. Shifting the processing clock by a half clock each other (Fig. 25), we call it "time interleaved sampling and kicking", the stability may get better. The result of the simulation (Fig. 26) supports this possibility. This is an intermediate plan of the feedback improvement for beam power upgrade.

### SUMMARY

Present knowledge on the transverse instabilities in the J-PARC MR is reviewed: (1) vertical plane is more unstable than the horizontal, which is reasonable considering vacuum duct geometry, (2) resistive wall seems dominant source, then kickers, more precisely under study, (3) space charge instability suppression is observed.

The intra-bunch feedback system works well up to the beam power ~ 500 kW. Above 500 kW some improvements of the feedback are necessary: (1) time interleaved

sampling and kicking with the current processing frequency,  $64 \times f_{RF}$  (or slightly higher  $96 \times f_{RF}$ ), (2) doubling the processing clock frequency from  $64 \times f_{RF}$  to  $128 \times f_{RF}$ .

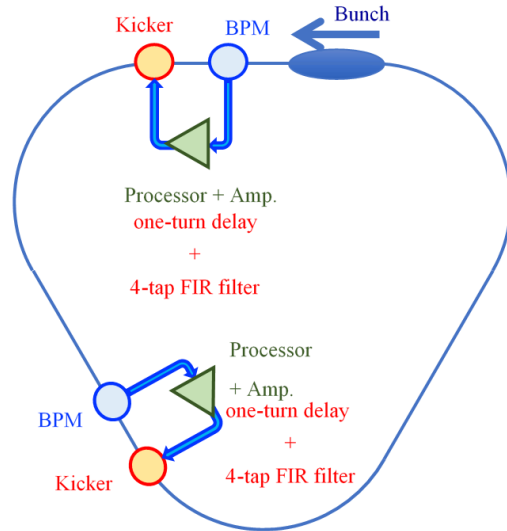


Figure 24: Two feedback systems in the MR.

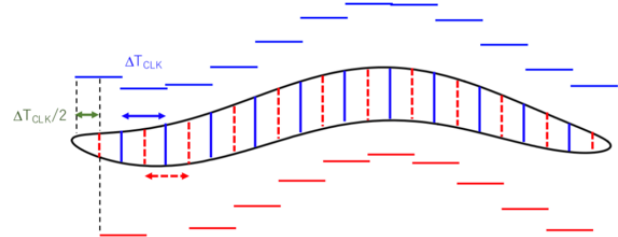


Figure 25: Sampling timings of the two systems, shifted by  $\Delta T_{CLK}/2$ .

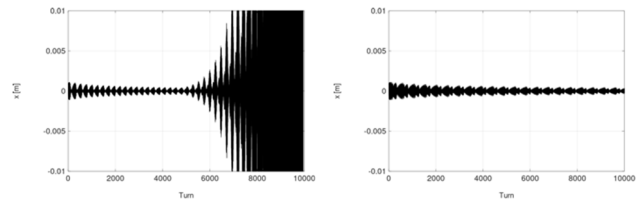


Figure 26: Simulated results w/o and with the time interleaved sampling and kicking by two feedback system. Left: the same timing Right: interleaved sampling and kicking with  $\Delta T_{CLK}/2$  shift.

### ACKNOWLEDGEMENTS

We gratefully acknowledge Y. H. Chin, T. Obina, K. Nakamura, Y. Kurimoto, S. Hiramatsu for their important contribution in an earlier stage of this project, D. Teytelman for his supply of the key instruments, iGp12H, and his subsequent adjustments of the instrument. The author got useful comments and data from R. Muto, Y. Sato and M. Tomizawa in the preparatory stage of this presentation.

### REFERENCES

- [1] S. Igarashi *et al.*, "Accelerator design for 1.3-MW beam power operation of the J-PARC Main Ring", *Prog. Theor. Exp. Phys.*, vol. 2021, p. 033G01, 2021. doi:10.1093/ptep/ptab011

- [2] M. Tomizawa *et al.*, “Slow Extraction Operation at J-PARC Main Ring”, presented at HB’21, Batavia, IL, USA, paper THDC1, this conference.
- [3] K. Nakamura *et al.*, “Transverse Intra-bunch Feedback in the J-PARC MR”, in *Proc. 5th Int. Particle Accelerator Conf. (IPAC’14)*, Dresden, Germany, Jun. 2014, pp. 2786-2788. doi:10.18429/JACoW-IPAC2014-THOAA03
- [4] Dimtel Inc., <https://www.dimtel.com/>
- [5] A. Kobayashi *et al.*, “Study of the transverse beam instability caused by the resistive-wall impedance at the J-PARC main ring”, in *Proceedings of the 17th Annual Meeting of Particle Accelerator Society of Japan*, September 2 - 4, 2020, pp. 684 – 688.
- [6] G. Sabbi, “Simulation of single-bunch collective effects in LEP by linear expansion of the distribution moments”, CERN, Geneva, Switzerland, CERN SL/95-25 (AP), 1995.

# EXPLORING QUASI-INTEGRABLE OPTICS WITH THE IBEX PAUL TRAP

J. A. D. Flowerdew\*, S. L. Sheehy, University of Oxford, Oxford, UK  
 D. J. Kelliher, S. Machida, STFC Rutherford Appleton Laboratory, Oxford, UK

## Abstract

An ideal accelerator built from linear components will exhibit bounded and stable particle motion. However, in reality, any imperfections in the magnetic field strength or slight misalignments of components can introduce chaotic and unstable particle motion. All accelerators are prone to these non-linearities but the effects are amplified when studying high intensity particle beams with the presence of space charge effects. This work aims to explore the non-linearities which arise in high intensity particle beams using a scaled experiment called IBEX. The IBEX experiment is a linear Paul trap which allows the transverse dynamics of a collection of trapped particles to be studied. It does this by mimicking the propagation through multiple quadrupole lattice periods whilst remaining stationary in the laboratory frame. IBEX is currently undergoing a nonlinear upgrade with the goal of investigating Quasi-Integrable Optics (QIO), a form of Nonlinear Integrable Optics (NIO), in order to improve our understanding and utilisation of high intensity particle beams.

## INTRODUCTION

When designing new particle accelerators, constructing test accelerators can be costly in terms of both financial expense and energy consumption. Once an accelerator is built, it is often difficult to change the lattice structure and thus it is impractical to investigate beam properties over large parameter spaces. Therefore, research and development of accelerator lattices are often performed using simulations. Simulations are a vital part of the accelerator design process, however they struggle to reproduce the intricate physics of the many-body Coulomb interactions (space charge forces) over long timescales (tens of thousands of turns) and can never be a replacement for experimental verification.

These challenges led to the design and construction of linear Paul traps to investigate transverse beam dynamics more efficiently at Hiroshima University, Japan [1], Princeton University, US [2] and, most recently, the Intense Beams Experiment (IBEX), at the Rutherford Appleton Laboratories (RAL), UK [3]. IBEX is a table-top sized experiment that can replicate the transverse betatron motion in alternating gradient accelerators in a dispersion- and chromaticity-free environment.

This paper aims to test a lattice proposed by the theory of Nonlinear Integrable Optics (NIO) by exciting a 4th order resonance and measuring particle loss and phase space evolution. Two different octupole potentials are compared; a normal square wave octupole and an octupole with a strength that scales with the beta function to make the Hamiltonian

time-independent. The time-independent Hamiltonian becomes an invariant of motion and therefore creates a quasi-integrable lattice that should be robust to small perturbations.

## THE IBEX PAUL TRAP

The current IBEX trap consists of four stainless steel cylindrical rods and two sets of end caps, each made from four shorter cylinders as seen in the ionisation region of Fig. 1. Argon gas is introduced into the trap via a VAT Series 59 variable leak valve and is ionised with an electron gun. Typically, a sinusoidal RF voltage is applied to the central rods with a maximum peak-to-peak of 300 V and frequency of 1 MHz. Voltages of the same form but opposite polarity are applied to the blue and red outlined rods in Fig. 1 to provide transverse confinement of the ions. A sinusoidal voltage replicates a simple FODO lattice, although it is possible to create more complex lattices in IBEX. Longitudinal confinement of the ions is achieved by applying a DC offset to the end caps.

Adjusting the peak voltage applied to the rods is analogous to changing the quadrupole strength in an accelerator, which in turn changes the betatron tune in both the horizontal and vertical planes. Thus, scanning the rod voltage allows for a wide range of tunes to be scanned over in a short period of time. This is impractical in conventional accelerators and when studying space charge dominated beams over long timescales, it is also impractical to use simulations. Ions can be stored for around 1 s in IBEX, corresponding to  $10^6$  RF periods. The DC voltage on the end cap is then dropped and the ions are directed onto a Micro-Channel Plate (MCP) or Faraday Cup (FC) detector. The number of ions stored in the trap is controlled by adjusting the length of time that the electron gun is on. This allows for a wide range of intensities to be studied within the trap. Due to the low energy of the ions ( $< 1$  eV), high intensity beam loss studies can be carried out in the trap without damaging or activating components. IBEX has already been used to study coherent and incoherent resonances at high intensities [4].

## NONLINEAR UPGRADE TO IBEX

In IBEX's current quadrupolar rod configuration it is only possible to study linear lattice designs. Thus, in order to investigate QIO and NIO, a nonlinear upgrade to IBEX is required. The upgrade will duplicate the linear trap but will also include the addition of four plate electrodes positioned between the rods (shown in Fig. 1 side view). Grounding the four cylindrical rods whilst applying an equal voltage to all four plate electrodes will allow for octupole fields to be realised in the trap. Grounding the four plates while applying voltages of opposite polarity to the red and blue outlined rods will continue to create a quadrupole field. The additional

\* jake.flowerdew@physics.ox.ac.uk

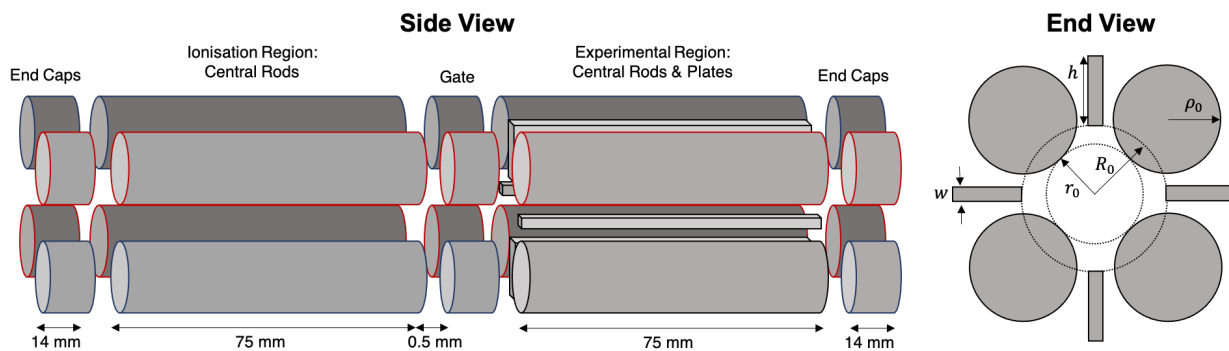


Figure 1: Schematic of the IBEX trap (ionisation region) and nonlinear upgrade (addition of experimental region). Opposing RF voltages are applied to the red and blue outlined rods for transverse confinement of ions. A DC voltage is applied to the end caps and gate electrodes to provide longitudinal trapping. In IBEX  $r_0 = 5$  mm and  $\rho_0 = 5.75$  mm. Four additional plates between the rods are present in the nonlinear trap at an inscribed radius of  $R_0$  to enable the creation of octupole fields.

electrodes will affect the quadrupole field quality within the trap, thus it is important to minimise these effects to ensure the upgrade has minimal impact on ion confinement.

The scalar potential  $\phi$  of the trapping field can be expressed as a sum of multipoles

$$\phi(r, \theta) = \sum_{n=1}^{\infty} c_n \left(\frac{r}{r_0}\right)^n \cos(n\theta). \quad (1)$$

The multipole coefficients  $c_n$  are calculated by evaluating  $\phi$  along the circumference of a circle within the trap aperture and taking the Fast Fourier Transform (FFT) of the solutions. The quadrupolar focusing potential in Eq. (1) corresponds to the  $c_2$  coefficient which will be the dominant term in the multipole expansion of the quadrupole field. Due to the symmetry of the trap, in the ideal case, only every fourth harmonic will be excited; the next two terms will thus be  $c_6$  (12-pole) and  $c_{10}$  (20-pole).

The width  $w$  and inscribed radius of the plates,  $R_0$  were optimised to reduce the  $c_6$  (12-pole) component of the quadrupole field in the experimental region. The results agree well with a previous study at Hiroshima University which found the optimum values to be  $R_0 = 8.5$  mm and  $w = 1$  mm [5]. With these values and perfect electrode alignment, the  $c_6$  component was found to be completely eliminated. The alignment tolerances of the new trap will be within  $10 \mu\text{m}$  to further reduce unwanted nonlinearities.

Argon gas will now be ionised and trapped in the linear ionisation region before being transported to the nonlinear experimental region of the trap (Fig. 1). Ions will then be stored in this region of the trap for the desired length of time before the end cap voltage is removed and the ions are detected on an MCP and phosphor screen. The current incident on the phosphor screen can be read out to get an ion count, or it can also be operated in a mode where the phosphor screen fluorescence is captured by a CCD camera to create an integrated image of the ion distribution. With this upgrade to the trap we hope to be able to test the proposed nonlinear, integrable lattices [6, 7].

## NONLINEAR INTEGRABLE OPTICS

Accelerators are mainly built from linear elements such as dipole and quadrupole magnets. Assuming no coupling between the horizontal and vertical particle motion, an ideal linear lattice is fully integrable. In other words, the Hamiltonian associated with a single particle is time-independent and can be separated into two invariants of motion. However, in reality these linear lattices are susceptible to perturbations, and so components such as sextupoles and octupoles are often used to apply higher order corrections. In general, the addition of these nonlinear components creates a non-integrable system, which limits the available area of phase-space where the particle motion is non-chaotic. Therefore, it is desirable to design a lattice which includes nonlinear components in such a way that it remains integrable. If an integrable, nonlinear lattice exists, then the system will always be close to an integrable solution, even when effects such as magnet misalignment and space charge are included.

The theory of NIO was laid out in 2010 by Danilov and Nagaitsev [6] in which they proposed an integrable, nonlinear lattice consisting of a linear T-insert and a drift region for a nonlinear magnet insert. The three conditions of the T-insert lattice are 1.  $n\pi$  (where  $n$  is an integer) phase advance over the linear section to provide quasi-periodic motion through the nonlinear region. 2. Equal beta functions in the nonlinear insert drift region ( $\beta_x = \beta_y$ ). 3. For Quasi-Integrable optics, the octupole strength will scale with  $1/\beta^3(s)$ .

Along with the conditions for integrability, the lattice is also constrained by the experimental set up of IBEX. The maximum beta function needs to be kept below around 1500 m to reduce scraping on the rods. The maximum voltage that can be applied to the rods is 150 V and the maximum voltage that can be applied to the plates is 500 V. The shortest voltage pulse duration is limited by the slew rate of the custom made high voltage amplifiers which is expected to be around  $1750 \text{ V}/\mu\text{s}$ . The beta functions are plotted for a T-insert lattice designed for IBEX in Fig. 2. The lattice length of  $s = 890$  m corresponds to a lattice time period of

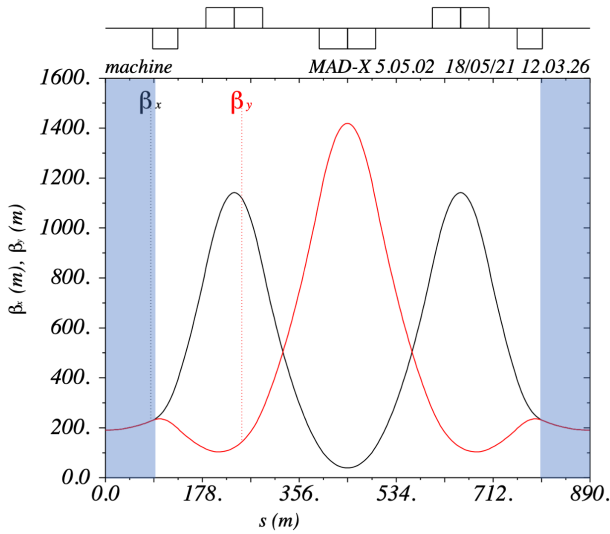


Figure 2: Beta functions of the T-insert lattice designed for the IBEX trap. Blue shaded region is the drift region for the nonlinear insert.

$T = s/c = 2.966 \mu\text{s}$  in IBEX, where we assume a particle bunch traveling at the speed of light,  $c$ .

The Integrable Optics Test Accelerator (IOTA), Fermilab [8] will test the fully integrable solution, which requires a complex elliptical potential in the nonlinear insert region. However, the elliptical potential is a challenge to create experimentally. Therefore, IBEX will first test the quasi-integrable case, which uses an octupole potential of the form

$$V(x, y, s) = \frac{\kappa}{\beta^3(s)} \left( \frac{x^4}{4} + \frac{y^4}{4} - \frac{3x^2y^2}{2} \right), \quad (2)$$

where  $\kappa$  is a constant and  $\kappa/\beta^3(s)$  defines the strength of the octupole field. Assuming equal beta functions in the horizontal and vertical direction ( $\beta_x(s) = \beta_y(s) = \beta(s)$ ), the octupole potential creates the time-independent Hamiltonian

$$H_N = \frac{p_{xN}^2 + p_{yN}^2}{2} + \frac{x_N^2 + y_N^2}{2} + U(x_N, y_N) \quad (3)$$

where  $U(x_N, y_N) = \beta(s)V(x, y, s)$  and the coordinate transform,  $z_N = z/\sqrt{\beta(s)}$  is used. The time-independent Hamiltonian becomes an integrable of motion, creating a quasi-integrable lattice which should be robust to small perturbations. In this work, the T-insert lattice was tested by applying an octupole perturbation, with and without applying an octupole field in the nonlinear insert, and measuring the particle loss and transverse phase space distribution.

## SIMULATION RESULTS

Previous work has shown that resonances driven by a small quadrupole perturbation are damped in a T-insert lattice with octupole insert [9]. In this paper, VSim 11 was used to simulate an octupole perturbation applied to the T-insert lattice in order to excite the 4th order resonance. Figure 3 plots the voltage waveform applied to the rods in IBEX to

create the beta functions of the T-insert shown in Fig. 2. The blue waveform corresponds to the voltage applied to one pair of opposing rods and the red waveform corresponds to a voltage, which is equal and opposite in magnitude, applied to the other pair of rods. The octupole perturbation is plotted as the black dashed line and corresponds to a sinusoidal voltage of  $V = A \sin(4 \cdot 2\pi Q/T)$  applied to the plates where  $A = 5.88 \text{ V}$  is the amplitude of the perturbation,  $Q = 0.6356$  is the horizontal and vertical tune of the lattice and  $T = 2.966 \mu\text{s}$  is the lattice time period. In the left plot of Fig. 3, no octupole is applied in the nonlinear insert region, only the octupole perturbation is present (black dashed). In the center plot of Fig. 3, a constant octupole field is applied in the nonlinear insert (green) in the presence of the octupole perturbation. As the octupole strength does not vary with the beta function, this lattice is no longer time independent and is non-integrable. The right plot of Fig. 3 shows the quasi-integrable lattice, where an octupole scaling as  $1/\beta^3(s)$  is applied in the nonlinear region of the perturbed T-insert lattice (black, solid).

A 2D Gaussian distribution of 25,865 particles was tracked in a VSim 11 model of IBEX for 200 T-insert lattice periods. A low number of particles was chosen to avoid space charge effects in these simulations. Figure 4 shows the initial phase space ( $x, x'$ ) of the particle distribution as well as the phase space after 50, 100 and 200 turns for the T-insert lattice with octupole perturbation but no octupoles turned on in the nonlinear insert (Fig. 3, left). The four tails forming in the phase space distribution show that the 4th order resonance is being excited by the octupole perturbation. Over the 200 lattice periods, 25.6% of particles were lost in the simulation.

Figure 5 shows the evolution of the phase space distribution for the perturbed, quasi-integrable lattice. An octupole with a strength that scales with the beta function is applied in the nonlinear insert (Fig. 3, right). The phase space distribution has been restored to one that resembles the initial distribution. The particle loss over the 200 lattice periods has been reduced from 25.6% to 5.1%. These results show that the T-insert lattice can successfully dampen the instability excited by the octupole perturbation with voltages that can be realistically achieved in the nonlinear IBEX trap.

In order to prove the true benefits of quasi-integrable optics, we must compare the quasi-integrable lattice to a lattice that creates an equal tune spread but is non-integrable. The simplest way to do this is with a lattice where a constant octupole is applied in the nonlinear insert, with an integrated octupole strength equal to the quasi-integrable lattice (Fig. 3, center). Tracking the particle distribution over 200 turns through this non-integrable lattice also gives a particle loss of 5.1% and has a similar phase space evolution to Fig. 5.

These results do not show a difference between the non-integrable and quasi-integrable lattices over the limited number of periods they were studied. The simulations will need to be run for many more lattice periods (>1000 lattice periods) to potentially show a significant difference. This will take days of computing time as it currently takes around 20

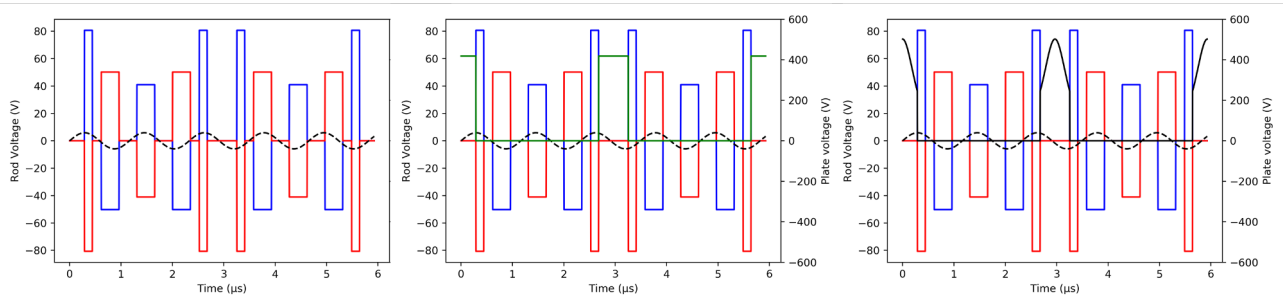


Figure 3: Two periods of the voltage waveform, applied to the rods in IBEX (red and blue) to create the T-insert lattice. A 5.88 V octupole perturbation is applied to the plates (black, dashed). **Left:** No octupoles applied in drift region. **Center:** Constant square wave octupole pulse applied in drift region (green). **Right:** Octupole pulse with  $1/\beta^3$  strength scaling (black, solid).

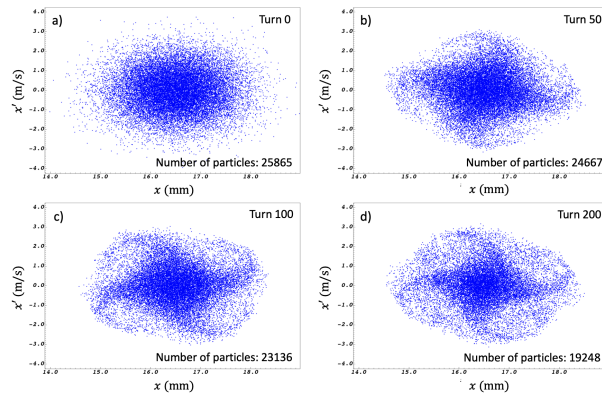


Figure 4: Phase space evolution when an octupole perturbation is applied to the T-insert lattice, at a frequency proportional to  $4Q$ , with the octupole potential switched off.

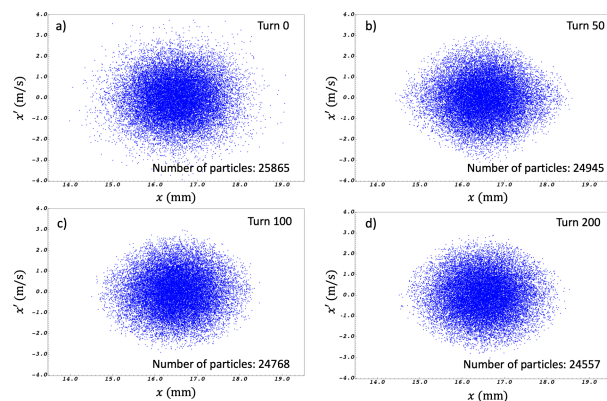


Figure 5: Phase space evolution when an octupole perturbation is applied to the T-insert lattice, at a frequency proportional to  $4Q$ , with the octupole potential switched on.

hours running on 16 cores to simulate the lattices for 200 periods. Extending these simulations to include space charge will make them even more computationally intensive.

Fortunately, with the nonlinear upgrade to IBEX, particles can be stored for tens of thousands of lattice periods in less

than a second to help probe the differences between the quasi-integrable and non-integrable lattices.

## CONCLUSION

A nonlinear upgrade to the IBEX Paul trap is currently underway which will allow for the simultaneous excitation of quadrupole and octupole fields in the experimental region of the trap. A T-insert lattice has been designed to create the conditions needed for QIO, while being constrained by realistic voltages applied to the rods ( $< 150$  V) and plates ( $< 500$  V) and the maximum beta functions to avoid scraping on the rods. Simulation results show that when trapping particles in the linear T-insert for 200 periods, whilst applying a small octupole perturbation to the plates, the octupole resonance is excited and 25.6 % particle loss is seen. When the octupoles are applied in the nonlinear region with correct scaling with beta function, the resonance is damped and only 5.1 % particle loss is seen. When compared to a non-integrable lattice with the same integrated octupole strength but constant in the nonlinear insert, the same particle loss of 5.1 % over 200 turns was observed. Although a significant difference between the quasi-integrable and non-integrable lattice was not observed, the simulations showed that the T-insert lattice with an octupole present in the nonlinear region was able to successfully dampen an octupole resonance. We hope that the nonlinear upgrade to IBEX will allow us to examine the differences between the quasi-integrable and non-integrable lattices over longer time scales.

## REFERENCES

- [1] H. Okamoto, Y. Wada, and R. Takai, “Radio-frequency quadrupole trap as a tool for experimental beam physics,” *Nuclear Instruments and Methods in Physics Research Section A: Accelerators, Spectrometers, Detectors and Associated Equipment*, vol. 485, no. 3, pp. 244–254, 2002. doi: 10.1016/S0168-9002(01)02139-8
- [2] R. C. Davidson, P. C. Efthimion, R. Majeski, H. Qin, and G. Shvets, “Paul trap experiment to simulate intense non-neutral beam propagation through a periodic focusing field configuration,” *Nuclear Instruments and Methods in Physics Research, Section A: Accelerators, Spectrometers, Detectors*

and Associated Equipment, vol. 464, pp. 502–511, 2001.  
 doi:10.1016/S0168-9002(01)00118-8

- [3] S. L. Sheehy, E. J. Carr, L. K. Martin, K. Budzik, D. J. Kelliher, S. Machida, and C. R. Prior, “Commissioning and first results of the Intense Beam Experiment (IBEX) linear Paul trap,” *Journal of Physics: Conference Series*, vol. 874, no. 1, pp. 4–10, 2017. doi:10.1088/1742-6596/874/1/012067
- [4] L. K. Martin, S. Machida, D. J. Kelliher, and S. L. Sheehy, “A study of coherent and incoherent resonances in high intensity beams using a linear Paul trap,” *New Journal of Physics*, vol. 21, no. 5, pp. 0–16, 2019. doi:10.1088/1367-2630/ab0e28
- [5] K. Fukushima and H. Okamoto, “Design Study of a Multipole Ion Trap for Beam Physics Applications,” *Plasma and Fusion Research*, vol. 10, no. 0, pp. 1401081–1401081, 2015. doi:10.1585/pfr.10.1401081
- [6] V. Danilov and S. Nagaitsev, “Nonlinear accelerator lattices with one and two analytic invariants,” *Physical Review Special Topics - Accelerators and Beams*, vol. 13, no. 8, pp. 1–10, 2010. doi:10.1103/PhysRevSTAB.13.084002
- [7] S. S. Baturin, “Hamiltonian preserving nonlinear optics,” pp. 1–14, 2020. arXiv:1908.03520
- [8] S. Antipov, D. Broemmelsiek, D. Bruhwiler, D. Edstrom, E. Harms, V. Lebedev, J. Leibfritz, S. Nagaitsev, C. S. Park, H. Piekarz, P. Piot, E. Prebys, A. Romanov, J. Ruan, T. Sen, G. Stancari, C. Thangaraj, R. Thurman-Keup, A. Valishev, and V. Shiltsev, “IOTA (Integrable Optics Test Accelerator): Facility and experimental beam physics program”, *Journal of Instrumentation*, vol. 12, p. T030002, 2017. doi:10.1088/1748-0221/12/03/T03002
- [9] J. A. D. Flowerdew, S. L. Sheehy, D. J. Kelliher, and S. Machida, “Exploring Accelerators for Intense Beams with the IBEX Paul Trap”, in *Proc. 12th Int. Particle Accelerator Conf. (IPAC’21)*, Campinas, Brazil, May 2021, pp. 1980–1983. doi:10.18429/JACoW-IPAC2021-TUPAB234

# SLOW EXTRACTION OPERATION AT J-PARC MAIN RING

M. Tomizawa\*, Y. Arakaki, T. Kimura, S. Murasugi, R. Muto, K. Okamura,  
 Y. Sugiyama, E. Yanaoka, M. Yoshii, ACCL, KEK, Tsukuba, Japan,  
 F. Tamura, JAEA/J-PARC, Tokai, Japan,  
 H. Nishiguchi, Y. Shirakabe, IPNS, KEK, Tsukuba, Japan,  
 K. Noguchi, Kyushu University, Fukuoka, Japan

## Abstract

A high-intensity proton beam accelerated in the J-PARC main ring (MR) is slowly extracted by using the third integer resonance and delivered to the experimental hall. A critical issue in slow extraction (SX) is a beam loss caused during the extraction. A dynamic bump scheme under an achromatic condition provides extremely high extraction efficiency. We have encountered a beam instability in the debunch formation process, which is estimated to be triggered by a longitudinal microstructure of the beam. To suppress this instability, the beam to the MR has been injected into the RF bucket with a phase offset. A newly developed RF manipulation, 2-step voltage debunch, has successfully pushed up the beam power up to 64.6 kW keeping a high extraction efficiency of 99.5%. A drastic beam loss reduction has been demonstrated in the beam test using a diffuser installed upstream of the first electrostatic septum (ESS1). 8 GeV-bunched slow extraction tests for the neutrino-less muon to electron conversion search experiment (COMET Phase-I) have been successfully conducted.

## INTRODUCTION

A high-intensity proton beam accelerated in the J-PARC main ring (MR) is slowly extracted by the third integer resonance and provided to the hadron experimental hall to drive various nuclear and particle physics experiments. Most of the proposed experiments are best performed using a coasting beam without an RF structure and a uniform beam intensity during the extraction time.

One of the critical issues in the slow extraction (SX) of a high intensity proton beam is an inevitable beam loss caused at an electrostatic septum (ESS). The slow extraction from the J-PARC MR has unique schemes to reduce the beam loss rate [1]. The first electrostatic septum (ESS1) is located in the section between adjacent focusing quadrupole magnets as shown in Fig. 1. The Courant-Snyder  $\beta_x$  function in this section is  $\sim 40$  m, which is highest in the MR. In this condition, a large step size (spiral step)  $\Delta$  at ESS1 can be chosen without causing any primary beam loss in other sections. The head-on hit rate of the beam on the septum in ESS1 can be reduced by the large  $\Delta$ . The long straight sections in the MR are dispersion-free. If horizontal chromaticity is set to near zero during the extraction, the momentum dependence of the third-integer resonant separatrix can be neglected. When a bump orbit, which moves the circulating beam toward the septum of ESS1, is fixed during extraction,

the outgoing arms from the separatrices can have different angles ( $x' = dx/ds$ ) at ESS1 over the start and the end of extraction (fixed bump scheme). The angles of the bump orbit at ESS1 can be moved to overlap these arms during extraction (dynamic bump scheme). The dynamic bump scheme reduces the side hit rate on the ESS1 septum and reduces the beam losses also at ESS2 and the downstream magnetic septa.

In the actual beam tunings, the transverse septum position of the ESSs and the followed magnetic septa (SMS1 and SMS2) are finely tuned to minimize the beam loss iteratively with the dynamic bump orbit tuning. The beam loss is sensitive to horizontal chromaticity, which is searched to minimize the beam loss rate [1]. We have encountered a transverse beam instability occurring in a debunching process above 30 kW beam power. The mitigations we adopted have played an essential role to rise up the beam power as described in the next section. A current performance of 30 GeV-slow extraction operations, 8 GeV-slow extraction tests COMET Phase-I and future plans toward a higher beam power 30 GeV SX operation are also reported.

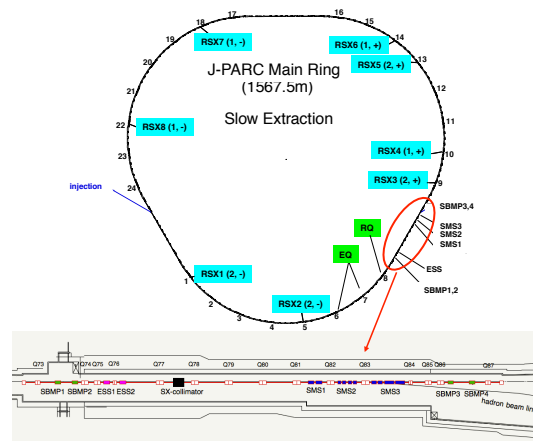


Figure 1: Layout of J-PARC slow extraction devices.

## BEAM INSTABILITY AND MITIGATIONS

We have encountered a beam loss increase in the slow extraction at the beam powers above 30 GeV. This involves a vacuum pressure rise in the whole ring. An electron cloud has been detected by electron cloud monitors at the debunch formation process [2]. The horizontal and vertical coherent oscillations have been also observed at the same timing. A transverse beam size growth has been observed by a profile

\* masahito.tomizawa@kek.jp

monitor located in the beam transport line to the beam dump. These observations shows a transverse instability related to an electron cloud is caused in the ring in the debunching.

A weak chromaticity correction could mitigate the instability. The horizontal and vertical chromaticities of  $-3.5$  and  $-2.0$  before acceleration are set to  $-5.0$  and  $-7.1$  at the flat top and keeping during the debunch formation process. Before the start of the slow extraction, the horizontal chromaticity is set near zero to make an achromatic condition. However this manipulation is not enough to suppress the observed instability.

Whenever this instability happens, a microstructure in the longitudinal beam distribution has been enhanced (see Fig. 2). We guess this transverse instability is triggered by a longitudinal coherent oscillation. A probable mechanism is that such a microstructure induces a vacuum pressure rise by e.g. a multipacting and brings electron clouds. The microstructure has broad frequency components up to  $\sim 300$  MHz. Any coupling impedance source in the MR is not yet clearly identified.

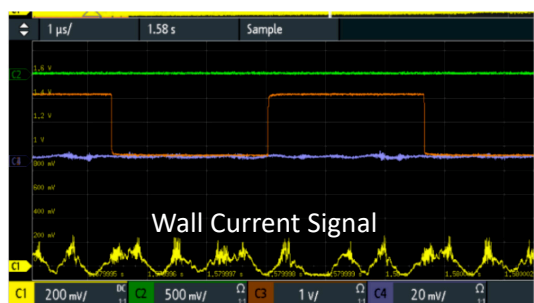


Figure 2: Microstructure observed by a wall current monitor.

In order to mitigate this instability, the beam bunch has been injected into the RF bucket with a phase offset of typically 50 to 60 deg as shown in Fig. 3 a) (phase offset injection) [3]. This manipulation spreads the longitudinal beam emittance and suppress the microstructure enhancement. The phase offset injection was very effective for a stable slow extraction operation up to 50 kW ( $5.4 \times 10^{13}$  protons). However, a phase offset larger than 60 deg. which is necessary to suppress the instability above 50 kW, partially spilled the beam out of the RF bucket at the acceleration start timing.

A new technique, called 2-step voltage debunch, has been implemented to achieve the beam power higher than 50 kW since Dec. 2020. An RF voltage of 256 kV for acceleration is normally non-adiabatically set to zero at the flat top start for the debunching. In the 2-step voltage debunch, the 256 kV voltage is non-adiabatically reduced at a very low voltage, and then is set to zero after a half synchrotron period as shown in Fig. 3 b). This manipulation changes the longitudinal beam distribution and helps suppressing the microstructure growth. This technique pushed up the SX beam power to 64.6 kW ( $7 \times 10^{13}$  protons).

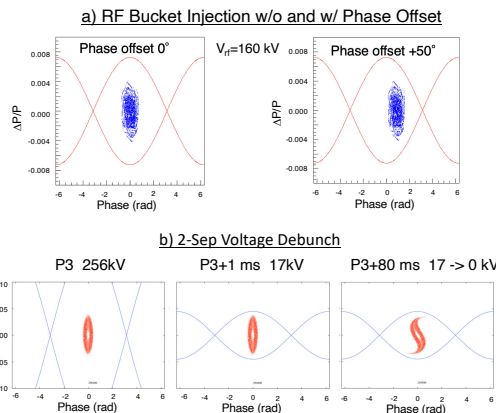


Figure 3: Phase offset injection and 2-step voltage debunch simulations.

## CURRENT BEAM PERFORMANCES

The current cycle time of the SX operation is 5.2 s, in which the acceleration time and the flat top time is 1.4 s and 2.61 s respectively. The beam power in the physics run achieved at 64.6 kW ( $7 \times 10^{13}$  p/pulse) in May, 2021. The instability in the debunch process has been well suppressed by a combination of the phase offset injection and the 2-step voltage debunch. In the latest SX operation, the phase offset was set at 50 deg. for a 165 kV RF bucket. The RF voltage was reduced from 256 kV to 23 kV at the flat top start, and then set at zero after 60 ms. The beam loss for the slow extraction was minimized by tuning the dynamic bump parameters and by tunings septa positions of ESS1, ESS2 and SMS1. Figure 4 a) to d) show the beam loss distribution around the SX area, the beam loss time structure during extraction in the SX area, the DCCT signal and the beam loss distribution in the whole ring. The beam loss distribution have a maximum at ESS1. The beam loss is flat during extraction. The red peaks in the MR collimator region and the SX area shown in Fig. 4 d) must be multiplied by 16 time comparing the blue peaks. The beam loss at the collimator region is mainly generated at the flat base and the beginning of the acceleration. The beam loss in the slow extraction is well localized around the SX area.

The beam spill time structure was measured by a spill monitor located in the beam line to the target. A spill feedback system, in which a DSP processes the spill monitor signal and control the fast response quadrupole (EQs and RQ) currents in real time, has been implemented to improve the spill time structure [4]. Transverse fields by two sets of horizontal strip line kickers have been applied to the circulating beam (transverse RFs) [5]. In the latest operation, the carrier frequencies corresponding to harmonics of the horizontal betatron frequency and its noise widths are 47.4719 MHz and 50 Hz for the D3 kicker, 0.239 MHz and 31.25 Hz for the D1 kicker, respectively. The spill feedback system and the transverse RFs pushed up the spill duty factor to 50–55% (ideal case 100%) [6]. Figure 4 e) shows a beam spill measured at 64.6 kW.

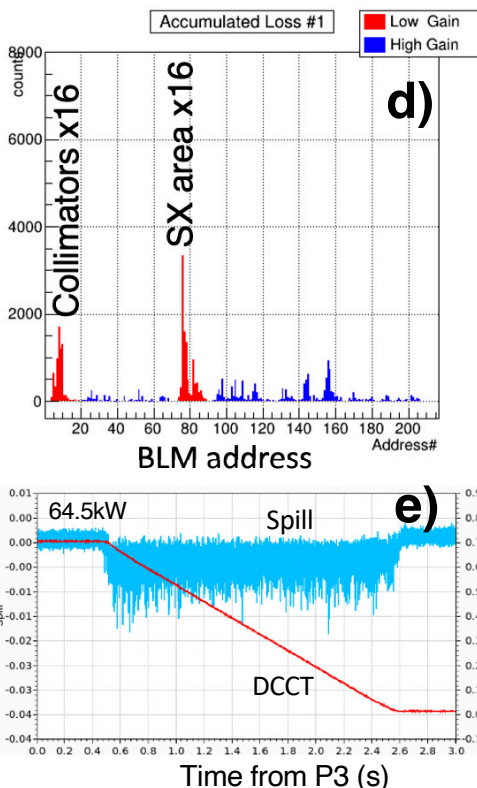
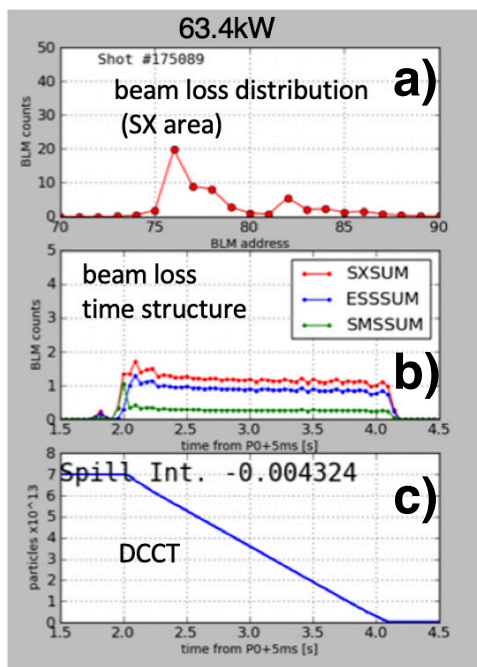


Figure 4: Current performances of 30 GeV slow extraction.

### BEAM TESTS FOR COMET

A planned muon to electron conversion search experiment (COMET Phase-I) needs 8 GeV bunched proton beam with a 1 MHz pulse structure in a long beam duration. In this experiment, the beam intensity ratio of inter-bunch to bunch, which is called extinction, should be less than  $1 \times 10^{-10}$ . In the ordinary 30 GeV operation, two bunches are accelerated

by a 3 GeV rapid cycle synchrotron (RCS) and 4 batches are injected into the MR (harmonics 9) at the K1 to K4 timings every 40 ms. To derive the beam with a MHz structure, the RCS accelerates one bunch for the COMET experiment and 4 batches are injected into the MR. The four bunches are accelerated up to 8 GeV (revolution time of 5.26  $\mu$ s) and they are slowly extracted keeping the bunch structure. An empty bucket in the RCS is produced by an RF chopper placed between the RFQ and the Drift Tube Linac (DTL). The residual beam intensity in the empty bucket is in  $10^{-6}$  level at the ratio for the main beam bucket. To reduce the residual beams in the empty bucket, the MR injection kicker timing is shifted by roughly one bucket length. The timing is shifted forward when the main beam is in a forward bucket (front injection) and reversely shifted backward in a backward bucket (rear injection). By such a kicker timing shift, the residual beam in the empty bucket can not be deflected along the injection orbit and then lost in the MR.

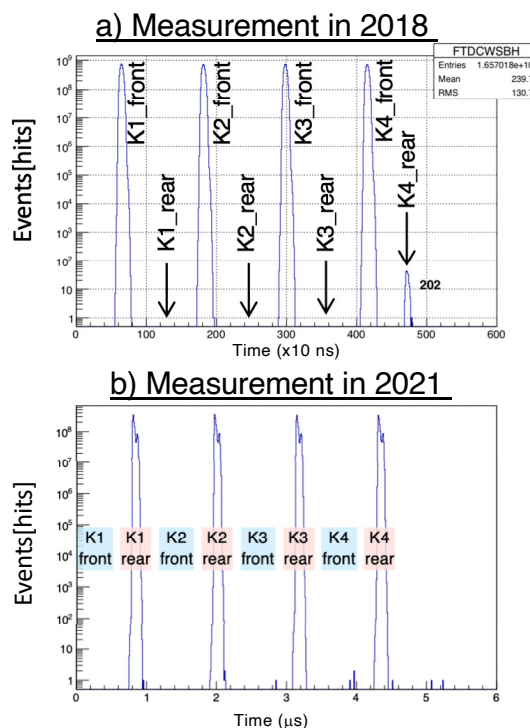


Figure 5: Time structures of extracted beams measured in 2018 and 2021.

The 8 GeV beam tests were conducted in 2018 and 2021. The acceleration pattern is swept in 2.48 s chosen in the COMET phase-I, and the repetition time of the MR is kept to 5.2 s, same as that of the 30 GeV operation avoiding a hard work to change the setting of the timing system. The particle number in the MR is  $7.3 \sim 7.4 \times 10^{12}$  per pulse, which corresponds to 3.2 kW at a 2.48 s cycle nominal for the COMET phase-I. The beam loss around the slow extraction area was drastically improved in the 2021 test by a careful dynamic bump tuning and the septa position optimization. A tentative slow extraction efficiency is above 99%, which should be calibrated in a similar way as done at 30 GeV. The

Content from this work may be used under the terms of the CC BY 3.0 licence (© 2021). Any distribution of this work must maintain attribution to the author(s), title of the work, publisher, and DOI

time structure has been also improved to be above 50% at the duty factor by the spill feedback tunings. The transverse RF used for the 30 GeV operation was not applied.

The extinction of the slow-extracted beam has been measured by an extinction monitor in an secondary beam line in the hadron experimental hall. Figure 5 a) shows a bunch structure of the secondary beam measured in the 2018 test [7]. Any residual beam has not been observed in the inter-bunch of the K1-K3 timings, however, the residual beam was seen in an empty bucket at the K4 timing. Though the residual beams injected at the K1 through K3 timings can be also circulated similar to that at the K4 timing, they can be lost by the kicker field at the followed K2 to K4 timings. The residual beam injected at the K4 timing can not be lost since the kicker field is not excited after the K4 timing. Figure 5 b) shows a bunched time structure measured in May, 2021 [8]. The beam was injected into the backward bucket and the kicker timing was shifted backward by 600 ns. Any peak seen for the front injection was not seen in the rear injection. A few events in random timing locations have been identified as accidental events in the extinction monitors by data analysis. The extinction rejecting such accidental events is less than  $1 \times 10^{-10}$ . In the 2021 test, two correction kickers were successfully applied to suppress a horizontal emittance growth by an undesirable reflection in the kicker transmission line.

## FUTURE PLANS

### Beam Loss Reductions

The power supplies for bending and quadrupole families in the MR will be replaced to shorten a cycle time from 2.48 to 1.3 s for a planned neutrino experiment program toward a 750 kW operation. This replacement will shorten a cycle time for the slow extraction from 5.2 s to 4.2 s finally. This means that the SX beam power can be pushed up by 1.23 times for the same proton number per pulse.

The beam loss reduction using a diffuser has been successfully demonstrated in CERN SPS [9]. Further beam loss reduction schemes are planned toward a higher intensity J-PARC SX operation. Two diffusers have been installed upstream of ESS1 as shown in Fig. 6. A multiple scattering in the diffusers reduces a head-on hit rate on the ESS1 septum. The beam loss reduction effect is sensitive to an angular spread of the beam coming into the diffusers. The dynamic bump which reduces the angular spread very well fits to the diffuser scheme. Further, we have a plan to boost up the effect by two diffusers combination. The sizes of the diffuser0 and the diffuser1 made of tantalum, have been optimized by a FLUKA simulation, 0.2 mm (W)×0.5 mm (L) and 0.1 mm (W)×2 mm (L), respectively [10]. A preliminary beam test using the diffuser0 has been conducted in 2021. Figure 6 shows the beam loss comparison with and without the diffuser0. The beam loss in all SX area except for the diffuser0 has been definitely reduced, especially becomes 1/2.7 at ESS1 of a maximum beam loss point. In the next beam test, a combination effect by the two diffusers, a high

beam intensity effect, a long term stability will be examined. To put them to practical use, the diffuser0 will be covered with a radiation shield.

A septum shadowing using a bent Si crystal would be a promising candidate as the diffusers [11]. Beams going through the crystal are deflected by a channeling effect and make a separation at the first ESS.

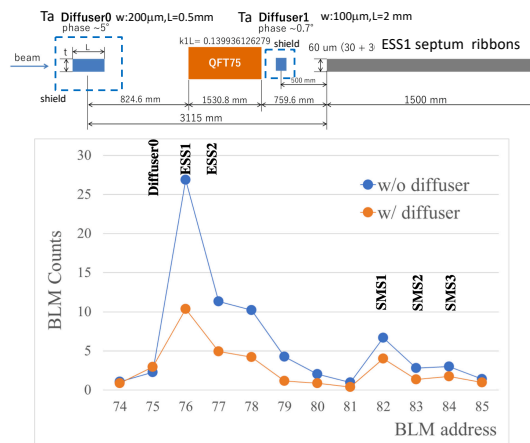


Figure 6: Diffusers configuration and beam loss distributions measured for w/ and w/o diffuser0.

The septa of the ESSs are made of a W/Re alloy with a large average atomic number [12]. If the septum of ESS1 can be made of a material with a low atomic number, the radioactivity around can be reduced. We have started a feasibility research using carbon-Nano Tube (CNT) wires developed by Hitachi Zosen (Hitz) as the septum material. In a high voltage test by a single CNT wire, we have achieved an electric field of 20 MV/m on the wire surface [13].

### Instability Mitigations

Mitigations for the instability occurring in the debunch process are crucial to rise up the beam intensity.

The RF voltage and its RF-off timing in the 2-step voltage debunch technique will be optimized. As its advanced technique, a multi-step voltage debunch will be also studied.

A beam coupling impedance reduction in the MR is important. A major longitudinal impedance source triggering the instability has not been clearly identified. However, a RF cavity impedance is supposed to be a candidate. The impedance measurement for newly installed cavities is underway. An impedance reduction way for the RF cavities are also discussed.

Phase and amplitude modulations by VHF cavities increase the longitudinal beam emittance uniformly are a promising way suppressing the instability. The VHF cavities have been already designed [14]. A funding to build them can be an issue.

If absolute value of a slippage factor  $|\eta|$  is enlarged during the debunch timing, a longitudinal microstructure is suppressed as expected from the well known longitudinal Keil-Schnell criterion. The MR ring has an imaginary transition  $\gamma_t$ . The  $\eta$  is -0.00192 at 30 GeV. The  $\eta$  can be changed

by tuning the field strength of four quadrupole families in the arc sections keeping horizontal and vertical tunes and an achromatic condition in the long straight sections. The slippage change optics will be tried in the next beam test.

### Beam Spill Improvements

The replaced bending and quadrupole power supplies in 2021–2022 have one order less ripple than the present ripples, order of  $10^{-4}$ . The improvement for the spill time structure will be expected from the next beam operation.

The two transverse RF fields have been applied to the beam at fixed frequencies and noise widths in the current operation. A feedback to the transverse RF fields from the spill signal will be planned. A voltage programmable attenuator added in the low level line in the exciters can be controlled by the spill feedback DSP. A time response of the extracted beam by the DSP command has been tested.

A ripple canceler, processes the total horizontal tune shift by FPGAs from the measured current ripples for the bending and quadrupole power supplies, set the current to cancel the processed total horizontal tune shift to the RQ magnet [15]. The beam test showed the performance similar to that of the current feedback system in the condition without the transverse RF.

The transverse RF frequencies corresponding to two different harmonics of the betatron oscillation frequency is applied to the circulating beam by the two strip line kickers to improve the spill structure. Multi-harmonic frequencies more than the current two frequencies will be applied in a test to improve the spill time structure [16].

## CONCLUSIONS

The 30 GeV-slow extracted beam has been stably delivered to the hadron experimental hall for various high energy and nuclear physics experiments. The current SX beam power have achieved to 64.6 kW, which corresponds to  $7 \times 10^{13}$  protons per pulse. An extremely high slow extraction efficiency of 99.5% is maintained also at the current operation. The beam instability occurring in the debunch formation process is crucial. The mitigations of the phase offset injection into the MR RF bucket and the 2-step voltage debunch technique have played an essential role to push up the beam power. The time structure of the extracted beam has been improved by a spill feedback to the fast response quadrupoles and applying transverse RF fields to the circulating beam.

The 8 GeV-bunched slow extraction tests have been successfully conducted for the planned  $\mu$ -e conversion experiment (COMET). The extinction measured for the extracted beam is  $< 1 \times 10^{-10}$ , which satisfies the requirement from the COMET Phase-I. The slow extraction efficiency and the spill time structure have been rather improved in the 8 GeV slow extraction test conducted in 2021.

## ACKNOWLEDGEMENTS

The authors would like to thank S. Igarashi, Y. Sato and T. Toyama for their cooperation for the MR beam commissioning and the beam measurements. We are grateful to J. Takano for his COD correction works. The authors also would like to thank the all MR staffs for their corporations for the slow extraction operation. We would like to thank Accelerator Beam Transfer Group in CERN for their collaboration on the diffuser design. The diffuser manufacture is supported by U.S.-Japan Science and Technology Cooperation Program in High Energy Physics, “Development in Slow Extraction for Higher Intensity Beams” by FNAL, BNL and KEK.

## REFERENCES

- [1] M. Tomizawa *et al.*, “Slow extraction from the J-PARC main ring using a dynamic bump”, *Nuclear Inst. and Methods in Physics Research A*, vol. 902, pp. 51-61, 2018. doi:10.1016/j.nima.2018.06.004
- [2] B. Yee-Rendón *et al.*, “Electron Cloud Measurements at J-PARC Main Ring”, in *Proc. 7th Int. Particle Accelerator Conf. (IPAC'16), Busan, Korea, May 2016*, pp. 137–139. doi:10.18429/JACoW-IPAC2016-MOPMB024
- [3] M. Tomizawa *et al.*, “Status and Beam Power Ramp-Up Plans of the Slow Extraction Operation at J-Parc Main Ring”, in *Proc. 61st ICFA Advanced Beam Dynamics Workshop on High-Intensity and High-Brightness Hadron Beams (HB'18)*, Daejeon, Korea, Jun. 2018, pp. 347–351. doi:10.18429/JACoW-HB2018-THA1WD03
- [4] A. Kiyomichi *et al.*, “Beam Spill Control for the J-PARC Slow Extraction”, in *Proc. 1st Int. Particle Accelerator Conf. (IPAC'10)*, Kyoto, Japan, May 2010, paper THPEB022, pp. 3933–3935.
- [5] M. Tomizawa *et al.*, “Performance of Resonant Slow Extraction from J-PARC Main Ring”, in *Proc. 3rd Int. Particle Accelerator Conf. (IPAC'12)*, New Orleans, USA, May 2012, paper MOPPD051, pp. 481–483.
- [6] R. Muto *et al.*, “Current Status of Slow Extraction from J-PARC Main Ring”, *IOP Journal of Physics Conference Series*, vol. 1350, p. 012105, 2019. doi:10.1088/1742-6596/1350/1/012105
- [7] H. Nishiguchi *et al.*, “Extinction Measurement of J-PARC MR with 8 GeV Proton Beam for the New Muon-to-Electron Conversion Search Experiment - COMET”, in *Proc. 10th Int. Particle Accelerator Conf. (IPAC'19), Melbourne, Australia, May 2019*, pp. 4372–4375. doi:10.18429/JACoW-IPAC2019-FRXXPLS2
- [8] K. Noguchi *et al.*, “Extinction Measurement at J-PARC MR with Slow-Extracted Pulsed Proton Beam for COMET Experiment”, in *Proc. 22nd Int. Workshop on Neutrinos from Accelerators. (NuFact'21)*, Cagliari, Italy, Sep. 2021, to be published.
- [9] B. Goddard *et al.*, “Reduction of 400 GeV/c slow extraction beam loss with a wire diffuser at the CERN Super Proton Synchrotron”, *Physical Review Accelerators and Beams*, vol. 23, p. 023501, 2020. doi:10.1103/physrevaccelbeams.23.023501

- [10] R. Muto *et al.*, “Simulation Study on Double Diffuser for Loss Reduction in Slow Extraction at J-PARC Main Ring”, in *Proc. 12th Int. Particle Accelerator Conf. (IPAC’21)*, Campinas, SP, Brazil, May 2021, pp. 3069–3072. doi:10.18429/JACoW-IPAC2021-WEPAB192
- [11] F. M. Velotti *et al.*, “Septum shadowing by means of a bent crystal to reduce slow extraction beam loss”, *Physical Review Accelerators and Beams*, vol. 22, p. 093502, 2019. doi:10.1103/PhysRevAccelBeams.22.093502
- [12] Y. Arakaki *et al.*, “Electrostatic Septum for 50GeV Proton Synchrotron in J-PARC”, in *Proc. 1st Int. Particle Accelerator Conf. (IPAC’10)*, Kyoto, Japan, May 2010, THPEB010, pp. 3900–3902.
- [13] M. Tomizawa *et al.*, “Initial Tests for Electrostatic Septum Using Carbon Nanotube Wires”, *JPS Conf. Proc.*, vol. 33, p. 011035, 2021. doi:10.7566/JPSCP.33.011035
- [14] Y. Morita *et al.*, “Design of VHF System in J-PARC Main Ring”, *JPS Conf. Proc.*, vol. 33, p. 011032, 2021. doi:10.7566/JPSCP.33.011032
- [15] D. Naito *et al.*, “Real-time correction of betatron tune ripples on a slowly extracted beam”, *Physical Review Accelerators and Beams*, vol. 22, p. 072802, 2019. doi:10.1103/PhysRevAccelBeams.22.072802
- [16] T. Shiokawa *et al.*, “Slow beam extraction method from synchrotron for uniform spill and fast beam switching using an RF knockout method of multi-band colored noise signal—POP Experiment and simulation”, *Nuclear Inst. and Methods in Physics Research A*, vol. 1010, p. 165560, 2021. doi:10.1016/j.nima.2021.165560

# COMMISSIONING OF THE ESS FRONT END

N. Milas\*, R. Miyamoto, C. S. Derrez, E. M. Donegani, M. Eshraqi, B. Gålnander,  
 H. Hassanzadegan, E. Laface, Y. Levinsen, M. Muñoz, E. Nilsson, C. Plostinar, A. G. Sosa,  
 R. Tarkeshian and C. Thomas  
 European Spallation Source ERIC, Lund, Sweden

## Abstract

The European Spallation Source, currently under construction in Lund, Sweden, will be the brightest spallation neutron source in the world, when the proton linac driver achieves the design power of 5 MW at 2 GeV beam energy. Such a high power requires production, efficient acceleration, and transport of a high current proton beam with minimal loss. This implies in a challenging design and beam commissioning of this machine. The linac features a long pulse length of 2.86 ms at a relatively low repetition rate of 14 Hz. The ESS ion source and low energy beam transport are in-kind contributions from INFN-LNS. Beam commissioning of this section started in September 2018 and continued until early July in 2019. This article presents highlights from a campaign of beam characterizations and optimizations during this beam commissioning stage.

## ION SOURCE AND LEBT OVERVIEW

European Spallation Source (ESS), currently under construction in Lund, Sweden, will be a spallation neutron source driven by a proton linac [1]. The beam commissioning of the ESS linac is being conducted in stages [2–4]. Commissioning of the first and stage, consisting of the Ion Source (IS) and LEBT, started in September 2018 and continued until early July in 2019. The IS of ESS is a microwave discharge type with the nominal extraction voltage of 75 kV. This type of source is known to produce a high current and high quality beam. As indicated in Table 1, the beam out of the IS includes other ion species, typically around 20% and primarily  $H_2^+$  and  $H_3^+$ , which are lost still within the LEBT section. After stable operation was established, the IS provided more than 400 hours of beam time by the end of the beam commissioning period.

Figure 1 is a schematic layout of the LEBT, showing the locations of the two solenoids and other devices. Each solenoid has an integrated pair of dipole correctors (*steerers*) acting on both transverse planes. In between the solenoids, inside the *Permanent Tank*, there are one Faraday Cup (FC), a set of Beam Induced Fluorescence Monitors (BIFMs) [5], and Emittance Measurement Units (EMUs) of Allison scanner type measuring for vertical plane. Beam Current Monitors (BCMs) measure the IS extraction current and also the LEBT output current. The LEBT also houses an iris, which is a movable diaphragm with six blades that mechanically restricts the aperture to adjust the beam current, and a chopper, which adjusts pulse length by deflecting the leading and

Table 1: ESS IS Possible Operational Parameters

Parameter	Value	Unit
Energy	~75	keV
Peak current (total)	~85	mA
Peak current (proton)	~70	mA
Proton fraction	~80	%
Pulse length	~6	ms
Pulse repetition rate	14	Hz
Duty cycle	~8	%

trailing parts of a pulse. During this first stage of beam commissioning a temporary tank, referred to as *Commissioning Tank*, was placed right after the collimator at the end of the LEBT, providing additional measurement locations closer to the RFQ interface. Inside this *Commissioning Tank* a second EMU (measurement the vertical plane as well) was installed and a second pair of BIFs was available. The use of the BIFMs in a LEBT is a relatively new idea and provided a tool to perform conventional diagnostics techniques, such as an emittance reconstruction based on a gradient scan, even for this part of the linac. Examples of characterizations based on the BIFMs will be presented when discussing the Linear Optics studies in the LEBT.

## SOURCE TUNING

In order to tune the IS a scan of 5 parameters is required: the 3 coils confining the magnetic field inside the plasma chamber (referred as Coil 1, 2, and 3, counting from the extraction side), the input RF power for the magnetron and the injected  $H_2$  flux. It was found the source output current was specially sensitive to the Coil 2 strength. Figure 2 shows

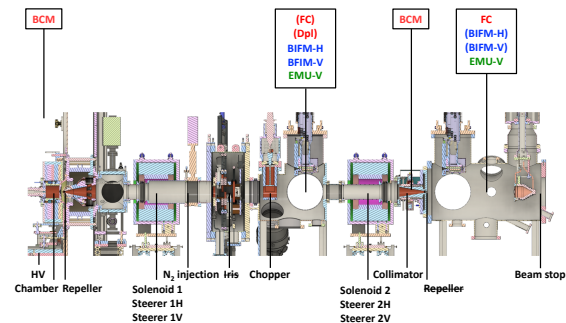


Figure 1: Schematics of the ESS IS and LEBT. a) Close-up of the IS plasma chamber and extraction system. b) IS and LEBT with diagnostics devices.

\* natalia.milas@ess.se

Content from this work may be used under the terms of the CC BY 3.0 licence (© 2021). Any distribution of this work must maintain attribution to the author(s), title of the work, publisher, and DOI

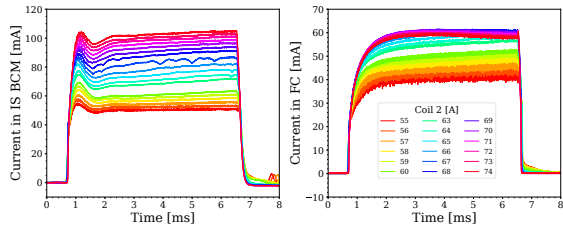


Figure 2: Beam pulses during a Coil 2 scan. a) Measurement with the IS BCM. b) Measurement with the FC in the Permanent Tank. (RF power, Coil 1 current, Coil 3 current, and H<sub>2</sub> flux were kept to 500 W, 120 A, 217 A, and 3.5 sccm.)

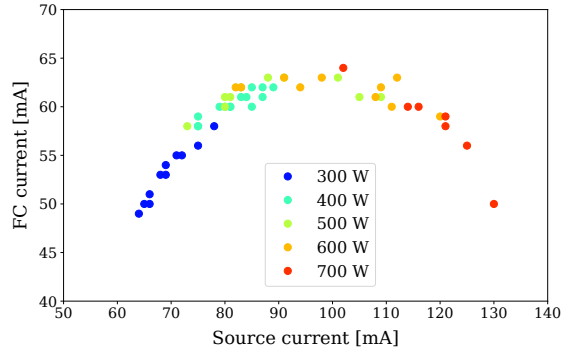


Figure 3: Relations between currents out the IS and those measured in Permanent Tank with the FC for various IS settings. (Strengths of Solenoid 1, Steerer 1H, and Steerer 1V were kept to 249 mT, -2.72 mT, and -0.35 mT.)

changes in beam pulse shapes during a scan of Coil 2 current, observed by the IS BCM (2a) and FC in Permanent Tank (2b). We defined the Coil 2 current of 67-68 A as the optimal setting, for the fixed values of the other four parameters. It was also found that a small increase in the H<sub>2</sub> flux tends to compensate the drooping effect. Thus, the H<sub>2</sub> flux was used to fine-tune the flatness after an optimal Coil 2 current was found.

During the study, the magnetron power and currents in Coil 1 and Coil 3 were scanned and a local optimal setting for each combination was found. Figure 3 summarizes the result of the study, showing the relations between the total currents (averaged over the 2.9 ms plateau) extracted from the IS and those measured by the FC in Permanent Tank. During the study, Solenoid 1 was kept to a fixed value to make an almost parallel (slightly converging) beam and likewise the first set of steerers were adjusted to maximize the current measured by the FC. As seen in the figure, the current out of the IS is correlated with the magnetron power, as expected, but also depends a lot on strengths of the coils. Another important feature is that the current reaching the Permanent Tank is highly correlated with the current out of the IS. This indicates that the condition of the meniscus and the initial divergence are also highly correlated with the extracted current.

Figure 4 shows the measured beam pulses and vertical phase space distributions for two settings, a Standard Setting where the standard current expected for this source in

nominal operations is extracted and a Low Setting with a extracted current of 60 mA from the source. The Low Setting has a slower rise time, and the extracted pulse length has to be extended to achieve the same level of flatness as the Standard Setting. Each setting has different values for the magnetron power and coils that were adjust in order to extract the best possible beam. The discrepancy between the LEBT BCM and FC has not been well understood [6], and further investigation has to be conducted. The phase space distribution of the Standard Setting not only has a larger emittance but also features the wing-like structure, often due to an imperfect meniscus condition or a solenoid aberration. The LEBT of ESS has an injection point of N<sub>2</sub> gas right after the IS extraction system which can be used to spool the vacuum level intentionally and increase the degree of space charge neutralization. The emittance measurements of Figures 4c and 4d were repeated for various levels of N<sub>2</sub> flux as well (0.1 to 9 sccm), but no positive effect was observed, indicating a large initial divergence at the IS which also causes a large beam size filling the aperture of Solenoid 1. This large initial beam divergence is still under study and more experiments are planned for the following commissioning round in 2021 in order to understand it.

## BEAM TRANSPORT IN THE LEBT

### Trajectory and Linear Optics

The LEBT section is required to transport the proton beam to the RFQ with minimal losses and provide the required Courant-Snyder parameters at the interface. In addition, the beam has to enter the RFQ with minimal position and angular offsets, since the transmission and output beam quality of the RFQ are sensitive against these offsets. A set of BIFMs at two different locations allow measurements and corrections

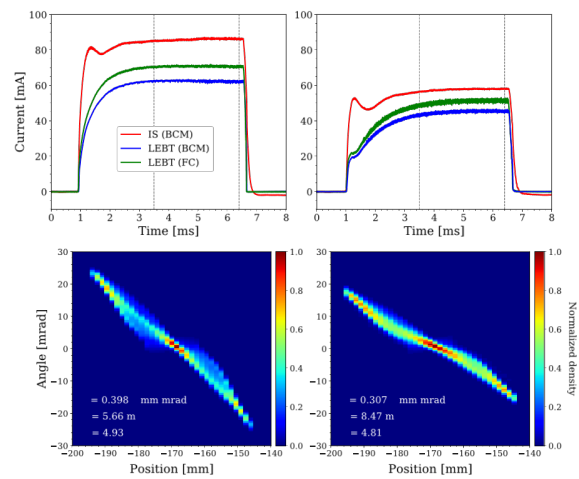


Figure 4: Measured beam pulses and phase distributions for Standard and Low Settings. a) Pulses for Standard Setting. b) Pulses for Low Setting. c) Vertical phase space distributions in Permanent Tank for Standard Setting. d) Vertical phase space distributions (vertical plane) in Permanent Tank for Low Setting.

of trajectory in the ESS LEBT. The conventional scheme of simply minimizing the offset at each monitor location was possible, but another method of characterizing the beam near the image point condition was adopted to identify error sources [7].

When the centroid position is measured near the image point of a lens (Solenoid 1) and its strength is scanned, information of error sources can be acquired as fit parameters to a model. Thus, the key to the method is to determine the Solenoid 1 strength to produce the image point at the BIFMs. Note that in the considered example, the main error sources are tilts of Solenoid 1 and the initial trajectory errors out of the IS. Solenoids offsets were estimated to be negligible compared to those errors, as long as they are within the specified alignment tolerances of 100-200  $\mu\text{m}$  [7]. Figure 5a shows a scan of the beam size as a function of Solenoid 1 strength. As seen in the figure, identifying the condition for the image point is fairly trivial. Figure 5b shows a more detailed scan around the image point; in this particular case, the strengths of Solenoid 1 to minimize the beam sizes at the BIFMs were 282.7 mT for the horizontal plane and 283.7 mT for the vertical plane. Once the condition for the image point is identified, the rest of method is relatively straightforward model fitting against the scan around the image point condition [7]. The curves of the beam sizes for Solenoid 1 strengths too weak or too strong flatten out. This indicates that the beam is being clipped at some element before the BIFMs, implying that the measurements are untrustworthy for both beam size and centroid position in those regions.

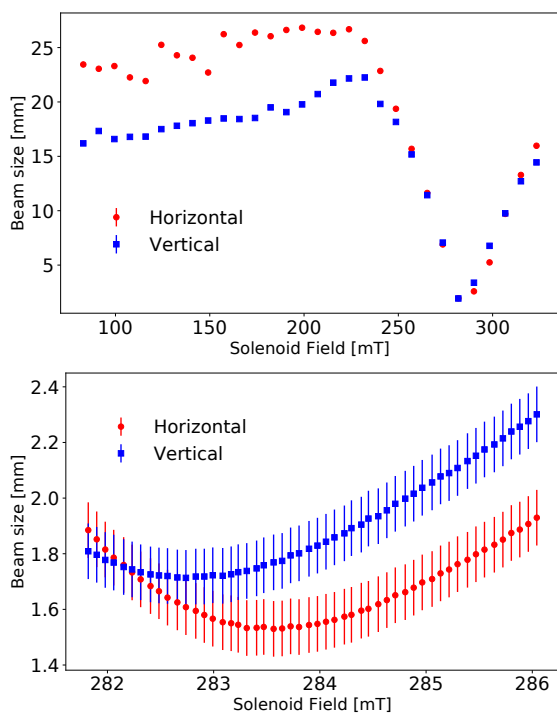


Figure 5: a) Beam size measured with the BIFMs in Permanent Tank as a function of Solenoid 1. b) Close-up around the image point.

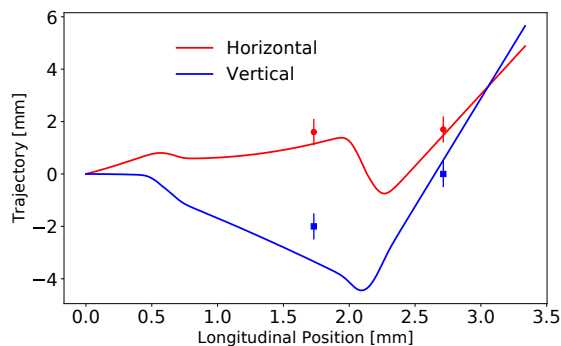


Figure 6: Comparison between the modeled trajectory (lines) and measured positions at BIFMs (markers) in the LEBT.

This situation ultimately affects accuracy of the corrected trajectory by always requiring high Solenoid 1 strengths for the measurements, which are not ideal for evaluating the initial angles at the IS.

Based on the method described above, a series of measurements were performed during the beam commissioning period to assess the initial angular error at the IS and solenoid tilts, and the mean values obtained for both solenoids tilts and source misalignment are listed in Table 2. Note, for the reconstruction of the solenoid tilts, the mean value of measurements from both planes are listed. A large tilt in each solenoid was predicted from the field measurement prior to their delivery and the presented method qualitatively confirmed this, but discrepancies are remaining in terms of magnitude. In order to verify the reconstructed solenoid tilts and initial angular errors at the IS, the beam trajectory was simulated through the LEBT with the reconstructed errors, for a set of solenoid strengths weaker than those corresponding to the image point condition (259.5 mT for Solenoid 1 and 211.4 mT for Solenoid 2), and the simulated centroid positions at both sets of BIFMs were compared with the measurements. As seen in Figure 6, the model predictions and measurements are in fairly good agreement.

### Solenoids Scan

The standard technique to match the beam to the RFQ is to scan the solenoids and find the strengths that maximize transmission. For a typical RFQ, such a condition almost coincides with that for the best emittance preservation, and this is also the case for the RFQ of ESS [8–11]. As seen in [12], the pattern of the LEBT output current during the solenoids scan could also provide indirect information of var-

Table 2: Measurements Results for Solenoid and Source Errors

Elements	$\theta$ [mrad]	$\phi$ [mrad]	$x_{p0}$ [mrad]	$y_{p0}$ [mrad]
<b>Source</b>	-	-	$1.3 \pm 0.3$	$0.0 \pm 0.4$
<b>Solenoid 1</b>	$-1.0 \pm 0.5$	$-4.0 \pm 0.1$	-	-
<b>Solenoid 2</b>	$2.0 \pm 0.7$	$7.0 \pm 2.0$	-	-

Content from this work may be used under the terms of the CC BY 3.0 licence (© 2021). Any distribution of this work must maintain attribution to the author(s), title of the work, publisher, and DOI

ious conditions of the IS and LEBT. Hence, the effects from the reconstructed solenoid tilts and initial angular errors, as well as (empirically acquired) larger initial RMS sizes and angles, were tested in simulations of the solenoids scan. The simulations were performed with TraceWin code [13] by assuming a space charge compensation level of 95%. Figure 7 shows the measured currents with the BCM at the RFQ interface for different sets of solenoid strengths (a) and their simulations (b, c and d). Comparison of Figure 7b and Figure 7c demonstrates the difference of taking into account those reconstructed errors. Better agreement with the measurement (a) is visible for the case with the errors (c), especially for the reduction in current in the region between the weak-focusing and strong-focusing regions. On the other hand, the region with a high transmission is still much larger for the simulation, and further improvements are expected if a more realistic initial distribution at the IS can be achieved. Measurements of emittance and Courant-Snyder parameters in the Permanent Tank indicated that the initial beam out the IS has an RMS angle larger than the simulated [14] and Figure 7d shows the simulation emulating such a larger initial RMS angle case, together with the reconstructed errors. Further improvement in agreement with the measurement (a) indicates the right direction of correcting the initial distribution for simulations.

### Matching to RFQ

For both IS settings, Standard and Low Settings discussed before, we performed EMU measurements in the Commissioning Tank for different sets of solenoid strengths. This was to understand a trend of the matching condition to the RFQ. As representative cases, three sets of measurements are shown in Figure 8. The reconstructed emittance and mis-

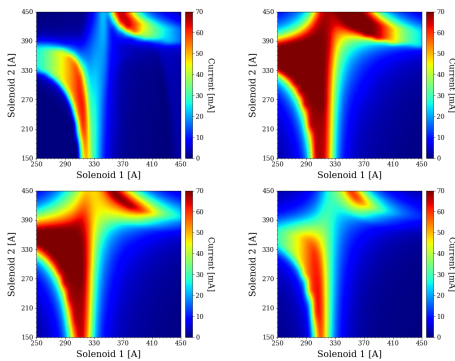


Figure 7: LEBT output current against scan of two solenoids. a) Measurements from the BCM at the RFQ interface. b) Simulation using the nominal simulated initial distribution with an emittance of  $0.144 \pi$  mm mrad,  $\beta = 0.44$  m and  $\alpha = -4.23$  and with no error. c) Simulation using the nominal initial distribution and with the reconstructed solenoid tilts and initial angular errors. d) Simulation using the initial distribution with increased initial  $\beta = 0.7$  m and  $\alpha = -10.0$  and with the reconstructed solenoid tilts and initial angular errors.

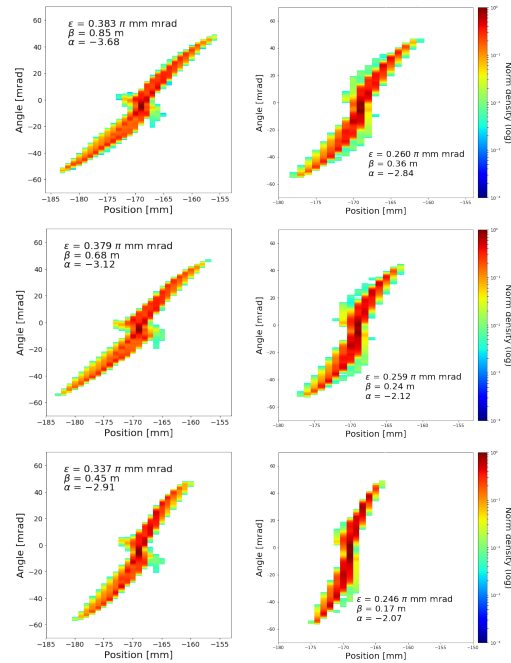


Figure 8: EMU measurements in Commissioning Tank with different solenoid strengths, for two IS setting. For the IS setting, left column: Standard Setting and right column: Low setting. For the solenoid strengths, top row: (258, 216) mT, middle row: (258, 207) mT and bottom row: (254, 216) mT.

match parameter [15] at the RFQ interface (with respect to  $\beta = 0.17$  and  $\alpha = 1.7$  from the most recent simulation [8]) are summarized in Table 3. Compared to the measurements in the Permanent Tank (Figure 4), there is a  $\sim 5\%$  reduction in emittance for the Standard Setting and  $\sim 15\%$  for the Low Setting. The reduction seen for the third set of the solenoid strengths is due to a small loss of current. The mismatch parameter at the RFQ interface, which is 149.5 mm upstream of the EMU, was estimated approximately by simple propagation of the Courant-Snyder parameters in a drift ignoring space charge. As seen in the table, the tested sets of solenoid strengths were not far from the well matched condition for the Low Setting, whereas this was not the case for Standard Setting. Preparing a good matching condition from direct measurement at the EMU in the Commissioning Tank is not at all trivial, since it depends strongly on beam current,

Table 3: Emittance and Estimated Mismatch at the RFQ Interface for Tested Sets of Solenoid Strengths

IS setting	Solenoids [mT]	Emittance [ $\pi$ mm mrad]	Mismatch [%]
Standard	(258, 216)	0.38	211
	(258, 207)	0.38	172
	(254, 216)	0.34	91
Low	(258, 216)	0.26	55
	(258, 207)	0.26	22
	(254, 216)	0.25	21

emittance, and even details in the distribution used initially. In addition, an accurate reconstruction of the beam parameters at the RFQ interface requires knowledge of the level of space charge compensation which is not available and for this reason the matching will rely strongly on optimization of the transmission through the RFQ.

## LESSONS LEARNED

At the very beginning of the commissioning we experienced grounding issues both at the IS and LEBT which delayed commissioning by approximately 5 months. The corrections required several months of consolidation works against high-frequency discharges, but afterwards achieved reliable and stable operation. Due to the lack of proper grounding some equipment were damaged, including power supplies that had a long fixing/replacing lead time. Since we started commissioning with no spare parts readily available for any of the systems, this resulted in several weeks of recommissioning, once the main grounding issue was resolved, with just partial systems active. Another issue that was present throughout commissioning was a constant struggle with the integration of many systems. As a consequence some of the equipment that was intended to be tested during the LEBT commissioning never became fully functional (as the Iris) or had very poor performance and will have to be retested or recommissioned, e.g. the cases for the LEBT Chopper and the repeller at the end of the LEBT. Since there was no time allocated for integrated tests before commissioning these obstacles should not have come as a surprise. For the next commissioning round we plan ahead to have integrated tests and dry runs before beam extraction in order to save commissioning time for beam tests only.

From the Beam Physics point of view, we were not able to explain the larger emittance ( $>0.4 \pi$  mm mrad for 70 mA protons out of LEBT) and larger initial divergence than the ones observed during the off-site commissioning [16, 17]. This large emittance is not reproducible with the extraction code and more investigation on this topic is of high importance for us to fully understand the IS. Another issue we observed was a large trajectory deviation, which resulted in the need to have larger kicks on the dipole correctors in order to maximize current transmission through the LEBT cone and which cannot be easily explained either. Given all these open issues, a test stand for source study and characterization is being assembled at ESS.

## CONCLUSION

This article presented selected highlights from the first beam commissioning activities at ESS for its IS and LEBT. The IS initially experienced grounding issues and required several months of consolidation works against high-frequency discharges, but afterwards achieved reliable and stable operation. It demonstrated great flexibility in tuning and production of the required level of current, but on the other hand the observed emittance was larger than the design value of  $0.25 \pi$  mm mrad near the RFQ interface, unless the

current was lowered significantly. The cause and mitigation of the emittance larger than expected, as well as impact to the downstream sections when such a beam is injected to the RFQ, will continue to be investigated as a part of preparations for the upcoming beam commissioning stages, covering the normal-conducting injector. In addition to the conventional Allison scanner type EMU, BIFMs were used for characterizations of the beam trajectory and profiles in the LEBT and proved to be extremely useful. During the IS and LEBT commissioning we faced a series of issues, from grounding to integration. Going forward, we included integrated test ahead of beam extraction in the schedule in order to minimize issues appearing during beam commissioning.

## REFERENCES

- [1] R. Garoby *et al.*, “The European Spallation Source Design”, *Phys. Scr.*, vol. 93, p. 014001, 2018. doi:10.1088/1402-4896/aa9bff
- [2] R. Miyamoto, M. Eshraqi, and M. Muñoz, “ESS Linac Plans for Commissioning and Initial Operations”, in *Proc. HB’16*, Malmö, Sweden, July 2016, pp. 342-347. doi:10.18429/JACoW-HB2016-TUPM5Y01
- [3] R. Miyamoto, M. Eshraqi, M. Muñoz, and C. Plostinar, “Beam Commissioning Planning Updates for the ESS Linac”, in *Proc. IPAC’17*, Copenhagen, Denmark, May 2017, pp. 2407-2410. doi:10.18429/JACoW-IPAC2017-TUPVA131
- [4] C. Plostinar *et al.*, “Opportunities and Challenges in Planning the Installation, Testing and Commissioning of Large Accelerator Facilities”, in *Proc. 9th Int. Particle Accelerator Conf. (IPAC’18)*, Vancouver, Canada, Apr.-May 2018, pp. 878-881. doi:10.18429/JACoW-IPAC2018-TUPAF065
- [5] C. A. Thomas *et al.*, “Commissioning of the Non-invasive Profile Monitors for the ESS LEBT”, in *Proc. 8th Int. Beam Instrumentation Conf. (IBIC’19)*, Malmö, Sweden, Sep. 2019, pp. 495-498. doi:10.18429/JACoW-IBIC2019-WEC004
- [6] C. S. Derrez *et al.*, “Initial Performance of the Beam Instrumentation for the ESS IS & LEBT”, in *Proc. 10th Int. Particle Accelerator Conf. (IPAC’19)*, Melbourne, Australia, May 2019, pp. 2650-2653. doi:10.18429/JACoW-IPAC2019-WEPGW076
- [7] N. Milas *et al.*, “Beam Based Alignment of Elements and Source at the ESS Low Energy Beam Transport Line”, in *Proc. 8th Int. Beam Instrumentation Conf. (IBIC’19)*, Malmö, Sweden, Sep. 2019, pp. 600-604. doi:10.18429/JACoW-IBIC2019-WEP032
- [8] E. Nilsson, M. Eshraqi, J. F. Esteban Müller, Y. Levinsen, N. Milas, and R. Miyamoto, “Beam Dynamics Simulation with an Updated Model for the ESS Ion Source and Low Energy Beam Transport”, in *Proc. 10th Int. Particle Accelerator Conf. (IPAC’19)*, Melbourne, Australia, May 2019, pp. 1042-1045. doi:10.18429/JACoW-IPAC2019-MOPTS083
- [9] R. Miyamoto *et al.*, “Preparation towards the ESS Linac Ion Source and LEBT Beam Commissioning on ESS Site”, in *Proc. 9th Int. Particle Accelerator Conf. (IPAC’18)*, Vancouver, Canada, Apr.-May 2018, pp. 874-877. doi:10.18429/JACoW-IPAC2018-TUPAF064

- [10] Y. Levinsen *et al.*, “European Spallation Source Lattice Design Status”, in *Proc. 6th Int. Particle Accelerator Conf. (IPAC’15)*, Richmond, VA, USA, May 2015, pp. 3911–3914.
- [11] Y. Levinsen, L. Celona, M. Eshraqi, and L. Neri, “In-depth Analysis and Optimization of the European Spallation Source Front End Lattice”, in *Proc. 7th Int. Particle Accelerator Conf. (IPAC’16)*, Busan, Korea, May 2016, pp. 1274–1277. doi:10.18429/JACoW-IPAC2016-TUPMR020
- [12] Ø. Middtun, L. Celona, B. Cheymol, R. Miyamoto, L. Neri, and C. Thomas, “Measurements and Simulations of the Beam Extraction from the ESS Proton Source”, in *Proc. 17th Int. Conf. on Ion Source*, Geneva, Switzerland, Oct. 2017, p. 080022. doi:10.1063/1.5053377
- [13] D. Uriot and N. Pichoff, “Status of TraceWin Code”, in *Proc. 6th Int. Particle Accelerator Conf. (IPAC’15)*, Richmond, VA, USA, May 2015, pp. 92–94. doi:10.18429/JACoW-IPAC2015-MOPWA008
- [14] Ø. Middtun, “Off-site commissioning report for the ESS proton source and LEBT”, ESS Rep. ESS-0190279, 2018.
- [15] K. R. Crandall and D. P. Rusthoi, “TRACE 3-D documentation, third edition”, Los Alamos Rep. LA-UR-90-4146, 1997.
- [16] L. Neri *et al.*, “Beam Commissioning of the High Intensity Proton Source Developed at INFN-LNS for the European Spallation Source”, in *Proc. 8th Int. Particle Accelerator Conf. (IPAC’17)*, Copenhagen, Denmark, May 2017, pp. 2530–2532. doi:10.18429/JACoW-IPAC2017-WE0BB2
- [17] L. Celona *et al.*, “Ion Source and Low Energy Beam Transport Line Final Commissioning Step and Transfer from INFN to ESS”, in *Proc. 9th Int. Particle Accelerator Conf. (IPAC’18)*, Vancouver, Canada, Apr.-May 2018, pp. 1712–1714. doi:10.18429/JACoW-IPAC2018-TUPML073

# BEAM ACCELERATION WITH THE UPGRADED RIKEN HEAVY-ION LINAC

T. Nishi\*, M. Fujimaki, N. Fukunishi, H. Imao, O. Kamigaito, T. Nagatomo,  
 N. Sakamoto, A. Uchiyama, T. Watanabe, Y. Watanabe, K. Yamada  
 RIKEN Nishina Center, Wako, Japan

## Abstract

The performance of the RIKEN heavy-ion linac (RILAC) has been upgraded with a new electron cyclotron resonance ion source and superconducting linac booster (SRILAC). It is expected to have a major role in the synthesis of superheavy elements (SHEs), development of the technologies for production of medical radioisotopes, and as a powerful injector to the RI Beam Factory. Here, we report on the beam delivery for the SHE experiment that began in June 2020, particularly on the adjustment of the optics based on the measured phase ellipse.

## INTRODUCTION

The RIKEN Nishina Center has been conducting experiments to search for new superheavy elements using RIKEN heavy-ion linac (RILAC) [1]. Recently, a new 28-GHz electron cyclotron resonance (ECR) ion source [2] and superconducting linear accelerator (SRILAC) [3] were constructed to increase the beam intensity and beam energy. The low-energy beam-transport (LEBT) system is equipped with slit triplets that control the beam emittance in the RILAC. The beam energy and beam positions are measured using eight sets of capacitive pickups called BEPM (beam energy position monitor) installed in the cold section of the SRILAC [4, 5].

In January 2020, we obtained the first beam from SRILAC. The  $\text{Ar}^{11+}$  with an intensity of  $2 \mu\text{A}$  was accelerated up to  $5 \text{ MeV/u}$  [6]. From July 2020, we began to deliver the high-intensity  $\text{V}^{13+}$  beam with energy of  $6 \text{ MeV/u}$  to the GARIS-III [7] experiment. To transport the high-intensity heavy ion beam to the GARIS-III target with acceptable beam loss, we have established a method of measuring the phase ellipse and adjusting the optics based on the measured phase ellipse and optical simulation. This method enables us to optimize the optics flexibly according to the beam state, which varies depending on the ion source and slit conditions, as well as the experimental requirements.

## HIGH ENERGY BEAM TRANSPORT LINE

The heavy ion beam, accelerated to approximately  $6 \text{ MeV/u}$  in the SRILAC, passes through a differential pumping system [8] and is then transported to GARIS-III through a beam transport called the high-energy beam transfer (HEBT) line (Fig. 1). The inner diameter of this beam transport is  $62 \text{ mm}$ , and its configuration is TQ - TQ - D - SQ - SQ - DQ (TQ = triplet quadrupole, D = dipole, SQ = singlet quadrupole, DQ = doublet quadrupole). D is a  $90^\circ$  bending

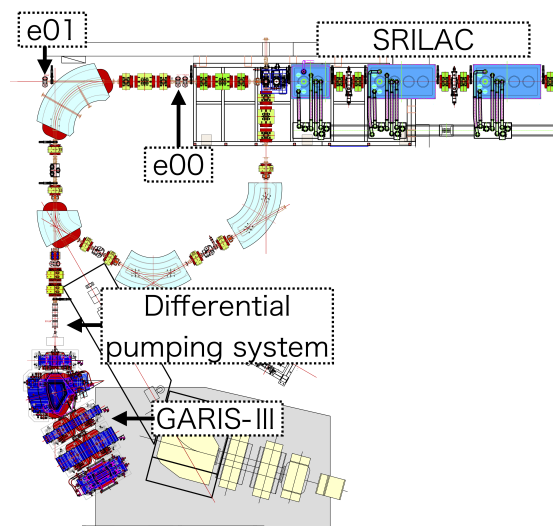


Figure 1: Top view of SRILAC, high-energy beam transfer line, and GARIS-III. A middle point denoted as e00 is considered the object point for optical calculation.

magnet with edges cut at  $25^\circ$  at both ends. Additionally, a bending magnet is placed between SQ and DQ, but it is not excited during the beam transport to GARIS-III. GARIS-III is filled with He gas at  $\approx 70 \text{ Pa}$  during the experiment, while the vacuum of the HEBT line must be maintained at  $10^{-5}$ – $10^{-6} \text{ Pa}$ . Therefore, the inner diameter of the beam pipe immediately before the target is narrowed to  $\phi 25$ – $15 \text{ mm}$ , and the gas is continuously evacuated by a vacuum pump. The requirements for the beam transport of the HEBT line are (A) a beam loss less than a few percent and (B) the adjustability of beam spot shape on the GARIS-III target depending on the experimental conditions. The first requirement is particularly important for maintaining for the radiation safety. Since the side wall of GARIS-III is relatively thin, it is necessary to measure and confirm the radiation while optimizing the beam transport. For the second requirement, a horizontally flatted ellipse is desired in the production run to prevent local depletion of the rotating target, while a large circle shape is desired in the calibration run. To satisfy these requirements, the beam envelope should be narrower immediately before the target, where the acceptance is relatively smaller and wider at the target.

## PHASE ELLIPSE MEASUREMENT AND OPTICS TUNING

In the operations of the upgraded RILAC, the optical system was adjusted in two steps. First, phase ellipse of the beam at e00, defined as the object point in the optical

\* takahiro.nishi@riken.jp

Content from this work may be used under the terms of the CC BY 3.0 licence (© 2021). Any distribution of this work must maintain attribution to the author(s), title of the work, publisher, and DOI

design, was measured using the wire scanner at e00 and e01 (Fig. 1). The phase ellipse at e00 was adjusted to be upright using a triplet quadrupole upstream of e00 based on optical calculation. Second, the optics from the object point to the target of GARIS-III experiment were tuned using optical simulation based on the adjusted phase ellipse at e00 and experimental requirement for beam spot shape. Details of these steps are described below.

### (1) Phase Ellipse Measurement and Adjustment

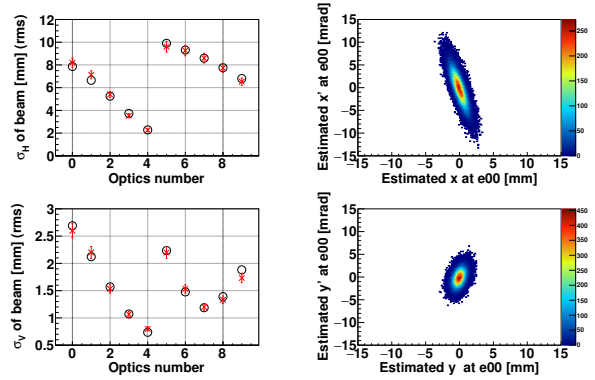
The phase ellipse at the object point was measured using wire scanners and triplet quadrupole magnets in the straight line from e00 to e01 (Fig. 1). The beam widths in horizontal and vertical directions were measured using 10 different settings of quadrupoles inbetween. The phase ellipse at e00 was estimated to reproduce the beam widths in all settings simultaneously. These 10 optical systems were selected to be sensitive to any type of phase ellipses using optical simulation.

The measured phase ellipse was adjusted to be upright using the triplet quadrupole magnets located upstream of e00. Based on the current magnetic field of these magnets and the measured phase ellipse, a new optics was calculated and adopted. Figure 2 shows an example of the estimated phase ellipse at e00 before and after the phase ellipse adjustment. These measurements were performed on an approximately 100 enA  $V^{13+}$  beam accelerated to 6 MeV/u. The graph on the left shows the beam widths (rms) measured at e01 for each optical setting, where the red crosses represent the measured values and the black circles represent the fitted results. The contour plots on the right are the phase ellipses at e00 estimated from the fitted results. Here, the phase ellipse was assumed to have a two-dimensional normal distribution. As shown in the figures, the phase ellipse was tilted before adjustment and became upright after the adjustment as calculated. The measured emittances in these measurements were  $\epsilon_h = 5.73$  and  $\epsilon_v = 3.30$  before the adjustment and  $\epsilon_h = 5.67$  and  $\epsilon_v = 3.27$  after the adjustment (both corresponding to 4 rms, unit is [ $\pi$  mm mrad]), which were in good agreement with each other.

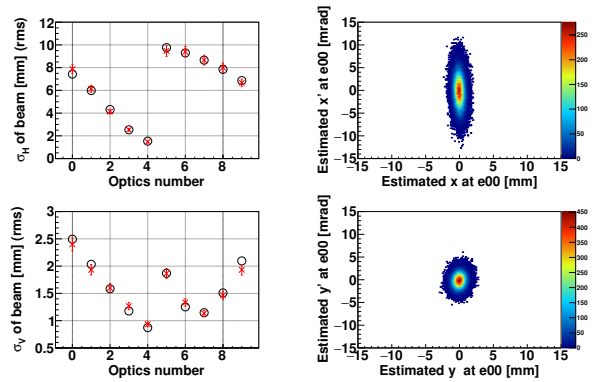
Some of the emittance values measured from January 2020 to July 2021 are summarized in Table 1. The emittance values measured at e00 were approximately 2 to 7 [ $\pi$  mm mrad] for both  $\epsilon_h$  and  $\epsilon_v$ . As shown in the table, the values of emittance varied in each measurement. Therefore, it is important to measure the phase ellipse at each operation of the ion source and accelerator and to optimize the optics to the phase ellipse as in the method used in this study.

The data in 2nd and 3rd rows or 5th and 6th rows correspond to the beam emittance in the series operations before and after acceleration by SRILAC, respectively. These data indicate that the beam emittance reduced by the SRILAC acceleration to almost the expected values.

" $\epsilon$  at upstream" in Table 1 is the emittance measured at the pepperpot placed upstream of the radio frequency quadrupole (RFQ). Considering the energy of the particles here ( $\approx 3$  keV/u), the emittance downstream increased by a



(a) Measured beam widths and estimated phase ellipse before adjustment.



(b) Measured beam widths and estimated phase ellipse after adjustment.

Figure 2: Data of emittance measurement before (a) / after (b) adjustment of phase ellipse at an object point e00.

factor of approximately 1.5 to 6 of the expected value. The detailed cause of this results is currently under analysis.

The measurement of the phase ellipse and upright adjustment of the phase ellipse were almost automated except for the data acquisition by the wire scanners. The phase ellipse measurement required approximately 30 min and the entire procedure to measure and adjust the phase ellipse required 1 hour.

### (2) Optics Tuning to a Target for GARIS-III

After confirming that the phase ellipse was upright at e00, we optimized the optical system from e00 to the GARIS-III target based on the measured phase ellipse. In the basic optical system, the image magnification from e00 to GARIS-III was set to 1.0 in both horizontal and vertical directions. The optics was adjusted to satisfy the required spot shape and acceptable beam loss simultaneously using the optical simulation code GICOSY [9] and Monte Carlo simulation MOCADI [10]. Finally, the optical system was optimized by fine-tuning the steerer and the magnetic field of each magnet based on the viewer on the target, baffles located upstream of the target, and beam current measured using a Faraday cup.

Table 1: Measured Emittance of Heavy-Ion Beams Accelerated by SRILAC

Ion	Energy [MeV/u]	$\epsilon_h$ at e00 [ $\pi$ mm mrad]	$\epsilon_v$ at e00 [ $\pi$ mm mrad]	$\epsilon_h$ at upstream [ $\pi$ mm mrad]	$\epsilon_v$ at upstream [ $\pi$ mm mrad]
Ar <sup>13+</sup>	4	3.6	2.7	—	—
Ar <sup>13+</sup>	4	5.5	2.7	—	—
Ar <sup>13+</sup>	6	3.9	2.3	—	—
Ar <sup>13+</sup>	6	4.0	6.0	34.2	41.2
Ar <sup>13+</sup>	4	4.7	6.8	92.9	83.2
Ar <sup>13+</sup>	6	3.6	4.3	—	—
Ar <sup>13+</sup>	6	3.2	3.2	99.3	63.5
Ar <sup>11+</sup>	5	3.1	6.5	—	—
Ar <sup>11+</sup>	5	2.2	1.6	—	—
V <sup>13+</sup>	6	5.9	4.5	84.1	66.4
V <sup>13+</sup>	6	5.7	3.3	—	—

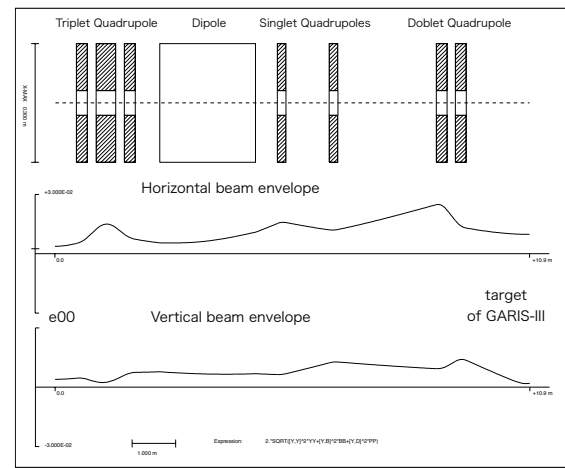
Figure 3 (a) depicts to the optics used for the beam transport with the phase ellipse in Fig. 2 (b). The top row of the figure shows the optical elements after e00 of the HEBT line, and the second and third rows show the beam envelopes in the horizontal and vertical directions, respectively. These images were created using GICOSY. The image magnification was set to 2.5 in the horizontal direction and 0.5 in the vertical direction to realize a horizontal elliptical spot. Figure 3 (b) shows a charge-coupled device (CCD) camera image of the beam spot on the target after the adjustment of the steerer, etc. Although the emittance was almost twice as large in the vertical direction, the beam spot was wide in the horizontal direction as required by adjusting the optical system. In this transportation, the beam loss was suppressed to a few percent. The outdoor radiation level was measured and confirmed to be within the acceptable level.

## REAL-TIME EMITTANCE MEASUREMENT USING THE BEPM

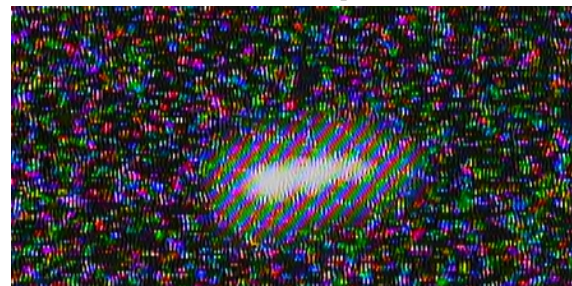
While beam emittance measurement with wire scanners in SRILAC is effective as described above, the method requires the beam current to be reduced to less than 100 enA and the magnetic currents to be changed. To realize more effective optimization of optics in the HEBT line in long-term operations, we require real-time emittance measurement.

We are developing a new method of measuring beam emittance using non-destructive diagnostics: beam energy position monitor (BEPM). Eight BEPMs are installed in-between quadrupole magnets in the SRILAC. The BEPM consists of four electrodes and measures the beam position and time of flight in-between using the induced voltage on the electrodes. Now, we are attempting to utilize the detectors to estimate the beam phase ellipse.

The asymmetry of signal strength of four electrodes reflect the flatness of a beam ellipse [11, 12]. The standard deviation of horizontal and vertical beam position distribution  $\sigma_x$  and



(a) Calculated beam envelope in HEBT line.



(b) Beam spot on target.

Figure 3: (a) Top figure represents optical elements. The middle and bottom figures show the beam envelope in horizontal and vertical directions, respectively. (b) Beam spot captured using a CCD camera on a viewer at the GARIS-III target. The beam spot was horizontally flatted ellipse as expected.

$\sigma_y$  can be related to the BEPM signals as

$$Q \equiv \sigma_x^2 - \sigma_y^2 = kq \frac{V_L + V_R - V_U - V_D}{V_L + V_R + V_U + V_D} - \langle x \rangle^2 + \langle y \rangle^2, \quad (1)$$

where  $V_L$ ,  $V_R$ ,  $V_U$ , and  $V_D$  are the induced voltages of left, right, up, and down electrodes, respectively, and  $k_q$  is a con-

stant number measured previously. This value of  $Q$  is measured in each BEPM position, and it can be also calculated using components of sigma matrix and transfer matrices as

$$\begin{pmatrix} Q_1 \\ Q_2 \\ \vdots \\ Q_8 \end{pmatrix} = (\mathbf{H}, \mathbf{V}) \begin{pmatrix} \sigma_{xx}(0) \\ \sigma_{xa}(0) \\ \sigma_{aa}(0) \\ \sigma_{yy}(0) \\ \sigma_{yb}(0) \\ \sigma_{bb}(0) \end{pmatrix}, \quad (2)$$

where

$$\mathbf{H} \equiv \begin{pmatrix} (M_{11}^{01})^2, 2M_{11}^{01}M_{12}^{01}, (M_{12}^{01})^2 \\ \vdots \\ (M_{11}^{08})^2, 2M_{11}^{08}M_{12}^{08}, (M_{12}^{08})^2 \\ \vdots \\ -(M_{33}^{01})^2, -2M_{33}^{01}M_{34}^{01}, -(M_{34}^{01})^2 \\ \vdots \\ -(M_{33}^{08})^2, -2M_{33}^{08}M_{34}^{08}, -(M_{34}^{08})^2 \end{pmatrix},$$

$$\mathbf{V} \equiv \begin{pmatrix} \vdots \\ \vdots \end{pmatrix}.$$

In these equations,  $\sigma(0)$  indicates the elements of the sigma matrix of the beam at the upstream position denoted as 0, and  $M_{ij}^{0n}$  is the  $(i, j)$ -th element of transfer matrix from position 0 to the position of the  $n$ -th BEPM.

Figure 4 shows  $Q_8$  measured using the most downstream BEPM and the estimated  $Q_8$ , which is calculated based on the calculated transfer matrices and sigma matrix obtained using wire scanner measurements. As shown in the figure, the two values have a clear positive correlation. We will investigate the origin of the offset and attempt to reconstruct beam emittance by combining  $Q_1 - Q_8$ .

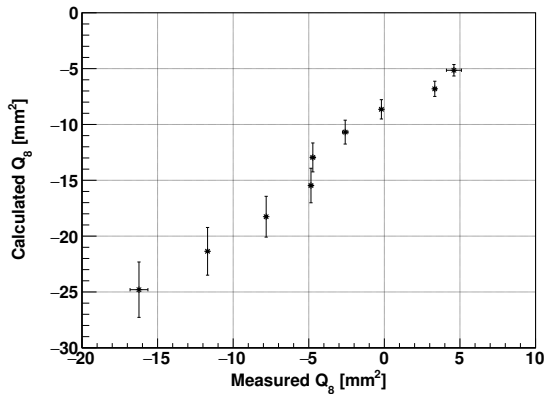


Figure 4: Comparison of the  $Q_8$  measured using the most downstream BEPM and the estimated  $Q_8$ , which is calculated based on the calculated transfer matrices and sigma matrix obtained using wire scanner measurements. The sigma matrix at position 0 is calculated with the phase ellipse at e00 and transfer matrix in between.

## CONCLUSION

The performance of the RIKEN heavy-ion linac (RILAC) has been upgraded with a new ECR ion source and superconducting linac booster (SRILAC). We obtained the first beam in January 2020 and began to supply the  $V^{13+}$  beam to the experiment for the synthesis of super-heavy elements. In

the operation, we established the beam transport adjustment method and realized small beam loss and required beam spot shape simultaneously using wire scanners and simulation code. A new method to estimate the phase ellipse with non-destructive detector BEPMs is under development for the real-time measurement and optimization of the beam transport.

## REFERENCES

- [1] K. Morita *et al.*, “New result in the production and decay of an isotope,  $^{278}113$ , of the 113th element”, *J. Phys. Soc. Jpn.*, vol. 81, p. 103201, 2012. doi:10.1143/JPSJ.81.103201
- [2] T. Nagatomo *et al.*, “High intensity vanadium beam for synthesis of new superheavy elements with well-controlled emittance by using slit triplet”, *Rev. Sci. Instrum.*, vol. 91, p. 023318, 2020. doi:10.1063/1.5130431
- [3] N. Sakamoto *et al.*, “Development of Superconducting Quarter-Wave Resonator and Cryomodule for Low-Beta Ion Accelerators at RIKEN Radioactive Isotope Beam Factory”, in *Proc. SRF2019*, Dresden, Germany, 2019, pp. 750–757. doi:10.18429/JACoW-SRF2019-WETEB1
- [4] T. Watanabe *et al.*, “Calibration for Beam Energy Position Monitor System for Riken Superconducting Acceleration Cavity”, in *Proc. IBIC2019*, Malmö, Sweden, 2019, pp. 526-529. doi:10.18429/JACoW-IBIC2019-WEPP007
- [5] T. Watanabe *et al.*, “Commissioning of the beam energy position monitoring system for the superconducting RIKEN heavy-ion linac”, in *Proc. IBIC2020*, Santos, Brazil, pp. 295-302. doi:10.18429/JACoW-IBIC2020-FRA004
- [6] K. Yamada *et al.*, “Construction of Superconducting Linac Booster for Heavy-Ion Linac at RIKEN Nishina Center”, in *Proc. SRF2019*, Dresden, Germany, 2019, pp. 502-507. doi:10.18429/JACoW-SRF2019-TUP037
- [7] H. Haba and for RIKEN SHE Collaboration, “Present Status and Perspectives of SHE Researches at RIKEN”, in *Proc. EXON-2018*, Petrozavodsk, Russia, 2019, 192-199. doi:10.1142/9789811209451\_0027
- [8] H. Imao *et al.*, “Non-Evaporative Getter-Based Differential Pumping System for SRILAC at RIBF”, in *Proc. SRF2019*, Dresden, Germany, 2019, p. 419–423. doi:10.18429/JACoW-SRF2019-TUP013
- [9] “GICOSY” on web page: <https://web-docs.gsi.de/~weick/gicosy/>
- [10] N. Iwasa, H. Geissel, G. Münzenberg, C. Scheidenberger, T. Schwab, and H. Wollnik, “MOCADI, a universal Monte Carlo code for the transport of heavy ions through matter within ion-optical systems”, *Nucl. Instrum. Methods Phys. Res., Sect. B*, vol. 126, pp. 284-289, 1997. doi:10.1016/S0168-583X(97)01097-5
- [11] R. H. Miller, J. E. Clendenin, M. B. James, and J. C. Shepard, “Nonintercepting emittance monitor”, in *Proc. HEAC’83*, Fermilab, IL, USA, 1983, pp. 602-605. <http://slac.stanford.edu/pubs/slacpubs/3000/slac-pub-3186.pdf>
- [12] T. Suwada, “Multipole Analysis of Electromagnetic Field Generated by Single-Bunch Electron Beams”, *Jpn. J. Appl. Phys.*, vol. 40, pp. 890-897, Jan. 2001.

## List of Authors

**Bold** papercodes indicate primary authors; ~~crossed-out~~ papercodes indicate 'no submission'

### — A —

Abell, D.T. MOP25  
 Ainsworth, R. MOP22  
 Akagi, T. WEDC2  
 Albright, S.C.P. MOP06, MOP18, MOP19  
 Alexahin, Y.I. MOP21, MOP24  
 Ambrosio, G. MOCC2  
 Amorim, D. TUAC3  
 Antipov, S.A. TUAC3  
 Antoniazzi, L. WEDC2  
 Antoniou, F. MOP06, MOP14, MOP18,  
 MOP19  
 Arakaki, Y. THDC1  
 Argyropoulos, T. MOP16  
 Asvesta, F. MOP06, MOP14, MOP18,  
 MOP19, MOP20  
 Avati, V. MOCC3

### — B —

Bartosik, H. MOP06, MOP12, MOP14,  
 MOP18, MOP19, TUAC2  
 Baumann, P. MOCC4  
 Bazzani, A. MOP08  
 Bellan, L. WEDC2  
 Belmans, J. WEBC3  
 Ben Abdillah, Dr. WEBC3  
 Bhat, C.M. MOP02, MOP23  
 Biancacci, N. TUAC3  
 Blokland, W. FRPS5  
 Boine-Frankenheim, O. WEIPI2, TUAC1  
 Bolzon, B. WEDC2  
 Bouly, F. WEBC3  
 Boussa, S. WEBC3  
 Bracco, C. MOP06, MOP18, MOP19  
 Broemmelsiek, D.R. TUEC1  
 Bruce, R. MOCC3, MOP09  
 Bruchon, N. TUEC4  
 Bruhwiler, D.L. MOP25  
 Buffat, X. MOP07, TUAC3  
 Burov, A.V. MOP22, MOP24  
 Butcher, M.E.J. MOCC3

### — C —

Capoani, F. MOP08  
 Cara, P. WEDC2  
 Carin, Y. WEDC2  
 Carlà, M. MOP12  
 Carlson, K. TUEC1  
 Carneiro, J.-P. MOP03  
 Carver, L.R. MOP12  
 Casagrande, F. WEDC3  
 Chattopadhyay, S. TUEC1  
 Chaurize, S. MOP02  
 Chauvin, N. WEDC2

Chen, Q. WEIPI1  
 Chen, W.L. WEIPI1  
 Chen, Y.X. WEIPI1  
 Cheon, Y.L. THAC2, THBC2  
 Chung, M. THAC2, THBC2, FRPS3  
 Coleman, S.J. MOP25  
 Comblin, J.F. MOP14  
 Comunian, M. WEDC2, FRPS4  
 Cousineau, S.M. FRPS4

### — D —

Dadiani, E. MOP10  
 Damerau, H. MOP11, MOP15, MOP17  
 D'Andrea, M. MOCC3  
 Davin, F. WEBC3  
 De Cock, W. WEBC3  
 De florio, V.R.A. WEBC3  
 De Maria, R. MOP09  
 Deile, M. MOCC3  
 Derrez, C.S. THDC2  
 Derwent, P. MOP02  
 Di Castro, M. MOCC3  
 Di Giovanni, G.P. MOP06, MOP14, MOP18,  
 MOP19  
 Dick, A.J. TUEC1  
 Domeier, M.W. MOP02  
 Donegani, E.M. THDC2  
 Dou, W.P. WEIPI1  
 Doucet, F. WEBC3  
 Duperrex, P.-A. MOCC4  
 Dziejczak, B.S. MOCC3  
 Dzitko, H. WEDC2

### — E —

Eddy, N. MOP22, MOP23  
 Edstrom, D.R. TUEC1  
 El Baz, M. MOP03  
 Eldred, J.S. MOIPI2, FRPS1  
 Eshraqi, M. THDC2  
 Evans, N.J. MOAC3, TUEC2

### — F —

Fagotti, E. WEDC2  
 Fedotov, A.V. MOAC2  
 Feng, C. WEIPI1  
 Ferdinand, R. WEBC4  
 Fischer, W. FRPS1  
 Flowerdew, J.A.D. THAC3  
 Fomin, A.S. MOP26  
 Forck, P. FRPS5  
 Franck, D. TUEC1  
 Froidefond, E. WEBC3  
 Fujimaki, M. THBC1  
 Fukunishi, N. THBC1  
 Fukushima, K. WEDC3

Content from this work may be used under the terms of the CC BY 3.0 licence (© 2021). Any distribution of this work must maintain attribution to the author(s), title of the work, publisher, and DOI

Furuseth, S.V.	MOP07	Kamigaito, O.	THBC1
<b>— G —</b>		Kanemura, T.	WEDC3
Galambos, J.	TUIPI1	Karpov, I.	MOP11, MOP15, MOP16
Gålander, B.	THDC2	Kašpar, J.	MOCC3
Gao, Z.	WEIPI1	Kayran, D.	MOAC2
Garcia Morales, H.	MOCC3	Kelliher, D.J.	THAC3
Gatera, A.	WEBC3	Kettle, P.R.	MOCC4
Gavrikov, Yu.A.	MOCC3	Kikoła, D.	MOP26
Giacchini, M.G.	WEDC2	Kim, S.H.	WEDC3
Giovanozzi, M.	MOP08, MOP09	Kimura, T.	THDC1
Gorlov, T.V.	MOAC3	Kinsho, M.	MOIPI1
Grespan, F.	WEDC2	Kiselev, D.C.	MOCC4
Grzelak, V.M.	MOP02	Kobayashi, A.	THAC1
<b>— H —</b>		Kondo, K.	WEDC2
Haj Tahar, M.	MOCC4	Kondo, Y.	MOP04
Hanna, B.M.	MOP03	Korcyl, K.M.	MOCC3
Harada, H.	MOIPI1	Kostoglou, S.	TUAC2
Hassanzadegan, H.	THDC2	<b>— L —</b>	
Hayashi, N.	MOIPI1, FRPS5	Laface, E.	THDC2
He, Y.	WEIPI1, FRPS2	Lagniel, J.-M.	WEBC4
He, Y.C.	MOP27	Lamas Garcia, I.	MOCC3
Hermes, P.D.	MOP09	Lasheen, A.	MOP13, MOP17
Hiller, K.H.	MOCC3	Latina, A.	MOP21
Hirlander, S.	TUEC4	Laube, D.	MOCC4
Hofmann, I.	TUAC1, FRCLS1	Laut, A.J.	MOP13
Holmes, J.A.	MOAC3	Lebedev, V.A.	MOAC1, TUEC1
Hoover, A.M.	MOAC3	Levinsen, Y.	THDC2
Hostettler, M.	MOP14	Li, J.Y.	MOP01
Hotchi, H.	MOIPI1	Li, K.S.B.	MOP12
Hu, T.	MOP01	Lidia, S.M.	WEDC3
Huang, G.	WEIPI1	Liu, S.H.	WEIPI1
Huang, M.Y.	WEDC1	Lobach, I.	TUEC1
Hulsart, R.L.	TUEC3	<b>— M —</b>	
Huschauer, A.	MOP14	Machicoane, G.	WEDC3
<b>— I —</b>		Machida, S.	THAC3
Igarashi, S.	FRPS4	Maclean, E.H.	MOP06, MOP18
Ikegami, M.	WEDC3	Madysa, N.	TUEC4
Iliakis, K.	MOP17	Maekawa, F.	MOP04
Imao, H.	THBC1	Marroncle, J.	WEDC2
Intelisano, L.	MOP15	Maruta, T.	WEDC3
<b>— J —</b>		Masi, A.	MOCC3
Jakobsen, S.	MOCC3	Masuda, K.	WEDC2
Jang, J.-H.	THAC2	Meigo, S.I.	MOP04
Jarvis, J.D.	TUEC1	Mereghetti, A.	MOCC3, MOP09
Jeon, D.	THAC2, THBC2	Métral, E.	MOP10, MOP12, TUAC3, FRPS1, FRCLS1
Jia, H.	WEIPI1	Mikulec, B.	MOP06, MOP14, MOP18, MOP19
Jiang, T.C.	WEIPI1	Milas, N.	THDC2
Jimenez-Rey, D.	WEDC2	Minty, M.G.	FRPS5
Jin, D.P.	MOP27	Mirarchi, D.	MOCC3, MOP09, MOP26
Jollet, S.	MOCC4	Miyamoto, R.	TUIPI2, THDC2
Joly, C.	WEBC3	Montis, M.	WEDC2
Joray, S.	MOCC4	Moon, S.H.	THBC2
<b>— K —</b>		Morris, D.G.	WEDC3
Kain, V.	TUEC4	Mounet, N.	MOP10, TUAC3

Moya, I. **WEDC2**  
 Muñoz, M. **THDC2**  
 Murasugj, S. **THDC1**  
 Muto, R. **THDC1**

— N —

Nagaitsev, S. **TUEC1**  
 Nagatomo, T. **THBC1**  
 Nakamura, T. **THAC1**  
 Nash, B. **MOP25**  
 Nese, S. **MOP16**  
 Nilsson, E. **THDC2**  
 Nishi, T. **THBC1**  
 Nishiguchi, H. **THDC1**  
 Noguchi, K. **THDC1**  
 Nonglaton, J.-M. **MOP14**  
 Normand, G. **WEBC4**

— O —

Obrycki, O. **TUEC1**  
 Oeftiger, A. **TUAC1, TUAC3**  
 Okabe, K. **MOIPI1**  
 Okada, M. **THAC1**  
 Okamura, K. **THDC1**  
 Okuno, H. **MOCC1**  
 Orduz, A.K. **WEBC4**  
 Ostroumov, P.N. **WEDC3, FRPS2**

— P —

Palmieri, A. **WEDC2**  
 Papa, A. **MOCC4**  
 Papaphilippou, Y. **TUAC2**  
 Papotti, G. **MOP11**  
 Perez, L. **WEBC3**  
 Patecki, M. **MOP26**  
 Pellico, W. **MOP02**  
 Perrot, L. **WEBC3**  
 Peters, C.C. **WEDC4**  
 Piekarz, H. **TUEC1**  
 Piot, P. **TUEC1**  
 Pisent, A. **WEDC2**  
 Plaçais, A. **WEBC3**  
 Plastun, A.S. **WEDC3**  
 Plostinar, D.C. **THDC2, FRPS2**  
 Podadera, I. **WEDC2**  
 Podlech, H. **WEBC3**  
 Poggi, M. **WEDC2**  
 Pogorelov, I.V. **MOP25**  
 Pompon, F. **WEBC3**  
 Ponton, A. **WEBC3**  
 Popielarski, J.T. **WEDC3**  
 Prebibaj, T. **MOP06, MOP14, MOP18, MOP19**

— Q —

Qiang, J. **WEBC1**  
 Quartullo, D. **MOP11**

— R —

Rahemtulla, A. **MOP10**  
 Raparia, D. **WEBC2**  
 Redaelli, S. **MOCC3, MOP09, MOP26, THIPI1**  
 Reggiani, D. **MOCC4**  
 Reid, J. **MOP02**  
 Renner, E. **MOP06, MOP18, MOP19**  
 Renshall, H. **MOP21**  
 Romanov, A.L. **TUEC1**  
 Rostomyan, T. **MOCC4**  
 Ruan, J. **TUEC1**  
 Rumolo, G. **MOP12**

— S —

Saewert, G.W. **MOP05**  
 Saha, P.K. **MOIPI1**  
 Saini, A. **MOP05**  
 Sakamoto, N. **THBC1**  
 Salvachua, B. **MOCC3**  
 Salvant, B. **MOP12**  
 Santucci, J.K. **TUEC1**  
 Scantamburlo, F. **WEDC2**  
 Schenk, M. **MOP12**  
 Schmidt, F. **MOP20, MOP21**  
 Schupbach, B.A. **MOP02**  
 Schwendimann, P. **MOCC4**  
 Seletskiy, S. **MOAC2**  
 Semenov, A. **MOP22**  
 Serrano Galvez, P. **MOCC3**  
 Shaposhnikova, E.N. **MOP11, MOP16**  
 Sheehy, S.L. **THAC3**  
 Shemyakin, A.V. **MOP05**  
 Shiltsev, V.D. **MOP24**  
 Shirakabe, Y. **THDC1**  
 Shishlo, A.P. **WEDC4**  
 Shobuda, Y. **MOIPI1, THAC1**  
 Skowroński, P.K. **TUEC4**  
 Sobbia, R. **MOCC4**  
 Solfaroli Camillocci, M. **MOCC3**  
 Sosa, A.G. **THDC2**  
 Stancari, G. **MOP09, TUEC1**  
 Sterbini, G. **TUAC2**  
 Stern, E.G. **MOP24**  
 Sugimoto, M. **WEDC2**  
 Sugiyama, Y. **THDC1**

— T —

Talanov, V. **MOCC4**  
 Tamura, F. **MOIPI1, THDC1**  
 Tamura, J. **MOP04, WEBC3**  
 Tan, C.-Y. **MOP02, FRPS3**  
 Tarkeshian, R. **THDC2**  
 Thomas, C.A. **THDC2**  
 Tobiyama, M. **THAC1**  
 Tomizawa, M. **THDC1**  
 Toyama, T. **THAC1**

Content from this work may be used under the terms of the CC BY 3.0 licence (© 2021). Any distribution of this work must maintain attribution to the author(s), title of the work, publisher, and DOI

Triplett, A.K.	<b>MOP02</b>
Turini, N.	<b>MOCC3</b>
<b>— U —</b>	
Uchiyama, A.	<b>THBC1</b>
Uriot, D.U.	<b>WEBC4</b>
<b>— V —</b>	
Valentino, G.	<b>TUEC4</b>
Valishev, A.	<b>TUEC1</b>
Valuch, D.	<b>TUAC3</b>
Vandeplassche, D.	<b>WEBC3</b>
Velotti, F.M.	<b>MOP19</b>
Verhagen, E.	<b>WEBC3</b>
Vicentini, G.	<b>MOP07</b>
Vojskovic, I.	<b>TUEC4</b>
<b>— W —</b>	
Wang, L.	<b>MOP27</b>
Wang, S.	<b>WEDC1, FRPS4</b>
Wang, Z.J.	<b>WEIPI1</b>
Watanabe, T.	<b>THBC1</b>
Watanabe, Y.	<b>THBC1</b>
Wei, J.	<b>WEDC3</b>
Willeke, F.J.	<b>THIPI2</b>
Wollmann, D.	<b>FRPS3</b>
Wu, X.	<b>MOP27</b>
<b>— X —</b>	
Xu, H.G.	<b>MOP01</b>
Xu, S.Y.	<b>WEDC1</b>

Xu, T.	<b>WEDC3</b>
Xue, K.	<b>MOP27</b>
<b>— Y —</b>	
Yamada, K.	<b>THBC1</b>
Yamamoto, K.	<b>MOIPI1</b>
Yamamoto, M.	<b>MOIPI1</b>
Yanaoka, E.	<b>THDC1</b>
Yang, F.	<b>WEIPI1</b>
Yang, J.	<b>MOP01</b>
Yee-Rendón, B.	<b>MOP04</b>
Yoshii, M.	<b>THDC1</b>
Yoshimoto, M.	<b>MOIPI1</b>
<b>— Z —</b>	
Zannini, C.	<b>MOP10, MOP12</b>
Zeng, B.Q.	<b>MOP01</b>
Zhang, C.	<b>WEBC3</b>
Zhang, H.	<b>MOP25</b>
Zhang, S.H.	<b>WEIPI1</b>
Zhang, T.	<b>WEDC3</b>
Zhang, Y.L.	<b>MOP27</b>
Zhao, H.	<b>MOAC2</b>
Zhao, H.W.	<b>WEIPI1</b>
Zhao, Q.	<b>WEDC3</b>
Zhao, S.	<b>WEDC3</b>
Zhu, P.	<b>MOP27</b>
Zisou, C.	<b>MOP11</b>

## Institutes List

### BNL

Upton, New York, USA

- Fedotov, A.V.
- Fischer, W.
- Hulsart, R.L.
- Kayran, D.
- Minty, M.G.
- Raparia, D.
- Seletskiy, S.
- Willeke, F.J.
- Zhao, H.

### Bologna University

Bologna, Italy

- Bazzani, A.

### CEA-DRF-IRFU

France

- Marroncle, J.
- Uriot, D.U.

### CEA-IRFU

Gif-sur-Yvette, France

- Bolzon, B.
- Chauvin, N.

### CERN

Meyrin, Switzerland

- Albright, S.C.P.
- Antoniou, F.
- Argyropoulos, T.
- Avesta, F.
- Avati, V.
- Bartosik, H.
- Biancacci, N.
- Bracco, C.
- Bruce, R.
- Buffat, X.
- Butcher, M.E.J.
- Capoani, F.
- Carlà, M.
- Comblin, J.F.
- D'Andrea, M.
- Dadiani, E.
- Damerau, H.
- De Maria, R.
- Deile, M.
- Di Castro, M.
- Di Giovanni, G.P.
- Fomin, A.S.
- Furuseh, S.V.
- Garcia Morales, H.
- Giovannozzi, M.
- Hermes, P.D.
- Hostettler, M.
- Huschauer, A.
- Iliakis, K.
- Intelisano, L.
- Jakobsen, S.
- Kain, V.

- Karpov, I.
- Kašpar, J.
- Kostoglou, S.
- Lamas Garcia, I.
- Lasheen, A.
- Latina, A.
- Laut, A.J.
- Li, K.S.B.
- Maclean, E.H.
- Madysa, N.
- Masi, A.
- Mereghetti, A.
- Mikulec, B.
- Mirarchi, D.
- Mounet, N.
- Métral, E.
- Nonglaton, J.-M.
- Papaphilippou, Y.
- Papotti, G.
- Prebibaj, T.
- Quartullo, D.
- Redaelli, S.
- Renner, E.
- Renshall, H.
- Rumolo, G.
- Salvachua, B.
- Salvant, B.
- Schmidt, F.
- Serrano Galvez, P.
- Shaposhnikova, E.N.
- Skowroński, P.K.
- Solfaroli Camillocci, M.
- Sterbini, G.
- Valuch, D.
- Velotti, F.M.
- Vicentini, G.
- Vojskovic, I.
- Wollmann, D.
- Zannini, C.
- Zisou, C.

### CIEMAT

Madrid, Spain

- Jimenez-Rey, D.
- Podadera, I.

### DESY

Hamburg, Germany

- Antipov, S.A.

### DESY Zeuthen

Zeuthen, Germany

- Hiller, K.H.

### EPFL

Lausanne, Switzerland

- Furuseh, S.V.
- Rahemtulla, A.
- Schenk, M.

## ESRF

Grenoble, France

- Carver, L.R.

## ESS

Lund, Sweden

- Derrez, C.S.
- Donegani, E.M.
- Eshraqi, M.
- Gålander, B.
- Hassanzadegan, H.
- Laface, E.
- Levinsen, Y.
- Milas, N.
- Miyamoto, R.
- Muñoz, M.
- Nilsson, E.
- Plostinar, D.C.
- Sosa, A.G.
- Tarkeshian, R.
- Thomas, C.A.

## F4E

Germany

- Carin, Y.
- Dzitko, H.

## Fermilab

Batavia, Illinois, USA

- Ainsworth, R.
- Alexahin, Y.I.
- Ambrosio, G.
- Bhat, C.M.
- Broemmelsiek, D.R.
- Burov, A.V.
- Carlson, K.
- Carneiro, J.-P.
- Chaurize, S.
- Derwent, P.
- Domeier, M.W.
- Eddy, N.
- Edstrom, D.R.
- Eldred, J.S.
- Franck, D.
- Grzelak, V.M.
- Hanna, B.M.
- Jarvis, J.D.
- Lebedev, V.A.
- Nagaitsev, S.
- Obrycki, O.
- Pellico, W.
- Piekarz, H.
- Reid, J.
- Romanov, A.L.
- Ruan, J.
- Saewert, G.W.
- Saini, A.
- Santucci, J.K.
- Schupbach, B.A.
- Semenov, A.
- Shemyakin, A.V.
- Shiltsev, V.D.

- Stancari, G.
- Stern, E.G.
- Tan, C.-Y.
- Triplett, A.K.
- Valishev, A.

## FRIB

East Lansing, Michigan, USA

- Casagrande, F.
- Fukushima, K.
- Ikegami, M.
- Kanemura, T.
- Kim, S.H.
- Lidia, S.M.
- Machicoane, G.
- Maruta, T.
- Morris, D.G.
- Ostroumov, P.N.
- Plastun, A.S.
- Popielarski, J.T.
- Wei, J.
- Xu, T.
- Zhang, T.
- Zhao, Q.
- Zhao, S.

## Fusion for Energy

Garching, Germany

- Moya, I.

## GANIL

Caen, France

- Ferdinand, R.
- Lagniel, J.-M.
- Normand, G.
- Orduz, A.K.

## GS1

Darmstadt, Germany

- Boine-Frankenheim, O.
- Forck, P.
- Hofmann, I.
- Oeftiger, A.
- Zhang, C.

## HUST

Wuhan, People's Republic of China

- Hu, T.
- Li, J.Y.
- Yang, J.
- Zeng, B.Q.

## IAP

Frankfurt am Main, Germany

- Podlech, H.
- Prebibaj, T.

## IBS

Daejeon, Republic of Korea

- Jang, J.-H.
- Jeon, D.

## IFJ-PAN

Kraków, Poland

- Dzedzic, B.S.
- Korcyl, K.M.

### IFMIF/EVEDA

Rokkasho, Japan

- Cara, P.
- Scantamburlo, F.

### IHEP

Beijing, People's Republic of China

- He, Y.C.
- Huang, M.Y.
- Jin, D.P.
- Wang, S.
- Xu, S.Y.
- Zhang, Y.L.
- Zhu, P.

### IHEP CSNS

Guangdong Province, People's Republic of China

- Wang, L.
- Wu, X.
- Xue, K.

### IMP/CAS

Lanzhou, People's Republic of China

- Chen, Q.
- Chen, W.L.
- Chen, Y.X.
- Dou, W.P.
- Feng, C.
- Gao, Z.
- He, Y.
- Huang, G.
- Jia, H.
- Jiang, T.C.
- Liu, S.H.
- Wang, Z.J.
- Yang, F.
- Zhang, S.H.
- Zhao, H.W.

### INFN-Pisa

Pisa, Italy

- Papa, A.

### INFN/LNL

Legnaro (PD), Italy

- Antoniazzi, L.
- Bellan, L.
- Comunian, M.
- Fagotti, E.
- Giacchini, M.G.
- Grespan, F.
- Montis, M.
- Palmieri, A.
- Pisent, A.
- Poggi, M.

### JAEA/J-PARC

Tokai-mura, Japan

- Harada, H.
- Hayashi, N.
- Kinsho, M.
- Kondo, Y.
- Maekawa, F.

- Meigo, S.I.
- Okabe, K.
- Saha, P.K.
- Shobuda, Y.
- Tamura, F.
- Tamura, J.
- Yamamoto, K.
- Yamamoto, M.
- Yee-Rendón, B.
- Yoshimoto, M.

### JLab

Newport News, Virginia, USA

- Zhang, H.

### KEK

Ibaraki, Japan

- Arakaki, Y.
- Hotchi, H.
- Igarashi, S.
- Kimura, T.
- Kobayashi, A.
- Murasugi, S.
- Muto, R.
- Nakamura, T.
- Nishiguchi, H.
- Okada, M.
- Okamura, K.
- Shirakabe, Y.
- Sugiyama, Y.
- Tobiyama, M.
- Tomizawa, M.
- Toyama, T.
- Yanaoka, E.
- Yoshii, M.

### Kyushu University

Fukuoka, Japan

- Noguchi, K.

### LBNL

Berkeley, California, USA

- Qiang, J.

### LPSC

Grenoble Cedex, France

- Bouly, F.
- Froidefond, E.
- Plaçais, A.

### Northern Illinois University

DeKalb, Illinois, USA

- Chattopadhyay, S.
- Dick, A.J.
- Piot, P.

### ORNL

Oak Ridge, Tennessee, USA

- Blokland, W.
- Cousineau, S.M.
- Galambos, J.
- Gorlov, T.V.
- Holmes, J.A.
- Shishlo, A.P.

64<sup>th</sup> ICFA ABDW on High-Intensity and High-Brightness Hadron Beams HB2021, Batavia, IL, USA JACoW Publishing  
 ISBN: 978-3-95450-225-7 ISSN: 2673-5571

Content from this work may be used under the terms of the CC BY 3.0 licence (© 2021). Any distribution of this work must maintain attribution to the author(s), title of the work, publisher, and DOI

**ORNL RAD**  
 Oak Ridge, Tennessee, USA

- Evans, N.J.
- Peters, C.C.

**PNPI**  
 Gatchina, Leningrad District, Russia

- Gavrikov, Yu.A.

**PSI**  
 Villigen PSI, Switzerland

- Baumann, P.
- Duperrex, P.-A.
- Haj Tahar, M.
- Jollet, S.
- Joray, S.
- Kettle, P.R.
- Kiselev, D.C.
- Laube, D.
- Papa, A.
- Reggiani, D.
- Rostomyan, T.
- Schwendimann, P.
- Sobbia, R.
- Talanov, V.

**QST**  
 Aomori, Japan

- Akagi, T.
- Kondo, K.
- Masuda, K.
- Sugimoto, M.

**RadiaSoft LLC**  
 Boulder, Colorado, USA

- Abell, D.T.
- Bruhwiler, D.L.
- Coleman, S.J.
- Nash, B.
- Pogorelov, I.V.

**RIKEN Nishina Center**  
 Wako, Japan

- Fujimaki, M.
- Fukunishi, N.
- Imao, H.
- Kamigaito, O.
- Nagatomo, T.
- Nishi, T.
- Okuno, H.
- Sakamoto, N.
- Uchiyama, A.
- Watanabe, T.
- Watanabe, Y.
- Yamada, K.

**Sapienza University of Rome**  
 Rome, Italy

- Quartullo, D.

**SCK•CEN**  
 Mol, Belgium

- Belmans, J.

- Boussa, S.
- Davin, F.
- De Cock, W.
- De florio, V.R.A.
- Doucet, F.
- Gatera, A.
- Perez, L.
- Pompon, F.
- Ponton, A.
- Vandeplasseche, D.
- Verhagen, E.

**SINR**  
 Jiading, Shanghai, People's Republic of China

- Xu, H.G.

**SOLEIL**  
 Gif-sur-Yvette, France

- Amorim, D.

**STFC/RAL/ASTeC**  
 Chilton, Didcot, Oxon, United Kingdom

- Kelliher, D.J.
- Machida, S.
- Sheehy, S.L.

**TEMF, TU Darmstadt**  
 Darmstadt, Germany

- Boine-Frankenheim, O.

**UNISI**  
 Siena, Italy

- Turini, N.

**UNIST**  
 Ulsan, Republic of Korea

- Cheon, Y.L.
- Chung, M.
- Moon, S.H.

**University of Bergen**  
 Bergen, Norway

- Nese, S.

**University of Chicago**  
 Chicago, Illinois, USA

- Lobach, I.

**University of Malta, Information and Communication Technology**  
 Msida, Malta

- Hirlander, S.
- Valentino, G.

**University of Oxford**  
 Oxford, United Kingdom

- Flowerdew, J.A.D.

**University of Trieste**  
 Trieste, Italy

- Bruchon, N.

**Université Paris-Saclay, CNRS/IN2P3, IJCLab**  
 Orsay, France

- Ben Abdillah, Dr.
- El Baz, M.
- Joly, C.
- Perrot, L.

**UTK**

Knoxville, Tennessee, USA

- Hoover, A.M.

**Warsaw University of Technology**

Warsaw, Poland

- Kikoła, D.
- Patecki, M.